THE EVOLUTION OF APATITE IN IRON-OXIDE-COPPER-GOLD MINERALIZATION OF THE OLYMPIC CU-AU PROVINCE: UNRAVELING MAGMATIC AND HYDROTHERMAL HISTORIES THROUGH CHANGES IN MORPHOLOGY AND TRACE ELEMENT CHEMISTRY

SASHA KRNETA

This thesis is submitted for the degree of Doctor of Philosophy

in the

School of Physical Sciences, Department of Earth Sciences,

at

The University of Adelaide

THE UNIVERSITY of ADELAIDE

November 2017

TABLE OF CONTENTS

ABSTRACT

Iron-oxide-copper-gold (IOCG) mineralization is expressed in various forms across some 700 km of the eastern Gawler Craton throughout the N-S striking Olympic Cu-Au Province. In all instances, IOCG mineralisation and the rocks that host it contain variable concentrations of apatite with varying morphological and chemical characteristics. A large body of work has demonstrated apatite's ability to chemically reflect the physiochemical conditions under which it formed and act as tracers of magmatic and hydrothermal processes. This is confirmed throughout the IOCG deposits and prospects studies as part of this work.

Magmatic apatite hosted within the Roxby Downs Granite, the dominant host to the Olympic Dam deposit displays characteristics indicative of a complex magmatic history. Namely, nano-scale, oriented inclusions of pyrrhotite and fluorite within the cores of apatite closely associated with mafic enclaves are indicative of the granites protracted interaction with mafic melts. Their chondrite-normalized rare earth element (REE) fractionation trends are light REE (LREE) enriched and vary when altered by hydrothermal fluids along with the concentrations of several other elements. Magmatic apatite hosted in other intrusives displays similar behaviour when altered, but contains higher concentrations of Cl, Sr, and lower Mn which vary systematically with regards to bulk rock basicity.

Many of the deposits and prospects within the Olympic Cu-Au Province exhibit a chemical and mineralogical zoning grading from early, reduced and later, oxidized hydrothermal assemblages as evidenced by changes in the dominant Fe-oxide, Cu-Fe-sulphide species and as we report herein, changes in apatite. Within the early, reduced, high-temperature expressions of IOCG mineralisation throughout the Province, apatite is abundant, making up, alongside magnetite, the bulk of the mineralisation. Such apatite is dominantly near end-

member fluorapatite characterized by LREE-enriched chondrite-normalized signatures and variable but measurable concentrations of S and Cl.

Overprinting of the magnetite-dominant reduced assemblages by later oxidised hematite-sericite altering fluids results in LREE-loss within the early, hydrothermal and magmatic apatite. Such hematite-sericite altered zones along with newly formed apatite display middle REE (MREE) enriched signatures and are devoid of many of the other trace elements present in magmatic and early hydrothermal apatite, such as S and Cl. This behaviour is observed within the Olympic Dam deposit, as well as the Wirrda Well and Acropolis prospects.

Late apatite hosted within the high-grade massive bornite mineralisation of Olympic Dam and within chalcopyrite-barite-rich zones of the Acropolis prospects displays extreme MREE-enriched REE-signatures with positive Eu-anomalies. The latter characteristic is unique amongst all other apatite examined as part of this study and highly anomalous globally. Numerical modeling shows that the evolution in apatite trace elements, and in particular REE signatures is the direct result of fluid evolution within IOCG systems. Given this association, the various assemblages within IOCG systems are classified according to REE-signature and the use of apatite in mineral exploration and as a petrogenetic tool is discussed in detail.

The modeling of REE behaviour in hydrothermal fluids typical of IOCG mineralised systems has offered important insights into the transport and deposition of REE within Olympic Dam and possibly other IOCG systems. Specifically, REE are transported primarily as REE-Cl species and deposited under conditions of suppressed REE-Cl activity. The propensity of the LREE to occur as Cl-complexes explains both their significantly greater enrichment in IOCG systems when compared to the HREE, as well as their preferential depletion in apatite during hematite-sericite alteration.

DECLARATION

I certify that this work contains no material which has been accepted for the award of any other degree or diploma in my name, in any university or other tertiary institution and, to the best of my knowledge and belief contains no material previously published or written by another person, except where due reference has been made in the text. In addition, I certify that no part of this work will, in the future, be used in a submission in my name, for any other degree or diploma in any university or other tertiary institution without the prior approval of the University of Adelaide and where applicable, any partner institution responsible for the joint-award of this degree.

I give consent to this copy of my thesis when deposited in the University Library, being made available for loan and photocopying, subject to the provisions of the Copyright Act 1968.

I acknowledge that copyright of published works contained within this thesis resides with the copyright holder(s) of those works.

I also give permission for the digital version of my thesis to be made available on the web, via the University's digital research repository, the Library search and also through web search engines, unless permission has been granted by the University to restrict access for a period of time.

Signed

Date 7/11/2017

ACKNOWLEDGEMENTS

Firstly, I would like to express my deepest gratitude to the two hardest working and most passionate geologists at the University of Adelaide, my academic supervisors Prof. Nigel Cook and Dr. Cristiana Ciobanu. Thank you for your tireless support, encouragement and advice. I feel fortunate to have been your student. The knowledge that I have acquired thanks to your willingness to go above and beyond stands as the solid foundation on which my future success, professional and otherwise, will be built. For this I am forever grateful. Thank you Nigel for your patience and support, particularly with regards to the energy you invested in making me a better writer. Cristi, thank you for your unwavering support and for pushing me to accomplish even the most impossible tasks, for the late nights on the SEM and the Sunday afternoons.

I would also like to express my gratitude to my external supervisor, Dr Kathy Ehrig for her support, advice, encouragement and for her willingness to make time for, and entertain the ideas of a young geologist. Thank you for your genuine interest and support, thank you for all the discussions, not only with regards to the research, but the mining industry and life in general. I would also like to express my gratitude for the financial support that I received from BHP and the site visits to Olympic Dam that you made possible. The next coffee is on me.

Thank you to all of the staff at Adelaide Microscopy for their assistance on countless occasions. In particular Mr. Angus Netting, Mr. Ken Neubauer, Ms Aoife McFadden, Dr Animesh Basak and the especially "the man with the plan" Dr. Benjamin Wade.

I would also like to thank my fellow Ph.D students Luke George, Matthew Paul and especially my dear friend Alkis Kontonikas-Charos for all of your support, advice and all the good times that we have shared over the years.

A big thank you to all of the friends and family that I am so fortunate to have, especially my parents Zlatko and Aldina Krneta and my younger siblings Sanja and Sara for their support and encouragement, particularly during those times that were the hardest, and for making me the man that I am today. Thank you, to my close friends Ben Crago and Petar Kolundzic and my fiancées family for all of their encouragement and support.

Lastly, I would like to thank my fiancée Rhiannon for the support and encouragement that she has given me over the course of my Ph.D and for her unwavering belief that I could do it. Thank you.

"Our virtues and our failings are inseparable, like force and matter. When they separate, man is no more."

-Nikola Tesla

"Life without dreams is meaningless, impoverished and grey."

-Dr. Nele Karajlic

PREFACE

This thesis comprises of a portfolio of manuscripts which have been published or prepared for submission, in international peer-reviewed journals. The journals in which these papers have been published are *'Lithos'* (Chapter 2, published), *'Minerals'* (Chapter3, published), *'Journal of Geochemical Exploration'* (Chapter 4, published). Chapters 5 and 6 will be submitted for publication in a revised and abridged form. All five chapters are closely related, and summarize key findings and interpretations of apatite morphology and geochemistry within iron-oxide copper-gold systems, that were made as part of this project. Recommendations have been made at the end of this thesis as a direct result of the key findings of this research, and it is hoped that these are explored at a later date.

The five chapters which form the basis of this thesis are:

2. Krneta, S., Ciobanu, C.L., Cook, N.J., Ehrig, K. and Kontonikas-Charos, A., 2016. Apatite at Olympic Dam, South Australia: a petrogenetic tool. Lithos, 262, 470-485.
3. Krneta, S., Ciobanu, C.L., Cook, N.J., Ehrig, K. and Kontonikas-Charos, A. 2017. Rare earth element behaviour in apatite from the Olympic Dam Cu-U-Au-Ag deposit, South Australia. Minerals 7(8), 135.
4. Krneta, S., Cook, N.J., Ciobanu, C.L., Ehrig, K. and Kontonikas-Charos, A., 2017. The Wirrda Well and Acropolis prospects Gawler Craton, South Australia: insights into evolving fluid conditions through apatite chemistry. Journal of Geochemical Exploration 181, 276-291.
5. Krneta, S., Ciobanu C.L., van der Kerke, K, Cook, N.J., Ehrig, K. and Basak, A. Crystal structural modification and mineral inclusions in apatite from Olympic Dam, South Australia. (*to be submitted in a revised and abridged form*)

6. Krneta, S., Ciobanu, C.L., Cook, N.J. and Ehrig, K. Numerical modeling of REE trends in fluorapatite: snapshots of fluid evolution in a giant hydrothermal system. (*to be submitted in a revised and abridged form*)

Key findings and implications of this work, as well as future avenues of research, are summarized in Chapter 7.

Chapter 8 contains all supplementary material for the main papers outlined above, as well as additional conference abstracts, and other co-authored publications that have been generated during the PhD candidature. The additional material is as follows:

A. Supplementary material for Chapter 2 (Paper 1).

B. Supplementary material for Chapter 3 (Paper 2).

C. Supplementary material for Chapter 4 (Paper 3).

D. Supplementary material for Chapter 6.

E. Krneta, S., Ciobanu, C.L., Cook, N.J., Ehrig, K. and Kamenetsky, V.S., 2016. REY-signatures in apatite monitor the evolution of IOCG systems:examples from Olympic Dam and Acropolis, South Australia. Abstract, Australian Earth Science Convention, Adelaide, 26-30 June, 2016, unpaginated.

F. Krneta, S., Ciobanu, C.L., Cook, N.J., Ehrig, K., Kamenetsky, V.S., 2015. Apatite in the Olympic Dam Cu–U–Au–Ag deposit. In: Mineral Resources in a Sustainable World, Proceedings, 13th Biennial SGA Meeting, Nancy, France, August 2015, Vol. 3, pp. 1103-1106.

G. Krneta, S., Ciobanu, C.L., Cook, N.J., Ehrig, K. and Kamenetsky, V.S., 2016. REY-signatures in apatite monitor the evolution of IOCG systems: examples from

Olympic Dam and Wirrda Well, South Australia. Abstract, International Geological Conference, Cape Town, South Africa, August 27- September 4 2016, unpaginated.

H. Krneta, S., Ciobanu, C.L., Cook, N.J., Ehrig, K. and Kamenetsky, V.S., 2015. Apatite in the Olympic Dam IOCG system and adjacent prospects insights into magmatic and hydrothermal evolution. Abstract, Society of Economic Geologists Conference, Hobart, TAS, September 27-30, unpaginated.

I. Krneta, S., Ciobanu, C.L., Cook, N.J., Ehrig, K. and Kamenetsky, V.S., 2016. Apatite in the Olympic Dam IOCG system and adjacent prospects insights into magmatic and hydrothermal evolution. Conference poster, Society of Economic Geologists Conference, Hobart, TAS, September 27-30.

J. Kontonikas-Charos, A., Ciobanu, C.L., Cook, N.J., Ehrig, K., Krneta, S.K., Kamenetsky, V.S., 2017. Feldspar evolution in the Roxby Downs Granite host to Fe-oxide Cu-Au-(U) mineralisation at Olympic Dam, South Australia. Ore Geology Reviews 80, 838-859.

The final chapter of this thesis consists of a complete reference list of all publications cited within any of the manuscripts, chapters, supplementary and additional material submitted as a component this thesis.

CHAPTER 1

INTRODUCTION

CHAPTER 1: INTRODUCTION

Apatite is the Earth's most abundant phosphate, and 10th most abundant mineral overall (Hughes and Rakovan, 2002). Perhaps like that of no other mineral, its study spans a wide breadth of disciplines including material sciences, dentistry, medicine, agriculture, astrophysics and various sub disciplines of geology (Chew and Spikings, 2015, Harlov, 2015, Hughes and Rakovan, 2015, Jungck and Niederer, 2017). Notwithstanding the importance of apatite to modern civilisation as a fertiliser and a crucial component of the global chemical industry, its impact on geological processes can be profound due to its significant capacity to incorporate a wide range of trace elements (Hughes, 2014, Hughes and Rakovan, 2015, Harlov, 2015, Webster and Piccoli, 2015). As such apatite has seen extensive use in the study of geological processes and in particular the study of hydrothermal mineral deposits and the various rocks associated with their formation (e.g., Belousova et al., 2001, 2002, Cao et al., 2012, Mao et al., 2016).

The morphology, mineral associations and chemistry of magmatic apatite are extremely variable (Piccoli and Candela, 2002) and extensively studied due to the insights they provide into processes, such as magma mixing, cooling history, volatile concentrations, magmatic differentiation, degassing and the fugacity of O_2 and SO_4 (e.g., Streck and Dilles, 1998, Cao et al., 2012, Barkov and Nikiforov, 2016, Takashima et al., 2017). Equally, hydrothermal apatite has proven just as useful in the study of metasomatic processes, particularly in instances where repeated interaction with evolving fluids is expressed within it as distinct compositional domains (Harlov, 2015, Harlov et al., 2002, Bonyadi et al., 2011, Krause et al., 2013, Krneta et al., 2016, 2017b, Xing and Wang, 2017). As such, apatite is able to effectively create a chemical fingerprint of its environment, and act as a tracer of petrogenesis

and provenance (Belousova et al., 2002, Brauand et al., 2017). It is no surprise that apatite has received so much attention as a potential mineral pathfinder (Kelley et al., 2011, Bouzari et al., 2016).

Iron-Oxide-Copper-Gold (IOCG) deposit is a broad term which encompasses an expansive group of mineralised systems spanning a variety of tectonic settings and geologic time (Hitzman et al., 1992, Barton, 2014). Deposits classified as IOCGs do, however, display much variation, with respect to parameters, such as Cu and Au concentrations, dominant Fe-oxide species and style of alteration (Williams et al., 2005, Groves et al., 2010, Kontonikas-Charos et al., 2017a). Nevertheless, they all commonly contain apatite as a significant component, particularly those classified within the high-temperature, magnetite-dominant Iron-Oxide-Apatite (IOA) and IOCG skarn sub-groups (Cross, 1993, Harlov et al., 2002, Ismail et al., 2014). Although the mechanisms of IOCG-formation remain much debated (Hitzman et al., 1992, Haynes et al., 1995, Williams et al., 2005, Skirrow et al., 2007, Barton, 2014), study of apatite within these deposits has given significant insights into the fluid responsible for their formation and the behaviour of numerous trace elements, particularly rare earth elements and yttrium (REY) (Harlov et al., 2002, Bonyadi et al., 2011). Within the Olympic Cu-Au province, on the eastern margin of the Gawler Craton, South Australia, one of the world's largest IOCG-mineralised belts, such studies have defined clear associations between apatite chemistry and specific hydrothermal assemblages, effectively tracking the evolution of these systems (Ismail et al., 2014, Kontonikas-Charos et al., 2014).

The abundance of apatite within IOCG-mineralisation and its capacity to offer insights into parameters of metallogenic interest presents a unique opportunity for the study of processes associated with the formation of the world's largest and one of the most strongly mineralised

IOCG deposits, Olympic Dam, as well as other prospects within the Olympic Cu-Au province, along with assessing the role of apatite in their formation.

This chapter provides a summary of background information on apatite chemistry and crystal structure as well an account of the controls on elemental uptake. Geochemical trends in both magmatic and hydrothermal apatite are discussed in the context of magmatic and hydrothermal processes. Summary background information regarding IOCG-type deposits, regional geology of the Olympic Cu-Au province and descriptions of the Olympic Dam deposit as well as other study cases are provided along with a list and descriptions of the samples used in the preceding studies. Finally, the last part of this chapter describes the key objectives of the research undertaken within this thesis along with a chapter-by-chapter explanation of the thesis structure.

1.1 Apatite chemistry and crystal structure

The apatite supergroup (Pasero et al., 2010) constitutes a large group of unique minerals the existence of which is primarily owed to the high flexibility of the apatite structure (e.g., White and Dong, 2002) which gives it the capacity to integrate a wide variety of elements (Figure 1.1 after Hughes and Rakovan, 2015). This element incorporating capacity coupled with the ubiquitous presence of apatite in almost all geological environments has resulted in the huge variability in the chemistry of natural apatite (e.g., Belousova et al., 2002, Mao et al., 2016).

The general formula of the apatite supergroup is given as $A_5(XO_4)_3Z$ (Pasero et al., 2010) where the A position is most commonly occupied by Ca^{2+}, but can be substituted by a variety of other divalent, trivalent, and tetravalent cations, such as Na^{+}, Sr^{2+}, Pb^{2+}, Ba^{2+}, Mn^{2+}, Fe^{2+}, Mg^{2+}, Ni^{2+}, Co^{2+}, Cu^{2+}, Zn^{2+}, Sn^{2+}, Cd^{2+}, Eu^{2+}, REE^{3+}, Y^{3+}, Zr^{4+}, Ti^{4+}, Th^{4+}, U^{4+}, S^{4+}, as well as U^{6+}. The X position is dominantly occupied by P, as PO_4^{3-}, but can also host SO_4^{2-}, AsO_4^{3-},

VO_4^{3-}, SiO_4^{4-}, CO_3^{2-} , CrO_4^{2-} , CrO_4^{3-}, GeO_4^{4-}, SeO_4^{4-}, and WO_4^{3-}. Finally, the Z position is most often occupied by F in most natural apatite but also readily hosts Cl, OH^- and defines the three end-members fluorapatite, chlorapatite, and hydroxyapatite (defined as apatite *sensu stricto* by Hughes and Rakovan, 2002), although most natural apatite are binary or ternary (Hughes and Rakovan, 2015). Other halogens such as Br^- and I^-, as well as S^{2-}, CO_3^{2-}, and a variety of O and N complexes, have been identified in this position in natural or synthetic apatite (Pan and Fleet, 2002).

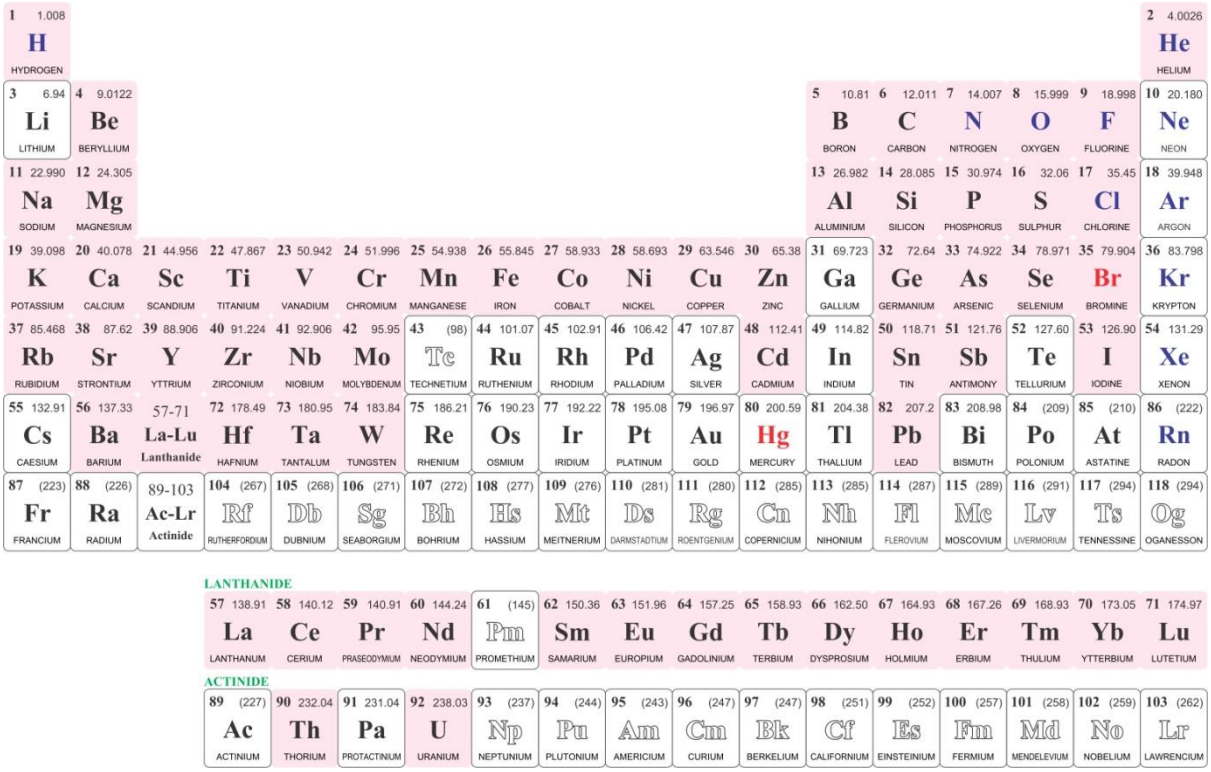

Figure 1.1: Periodic table with elements measured in apatite supergroup minerals in concentrations from several ppm to weight percent shown in pink (Pan and Fleet, 2002, Cao et al., 2012, Chew and Spikings, 2015, Mao et al., 2016).

The apatite supergroup exhibits a number of structural variants (e.g., Pasero et al., 2010, Kampf and Housley, 2011, Demartin et al., 2010) largely owing to the slight structural distortions caused by chemical substitutions of Ca and P and variations in Z position geometry. Nevertheless, these variants are all sub-symmetries of the apatite *sensu stricto*

which are hexagonal minerals with a holosymmetric structure in space group $P6_3/m$, made up of 3 cation polyhedra; a rigid XO_4 tetrahedron and two polyhedrons Ca_1O_9, a nine-fold coordinated tri-capped trigonal prism (Mercier et al., 2005) and Ca_2O_6Z, a seven-fold coordinated distorted pentagonal bipyramid (Dolivo-Dobrovolsky, 2006), which constitute the two Ca positions, Ca1 and Ca2, respectively (Figure 1.2, Hughes and Rakovan, 2002, 2015). The second of these, (Ca2), preferentially accommodates many of the elements that substitute for Ca and is connected to the Z position hosting F, Cl, and OH^- (Figure 1.2).

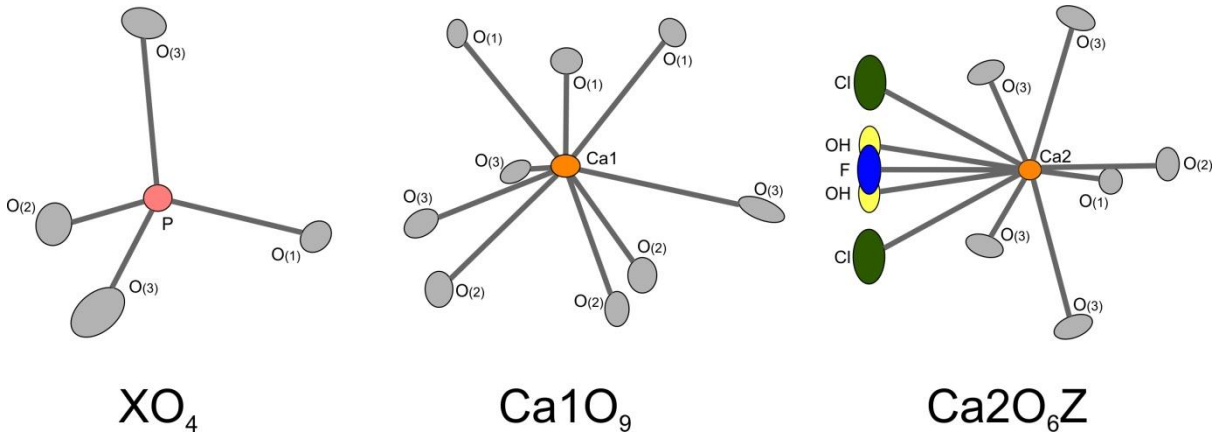

Figure 1.2: The three apatite cation polyhedra.

Elemental preferences for the two Ca positions are summarised in Table 1.1 after Mao et al., (2016) with references therein. However, Ca position occupancy can be significantly impacted by changes in the dominant occupant of the Z position (F, Cl, and OH^-). For example, elements such as U^{4+} and Th^{4+} preferentially occupy the Ca2 position in fluorapatite (Luo et al., 2011), whereas in chlorapatite they occupy both the Ca1 and Ca2 positions (Luo et al., 2009). This stems from the tendency for Cl^- and OH^- to distort the size of the Ca2 position by creating a Markovian offset sequence, whereby the position of one anion is affected by the position of the one preceding, and will affect the position of the following anion. This is due to the larger atomic radius of Cl and OH^- compared to F (Figure 1.2, Hughes et al., 1989, Hughes and Rakovan, 2002). Such distortions are a topic of extensive study given the structure of binary and ternary apatite is generally poorly understood (Hughes

et al., 2014, Kelly et al., 2017). However, distortions to the apatite structure are not limited to substitutions in the Z position as evidenced by the slight structural variability in all apatite supergroup minerals (e.g., Demartin et al., 2010, Yi et al., 2013, Gianfagna and Mazziotti, 2014).

Elements other than Ca and P substitute into apatite either directly in which case the substituting element and the element it displaces share the same valance, or by coupled charge compensated substitution where the substitution of one element is accompanied by the substitution of another, maintaining overall charge balance (Pan and Fleet, 2002, Rønsbo, 1989).

Cation	**Ca1 site: $^{IX}Ca^{2+}$ (Å)**	**Ca2 site: $^{VII}Ca^{2+}$ (Å)**	**Site preference**
Ca^{2+}	1.18	1.06	Stoichiometric
Sr^{2+}	1.31	1.21	Ca2 (almost exclusively)
Ba^{2+}	1.47	1.38	Ca2
Mg^{2+}	0.89 (VIII)	0.72 (VI)	Possibly Ca1 in REE-rich environment
Mn^{2+}	0.96 (VIII)	0.9	Ca1
Fe^{2+}	0.92 (VIII)	0.78 (VI, HS)	Ca1
Eu^{2+}	1.3	1.2	Ca2
Pb^{2+}	1.35	1.23	Ca2
Na^{+}	1.24	1.12	Ca1
Y^{3+}	1.075	0.96	Ca2
REE^{3+} (La-Lu)	1.042-1.216	0.925-1.10	Dominantly Ca2
Th^{4+}	1.09	0.94	Ca2 (both in Cl-rich)
U^{4+}	1.05	0.95	Ca2 (both in Cl-rich)
Zr^{4+}	0.89	0.78	Incompatible

Table 1.1: Radius and site occupancy of common cations substituting for Ca in apatite (Mao et al., 2016, and references therein)

This can also be achieved by means of a vacancy, such as in the case of U^{4+} and Th^{4+}. Below is a comprehensive list of proposed substitutions in apatite after Pan and Fleet (2002) and references therein.

$$A^{2+} = Ca^{2+}$$
$$\square + 2\square = Ca^{2+} + 2\ F^{-}$$

$$\square + 2\ XO_4^{2-} = Ca^{2+} + 2\ PO_4^{3-}$$
$$A^+ + \square = Ca^{2+} + F^-$$
$$2\ A^+ = Ca^{2+} + \square$$
$$A^+ + A^{3+} = 2\ Ca^{2+}$$
$$A^+ + XO_4^{2-} = Ca^{2+} + 2\ PO_4^{3-}$$
$$A^{3+} + XO_4^{4-} = Ca^{2+} + PO_4^{3-}$$
$$2\ A^{3+} + \square = 3Ca^{2+}$$
$$2\ A^{3+} + XO_4^{5-} = Ca^{2+} + PO_4^{3-}$$
$$A^{4+} + \square = 2\ Ca^{2+}$$
$$XO_4^{2-} = PO_4^{3-}$$
$$2\ XO_4^{2-} + \square = PO_4^{3-} + Ca^{2+}$$
$$XO_4^{2-} + A^+ = PO_4^{3-} + Ca^{2+}$$
$$XO_4^{2-} + XO_4^{4-} = 2\ PO_4^{3-}$$
$$XO_4^{4-} + \square = PO_4^{3-} + F^-$$
$$XO_4^{4-} + A^{3+} = PO_4^{3-} + Ca^{2+}$$
$$XO_4^{5-} + 2\ A^{3+} = PO_4^{3-} + Ca^{2+}$$
$$XO_4^{2-} + XO_3^{2-} = 2\ PO_4^{3-}$$
$$Z^- = F^-$$
$$\square + X^{2-} = 2F^-$$
$$\square + A^+ = F^- + Ca^{2+}$$
$$2\square + \square = 2F^- + Ca^{2+}$$
$$\square + XO_4^{4-} = F^- + PO_4^{3-}$$
$$X^{2-} + A^{3+} = F^- + Ca^{2+}$$

1.1.1 Controls on elemental uptake

The controls which govern apatite chemistry can be largely divided into those intrinsic to the apatite crystal structure and external controls (Pan and Fleet, 2002). Although the sheer number of parameters which interplay to ultimately result in the chemical signature of a particular apatite can be highly convoluted, numerous studies have shown that they are usually resolvable and their interpretation can provide valuable information about the host intrusive or hydrothermal assemblage (e.g., Belousova et al., 2002, Harlov, 2015, Harlov et al., 2002, Bonyadi et al., 2011, Cao et al., 2012, Mao et al., 2016, Bouzari et al., 2016).

Substitution in apatite is primarily controlled by Goldschmidt's Rules (Goldschmidt, 1937), whereby elements with atomic radii most closely resembling that of the substituting position are most easily substituted. This is most easily observed with respect the REE, which display a systematic decrease in atomic radius with increasing atomic number (Table 1.1), resulting in apatite incorporating REE in the range of Nd-Gd most strongly with decreasing rates of

incorporation in REE above and below this range (Pan and Fleet, 2002). However, significant distortions to normal crystal controlled partitioning can be brought about by external physiochemical controls and the presence of co-crystallising trace element scavenging species. Multiple external controls may exert an effect on apatite chemistry in any particular environment and their interplay is often complex. However, in essence, these controls will either result in the lack of REE within the melt or fluid, or their presence in a form incompatible with incorporation into apatite. The controls include physical-chemical parameters such as fO_2, pH, and temperature, as well as the composition of the melt or fluid.

Although a single parameter can affect apatite composition in both magmatic and hydrothermal environments, its importance can vary significantly between the two. For instance, apatite preferentially incorporates Eu^{3+} over Eu^{2+} making its incorporation very sensitive to fO_2 in the magmatic environment (e.g., Cao et al., 2012). In hydrothermal fluids, however, the dominance of one Eu species over the other is largely controlled by pH (Brugger et al., 2008). Notwithstanding this particular example, fO_2 affects apatite chemistry in both environments due to its ability to alter the oxidation state of many commonly substituting elements and apatite's ability to incorporate one form and not others. Although evidence contrary to this has emerged recently with respect to As and S and their incorporation into apatite (albeit in small concentrations, and under laboratory conditions) in forms other than As^{5+}, S^{6+} (Konecke et al., 2017, Liu et al., 2017), it has not discredited earlier studies, which have interpreted changes in the concentration of these elements in apatite as evidence of fO_2 variability (Streck and Dilles, 1998).

In spite of the examples provided above where the concentration of a particular element in apatite can be attributed to a single external parameter in a specific melt or fluid, generalisation of such associations to environments beyond a particular study case are

oversimplified and prone to misinterpretation. This was pointed out by Marks et al. (2014) with respect to the proposed use of Mn-in-apatite as a fO_2 proxy in felsic magmas (Miles et al., 2014). As such the various controls on apatite chemistry are discussed below in the context of well-defined and well-constrained trends in apatite chemistry in magmatic and hydrothermal environments.

1.1.2 Geochemical trends in magmatic apatite

Apatite is a very common magmatic accessory and readily found in igneous phases spanning the entire range of whole rock compositions, where it hosts the majority of whole rock P (Piccoli and Candela, 2002). Given its ability to incorporate so many elements, its presence can significantly impact trace element behaviour within magmatic rocks along with recording magmatic processes (Hughes and Rakovan, 2015, Brauand et al., 2017). This is often expressed as core to rim variations in the concentration of a multitude of magmatic process sensitive elements (e.g., Streck and Dilles, 1998, Cawthorn, 2013).

The relative ease with which trace elements are incorporated into apatite are evident in its suitability as a host for U, Th, and Pb, and, as a result, the widespread use of apatite in geochronology and thermochronology (e.g., Chew and Spikings, 2015). For the same reason, apatite has been touted as a storage medium for radioactive waste (Oelkers and Montel, 2008).

Until recently, the chemistry of apatite has been used to gain extensive insights into the magmatic environment, of which perhaps the most complex, but widely studied area has been the relationships between apatite F, Cl, and OH^- concentrations and the volatile contents of magmas and their degassing processes (e.g., Boudreau and McCallum, 1990, Webster et al., 2009, Barkov and Nikiforov, 2016). Ternary apatite spaning all possible concentrations of F,

Cl and OH are observed in nature and exhibit the greatest variability in layered mafic intrusions (Figure 1.3; Boudreau and Krugger, 1990, Barkov and Nikiforov, 2016).

The controls on apatite composition in the F-Cl-OH^- space were outlined by Zhu and Sverjensky (1991) as 1) the melt or fluid composition, 2) the presence of other phases competing for these elements (such as biotite), and 3) P-T conditions, allowing Piccoli and Candela (1994) to develop a method for the estimation of initial F-Cl concentrations in a melt at the time of apatite crystallisation (given as the apatite saturation temperature, unique to a melt of a particular composition (Harrison and Watson, 1984, Bea et al., 1992). However, more recent work has brought these methods into questions due to the non-ideal mixing exhibited by F, Cl and OH, further emphasising the complex relationship between apatite composition and volatile concentrations in host melt/fluid (Li and Hermann, 2017).

In general, apatite hosted in mafic rocks contains higher concentrations of Cl and OH^- than intermediate and felsic rocks (Figure 1.3; Belousova et al., 2002, Mao et al., 2016).

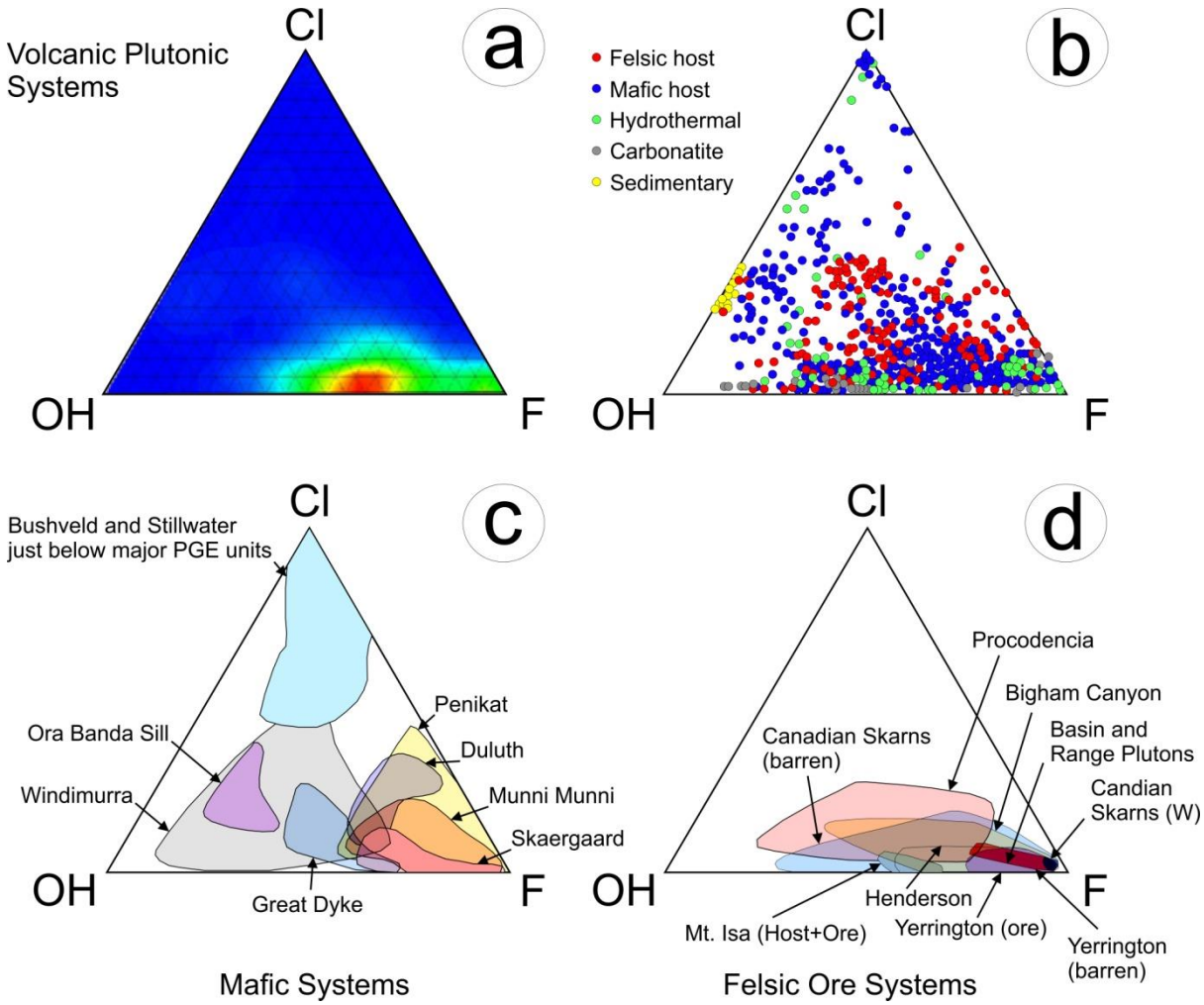

Figure 1.3: Plots of halogen content in apatite (in molar proportions) after Webster and Piccoli (2015). a) Host environment, where hotter colours indicate more analyses. b) Host rock composition. c) Mafic layered intrusions. d) Felsic ore systems.

Although systematic relationships between Cl-concentrations in apatite and the level of magmatic differentiation are noted on a terrain scale (Marks et al., 2012, Ladenburger et al., 2016), a large body of work has attributed these elevated Cl and OH concentrations to late stage movement of Cl- and H_2O-rich vapours through a solidifying magma, possibly as part of degassing processes (e.g., Ustunisik et al., 2011, Barkov and Nikiforov, 2016). Evidence in support of this can be observed in the preferential uptake of F over Cl, Cl over OH^-, and the ability of fluids or melts with low F activity to produce F-rich apatite (Zhu and Sverjensky, 1991). This suggests that generation of a Cl- or OH^--rich apatite requires conditions where

these elements have a very high activity. Therefore, the higher Cl concentrations seen in hydrothermal apatite and in some mafic rocks may be reconcilable with the strong affinity that Cl and OH^- have for the fluid phase in a cooling melt (Piccoli and Candela, 1994).

Other elements incorporated into magmatic apatite display much clearer trends with regards to magmatic differentiation and whole rock chemistry. Strontium concentrations display a strong negative correlation with whole rock SiO_2 and are highest in carbonatites and alkaline rocks (~1.5 wt. %), and lowest in pegmatites and granitoids (~tens of ppm; Belousova et al., 2002, Teiber et al., 2015, Mao et al., 2016, Ladenburger et al., 2016). Thorium mirrors this behaviour, but Mn displays the opposite trend and attains concentrations exceeding ~10,000 ppm in some pegmatite- and granitoid-hosted apatite. Furthermore, Mn along with a number of other elements that can exist in multiple valance states, exhibits significant sensitivity to fO_2. Miles et al. (2014) demonstrated the potential of Mn-in-apatite concentrations as a fO_2 proxy in silicic magmas. However, Marks et al. (2014) expressed significant doubt with regards to this due to the significant interplay between the Mn concentrations in apatite, temperature, whole rock compositions, and the co-partitioning of Mn between apatite and other minerals, emphasising that the utility of apatite chemistry is often highly localised to a specific intrusive or group of intrusives. Moreover, this emphasizes the importance of understanding apatite chemistry in the context of the host assemblage.

Other elements which exhibit a high sensitivity to fO_2 include S, As, and V, along with Ce and Eu. Both these rare earths will often display anomalies in apatite (calculated as the relative concentration of Ce and Eu with reference to the adjacent REE). Such anomalies stem from the ability of these two elements (unlike other REE) to exist in oxidation states other than REE^{3+} (Eu^{2+} and Ce^{4+}) and the increased partitioning of one species (Eu^{3+} and Ce^{4+}) into apatite over the other. Negative Eu-anomalies are very common in apatite and highly sensitive

to the fO_2 conditions of the host melt (Cao et al., 2012). However, this relationship is much more complex in hydrothermal apatite (Brugger et al., 2008).

Sulphur concentrations are particularly instructive in oxidised arc magmas where they have been used to correlate between volcanic ignimbrites (Takashima et al., 2017) and in the recognition of the onset of anhydrite crystallisation in plutonic rocks (Streck and Dilles, 1998), although with some limitations (Peng et al., 1997). In contrast, As concentrations are commonly very low in magmatic apatite, reaching their highest concentrations in pegmatite hosted grains (Teiber et al., 2015).

Silica and Na in magmatic apatite often exhibit strong correlations with REE and S due to their involvement in charge compensated coupled substitutions accommodating the incorporation of the latter two elements (Pan and Fleet, 2002, Rønsbo, 1989). Sodium performs this role more commonly in mafic rocks and its concentrations are often higher in the same (Rønsbo, 1989). The concentrations of REE and Y (REY) are generally higher in evolved igneous phases, particularly pegmatites and lower in mafic rocks (Belousova et al., 2002, Cao et al., 2012, Teiber et al., 2015, Mao et al., 2016). However, the positive correlation between ΣREY and magmatic differentiation is not particularly strong given the wide range in ΣREY values measured in rocks of all compositions, suggesting that there are multiple controls on ΣREY incorporation in magmatic apatite. Despite this variability in ΣREY concentrations, the chondrite-normalised REY-signatures of magmatic apatite are almost ubiquitously light-REE (LREE)-enriched with negative Eu-anomalies (e.g., Belousova et al., 2002, Cao et al., 2012, Mao et al., 2016).

1.1.3 Geochemical trends in hydrothermal apatite

The chemistry of hydrothermal apatite is dictated by much the same controls as magmatic apatite (i.e., fluid composition, fO_2, and the presence of other trace element consuming species). However, deciphering the chemistry of hydrothermal apatite and making inferences about the physiochemical conditions at the time of apatite crystallisation can be significantly more complicated due to the speciation of elements transported in hydrothermal fluids and the effects that parameters such as temperature, pressure, pH, composition, salinity and, in particular, the presence or absence of particular complexing ligands can have on the chemistry of hydrothermal minerals (van Hinsberg et al., 2010, Brugger et al., 2008).

Moreover, the capacity of hydrothermal environments to concentrate certain elements (e.g., U, Th, REE, S) to levels high enough for the formation of discrete minerals (primarily made up of the aforementioned elements) can affect the chemistry of a co-crystallising apatite significantly by the creation of complex co-partitioning relationships. This is perhaps best demonstrated by the contrasting levels of absolute concentrations of substituted elements in magmatic and hydrothermal apatite. Magmatic apatite commonly contains higher concentrations of elements other than Ca and P, thus revealing the much greater role apatite plays as a host for a variety of trace elements in the magmatic, compared to the hydrothermal environment (Mao et al., 2016).

The evolving nature of many hydrothermal fluids and the presence of multiple overprinting events in many hydrothermal systems is often reflected in apatite as grain-scale chemical zoning related to fracturing, commonly with inclusions of minerals of the overprinting assemblage (e.g., Harlov et al., 2002, Bonyadi et al., 2011, Harlov, 2015, Krneta et al., 2016, 2017a, b). Similar post-crystallising alteration of magmatic apatite is readily observed in hydrothermally altered rocks (e.g., Krause et al., 2013, Bouzari et al., 2016). Such alteration

of apatite is achieved via coupled dissolution reprecipitation reactions (CDRR; Wang et al., 1995, Putnis, 2002, Harlov et al., 2002) and commonly does not affect the apatite grain shape.

As in magmatic apatite, the chemistry of hydrothermal grains in F-Cl-OH space is heavily dominated by fluorapatite with lesser concentrations of Cl and OH^- (e.g., Zhu and Sverjensky, 1991, Harlov, 2015, Mao et al., 2016). Apatite formed from high-salinity fluids such as those associated with IOA systems commonly contains elevated Cl-concentrations along with appreciable S and REY (Harlov et al., 2002, Bonyadi et al., 2011, Krneta et al., 2017a). However, such early hydrothermal apatite along with magmatic grains exhibits significant loss of Cl, S, and REY when overprinted by later fluids of lower salinity, forming inclusions of monazite (e.g., Majka et al., 2016) and lesser xenotime via the reaction proposed by Harlov et al. (2002):

$$\text{(REE-rich) apatite} + (Ca^{2+} + P^{5+})_{aq} \Leftrightarrow \text{(REE-rich) apatite} + \text{(REE-rich) monazite} + (Si^{4+} + Na^{+})_{aq}$$

Although such overprinting tends to be associated with increases in F-concentrations in the affected apatite, increases in Cl have also been observed (Krause et al., 2013). Such cases appear, however, to be significantly rarer and restricted to mafic intrusive rocks.

Such localised element re-distribution has been proposed in explaining other phenomena, such as the crystallisation of apatite with weak-negative to strongly positive Eu-anomalies in grains associated with the sericitization of feldspars. Liberation of the significantly Eu-enriched REY-budget from a feldspar (Alderton et al., 1980, van Dongen et al., 2010) would increase the amount of Eu partitioning into apatite over the other REY (Mao et al., 2016). However, this explanation may be somewhat oversimplified given how complex REY behaviour in hydrothermal fluids can be (e.g., Bau and Dulski, 1995, Haas et al., 1995,

Lottermoser et al., 1992, Brugger et al., 2008, Migdisov and Williams-Jones, 2014, Migdisov et al., 2016).

Possibly, due to this complexity, the REY-signatures of hydrothermal apatite display much more variability that those of magmatic grains. This is due to the highly varied behaviour of the REY collectively with individual complexing ligands, i.e., F, Cl, SO_4, and CO_2, as well as individually, or as groups (LREE *vs.* HREE; Migdisov et al., 2016). Such contrasts, primarily expressed as the variable stability or solubility of REY-complexes, can result, for example, in complete spatial disassociation between the LREE from the HREE in selected hydrothermal systems (Migdisov et al., 2016). They may feature MREE- (Brugger et al., 2000, Mao et al., 2016), or heavy-REE (HREE)-enrichment (Ismail et al., 2014, Broom-Fendley et al., 2017), suggesting that apatite readily records the complex behaviour of the REY.

Transport of the REY in hydrothermal fluids has historically been attributed to REE-F species (e.g., Smith and Henderson, 2000, Williams-Jones et al., 2000). However, a large body of more recent experimental work determining the stabilities and solubilities of various REY complexes has shown this to be unlikely due to the extremely low solubilities of REY-F species at the hydrothermal conditions measured for many orebodies. Instead, it is suggested that they are primarily transported by highly stable and soluble REY-Cl and REY-SO_4 complexes (Migdisov and Williams-Jones, 2006a, b, 2008, 2014, Migdisov et al., 2006, 2008, 2009, 2016). The solubilities and stabilities of various REY species display significant internal heterogeneities as well, whereby the LREE are much more stable as soluble Cl complexes than the HREE, making them much more easily transported and allowing for their complete spatial disassociation from the HREE in many hydrothermal systems (Migdisov et al., 2016). Such a discrepancy could possibly explain the often observed LREE-depletion in

apatite during alteration (Harlov et al., 2002, Broom-Fendley et al., 2016, Krneta et al., 2017a, b).

Numerous authors have studied REY behaviour in hydrothermal systems and attempted to model fluid-mineral REY partitioning through the use of programs such as the Geochemist's Workbench® (Bethke and Yeakel, 2016), in an attempt to reconcile chondrite-normalised REY-signatures measured in particular minerals with certain fluid conditions (i.e., Smith et al., 2004, Brugger et al., 2008). Recently published thermodynamic data for a large number of REY-complexes (Migdisov et al., 2016, with references therein) has enhanced the validity of such work, which when paired with robust empirical measurements of hydrothermal fluid chemistry (by means of fluid inclusions studies) and/or sound assumptions backed up by the host assemblage, can contribute significantly to explaining particular REY-trends in hydrothermal apatite.

1.2 IOCG deposits and the Olympic Cu-Au Province

1.2.1 IOCG deposits

The IOCG deposit class was defined following the discovery of the Olympic Dam deposit (Hitzman et al., 1992). The identity of IOCG systems within any hierarchical classification of ore deposits remains a topic of intense discussion, particularly with respect to which deposits are true IOCG's and which are genetically distinct Fe-oxide-rich systems, albeit with some shared features. This has resulted in several classification protocols with some including individual mineralisation types and deposits, and excluding others (Hitzman et al., 1992, Williams et al., 2005, Groves et al., 2010, Porter, 2010, Barton, 2014). Williams et al. (2005) limited the classification primarily to hydrothermal deposits with economic concentrations of Cu, containing abundant low Ti Fe-oxide minerals (magnetite-hematite) and lacking a clear

spatial association with igneous intrusions. This effectively removed a number significant deposits from the classification such as the carbonatite-hosted Phalabowra deposit, the Vergenoeg Fe-F deposit and the IOA or Kiruna-type mineralisation. The work of Groves et al. (2010) restricted the term IOCG to the Olympic Dam deposit and others like it (IOCG *sensu stricto*), whilst grouping them into a wider class of deposits termed as "iron-oxide associated", which included the aforementioned IOA and carbonatite-hosted types along with Fe-oxide rich porphyry deposits such as Yerington. In the most recent review of IOCG deposits, Barton (2014) outlines the significant arguments still surrounding aspects such as geodynamic setting, classification, alteration, metal sources and the chemistry and importance of intrusive rocks.

Several different formation mechanisms have been proposed for the IOCG deposit class ranging from formation from immiscible Fe-F-P melts in the case of the IOA (Chen et al., 2010), through mechanisms involving only magmatic fluids (Hitzman et al., 1992, Pollard, 2006, Groves et al., 2010), to those involving the mixing of magmatic and basinal fluids (Haynes et al., 1995). Tectonic setting is dominantly considered as being anorogenic and regionally to locally divergent allowing for mantle underplating and melting of the SCLM and lower crust (Groves et al., 2010, Barton, 2014). Groves et al. (2010) note that most IOCG deposits are confined to within 100 km of cratonic margins, locations which could have allowed for the tapping of the deep mantle-derived mamas necessary for IOCG formation. Groves et al. (2010) note that major episodes of IOCG formation are coincident with the breakup of major supercontinents. IOA-type deposits, on the other hand, appear tied to convergent settings preceding supercontinent amalgamation.

Alteration within IOCG systems can be characterised as high-temperature deep seated Na-Ca-K-metasomatism associated with deposition of Fe-oxides ± Fe-Cu-sulphides. This is locally

manifested via albitization of pre-existing feldspars (Kontonikas-Charos et al., 2014, 2017a, b) and the formation of hydrothermal K-feldspar, biotite and calc-silicates along with high-level, lower temperature, oxidised hydrolytic alteration characterised by sericitization of feldspars and chloritization of mafic minerals commonly in concerts with Fe-oxide ± Fe-Cu-sulphide deposition (Hitzman et al., 1992, Williams et al., 2005, Groves et al., 2010, Porter, 2010, Barton, 2014). Hydrolytic alteration is much less voluminous and commonly centred around high-level deposits, whereas Na-Ca-K metasomatism is regional in many IOCG districts (Barton, 2014).

Metal concentrations can be highly variable, ranging from Fe-only deposits (Salobo, Acropolis, Cairn Hill), to those with significant concentrations of Cu and Au (Olympic Dam, Prominent Hill, Carrapateena) and others with high to economic concentrations of one or more of the following: REE, P, U, Ag, and Co (Barton, 2014). The strength of Cu mineralisation has been attributed to variable levels of mantle input into the hydrothermal fluids, as determined using Cl and Nd isotopes (Skirrow et al., 2007, Storey and Smith, 2017) and to the presence or absence of a suitable precipitation mechanism (Haynes et al., 1995, Bastrakov et al., 2007).

1.2.2 Olympic Cu-Au province geology

The eastern Gawler Craton, South Australia is host to the world-class Olympic Cu-Au province (Skirrow et al., 2007). This is a heavily mineralised IOCG belt, spanning some 700 km along a roughly N-S-strike (Figure 1.4). The entire province is obscured by tens to thousands of meters of modern to Neoproterozoic flat-lying sediments (Skirrow et al., 2002). The extent of the Olympic Cu-Au province has been defined through several decades of exploration beginning with the discovery of Olympic Dam in 1975 by WMC Resources and the recognition of a new deposit type highly suited to geophysically targeted exploration. The

discovery of numerous IOCG deposits and prospects followed over the last 40 years. Notably, Wirrda Well and Acropolis, which although located only ~25 km SSE and SW of Olympic Dam, differ from it significantly, particularly with regards to the concentrations of Cu and Au and other characteristics detailed in this thesis (Krneta et al., 2017a). More recently, further discoveries (Figure 1.4) have emphasised the variable ways in which IOCG mineralisation is expressed throughout the province as classified according to the dominant style of alteration. These range from deep-seated magnetite-dominant, Cu-poor mineralization at Cairn Hill (Clark et al., 2014), through high-temperature, reduced-Fe, magnetite-(Na/K)-feldspar-calc-silicate ± biotite ± Fe-Cu sulphide + skarn mineralisation (Hillside, Moonta-Wallaroo; Conor et al., 2010, Ismail et al., 2014), and skarn hosted mineralisation within the Moonta-Wallaroo group (Punt Hill and SAR9; Reid et al., 2011) to oxidised-Fe, hematite-sericite ± chlorite alteration associated with polyphase brecciation and Cu-Fe-sulphides (Olympic Dam, Prominent Hill and Carrapateena; Ehrig et al., 2012, Belperio et al., 2007, Vella and Cawood, 2006, Schlegel and Heinrich, 2015, Bowden et al., 2017, Krneta et al., 2017a, Schlegel et al., in press).

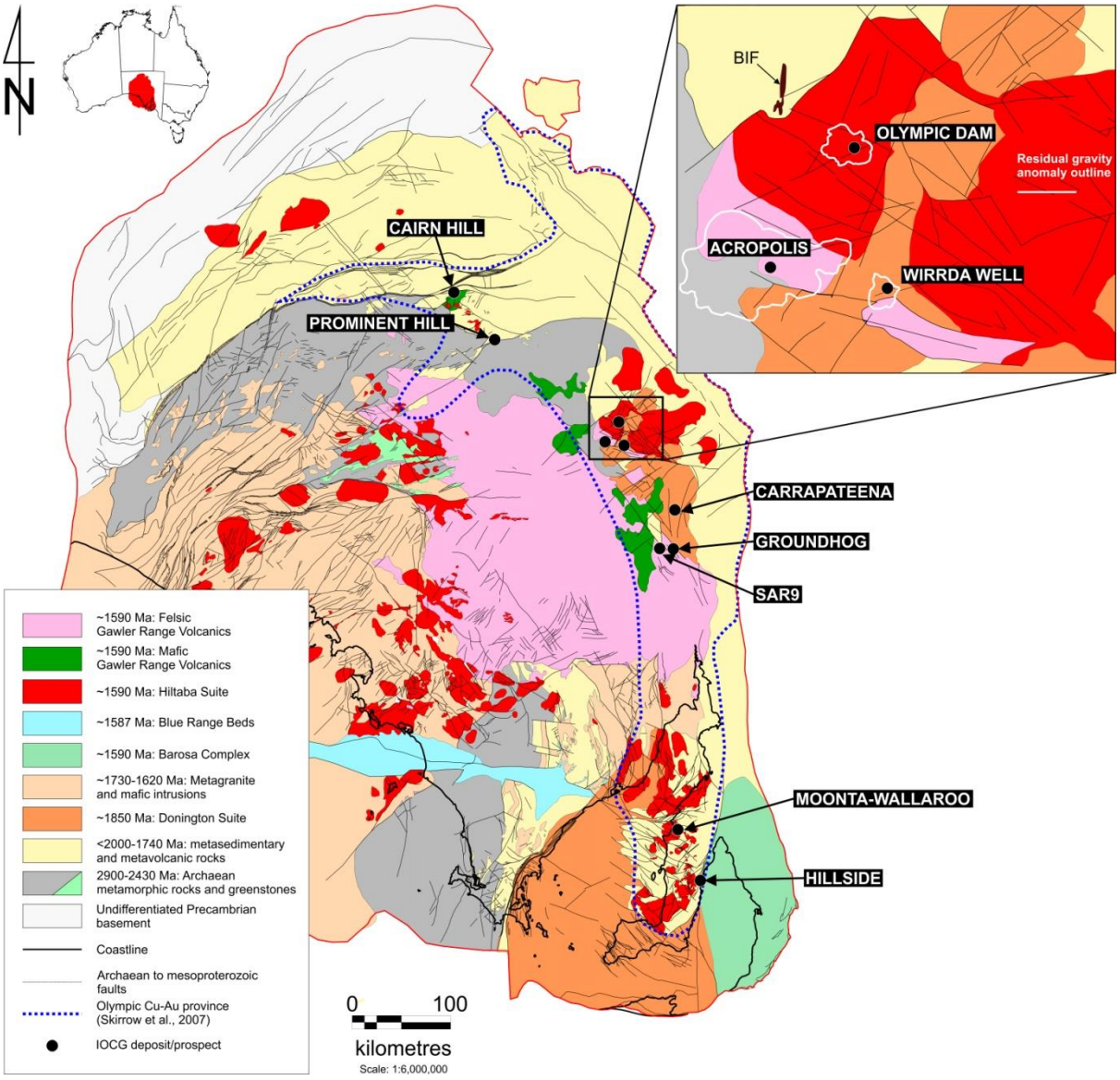

Figure 1.4: Simplified geological map of the Gawler Craton showing Archaean to Mesoproterozoic lithologies and structure, the extent of the Olympic Cu-Au province and the locations of prominent IOCG deposits and prospects. The inset is of the Burgoyne Batholith. Map sourced from "https://map.sarig.sa.gov.au/".

Multiple assemblages are often represented within the same system and overprint one another (e.g., Krneta et al., 2017a, Ehrig et al., 2017). Notwithstanding this variety, all IOCG mineralisation within the Province is related to the same Mesoproterozoic (~1.6 Ga) thermal event. This is expressed by emplacement of Hiltaba Suite (HS) intrusive rocks consisting of A- and I-type granites and mafic magmas (Creaser, 1989), and coeval voluminous eruption of

mafic, intermediate and felsic Gawler Range Volcanics (GRV; Blissett et al., 1993, Allen et al., 2008). Affiliation of IOCG mineralization to the ~1.6 Ga event has been determined through dating of magmatic and hydrothermal minerals (Johnson and Cross, 1995, Ciobanu et al., 2013, Jagodinski, 2005, 2014, Courtney-Davies et al., 2016, Apukhtina et al., 2017).

These magmas intruded the Archaean crystalline basement consisting of the Sleaford and Mulgathing Complexes, intrusive rocks of the ~1850 Ma Donington Suite and metasediments of the ~1.76-1.74 Wallaroo Group (Figure 1.4; Fanning et al., 2007). Unlike the aforementioned lithologies the HS and GRV are un-deformed, un-metamorphosed and dominantly flat-lying in the case of the GRV. Mineralisation in all instances shows a strong structural component and is emplaced commonly along E-NE to NE-extensional faults near their intersection with major NNE to NW-trending structures, during a hypothetical short-lived period of NNE-SSE extension (Hayward and Skirrow, 2010). Hiltaba Suite granitoids are, however, not exposed in several deposits, notably Moonta, Prominent Hill, and Carrapateena.

1.2.3 Olympic Dam

Discovered through a targeted exploration campaign based on a sediment-hosted stratabound Cu-deposit model and initially classified as such (Roberts and Hudson, 1983), the Olympic Dam Cu-U-Au-Ag deposit has since been reclassified as a magmatic-hydrothermal IOCG deposit (Oreskes and Einaudi, 1990, 1992, Reeve et al., 1990, Hitzman et al., 1992, Haynes et al., 1995, Johnson and Cross, 1995). The deposit possibly formed below and partially within a sedimentary basin (McPhie et al., 2011, 2016). Olympic Dam contains a resource of 10,400 Mt at 0.77% Cu, 0.25 kg/t, 0.32 g/t Au and 1 g/t Ag which continues to expand as new parts of the deposit are explored despite mining associated depletion (BHP, 2016). The deposit is hosted within one major and a multitude of minor intrusive phases, breccias and bedded

clastic facies collectively referred to as the Olympic Dam Breccia Complex (Reeve et al., 1990; McPhie et al., 2016). This is, in turn, hosted within the Roxby Downs Granite a medium- to coarse-grained, pink, two-feldspar, granite of the Hiltaba Suite, which displays local rapakivi textures (Creaser, 1989; Kontonikas-Charos et al., 2017a). The RDG contains apatite, locally in high concentrations associated with mafic enclaves (Krneta et al., 2016). Alteration is most intense near the deposit and weakens away from it, but is still visible several km away from the main resource (Krneta et al., 2016, Kontonikas-Charos et al., 2017a). Albitization precedes hematite-sericite alteration. The latter eventually obliterates all magmatic minerals, including apatite (Krneta et al., 2016). Albitization is preserved at depth in a few locations within the resource outline (Kontonikas-Charos et al., 2017a).

The transition from unaltered RDG to the centre of the deposit is gradational forming a continuum (observable in whole rock assays as increases in Fe and decreases in Si concentrations) from weakly through to pervasively hematite-sericite altered RDG, granite-rich breccias and finally hematite-rich breccias. Mineralisation is primarily hosted within the latter two lithologies as fine-grained disseminations and lesser vein-hosted mineralisation in the granite breccias on the edge of the deposit (Ehrig et al., 2012). Massive sulphide mineralisation is very rare but m- to dm-sized zones such as those described in Ciobanu et al. (2013) are noted. Chalcopyrite, bornite and chalcocite are the main Cu-hosts with the uranium primarily hosted in uraninite, brannerite and coffinite as well as hematite (Ehrig et al., 2012). Gold and silver occur primarily as electrum and subordinate Ag(±Au) tellurides, acanthite, and as trace elements within sulphides. Apatite is present throughout the orebody but most abundant in association with magnetite on the margins of the deposit (Krneta et al., 2016).

The deposit is enriched in a multitude of elements over crustal averages besides those for which it is exploited, including F, S, C, As, Ba, Bi, Cd, Co, Cr, Fe, In, Mo, Nb, Ni, P, Pb, Sb,

Se, Sn, Te, V, W, Y, Zn and REE, and displays a deposit wide zoning with respect to the mineralogy of the dominant Cu-Fe-sulphides and Fe-oxides whereby hematite+sericite dominate centrally and high within the deposit whereas on its margins and at depth it is subordinate to magnetite (Ehrig et al., 2012, Ciobanu et al., 2017). The deepest and most distal parts of the deposit are dominated by pyrite which transitions into chalcopyrite- followed by bornite- and finally chalcocite-dominant ore with the centre of the deposit being taken up by the barren hematite-quartz-barite breccias (Ehrig et al., 2012).

Zones of high-grade Au-mineralisation, characterised by complex geometries and bonanza grade zones of coarse native gold dominate in domains surrounding the barren hematite-quartz-barite breccias and on the margins of the bedded clastic facies (Reeve, 1990, Hodgkin, 1996, Ehrig et al., 2012). The formation of the high-grade Au-mineralisation has been suggested as being the result of hydrothermal overprinting during the ~514-500 Ma Delamerian Orogeny (Kamenetsky, pers. comm., 2017).

Evidence for hydrothermal overprinting is recorded in numerous hydrothermal minerals from across the deposit (e.g., Ciobanu et al., 2013; Apukhtina et al., 2017). Kirchenbaur et al. (2016) identified significant U-redistribution throughout the deposit accompanying recrystallisation of ~1.6 Ga U-minerals, and moreover, evidence to support addition of U to the deposit during these subsequent events. Such studies have highlighted the complex effects of post-1.6 Ga processes within the deposit. Although the majority of hydrothermal activity and metal deposition is easily attributed to the 1.6 Ga event associated with Hiltaba Suite emplacement and contemporary with the breakup of the Columbia supercontinent. Similarly, overprints associated with regionally significant tectonic events such as the ~1450 Kararan and ~1200-1160 Ma Musgravian orogenies are observed. Moreover, the emplacement of the volumetrically significant Gairdner dyke swarm associated with the breakup of Rodinia and

the aforementioned ~514-500 Ma Delamerian Orogeny, a local expression of Gondwana assembly, are recorded (Ehrig et al., 2016).

Regionally, the Olympic Dam deposit, along with the Wirrda Well and Acropolis prospects, is hosted within a prominent ENE-trending fault-bound block on the southern margin of the Burgoyne Batholith, a 35 by 50 km basement high consisting of felsic and lesser mafic Hiltaba Suite intrusives sub-classified into the Wirrda and White Dam suites (Creaser, 1989), ~1850 Ma Donington suite intrusives (predominantly granite) and metasediments of the 1790-1740 Ma Moonta-Wallaroo Formation. Various felsic through to ultramafic dykes belonging to the Hiltaba Suite, as well as later mafic dykes associated with the Gairdner Dyke Swarm are abundant throughout the Burgoyne Batholith and the deposit itself (Huang et al., 2015, 2016, Apukhtina et al., 2016). Parts of the area are overlain by the Mesoproterozoic Pandurra Formation which may be present within Olympic Dam itself (Cherry, 2017, pers. comm.).

1.2.4 Wirrda Well

The Wirrda Well prospect was discovered shortly after Olympic Dam and has a very similar geophysical response forming a near circular 4 km-wide gravity anomaly, ~6 mGal above background with an overlapping ~1800 nT magnetic anomaly (Vella, 1997). The prospect is obscured by a minimum of 330 m of barren Stuart Shelf sediments and hosted within altered and locally deformed megacrystic K-feldspar granite and mafic dykes of the ~1850 Ma Donington suite (Ehrig, 2013). Mineralisation is developed within a circular steeply-plunging pipe, with multiple apophyses defining the main mineralised zones (North and South). Brecciation and mineralisation is most strongly developed on the granite-mafic contacts (Ehrig et al., 2013). Post-Donington Suite lithologies are represented throughout the prospect as various syn- and post mineralisation mafic dykes and felsic GRV contained to a post-mineralising faulted block in the Northern zone (Ehrig et al., 2013, Huang et al., 2016, Krneta

et al., 2017a). Mineralisation within the prospect has been defined from just below the unconformity to depths in excess of 1.8 km and consists of breccias and vein networks containing magnetite, apatite (±hematite ± carbonate ± quartz ± sulphides) with widespread chlorite and sericite alteration (Krneta et al., 2017a). Wirrda Well displays mineralogical zoning comparable to that of Olympic Dam with regards to Fe-oxides and Cu-(Fe)-sulphides. Deep, high-temperature magnetite-pyrite-apatite assemblages transition with increasing hematite dominance into pyrite-chalcopyrite through chalcopyrite-bornite and finally bornite-chalcocite zones (Ehrig et al., 2013, Krneta et al., 2017a). Apatite is present in both hematite- and magnetite-dominant zones and abundant in the former.

1.2.5 Acropolis

Of the three examples of IOCG mineralisation discussed in detail in this chapter the Acropolis prospect by far has the largest footprint (~50 km^2) as defined by drilling and its almost co-incident 15 km-long magnetic and gravity anomalies (Figure 1.4) and the lowest discovered concentrations of Cu and Au in association with the prolific Fe-oxide mineralisation (e.g., Paterson, 1986). Mineralisation is hosted predominantly within sericite-altered, rhyolitic and dacitic lavas and rare localised dacitic ignimbrite and andesitic lavas of the GRV along with minor thin clastic bedded facies within them as large tabular masses of coarse-grained magnetite (in places replaced by hematite), coarse-grained apatite along with very minor sulphides. Other lithologies in the area include Donington Suite Granite, which is believed to underlie the GRV in the area as well as numerous mafic and felsic dykes that intrude the volcanic pile along with a small Hiltaba Suite Granite (McPhie, pers. comm. 2016). The later intrusives along with the broader SW-portion of the prospect hosts the strongest mineralisation. The high temperature mineralisation, which dominates the prospect consists of a magnetite-apatite-carbonate-K-feldspar-biotite-quartz assemblage that is locally

significantly overprinted by hematite-sericite-chlorite and more rarely carbonate alteration (Krneta et al., 2017a).

1.3 Sample Material

The sample material used in the proceeding studies was sourced from drill core located at the Olympic Dam mine. The sampled drillholes were logged and photographed. Sample selection was made based on collecting material representative of all of the lithologies and hydrothermal assemblages important to the wider hydrothermal environment within Olympic Dam and the two prospects. This was greatly aided by the provision of down-hole assays along with density and magnetic susceptibility data by the company. Samples were prepared as thin sections and polished blocks and examined using optical, scanning electron and cathodoluminescence microscopy.

	Drill hole no.	Depth (m)	Sample ID	Sample Category/Rock type	Chapter
Olympic Dam	Underground grab sample		OD10.1	**High grade Cu-Au ore-** The samples consist of massive bornite with abundant hematite inclusions. Apatite occurs as grains and/or aggregates within bornite and also as milled fragments along veinlets in bornite. No sericite is present but minor chlorite and occasional barite. Other accessories are zircon (metamict) with halos of xenotime, abundant, fine-grained (few μm) florencite as rims along other mineral boundaries, coffinite and brannerite. Trace minerals include U-, REY-bearing phases as dusty inclusions within altered hematite and molybdenite in bornite.	3, 6
			OD10.2		3, 6
			OD10.3		3, 6
	RD2274	372.5	2274-1	**Horn Ridge Quartz Monzonite**-Equigranular, medium-grained K-feldspar-quartz-plagioclase Quartz Monzonite. Lightly hematite-sericite-chlorite altered. Abundant biotite and hornblende has been altered to chlorite. Some ilmenite remains. Abundant apatite in association with accessory magnetite, ilmenite and zircon.	2, 3
	RD2929	401.3	RX7913	**Dolerite dyke**-intensely hematite-sericite-chlorite-carbonate altered dolerite. The majority of primary silicates are replaced by secondary minerals but accessory apatite and Fe-Ti-oxides (hemoilmenite) are largely preserved.	2, 3
		411.1	RX7914		2, 3
	RD2494	588.2	RX7860	**Roxby Downs Granite**- Equigranular, medium to coarse grained K-feldspar-quartz-plagioclase granite. Fresh to pervasively hematite-sericite-chlorite altered. Some samples contain spherical mafic enclaves. Fresh samples are characterised by the presence of biotite, edenite and ilmenite. Locally abundant apatite in association with other accessories such as magnetite, ilmenite and zircon.	2, 3
	RD2492	756	RX7864		2, 3
	RD2495	584	RX7866		2, 3
	RD2280	413	2280-1		2, 3
		416.5	-2		2, 3
		416.9	-3		2, 3
		440	-4		2, 3

		466	-5		2, 3, 5
		467.5	-6		2, 3, 6
		475.7	-7		2, 3
	RD2773	2208.5	2773-1	**Deep Mineralisation**- magnetite-chlorite-carbonate to hematite-sericite altered Roxby Downs Granite and Felsic Unit. Apatite occurs in a number of morphologies ranging from small, unzoned to large, zoned and fractured grains, in isolation as well as large aggregates.	2, 3, 6
		2261	-2		2, 3, 6
		2289.5	-3		2, 3, 6
		2309.5	-4		2, 3, 6
		1998.1	-5		2, 3, 6, 5
	RD2316	580.2	RX6685	**Distal Satellite-** magnetite-chlorite-sericite (minor) altered Roxby Downs Granite. Red-stained K-feldspar present, no plagioclase is present. Apatite occurs in a wide range of sizes. Larger grains are commonly zoned and occur in aggregates in close association to magnetite. Feldspars replaced by chlorite and by an unusual assemblage of molybdenite-bastnäsite.	2, 3
		588.2	RX6687		2, 3
		645.3	RX6691		2, 3
Wirrda Well	WRD33	1781.8	WRD33-1	**Wirrda Well deep zone** consists of chlorite-sericite altered Donington Suite Granite, containing well developed iron-oxide-apatite mineralisation with variable concentrations of pyrite-chalcopyrite. The mineralisation varies from early (magnetite-apatite-sulphide) veinlets through massive (magnetite-hematite-apatite-sulphide) veins and breccias. Iron-oxide dominance alternates locally between magnetite and hematite although overall the earlier is more abundant. Intense chlorite-sericite alteration is texturally destructive. Late apatite-calcite veins cross cut the altered granite and iron-oxide veins and breccias. In such instances the iron-oxides are commonly altered to siderite.	4
		1811	-2		4
		1819.8	-3		4
		1852.2	-4		4
		1854.2	-5		4
		1950.9	-6		4
		2009	-7		4
		2046.9	-8		4
		2057	-9		4
		2063.6	-10		4
	WRD50A	456.1	RX7575	**Wirrda Well Shallow zone** mineralisation is hosted in sericite-altered Donington Granite and coeval mafic dyke. Alteration of the host rock is for the most part texturally destructive although some remnant K-feldspar remains. Chlorite is absent to rare. Fine grained hematite is sometimes intergrown with the sericite along with irregular grains of rutile. Veins and breccias consist primarily of hematite, both primary and lesser martite. Remnant magnetite is observed in some grains. Bornite-chalcocite are the dominant sulphides and host the apatite. Barite is abundant in some samples.	4
		461.5	RX7576		4
		468.5	RX7577		4
		472.2	RX7578		4
		476.2	RX7579		4
Acropolis	ACD1	1025.5	ACD1-1	Magnetite-apatite-quartz-K-feldspar-carbonate-biotite veins and breccias hosted in partially to completely sericite altered rhyolitic and dacitic lavas along with localised dacitic ignimbrite and andesitic lavas all belonging to the GRV and very thin intervals of bedded clastic facies. Fe-oxide veins are most strongly developed in the rhyolitic lavas. Widespread overprinting of the original hydrothermal assemblage is observed as martitization of the magnetite, sericitizations of the hydrothermal K-feldspar and chlorite replacement of biotite. Elsewhere significant replacement of the martite by siderite occurs. Increased copper concentrations are seen in samples where the original assemblage is overprinted by significant sericite, chlorite, barite, hematite and chalcopyrite.	4
		1034.3	-2		4
		1046	-3		4
		1058.9	-4		4
		1082.5	-5		4
		1083.5	-6		4
	ACD2	576.9	ACD2-1		4
		599.5	-2		4
		639.1	-3		4
		647.2	-4		4
	ACD21	675.7	ACD21.2A		4

Table 1.2: Samples examined in the proceeding studies.

1.4 Research objectives and thesis structure

Apatite has been studied previously as a means of gaining insights into the formation of magmatic-hydrothermal deposits. However, such studies have primarily focused on the chemistry of magmatic apatite hosted in the intrusives interpreted as the source of the mineralising fluids (e.g., Belousova et al., 2001, 2002, Cao et al., 2012). Others, focusing on hydrothermal apatite have primarily concentrated their efforts on the study of its role in IOA systems (e.g., Harlov et al., 2002, Bonyadi et al., 2011) and in the context of large studies that compare and contrast the chemistry of many different magmatic and hydrothermal apatite (Mao et al., 2016). In contrast studies which have explored the chemistry and morphology of apatite across the magmatic-to-hydrothermal transition and from various overprinting hydrothermal assemblages are rare (Ismail et al., 2014, Bouzari et al., 2016). These studies have shown that apatite can track the evolution of a hydrothermal system and offer insights into the behaviour of numerous elements, particularly the REY.

Therefore, the study of apatite in the context of the world's largest IOCG deposits presents a unique opportunity to gain insights into its formation and the role played therein by apatite. Similarly, studying apatite in the nearby Wirrda Well and Acropolis prospects could possibly illuminate the key processes and conditions which resulted in the significant differences between them and Olympic Dam. Moreover, geochemically fingerprinting particular processes, fluid conditions or other characteristics associated with the formation of high-grade Cu-Au ore could lead to the development of an important exploration tool.

The samples were examined using optical and scanning electron microscopy. Mineral chemistry was measured using Electron-Probe-Micro-Analysis (EPMA) and Laser-Ablation-Inductively-Coupled-Plasma-Mass-Spectroscopy (LA-ICP-MS). Each chapter (2-6) contains a detailed methodology section outlining the data collection procedures.

Chapter 2 provides a detailed account of the minor element chemistry and morphology of apatite within the Olympic Dam Cu-U-Au-Ag deposit and its host rocks. Samples of Hiltaba Suite intrusive rocks ranging from least-altered through to pervasively altered RDG, HQRM and dolerite dyke, as well as hydrothermal apatite from the periphery of the deposit and at depth were studied. An account of apatite evolution across the magmatic-to-hydrothermal transition is given, together with insights into the magmatic history of the host RDG.

Chapter 3 provides an account of the behaviour of the REY and other trace elements across the same samples, as well as in samples of massive bornite ore containing apatite. This chapter demonstrates the transition in REY chemistry in apatite, marked by a transition from LREE- to MREE-enrichment, from unaltered granite through to early magnetite-dominant hydrothermal assemblages and finally high-grade ore.

Chapter 4 provides an account of apatite morphology as well as trace and minor element chemistry in samples from the Wirrda Well and Acropolis prospects and discusses the differences and similarities between these and from Olympic Dam. The chapter goes on to discuss the potential changes in hydrothermal conditions which could account for the observed changes in apatite REY-signatures along with a discussion of the potential applications of apatite as a pathfinder in mineral exploration.

Following the discovery of minute elongated inclusions of Fe-sulphide minerals within RDG-hosted apatite associated with mafic enclaves, a nanoscale study of this apatite and the contained inclusions was undertaken. Results are described in **Chapter 5.**

In **Chapter 6,** the switch from LREE- to MREE-enriched apatite, which accompanies the transition from magnetite- to hematite-dominant assemblages, has been modelled with regards to REE speciation and activities. This is achieved through utilisation of new thermodynamic data (Migidisov et al., 2016), as well fluid chemistries and parameters derived from published

fluid inclusion data along with previous modelling protocols and assumptions grounded in the mineralogy and petrography of the wider observed mineral assemblage.

Chapter 7, summarises the key findings of all the work conducted as part of this project and goes on to offer some suggestions as to the potential future study directions. This compilation of work has explained some aspects of apatites role in IOCG deposits and the insights it can provide into their formation. However, it has also raised a number of questions and opened up additional avenues for future research. Additional material, including co-authored publications, appendices and conference contributions are given in **Chapter 8**. All references cited within this thesis can be found in **Chapter 9**.

References

Alderton, D.H.M., Pearce, J.A. and Potts, P.J., 1980. Rare earth element mobility during granite alteration: Evidence from southwest England. Earth and Planetary Science Letters 49, 149–165.

Allen, S., McPhie, J., Ferris, G. and Simpson, C., 2008. Evolution and architecture of a large felsic igneous province in western Laurentia: the 1.6 Ga Gawler Range Volcanics, South Australia. Journal of Volcanology and Geothermal Research 172, 132–147.

Apukhtina, O.B., Kamenetsky, V.S., Ehrig, K., Kamenetsky, M.B., McPhie, J., Maas, R., Meffre, S., Goermann, K., Rodermann, T., Cook, N.J. and Ciobanu, C.L., 2016. Postmagmatic magnetite–apatite assemblage in mafic intrusions: a case study of dolerite at Olympic Dam, South Australia. Contributions to Mineralogy and Petrology 171:2 DOI 10.1007/s00410-015-1215-7

Apukhtina, O.B., Kamenetsky, V.S., Ehrig, K., Kamenetsky, M.B., Mass, R., McPhie, J., Ciobanu, C.L. and Cook, N.J., 2017. Deep, early mineralisation at the Olympic Dam Cu-U-Au-Ag deposit, South Australia. Economic Geology, 112 (6), 1531-1542.

Barkov, A.Y. and Nikiforov, A.A., 2016. Compositional variations of apatite, fractionation trends, and a PGE-bearing zone in the Kivakka layered intrusion, nothern Karelia, Russia. The Canadian Mineralogist 54, 475–490.

Barton, M., 2014. Iron oxide (–Cu–Au–REE–P–Ag–U–Co) systems. Treatise on Geochemistry (second edition, volume 13): Amsterdam, Elsevier, 515–541.

Bastrakov, E.N., Skirrow, R.G. and Davidson, G.J., 2007. Fluid evolution and origins of iron oxide Cu-Au prospects in the Olympic Dam District, Gawler Craton, South Australia: Economic Geology 102, 1415–1440.

Bau, M. and Dulski, P., 1995. Comparative study of yttrium and rare-earth element behaviours in fluorine-rich hydrothermal fluids. Contributions to Mineralogy and Petrology 119, 213–223.

Bea, F., Fershater, G. and Corretge, L.G., 1992. The geochemistry of phosphorus in granite rocks and the effect of aluminium. Lithos 29, 43–56.

Belousova, E.A., Walters, S., Griffin, W.L. and O'Reilly, S.Y., 2001. Trace-element signatures of apatites in granitoids from the Mt Isa Inlier, northwestern Queensland. Australian Journal of Earth Sciences 48, 603–619.

Belousova, E.A., Griffin, W.L., O'Reilly, S.Y. and Fisher, N.I., 2002. Apatite as an indicator mineral for mineral exploration: trace-element compositions and their relationship to host rock type. Journal of Geochemical Exploration 76, 45–69.

Belperio, A., Flint, R. and Freeman, H., 2007. Prominent Hill: A hematite-dominated, Iron Oxide Copper-Gold System. Economic Geology 102, 1499–1510.

Bethke, C. and Yeakel, S., 2016, The Geochemist's Workbench® Release 11 - GWB Essentials Guide. https://www.gwb.com/pdf/GWB11/GWBessentials.pdf

BHP, 2016. http://www.bhp.com/-/media/bhp/documents/investors/annual-reports/2016/bhpbillitonannualreport2016.pdf?la=en

Blissett, A.H., Creaser, R.A., Daly, S.J, Flint, D.J. and Parker, A.J., 1993. Gawler Range Volcanics. In: Drexel, J. F., Preiss, W.V., Parker, A.J. (eds.), The Geology of South Australia. Volume 1, The Precambrian: Adelaide, Geological Survey of South Australia, Bulletin 54, 107–131.

Bonyadi, Z., Davidson, G.J., Mehrabi, B., Meffre, S. and Ghazban, F., 2011. Significance of apatite REE depletion and monazite inclusions in the brecciated Se–Chahun iron oxide–apatite deposit, Bafq district, Iran: Insights from paragenesis and geochemistry. Chemical Geology 281, 253–269.

Boudreau A.E. and Krugger F.J. 1990. Variation in the composition of apatite through the Merensky cyclic unit in the western Bushveld Complex. Economic Geology 85, 737–745.

Boudreau, A.E. and McCallum, I.S., 1990. Low temperature alteration of REE-rich chlorapatite from the Stillwater Complex, Montana. American Mineralogist 75, 687–693.

Bouzari, F., Hart, J.R.H., Bissig, T. and Barker, S., 2016. Hydrothermal alteration revealed by apatite luminescence and chemistry: A potential indicator mineral for exploring covered Porphyry Copper Deposits. Economic Geology 111, 1397–1410.

Bowden, B., Fraser, G., Davidson, G.J., Meffre, S., Skirrow, R., Bull, S. and Thompson, J., 2017. Age constraints on the hydrothermal history of the Prominent Hill iron oxide copper-gold deposit, South Australia. Mineralium Deposita 52, 863–881.

Brauand, E., Fowler, M., Storey, C. and Darling, J., 2017. Apatite trace element and isotope applications to petrogenesis and provenance. American Mineralogist, 102, 75–84.

Broom-Fendley, S., Styles, M.T., Appleton, J.D., Gunn, G. and Wall, F., 2016. Evidence for dissolution-reprecipitation of apatite and preferential LREE mobility in carbonatite-derived late-stage hydrothermal processes. American Mineralogist 101, 596–611.

Broom-Fendley, S., Brady, A.E., Wall, F., Gunn, G. and Dawes, W., 2017. REE minerals at the Songwe Hill carbonatite, Malawi: HREE-enrichment in late-stage apatite. Ore Geology Reviews 81, 23–41.

Brugger, J., Lahaye, Y., Costa, S., Lambert, D. and Bateman, R. 2000. Inhomogenous distribution of REE in scheelite and dynamics of Archean hydrothermal systems (Mt. Charlotte and Drysdale gold deposits, Western Australia). Contributions to Mineralogy and Petrology 139, 251–264.

Brugger, J., Etschmann, B., Pownceby, M., Liu, W., Grundler, P. and Brewe, D., 2008. Oxidation state of europium in scheelite: Tracking fluid-rock interaction in gold deposits. Chemical Geology 257, 26–33.

Cao, M., Li, G., Qin, K., Seitmuratova, E.Y. and Liu, Y., 2012. Major and trace element characteristics of apatites in granitoids from Central Kazakhstan: Implications for petrogenesis and mineralization. Resource Geology 62, 63–83.

Cawthorn, R.G., 2013. Rare earth element abundances in apatite in the Bushveld Complex- A consequence of the trapped liquid shift effect. Geology 41, 603–606.

Chen, H.Y., Clark, A.H. and Kyser, T.K., 2010. The Marcona magnetite deposit, Ica, central south Peru: A product of hydrous, iron oxide-rich melt. Economic Geology 105, 1441–1456.

Chew, D.M. and Spikings, R.A., 2015. Geochronology and thermochronology using apatite: time and temperature, lower crust to surface. Elements 11, 189–194.

Ciobanu, C.L., Wade, B., Cook, N.J., Schmidt Mumm, A. and Giles, D., 2013. Uranium-bearing hematite from the Olympic Dam Cu-U-Au deposit, South Australia; a geochemical tracer and reconnaissance Pb-Pb geochronometer: Precambrian Research 238, 129–147.

Ciobanu, C.L., Cook, N.J. and Ehrig, K., 2017. Ore minerals down to the nanoscale: Cu-(Fe)-sulphides from the Iron Oxide Copper Gold deposit at Olympic Dam, South Australia. Ore Geology Reviews 81, 1218–1235.

Clark, J.M., Cook, N.J., Reid, A., Ciobanu, C.L. and Hill, P., 2014. Defining the Style of Mineralisation at the Cairn Hill Magnetite-Sulphide Deposit, Mount Woods Inlier, Gawler Craton, South Australia. Gold14@Kalgoorlie – Western Australia Abstract volume, p. 19–20.

Conor, C., Raymond, O., Baker, T., Teale, G., Say, P. and Lowe, G., 2010. Alteration and Mineralisation in the Moonta-Wallaroo Cu-Au Mining Field Region, Olympic Domain, South Australia. Hydrothermal Iron Oxide Copper-Gold and Related Deposits: A Global Perspective 3, 1–24.

Courtney-Davies, L., Zhu, Z., Ciobanu, C.L., Wade, B.P., Cook, N.J., Ehrig, K., Cabral, A.R. and Kennedy, A., 2016. Matrix-matched iron-oxide laser ablation ICP-MS U-Pb geochronology using mixed solutions standards. Minerals, 6, 85.

Creaser, R.A., 1989. The geology and petrology of Middle Proterozoic felsic magmatism of the Stuart Shelf, South Australia. Unpublished Ph.D. thesis, La Trobe University, Melbourne.

Cross, K.C., 1993. Acropolis and Wirrda Well, in: Drexel, J.F., Preiss, W.V., Parker, A.J., (Eds.), The geology of South Australia. Vol. 1, The Precambrian. Geological Survey of South Australia, South Australia, pp. 138.

Demartin, F., Gramaccioli, C.M., Campostrini, I. and Pilati, T. 2010. Aiolosite, $Na_2(Na_2Bi)(SO_4)_3Cl$, a new sulfate isotypic to apatite from La Fossa Crater, Vulcano, Aeolian Islands, Italy. American Mineralogist 95, 382–385.

Dolivo-Dobrovolsky, V.V. 2006. About a common mistake in treating the crystal structure of apatite. Zapiski Vserossijskogo mineralogičeskogo obseŝtva 135, 123–125.

Ehrig, K., 2013. Geology of the Wirrda Well IOCG deposit. Powerpoint presentation, 10th Annual SA Exploration and Mining Conference, Adelaide. http://www.saexplorers.com.au

Ehrig, K., 2016. The Olympic Dam Fe-oxide Cu-U-Au-Ag deposit: 40 years since discovery. Powerpoint presentation, Australian Earth Sciences Convention 2016, Adelaide.

Ehrig, K., McPhie, J. and Kamanetsky, V.S., 2012. Geology and mineralogical zonation of the Olympic Dam iron oxide Cu-U-Au-Ag deposit, South Australia. In: Hedenquist, J.W., Harris, M., Camus, F. (Eds.), Geology and Genesis of Major Copper Deposits and Districts of the World, a Tribute to Richard Sillitoe. Society of Economic Geologists Special Publication 16, 237–268.

Ehrig, K., Kamenetsky, V.S., McPhie, J., Apukhtina, O., Ciobanu, C.L., Cook, N.J., Kontonikas-Charos, A. and Krneta, S. 2017. The IOCG-IOA Olympic Dam Cu-U-Au-Ag deposit and nearby prospects, South Australia. In: Mineral Resources to Discover, Proceedings 14th SGA Biennial Meeting, Quebec, Canada, August 2017, Volume 3, p. 823-826.

Fanning, C.M., Reid, A. and Teale, G., 2007. A geocronological framework for the Gawler Craton, South Australia. South Australian Geological Survey Bulletin, 55, 258.

Gianfagna, A. and Mazziotti-Tagliani, S., 2014. As-rich apatite from Mt. Calvario: Characterization by micro-raman spectroscopy. The Canadian Mineralogist 52, 799–808.

Goldschmidt, V.M. 1937. The principles of distribution of chemical elements in minerals and rocks. The seventh Hugo Müller Lecture, delivered before the Chemical Society on March 17th, 1937. Journal of the Chemical Society (Resumed), 655–673.

Groves, D.I., Bierlein, F.P., Meinert, L.D. and Hitzman, M.W., 2010. Iron Oxide Copper-Gold (IOCG) Deposits through Earth History: Implications for Origin, Lithospheric Setting, and Distinction from Other Epigenetic Iron Oxide Deposits. Economic Geology 105, 641–654.

Haas, J.R., Shock, E.L. and Sassani, D.C., 1995. Rare earth elements in hydrothermal systems: Estimates of standard partial molal thermodynamic properties of aqueous complexes of the rare earth elements at high pressures and temperatures. Geochimica at Cosmochimica Acta 59, 4329–4350.

Harlov, D.E., 2015. Apatite: a fingerprint for metasomatic processes. Elements 11, 171–176.

Harlov, D.E., Andersson, U.B., Förster, H-J., Nyström, J.O., Dulski, P. and Broman, C., 2002. Apatite–monazite relations in the Kiirunavaara magnetite–apatite ore, northern Sweden: Chemical Geology 191, 47–72.

Harrison, T.M. and Watson, E.B., 1984. The behaviour of apatite during crustal anatexis: equilibrium and kinetic considerations. Geochimica et Cosmochimica Acta 48, 1467–1477.

Haynes, D.W., Cross, K.C., Bills, R.T. and Reed, M.H., 1995. Olympic Dam ore genesis: A fluid-mixing model. Economic Geology 90, 281–307.

Hayward, N. and Skirrow, R.G., 2010. Geodynamic setting and controls on iron oxide Cu-Au (±U) ore in the Gawler Craton, South Australia. In: Porter, T.M (Ed.), Hydrothermal iron oxide copper-gold & related deposits: A global perspective, Volume 3, PGC Publishing, Adelaide,1–27.

Hitzman, M.W., Oreskes, N. and Einaudi, M.T., 1992. Geological characteristics and tectonic setting of Proterozoic iron oxide (Cu-U-Au-REE) deposits. Precambrian Research 58, 241–287.

Hodgkin, T., 1996. High-grade gold occurrence at Olympic Dam Mine. Mesa Journal 1, 24.

Huang, Q., Kamenetsky, V.S., McPhie, J., Ehrig, K., Meffre, S., Maas, R., Thompson, J., Kamenetsky, M., Chambefort, I., Apukhtina, O. and Hu, Y., 2015. Neoproterozoic (ca. 820-830 Ma) mafic dykes at Olympic Dam, South Australia: Links with the Gairdner Large Igneous Province. Precambrian Research 271, 160–172.

Huang, Q., Kamenetsky, V.S., Ehrig, K., McPhie, J., Kamenetsky, M., Cross, K., Meffre, S., Agangi, A., Chambefort, I., Direen, N.G., Maas, R. and Apukhtina, O., 2016. Olivine-phyric basalt in the Mesoproterozoic Gawler silicic large igneous province, South Australia: Examples at the Olympic Dam Iron Oxide Cu–U–Au–Ag deposit and other localities. Precambrian Research 281, 185–199.

Hughes, J.M., 2015. The many facets of apatite. American Mineralogist 100, 1033–1039.

Hughes, J.M. and Rakovan, J.F., 2002. The crystal structure of apatite, $Ca_5(PO4)_3$ (F,OH,Cl). Reviews in Mineralogy and Geochemistry 48, 1–12.

Hughes, J.M. and Rakovan, J.F., 2015. Structurally robust, chemically diverse: Apatite and apatite supergroup minerals. Elements 11, 165–170.

Hughes, J.M., Cameron, M. and Crowley, K.D. 1989. Structural variations in natural F, OH and Cl apatites. American Mineralogist 74, 870–876.

Hughes, J.M., Heffernan, K.M., Goldoff, B. and Nakvasil, H. 2014. Cl-rich fluorapatite, devoid of OH, from the three peaks area, Utah: The first reported structure of natural Cl-rich fluorapatite. The Canadian Mineralogist 52, 643–652.

Ismail, R., Ciobanu, C.L., Cook, N.J., Teale, G.S., Giles, D., Schmidt Mumm, A. and Wade, B., 2014. Rare earths and other trace elements in minerals from skarn assemblages, Hillside iron oxide–copper–gold deposit, Yorke Peninsula, South Australia. Lithos 184–187, 456-477.

Jagodzinski, E.A., 2005. Compilation of SHRIMP U-Pb Geochronological Data. Olympic Domain, Gawler Craton, South Australia, 2001-2003. Geoscience Australia, Record 2005/20.

Jagodzinski, E.A., 2014. The age of magmatic and hydrothermal zircon at Olympic Dam, Australian Earth Sciences Convention Proceedings, Geological Society of Australia Abstracts 110, 260.

Johnson, J.P. and Cross, K.C., 1995. U-Pb geochronological constraints on the genesis of Olympic Dam Cu-U-Au-Ag deposit, South Australia. Economic Geology 88, 1046–1063.

Jungck, M.H.A. and Niederer, F.R., 2017. From supernova to Solar System: Few years only; first Solar System components apatite and spinel determined. Polar Science 11, 54–71.

Kampf, A.R. and Housley, R.M. 2011. Fluorphosphohedyphane, $Ca_2Pb_3(PO_4)_3F$, the first apatite supergroup mineral with essential Pb and F. American Mineralogist 96, 423–429.

Kelley, K.D., Eppinger, R.G., Lang, J., Smith, S.M. and Fey, D.L., 2011. Porphyry Cu indicator minerals in till as an exploration tool: example from the giant Pebble porphyry Cu-Au-Mo deposit, Alaska, USA. Geochemistry: Exploration, Environment, Analysis 11, 321–334.

Kelly, S.R., Rakovan, J. and Hughes, J.M., 2017. Column anion arrangements in chemically zoned ternary chlorapatite and fluorapatite from Kurokura, Japan. American Mineralogist 102, 720–727.

Kirchenbaur, M., Maas, R., Ehrig, K., Kamenetsky, V.S., Strub, E., Ballhaus, C. and Munker, C., 2016. Uranium and Sm isotope studies of the supergiant Olympic Dam Cu-Au-U-Ag deposit, South Australia. Geochimica et Cosmochimica Acta 180, 15–32.

Konecke, B.A., Fiege, A., Simon, A.C., Parat, F. and Stechern, A., 2017. Co-variability of S^{6+}, S^{4+}, and S^{2-} in apatite as a function of oxidation state: Implications for a new oxybarometer. American Mineralogist 102, 548–557.

Kontonikas-Charos, A., Ciobanu, C.L. and Cook, N.J., 2014. Albitization and redistribution of REE and Y in IOCG systems: Insights from Moonta-Wallaroo, Yorke Peninsula, South Australia. Lithos 208, 178–201.

Kontonikas-Charos, A., Ciobanu, C.L., Cook, N.J., Ehrig, K., Krneta, S. and Kamenetsky, V.S. 2017a. Feldspar evolution in the Roxby Downs Granite, host to Fe-oxide Cu-Au-(U) mineralisation at Olympic Dam, South Australia. Ore Geology Reviews 80, 838–859.

Kontonikas-Charos, A., Ciobanu, C.L., Cook, N.J., Ehrig, K., Ismail, R., Krneta, S. and Basak, A., 2017b. Feldspar mineralogy and rare earth element (re)mobilization in iron-oxide copper gold systems from South Australia: a nanoscale study. Mineralogical Magazine. (in press) DOI: 10.1180/minmag.2017.081.040.

Krause, J., Harlov, D.E., Pushkarev, E.V. and Brugmann, E.G., 2013. Apatite and clinopyroxene as tracers for metasomatic processes in nepheline clinopyroxenites of Uralian-Alaskan-type complexes in the Ural Mountains, Russian Federation. Geochimica et Cosmochimica Acta 121, 503–521.

Krneta, S., Ciobanu, C.L., Cook, N.J., Ehrig, K. and Kontonikas-Charos, A., 2016. Apatite at Olympic Dam, South Australia: a petrogenetic tool. Lithos 262, 470–485.

Krneta, S., Cook, N.J., Ciobanu, C.L., Ehrig, K. and Kontonikas-Charos, A., 2017a. The Wirrda Well and Acropolis prospects Gawler Craton, South Australia: insights into evolving fluid conditions through apatite chemistry. Journal of Geochemical Exploration 181, 276–291.

Krneta, S., Ciobanu, C.L., Cook, N.J., Ehrig, K. and Kontonikas-Charos, A. 2017b. Rare earth element behaviour in apatite from the Olympic Dam Cu-U-Au-Ag deposit, South Australia. Minerals 7(8), 135.

Ladenburger, S., Marks, M.A.W., Upton, B., Hill, P., Wenzel, T., and Markl, G., 2016. Compositional variation of apatite from rift-related alkaline igneous rocks of the Gardar Province, South Greenland. American Mineralogist 101, 612–626.

Li, H., and Hermann, J., 2017. Chlorine and fluorine partitioning between apatite and sediment melt at 2.5 GPa, 800 ^{o}C: A new experimentally derived thermodynamic model. American Mineralogist 102, 580–594.

Liu, W., Mei, Y., Etschmann, B., Brugger, J., Pearce, M., Ryan, C.G., Borg, S., Wykes, J., Kappen, P., Paterson, D., Boesenberg, U., Garrevoet, J., Moorhead, G. and Falkenberg, G.,

2017. Arsenic in hydrothermal apatite: Oxidation state, mechanism of uptake, and comparison between experiments and nature. Geochimica et Cosmochimica Acta 196, 144–159.

Lottermoser, B.G., 1992. Rare earth elements and hydrothermal ore formation processes. Ore Geology Reviews 7, 25–41.

Luo, Y., Hughes, J.M., Rakovan, J. and Pan, Y.M. 2009. Site preference of U and Th in Cl, F, and Sr apatites. American Mineralogist 94, 345–351.

Luo, Y., Rakovan, J., Tang, Y., Lupulescu, M., Hughes, J.M. and Pan, Y., 2011. Crystal chemistry of Th in fluorapatite. American Mineralogist 96, 23–33.

Majka, J., Harlov, D.E., Jonsson, E., Högdahl, K. and Persson-Nilsson, K., 2016. Fluorapatite-monazite-allanite relations in the Grängesberg apatite-iron oxide ore district, Bergslagen, Sweden. American Mineralogist 101, 1769–1783.

Mao, M., Rukhlov, A.S., Rowins, S.M., Spence, J. and Coogan, L.A., 2016. Apatite trace element compositions: A robust new tool for mineral exploration. Economic Geology 111, 1187–1222.

Marks, M.A.W., Thomas, W., Whitehouse, M.J., Loose, M., Zack, T., Barth, M., Worgard, L., Krasz, V., Eby, G.N., Stosnach, H. and Markl, G., 2012. The volatile inventory (F, Cl, Br, S, C) of magmatic apatite: An integrated analytical approach. Chemical Geology 291, 241–255.

Marks, A.W., Scharrer, M., Landenburger, S. and Markl, G., 2014. Comment on "Apatite: A new redox proxy for silicic magmas?". Geochimica et Cosmochimica Acta 183, 267–270.

McPhie, J., Kamenetsky, V., Chambefort, I., Ehrig, K. and Green, N., 2011. Origin of the supergiant Olympic Dam Cu-U-Au-Ag deposit, South Australia: Was a sedimentary basin involved? Geology 39, 795–798.

McPhie, J., Orth, K., Kamenetsky, V., Kamenetsky, M. and Ehrig, K., 2016. Characteristics, origin and significance of Mesoproterozoic bedded clastic facies at the Olympic Dam Cu-U-Au-Ag deposit, South Australia. Precambrian Research 276, 85–100.

Mercier, P.H.J., Le Page, Y., Whitfield, P.S., Mitchell, L.D., Davidson, I.J. and White, T.J. 2005. Geometrical parameterization of the crystal chemistry of P63/m apatites: comparison with experimental data and *ab initio* results. Acta Crystallographica B61, 635–655.

Migdisov, A.A. and Williams-Jones, A.E., 2006a. A spectrophotometric study of Erbium (III) speciation in chloride solutions at elevated temperatures. Chemical Geology 234, 17–27.

Migdisov, A.A. and Williams-Jones, A.E., 2006b. An experimental study of the solubility and speciation of neodymium (III) fluoride in F-bearing aqueous solutions. Geochimica et Cosmochimica Acta 71, 3056–3069.

Migdisov, A.A. and Williams-Jones, A.E., 2008. A spectrophotometric study of Nd(III), Sm(III) and Er(III) complexation in sulfate-bearing solutions at elevated temperatures. Geochimica et Cosmochimica Acta 72, 5291–5303.

Migdisov, A.A. and Williams-Jones, A.E., 2014. Hydrothermal transport and deposition of the rare earth elements by fluorine-bearing aqueous liquids. Mineralium Deposita 49, 987–997.

Migdisov, A.A., Reukov, V.V. and Williams-Jones, A.E., 2006. A spectrophotometric study of neodymium(III) complexation in sulfate solutions at elevated temperatures. Geochimica et Cosmochimica Acta 70, 983–992.

Migdisov, A.A., Williams-Jones, A.E., Normand, C. and Wood, S.A., 2008. A spectrophotometric study of samarium (III) speciation in chloride solutions at elevated temperatures. Geochimica et Cosmochimica Acta 72, 1611–1625.

Migdisov, A.A., Williams-Jones, A.E. and Wagner, T., 2009. An experimental study of the solubility and speciation of the Rare Earth Elements (III) in fluoride- and chloride-bearing

aqueous solutions at temperatures up to 300 ^{o}C. Geochimica et Cosmochimica Acta 73, 7087–7109.

Migdisov, A.A., Williams-Jones, A.E., Brugger, J., and Caporuscio, F.A., 2016. Hydrothermal transport, deposition, and fractionation of the REE: Experimental data and thermodynamic calculations. Chemical Geology 439, 13–42.

Miles, A.J., Graham, C.M., Hawkesworth, C.J., Gillespie, M.R., Hinton, R.W., Bromiley, G.D. and EMMAC, 2014. Apatite: A new redox proxy for silicic magmas?". Geochimica et Cosmochimica Acta 132, 101–119.

Oelkers, E.H. and Montel, J-M., 2008. Phosphates and nuclear waste storage. Elements 4, 113–116.

Oreskes, M. and Einaudi M.T., 1990. Origin of rare earth element-enriched heamatite breccias at the Olympic Dam Cu-U-Au-Ag deposit, Roxby Downs, South Australia. Economic Geology 85, 1–28.

Oreskes, M. and Einaudi M.T., 1992. Origin of Hydrothermal Fluids at Olympic Dam: Preliminary Results from Fluid Inclusions and Stable Isotopes. Economic Geology 87, 64–90.

Pan, Y. and Fleet, M.E., 2002. Compositions of the apatite-group minerals: Substitution mechanisms and controlling factors. Reviews in Mineralogy and Geochemistry 48, 13–49.

Pasero, M., Kampf, A., Ferraris, C., Pekov, I.V., Rakovan, J. and White, T., 2010. Nomenclature of the apatite supergroup minerals. European Journal of Mineralogy 22, 163–179.

Paterson, A.J., 1986. The Acropolis Prospect. In: A.J Parker, C.M. Horn, B.P.J Stevens, H.L Paterson (eds.), Geological Excursions of the Adelaide Geosyncline, Gawler Craton and Broken Hill Regions. Geological Society of Australia (S.A. Division), p. 17–27.

Peng, G., Luhr, J.F. and McGee, J.J., 1997. Factors controlling sulfur concentrations in volcanic apatite. American Mineralogist 82, 1210–1224.

Piccoli, P.M. and Candela, P.A., 1994. Apatite in felsic rocks: a model for the estimation on initial halogen concentrations in the Bishop Tuff (Long Valley) and Tuolumne Intrusive Suite (Sierra Nevada Batholith) magmas. American Journal of Science 294, 92–135.

Piccoli, P.M. and Candela, P.A., 2002. Apatite in Igneous Systems. Reviews in Mineralogy and Geochemistry 48, 255–292.

Pollard, P.J., 2006. An intrusion-related origin for Cu–Au mineralization in iron oxide–copper–gold (IOCG) provinces. Mineralium Deposita 41, 187.

Porter, T.M., 2010. Current understanding of iron oxide associated-alkali altered mineralised systems. Part 1. An overview, in Porter, T.M., ed., Hydrothermal iron oxide copper-gold & related deposits: A global perspective: Adelaide, Australia, PGC Publishing 3, 5–32.

Putnis, A., 2002. Mineral replacement reactions: from macroscopic observations to microscopic mechanisms. Mineralogical Magazine 66, 689–708.

Reeve, J.S. 1990. The discovery and evaluation of gold mineralization within the Olympic Dam deposit, South Australia, in Glasson, K.R., Rattigan, J.H. (eds.), Geological aspects of the discovery of some important mineral deposits in Australia: Australasian Institute of Mining and Metallurgy, Monograph 17, 57–58.

Reeve, J.S., Cross, K.C., Smith, R.N. and Oreskes, N., 1990. Olympic Dam copper-uranium-gold-silver deposit. In: Hughes, F.E. (ed.), Geology of the Mineral Deposits of Australia and Papua New Guinea: Australasian Institute of Mining and Metallurgy, Monograph 14, 1009–1035.

Reid, A.J., Swain, G.S., Mason, D. and Maas, R., 2011. Nature and timing of Cu-Au-Zn-Pb mineralisation at Punt Hill, eastern Gawler Craton. MESA Journal 60, 7–17.

Roberts, D.E. and Hudson, G.R.T., 1983. The Olympic Dam copper-uranium-gold deposit, Roxby Downs, South Australia. Economic Geology 78, 799–822.

Rønsbo, J.G., 1989. Coupled substitutions involving REE's and Na and Si in apatites in alkaline rocks from Ilimaussaq, South Greenland, and the petrological implications. American Mineralogist 74, 896–901.

Schlegel, T.U. and Heinrich, C.A., 2015. Lithology and hydrothermal alteration control the distribution of copper grade in the Prominent Hill Iron Oxide-Copper-Gold deposit (Gawler Craton, South Australia). Economic Geology 110, 1953–1994.

Schlegel, T.U., Wagner, T., Boyce, A. and Heinrich, C.A., 2016. A magmatic source of hydrothermal sulfur for the Prominent Hill deposit and associated prospects in the Olympic iron oxide copper-gold (IOCG) province of South Australia. Ore Geology Reviews (*in press*), doi: 10.1016/j.oregeorev.2016.09.002

Skirrow, R.G., Bastrakov, E.N., Davidson, G., Raymond, O.L. and Heithersay, P., 2002. The geological framework, distribution and controls of Fe-oxide Cu-Au mineralisation in the Gawler Craton, South Australia. Part II- Alteration and mineralisation. In: Porter, T.M (Ed.), Hydrothermal Iron Oxide Copper-Gold & Related Deposits: A Global Perspective, Volume 2, PGC Publishing, Adelaide, 33–47.

Skirrow, R.G., Bastrakov, E.N., Barovich, K., Fraser, G.L., Creaser, R., Fanning, M.C., Raymond, O.L. and Davidson, G.J., 2007. Timing of iron oxide Cu-Au-(U) hydrothermal activity and Nd isotope constraints on metal sources in the Gawler craton, South Australia. Economic Geology 102, 1441–1470.

Smith, M. and Henderson, P., 2000. Preliminary fluid inclusions constraints on fluid evolution in the Bayan Obo Fe-REE-Nb deposit, Inner Mongolia, China. Economic Geology 95, 1371.

Smith, M., Henderson, P., Jeffries, T., Long, J. and Williams, C., 2004. The rare earth elements and uranium in garnets from the Beinn an Dubhaich Aureole, Skye, Scotland, UK: constraints on processes in a dynamic hydrothermal system. Journal of Petrology 45, 457–484.

Storey, C.D. and Smith, M.P., 2017. Metal source and tectonic setting of iron oxide-copper-gold (IOCG) deposits: Evidence from an in situ Nd isotope study of titanite from Norrbotten, Sweden. Ore Geology Reviews 81, 1287–1302.

Streck, M.J. and Dilles, J.H., 1998. Sulfur evolution of oxidized magmas as recorded in apatite from a porphyry copper batholith. Geology 26, 523–526.

Takashima, R., Kuwabara, S., Sato, T., Takemura, K. and Nishi, H., 2017. Utility of trace elements in apatite for discrimination and correlation of Quaternary ignimbrites and co-ignimbrite ashes, Japan. Quaternary Geochronology 41, 151–162.

Teiber, H., Marks, M.A.W., Arzamastsev, A.A., Wenzel, T. and Markl, G., 2015. Compositional variation in apatite from various host rocks: clues with regards to source composition and crystallization conditions. Journal of Mineral Geochemistry 192, 151–167.

Ustunisik, G., Nekvasil, H. and Lindsley, D., 2011. Differential degassing of H_2O, Cl, F and S: Potential effects on lunar apatite. American Mineralogist 96, 1650–1653.

van Dongen, M., Weinberg, R.F. and Tomkins, A.G., 2010. REE-Y, Ti, and P remobilization in magmatic rocks by hydrothermal alteration during Cu-Au Deposit formation. Economic Geology 105, 763–776.

van Hinsberg, V.J., Migdisov, A.A and Williams-Jones, A.E. 2010. Reading the mineral record of fluid composition from element partitioning. Geology 38, 847–850.

Vella, L., 1997. Interpretation and modelling, based on petrophysical measurements, of the Wirrda Well potential field anomaly, South Australia. Exploration Geophysics 28, 299–306.

Vella, L. and Cawood, M., 2006. Carrapateena: discovery of an Olympic Dam – style deposit. Preview, Issue 122 (June 2006), CSIRO Publishing, 26–30.

Wang, Y., Wang, Y. and Merino, E., 1995. Dynamic weathering model: Constraints required by coupled dissolution and pseudomorphic replacement. Geochimica et Cosmochimica Acta 59, 1559–1570.

Webster, J.D. and Piccoli, P.M., 2015. Magmatic apatite: a powerful, yet deceptive mineral. Elements 11, 177–182.

Webster, J.D., Tappen, D. and Mandeville, C.W., 2009. Partitioning behaviour of chlorine and fluorine in the system apatite-melt-fluid: II. Felsic silicate systems at 200 MPa. Geochimica et Cosmochimica Acta 73, 559–581.

White, T.J. and Dong, Z.L., 2002. Structural derivation and crystal chemistry of apatites. Acta Crystallographica B59, 1–16.

Williams, P.J., Barton, M.D., Johnson, D.A., Fontboté, L., De Haller, A., Mark, G., Oliver, N.H. and Marschik, R., 2005. Iron oxide copper-gold deposits: Geology, space-time distribution, and possible modes of origin. Economic Geology, 371–405.

Williams-Jones, A.E., Samson, I.M. and Olivo, G.R., 2000. The genesis of hydrothermal fluorite-REE deposits in the Gallinas Mountains, New Mexico. Economic Geology 95, 327–341.

Xing, C.M. and Wang, C.Y., 2017. Cathodoluminescence images and trace element compositions of fluorapatite from the Hongge layered intrusion in SW China: A record of prolonged crystallization and overprinted fluid metasomatism. American Mineralogist 102, 1390–1401.

Yi, H., Balan, E., Gervais, C., Segalen, L., Fayon, F., Roche, D., Person, A., Morin, G., Guillaumet, M., Blanchard, M., Lazzeri, M. and Babonneau, F., 2013. A carbonate-fluoride defect model for carbonate-rich fluorapatite. American Mineralogist 98, 1066–1069.

Zhu, C. and Sverjensky, D.A., 1991. Partitioning of F–Cl–OH between minerals and hydrothermal fluids. Geochimica et Cosmochimica Acta 55, 1837–1858.

CHAPTER 2

APATITE AT OLYMPIC DAM, SOUTH AUSTRALIA: A PETROGENETIC TOOL

Sasha Krneta[1], Cristiana L. Ciobanu[2], Nigel J. Cook[2], Kathy Ehrig[3], Alkis Kontonikas-Charos[1]

[1]*School of Physical Sciences, The University of Adelaide, Adelaide, S.A., 5005, Australia*

[2]*School of Chemical Engineering, The University of Adelaide, Adelaide, S.A., 5005, Australia*

[3]*BHP Olympic Dam, Adelaide, SA 5000, Australia*

Paper published in Lithos, 262, 470-485

Statement of Authorship

Title of Paper	Apatite at Olympic Dam, South Australia: A petrogenetic tool
Publication Status	☑ Published ☐ Accepted for Publication ☐ Submitted for Publication ☐ Unpublished and Unsubmitted w ork w ritten in manuscript style
Publication Details	Krneta, S., Ciobanu, C.L., Cook, N.J., Ehrig, K. and Kontonikas-Charos, A., 2016. Apatite at Olympic Dam, South Australia: a petrogenetic tool. Lithos, 262, 470-485.

Principal Author

Name of Principal Author (Candidate)	Sasha Krneta
Contribution to the Paper	Collected sample material, devised a plan for and performed analytical work, processed and interpreted data , wrote manuscript and acted as corresponding author.
Overall percentage (%)	60
Certification:	This paper reports on original research I conducted during the period of my Higher Degree by Research candidature and is not subject to any obligations or contractual agreements with a third party that would constrain its inclusion in this thesis. I am the primary author of this paper.
Signature	Date 13/9/17

Co-Author Contributions

By signing the Statement of Authorship, each author certifies that:

the candidate's stated contribution to the publication is accurate (as detailed above);

permission is granted for the candidate in include the publication in the thesis; and

the sum of all co-author contributions is equal to 100% less the candidate's stated contribution.

Name of Co-Author	Cristiana Ciobanu
Contribution to the Paper	Supervised development of work, assisted in defining direction of research, provided assistance in the collection of analytical data, assisted with data interpretation and helped with manuscript preparation.
Overall percentage (%)	25
Signature	Date 13. Sept 2017

Name of Co-Author	Nigel Cook
Contribution to the Paper	Supervised development of work, assisted in defining direction of research, assisted with data interpretation and helped with manuscript preparation.
Overall percentage (%)	12
Signature	Date 13/9/17

Name of Co-Author	Kathy Ehrig		
Contribution to the Paper	Assisted in defining the direction of research, assisted with data interpretation and evaluated manuscript.		
Overall percentage (%)	2		
Signature		Date	13/09/17

Name of Co-Author	Alkis Kontonikas-Charos		
Contribution to the Paper	Provided advice on samples and evaluated manuscript.		
Overall percentage (%)	1		
Signature		Date	13/09/17

Lithos 262 (2016) 470–485

Contents lists available at ScienceDirect

Lithos

journal homepage: www.elsevier.com/locate/lithos

Apatite at Olympic Dam, South Australia: A petrogenetic tool

Sasha Krneta [a,*], Cristiana L. Ciobanu [b], Nigel J. Cook [b], Kathy Ehrig [c], Alkis Kontonikas-Charos [a]

[a] School of Physical Sciences, University of Adelaide, Adelaide, SA 5000, Australia
[b] School of Chemical Engineering, University of Adelaide, Adelaide, SA 5000, Australia
[c] BHP Billiton, Olympic Dam, Adelaide, SA 5000, Australia

ARTICLE INFO

Article history:
Received 26 April 2016
Accepted 24 July 2016
Available online 6 August 2016

Keywords:
Fluorapatite
Olympic Dam
Chemical composition
Hydrothermal fluids
Grain-scale zoning

ABSTRACT

The >10,000 million tonne Olympic Dam Cu–Au–U–Ag deposit, (eastern Gawler Craton, South Australia) is one of the largest orebodies in the World. The deposit is hosted within the Olympic Dam Breccia Complex, placed at the centre of, and resulting from multiple brecciation and Fe-metasomatism of the Roxby Downs Granite (RDG). The latter is part of a larger batholith emplaced at ~1.6 Ga. Apatite petrography and chemistry were studied in non-mineralised RDG and coeval granitoids and dolerites, as well as in mineralised RDG from deep (>2 km) and distal (2.7 km to NE) locations. In both latter cases, although the mineralisation corresponds to the same, early chalcopyrite–pyrite–magnetite ± hematite stage identified in the outer and deeper zones of the deposit itself, the character of granite alteration differs: sericite–chlorite alteration with all feldspar replaced in the deep location; and red-stained K-feldspar on top of prevailing albitization in the distal location. Close-to end-member fluorapatite is a key accessory mineral in all igneous rocks and a common product of early hydrothermal alteration within mineralised granite. Variations in habit, morphology and textures correlate with chemical trends expressed as evolving Cl/F ratios, and concentrations of REE + Y (hereafter REY), Sr, Mn, S, Si and Na. Magmatic apatite is unzoned in the dolerite but features core to REY-enriched rim zonation in the granitoids. Increases in Cl- and Sr-contents correlate with rock basicity. Calculation of Cl in the vapour phase relative to melt at the apatite saturation temperature for zoned apatite in the RDG shows higher values for grains with inclusion-rich cores associated with mafic enclaves, concordant with assimilation of exotic material during magma crystallisation. Hydrothermal alteration of magmatic apatite is most varied in the dolerite where interaction with fluids is expressed as subtle changes in Cl- versus F- and REY-enrichment, and most importantly, S-enrichment in grains adjacent to crosscutting, carbonate–sulphide-bearing veins. Highly acidic fluids, which not only corroded apatite but also quartz, led to recycling of REY via subsequent crystallisation of discrete REY-bearing species, notably monazite. Hydrothermal apatite often occurs as interstitial aggregates and displays a wider range of textures indicating variability in local growth conditions and/or sustained interaction with evolving hydrothermal fluids. Apatite from the deep mineralisation is richer in Cl whereas increases in ΣREY and S correlate with higher Si in both deep and distal cases. The co-correlation between Na and S in apatite from distal mineralisation ties apatite crystallisation to replacement of albite by sericite + chlorite. The textural and chemical variation of apatite relative to magmatic to hydrothermal transition suggests that the mineral represents a petrogenetic tool to gain insights into mineralising processes at Olympic Dam. Apatite evolution clearly played a key contributing role in the elevated REY-concentrations seen at Olympic Dam. The marked differences in apatite chemistry between mineralised and non-mineralised lithologies show promise for potential application as a tool in mineral exploration, in which apatite chemistry represents a means for outlining spatial position within an alteration envelope, or identifying if a particular alteration system is barren or fertile with respect to Cu–Au mineralisation.

1. Introduction

Apatite is a ubiquitous accessory component in igneous rocks, as well as a common hydrothermal mineral. It generally hosts the majority of the whole rock P and a significant portion of the total budget of rare earth elements (REE) and Y (Piccoli and Candela, 2002).

Apatite chemistry is complex and can be defined by the formula $A_5(XO_4)_3Z$ (Pasero et al., 2010), where A is largely occupied by Ca^{2+} in two different positions. The 'A' site also hosts Sr^{2+}, Ba^{2+}, Mg^{2+}, Mn^{2+}, Fe^{2+}, Cd^{2+}, Na^{+}, Eu^{2+}, Y^{3+} and REE^{3+}. The X position is dominated by P^{5+}, as (PO_4), but can also host other small highly-

* Corresponding author.
E-mail address: Sasha.krneta@adelaide.edu.au (S. Krneta).

http://dx.doi.org/10.1016/j.lithos.2016.07.033
0024-4937/

charged cations such as V^{5+}, As^{5+}, Si^{4+} and S^{6+}. Halogens (F and Cl) and OH^{-} occupy the Z position and define the three named minerals, fluorapatite, chlorapatite and hydroxyapatite; most natural apatite contains all three end-members in varying proportions (cf. Hughes and Rakovan, 2015).

Although many of the aforementioned elements substitute directly into apatite, others, such as $(Y,REE)^{3+}$ or S^{6+}, require charge compensation via coupled substitution in order to be incorporated into the apatite structure in Ca^{2+} and P^{5+} positions, respectively. The proposed relevant coupled substitutions (Rønsbo, 1989; Pan and Fleet, 2002):

$$REE^{3+} + Na^{+} = 2Ca^{2+}$$
$$REE^{3+} + SiO_4^{4-} = Ca^{2+} + PO_4^{3-}$$
$$SO_4^{2-} + Na^{+} = PO_4^{3-} + Ca^{2+}$$
$$SO_4^{2-} + SiO_4^{4-} = 2PO_4^{3-}$$

Elemental substitution in apatite is governed by parameters inherent to the apatite structure, as seen in the uptake of REE^{3+} whereby those elements with atomic radii closest to Ca^{2+} (i.e., Sm–Nd) are most readily substituted. However, variation in apatite chemistry can depend on external parameters such that apatite is considered an ideal mineral to fingerprint metasomatic processes and as a tool for tracking fluid interaction in igneous and metamorphic rocks (e.g., Harlov, 2015; Webster and Piccoli, 2015).

Numerous studies have focused on apatite as a petrogenetic indicator of metallogenic processes in different settings. Examples include Iron-oxide–Apatite (Harlov et al., 2002; Bonyadi et al., 2011; Jonsson et al., 2016), Iron-oxide–Copper–Gold (IOCG) (Belousova et al., 2001; Ismail et al., 2014; Kontonikas-Charos et al., 2014), reef-type PGE (Boudreau and Kruger, 1990), and magmatic–hydrothermal systems (Streck and Dilles, 1998; Cao et al., 2012).

In this contribution, the textural and geochemical evolution of apatite is described in the context of the magmatic-to-hydrothermal transition associated with metasomatism and early mineralisation in the Olympic Dam Cu–Au–U–Ag deposit, South Australia. Apatite is described in relation to the igneous chemistry, different types of alteration, and mineralisation types, as well as in the context of magmatic evolution and interaction with hydrothermal fluids. Particular emphasis is placed on the utility of apatite to track changes in fluids, its potential use as a petrogenetic tool, and as a mineralisation pathfinder in IOCG systems.

2. Deposit background

The Olympic Dam (OD) Cu–Au–U–Ag deposit (10,100 Mt tonnes @ 0.78% Cu, 0.25 kg/t U_3O_8, 0.3 g/t Au, 2 g/t Ag; BHP Billiton, 2015) is located on the eastern margin of the Archean to Mesoproterozoic Gawler Craton, South Australia. It is by far the largest deposit within the Olympic Cu–Au Province (Skirrow et al., 2007), which stretches some 700 km N–S, and also encompasses other IOCG deposits and prospects such as Prominent Hill, Carrapateena, Hillside, Cairn Hill, Wirrda Well, and Acropolis. All are temporally and spatially associated with a major tectonothermal event at 1.6 Ga (e.g., Hayward and Skirrow, 2010).

The oldest rocks in the OD area comprise deformed, syntectonic granitoids of the ~1.85 Ga Donington Suite (Jagodzinski, 2005), located SE of the deposit area. Regionally, although well outside the deposit perimeter, these are overlain by ~1.76–1.74 Ga meta-sedimentary sequences of the Wallaroo Group (Jagodzinski, 2005). During the ~1.6 Ga tectonothermal event, extensive emplacement of felsic through to mafic–ultramafic intrusive rocks (Hiltaba Intrusive Suite; HIS) occurred coevally with the eruption of the volumetrically large bimodal Gawler Range Volcanics (GRV; Blissett et al., 1993). HIS granitoids include the Roxby Downs Granite (RDG) and Horn Ridge Quartz Monzonite (HRQM) (Creaser, 1989; Fig. 1). Olympic Dam and other deposits in the province are covered by Neoproterozoic, Cambrian, and later sedimentary successions up to hundreds of metres in thickness.

The OD deposit is confined to the Olympic Dam Breccia Complex (ODBC; Reeve et al., 1990), and is hosted within the Roxby Downs Granite (RDG) (1588 ± 4 Ma; Creaser, 1989; Johnson and Cross, 1995). The ODBC is made up primarily of various hydrothermal breccias,

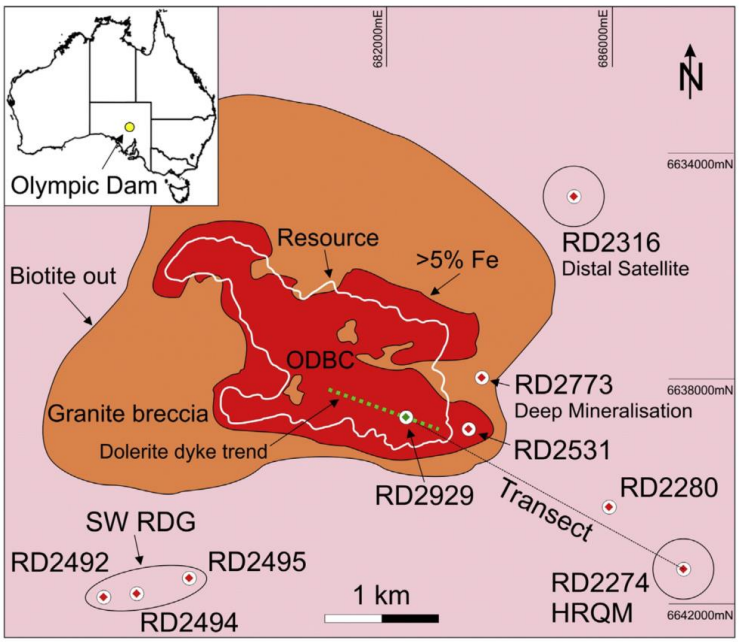

Fig. 1. Geological sketch map of the Olympic Dam deposit at RL-350 showing the location of the studied/sampled drillholes (modified from Ehrig et al., 2012). Insert shows the location of Olympic Dam.

variably altered RDG, coeval felsic through to mafic–ultramafic volcanics (Huang et al., 2016), and a series of bedded clastic facies rocks, all of which are enriched in Fe-oxides. Ehrig et al. (2012) define the boundary of the ODBC at >5% Fe (Fig. 1). Mafic dykes of 0.8 Ga age ('Gairdner dyke suite') crosscut the deposit (Huang et al., 2015; Apukhtina et al., 2016).

Ehrig et al. (2012) provide the most recent and comprehensive overview of the OD deposit, with particular emphasis on element and mineral zonation. Copper–Au–U mineralisation is associated with sericite- and iron-oxide alteration (hematite and subordinate magnetite at depth and at the deposit margins). The current resource broadly overlaps with the boundary of the ODBC (Fig. 1). Economic minerals are Cu–(Fe)-sulphides (chalcocite, bornite, and chalcopyrite), U-minerals (uraninite, brannerite, and coffinite), native gold, and electrum. The deposit also contains disseminations of pyrite and lesser but locally abundant galena, sphalerite, and molybdenite, and is also enriched in F, As, Ba, Bi, Cd, Co, Cr, In, Nb, Ni, Sb, Se, Sn, Sr, Te, V, W, Y, and REE. Deposit-scale zoning is defined by changes in the dominance of particular Cu- and Fe-species. Although apatite is not particularly abundant in the deposit itself (0.1029 wt.% based on 10,000-sample MLA dataset; Ehrig et al., 2012), it is a ubiquitous component of high-grade bornite ore from which the U-bearing hematite has been dated at 1577 ± 5 Ma (Ciobanu et al., 2013).

3. Sampling approach and methodology

The present study describes apatite from samples of two fresh granitoids: RDG (beyond the biotite-out boundary) and HRQM, as well from an intensely-altered, coeval dolerite dyke (Fig. 1), which forms part of a mafic–ultramafic suite of dikes crosscutting the orebody. The study also encompasses variably-altered RDG, both within and outside the biotite-out boundary, samples of mineralised RDG from locations at depths exceeding 2.0 km (hereafter 'deep mineralisation', DM), and samples from distal mineralisation outside the main brecciated granite, hereafter called 'distal satellite mineralisation' (Table 1; Fig. 1).

In order to understand the textural and chemical variation in apatite from the freshest granitoid in the ODBC, as well as to compare this with apatite from coeval igneous lithologies, three drillcores southwest of the deposit, as well as along a 5.6 km-long NW–SE transect, were sampled (Fig. 2). Although considered some of the freshest within the mine perimeter, RDG in the three drillholes from the southwest location display different intensities of albitization (Kontonikas-Charos et al., 2015) from one drillcore to another. This alteration can be readily seen in terms of K/Na ratio (Fig. 2). Samples were taken from the least altered interval in drillholes RD2494 and RD2495, and from a moderately-altered interval in drillhole RD2492. Similarly, samples along the transect record an increase in Na/K and Fe towards the deposit, corresponding with a marked decrease in the abundance of apatite relative to other phosphates. RDG intersected in drillhole RD2280 features abundant, heavily sericitized mafic enclaves, which were also sampled.

'Deep mineralisation' is hosted by RDG and an intensely-altered felsic rock with porphyritic appearance ("felsic unit"). Fig. 3 shows the variation in P, Fe, and Cu in drillhole RD2773, all of which correlate with one another, and are always higher where coarse-grained apatite is abundant. In the 'distal satellite' (DS) within drillhole RD2316 (Fig. 3), Fe-metasomatism increases towards depth, coincident with a decrease in K. The lowest part of the drillhole displays albitization. Copper, Mo, U, and LREE all correlate with the Fe content.

3.1. Analytical technique

Samples were prepared as 1-inch polished blocks. Each was imaged using a FEI Quanta 450 FEG ESEM equipped a with a back-scattered electron detector prior to electron probe microanalysis (EPMA). Analysed grains were selected based on textures, compositional zonation, and relationships to co-existing minerals.

Quantitative compositional data for apatite were obtained using two electron microprobes: a CAMECA SX-Five instrument at Adelaide Microscopy (University of Adelaide) and a Cameca SX100 (University of Tasmania). These instruments were both operated at accelerating voltages of 15 kV, and beam currents of 20 nA. X-ray lines, standards, count times, and typical minimum limits of detection are given as Electronic Appendix A. A spot size of 4 μm was used for most analyses in order to target distinct domains within individual grains but a larger spot size (10 μm) was used whenever possible to obtain optimal sensitivity for minor elements. Grain-scale cathodoluminescence (CL)

Table 1
Overview of lithologies and samples discussed in this study.

Drillhole no.	Sample ID	Depth (m)	Sample category/rock type
RD2494	RX7860	588.2	*Roxby Downs Granite* — Equigranular, medium to coarse grained K-feldspar–quartz–plagioclase granite. Fresh to pervasively hematite–sericite–chlorite altered. Some samples contain spherical mafic enclaves. Fresh samples are characterised by the presence of biotite, edenite and ilmenite. Locally abundant apatite in association with other accessories such as magnetite, ilmenite and zircon.
RD2492	RX7864	756	
RD2495	RX7866	584	
RD2280	2280-1	413	
	-2	416.5	
	-3	416.9	
	-4	440	
	-5	466	
	-6	467.5	
	-7	475.7	
RD2274	2274-1	372.5	*Horn Ridge Quartz Monzonite* — Equigranular, medium-grained K-feldspar–quartz–plagioclase Quartz Monzonite. Lightly hematite–sericite–chlorite altered. Abundant biotite and hornblende have been altered to chlorite. Some ilmenite remains. Abundant apatite in association with accessory magnetite, ilmenite and zircon.
RD2929	RX7913	401.3	*Dolerite dyke* — intensely hematite–sericite–chlorite–carbonate altered dolerite. The majority of primary silicates are replaced by secondary minerals but accessory apatite and Fe–Ti-oxides (hemoilmenite) are largely preserved.
	RX7914	411.1	
RD2773	2773-1	2208.5	*Deep mineralisation* — magnetite–chlorite–carbonate to hematite–sericite altered Roxby Downs Granite and Felsic Unit. Apatite occurs in a number of morphologies ranging from small, unzoned to large, zoned and fractured grains, in isolation as well as large aggregates.
	-2	2261	
	-3	2289.5	
	-4	2309.5	
	-5	1998.1	
RD2316	RX6685	580.2	*Distal satellite* — magnetite–chlorite–sericite (minor) altered Roxby Downs Granite. Red-stained K-feldspar present, no plagioclase present. Apatite occurs in a wide range of sizes. Larger grains are commonly zoned and occur in aggregates in close association with magnetite. Feldspars replaced by chlorite and by an unusual assemblage of molybdenite–bastnäsite–synchysite.
	RX6687	588.2	
	RX6691	645.3	

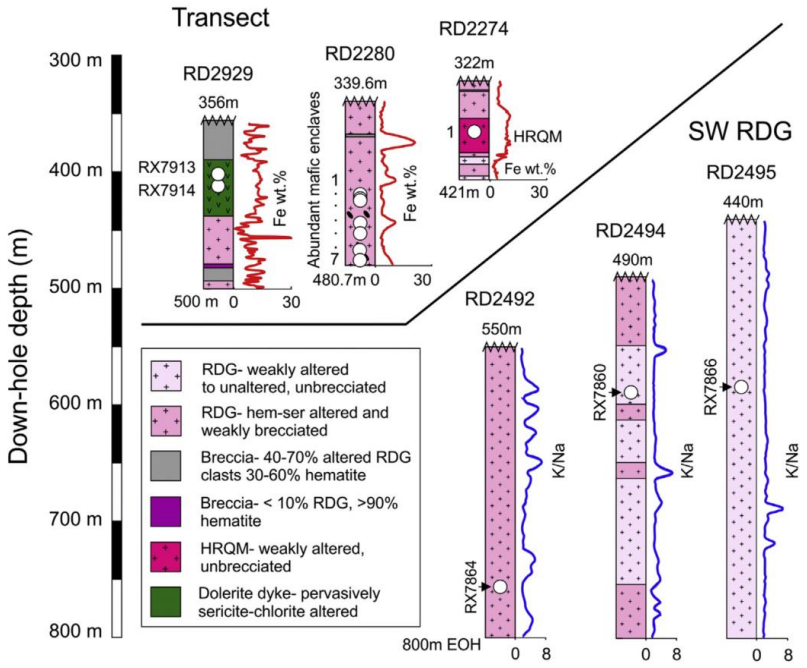

Fig. 2. Schematic representation of three drillholes southwest of the deposit, as well as along a 5.6 km-long NW–SE transect, sampled in this study. Variation in Fe content is indicated for the drillhole transect, and K/Na ratio for the drillholes southwest of the deposit.

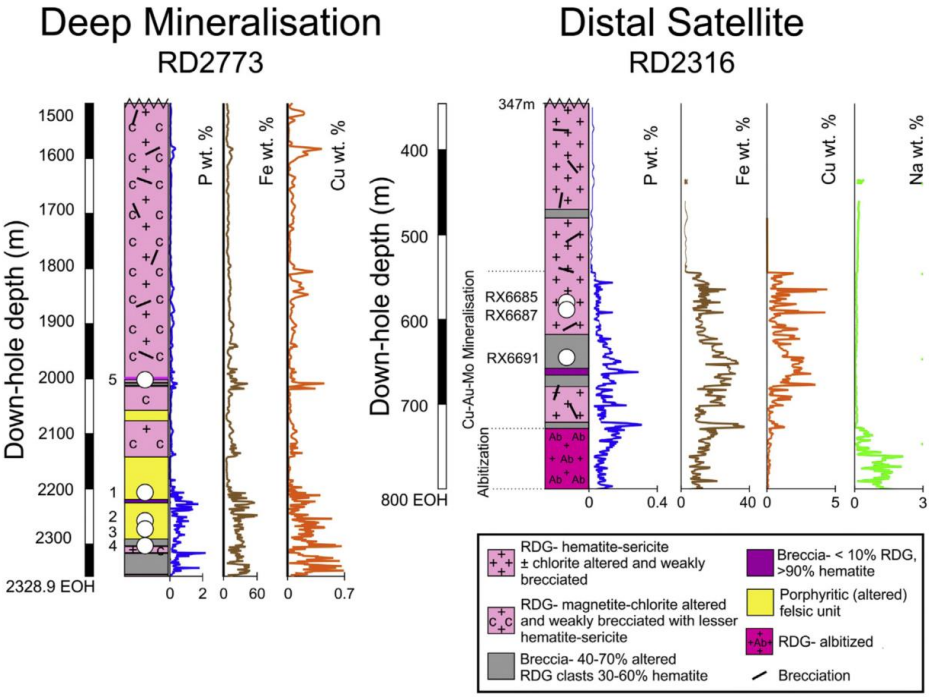

Fig. 3. Schematic representation of distal satellite mineralisation intersected in drillhole RD2316 and 'deep mineralisation' in drillhole RD2773. Variation in P, Fe, Cu, and Na across the sampled intervals.

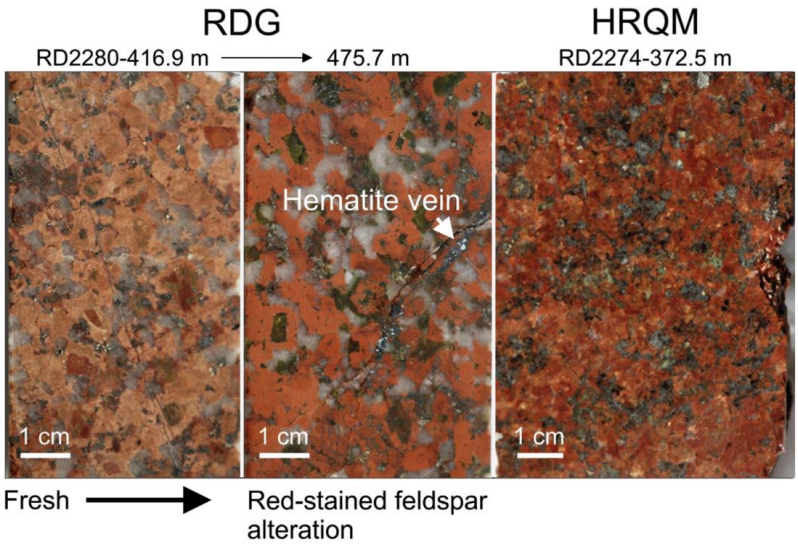

Fig. 4. Hand-specimen photographs showing the two granitoids from this study and variation in alteration in RDG as marked. Note the finer-grained and more mafic-rich character of the HRQM relative to RDG.

imaging was conducted using a Philips XL40 SEM fitted with a Gatan CL detector.

4. Petrography and apatite textural and chemical variation

Fig. 4 illustrates differences in hand-specimen appearance between granitoids. Differences in appearance can be seen even in the same drillhole (Fig. 4a, b), and are expressed as a reddening of feldspar and veining of hematite. Both are linked to hematite alteration. The HRQM is both fine-grained and richer in mafic minerals (Fig. 4c).

4.1. Roxby Downs Granite

Roxby Downs Granite (RDG) is a peraluminous, undeformed, equigranular granite (Kontonikas-Charos et al., 2015) and was sampled along the NW–SE transect and also from the SW locality (Fig. 1). This is a

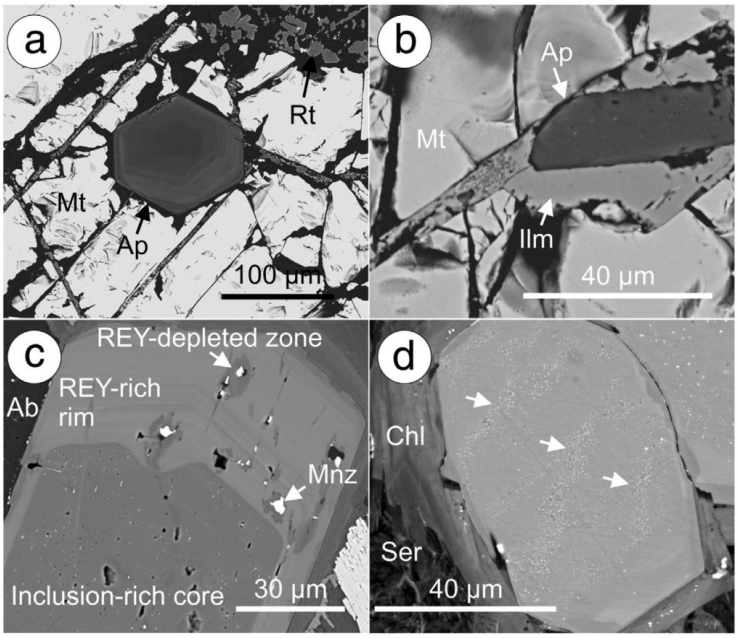

Fig. 5. Back-scatter electron (BSE) images showing the textural and morphological character of apatite in RDG. (a and b) Small, weakly zoned apatite hosted in Fe–Ti-oxides. (c) Dominant type of apatite with core–rim zonation expressed as a variation in REY. Note depletion in REY and monazite nucleation related to the fractures and pores. (d) Inclusion-rich apatite cores (arrowed) in apatite from RDG with mafic enclaves. Some of the coarser and brighter inclusions are monazite, the smaller are sulphides. Note the 'emulsion-like' texture of the bands with inclusions. Abbreviations: Ab — albite, Ap — apatite, Chl — chlorite, Ilm — ilmenite, Mnz — monazite, Mt — magnetite, Rt — rutile.

two-feldspar rapakivi granite that retains perthitic textures but with varying degrees of alteration at metre-scales, caused by deuteric coarsening, albitization, and formation of new, Ba-rich K-feldspar. Altered mafic enclaves, varying in size from mm- to dm-size are abundant in cores along the drillhole transect. The freshest samples preserve mafic minerals (edenite and biotite). Elsewhere, these are altered to chlorite, quartz, hematite, and rutile (Kontonikas-Charos et al., 2015). Mafic minerals in the enclaves are completely replaced by secondary chlorite + sericite. Iron–Ti-phases are abundant and preserved.

The RDG is rich in accessory minerals (zircon, apatite, Fe–Ti-phases), and in many instances, these occur together as clots up to mm-size. Apatite is enclosed within all Fe–Ti-phases (magnetite, Mn-bearing ilmenite, titanite), where it is typically small (tens of μm) and displays only weak zoning (Fig. 5a, b). The most abundant type of apatite in the RDG is, however, coarse single grains (reaching hundreds of μm in size) or aggregates with core-to-rim compositional zoning expressed as variation in REE + Y (hereafter REY), where the cores are REY-poor and the rims are REY-richer (Fig. 5c). Secondly, apatite shows distinct cores characterised by dense, sub-microscopic inclusions (hereafter 'inclusion-rich cores'; Fig. 5d), particularly in the granite with mafic enclaves from the transect location. Coarsening of these inclusions is observed along microfractures crosscutting the apatite. In this case, inclusions, a few μm in size, are identified as sulphides (pyrite, chalcopyrite and galena), and monazite using EDX–SEM. The smallest (<1 μm) inclusions, however, have elongate habit and show Fe:S ratios closer to pyrrhotite than pyrite. Some of the apatite grains feature a reshaping of the compositional zoning relative to the grain boundaries, sometimes with development of porosity and nucleation of monazite along microfractures (Fig. 5c). In the mafic enclaves, a greater proportion of the apatite grains display an elongate habit, and some have quartz cores (Krneta et al., 2015).

All aforementioned RDG apatites are end-member fluorapatite with negligible Cl content. However, apatite hosted within the mafic enclaves display slightly higher Cl concentrations. Compositional variation is expressed by differing REY concentrations (Electronic Appendix Table B1). All are considered magmatic apatite based on their association with Fe–Ti-phases, as well as the characteristic euhedral habit with REY zonation. In the most altered RDG, however, the apatite is corroded and replaced by either quartz (Fig. 6a), or sericite when hosted by altered feldspars (Fig. 6b). A final stage of apatite evolution, only seen in

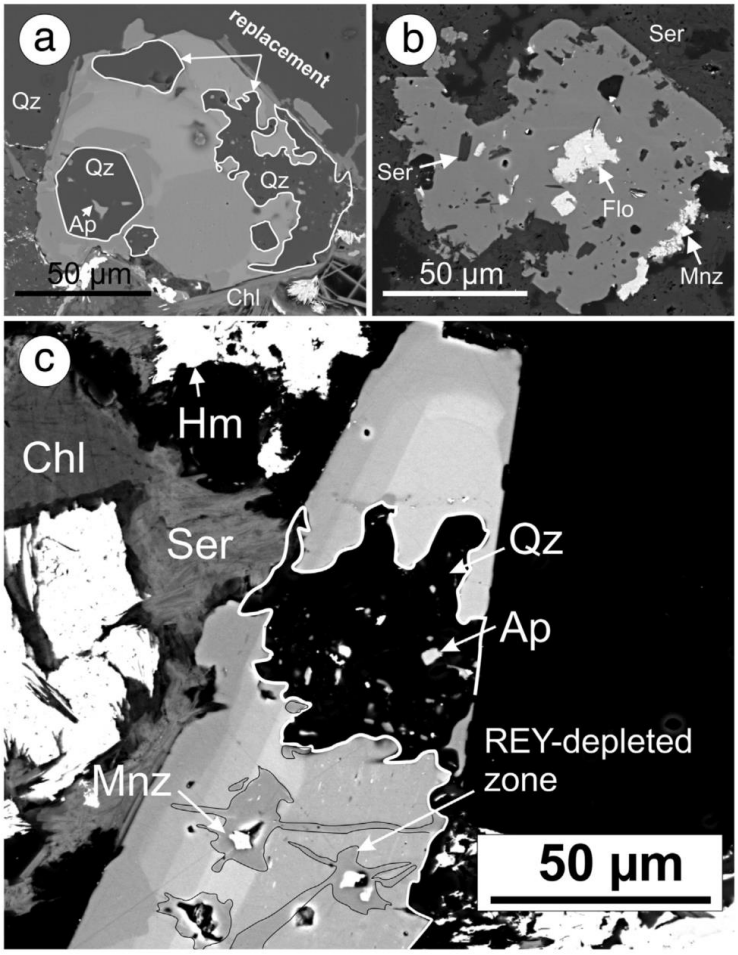

Fig. 6. BSE images showing the textural and morphological character of the hydrothermal alteration of apatite in RDG. (a) Quartz replacement of apatite. Changes in morphology of the replaced areas from pseudomorphic (hexagonal outline) to skeletal indicating a transition from coupled-dissolution reprecipitation to a fracture-porosity controlled replacement. (b) Unzoned apatite with atypical, hypidiomorphic morphology from intensively sericite-altered RDG along the drillhole transect. Coarse florencite and monazite are present. Although marginal replacement of apatite by sericite is observed, the irregular morphology of the sericite and florencite inclusions suggests late apatite crystallisation relative to these minerals. (c) Detail of apatite replacement by quartz accompanied by REY-depletion and monazite formation along fractures crosscutting patterns in apatite (REY-zonation and core–rim boundary). Abbreviations: Ap — apatite, Chl — chlorite, Flo — florencite, Hm — hematite, Mnz — monazite, Qz — quartz, Ser — sericite.

RDG displaying with more intense sericite–hematite alteration, is represented by replacement by quartz (containing monazite inclusions), and by fracture networks (also carrying inclusions of sericite and hematite) associated with the loss of REY from the apatite grains (Fig. 6c). In highly-altered RDG samples, containing base metal sulphides, hematite veinlets, and Nb-bearing rutile, magmatic apatite is largely obliterated and xenotime may be the dominant REE-phosphate. Samples from drillhole RD2513 at the margin of the ODBC along the transect (Fig. 1) do not contain apatite. The alteration assemblage is comprised of siderite, barite, fluorite, and sericite.

4.2. Horn Ridge Quartz Monzonite

The Horn Ridge Quartz Monzonite (HRQM) has been intersected in a drillhole ~4 km SE from the boundary between the altered and fresh RDG (biotite-out limit) and the outer limit of the ODBC (Fig. 1). The HRQM is similar in appearance to the RDG, although with greater proportions of both mafic minerals and accessory Fe–(Ti)-oxides, reflecting its less-evolved character (a QAP diagram is given by Kontonikas-Charos et al., 2015). At this location, mafic minerals in the HRQM are completely altered to chlorite, quartz, and rutile. Iron–Ti-oxides are abundant, and consist of magnetite and ilmenite, where the latter preserves domains of ulvöspinel, as well as more common decomposition to symplectites of hematite and rutile.

Apatite is an abundant component, occurring within the replaced mafic minerals, often together with clots of Fe–Ti-oxides, or at the boundaries of such clots (Fig. 7a). Some of the smallest apatite grains (down to ~5 μm) are un- or weakly-zoned, and are observed to be entirely enclosed within magnetite, either surrounded by coronas of decomposed ilmenite (Fig. 7b), or as euhedral grains oriented parallel to magnetite cleavage planes (Fig. 7c). In contrast with these, larger (up to a few hundred μm) individual, or aggregated apatite grains are seen outside Fe–Ti-oxides. Most such grains contain inclusion-rich cores, similar to those as described for the RDG above. The host apatite is zoned, either with preservation of core-to-rim geometry (Fig. 7d), or a more irregular outline between zones caused by reworking (Fig. 7e, f). Grains lacking inclusions are also seen outside the Fe–Ti-oxides. These vary in size from tens to hundreds of μm, and also show zoning, as well as reworking. The latter is expressed as pore-controlled nucleation of new apatite (Fig. 7g), overgrowths on rounded cores (Fig. 7h), and as patchy chemical zoning (Fig. 7i). The latter is associated with the nucleation of relatively coarse monazite and lesser xenotime.

Compositionally, all apatite grains are fluorapatite but with variable Cl and (inferred) OH content (Electronic Appendix Table B2). The smallest, magnetite-hosted grains are clearly magmatic because of their entrapment in magnetite during growth. They are the richest in Cl (up to 0.14 atoms per formula unit; apfu) but with variable REY content (ΣREY apfu 0.045–0.122). All other apatites contain zones with ~0.08–0.10 apfu Cl, but also zones that are Cl-depleted (<0.02 apfu).

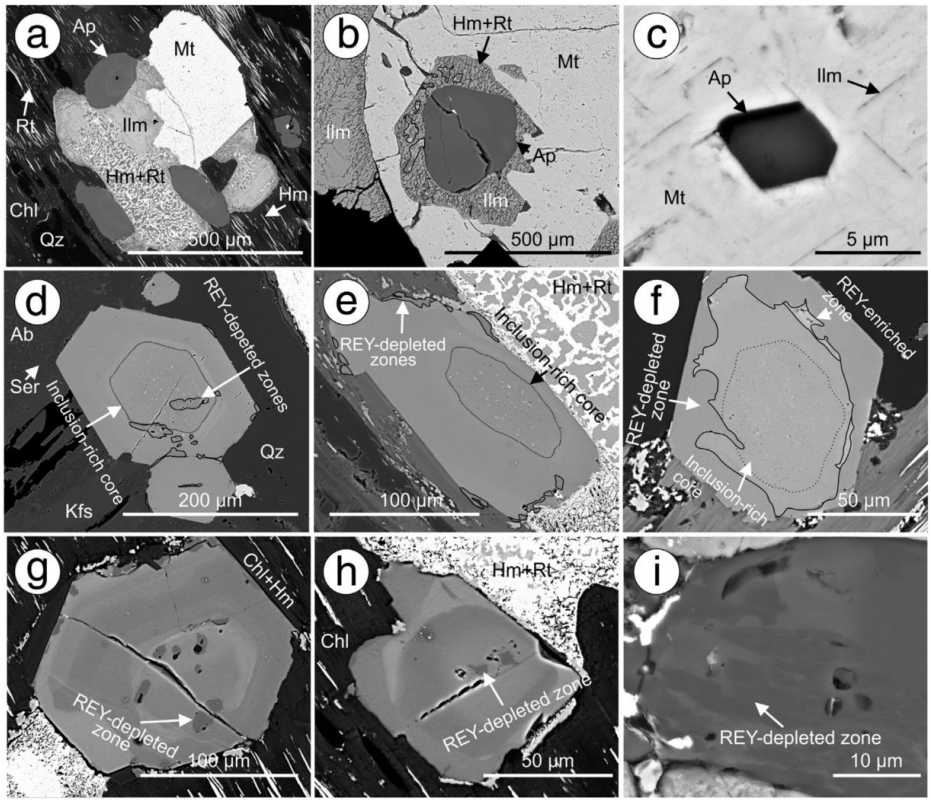

Fig. 7. BSE images showing the textural and morphological character of apatite in HRQM. (a) Apatite associated with Fe–Ti-oxides forming a clot within an altered mafic mineral. Note the decomposition of ilmenite into a rutile + hematite symplectite. (b and c) Fe–(Ti)-oxide hosted apatite. Note the lack of zoning and small size of apatite. In (c) see also the coherent orientation of the grains relative to the magnetite cleavages. (d, e and f) Inclusion-rich cores in dominant, coarse apatite with a euhedral morphology. Core–rim zoning (e) and core outline relative to margin (f), indicating superposed hydrothermal alteration expressed also as REY-depletion or local enrichment. (g and h) REY-zoned apatite with no obvious inclusion-rich cores. Further evidence for hydrothermal alteration is seen as pore-controlled nucleation of small, REY-depleted apatite. Rounding of the core with irregular overgrowth in apatite (h). (i) Detail of REY-depleted zones showing patchy morphology. Abbreviations: Ap — apatite, Chl — chlorite, Hm — hematite, Ilm — ilmenite, Kfs — K-feldspar, Mt — magnetite, Qz — quartz, Rt — rutile, Ser — sericite.

The Cl-rich zones in a given grain are associated with variable but generally higher REY, together accounting for the patterns seen on the BSE images.

4.3. Dolerite

The dolerite dyke from the mafic–ultramafic suite, coeval with RDG, has a dark-green to white-yellowish appearance in hand specimen due to intensive alteration to an assemblage of chlorite + sericite + carbonate + quartz. Carbonates, mainly siderite, occur as mm-scale veinlets throughout the rocks. Sulphides, such as pyrite and chalcopyrite, are found as scattered disseminations that increase in abundance along/within the veins. In most cases, chlorite + sericite ± carbonate assemblages occur as fine-grained intergrowths, with rhythmic layering within ovoid shapes.

The mafic–ultramafic origin of these rocks is evidenced by their Zr/Ti ratios and also by the high abundance of hemoilmenite as the main magmatic accessory phase. The latter occurs as aggregates or clots and preserves fields of dense ilmenite exsolutions. Rutile rather than titanite is the more abundant Ti-mineral, occurring either as acicular aggregates within hemoilmenite, or as tiny, abundant inclusions throughout the altered sericite–chlorite mass. Apatite is the other abundant accessory (Fig. 8). Zircon is present as rare grains, in some cases enveloped by sulphides. Although rare, K-feldspar is identified as small grains enclosed within both the Fe–Ti-oxides and apatite, indicating the presence of a potassic alteration stage that pre-dates carbonate–chlorite–sericite alteration.

Apatite ranges in size from 10 to 600 μm. It ranges in morphology from euhedral to subhedral (Fig. 8a, b), and rarely as acicular grains. The smallest grains, which are the least common, are compositionally homogenous, and have the highest Cl concentrations (up to 0.235 apfu; Electronic Appendix Table B3). The most common apatite grains are, however, larger and are characterised by either equant or corroded outlines. These are compositionally heterogeneous and display areas of patchiness (Fig. 8c). Abundant pores and μm-sized inclusions of monazite are often observed within the patchy zones.

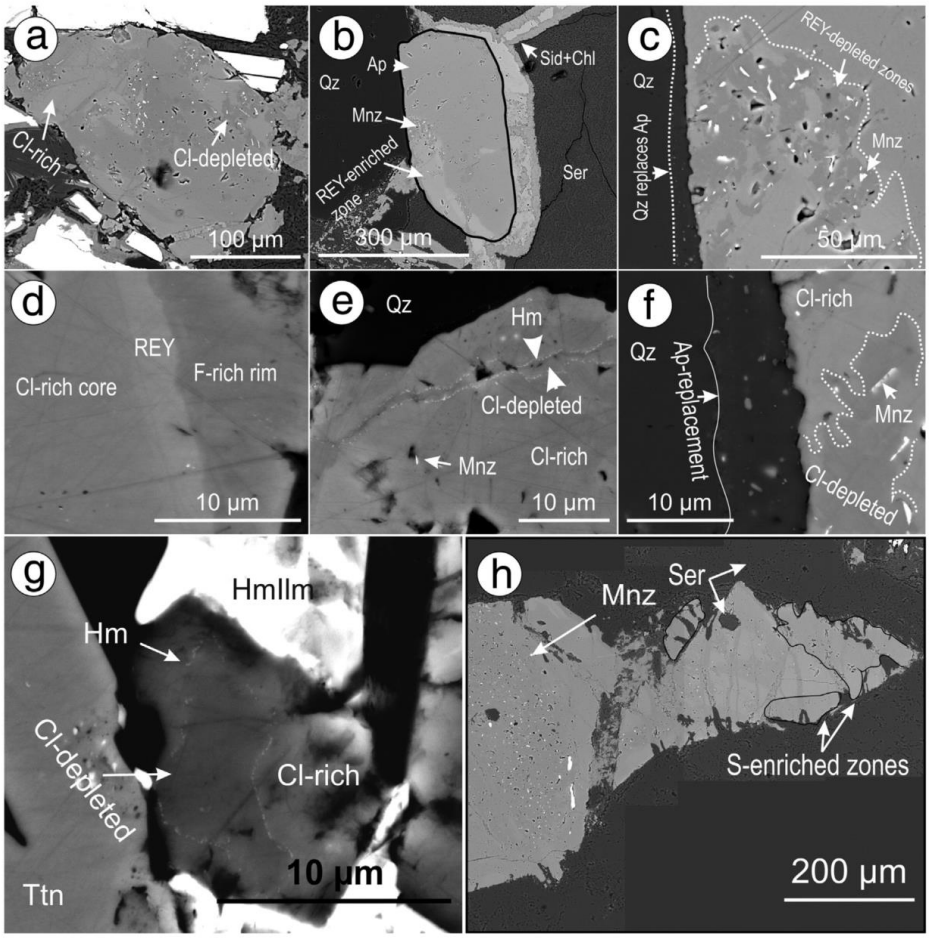

Fig. 8. BSE images showing apatite from the dolerite dyke (a–b). Coarse apatite with equant, slightly rounded morphology and with patchy Cl-rich, F-rich domains. In (b), carbonate partially envelopes a grain located at the junction of the fractures filled with secondary minerals. (c) Detail of a F-rich and Cl-REY-depleted zone showing the development of pores and monazite nucleation indicative of the superposed, hydrothermal alteration. (d–h) Various aspects of apatite alteration. In (d), a REY-rich band at the contact between the F-rich rim and a typical, Cl-rich apatite shows a reaction front with zonal development from margin to core. In (e), a Cl-depleted fracture is fringed by tiny platelets of hematite. Marginal replacement of apatite by quartz is marked by a scalloped outline — typical of a metasomatic reaction front. The adjacent zone in apatite with Cl-depletion and monazite inclusions has an irregular morphology indicating that the two alteration stages are distinct from one another. (g) Scalloped core morphology of a F-rich, Cl-depleted core marked by sub-μm hematite. (h) Sulphur-rich domains in apatite adjacent to a wide (cm-size) fracture filled by carbonate and sulphides. Note brittle fracturing of the apatite itself. Abbreviations: Ap — apatite, Chl — chlorite, Hm — hematite, Hmilm — hemoilmenite, Mnz — monazite, Qz — quartz, Ser — sericite, Sid — siderite, Ttn — titanite.

Zones of relative REY-enrichment (up to 0.087 apfu ΣREY in the bright areas on the BSE images; Electronic Appendix Table B3) are also present (Fig. 8b). The patchy zoning corresponds to the highest F (up to 0.998 apfu; Electronic Appendix Table B3). There are however, various relationships between the REY- and F-rich apatite zones. This can be seen either as a zonal arrangement of F- and REY-rich zones from the grain boundary inwards (Fig. 8d), or as patchy F-rich zones crosscutting the REY-rich zones (Fig. 8b). The F-rich zones are most varied texturally and clearly show association with microfractures fringed by hematite (Fig. 8e), or with apatite margins displaying scalloped morphologies against replacive quartz (Fig. 8f). The presence of tiny fragments of apatite within replacive quartz indicates the nature of this replacement as pseudomorphic. Cores of F-rich apatite are also observed within otherwise Cl-rich apatite (Fig. 8g). These cores have an irregular morphology and are sealed by dusty hematite inclusions, which suggests that they relate to an overprint event. The majority of apatite grains, however, display a combination of all the aforementioned textures.

A further category of apatite, observed in these rocks, is relatively SO_3-rich (up to 0.041 apfu S; Electronic Appendix Table B3) and occurs within angular terminations of larger, equant grains placed along the carbonate veins. In this case, textures clearly indicate an overlap of various categories of apatite as defined above. For example, the high-REE apatite zones are crosscut by F-rich veinlets, and only a few monazite inclusions occur within or adjacent to such veinlets (Fig. 8h). Areas of coarse pores and filling of the F-rich veinlets by sericite are also observed. The SO_3-rich zones are observed around the margins of, or adjacent to, crosscutting veins that occur at the boundaries between equant apatite and its angular edge.

4.4. Deep mineralisation

The deepest mineralisation is intersected in a 2.3 km-deep drillhole (RD2773) at the eastern boundary of the brecciated RDG (Fig. 1). Mineralisation is hosted by altered intrusive rocks (altered RDG and a felsic unit between 1500 and 2328 m), and intensifies over the lowermost ~300 m. The relationship between the RDG and felsic unit is, however, irregular with interfingering of one into the other over a 270 m-thick interval. Early emplacement of the 'felsic unit' relative to the RDG is suggested by contacts with fragments of the former incorporated within the latter. Mineralisation consists of sulphides (chalcopyrite + pyrite + sphalerite + galena) as disseminations and mm-size veinlets associated with a characteristic alteration assemblage comprising Fe-oxides (magnetite–hematite, with interconversion between the two), sericite, chlorite, carbonates, quartz, and locally abundant anhydrite. Carbonates are the most abundant within crosscutting late veins. Uranium minerals (uraninite, brannerite, and coffinite), as well as REE-minerals (monazite, synchysite, and bastnäsite), are also present. Alteration is patchy across the lower portion of the drillhole but zones of intense alteration, from mm up to as much as 4 m in size, are concentrated at the contacts between the RDG and felsic unit or along fractures.

Apatite is a ubiquitous component of the alteration irrespective of lithology, and displays a variety of grain sizes (up to cm-size), habits, and mineral associations. Although euhedral, REY-zoned grains comparable to those described from RDG are present (Fig. 9a). The majority and highest concentration of apatite occurs within cm-scale aggregates (Fig. 9b). Compositionally, apatite is close to end-member fluorapatite (Electronic Appendix Table B4) but with zones of higher Cl-content within any given grain (0.016–0.05 apfu Cl; i.e., higher than in RDG magmatic apatite). This variation in Cl-content is expressed as core-to-rim zoning (either with Cl in the cores or at the rims), as well as patchy zoning linked in some cases to microfractures (Fig. 9b–d). The Cl-rich zones also contain higher amounts of both REY and SO_3. Low-REY, F-rich zones are predominantly located along fractures and associated with inclusions of monazite (locally also hematite and chalcopyrite). When in contact with late quartz and calcite, apatite is typically brecciated and partially replaced. In contrast to magmatic apatite in RDG, F-enrichment clearly post-dates an early Cl-rich fluorapatite (Fig. 9c). Together with the close association with alteration, this indicates that apatite characteristic of deep levels, such as that intersected here, has a dominantly hydrothermal origin despite a similar equant habit in some cases. Although rare, potentially magmatic fluorapatite grains, characterised by very low Cl, but with relatively high ∑REY, are preserved as inclusions within Fe-oxides in altered RDG (Fig. 9e). Whereas monazite inclusions of varying size and density are common in all cases, in the deepest samples, bi-component (monazite + $ThSiO_4$) inclusions are conspicuous within F-rich, REE-poor zones in apatite, and also as splays crosscutting boundaries between the F- and Cl-rich domains (Fig. 9f). In detail, the $ThSiO_4$ (most likely huttonite) can be as abundant as the monazite (Fig. 9g). The inclusions may also be multi-component with hematite. Apatite may also contain inclusions of sulphides.

4.5. Distal satellite mineralisation

Mineralisation intersected in drillhole RD2316, 2.7 km NE from the ODBC, and 1 km from the biotite-out boundary within the RDG (Fig. 1), represents one of the distal satellite bodies in the OD area. The drillhole intersects 450 m of RDG below cover with zonation ranging from relatively fresh to mineralised and brecciated (below 543 m), with weakening of mineralisation towards the bottom of hole (800 m). Magmatic K-feldspar is partially preserved over the strongest mineralised interval and coexists with hydrothermal K-feldspar, whereas over the bottom 75 m, albitization is preserved (Fig. 3; Kontonikas-Charos et al., 2015). As in the DM, both magnetite and hematite (and their interconversion) are associated with pyrite, chalcopyrite, native gold, U-minerals, and an abundance of REE-minerals, particularly epitaxially intergrown REE fluoro-carbonates (e.g., bastnäsite, synchysite and parisite). In contrast to the DM, however, molybdenite is moderately abundant, and coexists, within lamellar intergrowths, with the REE-minerals. Alteration consists of chlorite (mostly associated with magnetite), sericite (with hematite), quartz, and rare carbonates.

In samples from the most intensely mineralised interval, apatite is abundant, occurring in close association with Fe-oxides (mostly martite), other alteration minerals, and sulphides. In this drillhole, the textures and chemistry of apatite differ markedly within individual samples, depending on the local association. Where closely associated with Fe-oxides and pyrite, apatite forms aggregates interstitial to other minerals, as in the uppermost sample (Fig. 10a). Such aggregates can either retain growth zoning and equilibrium textures, or display evidence of brecciation. Co-precipitation of apatite aggregates with a primary magnetite is suggested.

In contrast, in samples from deeper levels, apatite occurs as single grains that are brecciated and replaced by quartz, with REY-minerals or molybdenite marking the replacement front (Fig. 10b). A distinct, fine-grained apatite occurs within or at the margins of K-feldspar (Fig. 10c). The smallest apatite grains are seen in areas outside of the Fe-oxides and Cu-sulphides, and are characteristically unzoned and include fine-grained hematite in vugs and along trails (Fig. 10e). In some cases, apatite features more complex textures with both sectorial and oscillatory zonation (Fig. 10e). REY-depleted margins suggest hydrothermal overprinting on inherited magmatic grains.

All categories described here are end-member fluorapatite with negligible Cl content (Electronic Appendix Table B5). There is, however, variability with respect to the REY content, particularly core-enriched to margin-poor (Fig. 10e). All grains contain some S. Aggregates and large apatite grains are, however, markedly lower in S (0.01–0.02 apfu) than the smaller grains within and at the margins of K-feldspar (0.03–0.04 apfu). Although within each category, individual grains can contain domains that are completely depleted in S, the S-REE-rich domains also feature higher Na (up to 0.05 apfu) within the smaller grains that are located in and around K-feldspar (Fig. 10d).

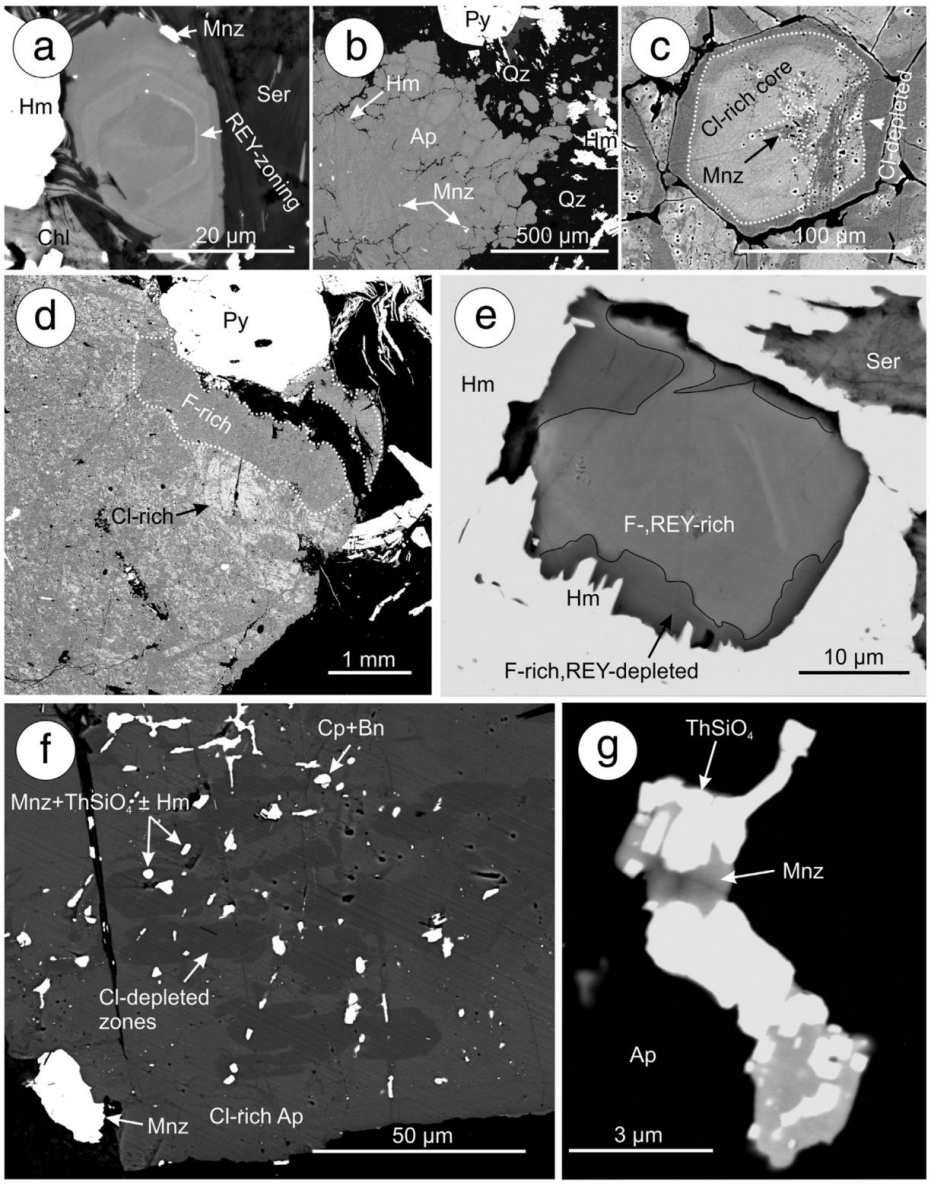

Fig. 9. BSE images showing apatite from the 'deep' mineralisation. (a) Rare, single grain of Cl-bearing hydrothermal apatite. (b) Typical large, Cl-rich apatite aggregate. (c) Detail of grains from (b) fractures and margins depleted in Cl and richer in F. (d) Detail of patchy Cl/F domains at the margin of an apatite where alteration is advanced (sulphides + hematite). (e) Marginal REY-depletion of a Cl-poor, REY-zoned fluorapatite embedded within hematite. This grain could be of magmatic origin. (f) Patchy Cl- and F-domains in apatite crosscut by trails of dominantly bi-component inclusions consisting of monazite-Th-rich silicate (huttonite?). Noteworthy is the presence of various sulphides and hematite. Such trails and inclusion variety indicate advanced hydrothermal alteration of apatite. (g) Detail of bi-component inclusions (monazite-huttonite?). Abbreviations: Ap — apatite, Bn — bornite, Cp — chalcopyrite, Hm — hematite, Mnz — monazite, Py — pyrite, Qz — quartz, Ser — sericite.

This can be attributed to a characteristic signature associated with the obliteration of albite in these samples during interaction with S-bearing fluids, particularly when such grains are formed.

5. Discussion

The ubiquitous character of apatite in igneous rocks and its ability to incorporate halogens, magmatic water, S, C, and trace elements, including Sr, REY, Th and U, are, if combined with careful textural and compositional analysis, considered important tools for understanding pluton building and associated mineralising systems (Webster and Piccoli, 2015). Magmatic apatite, the single mineral that accounts for the majority of the P content in melts, is of particular interest because both halogens (F, Cl) and OH are interdependent of one another since they are hosted in the same crystallographic site. The relative concentrations of these elements can therefore be linked to those of the parent melt.

Variation in the halogen content of magmatic apatite was initially considered predictive (Candela, 1986; Zhu and Sverjensky, 1991; Piccoli and Candela, 1994) and halogen variation, expressed as zonation

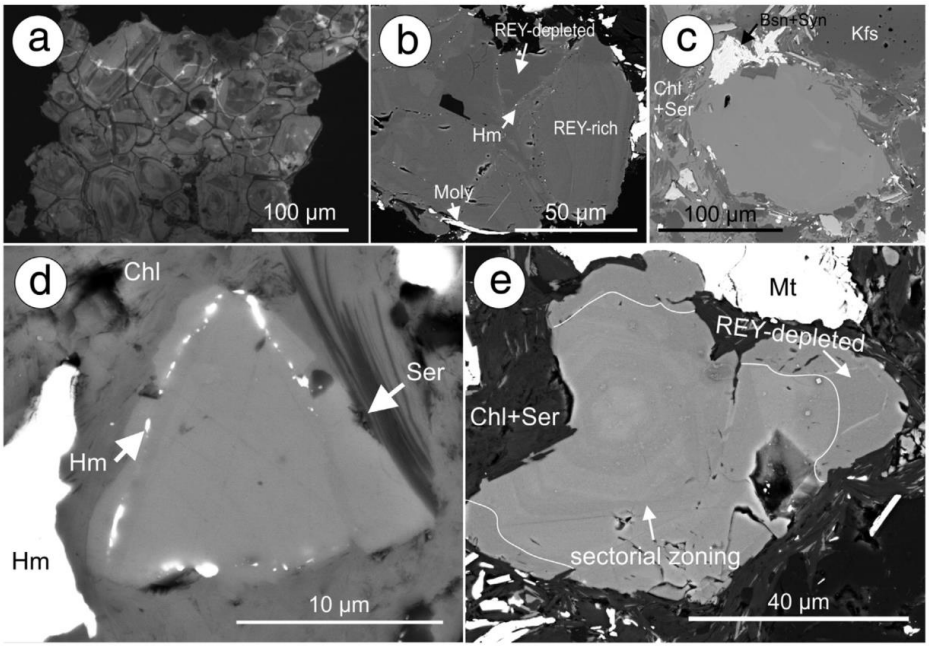

Fig. 10. Cathodoluminescence (a) and BSE (b–e) images showing apatite from the distal satellite mineralisation. (a) Aggregate of interstitial apatite with no obvious chemical zoning but with growth zones depicted in the CL image typical of the upper interval with lesser sulphides and more Fe-oxides. (b) Apatite aggregate with grain-boundaries marked by porosity and replacement by molybdenite. (c–d) Small, unzoned apatite formed within or along boundaries of K-feldspar with intense replacement by intergrown assemblage of bastnäsite, synchysite and molybdenite (c), and hematite trails (d). (e) Unusual sectorial zoning in apatite expressed as REY variation. Note that such grains (probably magmatic-inherited) are affected by marginal replacement (scalloped morphology) and overgrowth. Abbreviations: Chl — chlorite, Hm — hematite, Kfs — K-feldspar, Moly — molybdenite, Mt — magnetite, Ser — sericite.

within individual single grains or within an intrusion, was believed to be instructive for identifying igneous systems associated with ore generation. The predictability of halogen uptake into apatite has, however, been questioned (e.g., McCubbin and Jones, 2015). It is currently accepted that partitioning of halogen species into apatite is governed by fluid composition, the presence of other halogen-consuming species, P–T conditions, and other factors. Although all these factors can influence partitioning, plutonic apatite with >3.5 wt.% Cl is rare (Webster and Piccoli, 2015). Halogen partitioning within apatite can, however, be related to trends of magmatic evolution in a given orefield or region that share common magmatic reservoirs (e.g., Boudreau and Kruger, 1990).

Apatite composition in our samples can be expressed in terms of the following variables: halogens, REY, Si, Na, S, Sr, and Mn. Their variation correlates with specific textures observed in each of the five study cases described above. Collectively, the dataset shows a transition between magmatic to hydrothermal apatite recorded both as textures and as geochemical trends.

5.1. Magmatic apatite

Although the presence of almost-end-member fluorapatite in the RDG cannot be used to infer crystallisation from a F-rich magma, the relative concentration of halogens and other minor elements in apatite from igneous rocks at Olympic Dam shows systematic variation depending upon rock type and local context.

5.1.1. Magmatic differentiation and halogens in apatite

The most obvious compositional variable observed in magmatic apatite from the igneous rocks is the F/Cl ratio. This correlates with rock basicity, with the HRQM positioned midway between the RDG and the dolerite dyke, in agreement with the less-evolved character of the HRQM relative to the RDG (Fig. 11a). The Sr vs. Cl plot (Fig. 11b) is evidence for the control imposed by the fractionation character of the magma in determining the chemistry of igneous apatite (Belousova et al., 2001). In terms of the calculated OH component, the three rock types cannot be distinguished from one another. In all three lithologies, magmatic apatite displays a strong correlation between ΣREY and Si, although the absolute values of both variables are an order of magnitude lower in the dolerite dyke than in the granitoids. The highest ΣREY concentrations in granitoid apatites are observed in rims surrounding grain cores rich in mineral inclusions. In the granitoids, the smallest apatite grains, hosted by Fe–(Ti)-oxides, have ΣREY contents comparable to apatite from the inclusion-rich cores. Such apatite in the HRQM is also markedly enriched in Cl compared to the inclusion-rich cores.

Apatites from both RDG and HRQM plot in a similar region on a Sr vs. Mn plot (Fig. 11c), which is used as a measure of magmatic differentiation. They overlap with the granitoid field for occurrences elsewhere (Belousova et al., 2001, 2002) whereas apatites from the dolerite dyke plot astray, inferring that the dolerite dyke is a less-evolved magmatic phase.

5.1.2. Apatite crystallisation and Cl-concentration estimates in melt and volatile phase

Harrison and Watson (1984) considered P_2O_5 concentrations in the whole rock chemistry and the integral part they play in the cooling history of felsic melts. Taking the various parameters which affect apatite saturation into consideration, they conclude that, in the case of subaluminous granites, the greatest controls are exerted by silica concentrations and temperature. However, in the case of peraluminous granites, P_2O_5 solubility is enhanced, shifting apatite saturation to lower temperatures (Bea et al., 1992). Experimental work by Wolf and London (1995) provides further evidence of this phenomenon, observing that incongruent melting of apatite and the formation of monazite along grain margins can be achieved in peraluminous melts. Bea et al. (1992) incorporated the effects of Al_2O_3 concentrations into their

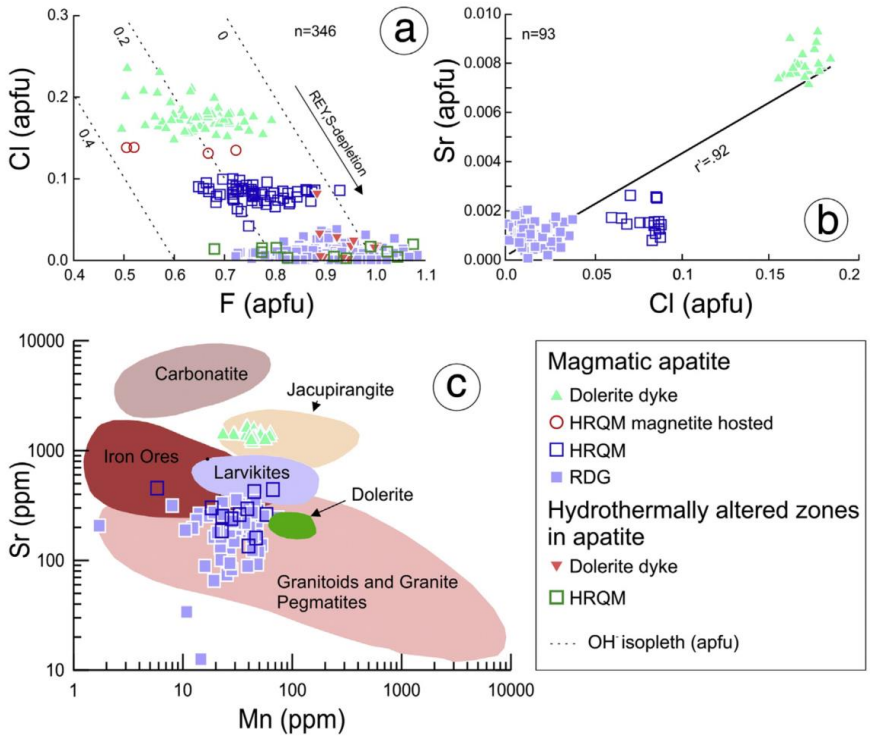

Fig. 11. Plots of (a) Cl vs. F, (b) Sr vs. Cl, and (c) Sr vs. Mn for magmatic apatite. Fields on (c) are from Belousova et al. (2002).

modified formula for calculating apatite saturation temperatures (AST) in peraluminous granites.

The presence of apatite with inclusion-rich cores, which are particularly abundant in RDG with mafic enclaves from the transect, raises the question of whether such apatite could be different relative to the majority of apatite in the RDG in terms of magma mixing and evolution, or it indicates the incorporation of exotic, compositionally-different material during magma crystallisation. Examples of such apatite with pyrrhotite-rich cores are reported from granitoids in the German Erzgebirge (Gottesmann and Wirth, 1997) and were interpreted to reflect assimilation of exotic material in the granite melt, possibly mafic material from the margins of the magma chamber. Attempts to definitively understand the identity of these inclusions are hampered by the fact that, in cores not affected by later fractures and coarsening of the inclusions, the inclusions are sub-μm size. Preliminary nanoscale studies, nevertheless, confirm that the enclave-hosted apatite from OD also includes pyrrhotite and fluorite (the latter as some of the smallest inclusions). This data will be published elsewhere.

Calculations of Cl in the melt relative to the volatile phase at AST were performed using whole rock assays from a limited number of samples from drillhole RD2495 (Fig. 1). These samples correspond to the freshest granites in which mafic minerals are still present. AST calculations were performed using formulae given by Harrison and Watson (1984) and Bea et al. (1992), using parameters such as the A/CNK ratio (Al/(Ca + Na + K) in molar terms) and the concentrations of SiO_2 and P_2O_5. Chlorine concentrations in melt and fluid were calculated following Piccoli and Candela (1994). Calculation details and formulae applied are described in Electronic Appendix C.

Calculated AST values overlap within error with temperatures obtained from feldspar–amphibole and two-feldspar geothermometric estimates on the same RDG samples (Kontonikas-Charos et al., 2015). Hovis and Harlov (2010) and Hovis et al. (2014) found, however, that F–Cl and F–OH mixing exhibits non-ideal characteristics thus reducing the accuracy with which F concentrations can be estimated. The calculations require the input of AST, pressure, and measured halogen concentrations in apatite (ideally also independently measured OH). We therefore calculated only Cl, because this is the parameter most sensitive to the distinct mafic vs. felsic categories of igneous rocks at OD.

The calculations are very sensitive to pressure (P) estimates. Here, we adopt the 2.2 kbar value derived from Al-in hornblende geobarometry (Creaser, 1989; Kontonikas-Charos (unpublished data)). Calculations were performed using average Cl concentrations

Table 2
Calculated Cl-concentrations (ppm) in coexisting melt and volatile phase at the time of AST in RDG.

Drillhole ID	Sample	Number of analyses	F (apfu)	Cl (apfu)	OH[a] (apfu)	Cl in volatile phase (ppm)	Error 2σ	Cl in melt (ppm)	Error 2σ
RD2492	RX7864	7	0.838	0.010	0.152	18,324	4396	29.0	10.7
RD2494	RX7860	21	0.913	0.011	0.076	42,744	10,255	67.8	25.0
RD2495	RX7866	1	0.840	0.005	0.154	9943	2385	15.8	5.8
RD2280	2280-2	19	0.919	0.005	0.077	17,079	4097	27.1	10.0
	2280-3	19	0.875	0.015	0.110	38,418	9217	60.9	22.5
	2280-5	41	0.917	0.014	0.069	59,600	14,299	94.5	34.8

[a] OH calculated.

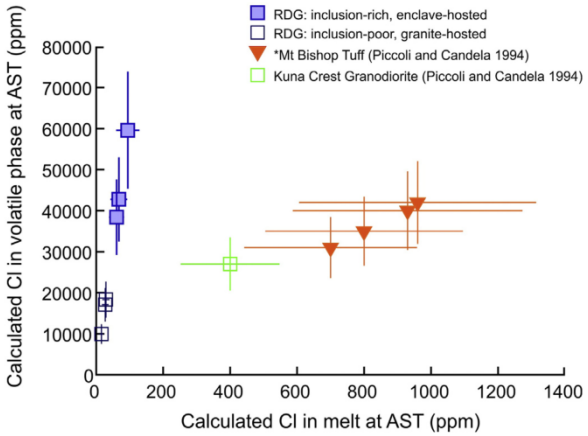

Fig. 12. Plot of calculated Cl (ppm) in volatile phase vs. calculated Cl (ppm) in melt at AST for magmatic apatite using grain core compositions. Note: Piccoli and Candela (1994) do not provide errors for their Mt. Bishop Tuff apatite halogen concentrations. Errors equivalent to those estimated for the Kuna Crest granodiorite have been used in the error calculations here.

from a number of grains and yield Cl values varying between 15 and 94 ppm (±6 to 35) Cl in the melt, and between 10,000 and 60,000 ppm (±2400 to ±14,300) Cl in the volatile phase (Table 2). Such values accord with the known behaviour of Cl to partition into the volatile phase over both apatite and the melt. Identical P and T values were used in calculations for all samples, and the variability in the calculated values can thus only be attributed to slight changes in Cl-concentration. The highest Cl-concentrations derive from apatite grains with inclusion-rich cores within samples dominated by mafic enclaves. The correlation of higher Cl in apatite, hosted by mafic enclaves within the RDG, is in agreement with observations made elsewhere (Piccoli and Candela, 2002). The dataset shows that the values for inclusion-bearing core apatite are statistically distinct from grains without such inclusions. For the sake of comparison, the plot (Fig. 12) also shows the fields for the un-mineralised Mt. Bishop Tuff and the Kuna Crest Granodiorite samples using values from Piccoli and Candela (1994). These latter two rocks show far higher Cl values in the melts than the RDG apatite, which is potentially a meaningful finding considering the very distinct tectonic settings of the Mt. Bishop Tuff and the Kuna Crest Granodiorite compared to the RDG, even if magma chemistry and pressure are the most important controls on apatite saturation temperatures and chemistry.

5.2. Hydrothermal apatite

Magmatic apatite shows textural and geochemical evidence of hydrothermal alteration in all cases. In addition, abundant hydrothermal apatite is recognisable in both mineralised granites, albeit with differences depending upon depth and alteration type.

5.2.1. Hydrothermal alteration of magmatic apatite

Apatite from the dolerite dike shows the most diverse range of alteration trends (Fig. 13). For example, in contrast to granitoids, the highest ΣREY values in apatites from the mafic dyke are observed in reaction zones on the margins of unaltered magmatic Cl-rich apatite grains often adjacent to REY-depleted zones in the same grains (e.g., Fig. 8e). Another important difference between the granitoids and the dolerite dyke is the measurable S content in the latter, with maximum concentrations in intensely altered grains in close proximity to the chlorite veins (Fig. 13). In apatite from all three igneous rocks, relatively F-rich zones, with negligible Cl, REY, Si, and S, crosscut pre-existing domains. Scattered coarse-grained monazite, and more rarely florencite (in the RDG), occur within such zones.

Common to all occurrences of magmatic apatite is the formation of monazite inclusions in areas affected by depletion in REY and enrichment in F relative to Cl (Fig. 6; see below).

5.2.2. Hydrothermal apatite in mineralised granitoids

Apatite in the mineralised RDG from the deep mineralisation contrasts markedly with igneous apatite from non-mineralised RDG in that it contains higher concentrations of Cl (Fig. 14a). Such Cl-rich apatite is less altered relative to F-rich zones in the same grain, which are characteristically superimposed onto the former. From this, it is clear that such apatite is typical of an early hydrothermal stage and distinct, both chemically and texturally from the magmatic apatite observed in the RDG. Inclusion-rich cores, diagnostic of magmatic apatite, are completely lacking in the hydrothermal grains. As in the RDG, the early hydrothermal apatite shows a strong correlation between REY and Si, in which the F-rich zones are REY-depleted (Fig. 14b). However, in contrast to the RDG, S also correlates with REY, Cl, and Si (Fig. 14c).

Apatite in the distal satellite contains negligible Cl but shows similar REY vs. Si and S vs. Si trends as the deep mineralisation (Fig. 14d, e). There is, however, a sub-population (the small unzoned grains), which plots with high S values, even higher than the apatite in the DM. This sub-population also shows the highest Na concentrations relative to other apatite populations in the DS (Fig. 14f). Noteworthy is the

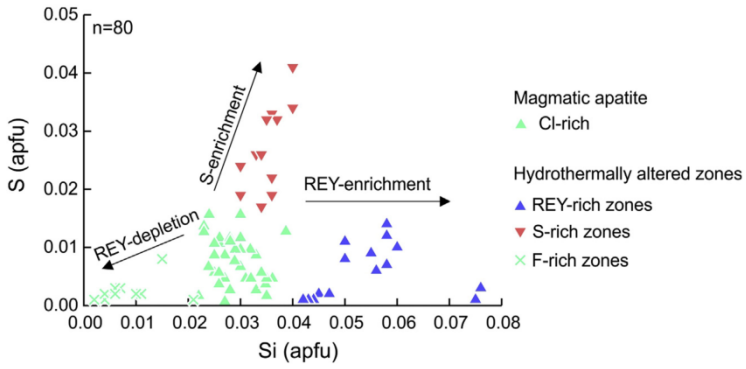

Fig. 13. Plot of S vs. Si illustrating compositional ranges of apatite from the dolerite dyke and key geochemical trends associated with hydrothermal alteration.

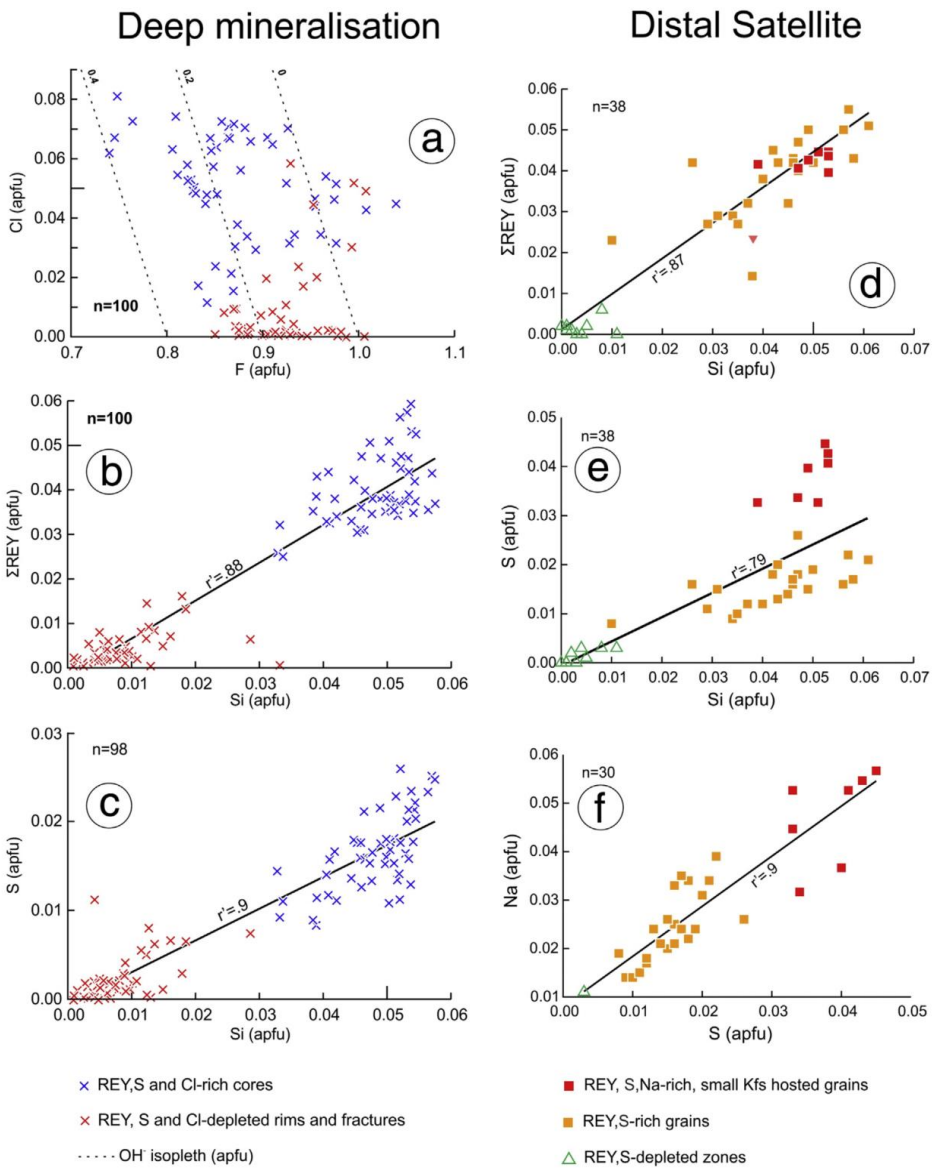

Fig. 14. (a–c) Compositional trends of apatite from Deep Mineralisation: (a) F vs. Cl; (b) ∑REY vs. Si; and (c) S vs. Si. (d–f) Compositional trends of apatite from distal satellite mineralisation: (d) ∑REY vs. Si; (e) S vs. Si; (f) Na vs. S.

excellent correlation between Na and S ($r^2 = 0.9$), which can be attributed to the obliteration of albite during apatite growth at the time of K-feldspar staining by Fe-oxides (Kontonikas-Charos et al., 2015). At this stage, Na can be assumed to be in the fluids (dissolution of albite), and will be readily incorporated in apatite particularly if S is also available. The latter can be also assumed since sulphides are formed at this stage. The strong correlation between S and Na (Fig. 14f) supports the idea that the two elements were incorporated at the same time in apatite via a coupled substitution mechanism (e.g., $SO_4^{2-} + Na^+ = PO_4^{3-} + Ca^{2+}$). Therefore the measured Na + S signature in this apatite, tied to areas around red-stained K-feldspar, can be related to progressive feldspar alteration in the RDG.

Despite the fact that the same style of mineralisation is observed in both locations, there are pronounced differences in the apatite compositions, i.e., Cl-rich in the DM, and Na-rich in the DS. These are features, which can be related to distinct stages of alteration. Similar to the non-mineralised granitoids, the F-rich, REY-poor, and S-poor zones crosscut earlier domains.

5.3. Apatite evolution at Olympic Dam

The evolution of apatite at Olympic Dam clearly spans both magmatic and hydrothermal stages. The composition of magmatic apatite reflects both the bulk rock chemistry of the host rock and its crystallisation history. Differences, both textural and geochemical, between apatite in the RDG and enclave-hosted apatite are indicative of the incorporation of exotic material into the RDG melt at the time of crystallisation. This interpretation rests on several lines of evidence: (i) the increased incidence

of pyrrhotite inclusions in apatite is closely tied to the presence of mafic enclaves in both RDG and HRQM; (ii) textural evidence for undercooling conditions during apatite crystallisation, e.g., abundance of acicular apatite in the enclaves, presence of small grains with quartz cores (Piccoli and Candela, 2002); (iii) neither RDG nor the HRQM granitoids contain pyrrhotite outside of the apatite cores; and (iv) whereas pyrrhotite inclusions are most likely to occur in apatite from mafic melts, the fluorite inclusions, present in the same cores, are likely be formed from felsic melts. All of these suggest that apatite co-crystallised with pyrrhotite + fluorite under conditions which were significantly different to those of each of the respective intrusive units, i.e., granitoids and mafic enclaves. Observations of pyrrhotite inclusions in apatite from granitic rocks elsewhere are also interpreted as 'foreign', possibly mafic material (Gottesmann and Wirth, 1997).

Hydrothermal apatite, hosted in early magnetite-dominant mineralisation in both mineralised locations, is interpreted to trace a high-temperature mineralising event in which the fluid is Cl-rich. The early generation is thus distinct from REY-, S-, and Cl-depleted apatite associated with later hematite–sericite alteration. Although not direct evidence, changes in the fluid salinities from early, hypersaline to late, diluted fluids spanning the magnetite dominant to hematite dominant alteration stages are put forward from fluid inclusion studies of various deposits and prospects in the Olympic Province; see summary and discussion in Bastrakov et al. (2007) and references therein. We can only speculate that the type of ligands for various metals and cations in fluids associated with alteration cycles would have also changed from Cl-dominant to others, e.g., fluoride, carbonate, and sulphate. Such changes are however far more complex considering the deposit scale variation in any given mineral association and geochemistry throughout the deposit area (Ehrig et al., 2012) but also the locally closed context that can form within a breccia environment.

Widespread, coarser, and generally irregular distribution of monazite inclusions in apatite is seen in all samples. These are readily identified and are interpreted as products of hydrothermal overprinting by their increased abundance in domains of intense hematite–sericite alteration, alteration of biotite to chlorite, breakdown of igneous ilmenite to hematite–rutile symplectites, an association with zones of hydrothermal interaction across grain margins and fractures, a close association with REY-depleted zones in apatite, and the presence of hydrothermal minerals along associated fractures and channels. Such monazite may be associated with what could be minor huttonite, i.e. monoclinic $ThSiO_4$ as opposed to tetragonal $ThSiO_4$ (thorite). The occurrence of monazite inclusions in apatite, and their interpretation as hydrothermal products, has been reported by Harlov (2015). These inclusions form from fluids of variable chemistry over a wide P–T range. REY-depletion and monazite formation are achieved by destabilisation of coupled substitution mechanisms involving Si^{4+} ($Si^{4+} + REE^{3+} = P^{5+} + Ca^{2+}$) and Na^{+} ($Na^{+} + REE^{3+} = 2Ca^{2+}$), which result in the inability of apatite to retain REY, in turn leading to monazite crystallisation via coupled dissolution–precipitation reactions (see Harlov, 2015, and references therein).

The rare presence of two-phase [monazite-$ThSiO_4$ (huttonite?)] inclusions (Fig. 9g) along distinct zones crosscutting earlier areas of REY depletion appears to indicate further reworking of apatite within the DM. Replacement of monazite by $ThSiO_4$ has been reproduced experimentally over a wide range of P–T conditions using Th-enriched fluids (Harlov et al., 2007).

Progressive hydrothermal overprinting modifies apatite-bearing assemblages, and ultimately leads to its obliteration. Direct textural observations suggest a two-stage process: (i) apatite replacement by quartz (Fig. 6), releasing Ca^{2+}, $(PO_4)^{2-}$, and F^{-} to hydrothermal fluid; and (ii) dissolution of that quartz, presumably under extremely acidic (HF-rich) conditions. Such sequential stages of alteration are clearly observed in RDG along the drillhole transect, where disappearance of apatite correlates with corrosion of quartz at the boundary to the orebody. We can only speculate that fluid changes that facilitated the precipitation of quartz that corrodes apatite, and the subsequent replacement of that quartz and ultimately, apatite dissolution, relate to changes in silica speciation and stabilities of dissolved species as a function of the availability of F (and, presumably, also other metals), e.g. Chemtob et al. (2015).

6. Implications and outlook

Previous studies of apatite have overwhelmingly focused on either gaining insights into magmatic processes (Streck and Dilles, 1998; Belousova et al., 2002; Cao et al., 2012), or on the evolution of apatite in response to hydrothermal processes (Bonyadi et al., 2011; Harlov, 2015). The advantage of combining these two approaches in the present study and examining magmatic apatite from distinct, yet related intrusives, has shown that the geochemical and textural responses of apatite to a particular mineralising fluid is largely independent of the magmatic heritage since they all show comparable alteration patterns. Such an observation is important in the study of apatite in magmatic–hydrothermal systems as mineralisation and associated alteration are superimposed onto multiple protoliths, and where the source and physicochemical nature of the hydrothermal fluid(s) are often poorly constrained relative to the sequence of magmatic events.

At OD, apatite evolution, from magmatic to early- and late-stage hydrothermal, is expressed both geochemically and texturally emphasising its potential as a petrogenetic tool. Whereas the petrography of RDG magmatic apatite points to the assimilation of exotic material, subtle changes in the mineral chemistry of hydrothermal apatite record transition in alteration stages. The replacement of apatite, to complete obliteration by highly acidic fluids, which not only corroded apatite but also quartz, led to recycling of REY via subsequent crystallisation of discrete REY-bearing species — notably monazite but also xenotime and florencite. As such, apatite evolution clearly played an important role and may have been integral in contributing to the elevated REY-concentrations seen at OD.

Future work would encompass accurate, independent measurements of OH in apatite, allowing for a more confident approach to fluid–melt–mineral partitioning, also considering the recent concept for an apatite-based hygrometer (McCubbin and Jones, 2015).

Given the marked differences between mineralised and non-mineralised lithologies at OD, apatite chemistry has potential application as a tool in mineral exploration. This rationale will be further explored by testing whether distinct chondrite-normalised REE-patterns in apatite may represent a means for outlining its spatial position within an alteration envelope, or identifying if a particular alteration system is barren or fertile with respect to Cu–Au mineralisation. Such an approach may be extended to include detrital apatite in the thick cover sequences that blanket much of the Olympic Cu–Au Province.

Work to ascertain whether the categories of apatite defined here can be fingerprinted with respect to trace element signatures is currently ongoing. In this, we will also include apatite hosted within high-grade Cu ore, as well as other IOCG systems and larger expressions of alteration yet without mineralisation within the Olympic Cu–Au Province.

Acknowledgements

This work is supported by BHP Billiton. We gratefully acknowledge microanalytical assistance from the staff at Adelaide Microscopy, notably Ben Wade, and from Karsten Goemann, Central Science Laboratory, University of Tasmania. N.J.C. and K.E. acknowledge support from the ARC Research Hub for Australian Copper–Uranium. CLC acknowledges support from the 'FOX' project (Trace elements in iron oxides), supported by BHP Billiton Olympic Dam and the South Australian Mining and Petroleum Services Centre of Excellence. We appreciate the helpful and insightful review comments received from Daniel Harlov and an anonymous reviewer, as well as editorial handling by *Lithos* Editor-in-Chief, Nelson Eby.

Appendix A. Supplementary data

Supplementary data to this article can be found online at http://dx.doi.org/10.1016/j.lithos.2016.07.033.

References

Apukhtina, O.B., Kamenetsky, V.S., Ehrig, K., Kamenetsky, M.B., McPhie, J., Maas, R., Meffre, S., Goemann, K., Rodemann, T., Cook, N.J., Ciobanu, C.L., 2016. Postmagmatic magnetite–apatite assemblage in mafic intrusions: a case study of dolerite at Olympic Dam, South Australia. Contributions to Mineralogy and Petrology 171 (2). http://dx.doi.org/10.1007/s00410-015-1215-7.

Bastrakov, E.N., Skirrow, R.G., Davidson, G.J., 2007. Fluid evolution and origins of iron oxide Cu–Au prospects in the Olympic Dam District, Gawler Craton, South Australia. Economic Geology 102, 1415–1440.

Bea, F., Fershater, G., Corretge, L.G., 1992. The geochemistry of phosphorus in granite rocks and the effect of aluminium. Lithos 29, 43–56.

Belousova, E.A., Walters, S., Griffin, W.L., O'Reilly, S.Y., 2001. Trace-element signatures of apatites in granitoids from the Mt Isa Inlier, northwestern Queensland. Australian Journal of Earth Sciences 48, 603–619.

Belousova, E.A., Griffin, W.L., O'Reilly, S.Y., Fisher, N.I., 2002. Apatite as an indicator mineral for mineral exploration: trace-element compositions and their relationship to host rock type. Journal of Geochemical Exploration 76, 45–69.

Billiton, B.H.P., 2015. http://www.bhpbilliton.com/~/media/bhp/documents/investors/annual-reports/2015/bhpbillitonannualreport2015.pdf.

Blissett, A.H., Creaser, R.A., Daly, S.J., Flint, D.J., Parker, A.J., 1993. Gawler Range Volcanics. In: Drexel, J.F., Preiss, W.V., Parker, A.J. (Eds.), The Geology of South Australia. The Precambrian: Adelaide, Geological Survey of South Australia, Bulletin 54 Vol. 1, pp. 107–131.

Bonyadi, Z., Davidson, G.J., Mehrabi, B., Meffre, S., Ghazban, F., 2011. Significance of apatite REE depletion and monazite inclusions in the brecciated Se–Chahun iron oxide–apatite deposit, Bafq district, Iran: insights from paragenesis and geochemistry. Chemical Geology 281, 253–269.

Boudreau, A., Kruger, F., 1990. Variation in the composition of apatite through the Merensky cyclic unit in the western Bushveld Complex. Economic Geology 85, 737–745.

Candela, P.A., 1986. Generalized mathematical models for the fractional evolution of vapor from magmas in terrestrial planetary crusts. In: Saxena, S.K. (Ed.), Advances in Physical GeochemistryPhysics and Chemistry of the Terrestrial Planets Vol. 6. Springer-Verlag, New York, pp. 362–398.

Cao, M., Li, G., Qin, K., Seitmuratova, E.Y., Liu, Y., 2012. Major and trace element characteristics of apatites in granitoids from Central Kazakhstan: implications for petrogenesis and mineralization. Resource Geology 62, 63–83.

Chemtob, S.M., Rossman, G.R., Young, E.D., Ziegler, K., Moynier, F., Eiler, J.M., Hurowitz, J.A., 2015. Silicon isotope systematics of acidic weathering of fresh basalts, Kilauea volcano, Hawai'i. Geochimica et Cosmochimica Acta 169, 63–81.

Ciobanu, C.L., Wade, B., Cook, N.J., Schmidt Mumm, A., Giles, D., 2013. Uranium-bearing hematite from the Olympic Dam Cu–U–Au deposit, South Australia; a geochemical tracer and reconnaissance Pb–Pb geochronometer. Precambrian Research 238, 129–147.

Creaser, R.A., 1989. The geology and petrology of Middle Proterozoic felsic magmatism of the Stuart Shelf, South Australia. Unpublished Ph.D. thesis, La Trobe University, Melbourne.

Ehrig, K., McPhie, J., Kamanetsky, V.S., 2012. Geology and mineralogical zonation of the Olympic Dam iron oxide Cu–U–Au–Ag deposit, South Australia. In: Hedenquist, J.W., Harris, M., Camus, F. (Eds.), Geology and Genesis of Major Copper Deposits and Districts of the World, a Tribute to Richard Sillitoe. Society of Economic Geologists Special Publication Vol. 16, pp. 237–268.

Gottesmann, B., Wirth, R., 1997. Pyrrhotite inclusions in dark pigmented apatite from granitic rocks. European Journal of Mineralogy 9, 491–500.

Harlov, D.E., 2015. Apatite: a fingerprint for metasomatic processes. Elements 11, 171–176.

Harlov, D.E., Andersson, U.B., Förster, H.-J., Nyström, J.O., Dulski, P., Broman, C., 2002. Apatite–monazite relations in the Kiirunavaara magnetite–apatite ore, northern Sweden. Chemical Geology 191, 47–72.

Harlov, D.E., Wirth, R., Hetherington, C.J., 2007. The relative stability of monazite and huttonite at 300–900 °C and 200–1000 MPa: metasomatism and the propagation of metastable mineral phases. American Mineralogist 92, 1652–1664.

Harrison, T.M., Watson, E.B., 1984. The behaviour of apatite during crustal anatexis: equilibrium and kinetic considerations. Geochimica et Cosmochimica Acta 48, 1467–1477.

Hayward, N., Skirrow, R.G., 2010. Geodynamic setting and controls on iron oxide Cu–Au (±U) ore in the Gawler Craton, South Australia. In: Porter, T.M. (Ed.)Hydrothermal Iron Oxide Copper–Gold & Related Deposits: A Global Perspective Vol. 3. PGC Publishing, Adelaide, pp. 1–27.

Hovis, G.L., Harlov, D.E., 2010. Solution calorimetric investigation of fluor-chlorapatite crystalline solutions. American Mineralogist 95, 946–952.

Hovis, G.L., McCubbin, F.M., Nekvasil, H., Ustunisik, G., Woerner, W.R., Lindsley, D.H., 2014. A novel technique for fluorapatite synthesis and the thermodynamic mixing behaviour of F–OH apatite crystalline solutions. American Mineralogist 99, 890–897.

Huang, Q., Kamenetsky, V.S., McPhie, J., Ehrig, K., Meffre, S., Maas, R., Thompson, J., Kamenetsky, M., Chambefort, I., Apukhtina, O., Hu, Y., 2015. Neoproterozoic (ca. 820–830 Ma) mafic dykes at Olympic Dam, South Australia: links with the Gairdner Large Igneous Province. Precambrian Research 271, 160–172.

Huang, Q., Kamenetsky, V.S., Ehrig, K., McPhie, J., Kamenetsky, M., Cross, K., Meffre, S., Agangi, A., Chambefort, I., Direen, N.G., Maas, R., Apukhtina, O., 2016. Olivine-phyric basalt in the Mesoproterozoic Gawler silicic large igneous province, South Australia: examples at the Olympic Dam Iron Oxide Cu–U–Au–Ag deposit and other localities. Precambrian Research 281, 185–199.

Hughes, J.M., Rakovan, J.F., 2015. Structurally robust, chemically diverse: apatite and apatite supergroup minerals. Elements 11, 165–170.

Ismail, R., Ciobanu, C.L., Cook, N.J., Teale, G.S., Giles, D., Schmidt Mumm, A., Wade, B., 2014. Rare earths and other trace elements in minerals from skarn assemblages, Hillside iron oxide–copper–gold deposit, Yorke Peninsula, South Australia. Lithos 184–187, 456–477.

Jagodzinski, E.A., 2005. Compilation of SHRIMP U–Pb Geochronological Data. Olympic Domain, Gawler Craton, South Australia, 2001–2003. Geoscience Australia, Record 2005/20.

Johnson, J.P., Cross, K.C., 1995. U–Pb geochronological constraints on the genesis of Olympic Dam Cu–U–Au–Ag deposit, South Australia. Economic Geology 88, 1046–1063.

Jonsson, E., Harlov, D.E., Majka, J., Högdahl, K., Persson-Nilsson, K., 2016. Fluorapatite-monazite-allanite relations in the Grängesberg apatite-iron oxide ore district, Bergslagen, Sweden. American Mineralogist 101, 1769–1782.

Kontonikas-Charos, A., Ciobanu, C.L., Cook, N.J., 2014. Albitization and redistribution of REE and Y in IOCG systems: insights from Moonta-Wallaroo, Yorke Peninsula, South Australia. Lithos 208, 178–201.

Kontonikas-Charos, A., Ciobanu, C.L., Cook, N.J., Ehrig, K., Kamenetsky, V.S., 2015. Deuteric coarsening and albitization in Hiltaba granites from the Olympic Dam IOCG deposit, South Australia. Proceedings, Mineral Resources in a Sustainable World, 13th Biennial SGA Meeting, Nancy, France, August 2015 Vol. 3, pp. 1099–1102.

Krneta, S., Ciobanu, C.L., Cook, N.J., Ehrig, K., Kamenetsky, V.S., 2015. Apatite in the Olympic Dam Cu–U–Au–Ag deposit. Proceedings, Mineral Resources in a Sustainable World, 13th Biennial SGA Meeting, Nancy, France, August 2015 Vol. 3, pp. 1103–1106.

McCubbin, F.M., Jones, R.H., 2015. Extraterrestrial apatite: planetary geochemistry to astrobiology. Elements 11, 183–188.

Pan, Y., Fleet, M.E., 2002. Compositions of the apatite-group minerals: substitution mechanisms and controlling factors. Reviews in Mineralogy and Geochemistry 48, 13–49.

Pasero, M., Kampf, A., Ferraris, C., Pekov, I.V., Rakovan, J., White, T., 2010. Nomenclature of the apatite supergroup minerals. European Journal of Mineralogy 22, 163–179.

Piccoli, P.M., Candela, P.A., 1994. Apatite in felsic rocks: a model for the estimation on initial halogen concentrations in the Bishop TuV (Long Valley) and Tuolumne Intrusive Suite (Sierra Nevada Batholith) magmas. American Journal of Science 294, 92–135.

Piccoli, M.P., Candela, P.A., 2002. Apatite in igneous systems. Reviews in Mineralogy and Geochemistry 48, 255–292.

Reeve, J.S., Cross, K.C., Smith, R.N., Oreskes, N., 1990. Olympic Dam copper–uranium–gold–silver deposit. In: Hughes, F.E. (Ed.), Geology of the Mineral Deposits of Australia and Papua New Guinea: Australasian Institute of Mining and Metallurgy. Monograph Vol. 14, pp. 1009–1035.

Rønsbo, J.G., 1989. Coupled substitutions involving REE's and Na and Si in apatites in alkaline rocks from Ilimaussaq, South Greenland, and the petrological implications. American Mineralogist 74, 896–901.

Skirrow, R.G., Bastrakov, E.N., Barovich, K., Fraser, G.L., Creaser, R., Fanning, M.C., Raymond, O.L., Davidson, G.J., 2007. Timing of iron oxide Cu–Au–(U) hydrothermal activity and Nd isotope constraints on metal sources in the Gawler craton, South Australia. Economic Geology 102, 1441–1470.

Streck, M.J., Dilles, J.H., 1998. Sulfur evolution of oxidized arc magmas as recorded in apatite from a porphyry copper batholith. Geology 26, 523–526.

Webster, J.D., Piccoli, P.M., 2015. Magmatic apatite: a powerful, yet deceptive, mineral. Elements 11, 177–182.

Wolf, M.B., London, D., 1995. Incongruent dissolution of REE- and Sr-rich apatite in peraluminous granitic liquids: differential apatite, monazite, and xenotime solubilities during anatexis. American Mineralogist 80, 765–775.

Zhu, C., Sverjensky, D.A., 1991. Partitioning of F–Cl–OH between minerals and hydrothermal fluids. Geochimica et Cosmochimica Acta 55, 1837–1858.

CHAPTER 3

RARE EARTH ELEMENT BEHAVIOUR IN APATITE FROM THE OLYMPIC DAM CU-U-AU-AG DEPOSIT, SOUTH AUSTRALIA

Sasha Krneta[1], Cristiana L. Ciobanu[2], Nigel J. Cook[2], Kathy Ehrig[3], Alkis Kontonikas-Charos[1]

[1]*School of Physical Sciences, The University of Adelaide, Adelaide, S.A., 5005, Australia*

[2]*School of Chemical Engineering, The University of Adelaide, Adelaide, S.A., 5005, Australia*

[3]*BHP Olympic Dam, Adelaide, SA 5000, Australia*

Paper published in Minerals 7, 135

Statement of Authorship

Title of Paper	Rare earth element behaviour in apatite from the Olympic Dam Cu-U-Au-Ag deposit, South Australia. Minerals 7(8), 135.
Publication Status	☑ Published ☐ Accepted for Publication ☐ Submitted for Publication ☐ Unpublished and Unsubmitted w ork w ritten in manuscript style
Publication Details	Krneta, S., Ciobanu, C.L., Cook, N.J., Ehrig, K. and Kontonikas-Charos, A. 2017. Rare earth element behaviour in apatite from the Olympic Dam Cu-U-Au-Ag deposit, South Australia. Minerals 7(8), 135.

Principal Author

Name of Principal Author (Candidate)	Sasha Krneta
Contribution to the Paper	Collected sample material, devised a plan for and performed analytical work, processed and interpreted data , wrote manuscript and acted as corresponding author.
Overall percentage (%)	60
Certification:	This paper reports on original research I conducted during the period of my Higher Degree by Research candidature and is not subject to any obligations or contractual agreements with a third party that would constrain its inclusion in this thesis. I am the primary author of this paper.
Signature	Date 13/9/17

Co-Author Contributions

By signing the Statement of Authorship, each author certifies that:

the candidate's stated contribution to the publication is accurate (as detailed above);

permission is granted for the candidate in include the publication in the thesis; and

the sum of all co-author contributions is equal to 100% less the candidate's stated contribution.

Name of Co-Author	Cristiana Ciobanu
Contribution to the Paper	Supervised development of work, assisted in defining direction of research, provided assistance in the collection of analytical data, assisted with data interpretation and helped with manuscript preparation.
Overall percentage (%)	25
Signature	Date 13. Sept. 2017

Name of Co-Author	Nigel Cook
Contribution to the Paper	Supervised development of work, assisted in defining direction of research, assisted with data interpretation and helped with manuscript preparation.
Overall percentage (%)	12
Signature	Date 13/9/17

Name of Co-Author	Kathy Ehrig
Contribution to the Paper	Assisted in defining the direction of research, provided samples, assisted with data interpretation and evaluated manuscript.
Overall percentage (%)	2
Signature	Date 13/09/17

Name of Co-Author	Alkis Kontonikas-Charos
Contribution to the Paper	Provided advice on samples and evaluated manuscript.
Overall percentage (%)	1
Signature	Date 13/09/17

minerals

MDPI

Article

Rare Earth Element Behaviour in Apatite from the Olympic Dam Cu–U–Au–Ag Deposit, South Australia

Sasha Krneta [1,*], Cristiana L. Ciobanu [2], Nigel J. Cook [2], Kathy Ehrig [3] and Alkis Kontonikas-Charos [1]

[1] School of Physical Sciences, The University of Adelaide, Adelaide, SA 5000, Australia; alkiviadis.kontonikas-charos@adelaide.edu.au
[2] School of Chemical Engineering, The University of Adelaide, Adelaide, SA 5000, Australia; cristiana.ciobanu@adelaide.edu.au (C.L.C.); nigel.cook@adelaide.edu.au (N.J.C.)
[3] BHP Billiton, Olympic Dam, Adelaide, SA 5000, Australia; Kathy.J.Ehrig@bhpbilliton.com
* Correspondence: sasha.krneta@adelaide.edu.au; Tel.: +61-433-254-401

Received: 4 July 2017; Accepted: 29 July 2017; Published: 2 August 2017

Abstract: Apatite is a common magmatic accessory in the intrusive rocks hosting the giant ~1590 Ma Olympic Dam (OD) iron-oxide copper gold (IOCG) ore system, South Australia. Moreover, hydrothermal apatite is a locally abundant mineral throughout the altered and mineralized rocks within and enclosing the deposit. Based on compositional data for zoned apatite, we evaluate whether changes in the morphology and the rare earth element and Y (REY) chemistry of apatite can be used to constrain the fluid evolution from early to late hydrothermal stages at OD. The ~1.6 Ga Roxby Downs granite (RDG), host to the OD deposit, contains apatite as a magmatic accessory, locally in the high concentrations associated with mafic enclaves. Magmatic apatite commonly contains REY-poor cores and REY-enriched margins. The cores display a light rare earth element (LREE)-enriched chondrite-normalized fractionation pattern with a strong negative Eu anomaly. In contrast, later hydrothermal apatite, confined to samples where magmatic apatite has been obliterated due to advanced hematite-sericite alteration, displays a conspicuous, convex, middle rare earth element (MREE)-enriched pattern with a weak negative Eu anomaly. Such grains contain abundant inclusions of florencite and sericite. Within high-grade bornite ores from the deposit, apatite displays an extremely highly MREE-enriched chondrite-normalized fractionation trend with a positive Eu anomaly. Concentrations of U and Th in apatite mimic the behaviour of ∑REY and are richest in magmatic apatite hosted by RDG and the hydrothermal rims surrounding them. The shift from characteristic LREE-enriched magmatic and early hydrothermal apatite to later hydrothermal apatite displaying marked MREE-enriched trends (with lower U, Th, Pb and ∑REY concentrations) reflects the magmatic to hydrothermal transition. Additionally, the strong positive Eu anomaly in the MREE-enriched trends of apatite in high-grade bornite ores are attributable to alkaline fluid conditions.

Keywords: apatite; rare earth elements; hydrothermal fluids; Olympic Dam

1. Introduction

The concentrations of trace elements within hydrothermal minerals and their variation can provide valuable information on fluid parameters and the conditions of ore deposition if the studied assemblages are well constrained with respect to their paragenetic position [1]. Rare earth elements and yttrium (REY) have proven particularly instructive, as they display a systematic decrease in atomic radius with an increased atomic number which causes a divergence in their geochemical behaviour [2]. REY behaviour has been demonstrated to be highly sensitive to changes in parameters such as pH, temperature, salinity, redox conditions and fluid composition [3–6], thus allowing for

the use of chondrite-normalized REY fractionation patterns as geochemical tracers that can assist interpretation of hydrothermal systems.

Chondrite-normalized REY fractionation patterns of apatite-group minerals [$Ca_5(PO_4)_3(F,Cl,OH)$] are recognized as valuable tools for the understanding of hydrothermal processes [7]. REY trends in apatite supergroup minerals are widely reported from a variety of rocks; however, these trends are, in general, remarkably consistent with one another, conspicuous by their consistent, downward-sloping chondrite-normalized REY fractionation trends featuring relative enrichment in LREE with negative Eu anomalies of variable strength [8–10]. Variation in the magnitude of Eu anomalies across rock suites spanning entire metallogenic provinces have been used to infer variability or change in redox conditions in magmatic apatite [8].

Apatite occurs in many magmatic-hydrothermal deposit types including iron-oxide copper gold (IOCG) systems. Apatite is particularly common in the early stage of evolution of IOCG deposits, in which the apatite-magnetite assemblages may resemble those in iron-oxide apatite (IOA)-type deposits such as Kiruna, Sweden [11], Pea Ridge, MO, USA [12], and the Bafq district of Iran [13,14].

Apatite may record hydrothermal events through changes in composition and thus provide information on the chemistry of the host intrusive rocks. Its refractory character in the burial or weathering environment allows those patterns to be preserved. For this reason, and its widespread presence within or associated with magmatic-hydrothermal deposits, apatite has accordingly received much attention as a potential pathfinder mineral in terranes obscured by residual glacial sediments [15,16].

The Olympic Cu–Au Province of South Australia [17] hosts several major deposits and many more prospects for IOCG and IOA-like mineralization [18]. Olympic Dam (OD) is by far the largest deposit in the province [19]. A recent study of fluorapatite from OD [20] has demonstrated significant compositional variation with respect to minor and trace elements among fluorapatite from rocks of igneous origin (variably altered granitoids and coeval mafic rocks). Apatite evolution is described in the context of the deposit-scale zoning, noting geochemically and morphologically distinct apatite types across the transition, from unaltered through altered to mineralized host rocks. The data also supports the incorporation of other substituting elements (notably Na) into apatite, hinting at a close relationship between apatite geochemistry and evolution of the mineralizing system from early-stage albitization involving the breakdown and replacement of feldspars [21] to magnetite alteration followed by hematite-sericite alteration. Crucially, each stage in this evolution is marked by distinct REY-signatures in apatite which are proportional to, and directly related to, hydrothermal conditions and, possibly, also to partitioning among other co-crystallising REY-bearing minerals.

In this work, we show chondrite-normalized REY fractionation patterns and trace element concentrations in fluorapatite from the same rocks described previously by Krneta et al. (2016) [20]. In addition, apatite from high-grade ore is also studied. We aim to show that REY signatures in apatite can trace the magmatic to hydrothermal transition in granite-hosted IOCGs. Secondly, the marked change in REY trends in apatite formed within the mineralizing environment responsible for high-grade Cu-Au ore.

The recognition of apatite trace element signatures associated with specific stages of mineralization may prove useful in the use of apatite as a mineral pathfinder in terranes like the Gawler Craton that are obscured by ubiquitous cover sequences [10].

2. Background

2.1. Deposit Geology

The Olympic Dam Cu–U–Au–Ag deposit, South Australia (10,400 Mt at 0.77% Cu, 0.25 kg/t, 0.32 g/t Au and 1 g/t Ag; [22]), is one of the world's largest orebodies and is anomalously rich in REY relative to crustal values [19]. The deposit is hosted within the Olympic Dam Breccia Complex (ODBC; [23]), a collective term used to describe the breccias, intrusive phases and minor bedded

sediments which host the deposit. This is hosted within the Roxby Downs granite (RDG), a medium- to coarse-grained, undeformed, pink, two-feldspar granite, locally displaying rapakivi textures [19] emplaced at ~1.6 Ga as part of the Hiltaba Suite (HS). Together with a second granitoid also sampled here, the Horn Ridge quartz monzonite (HRQM), HS rocks are part of the Burgoyne batholith, which makes up the basement of the northern Stuart Shelf [24]. Contemporaneous with the aforementioned granitoids, and also hosted within the ODBC, are a swarm of felsic to ultramafic dykes, including strongly altered olivine-phyric dolerites (dolerite dyke, DD) [20,25].

The OD deposit is an ideal subject for this study because it features a marked spatial zonation with respect to mineralogy. This is expressed by iron-oxides (magnetite is dominant laterally and at depth whereas inside the deposit, hematite and sericite assemblages prevail), and also with respect to Cu-Fe-sulphide speciation [18,26]. This transition in Fe-oxide species within OD, as well in other deposits and prospects regionally, is marked by a decrease in salinity (from 20–40 to 1–8 wt % NaCl equivalent) coincident with a decrease in temperature from ~400 °C to 150–300 °C [27,28].

Feldspar alteration processes, including albitization, have recently been characterized at OD [21,29]. Transformations in feldspar are preserved, especially in the least-altered RDG outside the deposit and at depth, but are largely obliterated within the deposit. This took place prior to the main stage of mineralization, which was marked by the precipitation of magnetite-pyrite assemblages. The albitization process is recognized as an in situ reaction controlled by a coupled dissolution-reprecipitation reaction. This requires no externally-sourced fluids but results in significant trace element redistribution [21].

Fluorapatite is present both as a primary magmatic accessory phase and as a product of early hydrothermal alteration. Fluorapatite is particularly abundant in locations marginal to, or outside, the ODBC [20,30]. Within the OD deposit, apatite is scarce, although it is present in, for example, high-grade ore samples such as those described in [31]. U–Pb and Pb–Pb hematite geochronology gives an age of ~1.6 Ga [31–33], concordant with the ages of magmatic and hydrothermal zircon within rocks hosting the deposit [34]. Apatite also occurs within the deposit where hydrothermal albite is preserved at depth. At OD, fluorapatite has been used to obtain U–Pb ages for deep, primary mineralization [35], coeval basalts and dykes [25], and for crosscutting mafic dykes [30,36].

2.2. Apatite Mineral Chemistry

The apatite supergroup [37] is defined by the formula $A_5(XO_4)_3Z$, where the A position is largely occupied by Ca^{2+}, along with lesser of Na^{+}, Sr^{2+}, Pb^{2+}, Ba^{2+}, Mn^{2+}, Fe^{2+}, Mg^{2+}, Ni^{2+}, Co^{2+}, Cu^{2+}, Zn^{2+}, Sn^{2+}, Cd^{2+}, Eu^{2+}, REE^{3+}, Y^{3+}, Ti^{4+}, Th^{4+} and U^{4+}. The X position is dominated by P^{5+}, as (PO_4), but can also host other highly-charged anions (SO_4^{2-}, AsO_4^{3-}, VO_4^{3-} and SiO_4^{4-}). The occupancy of the Z position (F^{-}, Cl^{-} and OH^{-}) defines the three end-members; fluorapatite; chlorapatite; and hydroxyapatite, respectively. Although the majority of natural apatites are F-dominated, they nevertheless contain all three anions components in different proportions [38].

Crystal structures of apatite group minerals are described by Hughes and Rakovan [39]. In detail, the atomic arrangement is made up of 3 cation polyhedra: a tetrahedron, XO_4, and two calcium positions; a tri-capped trigonal prism, $A1O_9$, and an irregular polyhedron, $A2O_6Z$, where Z is one of the anions F, Cl, OH.

The substitution of elements into apatite can either be direct, whereby the substituting element has a charge equal to that of the element it is replacing, or heterovalent, requiring either facilitation via coupled substitution or the presence of a vacancy [40,41]. Both types of mechanism are particularly relevant for the substitution of REY and other elements of interest in apatite (□ = vacancy):

$$REE^{3+} + Na^{+} = 2Ca^{2+}$$

$$REE^{3+} + SiO_4^{4-} = Ca^{2+} + PO_4^{3-}$$

$$U^{4+} + \square = 2Ca^{2+}$$

$$Th^{4+} + \square = 2Ca^{2+}$$

Substitution in apatite adheres to Goldschmidt's Rules, whereby elements with ionic radii closest to those of the substituted ion are most easily incorporated. REE and Y substitute for Ca and show distinct preferences for the two Ca positions; LREE preferring the Ca2 site and the HREE the Ca1 [39]. Although the selective incorporation of certain REY was considered to be crystallographically controlled [41], more recent work [42] has shown how external physiochemical parameters such as fluid composition or temperature can impact significantly on otherwise predictable patterns. Study of REY signatures in apatite has thus led to the recognition of individual signatures, or REY behaviours, attributable to specific fluid conditions within the evolution of a mineralized system [7,10]. The recent work of Migdisov et al. (2016) [6] has emphasized the variability of REY behaviour brought about by the dominance of certain REY complexes such as REY–Cl and $–SO_4$ over others, notably REY–F. Such variability can be tested against changes in fluid characteristics, as suggested from fluid inclusion studies—i.e., from early, high-T and salinity fluids to late, lower-T and salinity fluids, corresponding to magnetite and hematite stages, respectively, at OD [43]—and in other IOCG prospects from the Cu–Au Olympic Province [28]. Of particular relevance to apatite is how, under different conditions, LREE may be partitioned relative to HREE due to the increased stability and solubility as LREE–Cl complexes, thus explaining the LREE-enriched nature of many hydrothermal deposits, including IOCG systems [6].

Mao et al. (2016) [9] recognized that hydrothermal, and particularly ore-related, apatite may contain concentrations of trace elements, which are significantly lower than those of magmatic origin. This may relate to the co-crystallization, in ores, of apatite with other minerals that can incorporate certain trace elements more effectively than apatite but which seldom occur as magmatic accessories. Given the capacity of apatite to incorporate a variety of different elements, this contribution, although focused on REY, also reports concentrations of other trace elements.

3. Sample Suite

The samples investigated are the same as those described in [20], with the addition of one sample (three polished blocks) from massive bornite ore from the underground mine previously used for the U–Pb dating of hematite and zircon [31]. Overall, the sample suite encompasses Hiltaba-aged intrusive rocks (both felsic and mafic) displaying variable degrees of alteration, early magnetite-dominant mineralization (DM and DS), and high-grade bornite ore (Table 1, Figure 1).

The sample suite also covers apatite within two mineralized locations outside the main orebody, DM and DS. In the former, abundant apatite is found at the contact between RDG and a felsic volcanic unit at depths >2 km and this apatite is studied here. Apatite from DS is studied from the best mineralized interval hosted by red-stained K-feldspar altered granite. In both locations, the main mineralization consists of chalcopyrite and pyrite and is associated with co-existing magnetite and hematite; martite is also abundant along with sericite and chlorite.

The high-grade massive bornite samples, along with other similar cm to dm-sized pockets of massive Cu ore, are atypical of sulphide mineralization within the deposit, which is dominantly disseminated. Such massive mineralization is present throughout the orebody and may be representative of latest pulses of hydrothermal fluids associated with the evolution of the IOCG system at OD. Clustered inclusions of hematite are present in the bornite along with minor chlorite, however, no sericite is present, indicating that such assemblages are also atypical with respect to the description of "hematite-sericite alteration" considered for IOCGs.

Following [20], the distinct types of apatite at OD are classified according to their origin and association with particular intrusive rocks and hydrothermal assemblages as follows: (i) magmatic apatite within the RDG, HQRM and the DD; (ii) early hydrothermal magnetite–pyrite–apatite assemblages at depth within the "deep mineralization" (DM), as well as laterally outside of the main resource within "distal satellite" mineralization (DS); (iii) domains within magmatic and early hydrothermal apatite that relate to hematite-sericite alteration; and (iv) apatite associated with high-grade bornite ore. These categories represent the various stages of the magmatic-to-hydrothermal evolution identified at OD. Although IOCG-style mineralization at several locations in the Olympic Cu–Au province lacks a clear spatial association with intrusive

rocks likely to have been a source of hydrothermal fluids, thus prohibiting direct study of the magmatic-to-hydrothermal transition, the evolution in the REY signatures reported below may be nevertheless characteristic for the Cu–Au mineralization associated with similar intrusive rocks.

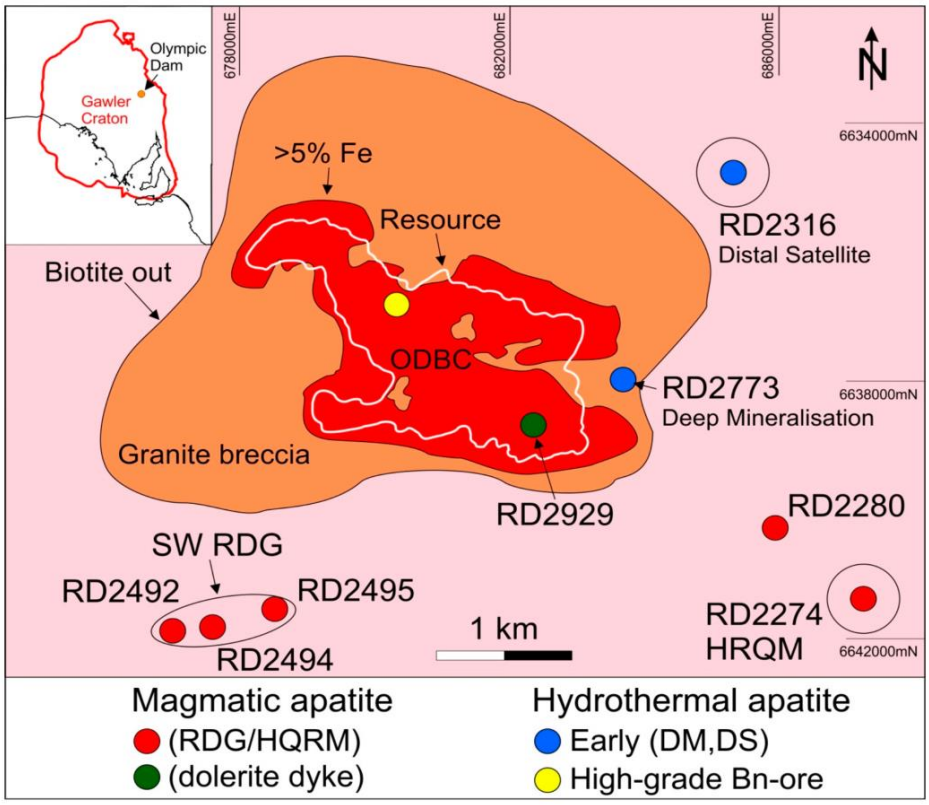

Figure 1. Geological sketch map of the Olympic Dam deposit at Relative level −350 m showing the location of the sampled drillholes/studied samples (modified from [19]). The insert map shows the location of Olympic Dam with respect to the Gawler Craton and South Australia.

4. Analytical Methodology

Laser ablation inductively coupled plasma mass spectrometry (LA-ICP-MS) spot analysis and element mapping was performed using a Resonetics M-50-LR 193 nm Excimer laser attached to an Agilent 7700cx Quadrupole ICP mass spectrometer (Adelaide Microscopy, The University of Adelaide). Ablation took place in an Ultra High Purity He (0.7 L/min) atmosphere, mixed after leaving the ablation cell with Ar (0.93 L/min). The mix was passed through a pulse-homogenizing device after which it was introduced to the torch. ICP-MS calibration was performed regularly so as to increase sensitivity. LA-ICP-MS analysis was performed with a laser beam energy output of 80 mJ and a spot size varying from 8 to 18 µm. Total acquisition time was 60 s for each analysis comprising a 30 s background measurement, 30 s of ablation and a 40 s delay between analysis allowing for adequate wash-out, gas stabilization and processing time. The following isotopes were analysed ^{23}Na, ^{24}Mg, ^{27}Al, ^{28}Si, ^{31}P, ^{34}S, ^{39}K, ^{43}Ca, ^{45}Sc, ^{47}Ti, ^{51}V, ^{55}Mn, ^{56}Fe, ^{57}Fe, ^{59}Co, ^{60}Ni, ^{63}Cu, ^{66}Zn, ^{75}As, ^{85}Rb, ^{88}Sr, ^{89}Y, ^{90}Zr, ^{93}Nb, ^{95}Mo, ^{118}Sn, ^{133}Cs, ^{137}Ba, ^{139}La, ^{140}Ce, ^{141}Pr, ^{146}Nd, ^{147}Sm, ^{153}Eu, ^{157}Gd, ^{159}Tb, ^{163}Dy, ^{165}Ho, ^{166}Er, ^{169}Tm, ^{172}Yb, ^{175}Lu, ^{181}Ta, ^{182}W, ^{204}Pb, ^{206}Pb, ^{208}Pb, ^{232}Th and ^{238}U.

Table 1. Overview of lithologies and samples discussed in this study.

Drill Hole No.	Depth (m)	Sample ID	Sample Category/Rock Type	Hydrothermal REY, Th and U Bearing Minerals								
				Apatite	Monazite	Thorite	Florencite	Xenotime	Bastnäsite	Uraninite	Coffinite	Brannerite
Underground grab sample	-	OD10.1	**High grade Cu–Au ore**—The samples consist of massive bornite with abundant hematite inclusions. Apatite occurs as grains and/or aggregates within bornite and also as milled fragments along veinlets in bornite. No sericite is present but minor chlorite and occasional barite. Other accessories are zircon (metamict) with halos of xenotime, abundant, fine-grained (few µm) florencite as rims along other mineral boundaries, coffinite and brannerite. Trace minerals include U-, REY-bearing phases as dusty inclusions within altered hematite and molybdenite in bornite.	x			x	x		x	x	x
	-	OD10.2		x			x	x		x	x	x
	-	OD10.3		x			x	x		x	x	x
RD2274	372.5	2274-1	**Horn Ridge quartz monzonite**—Equigranular, medium-grained, K-feldspar-quartz-plagioclase Quartz Monzonite. Slightly altered by hematite-sericite-chlorite altered. Abundant biotite and hornblende has been altered to chlorite. Some primary ilmenite remains. Abundant apatite in association with accessory magnetite, ilmenite, and zircon.	x	x							
RD2929	401.3	RX7913	**Dolerite dyke**—intensely hematite-sericite-chlorite-carbonate altered dolerite. The majority of primary silicates are replaced by secondary minerals but accessory apatite and Fe-Ti-oxides (hemoilmenite) are largely preserved.	x	x							
	411.1	RX7914		x	x							
RD2494	588.2	RX7860	**Roxby Downs granite**—Equigranular, medium to coarse grained K-feldspar-quartz-plagioclase granite. Fresh to pervasively hematite-sericite-chlorite altered. Some samples contain spherical mafic enclaves. Fresh samples are characterized by the presence of biotite, edenite and ilmenite. Locally abundant primary igneous apatite in association with other accessories such as magnetite, ilmenite and zircon.	x	x							
RD2492	756	RX7864		x	x							
RD2495	584	RX7866		x	x							
RD2280	413	2280-1		x	x							
	416.5	-2		x	x							
	416.9	-3		x	x							
	440	-4		x	x							
	466	-5		x	x							
	467.5	-6		x	x	x	x					
	475.7	-7			x		x					
RD2773	2208	2773-1	**Deep Mineralization**—magnetite-chlorite-carbonate to hematite-sericite altered Roxby Downs Granite and Felsic Unit. Apatite occurs in a number of morphologies ranging from small, unzoned to large, zoned and fractured grains, in isolation as well as large aggregates.	x	x							
	2261	-2		x	x					x		
	2289	-3		x	x				x	x		
	2309	-4		x	x							
	1998	-5		x	x	x						
RD2316	580.2	RX6685	**Distal Satellite Mineralization**—magnetite-chlorite-sericite (minor) altered Roxby Downs Granite. Red-stained K-feldspar present, no plagioclase is present. Apatite occurs in a wide range of sizes. Larger grains are commonly zoned and occur in aggregates in close association to magnetite. Feldspars replaced by chlorite and by an unusual assemblage of molybdenite-bastnäsite.	x	x				x			
	588.2	RX6687		x	x				x	x		
	645.3	RX6691		x	x				x			

The analyses of reference materials were performed after every ten sample analyses and comprised readings identical in every respect to that of the samples. Two analyses of NIST 612, followed by one of NIST 610 and a final two NIST 612 analyses comprised the standard run. Dwell times for each element were set to 0.01 s except for ^{75}As, ^{89}Y, ^{153}Eu, ^{157}Gd, ^{159}Tb, ^{163}Dy, ^{165}Ho, ^{166}Er, ^{169}Tm, ^{172}Yb, ^{175}Lu, ^{181}Ta, ^{182}W, ^{204}Pb, ^{206}Pb, ^{208}Pb, ^{232}Th and ^{238}U, which were set to 0.02 s to achieve better sensitivity. Data processing was performed using GLITTER data reduction software with P as an internal standard using values obtained via electron probe microanalysis (EPMA) and given in [20]. All analyses were examined in detail in time-resolved depth profiles to ensure negligible contamination from included or adjacent minerals during ablation. Typical minimum detection limits for the analyzed elements are given in Supplementary Material Table S1.

Quantitative compositional data for apatite were obtained using a CAMECA SX-Five instrument at Adelaide Microscopy (The University of Adelaide). It was operated at accelerating voltages of 15 kV, and beam currents of 20 nA. X-ray lines, standards, count times, and typical minimum limits of detection are given as Supplementary Material Table S2. A spot size of 1 μm was used.

5. Results

5.1. Apatite in Altered and Unaltered Igneous Rocks

Magmatic apatite from RDG features core (low) to rim (high) zonation with respect to REY concentrations (Table 2; Figure 2a–c). In many cases, apatite displays a mottled texture (Figure 2a) due to the presence of sub-micron to nanometre-scale inclusions of pyrrhotite and fluorite, which were observed in abundance in parts of RDG with numerous mafic enclaves. The occurrence of pores and a broader range of sulphide inclusions attached to these pores (including pyrite, chalcopyrite, etc.), as well as monazite inclusions, particularly in areas of strong hydrothermal fluid overprint (Figure 2c,d) is interpreted as fluid percolation. Nonetheless, both core and rim zones display LREE-enriched chondrite-normalized fractionation patterns with strong negative Eu anomalies (Figure 3a,b). ΣREY concentrations in the REY-rich rims are approximately double those in the core, and have a positive Ce anomaly (Figure 3b). Hydrothermally altered zones in apatite hosted in weakly-altered RDG become depleted slightly in both LREE and HREE when compared to the inclusion-rich cores (Figures 2c,d and 3b). They also display a marked decrease in the strength of the Eu anomaly (mean 0.4 vs. 0.24; Figure 3b). At shallow levels closer to the OD deposit, in pervasively hematite-sericite altered RDG, magmatic apatite has been obliterated.

Locally, in RDG with intervals of hematite-sericite alteration, unzoned apatite features abundant inclusions of florencite [$REEAl_3(PO_4)_2(OH)_6$] (Figure 2e). In this case, the trend changes markedly, displaying a MREE-enriched chondrite-normalized REY fractionation pattern with weak negative Eu anomalies (0.59) and slight negative Y-anomalies (0.6) (Figures 2e and 3b).

The HRQM contains igneous apatite grains that resemble those within the RDG in many ways, including the presence of inclusion-rich cores, hydrothermal rims and domains of REY-depletion (Table 3). However, both the hydrothermal rims and REY-depletion are poorly developed. HRQM apatite is LREE-enriched and almost indistinguishable from that hosted in the RDG although the negative Eu-anomaly is slightly stronger (Figure 3a).

Unzoned, Cl-bearing fluorapatite from the DD (Figure 2f) displays a LREE-enriched chondrite-normalized pattern with weak negative Eu- and Y-anomalies (Table 4; Figure 3c) with average ΣREY-concentrations approximately half compared to apatite from RDG and HRQM. Distinct hydrothermally REY-enriched zones in apatite from the DD mirror aspects seen in the RDG whereby ΣREY concentrations correlate with development of a weak Ce-anomaly (Figure 3b,d). Moreover, the REY-depletion seen along fractures and grain rims shows a preferential depletion in LREE, and is associated with a weaker negative Eu anomaly and a stronger negative Y anomaly (Figure 3c,d).

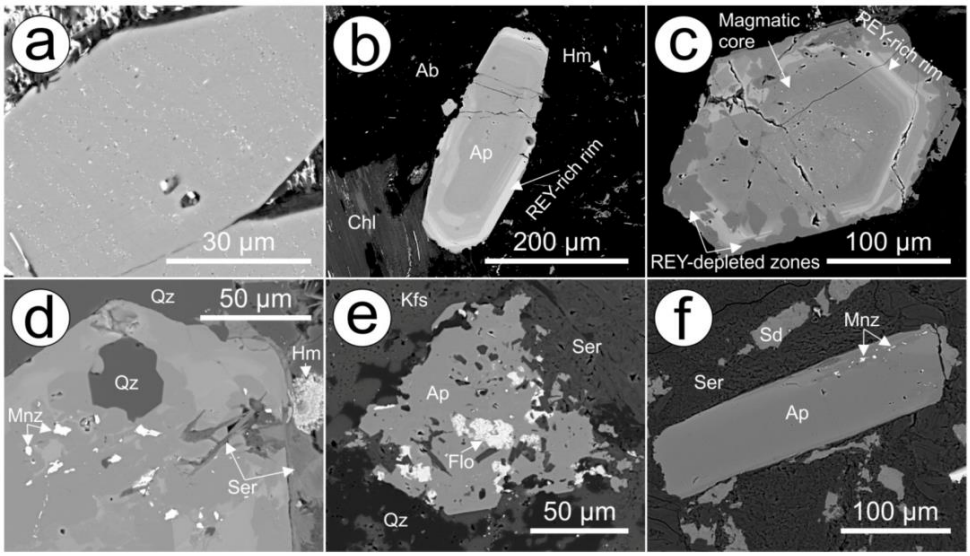

Figure 2. Back-scatter electron (BSE) images showing the textural and morphological character of apatite hosted in igneous rocks. (**a**) Magmatic apatite with numerous minute inclusions of a Fe-sulphide mineral; (**b**) Apatite grain displaying a rare earth element and Y (REY)-enriched rim and a magmatic core hosted within albite adjacent to biotite now replaced by chlorite; (**c**) Apatite grain showing a inclusion-rich magmatic core, REY-rich rim and zones of REY-depletion on the margin of the grain affecting both the magmatic core and REY-rich rim; (**d**) Magmatic apatite within pervasively altered Roxby Downs granite (RDG) displaying broad zones of REY-depletion that contain numerous inclusions of sericite and monazite; (**e**) Apatite associated with the hematite-sericite alteration of the RDG with numerous inclusions of sericite and florencite; (**f**) Unzoned apatite with a REY-depleted zone containing small grains of monazite (hematite-sericite altered dolerite dyke (DD)). Abbreviations: Ab-albite, Ap-apatite, Chl-chlorite, Flo-florencite, Hm-hematite, Kfs-K-feldspar, Mnz-monazite, Qz-quartz, Sd-siderite, Ser-sericite.

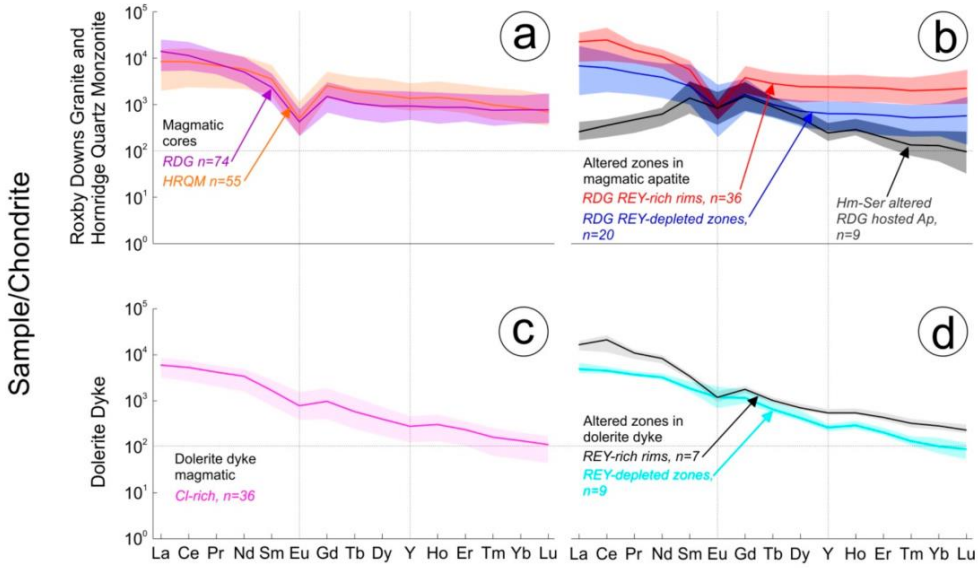

Figure 3. Chondrite-normalized [44] laser ablation inductively coupled plasma mass spectrometry (LA-ICP-MS) plots of apatite hosted in the igneous rock studied. Analyses were performed on multiple grains hosted within samples listed in captions for the respective tables. (**a**) Magmatic cores in RDG and HQRM apatite. (**b**) Hydrothermally altered zones in magmatic RDG hosted apatite. (**c**) Dolerite dyke magmatic apatite. (**d**) Hydrothermally altered zones in dolerite dyke magmatic apatite.

Table 2. Rare earth element (REE) and trace element concentrations in apatite from the Roxby Downs granite (ppm). Apatite analyses were performed on multiple grains in the following samples: RDG magmatic cores—2280-2, -3, -4, -5, -6, RX7860, RX7864, RX7866; REY-rich rims—2280-2, -3, -5; REY-depleted zones—2280-2, -3, -4, -5; Hm-Ser altered RDG hosted—2280-6. <mdl—below minimum detection limit.

RDG Magmatic Cores	**Na**	**Mg**	**Al**	**Si**	**S**	**K**	**Sc**	**Ti**	**V**	**Mn**	**Fe**	**Co**	**Ni**	**Cu**	**Zn**	**As**	**Rb**	**Sr**	**Zr**	**Nb**	**Mo**	**Sn**	**Cs**
Mean *n* = (74)	729	242	997	4865	252	454	1.86	63.6	20.3	400	3150	2.56	<mdl	<mdl	11.3	21.0	2.41	82.1	18.9	0.29	<mdl	<mdl	<mdl
S.D.	284	335	1813	3631	34.4	679	2.15	57.5	15.4	127	2981	3.15	<mdl	<mdl	16.5	11.0	1.94	20.7	35.4	0.39	<mdl	<mdl	<mdl
Min	176	15.6	0.97	1659	186	7.78	0.30	24.3	1.13	75.3	144	0.09	<mdl	<mdl	0.53	4.13	0.56	55.4	0.22	0.03	<mdl	<mdl	<mdl
Max	1356	1804	9474	14,497	361	2982	10.3	457	74.3	872	10,810	10.8	<mdl	<mdl	75.7	52.8	8.83	184	181	1.82	<mdl	<mdl	<mdl
Ba	Ta	W	^{204}Pb	^{206}Pb	^{208}Pb	Th	U	La	Ce	Pr	Nd	Sm	Eu	Gd	Tb	Dy	Y	Ho	Er	Tm	Yb	Lu	ΣREY
7.30	<mdl	<mdl	<mdl	9.21	37.5	120	23.8	3311	6968	707	2304	347	23.7	297	38.5	227	1463	47.9	139	18.8	123	18.9	16,035
14.1	<mdl	<mdl	<mdl	5.38	24.4	90.0	48.4	1020	2064	194	694	143	9.49	125	16.7	95.9	523	18.6	49.6	6.55	43.6	6.89	4409
0.24	<mdl	<mdl	<mdl	2.86	12.6	29.3	5.21	1256	3362	410	1254	164	11.8	134	17.6	99.7	738	21.4	69.5	8.74	62.9	9.85	8728
71.7	<mdl	<mdl	<mdl	21.6	116	528	385	6028	13,912	1374	4832	820	68.0	700	88.5	492	3033	101	276	40.8	256	43.2	31,774
REY-Rich Rims	**Na**	**Mg**	**Al**	**Si**	**S**	**K**	**Sc**	**Ti**	**V**	**Mn**	**Fe**	**Co**	**Ni**	**Cu**	**Zn**	**As**	**Rb**	**Sr**	**Zr**	**Nb**	**Mo**	**Sn**	**Cs**
Mean *n* = (36)	562	239	891	6558	240	137	2.32	55.0	4.90	483	2419	2.03	1.70	<mdl	7.07	38.2	1.69	71.0	11.6	0.35	<mdl	<mdl	<mdl
S.D.	164	438	1717	2187	25.7	171	3.84	33.8	4.98	96.1	2681	2.49	1.70	<mdl	11.4	10.4	1.39	16.5	30.0	0.57	<mdl	<mdl	<mdl
Min	215	24.4	2.36	3419	205	5.58	0.48	23.1	1.16	336	268	0.08	0.37	<mdl	0.49	15.9	0.65	41.2	0.61	0.04	<mdl	<mdl	<mdl
Max	974	1766	7000	14,134	296	566	18.7	188	25.0	760	9704	9.18	7.40	<mdl	47.9	57.5	6.76	116	174	2.19	<mdl	<mdl	<mdl
Ba	Ta	W	^{204}Pb	^{206}Pb	^{208}Pb	Th	U	La	Ce	Pr	Nd	Sm	Eu	Gd	Tb	Dy	Y	Ho	Er	Tm	Yb	Lu	ΣREY
<mdl	<mdl	0.24	<mdl	32.1	118	388	62.2	5567	15,739	1438	5106	873	49.5	783	106	621	3887	133	372	51.7	347	57.0	35,129
<mdl	<mdl	0.18	<mdl	15.3	42.3	134	30.4	1873	6535	372	1339	303	11.8	321	44.1	264	1508	55.8	142	21.8	166	36.4	10,309
<mdl	<mdl	0.04	<mdl	14.5	49.7	159	27.1	2132	5749	770	2904	399	27.6	364	47.8	288	1965	64.7	187	26.2	174	26.9	15,877
<mdl	<mdl	0.65	<mdl	66.7	235	713	136	9122	30,376	2145	7603	1395	70.8	1449	192	1187	7130	258	681	102	775	148	56,494
REY Depleted Zones	**Na**	**Mg**	**Al**	**Si**	**S**	**K**	**Sc**	**Ti**	**V**	**Mn**	**Fe**	**Co**	**Ni**	**Cu**	**Zn**	**As**	**Rb**	**Sr**	**Zr**	**Nb**	**Mo**	**Sn**	**Cs**
Mean *n* = (20)	572	541	2872	8011	305	665	6.15	111	20.9	241	4820	2.17	<mdl	<mdl	17.8	29.7	2.36	122	30.7	0.58	<mdl	<mdl	<mdl
S.D.	344	741	3288	5169	150	1076	5.69	100.0	22.4	156	3426	2.43	<mdl	<mdl	18.9	16.0	1.49	48.9	41.9	0.42	<mdl	<mdl	<mdl
Min	199	18.9	2.37	1897	204	37.5	0.66	36.1	0.61	65.5	495	0.10	<mdl	<mdl	0.96	6.18	0.57	65.1	1.53	0.08	<mdl	<mdl	<mdl
Max	1591	1611	9915	14,085	895	4085	19.5	446	70.5	525	10,805	7.90	<mdl	<mdl	56.0	58.4	4.70	199	123	1.25	<mdl	<mdl	<mdl
Ba	Ta	W	^{204}Pb	^{206}Pb	^{208}Pb	Th	U	La	Ce	Pr	Nd	Sm	Eu	Gd	Tb	Dy	Y	Ho	Er	Tm	Yb	Lu	ΣREY
13.0	<mdl	<mdl	<mdl	8.96	34.5	194	20.4	1679	3942	462	1841	386	49.2	341	37.3	184	1037	36.0	97.5	13.5	89.5	14.6	10,210
16.5	<mdl	<mdl	<mdl	5.09	20.1	195	14.6	1149	2447	257	986	247	33.7	175	19.0	112	677	24.1	70.1	9.96	64.6	10.6	5509
1.03	<mdl	<mdl	<mdl	2.18	7.90	30.0	5.56	394	1181	161	657	153	11.7	144	19.3	84.9	337	11.6	29.9	3.25	20.2	1.62	3738
57.7	<mdl	<mdl	<mdl	19.2	89.9	727	57.7	4452	8782	963	3749	1130	156	779	103	578	3341	119	343	47.4	305	41.9	22,275
Hm-Ser Altered RDG Hosted	**Na**	**Mg**	**Al**	**Si**	**S**	**K**	**Sc**	**Ti**	**V**	**Mn**	**Fe**	**Co**	**Ni**	**Cu**	**Zn**	**As**	**Rb**	**Sr**	**Zr**	**Nb**	**Mo**	**Sn**	**Cs**
Mean *n* = (9)	777	291	2082	6261	291	1442	3.17	118	9.55	78.9	5796	0.43	<mdl	<mdl	10.3	11.1	6.73	136	24.9	0.43	<mdl	0.85	<mdl
S.D.	550	477	1372	2340	77.4	706	2.50	104	10.1	54.7	5242	0.42	<mdl	<mdl	9.15	6.57	2.00	34.6	29.6	0.40	<mdl	0.47	<mdl
Min	151	12.2	536	3827	230	627	0.77	44.0	0.64	38.0	1023	0.11	<mdl	<mdl	2.47	4.78	5.39	79.6	0.72	0.06	<mdl	0.45	<mdl
Max	1511	1529	4491	9454	494	2600	8.31	401	31.5	199	13,372	1.09	<mdl	<mdl	28.6	25.0	9.03	189	92.7	1.39	<mdl	1.93	<mdl
Ba	Ta	W	^{204}Pb	^{206}Pb	^{208}Pb	Th	U	La	Ce	Pr	Nd	Sm	Eu	Gd	Tb	Dy	Y	Ho	Er	Tm	Yb	Lu	ΣREY
29.7	<mdl	<mdl	<mdl	29.7	7.84	50.0	168	84.5	258	47.0	280	195	44.6	290	32.0	125	399	16.3	32.8	3.62	24.1	2.70	1835
30.2	<mdl	<mdl	<mdl	27.6	4.81	34.2	164	50.9	89.0	11.4	82.6	122	26.9	160	12.6	42.0	162	6.02	15.4	2.08	15.8	2.24	431
2.76	<mdl	<mdl	<mdl	3.34	3.23	10.8	13.2	41.7	127	23.6	164	98.1	17.1	110	13.1	49.7	187	6.50	14.6	1.37	9.91	0.83	1261
95.6	<mdl	<mdl	<mdl	75.3	17.7	129	446	204	403	60.4	412	489	109	632	54.6	213	655	28.0	60.9	7.18	54.0	6.66	2698

Table 3. REE and trace element concentrations in apatite from the Horn Ridge quartz monzonite (ppm). Apatite analyses were performed on multiple apatite grains in sample 2274-1. <mdl—below minimum detection limit.

HRQM Magmatic Cores	Na	Mg	Al	Si	S	K	Sc	Ti	V	Mn	Fe	Co	Ni	Cu	Zn	As	Rb	Sr	Zr	Nb	Mo	Sn	Cs
Mean *n* = (55)	1122	174	348	2636	253	172	<mdl	205	16.0	530	1527	1.20	<mdl	<mdl	<mdl	26.0	1.79	157	0.94	<mdl	<mdl	<mdl	<mdl
S.D.	372	140	401	794	19.0	235	<mdl	608	6.58	161	1307	1.35	<mdl	<mdl	<mdl	9.10	1.84	23.6	0.58	<mdl	<mdl	<mdl	<mdl
Min	343	33.3	3.44	1313	211	4.97	<mdl	17.6	2.12	283	256	0.12	<mdl	<mdl	<mdl	15.4	0.19	110	0.24	<mdl	<mdl	<mdl	<mdl
Max	1753	649	1454	4731	299	874	<mdl	2830	29.0	955	4956	5.30	<mdl	<mdl	<mdl	52.0	8.29	237	2.62	<mdl	<mdl	<mdl	<mdl
Ba	Ta	W	^{204}Pb	^{206}Pb	^{208}Pb	Th	U	La	Ce	Pr	Nd	Sm	Eu	Gd	Tb	Dy	Y	Ho	Er	Tm	Yb	Lu	ΣREY
1.69	<mdl	0.33	<mdl	10.2	22.4	60.0	19.4	2009	5160	653	2631	523	28.1	505	69.1	404	2131	78.7	202	24.4	138	17.2	14,573
1.70	<mdl	0.22	<mdl	3.88	8.96	20.5	8.52	685	1689	202	786	148	9.04	132	18.2	109	557	21.4	56.0	7.15	42.0	4.83	4355
0.27	<mdl	0.05	<mdl	3.95	4.05	11.7	7.17	468	1436	206	990	240	11.5	269	36.2	211	1161	41.5	104	11.7	68.1	8.52	6217
7.61	<mdl	0.93	<mdl	24.3	48.1	97.1	50.8	3652	10,018	1272	5061	1051	63.8	1010	143	886	4507	173	433	57.3	331	40.5	28,692

Table 4. REE and trace element concentrations in apatite from the dolerite dyke (ppm). Apatite analyses were performed on multiple grains in the following samples: Cl-rich magmatic—RX7913, RX7914; REY-rich rims—RX7913; Depleted zones—RX7913, RX7914.

Cl-Rich Magmatic	Na	Mg	Al	Si	S	K	Sc	Ti	V	Mn	Fe	Co	Ni	Cu	Zn	As	Rb	Sr	Zr	Nb	Mo	Sn	Cs
Mean *n* = (36)	666	1904	530	2428	244	118	1.68	51.7	30.2	553	3583	1.19	<mdl	<mdl	9.49	11.2	<mdl	1182	9.42	<mdl	<mdl	<mdl	<mdl
S.D.	199	359	855	1720	25.6	248	0.52	11.9	12.1	43.7	1335	1.14	<mdl	<mdl	11.8	4.31	<mdl	75.0	13.9	<mdl	<mdl	<mdl	<mdl
Min	434	1250	0.54	1095	212	4.40	0.97	36.6	14.3	426	2517	0.21	<mdl	<mdl	0.76	3.79	<mdl	1021	2.38	<mdl	<mdl	<mdl	<mdl
Max	1154	2486	2563	8646	299	928	3.21	90.2	53.5	646	9012	5.00	<mdl	<mdl	56.6	21.2	<mdl	1283	65.9	<mdl	<mdl	<mdl	<mdl
Ba	Ta	W	^{204}Pb	^{206}Pb	^{208}Pb	Th	U	La	Ce	Pr	Nd	Sm	Eu	Gd	Tb	Dy	Y	Ho	Er	Tm	Yb	Lu	ΣREY
28.5	<mdl	0.14	<mdl	3.21	17.5	44.0	5.83	1328	3050	369	1475	236	41.7	184	20.1	94.3	423	16.1	36.4	3.91	21.2	2.66	7301
6.35	<mdl	0.13	<mdl	1.60	10.5	32.8	6.29	339	845	107	441	82.9	16.0	71.1	7.83	34.5	145	5.61	12.2	1.32	7.13	0.91	2090
19.0	<mdl	0.02	<mdl	1.23	6.75	13.0	1.82	711	1537	179	688	108	20.6	76.3	8.49	40.3	189	7.04	16.5	1.56	8.43	1.07	3601
47.3	<mdl	0.56	<mdl	7.70	51.8	141	24.4	1922	4287	514	2112	400	83.1	354	39.4	172	698	26.4	54.8	6.21	32.0	4.05	10,218
REY-Rich Rims	**Na**	**Mg**	**Al**	**Si**	**S**	**K**	**Sc**	**Ti**	**V**	**Mn**	**Fe**	**Co**	**Ni**	**Cu**	**Zn**	**As**	**Rb**	**Sr**	**Zr**	**Nb**	**Mo**	**Sn**	**Cs**
Mean *n* = (7)	1101	1010	150	2793	238	43.1	1.33	43.2	15.6	475	2521	0.28	<mdl	<mdl	2.32	33.6	<mdl	835	16.9	<mdl	<mdl	<mdl	<mdl
S.D.	370	322	328	1056	26.1	74.1	1.27	13.3	5.07	87.6	699	0.10	<mdl	<mdl	1.39	9.38	<mdl	198	28.3	<mdl	<mdl	<mdl	<mdl
Min	459	612	0.47	2024	218	7.07	0.46	27.5	9.07	342	1874	0.12	<mdl	<mdl	0.52	16.6	<mdl	595	4.73	<mdl	<mdl	<mdl	<mdl
Max	1411	1483	737	5110	293	194	4.06	67.8	22.6	581	3890	0.39	<mdl	<mdl	3.80	42.0	<mdl	1114	81.1	<mdl	<mdl	<mdl	<mdl
Ba	Ta	W	^{204}Pb	^{206}Pb	^{208}Pb	Th	U	La	Ce	Pr	Nd	Sm	Eu	Gd	Tb	Dy	Y	Ho	Er	Tm	Yb	Lu	ΣREY
16.3	<mdl	0.15	<mdl	7.59	52.1	164	13.8	3672	12,067	947	3561	477	63.6	335	34.9	165	821	28.8	66.9	7.81	44.0	5.50	22,297
5.02	<mdl	0.12	<mdl	2.29	31.7	94.2	4.77	622	2967	128	475	63.0	13.9	46.4	3.63	16.9	79.4	3.23	8.59	1.18	5.78	0.90	4258
9.39	<mdl	0.04	<mdl	3.76	18.5	57.2	6.10	2757	6547	710	2776	402	49.7	281	30.5	147	738	26.4	57.1	6.33	36.3	4.68	14,581
22.9	<mdl	0.32	<mdl	9.68	110	353	19.5	4412	15,150	1102	4199	549	85.6	394	41.2	200	990	35.7	84.4	9.69	53.7	7.17	27,302
REY-Depleted Zones	**Na**	**Mg**	**Al**	**Si**	**S**	**K**	**Sc**	**Ti**	**V**	**Mn**	**Fe**	**Co**	**Ni**	**Cu**	**Zn**	**As**	**Rb**	**Sr**	**Zr**	**Nb**	**Mo**	**Sn**	**Cs**
Mean *n* = (9)	860	1509	365	2963	264	44.5	1.72	56.1	27.6	426	3642	2.17	1.82	3.97	9.86	17.7	0.36	1074	22.4	<mdl	0.27	<mdl	<mdl
S.D.	178	249	460	1995	17.2	32.0	0.88	10.7	6.17	71.0	1620	2.14	1.60	1.11	5.72	8.34	0.27	71.2	22.5	<mdl	0.05	<mdl	<mdl
Min	581	1141	22.0	1373	235	16.0	0.92	40.4	20.9	300	1978	0.33	0.52	2.34	2.57	7.34	0.06	971	2.77	<mdl	0.22	<mdl	<mdl
Max	1208	1792	1234	6655	282	87.1	3.16	70.4	38.7	511	5949	5.75	5.16	5.95	17.4	28.5	0.78	1202	54.9	<mdl	0.35	<mdl	<mdl
Ba	Ta	W	^{204}Pb	^{206}Pb	^{208}Pb	Th	U	La	Ce	Pr	Nd	Sm	Eu	Gd	Tb	Dy	Y	Ho	Er	Tm	Yb	Lu	ΣREY
29.5	<mdl	0.24	<mdl	5.07	39.2	102	5.99	1089	2602	324	1397	261	63.6	220	22.4	99.6	396	15.4	31.6	3.23	16.0	2.11	6545
6.69	<mdl	0.28	<mdl	3.16	19.8	60.9	3.84	197	322	36.8	156	44.0	21.4	50.4	4.08	17.7	48.2	2.21	4.22	0.52	4.07	0.52	712
21.5	<mdl	0.06	<mdl	2.32	21.3	30.9	2.37	884	2217	290	1223	219	37.0	162	18.6	87.2	329	12.6	27.0	2.56	11.2	1.28	5756
37.5	<mdl	0.85	<mdl	10.7	83.0	228	11.4	1483	3202	386	1686	360	108	332	31.7	141	469	19.4	40.2	4.07	24.5	2.89	7724

5.2. Early Hydrothermal Apatite

Early hydrothermal apatite is observed in both the DM (*REY, S and Cl-rich cores*; Figure 4a–c) and the DS mineralization (*REY and S-rich grains*; Figure 4d). It displays similar, almost indistinguishable LREE-enriched chondrite-normalized REY fractionation patterns featuring moderate negative Eu anomalies (Tables 5 and 6; Figure 5a). Such patterns most resemble those of igneous apatite in the RDG and HRQM, although the negative Eu anomalies are weaker.

Although poorly developed and only rarely seen in DS apatite, zones of alteration in early hydrothermal apatite featuring depletion in REY are widespread throughout DM apatite. These are visible on BSE images as darker domains that are concentrated along fractures and grain rims and commonly contain inclusions of hematite, sericite and monazite (*REY, S and Cl-depleted zones*; Figure 4a,b). The depletion in such zones primarily affects the LREE, significantly flattening the REY-signature and weakening the negative Eu anomaly. In instances where such altered zones within apatite are adjacent to texturally late chalcopyrite (*REY, S and Cl-depleted zones adjacent to chalcopyrite*; Figure 4b), both LREE and HREE are affected. Such domains in apatite display MREE-enriched trends with weak negative Eu and Y anomalies (Figure 5b) similar in appearance to the MREE-enriched signatures of apatite with florencite inclusions (Figures 2e and 3b).

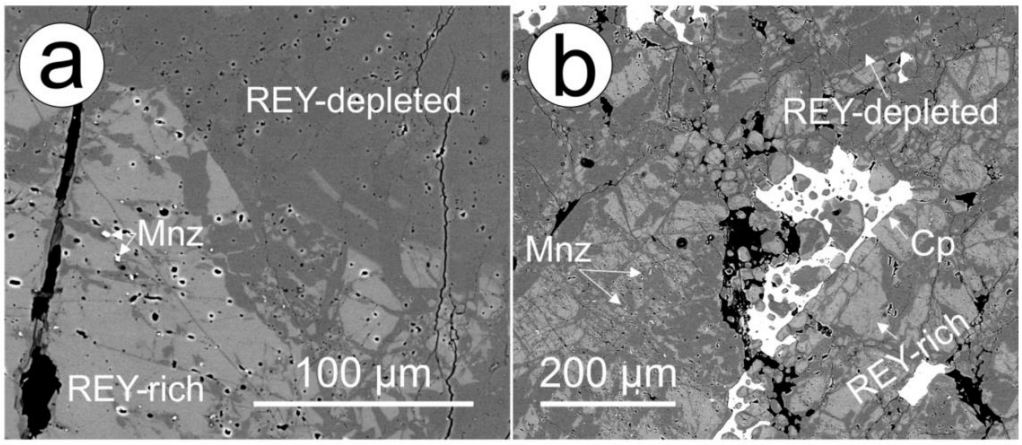

Figure 4. Back-scatter electron (BSE) images showing the textural and morphological character of early hydrothermal apatite from the magnetite-dominant mineralization (DM). (**a**) REY, Cl and S-rich zone (bright) adjacent to zones depleted in these elements (dark) related to fractures and associated with crystallization of monazite; (**b**) Extensive REY, Cl and S depletion in apatite associated with fracturing and the formation of monazite with late chalcopyrite infill. Abbreviations: Ap: apatite; Cp: chalcopyrite; Mnz: monazite.

5.3. High-Grade Bornite Ore

Fluorapatite is a relatively rare component of the ores themselves, making up just 0.103% of the orebody based on mineral liberation analysis of 10,000 samples [18]. However, in samples of high-grade massive bornite, apatite is present as a minor but pervasively distributed and intrinsic mineral component in the assemblage (Table 7, Figure 6a). Besides bornite, the second most abundant mineral is hematite, also in terms of its pervasive distribution. Hematite occurs as two generations defined by textures and trace element signatures [45]. These are: (i) coarser, brecciated, porous and rounded grains poor in U-W-Mo, hosting discrete inclusions of REY- and U-minerals; and (ii) acicular aggregates with U-W-Mo-oscillatory zonation patterns; the latter was dated at 1577 ± 5 Ma [31]. Based on textures and trace elements patterns, the acicular hematite is younger than type (i), and hematite type (ii) is co-genetic with the studied apatite because it is observed to grow within it (Figure 6b,c). In addition, fragments of milled hematite-(i) and bornite are found within apatite, which has undergone crystallization (developing crystal faces) as it seals brecciation within the bornite-hematite assemblage (Figure 6d).

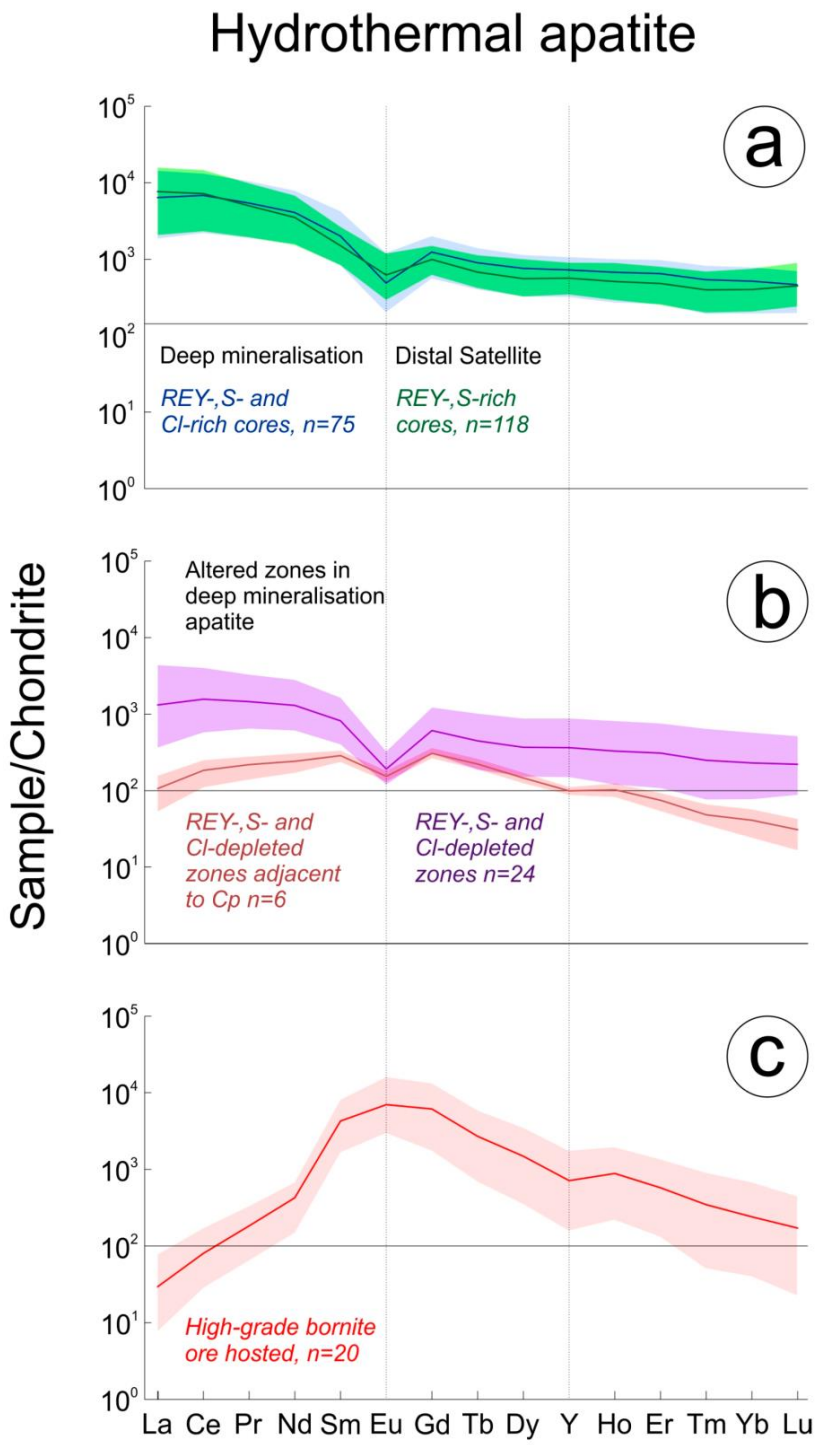

Figure 5. Chondrite-normalized [44] LA-ICP-MS plots of hydrothermal apatite. Analyses were performed on multiple grains hosted within samples listed in the captions to the respective tables. (**a**) Hydrothermal apatite hosted in the Deep and Distal Satellite Mineralization. (**b**) Altered zones in Deep Mineralization hosted apatite related. (**c**) Apatite hosted within the high-grade bornite ore.

Table 5. REE and trace element concentrations in apatite from the Deep Mineralization (ppm). Apatite analyses were performed on multiple grains in the following samples: REY, S and Cl-rich cores—2773-1, -2, -3, -4, -5; REY, S and Cl-depleted zones—2773-1, -2, -5; REY, S and Cl-depleted zones adjacent to Cp—2773-4. <mdl—below minimum detection limit.

REY, S and Cl-Rich Cores	**Na**	**Mg**	**Al**	**Si**	**S**	**K**	**Sc**	**Ti**	**V**	**Mn**	**Fe**	**Co**	**Ni**	**Cu**	**Zn**	**As**	**Rb**	**Sr**	**Zr**	**Nb**	**Mo**	**Sn**	**Cs**
Mean *n* = (75)	1272	79.9	192	2676	257	79.6	0.57	44.6	1.25	91.7	597	0.23	<mdl	<mdl	7.28	112	4.46	387	0.24	0.19	<mdl	<mdl	<mdl
S.D.	670	23.2	364	1111	24.2	166	0.37	15.4	1.60	26.8	305	0.12	<mdl	<mdl	6.44	24.5	7.51	57.9	0.19	0.27	<mdl	<mdl	<mdl
Min	409	28.2	0.45	1001	211	3.98	0.25	22.8	0.11	50.5	232	0.06	<mdl	<mdl	0.79	50.8	0.06	240	0.04	0.01	<mdl	<mdl	<mdl
Max	3557	149	1461	5517	334	826	2.41	95.1	9.17	188	1891	0.57	<mdl	<mdl	30.2	171	35.0	624	1.07	1.92	<mdl	<mdl	<mdl
Ba	Ta	W	^{204}Pb	^{206}Pb	^{208}Pb	Th	U	La	Ce	Pr	Nd	Sm	Eu	Gd	Tb	Dy	Y	Ho	Er	Tm	Yb	Lu	ΣREY
7.58	<mdl	0.50	<mdl	17.5	26.0	35.5	27.6	1520	4192	504	1868	298	27.4	247	32.5	187	1138	37.2	104	13.5	83.3	11.4	10,263
9.80	<mdl	0.87	<mdl	11.3	34.6	20.2	16.3	602	1486	178	626	97.0	6.95	68.7	9.24	56.3	339	11.5	33.0	4.46	26.7	3.32	3408
0.44	<mdl	0.03	<mdl	2.35	2.99	2.37	2.38	441	1344	177	720	123	11.4	111	14.5	79.6	495	14.9	41.3	4.83	31.3	4.87	3790
52.6	<mdl	4.16	<mdl	70.5	201	70.4	54.4	3386	8066	970	3596	627	67.5	398	46.9	279	1674	54.9	156	20.5	126	17.2	18,312
REY, S and Cl-Depleted Zones	**Na**	**Mg**	**Al**	**Si**	**S**	**K**	**Sc**	**Ti**	**V**	**Mn**	**Fe**	**Co**	**Ni**	**Cu**	**Zn**	**As**	**Rb**	**Sr**	**Zr**	**Nb**	**Mo**	**Sn**	**Cs**
Mean *n* = (24)	355	40.2	217	1565	264	101	0.52	43.2	0.62	125	268	0.29	0.46	9.35	6.34	103	<mdl	388	0.32	0.06	<mdl	<mdl	<mdl
S.D.	169	27.7	463	1500	29.2	173	0.54	12.7	0.80	35.9	178	0.18	0.19	9.83	4.53	48.4	<mdl	85.5	0.62	0.04	<mdl	<mdl	<mdl
Min	122	18.4	0.47	662	218	3.26	0.15	28.0	0.07	47.6	109	0.09	0.10	1.63	0.93	32.9	<mdl	195	0.02	0.01	<mdl	<mdl	<mdl
Max	774	128	1854	5993	332	570	2.60	86.6	2.99	200	924	0.81	0.75	35.8	19.6	213	<mdl	581	2.59	0.14	<mdl	<mdl	<mdl
Ba	Ta	W	^{204}Pb	^{206}Pb	^{208}Pb	Th	U	La	Ce	Pr	Nd	Sm	Eu	Gd	Tb	Dy	Y	Ho	Er	Tm	Yb	Lu	ΣREY
8.78	<mdl	1.00	6.93	6.45	15.8	13.9	6.25	314	966	136	598	122	10.8	122	16.2	91.1	576	18.2	49.8	6.28	37.3	5.47	3069
11.1	<mdl	1.64	6.31	5.07	14.9	16.1	5.69	242	586	72.2	288	54.5	3.36	52.3	8.34	49.7	320	10.4	29.0	3.84	22.4	3.00	1629
0.85	<mdl	0.05	2.01	0.785	1.86	0.73	0.84	87.4	355	60.4	280	60.0	6.75	61.2	6.83	37.0	237	6.64	17.3	1.92	12.5	2.18	1425
46.9	<mdl	4.93	19.8	23.1	62.2	58.5	21.4	1041	2474	306	1289	244	18.3	244	36.0	216	1385	44.8	121	16.1	92.5	12.7	7013
REY, S and Cl-Depleted Zones Adjacent to Cp	**Na**	**Mg**	**Al**	**Si**	**S**	**K**	**Sc**	**Ti**	**V**	**Mn**	**Fe**	**Co**	**Ni**	**Cu**	**Zn**	**As**	**Rb**	**Sr**	**Zr**	**Nb**	**Mo**	**Sn**	**Cs**
Mean *n* = (6)	138	16.5	<mdl	573	241	<mdl	<mdl	73.2	<mdl	189	115	<mdl	<mdl	<mdl	3.22	<mdl	<mdl	326	<mdl	<mdl	<mdl	<mdl	<mdl
S.D.	62.1	0.97	<mdl	60.1	24.4	<mdl	<mdl	16.2	<mdl	31.7	39.2	<mdl	<mdl	<mdl	1.31	<mdl	<mdl	102	<mdl	<mdl	<mdl	<mdl	<mdl
Min	72.1	14.8	<mdl	518	214	<mdl	<mdl	52.7	<mdl	151	75.1	<mdl	<mdl	<mdl	2.19	<mdl	<mdl	214	<mdl	<mdl	<mdl	<mdl	<mdl
Max	230	17.6	<mdl	653	277	<mdl	<mdl	98.2	<mdl	237	178	<mdl	<mdl	<mdl	5.09	<mdl	<mdl	466	<mdl	<mdl	<mdl	<mdl	<mdl
Ba	Ta	W	^{204}Pb	^{206}Pb	^{208}Pb	Th	U	La	Ce	Pr	Nd	Sm	Eu	Gd	Tb	Dy	Y	Ho	Er	Tm	Yb	Lu	ΣREY
1.68	<mdl	<mdl	<mdl	0.566	1.97	0.24	0.25	25.4	113	20.5	111	42.7	8.66	61.3	8.05	36.1	156	5.66	12.0	1.21	6.63	0.76	610
1.03	<mdl	<mdl	<mdl	0.326	1.58	0.19	0.23	10.4	37.7	5.47	25.8	5.45	0.97	8.25	1.12	4.93	16.0	0.78	2.43	0.32	2.12	0.28	93
0.42	<mdl	<mdl	<mdl	0.314	0.455	0.06	0.04	12.7	68.2	13.1	78.5	35.3	7.41	53.0	6.87	30.8	139	4.56	8.69	0.89	3.92	0.41	498
2.85	<mdl	<mdl	<mdl	1.13	4.57	0.50	0.47	37.3	154	26.0	141	49.8	10.2	72.2	9.43	42.4	175	6.87	14.9	1.66	9.21	1.05	741

Table 6. REE and trace element concentrations in apatite from the Distal Satellite (ppm). Apatite analyses were performed on multiple grains in the following samples: RX6685, RX6687, RX6691. <mdl—below minimum detection limit.

REY-,S-Rich Cores	Na	Mg	Al	Si	S	K	Sc	Ti	V	Mn	Fe	Co	Ni	Cu	Zn	As	Rb	Sr	Zr	Nb	Mo	Sn	Cs
Mean n = (118)	1476	338	968	6140	250	911	1.45	66.3	4.40	86.0	1355	<mdl	<mdl	<mdl	8.22	91.0	4.47	208	32.0	<mdl	<mdl	<mdl	<mdl
S.D.	711	506	1731	6806	21.7	2028	1.43	79.8	4.03	81.6	2342	<mdl	<mdl	<mdl	12.6	32.4	9.08	29.0	49.8	<mdl	<mdl	<mdl	<mdl
Min	287	18.9	1.10	1477	194	5.55	0.29	2.04	1.09	35.5	93.9	<mdl	<mdl	<mdl	0.35	21.5	0.05	62.9	0.05	<mdl	<mdl	<mdl	<mdl
Max	3361	2294	7173	31,824	303	9425	7.30	534	20.4	460	16,780	<mdl	<mdl	<mdl	70.3	209	49.8	279	201	<mdl	<mdl	<mdl	<mdl
Ba	Ta	W	^{204}Pb	^{206}Pb	^{208}Pb	Th	U	La	Ce	Pr	Nd	Sm	Eu	Gd	Tb	Dy	Y	Ho	Er	Tm	Yb	Lu	ΣREY
9.62	<mdl	<mdl	<mdl	7.88	4.74	14.9	23.6	1816	4426	466	1610	223	35.0	198	24.5	137	887	28.2	77.2	9.96	64.6	11.0	10,013
13.2	<mdl	<mdl	<mdl	5.92	3.34	11.9	27.9	663	1499	138	438	48.2	8.01	38.4	4.92	31.1	176	6.28	17.3	2.43	16.1	3.06	2868
0.33	<mdl	<mdl	<mdl	1.42	0.299	0.69	2.79	490	1418	180	705	124	16.4	124	15.2	80.0	543	16.0	40.7	5.01	33.2	5.92	3922
72.1	<mdl	<mdl	<mdl	25.0	17.2	63.1	145	3747	8980	920	3117	395	66.6	298	40.7	248	1416	49.4	128	17.3	121	22.1	18,700

The massive bornite samples show multiple stages of overprint, including metamictization of zircon with recrystallized domains that were dated at 1343 ± 47 Ma [31] and surrounded by haloes of xenotime (Figure 6a, inset). Furthermore, the overprint is illustrated by the presence of a variety of trace minerals tied to fractures within hematite and grain boundaries, such as common florencite, a few μm in size, or rare interstitial U-bearing minerals (fine-grained coffinite-brannerite intergrowths), dusty inclusions of U and REY-bearing phases within altered hematite, as well as tiny flakes of molybdenite in bornite. Lamellar chalcopyrite exsolutions occur in bornite adjacent to xenotime and rare, μm-sized chalcocite forms within fractured hematite of generation (i). Florencite contains nanometre-sized inclusions of hematite [31]. In addition, fractures containing milled, dusty fragments of all minerals in the assemblage are also present.

Compositionally, the apatite is unzoned and F-rich with low, only sporadically measurable Cl, or calculated OH^-, concentrations (Table 8). The chondrite-normalized REY fractionation patterns for this fluorapatite are conspicuously enriched in MREE (Figure 5c). A positive Eu anomaly and strong negative Y anomaly contribute to making it completely distinct from both the igneous and early hydrothermal apatite types.

Most other trace elements are depleted in apatite from the massive bornite samples, except for Sr which is present at concentrations one to two orders of magnitude higher (mean ~1350 ppm) than those measured in early hydrothermal (DM REY-, S- and Cl-rich cores mean ~390 ppm) and RDG-hosted apatite (magmatic cores mean ~80 ppm), respectively.

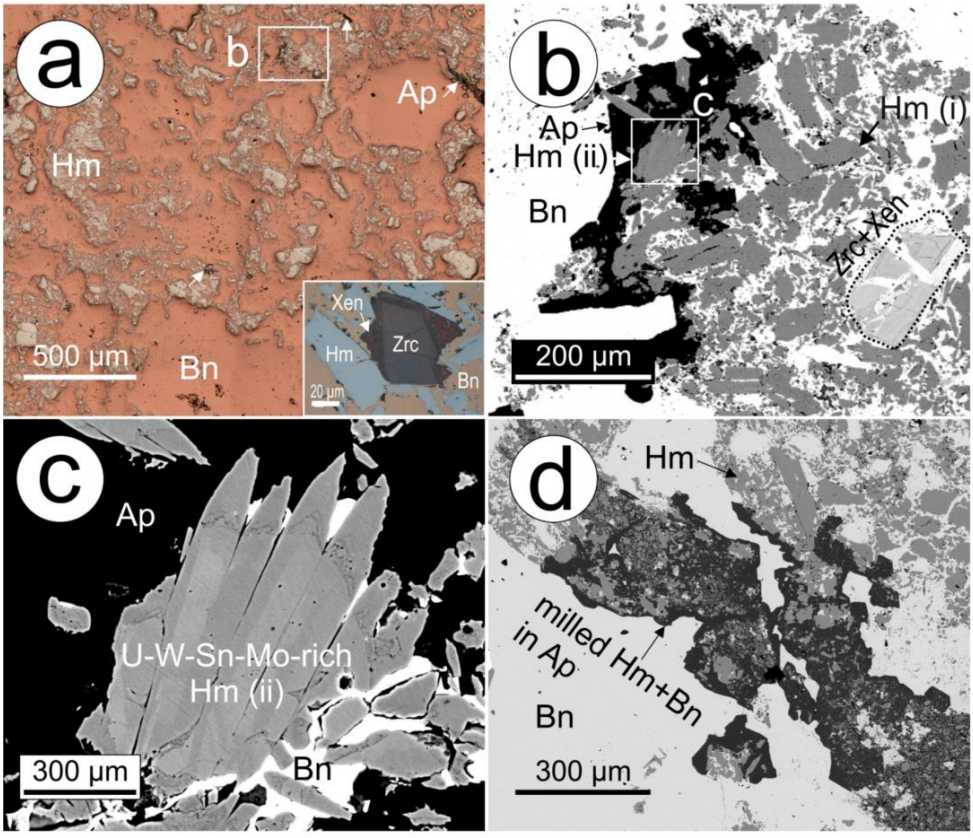

Figure 6. Reflected light microscopy map (**a**) and BSE images (**b**,**c**) showing aspects of apatite and associated minerals in the high-grade bornite ore. Inset in (**a**) shows zircon surrounded by xenotime. (**b**) Apatite at the boundary between bornite and a hematite-richer domain; most of the coarse hematite is early. Note inclusions of acicular grains/aggregates of oscillatory-zoned hematite (ii) within the apatite and brecciated zircon surrounded by xenotime. (**c**) Detail of zoned hematite within apatite from (**a**). (**d**) Apatite with milled fragments of hematite and bornite. Abbreviations: Ap: apatite; Bn: bornite; Hm: hematite; Xen: xenotime; Zrc: zircon.

5.4. Apatite as a Host for U, Th and Pb

The chemical-structural formula of apatite group minerals allows for the incorporation of a wide range of minor and trace elements. These include U, Th and Pb, making apatite a potential host for radionuclides from the ^{238}U, ^{235}U and ^{232}Th decay chains. Hydrothermal apatite in the high-grade bornite ore contains no more than a few ppm U or Th (mean values in individual samples 3–4 ppm Th, 1–3 ppm U, Table 7), increasing to a few tens of ppm Th and U in deep mineralization, preferentially within the *REY, S and Cl-rich cores* of apatite grains. In contrast, igneous apatite in altered host RDG is appreciably richer in both elements (high tens to low hundreds of ppm Th, typically tens of ppm U but 360 ppm in apatite in one sample). Magmatic cores in both the RDG and HRQM contain high U and Th concentrations of tens to ~100 ppm for both elements. These concentrations increase further in the REY-rich rims of RDG apatite, approximately tripling in both cases and in agreement with REY-behaviour.

The U/Th ratio remains largely constant within the magmatic apatite and the altered zones contained within it (0.1 to 0.6), but these do show a far broader range in hydrothermal apatite, commonly spanning several orders of magnitude (0.1 to 10) within a single sample. Lead in all apatite types examined is dominated by ^{206}Pb and ^{208}Pb with ^{204}Pb concentrations almost consistently below the minimum limits of detection. Concentrations of ^{206}Pb and ^{208}Pb show a very strong correlation with U, Th and REY across the sample suite.

These data show (Tables 2–7) that, despite variability and local enrichment, apatite is not a significant carrier of U, Th or Pb on the deposit scale. In the magmatic environment, U and Th partition strongly into apatite whereas in hydrothermal apatite, U and Th are likely partitioned into other phases, notably discrete U-minerals and hematite. Measurable concentrations of U and Th are also found within REY-mineral inclusions (bastnäsite, monazite, etc.) within apatite.

5.5. Trace Element Patterns

Many fluorapatite grains, both magmatic and hydrothermal, display grain-scale compositional zoning on BSE images. Such zoning primarily relates to the concentration of REY, as well as other elements, notably U, Th and Pb, which correlate positively with REY. Zoning is also related to hydrothermal alteration of apatite along grain margins and fractures. This is particularly obvious in RDG and HQRM-hosted apatite (Figure 7) where REY-rich rims also show high concentrations of U, Th and Pb. Early hydrothermal apatite within the DM also displays compositional zoning related to variation in concentration of the same elements. However, in this case and in marked contrast with magmatic apatite, the high concentrations of REY, U, Th and Pb are confined to grain cores, which represent the earliest hydrothermal fluid. These same elements are depleted along fractures and grain rims (Figure 8). Interestingly, concentrations of As show an inverse trend. Zoned apatite is for the most part lacking in the DS and particularly so in the high-grade bornite ore whereas zoning within apatite hosted by the DD is confined to discrete fracture related zones. Petrographic work by Krneta et al. (2016) [20] provides a framework to consider the evolution of trace element-signatures in apatite. Clear associations between compositionally-distinct apatite, or constituent zones thereof, with certain hydrothermal assemblages, and comparisons of those compositions with magmatic apatite, allow for variation in trace element concentrations to be viewed in the context of the physiochemical conditions at the time of formation of the mineral assemblage.

Table 7. REE and trace element concentrations in apatite from high-grade bornite ore (ppm). Apatite analyses were performed on multiple grains in samples: OD10.1, 10.2, 10.3.

High-Grade Bornite Ore Hosted	Na	Mg	Al	Si	S	K	Sc	Ti	V	Mn	Fe	Co	Ni	Cu	Zn	As	Rb	Sr	Zr	Nb	Mo	Sn	Cs
Mean *n* = (20)	521	20.1	104	528	221	50.6	0.53	86.3	1.12	56.2	2474	<mdl	<mdl	19.2	<mdl	<mdl	0.45	1351	<mdl	2.00	<mdl	<mdl	<mdl
S.D.	227	15.0	149	151	37.4	52.8	0.21	38.1	1.06	12.1	4510	<mdl	<mdl	20.6	<mdl	<mdl	0.31	676	<mdl	3.26	<mdl	<mdl	<mdl
Min	117	10.7	1.08	367	160	3.75	0.32	24.6	0.05	38.3	6.67	<mdl	<mdl	1.89	<mdl	<mdl	0.18	738	<mdl	0.11	<mdl	<mdl	<mdl
Max	953	65.3	491	874	298	189	1.01	198	3.16	89.9	13,448	<mdl	<mdl	55.4	<mdl	<mdl	1.08	3138	<mdl	10.1	<mdl	<mdl	<mdl
Ba	Ta	W	^{204}Pb	^{206}Pb	^{208}Pb	Th	U	La	Ce	Pr	Nd	Sm	Eu	Gd	Tb	Dy	Y	Ho	Er	Tm	Yb	Lu	ΣREY
4.28	<mdl	<mdl	<mdl	5.41	3.04	3.42	1.06	6.98	48.9	17.0	194	631	391	1217	96.6	365	1118	48.6	91.6	8.65	38.6	4.21	4277
5.79	<mdl	<mdl	<mdl	6.78	3.02	2.06	0.87	4.74	20.9	6.23	70.0	232	164	537	47.2	195	669	25.6	52.4	5.50	26.1	2.76	1939
0.47	<mdl	<mdl	<mdl	0.416	0.238	0.38	0.21	1.84	17.5	6.05	68.3	246	166	348	24.9	87.1	250	12.1	21.2	1.28	6.51	0.56	1490
19.8	<mdl	<mdl	<mdl	25.1	10.1	7.47	3.32	18.3	104	30.6	308	1191	893	2622	210	855	2730	106	216	22.5	109	10.9	9282

Table 8. EPMA data for the high-grade bornite-ore hosted apatite, <mdl—below minimum detection limit.

Analysis	F	Cl	Na_2O	SiO_2	Al_2O_3	MgO	P_2O_5	SO_3	K_2O	CaO	TiO_2	Cr_2O_3	MnO	FeO	As_2O_3	SrO	Y_2O_3	La_2O_3	Ce_2O_3	Nd_2O_3	Total
1	3.63	0.173	0.144	0.188	<mdl	<mdl	42.25	0.445	<mdl	55.22	<mdl	<mdl	0.015	1.088	<mdl	0.118	0.019	<mdl	0.184	0.255	103.73
2	3.59	<mdl	0.049	0.025	<mdl	<mdl	42.27	0.010	<mdl	55.71	0.002	<mdl	<mdl	0.156	<mdl	0.112	0.272	<mdl	<mdl	0.158	102.35
3	3.65	<mdl	0.063	0.012	<mdl	<mdl	42.15	<mdl	<mdl	55.94	<mdl	<mdl	<mdl	0.145	<mdl	0.107	0.214	<mdl	<mdl	0.160	102.44

Calculated Formula (9 apfu)

Ca	Mg	Mn	Sr	Y	La	Ce	Nd	Na	K	Fe	Ti	Al	Cr	Total	SREY	P	S	As	Si	Total	F	Cl	OH	Total
4.886	-	0.001	0.006	0.001	-	0.006	0.008	0.023	-	0.075	-	-	-	5.005	0.014	2.954	0.028	-	0.016	2.997	0.947	0.024	0.029	1.000
4.977	-	0.000	0.005	0.020	-	-	0.005	0.008	-	0.011	0.000	-	-	5.026	0.025	2.984	0.001	-	0.002	2.986	0.946	-	0.054	1.000
5.002	-	-	0.005	0.016	-	-	0.005	0.010	-	0.010	-	-	-	5.048	0.020	2.978	-	-	0.001	2.979	0.963	-	0.037	1.000

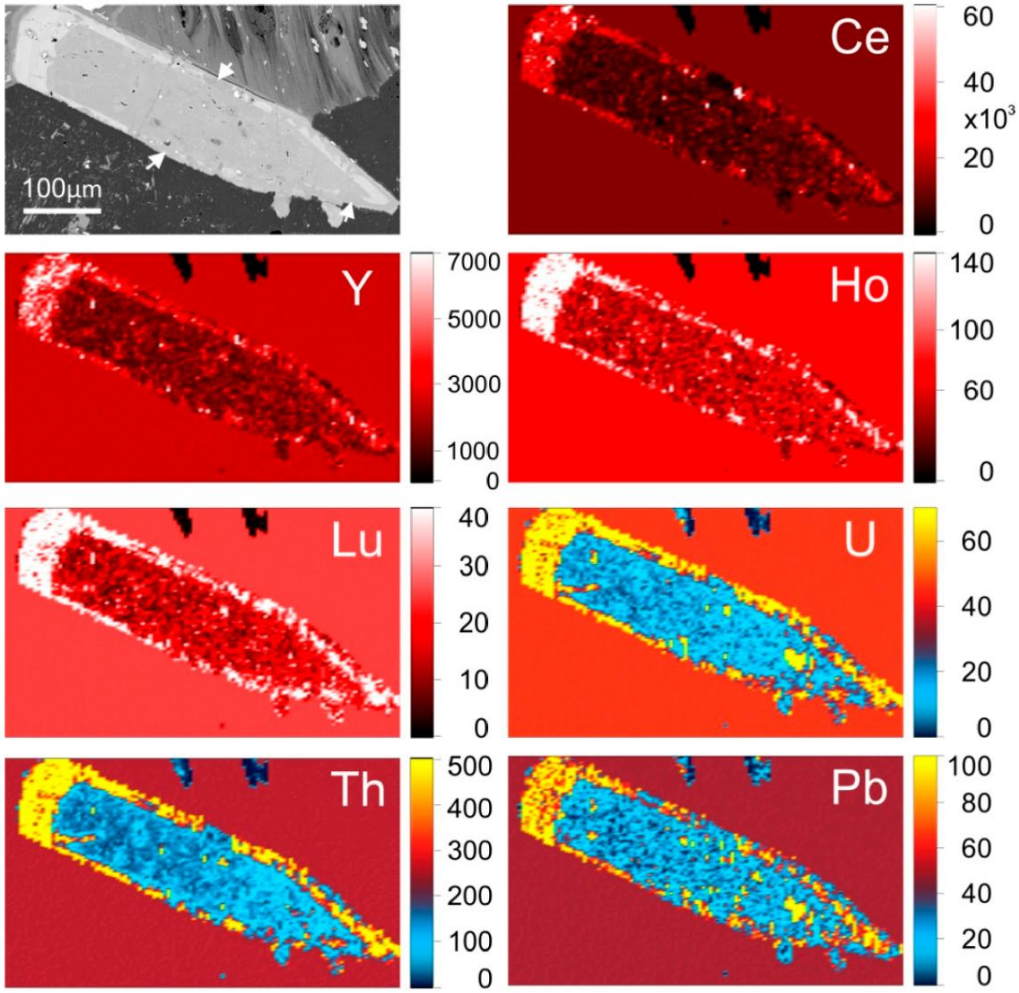

Figure 7. LA-ICP-MS map of a partially altered magmatic apatite grain hosted in hematite-sericite altered RDG (sample 2280-3, Figure 1, Table 1) showing a magmatic, inclusion-rich core and a REY- and U–Th–Pb-enriched rim, both of which have been affected by REY-depletion along fractures and the grain rim marked by the white arrows on the SEM image. All scales are in ppm.

6. Discussion

6.1. REY-Signatures in Apatite and the Transition from Magmatic to Hydrothermal Stages

REY-signatures measured in magmatic apatite of the RDG, HRQM and DD closely resemble those for apatite from analogous intrusive elsewhere [8,9,46]. Similarly, the LREE-enriched signatures characteristic for DM and DS apatite (REY-, S- and Cl-rich cores and REY-, S-rich cores, respectively) are almost identical to apatite REY-signatures measured in apatite from similar magnetite-apatite ± pyrite assemblages elsewhere within the Olympic Cu–Au Province [1,10,47], as well as globally [11,14]. Such an observation reinforces the interpretation of Krneta et al. (2017) [10] that although not unique to early high-temperature apatite associated with magnetite ± pyrite assemblages in IOCG systems, LREE-enriched apatite signatures are certainly characteristic for such apatite. In contrast, the characteristics that define the signatures of later generations of apatite associated with hematite-sericite alteration and high-grade ore (MREE-enrichment, positive Eu- and negative Y-anomalies) are less commonly reported. MREE-enriched REY-signatures with weak positive Eu anomalies are particularly scarce in the literature and their description has thus far been limited to orogenic-Au deposits [9,48] and IOCG mineralization within the Olympic Cu–Au belt [10].

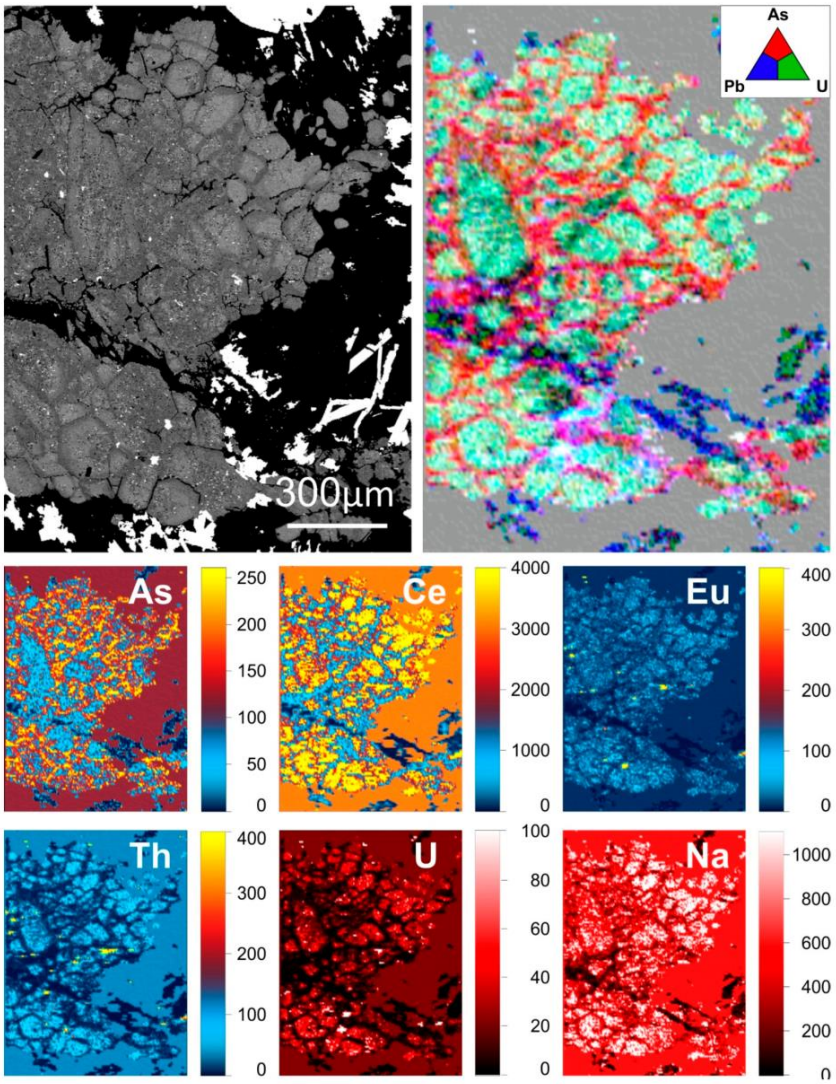

Figure 8. LA-ICP-MS map of a large aggregate of apatite grains (sample 2773-3, Figure 1, Table 1) displaying core-to-rim- and fracture-related zoning consisting of cores rich in REY and REY-depleted rims and fractures. Note relative enrichment of As along grain rims and attributed to crystallization from more oxidized fluids that the core. All scales are in ppm.

A preferential depletion of LREE from apatite has been noted elsewhere in IOCG and IOA deposits [10,11] and corresponds to a shift in fluid conditions as determined by a significant overprinting of the magmatic or early hydrothermal minerals in the host rock. Where it is LREE-depleted, the apatite commonly contains inclusions of minerals belonging to the overprinting assemblage (hematite, sericite). This preferential LREE-depletion, either where pre-existing apatite is present or where new grains of MREE-enriched apatite are formed, can be attributed to an increased proportion of LREE in the fluid occurring as highly mobile REY–Cl complexes at hydrothermal conditions characteristic of the hematite-sericite dominant assemblage. This causes LREE to be effectively partitioned away from apatite [6]. Therefore, an evolution in the speciation of REY-complexes in the fluid brought about by changing physicochemical conditions could explain the switch in REY-signatures. However, this does not address the weakening of the negative Eu anomaly in the hematite-sericite altered zones, or the presence of a positive Eu anomaly in the high-grade bornite ore.

The weakening of the negative Eu anomaly in apatite associated with hematite-sericite alteration may be the result of crystallization from fluids enriched in Eu relative to other REE by the sericitization of feldspars, which are characterized by Eu-enrichment [9]. Similarly, the marked

negative Y-anomaly in these apatites may be inherited from the feldspars, as they display a negative Y-anomaly within the RDG [21]. However, development of the negative Y-anomaly may be attributed to the behaviour of Y as a pseudo-lanthanide heavier than Lu effectively partitioning away from adjacent REE in F-rich fluids [49]. Such conditions may be justifiable given the marked F-rich character of the deposit.

Although evolution from LREE to MREE-enriched apatite (with positive Eu anomalies and negative Y anomalies) most probably stems from changes in fluid parameters, it also correlates with changes in the dominant hydrothermal assemblage hosting the apatite. This demonstrates that REY-signatures in apatite can fingerprint individual assemblages and are reflective of significant changes in REY-behaviour during the formation of OD (Figure 9a,b).

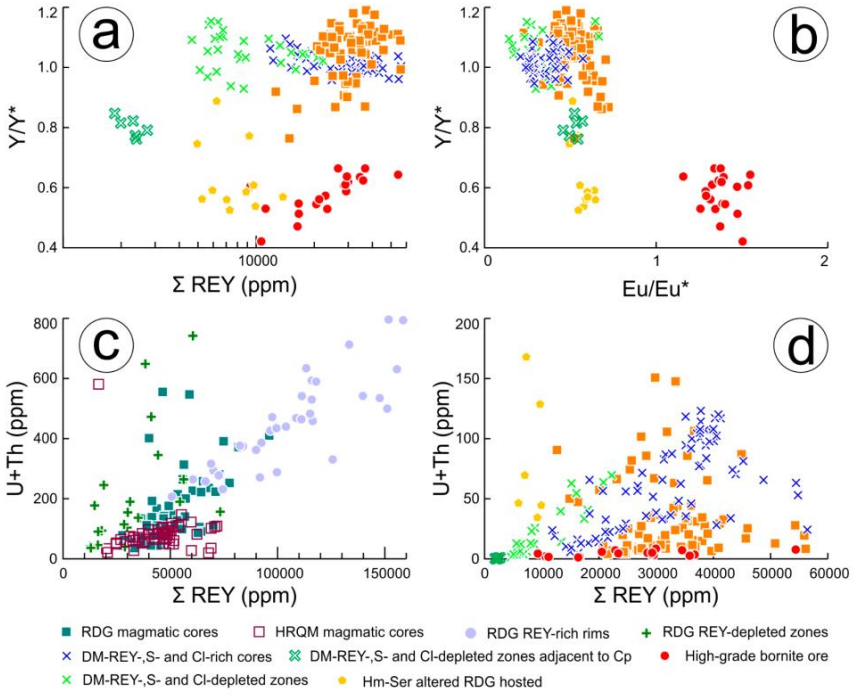

Figure 9. LA-ICP-MS plots of magmatic and hydrothermal apatite: (**a**) ΣREY (ppm) vs. (Y/Y* = $Y_{CN}/[(Dy_{CN} + Ho_{CN})/2]$); (**b**) (Eu/Eu* = $Eu_{CN}/[(Sm_{CN} + Gd_{CN})/2]$) vs. (Y/Y* = $Y_{CN}/[(Dy_{CN} + Ho_{CN})/2]$); (**a**,**b**) The evolution from early magnetite associated to later hematite-sericite and ore-related apatite is emphasized by changes is ΣREY as well as Eu and Y anomalies; (**c**) ΣREY (ppm) vs. (U + Th) (ppm); (**d**) ΣREY (ppm) vs. (U + Th) (ppm). (**c**,**d**) U and Th concentrations are strongly tied to that of ΣREY, particularly in magmatic apatite and hydrothermal zones therein.

6.2. REY Signatures in Apatite Associated with High-Grade Ores

Apatite preferentially incorporates Eu^{3+} over Eu^{2+}, and although the greatest control on the proportion of the two species is exerted by fO_2 in the magmatic environment [8], their speciation in hydrothermal fluids is primarily controlled by H^+ activity whereby Eu^{3+} complexes dominate at high pH conditions (>7 at 300 °C; [50]). Such alkaline conditions are unrealistic for the fluids responsible for the broad hematite-sericite alteration due to the low pH required for sericite stability at this temperature.

The positive Eu anomaly in the high-grade bornite ore hosted apatite may, however, be the result of crystallization from an alkaline, CO_2–HCO_3^- buffered fluid analogous to that invoked by [50] to explain comparable trends, observed and thermodynamically assessed, in scheelite from orogenic Au deposits (Mt. Charlotte and Drysdale, Western Australia). Evidence for the existence of such volatile-rich fluids (CO_2) accounting for high-grade ore deposition can be inferred from the presence of inclusions of milled hematite-(i) and bornite in apatite undergoing crystallization (Figure 6d). Moreover, the scenario of fluid pulses with unusual chemistry relative to those

accounting for the bulk of ores associated with hematite-sericite alteration but still affiliated with the IOCG event at ~1.6 Ga is feasible based on ongoing U–Pb hematite geochronology at OD.

Growth of U-rich, zoned hematite within apatite with such a distinct trend (Figures 5c and 6b,c) ties the formation of apatite at ~1.6 Ga, rather than during the later overprinting event recorded by zircon (1577 ± 5 Ma and 1343 ± 47 Ma, respectively, [31]. The hematite age is clearly younger by ~20–10 Ma than the earliest hematite, for which high-precision ID-TIMS dating of samples from the deepest, chalcopyrite + pyrite zone in the SE lobe give ages concordant with those of magmatic zircon in RDG [33]. Although similar U–W–Sn–Mo-rich and zoned hematite are observed across the ~6 km strike and ~2 km depth of the deposit [51], preliminary dating of such hematite throughout the deposit shows variation in ages, including younger dates, obtained from hematite in high-grade bornite ore from another location (NW arm) than the sample discussed here [33].

6.3. The Role of Apatite as a Host for U, Th and Pb

The affinity for U, Th and Pb shown by apatite is well known, and the mineral is increasingly finding application as a valuable geochronometer and in thermochronology [52]. The ease with which apatite incorporates U and Th has been exploited as a medium for radionuclide removal and long-term storage [53].

All three elements replace Ca in apatite. The incorporation of U and Th is as 4+ species requiring a vacancy to maintain charge balance [41], whereas Pb^{2+} substitutes directly for Ca^{2+}. Uranium and Th show a very strong affinity for the Ca2 position in fluorapatite [54], analogous to the LREE, although such a relationship might normally put them in direct competition for this position and lead to a negative correlation between the two elements, as is commonly the case between As and Si in the P site [10]. The evidence here, however, shows that their behaviour mirrors that of the REY in both magmatic and hydrothermal fluorapatite (Figures 9c,d).

Uranium and Th show very strong correlations with their respective daughter lead isotopes, ^{206}Pb and ^{208}Pb (Figure 10a), although hydrothermal apatite displays significantly greater scatter (Figure 10b). The U/Th ratios appear to track differentiation in RDG and HQRM magmatic apatite (Figure 10c), akin to Sr concentrations [20] whereas this ratio varies considerably in hydrothermal apatite, both within individual apatite types and between them (Figure 10d).

The decrease in the concentration of several trace elements in fluorapatite from magmatic through to early hydrothermal and finally ore-hosted apatite suggests that apatite strongly partitions trace elements in the magmatic environment. including the REY, U and Th. Apatite may thus be one of the major REY hosts in unaltered RDG and HQRM, and could also, alongside zircon and rare *uranothorite* [18], be a significant host for U and Th in those rocks. The lower concentration of these elements in hydrothermal apatite can be attributed to the increased abundance of uraninite, brannerite, coffinite and hematite in the case of U [55,56], and (probably) monazite in the case of Th, which are able to partition them more efficiently than apatite. Citing the comparable behaviour of decreasing trace element concentrations in feldspars from magmatic to hydrothermal within the deposit, Kontonikas-Charos et al. (2017) [21] reached similar conclusions, suggesting that a significant metal contribution was made to the deposit via the hydrothermal alteration of feldspars. Although apatite is a far smaller component of the RDG than feldspar, replacement of magmatic apatite associated with hematite-sericite alteration, may have also contributed REY, U and Th to the overall metal budget at Olympic Dam.

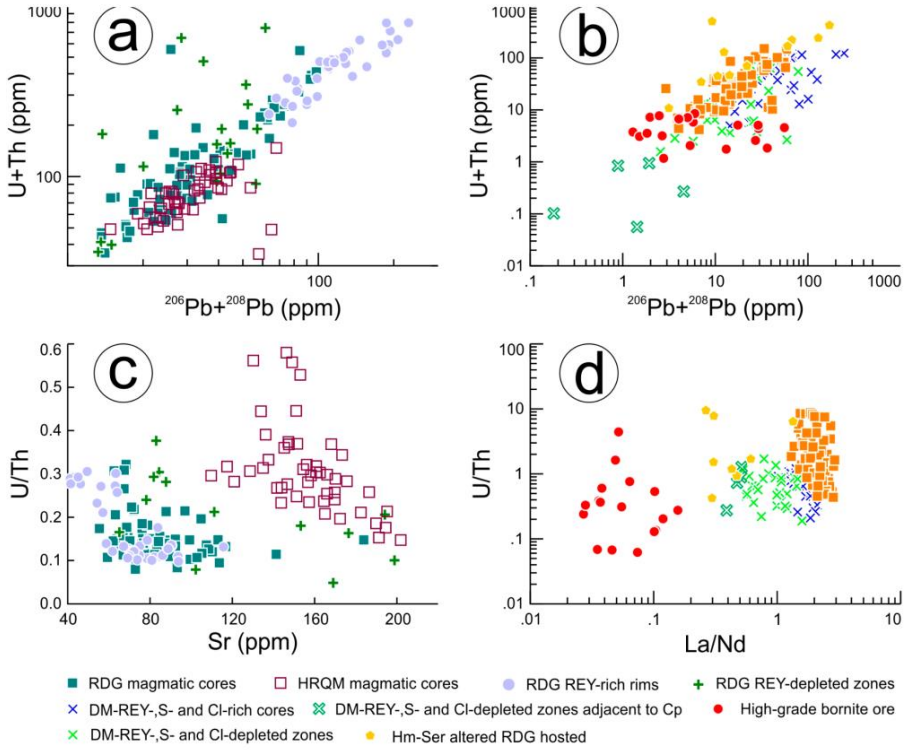

Figure 10. LA-ICP-MS plots of magmatic and hydrothermal apatite: (**a**) log(^{206}Pb + ^{208}Pb ppm) vs. (U + Th) (ppm); (**b**) log(^{206}Pb + ^{208}Pb ppm) vs. log(U + Th ppm); (**a**,**b**) U and Th concentrations exhibit a strong linear relationship with their lead daughter isotopes; (**c**) Sr (ppm) vs. (U + Th) (ppm); (**d**) La/Nd (ppm) vs. log(U + Th) (ppm).

7. Conclusions

Magmatic and early hydrothermal apatite within the OD deposit carry chemical signatures, particularly with respect to the REY, which are characteristic of the host's intrusive or early hydrothermal assemblage. The LREE-enriched signatures measured in these apatites are concordant with REY-signatures in apatite hosted in analogous intrusive rocks globally, as well as from magnetite-apatite ± pyrite assemblages in some IOCG and IOA deposits.

The transition from LREE to MREE-enriched apatite coincident with a weakening of negative Eu anomalies and the formation of negative Y anomalies appears to track an evolution from the magmatic, through early magnetite-associated hydrothermal to hematite-sericite-associated and finally high-grade bornite ore-hosted apatite. Such a transition has been noted at the Wirrda Well and Acropolis prospects and may be characteristic of IOCG systems with alteration patterns similar to OD.

In the magmatic environment, and to a lesser extent under hydrothermal conditions characteristic of early magnetite-associated mineralization, apatite appears to heavily partition several trace elements including U and Th. Concentrations of these and other trace elements weaken significantly in later apatite generations most likely due to the increased abundance of other phases competing for the same trace elements. This is best seen by comparing U concentrations in primary magmatic apatite with those in hydrothermal apatite hosted by massive bornite ore. The least-altered RDG contains whole rock U concentrations of approximately 13 ppm, whereas samples akin to the massive bornite mineralization commonly contain U in the range of 125–495 ppm U [19]. Apatite hosted within these rocks shows, however, the opposite trend. The replacement of magmatic apatite by other minerals, e.g., monazite, florencite, may have contributed to the overall U, Th and REY budget at OD.

Remarkably, the MREE-enriched fractionation trend displayed by apatite, with its strong positive Eu anomaly, is indicative of alkaline, CO_2-HC 0_3^- buffered fluids accounting for

high-grade ore formation across a spectrum of hydrothermal deposits spanning IOCG and orogenic Au systems.

Supplementary Materials: The following are available online at www.mdpi.com/2075-163X/7/8/135/s1, Table S1: Typical minimum detection limits (mdl) for LA-ICP-MS analysis, Table S2: Standards, X-ray lines, count times and typical minimum detection limits (mdl) for electron probe microanalysis.

Acknowledgments: This work is supported by BHP Billiton Olympic Dam. We gratefully acknowledge microanalytical assistance from the staff at Adelaide Microscopy, notably Ben Wade. Nigel J. Cook. and Kathy Ehrig acknowledge support from the ARC Research Hub for Australian Copper–Uranium. Cristiana L. Ciobanu acknowledges support from the "FOX" project (Trace Elements in Iron Oxides), supported by BHP Billiton Olympic Dam and the South Australian Mining and Petroleum Services Centre of Excellence. The authors extend thanks to the three anonymous reviewers whose pertinent comments assisted us to present our results, and to the *Minerals* editorial team for assistance and handling of the manuscript.

Author Contributions: Sasha Krneta performed all analytical work and data processing under the guidance of Cristiana L. Ciobanu and Nigel J. Cook; Kathy Ehrig contributed samples and deposit information; Alkis Kontonikas-Charos contributed data and knowledge on the samples. Sasha Krneta, Nigel J. Cook and Cristiana L. Ciobanu wrote the paper, assisted by all other authors. The work is part of the PhD project of Sasha Krneta.

Conflicts of Interest: The authors declare no conflict of interest. The project sponsors approve publication of the manuscript.

References

1. Ismail, R.; Ciobanu, C.L.; Cook, N.J.; Teale, G.S.; Giles, D.; Schmidt Mumm, A.; Wade, B. Rare earths and other trace elements in minerals from skarn assemblages, Hillside iron oxide–copper–gold deposit, Yorke Peninsula, South Australia. *Lithos* **2014**, *184–187*, 456–477.
2. Goldschmidt, V.M. The principles of distribution of chemical elements in minerals and rocks. The seventh Hugo Müller Lecture, delivered before the Chemical Society on March 17th, 1937. *J. Chem. Soc. (Resumed)* **1937**, 655–673.
3. Bau, M. Rare-earth element mobility during hydrothermal and metamorphic fluid-rock interaction and the significance of the oxidation state of europium. *Chem. Geol.* **1991**, *93*, 219–230.
4. Haas, J.R.; Shock, E.L.; Sassani, D.C. Rare earth elements in hydrothermal systems: Estimates of standard partial molal thermodynamic properties of aqueous complexes of the rare earth elements at high pressures and temperatures. *Geochim. Cosmochim. Acta* **1995**, *59*, 4329–4350.
5. Migdisov, A.A.; Williams-Jones, A. Hydrothermal transport and deposition of the rare earth elements by fluorine-bearing aqueous liquids. *Mineral. Deposita* **2014**, *49*, 987–997.
6. Migdisov, A.A.; Williams-Jones, A.E.; Brugger, J.; Caporuscio, F.A. Hydrothermal transport, deposition, and fractionation of the REE: Experimental data and thermodynamic calculations. *Chem. Geol.* **2016**, *439*, 13–42.
7. Harlov, D.E. Apatite: A fingerprint for metasomatic processes. *Elements* **2015**, *11*, 171–176.
8. Cao, M.; Li, G.; Qin, K.; Seitmuratova, E.Y.; and Liu, Y. Major and Trace element characteristics of apatites in granitoids from Central Kazakhstan: Implications for petrogenesis and mineralization. *Resource Geol.* **2012**, *62*, 63–83.
9. Mao, M.; Rukhlov, A.S.; Rowins, S.M.; Spence, J.; Coogan, L.A. Apatite trace element compositions: A robust new tool for mineral exploration. *Econ. Geol.* **2016**, *111*, 1187–1222.
10. Krneta, S.; Ciobanu, C.L.; Cook, N.J.; Ehrig, K.; Kontonikas-Charos, A. 2017. The Wirrda Well and Acropolis prospects Gawler Craton, South Australia: Insights into evolving fluid conditions through apatite chemistry. *J. Geochem. Explor.* **2017**, under review.
11. Harlov, D.E.; Andersson, U.B.; Förster, H-J.; Nyström, J.O.; Dulski, P.; Broman, C. Apatite–monazite relations in the Kiirunavaara magnetite–apatite ore, northern Sweden. *Chem. Geol.* **2002**, *191*, 47–72.
12. Day, W.C.; Slack, J.F.; Auyso, R.; Seeger, C.M. Regional Geologic and Petrologic Framework for Iron Oxide ± Apatite ± Rare Earth Element and Iron Oxide Copper-Gold Deposits of the Mesoproterozoic St. Francois Mountains Terrane, Southeast Missouri, USA. *Econ. Geol.* **2016**, *11*, 1825–1858.
13. Daliran, F.; Stosch, H.-G.; Williams, P.J.; Jamali, H.; Dorri, M.B. Early Cambrian iron oxide-apatite-REE (U) deposits of the Bafq district, east-central Iran. *Geol. Assoc. Canada Short Course Notes* **2010**, *20*, 147–159.

14. Bonyadi, Z.; Davidson, G.J.; Mehrabi, B.; Meffre, S.; Ghazban, F. Significance of apatite REE depletion and monazite inclusions in the brecciated Se–Chahun iron oxide–apatite deposit, Bafq district, Iran: Insights from paragenesis and geochemistry. *Chem. Geol.* **2011**, *281*, 253–269.
15. Kelley, K.D.; Eppinger, R.G.; Lang, J.; Smith, S.M.; Fey, D.L. Porphyry Cu indicator minerals in till as an exploration tool: Example from the giant Pebble porphyry Cu-Au-Mo deposit, Alaska, USA. *Geochem. Explor. Environ. Analysis* **2011**, *11*, 321–334.
16. Bouzari, F.; Hart, J.R.H.; Bissig, T.; Barker, S. Hydrothermal Alteration Revealed by Apatite Luminescence and Chemistry: A Potential Indicator Mineral for Exploring Covered Porphyry Copper Deposits. *Econ. Geol.* **2016**, *111*, 1397–1410.
17. Skirrow, R.G.; Bastrakov, E.N.; Barovich, K.; Fraser, G.L.; Creaser, R.; Fanning, M.C.; Raymond, O.L.; Davidson, G.J. Timing of iron oxide Cu–Au–(U) hydrothermal activity and Nd isotope constraints on metal sources in the Gawler craton, South Australia. *Econ. Geol.* **2007**, *102*, 1441–1470.
18. Ehrig, K.; Kamenetsky, V.S.; McPhie, J.; Apukhtina, O.; Ciobanu, C.L.; Cook, N.J.; Kontonikas-Charos, A.; Krneta, S. The IOCG-IOA Olympic Dam Cu-U-Au-Ag deposit and nearby prospects, South Australia. In Proceedings of the 14th Biennial SGA Conference, Quebec City, QC, Canada, 20–23 August 2017.
19. Ehrig, K.; McPhie, J.; Kamenetsky, V.S. Geology and mineralogical zonation of the Olympic Dam iron oxide Cu-U-Au-Ag deposit, South Australia. In *Geology and Genesis of Major Copper Deposits and Districts of the World, a Tribute to Richard Sillitoe*; Hedenquist, J.W., Harris, M., Camus, F., Eds.; Society of Economic Geologists: Littleton, CO, USA, 2012; Volume 16, pp. 237–268.
20. Krneta, S.; Ciobanu, C.L.; Cook, N.J.; Ehrig, K.; Kontonikas-Charos, A. Apatite at Olympic Dam, South Australia: A petrogenetic tool. *Lithos* **2016**, *262*, 470–485.
21. Kontonikas-Charos, A.; Ciobanu, C.L.; Cook, N.J.; Ehrig, K.; Krneta, S.; Kamenetsky, V.S. Feldspar evolution in the Roxby Downs Granite, host to Fe-oxide Cu-Au-(U) mineralisation at Olympic Dam, South Australia. *Ore Geol. Rev.* **2017**, *80*, 838–859.
22. BHP Billiton. Annual Report. 2016. Available online: http://www.bhpbilliton.com/-/media/bhp/documents/investors/annual-reports/2016/bhpbillitonannualreport2016.pdf?la=en (accessed on 21 September 2016).
23. Reeve, J.S.; Cross, K.C.; Smith, R.N.; Oreskes, N. Olympic Dam copper–uranium–gold–silver deposit. In *Geology of the Mineral Deposits of Australia and Papua New Guinea*; Hughes, F.E., Ed.; Australasian Institute of Mining and Metallurgy: Melbourne, Australia, 1990; Volume 14, pp. 1009–1035.
24. Creaser, R.A. The Geology and Petrology of Middle Proterozoic Felsic Magmatism of the Stuart Shelf. Ph.D. Thesis, La Trobe University, Melbourn, South Australia, 1989, Unpublished work.
25. Huang, Q.; Kamenetsky, V.S.; Ehrig, K.; McPhie, J.; Kamenetsky, M.; Cross, K.; Meffre, S.; Agangi, A.; Chambefort, I.; Direen, N.G.; et al. Olivine-phyric basalt in the Mesoproterozoic Gawler silicic large igneous province, South Australia: Examples at the Olympic Dam Iron Oxide Cu–U–Au–Ag deposit and other localities. *Precambr. Res.* **2016**, *281*, 185–199.
26. Ciobanu, C.L.; Cook, N.J.; Ehrig, K. Ore minerals down to the nanoscale: Cu-(Fe)-sulphides from the Iron Oxide Copper Gold deposit at Olympic Dam, South Australia. *Ore Geol. Rev.* **2017**, *81*, 1218–1235.
27. Oreskes, M.; Einaudi, M.T. Origin of Hydrothermal Fluids at Olympic Dam: Preliminary Results from Fluid Inclusions and Stable Isotopes. *Econ. Geol.* **1992**, *87*, 64–90.
28. Bastrakov, E.N.; Skirrow, R.G.; Davidson, G.J. Fluid evolution and origins of iron oxide Cu-Au prospects in the Olympic Dam District, Gawler Craton, South Australia. *Econ. Geol.* **2007**, *102*, 1415–1440.
29. Mauger, A.J.; Ehrig, K.; Kontonikas-Charos, A.; Ciobanu, C.L.; Cook, N.J.; Kamenetsky, V.S. Alteration at the Olympic Dam IOCG-U deposit: Insights into distal to proximal feldspar and phyllosilicate chemistry from infrared reflectance spectroscopy. *Aust. J. Earth Sci.* **2016**, *63*, 959–972.
30. Apukhtina, O.B.; Kamenetsky, V.S.; Ehrig, K.; Kamenetsky, M.B.; McPhie, J.; Maas, R.; Meffre, S.; Goermann, K.; Rodermann, T.; Cook, N.J.; et al. 2016. Postmagmatic magnetite–apatite assemblage in mafic intrusions: A case study of dolerite at Olympic Dam, South Australia. *Contrib. Mineral. Petrol.* **2016**, *171*, doi:10.1007/s00410-015-1215-7.
31. Ciobanu, C.L.; Wade, B.; Cook, N.J.; Schmidt Mumm, A.; Giles, D. Uranium-bearing hematite from the Olympic Dam Cu-U-Au deposit, South Australia; a geochemical tracer and reconnaissance Pb-Pb geochronometer. *Precambr. Res.* **2013**, *238*, 129–147.
32. Courtney-Davies, L.; Zhu, Z.; Ciobanu, C.L.; Wade, B.P.; Cook, N.J.; Ehrig, K.; Cabral, A.R.; Kennedy, A. Matrix-matched iron-oxide laser ablation ICP-MS U-Pb geochronology using mixed solutions standards. *Minerals* **2016**, *6*, 85, doi:10.3390/min6030085.

33. Courtney-Davies, L.; Ciobanu, C.L.; Tapster, S.; Condon, D.; Kennedy, A.; Cook, N.; Ehrig, K.; Wade, B.; Richardson, M. Steps to developing iron-oxide U-Pb geochronology for robust temporal insights into IOCG and BIF mineralisation, *Appl. Earth Sci.* **2017**, *126*, 51–52, doi:10.1080/03717453.2017.1306241.
34. Jagodzinski, E.A. The Age of Magmatic and Hydrothermal Zircon at Olympic Dam. In Proceedings of 2014 Australian Earth Sciences Convention (AESC), Sustainable Australia, Newcastle, NSW, Australia, 7–10 July 2014; Volume 110, p. 260.
35. Apukhtina, O.B.; Kamenetsky, V.S.; Ehrig. K.; Kamenetsky, M.B.; Maas, R.; Thompson, J.; McPhie, J.; Ciobanu, C.L.; Cook, N.J. Early, deep magnetite-fluorapatite mineralization at the Olympic Dam Cu-U-Au-Ag deposit, South Australia. *Econ. Geol.* **2017**, in press.
36. Huang, Q.; Kamenetsky, V.S.; McPhie, J.; Ehrig, K.; Meffre, S.; Maas, R.; Thompson, J.; Kamenetsky, M.; Chambefort, I.; Apukhtina, O.; et al. Neoproterozoic (ca. 820–830 Ma) mafic dykes at Olympic Dam, South Australia: Links with the Gairdner Large Igneous Province. *Precambr. Res.* **2015**, *271*, 160–172.
37. Pasero, M.; Kampf, A.; Ferraris, C.; Pekov, I.V.; Rakovan, J.; White, T. Nomenclature of the apatite supergroup minerals. *Eur. J. Mineral.* **2010**, *22*, 163–179.
38. Hughes, J.M.; Rakovan, J.F. Structurally robust, chemically diverse: Apatite and apatite supergroup minerals. *Elements* **2015**, *11*, 165–170.
39. Hughes, J.M.; Rakovan, J.F. The crystal structure of apatite, $Ca_5(PO_4)_3(F,OH,Cl)$. *Rev. Mineral. Geochem.* **2002**, *48*, 1–12.
40. Rønsbo, J.G. Coupled substitutions involving REE's and Na and Si in apatites in alkaline rocks from Ilimaussaq, South Greenland, and the petrological implications. *Am. Mineral.* **1989**, *74*, 896–901.
41. Pan, Y.; Fleet, M.E. Compositions of the apatite-group minerals: Substitution mechanisms and controlling factors. *Rev. Mineral. Geochem.* **2002**, *48*, 13–49.
42. Van Hinsberg, V.J.; Migdisov, A.A.; Williams-Jones, A.E. Reading the mineral record of fluid composition from element partitioning. *Geology* **2010**, *38*, 847–850.
43. Oreskes, M.; Einaudi, M.T. Origin of Rare Earth Element-Enriched Hematite Breccias at the Olympic Dam Cu-U-Au-Ag Deposit, Roxby Downs, South Australia. *Econ. Geol.* **1990**, *85*, 1–28.
44. McDonough, W.F.; Sun, S.-S. Composition of the Earth. *Chem. Geol.* **1995**, *120*, 223–253.
45. Cook, N.J.; Ciobanu, C.L.; George, L.; Ehrig, K. Trace Element Analysis of Minerals in Magmatic-Hydrothermal Ores by Laser Ablation Inductively-Coupled Plasma Mass Spectrometry: Approaches and Opportunities. *Minerals* **2016**, *6*, 111, doi:10.3390/min6040111.
46. Belousova, E.A.; Griffin, W.L.; O'Reilly, S.Y.; Fisher, N.I. Apatite as an indicator mineral for mineral exploration: Trace-element compositions and their relationship to host rock type. *J. Geochem. Explor.* **2002**, *76*, 45–69.
47. Kontonikas-Charos, A.; Ciobanu, C.L.; Cook, N.J. Albitization and redistribution of REE and Y in IOCG systems: Insights from Moonta-Wallaroo, Yorke Peninsula, South Australia. *Lithos* **2014**, *208*, 178–201.
48. Brugger, J.; Lahaye, Y.; Costa, S.; Lambert, D.; Bateman, R. Inhomogenous distribution of REE in scheelite and dynamics of Archean hydrothermal systems (Mt. Charlotte and Drysdale gold deposits, Western Australia). *Contrib. Mineral. Petrol.* **2000**, *139*, 251–264.
49. Bau, M.; Dulski, P. Comparative study of yttrium and rare-earth element behaviours in flourine-rich hydrothermal fluids. *Contrib. Mineral. Petrol.* **1995**, *119*, 213–223.
50. Brugger, J.; Etschmann, B.; Pownceby, M.; Liu, W.; Grundler, P.; Brewe, D. Oxidation state of europium in scheelite: Tracking fluid-rock interaction in gold deposits. *Chem. Geol.* **2008**, *257*, 26–33.
51. Verdugo-Ihl, M.R.; Ciobanu, C.L.; Cook, N.J.; Courtney-Davies, L.; Ehrig, K.; Gilbert, S. Trace element signatures in U-W-Sn-Mo zoned hematite from the IOCG deposit at Olympic Dam, South Australia. In Proceedings of the 14th Biennial SGA Conference, Quebec City, QC, Canada, 20–23 August 2017.
52. Chew, D.M.; Spikings, R.A. Geochronology and Thermochronology using apatite: Time and temperature, lower crust to surface. *Elements* **2015**, *11*, 189–194.
53. Chen, B.; Wang, J.; Kong, L.; Mai, X.; Zheng, N.; Zhong, Q.; Liang, J.; Chen, D. Adsorption of uranium from uranium mine contaminated water using phosphate rock apatite using (PRA): Isotherm, kinetic and characterization studies. *Colloids Surf. A Physiochem. Eng. Asp.* **2017**, *520*, 612–621.
54. Luo, Y.; Hughes, J.M.; Rakovan, J.; Pan, Y. Site preference of U and Th in Cl, F, and Sr apatites. *Am. Mineral.* **2009**, *94*, 345–351.

55. Macmillan, E.; Cook, N.J.; Ehrig, K.; Ciobanu, C.L.; Pring, A. Uraninite from the Olympic Dam IOCG-U-Ag deposit: Linking textural and compositional variation to temporal evolution. *Am. Mineral.* **2016**, *101*, 1295–1320.
56. Macmillan, E.; Cook, N.J.; Ehrig, K.; Pring, A. Chemical and textural interpretation of late stage coffinite and brannerite from the Olympic Dam IOCG-Ag-U deposit. *Mineral. Mag.* **2017**, in press, doi:10.1180/minmag.2017.081.006.

CHAPTER 4

THE WIRRDA WELL AND ACROPOLIS PROSPECT, GAWLER CRATON, SOUTH AUSTRALIA: INSIGHTS INTO EVOLVING FLUID CONDITIONS THROUGH APATITE CHEMISTRY

Sasha Krneta[1], Nigel J. Cook[2], Cristiana L. Ciobanu[2], Kathy Ehrig[3], Alkis Kontonikas-Charos[1]

[1]*School of Physical Sciences, The University of Adelaide, Adelaide, S.A., 5005, Australia*

[2]*School of Chemical Engineering, The University of Adelaide, Adelaide, S.A., 5005, Australia*

[3]*BHP Olympic Dam, Adelaide, SA 5000, Australia*

Paper published in the Journal of Geochemical Exploration, 181, 276-291

Statement of Authorship

Title of Paper	The Wirrda Well and Acropolis prospects Gawler Craton, South Australia: insights into evolving fluid conditions through apatite chemistry
Publication Status	☑ Published ☐ Accepted for Publication ☐ Submitted for Publication ☐ Unpublished and Unsubmitted w ork w ritten in manuscript style
Publication Details	Krneta, S., Cook, N.J., Ciobanu, C.L., Ehrig, K. and Kontonikas-Charos, A., 2017. The Wirrda Well and Acropolis prospects Gawler Craton, South Australia: insights into evolving fluid conditions through apatite chemistry. Journal of Geochemical Exploration 181, 276-291.

Principal Author

Name of Principal Author (Candidate)	Sasha Krneta
Contribution to the Paper	Collected sample material, devised a plan for and performed analytical work, processed and interpreted data , wrote manuscript and acted as corresponding author.
Overall percentage (%)	70
Certification:	This paper reports on original research I conducted during the period of my Higher Degree by Research candidature and is not subject to any obligations or contractual agreements with a third party that would constrain its inclusion in this thesis. I am the primary author of this paper.
Signature	Date 13/9/17

Co-Author Contributions

By signing the Statement of Authorship, each author certifies that:

the candidate's stated contribution to the publication is accurate (as detailed above);

permission is granted for the candidate in include the publication in the thesis; and

the sum of all co-author contributions is equal to 100% less the candidate's stated contribution.

Name of Co-Author	Nigel Cook
Contribution to the Paper	Supervised development of work, assisted in defining direction of research, provided assistance in the collection of analytical data, assisted with data interpretation and helped with manuscript preparation.
Overall percentage (%)	15
Signature	Date 13/9/17

Name of Co-Author	Cristiana Ciobanu
Contribution to the Paper	Supervised development of work, assisted in defining direction of research, assisted with data interpretation and helped with manuscript preparation.
Overall percentage (%)	10
Signature	Date 17 July 2017

Name of Co-Author	Kathy Ehrig		
Contribution to the Paper	Assisted in defining the direction of research, provided samples, assisted with data interpretation and evaluated manuscript.		
Overall percentage (%)	3		
Signature		Date	13/09/17

Name of Co-Author	Alkis Kontonikas-Charos		
Contribution to the Paper	Provided advice on samples and evaluated manuscript.		
Overall percentage (%)	2		
Signature		Date	13/09/17

Journal of Geochemical Exploration 181 (2017) 276–291

Contents lists available at ScienceDirect

Journal of Geochemical Exploration

journal homepage: www.elsevier.com/locate/gexplo

The Wirrda Well and Acropolis prospects, Gawler Craton, South Australia: Insights into evolving fluid conditions through apatite chemistry

Sasha Krneta[a,*], Nigel J. Cook[b], Cristiana L. Ciobanu[b], Kathy Ehrig[c], Alkis Kontonikas-Charos[a]

[a] School of Physical Sciences, The University of Adelaide, Adelaide, SA 5000, Australia
[b] School of Chemical Engineering, The University of Adelaide, Adelaide, SA 5000, Australia
[c] BHP Olympic Dam, Adelaide, SA 5000, Australia

ARTICLE INFO

Keywords:
Apatite
Hydrothermal ore deposits
Wirrda Well
Acropolis
Olympic Cu-Au province
Pathfinder minerals
IOCG exploration
REE

ABSTRACT

The Wirrda Well and Acropolis prospects are located ~25 km SSE and SW, respectively, from the giant Olympic Dam Cu-U-Au-Ag deposit within the Olympic Cu-Au Province of South Australia. Mineralisation in the two prospects displays a temporal and spatial zonation characteristic of other IOCG-type deposits and prospects within the province, including Olympic Dam, in which an early high-temperature, magnetite-dominant mineralisation is transitional to a hematite-dominant mineralisation style, accompanied by subordinate and often localised carbonate alteration. Both prospects contain conspicuous hydrothermal apatite which is characteristic in terms of host assemblage and geochemical signature. Chondrite-normalised rare earth element (REE) fractionation patterns for apatite depict the evolution of hydrothermal fluids during ore formation. An early generation of apatite is abundant within magnetite-dominant mineralisation in both prospects, and displays a characteristic light-REE enriched fractionation trend. Overprinting of this initial high-temperature assemblage results in the loss of REE and Y (REY), as well as Cl, along fractures within this apatite, as well as the formation of new generations of apatite that are also depleted in these elements. The transition from early reduced, to later oxidised assemblages within both prospects is accompanied by an evolution of the REY signature of apatite in which LREE-enriched patters with negative Eu-anomalies are replaced by convex middle-REE (MREE)-enriched patterns, positive Eu-anomalies and the development of a conspicuous negative Y-anomaly. Comparable trends are recognised elsewhere within the district and are interpreted as the hallmark of productive mineralised IOCG ore systems. The evolution of chondrite-normalised REY patterns can be explained in terms of changes in fluid parameters, speciation of REY in ore-forming fluids, and the capacity of REY to precipitate and partition into apatite in ways that contrast with those expected by simple consideration of crystal structure. Results are concordant with modelling of REY-speciation, which show that, under hydrothermal conditions typical of IOCG mineralisation, a decrease in salinity, pH and temperature is associated with hematite-sericite alteration sufficient to produce MREE-enriched apatite. These data offer encouragement for the use of apatite geochemistry in mineral exploration within the Olympic Cu-Au Province, and potentially in analogous terranes elsewhere, given the clear association between MREE-enriched apatite and often well-mineralised, hematite-dominant domains within these large IOCG systems.

1. Introduction

In most magmatic and hydrothermal systems, apatite-group minerals account for the majority of whole rock phosphorus, and also a significant proportion of the rare earth element and yttrium (hereafter REY) budget (Piccoli and Candela, 2002). Broad application of apatite geochemistry to constrain hydrothermal processes has been demonstrated for several deposit types, including iron-oxide copper gold (IOCG) (Ismail et al., 2014; Kontonikas-Charos et al., 2014; Krneta et al., 2016) and in iron-oxide-apatite (IOA) deposits (Harlov et al., 2002a; Bonyadi et al., 2011; Majka et al., 2016). These studies have drawn attention to the ubiquitous presence and refractory nature of apatite in these ores, and to the sensitivity of apatite to reflect the conditions under which it formed due to its complex, diverse chemistry and ability to incorporate a broad range of minor and trace elements. In the case of hydrothermal apatite, marked similarities in the evolution of hydrothermal apatite signatures exist within the Olympic Dam IOCG system, South Australia (Krneta et al., 2016), and the Kiirunavaara IOA deposit, Sweden (Harlov et al. 2002a) where a similar evolution in fluid chemistry was hypothesised. In both cases, fluids undergo a drop in

* Corresponding author.
E-mail address: sasha.krneta@adelaide.edu.au (S. Krneta).

http://dx.doi.org/10.1016/j.gexplo.2017.08.004
Received 27 May 2017; Accepted 1 August 2017
Available online 09 August 2017

both temperature and salinity, coeval with overprinting of the wider hydrothermal assemblage as well as the apatite.

The apatite group is defined by the formula $A_5(XO_4)_3Z$ (Pasero et al., 2010). The A position is largely occupied by Ca^{2+}, along with lesser concentrations of Sr^{2+}, Ba^{2+}, Mg^{2+}, Mn^{2+}, Fe^{2+}, Cd^{2+}, Na^{+}, Eu^{2+}, Y^{3+} and REE^{3+}. The X position is dominated by P^{5+}, as (PO_4), but can also host other small, highly-charged cations (Si^{4+}, S^{6+}, As^{5+} and V^{5+}). The Z position is occupied by halogens (F and Cl) and OH^{-} defining the three end-members fluorapatite, chlorapatite and hydroxyapatite. Most natural apatite-group minerals contain all three anions in varying proportions (Hughes and Rakovan, 2015). Heterovalent substitution in apatite is facilitated by coupled substitution mechanisms (Rønsbo, 1989; Pan and Fleet, 2002). These are particularly relevant for substitution of the REE and other elements such as S:

$$REE^{3+} + Na^{+} = 2\,Ca^{2+}$$

$$REE^{3+} + SiO_4^{4-} = Ca^{2+} + PO_4^{3-}$$

$$SO_4^{2-} + Na^{+} = PO_4^{3-} + Ca^{2+}$$

$$SO_4^{2-} + SiO_4^{4-} = 2\,PO_4^{3-}$$

As in any other mineral, the apatite crystal structure, and particularly the atomic radii of the accommodating position, exerts the greatest control on elemental substitutions. In apatite, there are two sites for Ca: (i) tri-capped trigonal prism: Me_1O_9 (Ca1 position); and (ii) an irregular polyhedron, Me_2O_6X (Ca2 position), where X is one of the anions F, Cl, OH; whereas P is placed in a tetrahedron: TO_4. There is a preference of LREE and HREE over the Ca2 and Ca1 sites, respectively, whereas REEs near Nd, with the highest partitioning coefficients can be accommodated in either of the two sites (Hughes et al., 1991). External parameters can, however, impact on crystal-controlled substitution behaviour allowing for fingerprinting of metasomatic processes (e.g., Harlov, 2015; Krneta et al., 2017; Krneta, 2017). This is particularly true for REY since their speciation in hydrothermal fluids is highly sensitive to changes in parameters such as acidity and temperature (Migdisov et al., 2016). The latter authors emphasised the large discrepancies in the stability and solubility of various commonly occurring REY-complexes, and the capacity of some to transport, and for others to instigate deposition of REY. For example, at temperatures and salinities characteristic of many magmatic-hydrothermal systems LREE-Cl are much more stable than HREE-Cl complexes, thus allowing for the complete spatial dissociation of these two groups (Migdisov et al., 2016). Moreover, the predominance of Eu^{3+} over Eu^{2+} in hydrothermal fluids is primarily controlled by pH and given that most minerals able to incorporate REY have a preference for one over the other as controlled by the size of the accommodating position, the presence of Eu-anomalies both positive and negative along with changes therein can give insights into fluid pH conditions (Brugger et al., 2000, 2008).

The 700 km-long, N-S-striking Olympic Cu-Au Province of South Australia, within the eastern Gawler Craton (Skirrow et al., 2007), hosts widespread IOCG-style mineralisation. These deposits are associated with a major tectonothermal event at 1.6 Ga (e.g., Hayward and Skirrow, 2010). Of these, by far the largest yet discovered, is the Olympic Dam (OD) Cu-Au-U-Ag deposit (Ehrig et al., 2017). Most deposits and prospects across the province contain abundant apatite, both as a preserved magmatic accessory mineral and as a hydrothermal mineral contemporaneous with ore formation (Krneta et al., 2016).

The Wirrda Well (WW) and Acropolis (AC) prospects, located ~25 km SSE and SW from Olympic Dam, respectively (Fig. 1), resemble Olympic Dam in many ways, not least with respect to the iron-oxide dominated alteration, and in the case of Wirrda Well, the association between sulphide mineralisation and widespread brecciation. Apatite is a conspicuous component of mineralisation and host rock in both prospects.

Mineralisation in the Wirrda Well prospect is hosted by granite of the Paleoproterozoic Donington Suite (DS; Jagodzinski, 2005) and by contemporaneous mafic dykes (Huang et al., 2016), as vein networks and breccias containing hematite and magnetite. Mineral zonation within the prospect mimics that observed at Olympic Dam with respect to the dominant Fe-oxide and Cu-sulphide species although higher-grade zones containing bornite-chalcocite mineralisation are weakly developed and generally more limited in extent (Cross, 1993).

Mineralisation within the Acropolis prospect is hosted primarily by sericite-altered, rhyolitic and dacitic lavas of the ~1.6 Ga Gawler Range Volcanics (GRV; McPhie, pers. comm., 2016). Mineralisation occurs as vein networks containing magnetite + apatite ± hematite ± biotite ± K-feldspar ± quartz assemblages (Cross, 1993). Weak copper mineralisation is expressed as pockets of pyrite and subordinate chalcopyrite. Within both prospects and elsewhere in the district, a transition from high-temperature (> 400°C) magnetite-dominant to lower temperature hematite-dominant (150–300 °C) mineralisation has been inferred based on fluid inclusion studies and oxygen isotopes (Oreskes and Einaudi, 1992; Bastrakov et al., 2007). There are, however, no studies of this type on mineralisation at Wirrda Well.

In this contribution, we provide a description of the mineralisation and alteration styles within these two prospects, as well as a detailed account of apatite petrography and geochemistry. Apatite is considered in relation to the wider hydrothermal assemblage and changes in apatite chemistry are investigated in terms of fluid evolution within the individual prospects. The importance of middle-REE enrichment in apatite, and its marked association with areas of later hematite-sericite alteration and strong Cu-mineralisation, is discussed within a context of exploration targeting and the potential use of apatite as a geochemical pathfinder in what are otherwise large, largely barren, iron-oxide dominant systems.

2. Geological background

The eastern Gawler Craton, South Australia is host to one of the largest IOCG provinces on Earth, the Olympic Cu-Au province (Skirrow et al., 2007). Mineralisation relates to a Mesoproterozoic (~1.6 Ga) thermal event associated with emplacement of A-type, I-type granites and mafic magmas of the Hiltaba Suite (HS; Creaser, 1989) and coeval eruption of the GRV (Blissett et al., 1993). These magmas intruded Archaean crystalline basement (Sleaford and Mulgathing Complexes), felsic and mafic intrusive rocks of the ~1850 Ma DS, and metasediments of the ~1.76–1.74 Wallaroo Group. In the area surrounding OD, WW and AC, all the aforementioned lithologies are obscured by hundreds of metres of barren, flat-lying post-mineralisation cover comprising the Mesoproterozoic Pandurra Formation and younger Neoproterozoic and Cretaceous sedimentary rocks including limestones, dolomites sandstones and shales of the Wilpena and Umberata Groups (Vella, 1997).

The WW and AC prospects were discovered during a regional exploration campaign by Western Mining Corporation shortly after the discovery of Olympic Dam (1975) beneath a minimum 330 and 480 m of barren sedimentary cover rocks of the Stuart Shelf, respectively. They are located together with OD, within a prominent ENE-trending fault-bounded block on the southern margin of the Burgoyne Batholith. The latter is a large 50 by 35 km basement high consisting of ~1590 Ma intrusive rocks varying in composition from felsic to mafic (Reeve et al., 1990). The two prospects are characterised by prominent magnetic and gravity anomalies on regional datasets (Fig. 1; Hayward and Skirrow, 2010). In the case of WW, a near circular 4 km-wide gravity anomaly, ~6 mGal above background, corresponds to an overlapping magnetic anomaly with a peak intensity of ~1800 nT. Acropolis, on the other hand, is recognised on a 15 km-long complex, multi-sourced, NW-SE striking magnetic anomaly with peaks in excess of 6000 nT and an approximately coincident gravity anomaly of 22 mGal above background (Vella and Cawood, 2006).

Within the large concentric gravity and magnetic anomaly, the WW

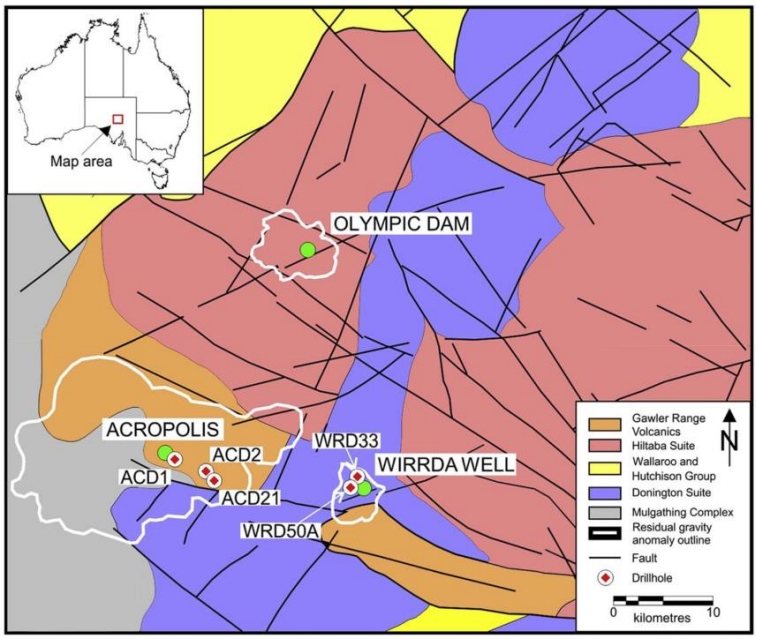

Fig. 1. Basement geological map of the Burgoyne Batholith showing the location of the Wirrda Well and Acropolis prospects, the Olympic Dam deposit, and studied/sampled drillholes. Insert shows the location of Olympic Dam.
Map sourced from https://map.sarig.sa.gov.au/.

prospect is made-up of a vertically-plunging breccia pipe with multiple apophyses. These are separated into two main mineralised zones (North and South), both characterised by weak brecciation and intense iron-oxide alteration. The mineralisation is primarily hosted within a sheared, and in places also mylonitised, megacrystic K-feldspar-bearing DS granite (~1850 Ma) and comparably deformed mafic dykes of the same age (Ehrig, 2013). A significant portion of the brecciation and mineralisation is concentrated along the contacts of the intrusive rocks. GRV rocks occur within a faulted block of possible post-mineralisation origin within the northern zone. Mafic dykes occur throughout the deposit and are recognised as pre- syn-and post-mineralisation in age (Huang et al., 2016). Notable among these are the picrites of post-mineralisation age (Fig. 2).

Mineralisation within the WW prospect consists of breccias and vein networks containing magnetite, apatite (± hematite ± carbonate ± quartz ± sulphides) accompanied by widespread chlorite-sericite alteration. The main iron-oxide (hematite vs. magnetite) and Cu-(Fe)-sulphide (pyrite-chalcopyrite vs. chalcopyrite-bornite vs. bornite-chalcocite) species changes upward throughout the deposit analogous to that observed at Olympic Dam. Magnetite-pyrite-apatite-chlorite assemblages are dominant at depth and grade upwards into zones of bornite-chalcocite mineralisation with increased abundance of hematite. The bornite-chalcocite and chalcopyrite-dominant zones are most strongly developed in the northern zone, where they also extend to greater depths than in the south (Ehrig, 2013). In comparison with OD, however, they are weakly mineralised and of more limited spatial extent, both laterally and vertically.

Iron-oxide-hosted mineralisation at Acropolis has been intersected by drilling across an area of approximately 50 km^2 and consists primarily of large, flat, tabular masses of coarse-grained magnetite, in places replaced by hematite (martite), along with a later generation of fine-grained hematite within sericite-altered, rhyolitic and dacitic lavas and rare localised dacitic ignimbrite and andesitic lavas of the GRV, along with an interbedded very thin clastic bedded facies within. The DS granite has been intersected by drilling in the central and eastern portions of the prospect and is believed to underlie the GRV in the area. Numerous post-mineralisation mafic and felsic dykes cross-cut the mineralisation with one drillhole intersecting a small HS granite. Mineralisation is most strongly developed in the south-western portion of the prospect within the rhyolitic lavas and the aforementioned HS granite (McPhie, pers. comm. 2016). Peripheral to the large tabular mineralisation, veins and vein-networks carrying iron-oxides extend some distance into the host rock. Magnetite-apatite-carbonate-K-feldspar-biotite-quartz assemblages dominate within the prospect. However, in places, this mineralisation is overprinted by assemblages of chlorite, sericite, hematite, and rarely, also siderite.

Abundant, locally very coarse-grained apatite, up to several cm in size, is closely associated with the iron-oxides, both within the locally abundant sulphide mineralisation, as well as in the surrounding vein networks. Although resembling OD in many ways, such as the intimate mineralogical association of copper, uranium and REE with iron-oxide mineralisation, the AC prospect differs in that concentrations of Cu, U, Au and REE are significantly lower, and AC is thus primarily an iron deposit with multiple, wide intersects averaging 60% Fe (Paterson, 1986). Moreover, the prospect lacks well-developed zones of bornite-chalcocite mineralisation with primary sulphides being represented by pyrite and chalcopyrite in which the latter commonly replaces pyrite often together with barite. Magnetite-dominant mineralisation from AC formed at comparable temperatures as OD (550–440 °C vs. 500 °C; Oreskes and Einaudi, 1992). These authors acknowledge, however, the lack of hematite dominant mineralisation within the AC prospect and the sub-economic nature of magnetite mineralisation within both systems, suggesting that the fluids responsible for transformation of magnetite to hematite were crucial for formation of economic Cu-ores with associated elevated Au and U.

3. Sampling approach and methodology

Distinct generations of hydrothermal apatite are identified and described from two contrasting zones within the WW prospect: a deep, magnetite-pyrite dominant zone; and a shallower hematite-bornite-chalcocite zone (hereafter, “Deep zone” DZ; and “Shallow zone” SZ, respectively), (Figs. 1 and 2; Table 1). Hydrothermal apatite in both zones is hosted almost exclusively in veins and breccia-fill and only

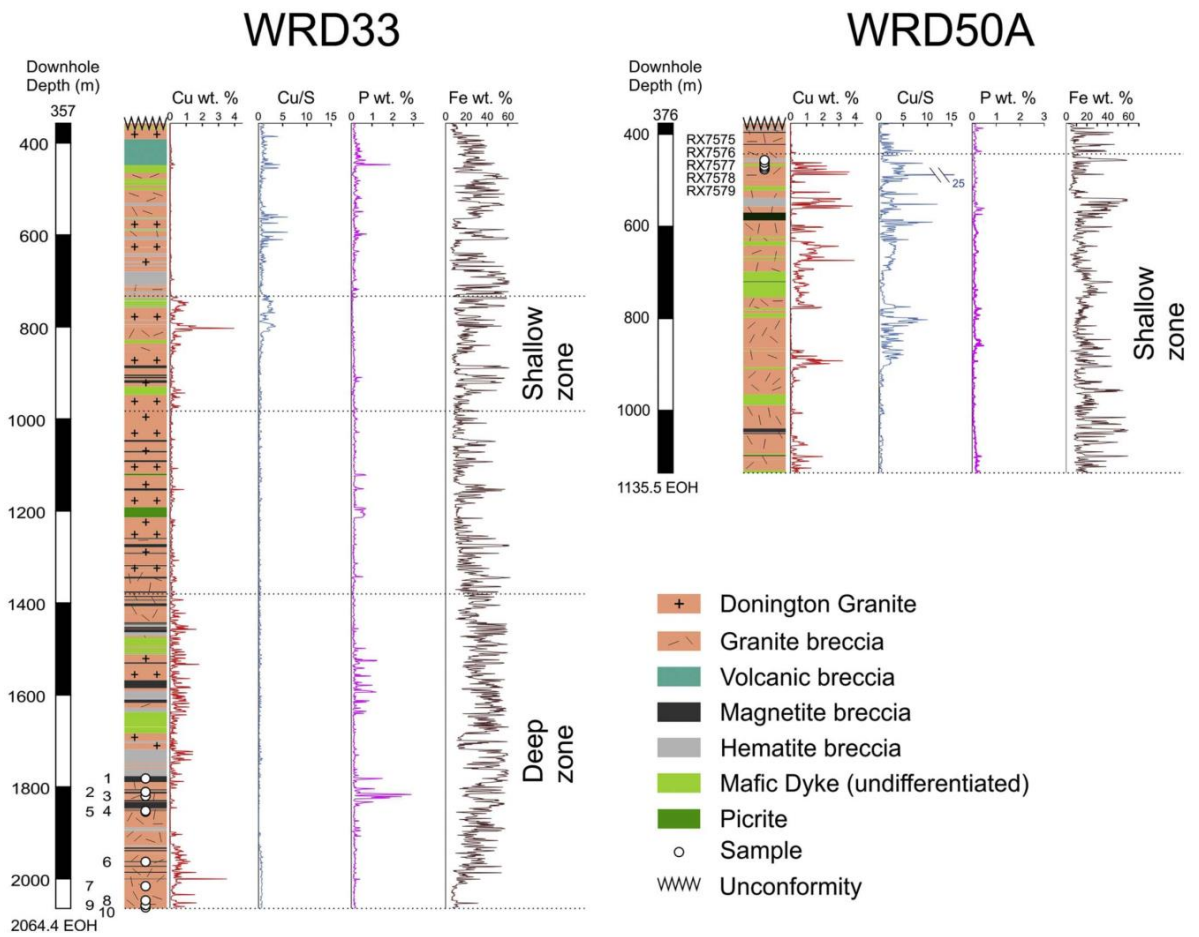

Fig. 2. Schematic representation of the Wirrda Well drillholes sampled in this study. Variations in the concentrations of Cu, P and Fe in whole rock are shown, together with whole rock Cu/S ratios. Note the difference in Cu/S ratios indicative of a dominance by chalcocite-bornite assemblages in the shallow zone. The unconformity shown separates the mineralised Archaean to Mesoproterozoic lithologies from the overlying younger non-mineralised sediments.

occasionally within the host DS granite. Subsequently, due to the highly altered character of the host granitoid, no magmatic apatite was considered in this study.

The DZ encompasses mineralisation intersected in the lower portions of drillhole WRD33, at depths below 1400 m through to the end of hole (2064.4 m). It is hosted exclusively within altered DS granite as iron-oxide-apatite veins and breccias with varying concentrations of magnetite and hematite. Pyrite and very much subordinate chalcopyrite are the dominant sulphides. In contrast, the SZ sampled from drillhole WRD50A consists of veins and breccias hosted within altered DS granite and coeval mafic dykes. Mineralisation is dominated by hematite as the main iron-oxide and bornite + chalcocite, the dominant sulphides in this interval, commonly in association with one another.

Samples examined from the AC prospect (Table 1) were collected from drillholes ACD1, ACD2 and ACD21 drilled on the eastern side of the coincident gravity and magnetic anomaly defining the prospect (Figs. 1 and 3). In the sampled drillholes, the character of the mineralisation varies considerably despite the shared felsic GRV host. Mineralisation in drillhole ACD1 consists primarily of coarse-grained magnetite whereas in the sampled portions of drillholes ACD2 and ACD21, the magnetite has been almost completely altered to hematite (martite) and in the case of ACD21 samples partially to siderite.

In both prospects emphasis during sample selection was placed on collecting a wide variety of apatite-bearing mineralised material so that apatite morphology and chemical signatures could be effectively tied to the enclosing mineral assemblage.

Considering the various mineral assemblages within which apatite is present in the two prospects, the present study will assess if apatite changes in chemical/trace elements signatures can be related to changes in the mineralising conditions.

3.1. Analytical techniques

Samples were prepared as 1-inch polished blocks. Each was imaged using a FEI Quanta 450 FEG environmental scanning electron microscope (ESEM) equipped with a back-scattered electron (BSE) detector and energy-dispersive X-ray spectrometry detector (EDS) prior to electron probe microanalysis (EPMA) and laser-ablation inductively coupled plasma-mass spectrometry (LA-ICP-MS). Analysed grains were selected based on textures, compositional zonation, and relationships to co-existing minerals.

Quantitative compositional data for apatite were obtained using two electron microprobes: a CAMECA SX-Five instrument at Adelaide Microscopy (The University of Adelaide); and a Cameca SX100 (Central Science Laboratory, University of Tasmania). Both were operated at accelerating voltages of 15 kV, and beam currents of 20 nA. X-ray lines,

Table 1
Overview of lithologies and samples discussed in this study.

	Drillhole no.	Depth (m)	Sample ID	Sample category/rock type
Wirrda Well	WRD33	1781.8	WRD33-1	Wirrda Well-Deep zone
		1811	− 2	Wirrda Well deep zone consists of chlorite-sericite altered Donington Suite Granite, containing well-developed iron-oxide-apatite mineralisation with variable concentrations of pyrite-chalcopyrite. The mineralisation varies from early (magnetite-apatite-sulphide) veinlets through massive (magnetite-hematite-apatite-sulphide) veins and breccias. Iron-oxide dominance alternates locally between magnetite and hematite although overall the earlier is more abundant. Intense chlorite-sericite alteration is texturally destructive. Late apatite-calcite veins cross-cut the altered granite and iron-oxide veins and breccias. In such instances the iron-oxides are commonly altered to siderite.
		1819.8	− 3	
		1852.2	− 4	
		1854.2	− 5	
		1950.9	− 6	
		2009	− 7	
		2046.9	− 8	
		2057	− 9	
		2063.6	− 10	
	WRD50A	456.1	RX7575	Wirrda Well-Shallow zone
		461.5	RX7576	Wirrda Well Shallow zone mineralisation is hosted in sericite-altered Donington Granite and coeval mafic dyke. Alteration of the host rock is for the most part texturally destructive although some remnant K-feldspar remains. Chlorite is absent to rare. Fine grained hematite is sometimes intergrown with the sericite along with irregular grains of rutile. Veins and breccias consist primarily of hematite, both primary and lesser martite. Remnant magnetite is observed in some grains. Bornite-chalcocite are the dominant sulphides and host the apatite. Barite is abundant in some samples.
		468.5	RX7577	
		472.2	RX7578	
		476.2	RX7579	
Acropolis	ACD1	1025.5	ACD1-1	Acropolis
		1034.3	− 2	Magnetite-apatite-quartz-K-feldspar-carbonate-biotite veins and breccias hosted in partially to completely sericite altered rhyolitic and dacitic lavas of the GRV. Fe-oxide veins are most strongly developed in the rhyolitic lavas. Widespread overprinting of the original hydrothermal assemblage is observed as martitization of the magnetite, sericitizations of the hydrothermal K-feldspar and chlorite replacement of biotite. Elsewhere significant replacement of the martite by siderite occurs. Increased copper concentrations are seen in samples where the original assemblage is overprinted by significant sericite, chlorite, barite, hematite and chalcopyrite.
		1046	− 3	
		1058.9	− 4	
		1082.5	− 5	
		1083.5	− 6	
	ACD2	576.9	ACD2-1	
		599.5	− 2	
		639.1	− 3	
		647.2	− 4	
	ACD21	675.7	ACD21.2A	

standards, count times, and typical minimum limits of detection are given as Electronic Appendix A. A spot size of 4 μm was used for most analyses to target distinct domains within individual grains but a larger spot size (10 μm) was used whenever possible to obtain optimal sensitivity for minor elements.

LA-ICP-MS spot analysis and element mapping was performed using a Resonetics M-50-LR 193 nm Excimer laser attached to an Agilent 7700cx Quadrupole ICP mass spectrometer at Adelaide Microscopy, University of Adelaide. Ablation took place in an UHP He (0.7 L/min) atmosphere, mixed after leaving the ablation cell with Ar (0.93 L/min). The mix was passed through a pulse-homogenising device after which it is introduced to the torch. ICP-MS calibration was performed regularly to increase sensitivity. LA-ICP-MS analysis was performed with a laser beam energy output of 80 mJ and a spot size ranging from 8 to 18 μm dependent on size of the analysed grain or domain within the grain. Zones of interest of limited size were tested using the smaller spot size but, for larger zones, a greater spot size was used in the interest of increasing accuracy and lowering trace element detections. Total acquisition time was 60 s for each analysis comprising a 30 s background measurement, 30 s of ablation, and a 40 s delay between analysis allowing for adequate wash-out, gas stabilisation and processing time. Typical minimum detection limits for the analysed elements are given in Electronic Appendix A.

The following isotopes were analysed ^{23}Na, ^{24}Mg, ^{27}Al, ^{28}Si, ^{31}P, ^{34}S, ^{39}K, ^{43}Ca, ^{45}Sc, ^{47}Ti, ^{51}V, ^{55}Mn, ^{56}Fe, ^{57}Fe, ^{59}Co, ^{60}Ni, ^{63}Cu, ^{66}Zn, ^{75}As, ^{85}Rb, ^{88}Sr, ^{89}Y, ^{90}Zr, ^{93}Nb, ^{95}Mo, ^{118}Sn, ^{133}Cs, ^{137}Ba, ^{139}La, ^{140}Ce, ^{141}Pr, ^{146}Nd, ^{147}Sm, ^{153}Eu, ^{157}Gd, ^{159}Tb, ^{163}Dy, ^{165}Ho, ^{166}Er, ^{169}Tm, ^{172}Yb, ^{175}Lu, ^{181}Ta, ^{182}W, ^{204}Pb, ^{206}Pb, ^{208}Pb, ^{232}Th and ^{238}U. Standard analyses were performed after every ten sample analyses and comprised readings identical in every respect to that of the samples. Each batch of standard analysis comprised two spots on NIST 612, followed by one NIST 610, and two analyses of NIST 612.

Dwell times for each measured isotope were set to 0.01 s except for ^{89}Y, ^{75}As, ^{153}Eu, ^{157}Gd, ^{159}Tb, ^{163}Dy, ^{165}Ho, ^{166}Er, ^{169}Tm, ^{172}Yb, ^{175}Lu, ^{181}Ta, ^{182}W, ^{204}Pb, ^{206}Pb, ^{208}Pb, ^{232}Th and ^{238}U which were set to 0.02 s. Data processing was performed using GLITTER data reduction software with P as an internal standard using EPMA values in Electronic Appendices B and C. Time-resolved LA-ICP-MS depth profiles for all spot analyses were examined in detail to ensure no contamination from inclusions or adjacent minerals during ablation.

4. Petrography and apatite textural and chemical variation

A lithological summary for the WW and AC prospects is provided in Figs. 4 and 5, respectively.

Although not completely unaltered in the samples studied, the host DS granite at Wirrda Well is characterised by the presence of megacrystic K-feldspar crystals (Fig. 4a). In instances where the granite is mylonitised and intensely altered, these are lacking (Fig. 4b). Elsewhere, chlorite alteration is visible on the macroscopic scale as replacement of the interpreted mafic minerals and feldspars, initially along cleavage planes in the latter (Fig. 4c, d). Sericite occurs in association with chlorite (Fig. 4e) and hematite, lending the host a green or red appearance, respectively (Fig. 4f). Several types of mineralisation are observed, varying primarily through reworking of aforementioned categories via repeated brecciation and changes in the proportion of magnetite to hematite. These range from veinlets in weakly-altered granite to massive magnetite-apatite veins (Fig. 4e) through to hematite-dominant veins and breccias (Fig. 4g–j).

Within the AC prospect, much of the mineralisation is hosted in felsic, porphyritic, sericite-altered GRV as locally massive iron-oxide replacement (Fig. 5a) and as veins and fracture networks (Fig. 5a–e), many of which show subsequent martitisation of magnetite with variable intensity (Fig. 5c–d). In some instances, apatite grains are very coarse-grained, in excess of several centimetres (Fig. 5e). Sample selection was based on incorporating all lithologies and mineralisation types mentioned above.

4.1. Wirrda Well

4.1.1. Deep zone

Within the DZ the earliest hydrothermal apatite (*magnetite-associated apatite*) is recognised in magnetite + chlorite + sericite + rutile ± hematite ± pyrite ± chalcopyrite veinlets in chlorite-sericite

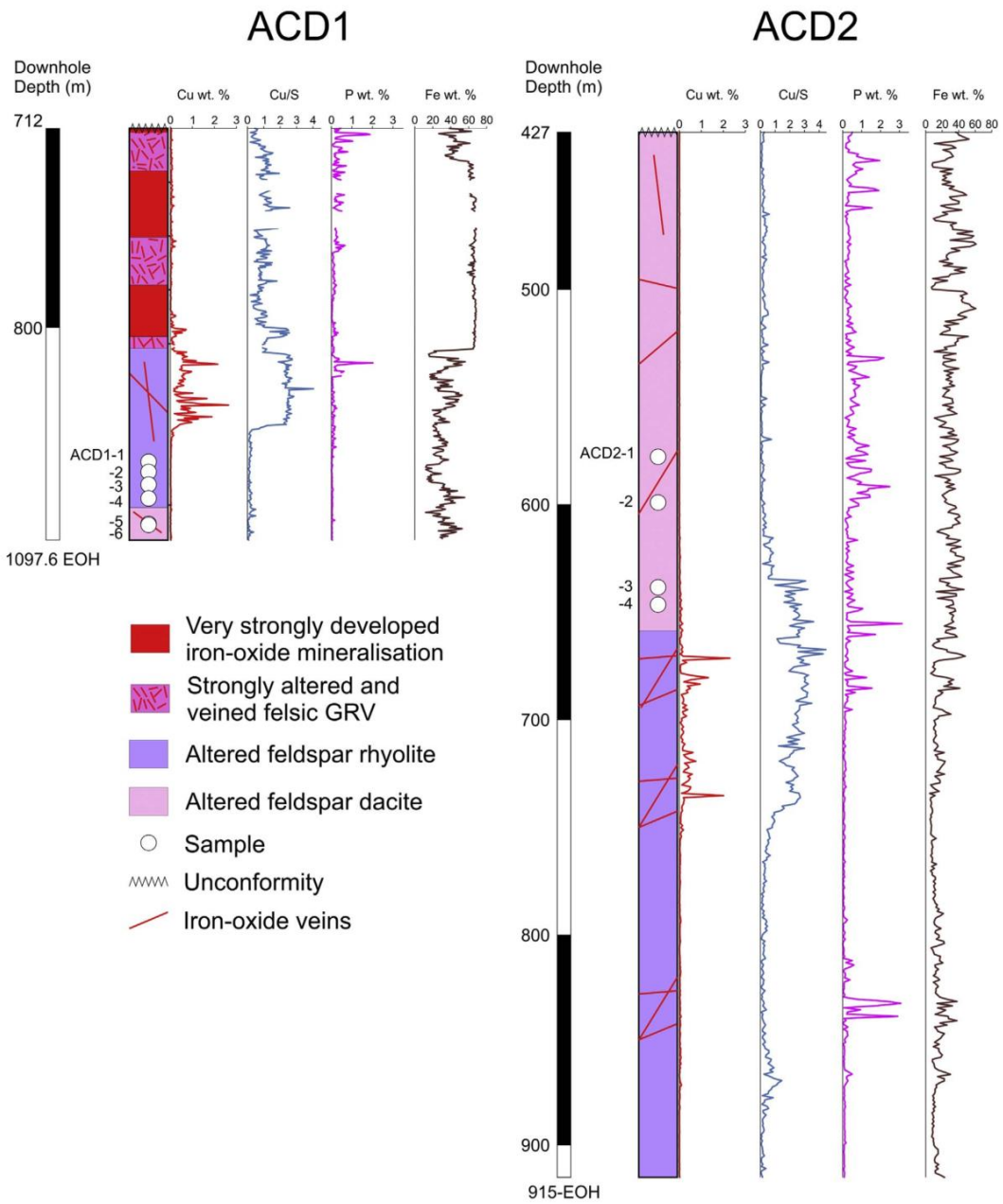

Fig. 3. Schematic representation of Acropolis mineralisation intersected in drillholes ACD1 and ACD2. Variations in the concentrations of Cu, P and Fe in whole rock are shown, together with whole rock Cu/S ratios. The unconformity shown separates the mineralised Archaean to Mesoproterozoic lithologies from the overlying younger non-mineralised sedimentary rocks.

altered DS granite (Fig. 6a). Such veins are mostly preserved in weakly mineralised areas, rarely measuring in excess of several mm in width, and are dominated by small rounded grains of magnetite and apatite along with larger, often fractured grains of the former (Fig. 6b). Initially, their development is localised to grain margins of weakly to partially altered K-feldspar megacrysts (Fig. 6c). Chlorite and sericite alter the K-feldspar individually and together, predominantly along cleavage planes and grain cores. Sericite is observed cross-cutting the chlorite, however never in reverse. Such altered zones within the feldspars commonly contain abundant inclusions of monazite and more seldom florencite (Fig. 6d). Chalcopyrite within the veins is seen replacing pyrite and magnetite (Fig. 6b, e). The component minerals within the veins, including apatite, are commonly fractured. However, zoning related to these fractures is not evident and in general the apatite is weakly concentrically zoned to unzoned in back-scattered electron (BSE) images (Fig. 6f).

Strongly mineralised zones are characterised by mafic dykes, veins and breccias ranging in size from several centimetres to several metres in width separated by zones of chlorite-sericite ± hematite altered granite. Their mineralogy is similar to that of the early veinlets, albeit

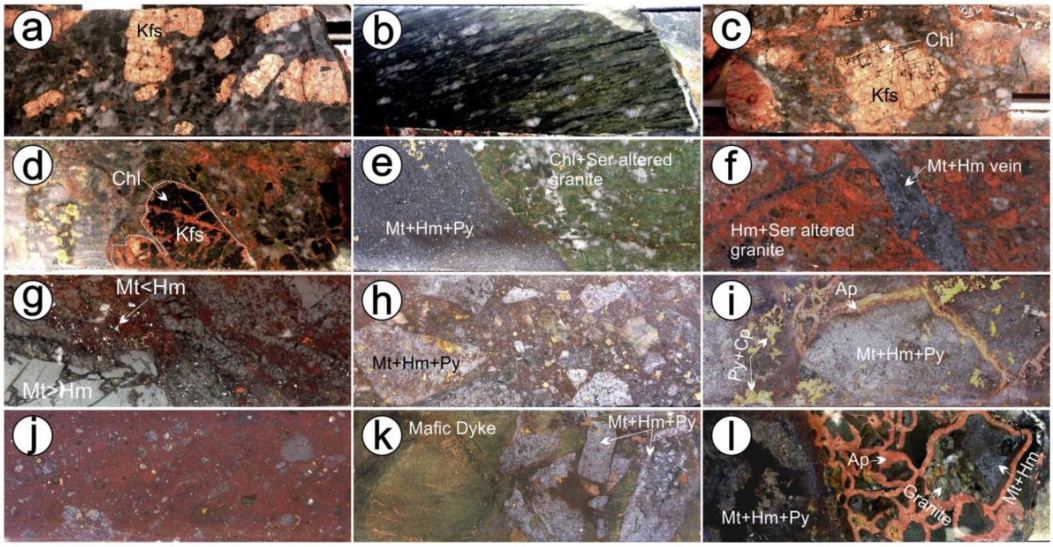

Fig. 4. Hand-specimen photographs showing key lithologies examined from Wirrda Well in this study. (a–f) Donington Suite granite in variable states of alteration. a) Weakly-altered granite with prominent megacrysts of K-feldspar. b) Mylonitised and chlorite-sericite-altered granite. c) Granite with early chlorite alteration of K-feldspar. d) Intensely chlorite-sericite altered granite. e) Sericite-chlorite altered granite on the margin of an iron oxide vein. f) Iron-oxide vein in hematite-sericite altered granite. g) Brecciation of earlier formed magnetite dominant iron-oxide mineralisation. h) Multistage iron-oxide breccia. i) Coarse apatite veins cross-cutting iron-oxide breccia. j) Hematite-dominant matrix supported polymictic breccia with rounded clasts. k) Post-mineralisation mafic dyke with brecciated clasts of iron-oxide mineralisation on the margin. i) Brecciated granite and iron-oxide mineralisation cemented by coarse-grained apatite. Note the composite granite-iron oxide breccia clast. Abbreviations: Ap-apatite, Chl-chlorite, Cp-chalcopyrite, Hm-hematite, Kfs-K-feldspar, Mt-magnetite, Py-pyrite, Ser-sericite.

with important differences, notably that iron-oxide species show greater variety with respect to grain size, mineral association and degree of re-working and inter-conversion into one another. Many of the magnetite and martite grains contain Si(± Al ± Mg ± Ca)-bearing phases too small to discern using SEM-EDS methods (Fig. 7a–b). Inclusion-free magnetite is present and commonly both varieties are altered to hematite. Zones of martite within the magnetite can be distinguished in high-contrast BSE images, whereby the earlier appears darker along with the surrounding blades of primary hematite (Fig. 7c). Along with pyrite (Fig. 7d), the aforementioned bladed hematite is the most common host for apatite within this mineralisation (Fig. 7e). As such, this apatite is termed *"hematite-pyrite associated apatite"*. The apatite itself is commonly small (10–300 μm), rounded to hexagonal in appearance, unzoned, and free of inclusions. Exceptions are seen in some larger grains where a weak fracture-related zoning is observed in BSE images along with numerous fluid and monazite inclusions

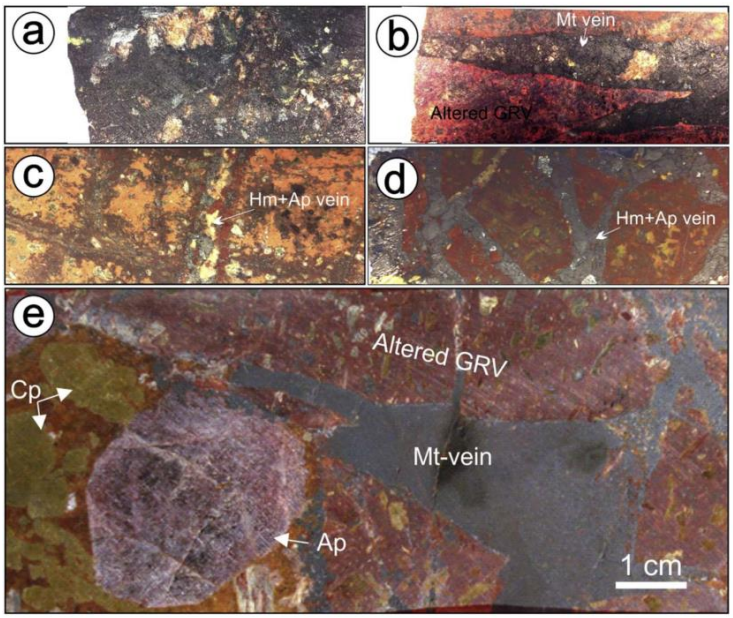

Fig. 5. Hand-specimen photographs showing key lithologies examined from the Acropolis prospect in this study. a) Massive iron-oxide-apatite mineralisation in felsic GRV. b) Magnetite-apatite vein in sericite-altered GRV. c) Multiple veins in sericite altered GRV. d) Hematite (martite)-apatite veins in sericite altered GRV. e) Very coarse apatite surrounded primarily by calcite and coarse-grained pyrite in sericite altered GRV adjacent to a magnetite vein. Abbreviations: Ap-apatite, Hm-hematite, Mt-magnetite, Py-pyrite.

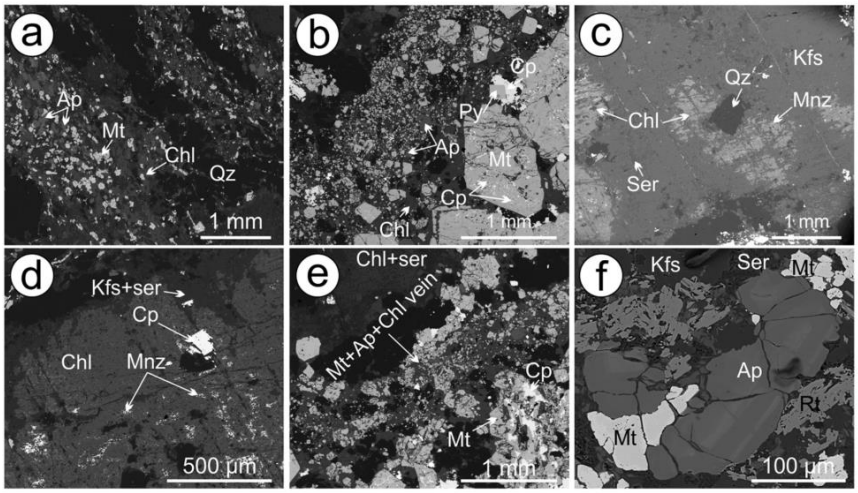

Fig. 6. Back-scatter electron (BSE) images showing the textural and morphological character of the magnetite-apatite veinlets in the Wirrda Well prospect. (a–b) magnetite-dominant vein showing the rounded character of the fine-grained apatite and magnetite with larger, fractured and partially chalcopyrite altered magnetite in b. (c) Image showing chlorite and lesser sericite alteration within a K-feldspar megacryst. (d) Abundant fine-grained monazite in chlorite altered K-feldspar. (e) Chalcopyrite replacement of magnetite and pyrite within a vein. (f) Fractures in weakly zoned apatite. Abbreviations: Ap-apatite, Chl-chlorite, Cp-chalcopyrite, Kfs-K-feldspar, Mnz-monazite, Mt-magnetite, Py-pyrite, Qz-quartz, Ser-sericite.

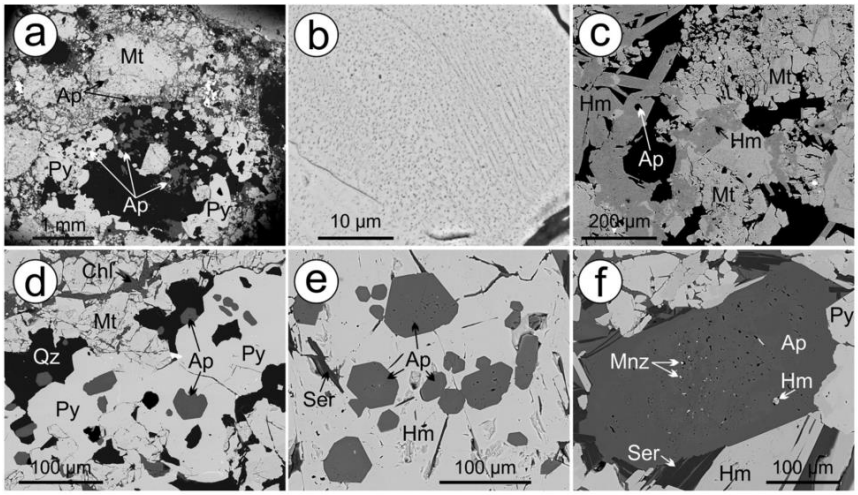

Fig. 7. Back-scatter electron (BSE) images showing the textural and morphological character of the hematite-pyrite associated apatite in strongly mineralised veins and breccias within the deep zone of the Wirrda Well prospect. (a–b) Images showing the coarse-grained, brecciated and inclusion-rich magnetite. (c) High-contrast image showing the difference in BSE intensity response between magnetite and martite, as well as bladed hematite. (d) Apatite hosted in pyrite. (e) Apatite in bladed hematite. (f) Rare, zoned apatite grain showing areas of weak BSE response associated with healed fractures and monazite inclusions. Abbreviations: Ap-apatite, Chl-chlorite, Hm-hematite, Mnz-monazite, Mt-magnetite, Py-pyrite, Qz-quartz, Ser-sericite.

(Fig. 7f).

Cross-cutting both the altered granite and mineralisation within the DZ, and commonly enveloping composite brecciated clasts of both, are coarse apatite and apatite-calcite veins (*calcite vein-hosted apatite*). Apatite within these veins is columnar, nucleating from the vein wall contact with aspect ratios exceeding 6:1 (Fig. 8a). Individual grains are several mm in length and intergrown with one another, forming a reticulated band of apatite visible in hand specimen (Fig. 4i, l). This apatite is inclusion-rich with abundant inclusions of calcite and subordinate hematite observed (Fig. 8b). In vein selvages, Mn-rich siderite is seen to replace hematite (Fig. 8c). In contrast, at contacts between apatite and calcite, small grains composed of fine, laminated intergrowths of bastnäsite-group minerals along with pyrite and hematite are observed (Fig. 8d).

4.1.2. Shallow zone

Shallow zone mineralisation studied from drillhole WRD50A (Table 1, Fig. 2) is hosted predominantly in sericite-hematite altered DS granite, and to a lesser extent in comparably altered coeval mafic dykes. This alteration has for the most part texturally obliterated textures in the igneous host, although some remnant magmatic K-feldspar is present. Sericite within the altered host rocks is, in some cases, intergrown with fine-grained hematite and with irregular grains of rutile in others. Mineralisation consists of hematite-dominant veins and breccias with abundant bornite and chalcocite and sporadic chalcopyrite, rutile, chlorite and florencite (Fig. 9a). Most hematite is restricted to fractures, where two distinct generations are observed: an earlier, coarse, and a later, fine-grained variety (Fig. 9b). Cu-(Fe)-sulphides, represented by symplectites of bornite and chalcocite, occur interstitial to the coarse hematite and are commonly cross-cut by (Fig. 9c), and in some instances almost completely replaced by, the fine-grained variety (Fig. 9b). Apatite is exclusively observed as inclusions in bornite-chalcocite (*bornite-chalcocite hosted apatite*) and commonly contains inclusions of Cu-(Fe)-sulphides along with hematite and sericite (Fig. 9d). The apatite is small (10–100 μm), rounded and unzoned (Fig. 9e). Along with the apatite the bornite and chalcocite contains inclusions of florencite and barite (Fig. 9f).

4.1.3. Wirrda Well apatite chemistry

Within the studied apatite grains, many of the elements commonly substituting for Ca, P and F are present at measurable concentrations (Appendix B). Common charge-compensated coupled substitutions, as

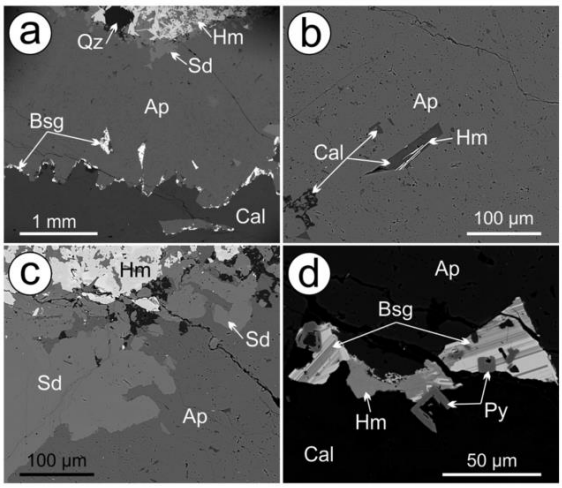

Fig. 8. Back-scatter electron (BSE) images showing the textural and morphological character of apatite in late apatite and apatite-calcite veins. (a) Apatite crystals nucleating from the hematite breccia in the upper part of the image growing into the interior of the vein. (b) Calcite and hematite inclusions in apatite. (c) Siderite inclusions in apatite. Note the siderite replacing the hematite in the upper part of the image. (d) Fine, rhythmically intergrown grains of bastnäsite group minerals along with pyrite and hematite on the apatite-calcite contact. Abbreviations: Ap-apatite, Bsg-bastnäsite group minerals, Cal-calcite, Hm-hematite, Py-pyrite, Qz-quartz, Sd-siderite.

described above, were confirmed. The apatite groups (*magnetite-associated apatite*, *hematite-pyrite associated apatite*, *calcite vein-hosted apatite*, *bornite-chalcocite hosted apatite*) display variation between one another but internal and intra-grain heterogeneity is minimal. Chemical variability is expressed primarily through ΣREY-concentrations and chondrite-normalised REY fractionation patterns, which vary from light rare earth element (LREE) to middle REE (MREE) enrichment, and in variability in both scale and sign of Eu and Y anomalies.

The *magnetite-associated* and *hematite pyrite-associated apatite* are chemically very similar (Electronic Appendices B and D). Both are F-rich, with negligible Cl and an average calculated (OH) component of ~0.1 apfu. Most element concentrations are comparable, with the exceptions of S and Na, which are higher in *hematite pyrite-associated apatite*, and ΣREY concentrations, which are slightly lower (mean ~6600 vs. 7300 ppm). The two sub-populations also differ in their chondrite-normalised REY fractionation patterns (Electronic Appendix D). The *magnetite-associated apatite* displays a LREE-enriched to flat REY pattern that differs from the *hematite pyrite-associated* sub-population, which features a much steeper LREE-segment and slightly weaker negative Eu-anomaly. On average, the *magnetite associated apatite* is also higher in both U and Th, has a higher U/Th ratio but is lower with respect to As concentration (35 vs. 90 ppm).

Compared with the iron-oxide-hosted apatite grains it cross-cuts, the *calcite vein apatite* is relatively pure, with low concentrations of all common elements substituting for Ca or P (Electronic Appendices B and D). ΣREY concentrations are particularly low *(mean* ~700 ppm) and are characterised by flat to MREE-enriched signatures with slight negative Eu-anomalies and moderately strong negative Y-anomalies. The *bornite-chalcocite hosted apatite*, if compared with the *calcite vein apatite*, has an almost indistinguishable REY-signature although with higher absolute ΣREY *(mean* ~3100 ppm). Most other elements are higher in the *bornite-chalcocite hosted apatite* with the notable exception of Mn (540 vs. 110 ppm).

4.2. Acropolis

4.2.1. Early apatite

The earliest recognised apatite within the Acropolis prospects (*early Cl- and REY-rich apatite*) is represented by coarse irregularly-shaped grains, generally at least a few mm in size and hosted within magnetite ± K-feldspar ± carbonate ± quartz veins, commonly as inclusions in rutile-rich magnetite and hematite (martite) (Fig. 10a), as well as carbonates with variable proportions of Mn, Mg and Fe (Fig. 10b). Biotite was not identified in the veins although abundant chlorite-sericite intergrowths may possibly represent pseudomorphic replacements of pre-existing biotite (Fig. 10c).

The early hydrothermal assemblage is overprinted in many samples. Magnetite is Ti-rich and contains exsolutions of ilmenite + rutile, as does the replacing hematite (Fig. 10d). K-feldspar is replaced by sericite with numerous inclusions of fine-grained hematite (Fig. 10e). Apatite hosted within veins with significant overprinting is fractured, rich in inclusions (hematite, sericite and monazite), and displays a zoning visible on BSE images which is controlled by the fractures (Fig. 10f). In some veins, overprinting is manifested primarily as replacement of iron-oxides by siderite (Fig. 11a). The apatite displays fracture-related zoning and contains abundant inclusions of hematite, sericite, monazite, barite and chalcopyrite (Fig. 11b). In both instances, darker

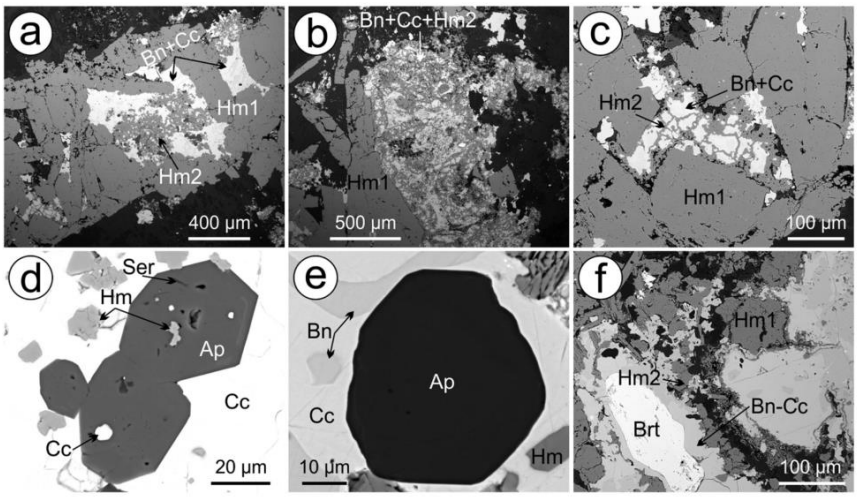

Fig. 9. Back-scatter electron (BSE) images showing the textural and morphological character of apatite within the shallow zone of Wirrda Well. (a–c) Images showing the relationship between the various generations of hematite and bornite-chalcocite symplectites. Note that the sulphide symplectites appear to postdate the coarse-grained hematite and are replaced by the finer-grained variety. (d–e) Apatite in bornite-chalcocite symplectites. In both instances the apatite is unzoned and in d contains inclusions of hematite, sericite and chalcocite. (f) Image showing a large barite grain within the copper-sulphides. Abbreviations: Ap-apatite, Bn-bornite, Brt-barite, Cc-chalcocite, Hm-hematite, Ser-sericite.

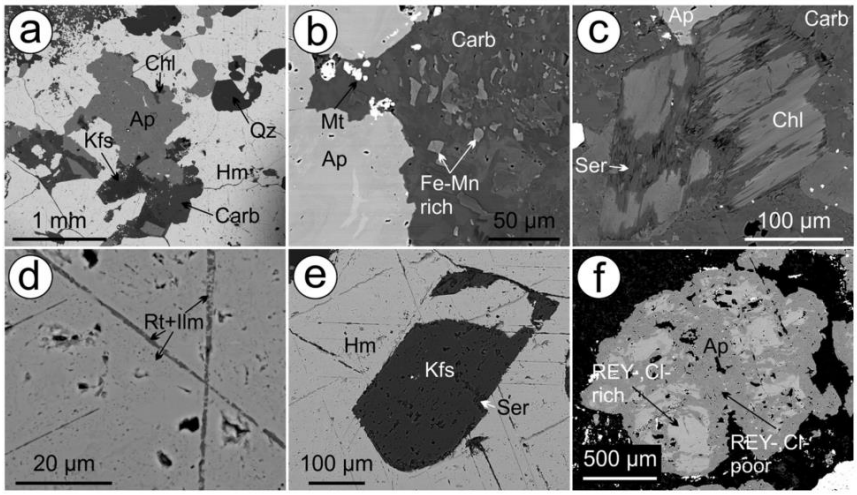

Fig. 10. Back-scatter electron (BSE) images showing the textural and morphological character of apatite within the Acropolis prospect. (a) Early (Cl-, REY)-rich apatite as an inclusion within martite alongside K-feldspar, chlorite, quartz and carbonate. (b) Apatite adjacent to carbonate with variable concentrations of Fe-Mn and Mg. The brightest portions are highest in Fe and Mn whereas the lighter are almost pure dolomite. (c) Possible former biotite grain on the margin of apatite, now mostly chlorite and sericite. (d) Rutile exsolutions in magnetite. (e) Partially sericite-altered K-feldspar in martite. (f) High-contrast image of a large apatite grain with significant fracture-related zoning. The bright domains are unaltered portions of the early (Cl-, REY)-rich apatite whereas the dark domains are LREE- and Cl-depleted. Abbreviations: Ap-apatite, Carb-carbonate, Chl-chlorite, Hm-hematite, Ilm-ilmenite, Kfs-K-feldspar, Mt.-magnetite, Qz-quartz, Rt-rutile, Ser-sericite, Chl-chlorite.

domains on the BSE images are depleted in Cl, Si, and REY, with corresponding increases in F, P and Ca (Fig. 12; Electronic Appendices C and E). However, the REY depletion appears to vary depending on the enclosing alteration. When occurring in veins where hematite-sericite is dominant, apatite displays LREE-depletion and is MREE-enriched (*LREE-Cl-depleted zones*). Conversely, where the surrounding alteration is siderite-dominated, REY are evenly depleted (*REY-Cl-depleted zones*).

4.2.2. Late apatite

Confined to samples in which hydrothermal K-feldspar is completely replaced by sericite, large areas commonly interstitial to coarse hematite (martite) host unzoned apatite grains intergrown with sericite (Fig. 11c, d). In some areas, these are hosted in quartz. Regardless of the host, fine trails of hematite both within and outside of the apatite define clearly visible margins of pre-existing minerals, often separating zones of porous and non-porous quartz (Fig. 11d). Apatite in such samples does not show a clear association with early magnetite-dominant assemblages but appears coeval with the sericite (*sericite associated apatite*).

Much of the Acropolis prospect contains only weak Cu-mineralisation and sulphides are relatively scarce. Samples containing higher concentrations of sulphides, particularly chalcopyrite, are however characterised by overprinting of the early magnetite-dominant assemblage by minor hematite-sericite-chlorite, and also abundant barite (Fig. 11e). Within such samples, apatite is characterised by irregular grain shapes and abundant hematite inclusions (*chalcopyrite-barite associated apatite*). Apatite is unzoned and forms coarse aggregates which occur in association with calcite and chlorite (Fig. 11e–f) interstitial to the early magnetite-dominant assemblage. The coarse magnetite grains are weakly altered to hematite only along grain margins, where abundant bladed hematite is commonly observed.

4.2.3. Acropolis apatite chemistry

Early (Cl, REY)-rich apatite grains are the most common throughout the prospect and are the only apatite generation carrying any appreciable quantities of Cl (mean ~0.03 apfu). They also contain the highest ΣREY concentrations (Fig. 12; Electronic Appendices C and E), and are characterised by a LREE-enriched REY fractionation pattern with a moderately-strong, negative Eu-anomaly and no Y-anomaly (Fig. 14b).

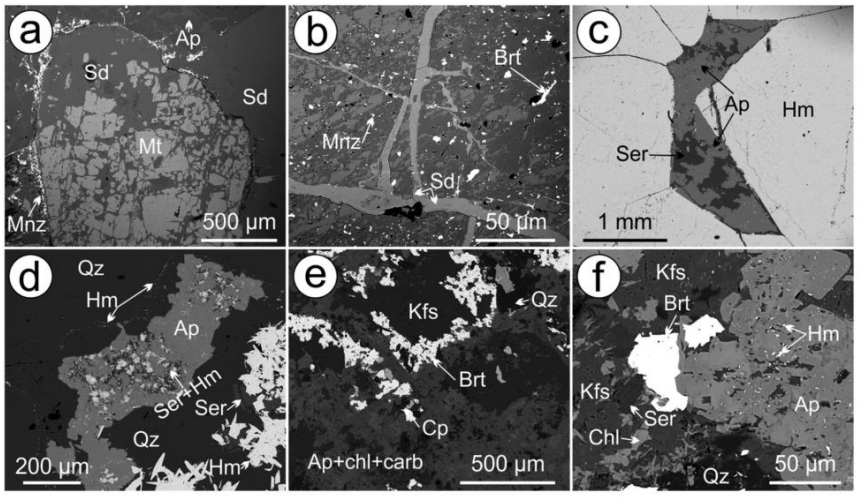

Fig. 11. Back-scatter electron (BSE) images showing the textural and morphological character of apatite within the Acropolis prospect. (a) Large martite grain partially altered to siderite. The former grain boundaries of the martite are marked by fine grained inclusions of monazite. (b) Large apatite with cross-cutting large siderite-filled fractures. The apatite displays a zoning where the bright areas represent unaltered early (Cl, REY)-rich apatite whereas the dark are REY- and Cl-depleted. (c) Angular zone interstitial to martite containing sericite (after K-feldspar) and abundant fine-grained apatite with abundant hematite and sericite inclusions. (d) Multiple hematite-sericite inclusion-rich apatite grains in quartz on the margin of a large accumulation of hematite (bottom-right). Note the line of hematite inclusions separating the inclusion-free and -rich and porous quartz. (e) Partially altered K-feldspar grains rimmed by barite and chalcopyrite in a groundmass of apatite-chlorite-carbonate. (f) Hematite-sericite inclusion-rich apatite on the margin of a barite grain hosted in a chlorite-carbonate groundmass. Abbreviations: Ap-apatite, Brt-barite, Carb-Carbonate, Chl-chlorite, Cp-chalcopyrite, Hm-hematite, Kfs-K-feldspar, Mnz-monazite, Mt.-magnetite, Qz-quartz, Sd-siderite, Ser-sericite.

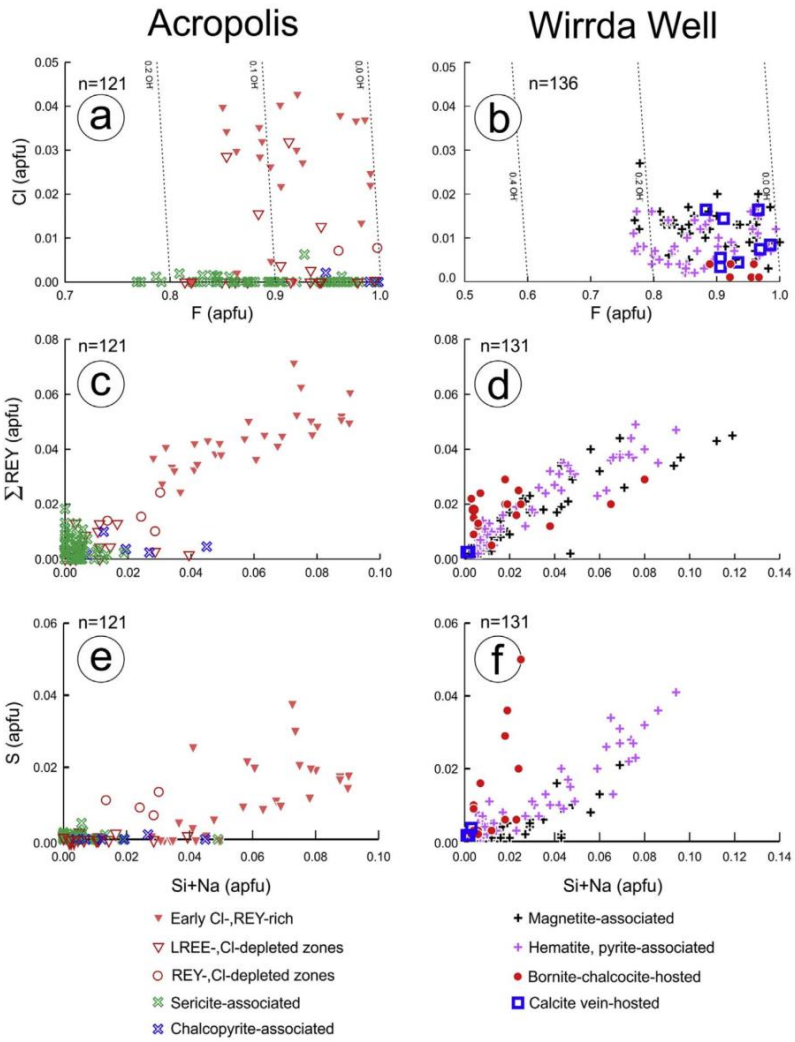

Fig. 12. EPMA Plots of Acropolis and Wirrda Well apatite. (a–b) Cl vs. F, (c–d) ΣREY (apfu) vs. Si + Na (apfu), and (f–g) S (apfu) vs. Si + Na (apfu).

Both the *LREE-Cl-depleted* and *REY-Cl-depleted zones* are found in the altered portions of *early Cl-REY-rich apatite*. In the case of the *REY-Cl-depleted* zones, the REY-signature is similar to that of the unaltered zones although ΣREY concentrations are lower (mean 5000 ppm compared to ~13,000 ppm). However, loss of LREE appears proportionally greater than other REY, lending the *LREE-Cl-depleted apatite* a marked MREE-enriched apatite signature with a weak, negative Eu-anomaly and a strong, negative Y-anomaly (Fig. 14b).

The two apatite generations coeval with overprinting of the initial hydrothermal assemblage (*LREE-Cl-depleted* and *REY-Cl-depleted zones*) display apatite REY-signatures which contrast dramatically with those of earlier apatite. The strongly MREE-enriched *chalcopyrite-barite-associated apatite* has a positive Eu-anomaly and a slight negative Y-anomaly. In contrast, *sericite-associated apatite* has a flat to MREE-enriched REY-signature with no Eu- or Y-anomalies. It also contains very low ΣREY concentrations (mean ~2500 ppm).

5. Discussion

A broad evolution from magnetite- through to hematite-dominant and much lesser, localised siderite-dominant or later carbonate alteration is observed within both prospects. Grains of apatite associated with specific assemblages are distinguished by unique, readily recognisable geochemical signatures, despite being separated by hundreds of meters vertically in a single drillhole, or even kilometres between different drillholes (Figs. 12 and 13; Electronic Appendices B–E). Furthermore, the geochemical signatures of apatite in both mineralised systems, which correlate with the host assemblage and by implication, the hydrothermal conditions, reflect a systematic pattern of fluid evolution. This is particularly true for changes in REY-signatures (Fig. 14; Electronic Appendices D and E). The following discussion is largely focused on the evolution of the two systems, and the manner in which this is reflected by changes in apatite chemistry. Emphasis is placed on the distinguishing characteristics of apatite in those parts of each prospect containing elevated Cu. Apatite REY-signatures are then compared to their equivalents in other ore systems within the Olympic Cu-Au Province, particularly, those from the Olympic Dam deposit (Krneta et al., 2017; Krneta, 2017).

5.1. Early hydrothermal apatite and subsequent overprinting

The flat to LREE-enriched REY-signatures observed in early

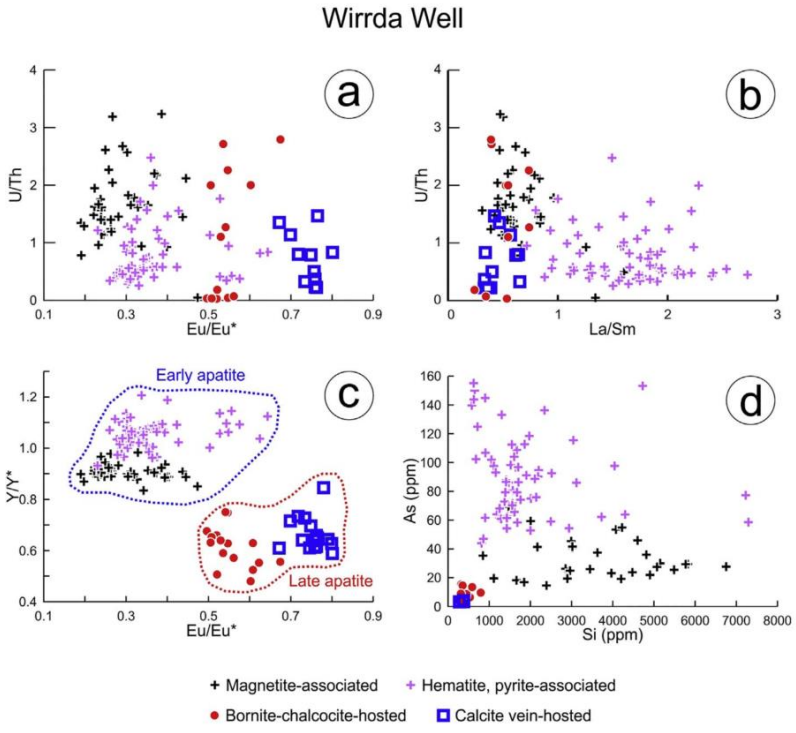

Fig. 13. LA-ICP-MS plots of Wirrda Well apatite. (a) U/Th vs. Eu-anomaly (b) U/Th vs. La/Sm (c) Y-anomaly vs. Eu-anomaly (d) As (ppm) vs. Si (ppm). $Eu/Eu^* = Eu_{CN} / [(Sm_{CN} + Gd_{CN}) / 2]$, $Y / Y^* = Y_{CN} / [(Dy_{CN} + Ho_{CN}) / 2]$.

generations of apatite from both prospects, i.e., *magnetite-associated apatite*, *hematite-pyrite associated apatite* and *early* (*Cl-REY*)*-rich apatite*, are typical of early hydrothermal apatite in the Olympic Cu-Au Province (Ismail et al., 2014; Kontonikas-Charos et al., 2014; Krneta et al., 2017; Krneta, 2017, Fig. 14a, b), and also globally within magmatic-hydrothermal mineralisation (Harlov et al., 2002a). Such signatures are thus not unique to IOCG systems although they are characteristic of early, high-temperature magnetite-dominant assemblages within them. Analogously, the presence and origin of monazite inclusions within apatite is a widespread phenomenon that has been addressed extensively (Harlov et al., 2002a, 2002b; Harlov and Forster, 2004). These studies concluded that the inclusions are hydrothermal products resulting from destabilisation of charge-compensated coupled-substitution mechanisms within apatite, liberating REY and facilitating monazite formation. Such REY-depleted, inclusion-rich zones are best developed in early AC apatite, within samples with significant overprinting of the original assemblage (Figs. 10f, 11b and 12a, c, f). Such zones are appreciably less common at WW but are observed nonetheless.

The recognition of REY-depleted zones and monazite inclusions as hydrothermal textures coeval with overprinting of the wider mineral assemblage presents an opportunity to examine the behaviour of individual REY under hydrothermal conditions characteristic of the overprinting event. REY form a variety of complexes in hydrothermal fluids with all commonly-occurring ligands, Cl, F, SO_4 and CO_3 (Migdisov et al., 2016). Critically, complexation of REY is highly sensitive to hydrothermal conditions and changes in fluid parameters, notably temperature and pH, can result in specific REY-complexes becoming dominant over others creating a wide variability in the stability and solubility among individual REY. This can lead to highly contrasted

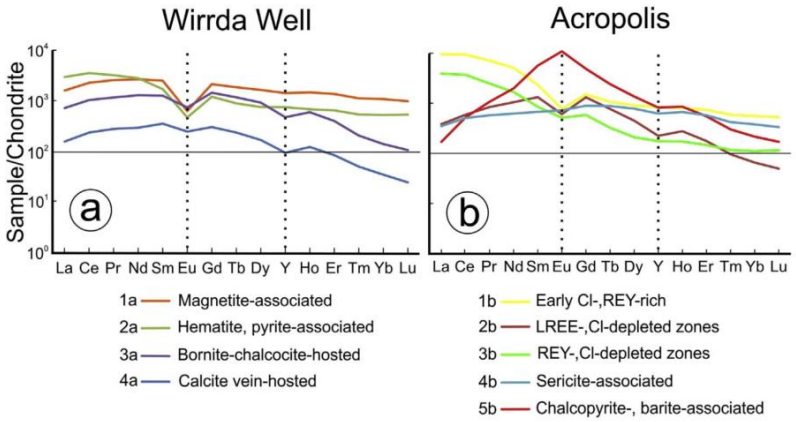

Fig. 14. LA-ICP-MS chondrite-normalised REY-plots of (a) Wirrda Well and (b) Acropolis apatite. Chonrite values after McDonough and Sun (1995).

partitioning behaviour, and even the complete spatial dissociation of individual REY within a hydrothermal system (Migdisov et al., 2016).

Early, magnetite-associated apatite within AC displays zones of REY depletion (*LREE-Cl)-depleted*, line 2b on Fig. 14b and (*REY-Cl)-depleted* zones, line 3b on Fig. 14b along fractures and grain rims. These are spatially related and coeval with hematite-sericite and carbonate alteration of the early hydrothermal assemblages, respectively. In both instances, significant REY loss is observed, although in the case of the hematite-sericite-hosted apatite, the depletion is greater for LREE and HREE, whereas MREE appear largely unaffected. Preferential depletion of LREE has been observed within IOA (Harlov et al., 2002a) and IOCG systems (Krneta et al., 2016, 2017; Krneta, 2017). The widespread nature of the phenomenon led Bonyadi et al. (2011) to suggest that LREE-depletion in apatite is characteristic of the late stages of IOA mineralisation. Addressing comparable depletion and the formation of late, MREE-enriched apatite from Olympic Dam, Krneta (2017) determined, using thermodynamic modelling, that changes in hydrothermal conditions associated with the transition from early to late assemblages at OD impacted on the speciation of REY to a sufficient extent to account for the observed switch from LREE- to MREE-enriched apatite. In detail, decreases in pH, temperature and fluid salinity, along with a rise in fO_2, are seen to result in an increased proportion of the LREE to speciate within the fluid as highly stable and soluble chloride complexes inhibiting their incorporation into apatite.

In the case of early AC apatite, the formation of MREE-enriched altered zones could be attributed to alteration by later, low-salinity, low-pH fluids, whereby LREE are preferentially depleted and remobilised a short distance into the growing monazite inclusions via a coupled dissolution-precipitation reaction (Putnis, 2002). This is shown in Eq.(1) modified after Harlov et al. (2002a):

$$\text{(LREE-rich) apatite} + (Ca^{2+} + P^{5+})_{aq}\text{n(MREE-rich) apatite} + \text{(LREE-rich) monazite} + (Si^{4+} + Na^{+})aq \quad (1)$$

In contrast, REY-depleted zones in early AC apatite associated with local carbonate alteration ((*REY-Cl)-depleted zones*) show a consistent level of depletion across all REY (line 3b on Fig. 14b). The abundance of carbonates both within and surrounding the apatite in these samples suggest high CO_2 concentrations in the fluid and offers a possible explanation for the uniform depletion in REY due to the uniform stability and solubility of REY-CO_3 complexes, and as such their inability to fractionate REY during remobilisation out of the apatite. Such an interpretation is somewhat weakened, however, given that the most recent thermodynamic and solubility data for REY-CO_3 complexes at typical hydrothermal temperatures and conditions is highly uncertain due to its extrapolation from experimental values obtained at 25 °C (Migdisov et al., 2016).

5.2. MREE-enrichment and the significance of positive Eu-anomalies in apatite

In both prospects, apatite associated with hematite-sericite alteration and increased Cu grades displays variable intensities of MREE-enrichment, a weak negative to moderately strong positive Eu-anomaly and a moderately strong negative Y-anomaly (Fig. 14a, b). An important exception to this rule are the *calcite vein-hosted apatite* grains which display MREE-enriched REY-signatures yet lack any association with Cu-mineralisation (Fig. 8 and line 4a on Fig. 14a). Elsewhere, in samples where significant Cu-mineralisation is absent and apatite is present, its REY-signature is flat with low ΣREY concentrations and lacking either Eu- or Y-anomalies (line 4b on Fig. 14b). Among the apatite signatures presented here, the strongest MREE-enrichment is observed in the *chalcopyrite-*, *barite-associated* apatite (line 5b on Fig. 14b), which, in contrast to the remainder of the grains, displays a strong positive Eu-anomaly.

In both prospects, the majority of the Cu-mineralisation displays a spatial and (probable) temporal separation from most of the early magnetite, and to a lesser extent some of the hematite mineralisation. For example, although the main Cu-rich zones within the AC prospect correspond to areas of elevated Fe-concentrations, they are dominantly found on the margins of the main bodies of Fe-rich mineralisation (Fig. 3). Moreover, chalcopyrite (the dominant Cu-sulphide) is rarely observed in association with early magnetite-dominant assemblages, except where it clearly replaces them. Such a relationship is also observed in WW (Fig. 6b). The lack of Cu in early magnetite-dominant mineralisation is significant in light of the observation that early high-temperature (> 400 °C) fluids in a number of IOCG-systems were very rich in Cu (> 500 ppm) yet no significant Cu-mineralisation was deposited due to the lack of a Cu-precipitating mechanism (Bastrakov et al., 2007). Haynes et al. (1995) proposed a model in which fluid mixing, associated with drops in pH, temperature and salinity induced copper deposition at Olympic Dam. Such a transition, particularly the drop in pH, can account for the widespread sericitization of feldspars. Krneta (2017) explored this transition via thermodynamic modelling in the context of REY-speciation and apatite REY-signatures, using similar conditions, and critically replicating the transition in all of the major Fe-oxide, Cu-Fe-sulphide and silicate species. They successfully explained the switch from LREE- to MREE-enriched apatite comparable to the one observed here through the increased presence of the LREE in the fluid as highly stable and soluble REY-Cl complexes, which inhibited their incorporation into the apatite. However, these models could not account for the presence of a positive Eu-anomaly under such acidic conditions (pH ~ 4.4).

A MREE-enriched signature and associated positive Eu-anomaly is anomalous for apatite (e.g., Brugger et al., 2000; Mao et al., 2016), and is seldom reported, either within magmatic or hydrothermal examples (e.g., Belousova et al., 2001, 2002; Cao et al., 2012). The positive Eu-anomalies are surprising given the dominance of Eu^{2+} over Eu^{3+} under the hydrothermal conditions determined for the hematite stage of IOCG-mineralisation (Krneta et al., 2017b), and the expected preference of apatite to incorporate Eu^{3+} (Pan and Fleet, 2002). Nevertheless, apatite can readily incorporate Eu^{2+} (Rakovan et al., 2001), and the positive Eu-anomaly may simply be the result of crystallisation from an Eu-enriched fluid associated with sericitisation of (and REY removal from) feldspars (Mao et al., 2016).

REY-depletion in feldspars during regional-scale alteration is a widespread phenomenon throughout the Olympic Cu-Au Province (Kontonikas-Charos et al., 2014, 2015, 2017a). This is interpreted as a significant contributor to the elevated REY concentrations observed in IOCG systems (Kontonikas-Charos et al., 2017b, 2017c). The strong positive Eu anomalies characteristic of magmatic feldspars would likely be transferred to the fluid and, in turn, into any apatite to crystallise from it. However, the argument that this mechanism was responsible for the formation of positive Eu-anomalies in apatite is weakened by the relatively low observed abundance of sericite in samples hosting the *chalcopyrite-*, *barite-associated* apatite, as well as the complete absence of sericite in samples hosting MREE-enriched apatite with positive Eu-anomalies within OD (Krneta et al., 2017). These positive Eu-anomalies can, alternatively, be accounted for by high pH conditions (> 7), under which Eu-speciation in the fluid, sensitive to pH transitions from Eu^{2+} to Eu^{3+} dominance, resulting in a greater proportion Eu partitioning into the apatite (Brugger et al., 2000, 2008; Krneta, 2017; Fig. 15).

5.3. Fluid evolution and apatite REY-signatures

Within both AC and WW, early magnetite-apatite ± K-feldspar ± biotite assemblages display significant overprinting by later hematite-sericite-carbonate mineralisation (Ehrig et al., 2017). Apatite is present in each stage of the mineralisation and displays chemical signatures characteristic of its host assemblage. These chemical signatures are, in some instances, subtly different with respect to the REY, as is the case with the early apatite of WW (lines 1a and 2a on Fig. 14a)

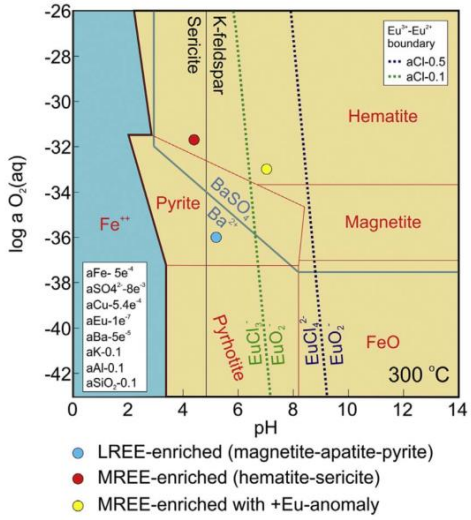

Fig. 15. Diagram showing the relative stabilities of iron-oxide and iron-sulphide species along with barite, K-feldspar and sericite at fluid conditions characteristic of the early magnetite-dominant mineralisation in IOCG deposits (Krneta, 2017). The green and purple dotted lines mark the conditions at which europium species transition from Eu^{2+}- to Eu^{3+}-dominance. Components are given as activities. At lower Cl-activities, this transition is depressed to a lower pH. The coloured dots correspond to interpreted fluid conditions which dominated during the formation of the various assemblages described. (For interpretation of the references to colour in this figure legend, the reader is referred to the web version of this article.)

but clearly discernible with respect to other elements, particularly those sensitive to changes in fluid parameters such as fO_2 (e.g., As; Fig. 13b, d). Moreover, early apatite associated with the magnetite-dominant assemblages displays higher concentrations of REY, most likely due to its crystallisation in the absence of any other REY-consuming phases (Figs. 12 and 13). Characteristics shared by later apatite generations in both WW and AC are the weakening of the negative Eu-anomaly and, in some instances, transition of that anomaly to a positive one, along with the development of a moderately strong negative Y-anomaly. Plotting these parameters against one another (Fig. 13c) allows for the clear separation of the early and later apatite generations, particularly within WW.

Broadly, the apatite encountered in this study can be grouped into: 1) LREE-enriched apatite associated with the earliest magnetite dominant assemblages; 2) MREE-enriched apatite associated with later overprinting by hematite-sericite-carbonate; and 3) MREE-enriched apatite with positive Eu-anomalies associated with later overprinting and, in the case of AC, copper mineralisation. Plotting the stabilities of the various minerals encountered in this study with respect to fO_2, pH, the transition in Eu^{2+}-Eu^{3+} dominance at 300 °C and elemental concentrations in line with Krneta (2017), we can demonstrate (Fig. 15) the approximate interpreted fluid conditions at the time of crystallisation for each of these three apatite groups. Importantly, such a diagram offers a possible solution to the development of the positive Eu-anomalies in apatite. Given that, at low Cl-activity, the transition from Eu^{2+}-to Eu^{3+}-dominance is depressed to lower pH conditions, the formation of positive Eu-anomalies may be the result of crystallisation from late, alkaline fluids. Although such fluids are highly uncharacteristic of magmatic-hydrothermal systems, they may possibly be representative of a late fluid pulse, rich in CO_2, resembling those inferred elsewhere (e.g., Brugger et al., 2000, 2008).

5.4. MREE-enriched apatite and significance to mineral exploration

Suitable pathfinders for magmatic-hydrothermal orebodies (e.g., Averill, 2007, 2011; Bouzari et al., 2016) must fulfil certain requirements. As one potential pathfinder mineral, apatite displays several prerequisite characteristics: (1) a common association with a number of magmatic-hydrothermal deposit types; (2) a chemistry highly sensitive to physiochemical conditions which allows for distinct apatite chemical signatures to be assigned to a particular deposit type (e.g., Cao et al., 2012; Mao et al., 2016), or specific zones within a particular deposit type (Bouzari et al., 2016; Krneta et al., 2016); and (3) a resistate character which allows it to survive chemical and/or physical weathering.

Much of the field testing of the potential of apatite as a pathfinder has been performed in terranes dominated by residual glacial sediments, and has been primarily focused on apatite concentration as a proximity guide to mineralisation. This has, however, produced variable results with some surveys successfully delineating mineralisation (Hashmi et al., 2015) whereas others produced apatite anomalies unrelated to target mineralisation (Kelley et al., 2011), thus highlighting the importance of distinguishing mineralisation-related apatite and false positives stemming from the erosion of unrelated apatite sources (Mao et al., 2016). Such studies nevertheless provide insights into the potential use of apatite as a pathfinder within the Olympic Cu-Au Province given that large portions are overlain by either Permian sediments consisting of basal glacial diamictites, moraines and eskers (Alley, 1995), or Mesoproterozoic fluvial red beds of the Pandurra Formation (Preiss, 1993). Both units have the capacity to incorporate and disperse material sourced from underlying IOCG mineralisation. Forbes et al. (2015) tested this hypothesis and discovered substantial dispersion of mineralised material in the interpreted down-ice direction from the Prominent Hill IOCG deposit represented by the presence of mineralised clasts and high-(La + Ce), low-(Th + Y) monazite. Interestingly, the authors noted a common association between apatite and monazite within this mineralisation which when considering the very low Th concentrations, (a characteristic of monazite derived from alteration of apatite; Harlov et al., 2002a), may indicate formation akin to that of monazite described from Olympic Dam and IOCG systems elsewhere (Krneta et al., 2016; Bonyadi et al., 2011).

Our work on apatite from Olympic Dam (Krneta et al., 2016, 2017; Krneta, 2017) has shown that in large complex ore deposits, apatite is not defined by a single geochemical signature but rather by multiple signatures that can be related to distinct zones and assemblages. These signatures include magmatic apatite as well as a range of spatially and temporally distinct hydrothermal apatite generations. Application of apatite as a pathfinder in the Olympic Cu-Au Province requires not only a consideration of what each distinct geochemical signature represents but also tailoring of methodologies to the type (brownfields vs. greenfields) and scale (regional vs. local) of exploration being undertaken. The most effective use of MREE-enriched apatite as a pathfinder in the Olympic Cu-Au Province would be in delineating zones of significant Cu-Au mineralisation within widespread sub-economic or barren magnetite-pyrite mineralisation (e.g., Skirrow et al., 2007; Bastrakov et al., 2007).

Application of geochemical vectoring using detrital apatite in the Olympic Cu-Au Province is untested. The high costs associated with drilling through thick sequences of barren sediments overlying IOCG mineralisation would make regional-scale efforts to identify pathfinder minerals in cover unrealistic. Although its use as a pathfinder may be impractical as a standalone exploration technique, it may nevertheless represent an efficient method to vector towards zones of high-grade Cu mineralisation within known prospects. The recognition of apatite signatures that reflect hydrothermal conditions responsible for formation of high-grade sulphide ore within larger, barren, or weakly mineralised iron-oxide-dominant envelopes is highly significant. The impracticalities of performing time-consuming and costly microanalysis on pathfinder minerals during routine drill programmes could potentially be alleviated by fingerprinting the cathodoluminescence response of MREE-enriched apatite, a technique found to be useful in exploration

for porphyry Cu mineralisation (Bouzari et al., 2016).

6. Implications and future work

To date, discovery of most known IOCG deposits and prospects within the Olympic Cu-Au Province has been the result of persistent drilling guided primarily by geophysical methods. The discovery of MREE-enriched apatite and its spatial association with hematite-sericite alteration within these systems can provide important additional vectoring in some areas of the province, potentially including those where interaction with overlying sediments has created dispersion halos. Future research should validate this hypothesis via collection of apatite from the overlying sequences and attempting to quantify the extent of such dispersion.

Future investigation of MREE-enriched apatite should focus on the underlying mechanisms for the development of a positive Eu-anomaly. The measurement of Eu^{2+}/Eu^{3+} ratios in apatite by XANES would indicate the main mechanism at play in their formation (Eu-enriched fluid vs. high pH).

Supplementary data to this article can be found online at http://dx.doi.org/10.1016/j.gexplo.2017.08.004.

Acknowledgements

This work is supported by BHP Olympic Dam. We gratefully acknowledge microanalytical assistance from staff at Adelaide Microscopy, notably Ben Wade, and from Karsten Goemann (Central Science Laboratory, University of Tasmania). C.L.C. acknowledges support from the 'FOX' project (Trace Elements in Iron Oxides), supported by BHP Olympic Dam and the South Australian Mining and Petroleum Services Centre of Excellence. N.J.C. and K.E. acknowledge support from the ARC Research Hub for Australian Copper-Uranium. The authors extend thanks to Ian T. Graham for constructive review of the manuscript and to Editor-in-Chief Robert Ayuso for the helpful comments.

References

Alley, N.F., 1995. Late Palaeozoic. In: Drexel, J.F., Preiss, W.V. (Eds.), The Geology of South Australia. Vol. 2. The Phanerozoic, Geological Survey of South Australia, Bulletin. 54. pp. 63–92.

Averill, S.A., 2007. Recent advances in base metal indicator mineralogy. Explore 134, 2–6.

Averill, S.A., 2011. Viable indicators in surficial sediments for two major base metal deposit types: Ni-Cu-PGE and porphyry Cu. Geochemistry: Exploration, Environment, Analysis 11, 279–292.

Bastrakov, E.N., Skirrow, R.G., Davidson, G.J., 2007. Fluid evolution and origins of iron oxide Cu-Au prospects in the Olympic Dam District, Gawler Craton, South Australia. Econ. Geol. 102, 1415–1440.

Belousova, E.A., Walters, S., Griffin, W.L., O'Reilly, S.Y., 2001. Trace-element signatures of apatites in granitoids from the Mt Isa Inlier, northwestern Queensland. Austral. J. Earth Sci. 48, 603–619.

Belousova, E.A., Griffin, W.L., O'Reilly, S.Y., Fisher, N.I., 2002. Apatite as an indicator mineral for mineral exploration: trace-element compositions and their relationship to host rock type. J. Geochem. Explor. 76, 45–69.

Blissett, A.H., Creaser, R.A., Daly, S.J., Flint, R.B., Parker, A.J., 1993. Gawler range volcanics. In: Drexel, J.F., Preiss, W.V., Parker, A.J. (Eds.), The Geology of South Australia. Vol. 1. The Precambrian, Geological Survey of South Australia, pp. 107–131.

Bonyadi, Z., Davidson, G.J., Mehrabi, B., Meffre, S., Ghazban, F., 2011. Significance of apatite REE depletion and monazite inclusions in the brecciated Se–Chahun iron oxide–apatite deposit, Bafq district, Iran: insights from paragenesis and geochemistry. Chem. Geol. 281, 253–269.

Bouzari, F., Hart, J.R.H., Bissig, T., Barker, S., 2016. Hydrothermal alteration revealed by apatite luminescence and chemistry: a potential indicator mineral for exploring covered porphyry copper deposits. Econ. Geol. 111, 1397–1410.

Brugger, J., Lahaye, Y., Costa, S., Lambert, D., Bateman, R., 2000. Inhomogenous distribution of REE in scheelite and dynamics of Archean hydrothermal systems (Mt. Charlotte and Drysdale gold deposits, Western Australia). Contrib. Mineral. Petrol. 139, 251–264.

Brugger, J., Etschmann, B., Pownceby, M., Liu, W., Grundler, P., Brewe, D., 2008. Oxidation state of europium in scheelite: tracking fluid-rock interaction in gold deposits. Chem. Geol. 257, 26–33.

Cao, M., Li, G., Qin, K., Seitmuratova, E.Y., Liu, Y., 2012. Major and trace element characteristics of apatites in granitoids from Central Kazakhstan: implications for petrogenesis and mineralization. Resour. Geol. 62, 63–83.

Creaser, R.A., 1989. The Geology and Petrology of Middle Proterozoic Felsic Magmatism of the Stuart Shelf, South Australia. Unpublished Ph.D. thesis La Trobe University, Melbourne.

Cross, K.C., 1993. Acropolis and Wirrda Well. In: Drexel, J.F., Preiss, W.V., Parker, A.J. (Eds.), The Geology of South Australia. Vol. 1. The Precambrian, Geological Survey of South Australia, South Australia, pp. 138.

Ehrig, K., 2013. Geology of the Wirrda Well IOCG deposit. Powerpoint presentation, 10th Annual SA Exploration and Mining Conference, Adelaide. http://www.saexplorers.com.au.

Ehrig, K., Kamenetsky, V.S., McPhie, J., Apukhtina, O., Ciobanu, C.L., Cook, N.J., Kontonikas-Charos, A., Krneta, S., 2017. The IOCG-IOA Olympic Dam Cu-U-Au-Ag deposit and nearby prospects, South Australia. In: Extended abstract, Mineral Resources to Discover, 14th Biennial Meeting of SGA 2017, Quebec, Canada, in press.

Forbes, C., Giles, D., Freeman, H., Sawyer, M., Normington, V., 2015. Glacial dispersion of hydrothermal monazite in the Prominent Hill deposit: an exploration tool. J. Geochem. Explor. 156, 10–33.

Harlov, D.E., 2015. Apatite: A fingerprint for metasomatic processes. Elements 11, 171–176.

Harlov, D.E., Forster, H.J., 2004. Fluid-induced nucleation of (Y + REE)-phosphate minerals within apatite: nature and experiment. Part II. Fluorapatite. Am. Mineral. 88, 1209–1221.

Harlov, D.E., Andersson, U.B., Förster, H.-J., Nyström, J.O., Dulski, P., Broman, C., 2002a. Apatite–monazite relations in the Kiirunavaara magnetite–apatite ore, northern Sweden. Chem. Geol. 191, 47–72.

Harlov, D.E., Förster, H.-J., Nijland, T.G., 2002b. Fluid-induced nucleation of REE-phosphate minerals in apatite: nature and experiment. Part I. Chlorapatite. Am. Mineral. 87, 245–261.

Hashmi, S., Ward, B.C., Plouffe, A., Leybourne, M.I., Ferbey, T., 2015. Geochemical and mineralogical dispersal in till from the Mount Polley Cu-Au porphyry deposit, central British Columbia, Canada. Geochemistry: Exploration, Environment, Analysis 15, 234–249.

Haynes, D.W., Cross, K.C., Bills, R.T., Reed, M.H., 1995. Olympic Dam ore genesis: a fluid mixing model. Econ. Geol. 90, 281–307.

Hayward, N., Skirrow, R.G., 2010. Geodynamic setting and controls on iron oxide Cu-Au (± U) ore in the Gawler Craton, South Australia. In: Porter, T.M. (Ed.), Hydrothermal Iron Oxide Copper-Gold & Related Deposits: A Global Perspective. Vol. 3. PGC Publishing, Adelaide, pp. 1–27.

Huang, Q., Kamenetsky, V.S., Ehrig, K., McPhie, J., Kamenetsky, M., Cross, K., Meffre, S., Agangi, A., Chambefort, I., Direen, N.G., Maas, R., Apukhtina, O., 2016. Olivine-phyric basalt in the Mesoproterozoic Gawler silicic large igneous province, South Australia: examples at the Olympic Dam iron oxide Cu–U–Au–Ag deposit and other localities. Precambrian Res. 281, 185–199.

Hughes, J.M., Rakovan, J.F., 2015. Structurally robust, chemically diverse: apatite and apatite supergroup minerals. Elements 11, 165–170.

Hughes, J.M., Cameron, M., Crowley, K.D., 1991. Ordering of divalent cations in apatite structure: crystal 3 structure refinements of natural Mn- and Sr-bearing apatites. Am. Mineral. 76, 1857–1862.

Ismail, R., Ciobanu, C.L., Cook, N.J., Teale, G.S., Giles, D., Schmidt Mumm, A., Wade, B., 2014. Rare earths and other trace elements in minerals from skarn assemblages, Hillside iron oxide–copper–gold deposit, Yorke Peninsula, South Australia. Lithos 184–187, 456–477.

Jagodzinski, E.A., 2005. Compilation of SHRIMP U–Pb geochronological data, Olympic Domain, Gawler Craton, South Australia, 2001–2003. Canberra ACT: Geoscience Australia Record 2005 (20), 21.

Kelley, K.D., Eppinger, R.G., Lang, J., Smith, S.M., Fey, D.L., 2011. Porphyry Cu indicator minerals in till as an exploration tool: example from the giant Pebble porphyry Cu-Au-Mo deposit, Alaska, USA. Geochemistry: Exploration, Environment, Analysis 11, 321–334.

Kontonikas-Charos, A., Ciobanu, C.L., Cook, N.J., 2014. Albitization and redistribution of REE and Y in IOCG systems: Insights from Moonta-Wallaroo, Yorke Peninsula, South Australia. Lithos 208, 178–201.

Kontonikas-Charos, A., Ciobanu, C.L., Cook, N.J., Ehrig, K., Kamenetsky, V.S., 2015. Deuteric coarsening and albitization in Hiltaba granites from the Olympic Dam IOCG deposit, South Australia. In: Proceedings, Mineral Resources in a Sustainable World, 13th Biennial SGA Meeting, Nancy, France. vol. 3.. pp. 1099–1102.

Kontonikas-Charos, A., Ciobanu, C.L., Cook, N.J., Ehrig, K., Krneta, S., Kamenetsky, V.S., 2017a. Feldspar evolution in the Roxby Downs Granite, host to Fe-oxide Cu-Au-(U) mineralisation at Olympic Dam, South Australia. Ore Geol. Rev. 80, 838–859.

Kontonikas-Charos, A., Ciobanu, C.L., Cook, N.J., Ehrig, K., Ismail, R., Krneta, S., Basak, A., 2017b. Feldspar mineralogy and rare earth element (re)mobilization in iron-oxide copper gold systems from South Australia: a nanoscale study. Mineral. Mag.. http://dx.doi.org/10.1180/minmag.2017.081.040. in press.

Kontonikas-Charos, A., Ciobanu, C.L., Cook, N.J., Ehrig, K., Krneta, S., Kamenetsky, V.S., 2017c. Rare earth element geochemistry of feldspars: examples from Fe-oxide Cu-Au systems in the Olympic Cu-Au Province, South Australia. Mineral. Petrol (in revision).

Krneta, S., Ciobanu, C.L., Cook, N.J., Ehrig, K., Kontonikas-Charos, A., 2016. Apatite at Olympic Dam, South Australia: a petrogenetic tool. Lithos 262, 470–485.

Krneta, S., Ciobanu, C.L., Cook, N.J., Ehrig, K., Kontonikas-Charos, A., 2017. Rare earth element behaviour in apatite from the Olympic Dam Cu-U-Au-Ag deposit, South Australia. Minerals 7 (8), 135. http://dx.doi.org/10.3390/min7080135.

Krneta, S., 2017. The evolution of apatite in Iron-Oxide-Copper-Gold mineralization of the Olympic Cu-Au Province: unraveling magmatic and hydrothermal histories through changes in morphology and trace element chemistry. Unpublished PhD

thesis The University of Adelaide.
Majka, J., Harlov, D.E., Jonsson, E., Högdahl, K., Persson-Nilsson, K., 2016. Fluorapatite-monazite-allanite relations in the Grängesberg apatite-iron oxide ore district, Bergslagen, Sweden. Am. Mineral. 101, 1769–1783.
Mao, M., Rukhlov, A.S., Rowins, S.M., Spence, J., Coogan, L.A., 2016. Apatite trace element compositions: a robust new tool for mineral exploration. Econ. Geol. 111, 1187–1222.
McDonough, W.F., Sun, S-S., 1995. The composition of the Earth. Chem. Geol. 120, 223–253.
Migdisov, A.A., Williams-Jones, A.E., Brugger, J., Caporuscio, F.A., 2016. Hydrothermal transport, deposition, and fractionation of the REE: experimental data and thermodynamic calculations. Chem. Geol. 439, 13–42.
Oreskes, M., Einaudi, M.T., 1992. Origin of hydrothermal fluids at Olympic Dam: preliminary results from fluid inclusions and stable isotopes. Econ. Geol. 87, 64–90.
Pan, Y., Fleet, M.E., 2002. Compositions of the apatite-group minerals: substitution mechanisms and controlling factors. Rev. Mineral. Geochem. 48, 13–49.
Pasero, M., Kampf, A., Ferraris, C., Pekov, I.V., Rakovan, J., White, T., 2010. Nomenclature of the apatite supergroup minerals. Eur. J. Mineral. 22, 163–179.
Paterson, A.J., 1986. The Acropolis prospect. In: Parker, A.J., Horn, C.M., Stevens, B.P.J., Paterson, H.L. (Eds.), Geological Excursions of the Adelaide Geosyncline. Gawler Craton and Broken Hill Regions. Geological Society of Australia (S.A. Division), pp. 17–27.
Piccoli, M.P., Candela, P.A., 2002. Apatite in igneous systems. Rev. Mineral. Geochem. 48, 255–292.
Preiss, W.V., 1993. Neoproterozoic. In: Drexel, J.F., Preiss, W.V., Parker, A.J. (Eds.), The Geology of South Australia, Vol. 1, The Precambrian. Geological Survey of South Australia Bulletin. Vol. 54. pp. 170–203.
Putnis, A., 2002. Mineral replacement reactions: from macroscopic observations to microscopic mechanisms. Mineral. Mag. 66, 689–708.
Rakovan, J., Newville, M., Sutton, S., 2001. Evidence for heterovalent europium in zoned Llallagua apatite using wavelength dispersive XANES. Am. Mineral. 86, 697–700.
Reeve, J.S., Cross, K.C., Smith, R.N., Oreskes, N., 1990. Olympic Dam copper-uranium-gold-silver deposit. In: Hughes, F.E. (Ed.), Geology of the Mineral Deposits of Australia and Papua New Guinea. vol. 2. The AusIMM, Melbourne, pp. 1009–1035.
Rønsbo, J.G., 1989. Coupled substitutions involving REE's and Na and Si in apatites in alkaline rocks from Ilimaussaq, South Greenland, and the petrological implications. Am. Mineral. 74, 896–901.
Skirrow, R.G., Bastrakov, E.N., Barovich, K., Fraser, G.L., Creaser, R., Fanning, M.C., Raymond, O.L., Davidson, G.J., 2007. Timing of iron oxide Cu-Au-(U) hydrothermal activity and Nd isotope constraints on metal sources in the Gawler craton, South Australia. Econ. Geol. 102, 1441–1470.
Vella, L., 1997. Interpretation and modelling, based on petrophysical measurements, of the Wirrda Well potential field anomaly, South Australia. Explor. Geophys. 28, 299–306.
Vella, L., Cawood, M., 2006. Carrapateena: Discovery of an Olympic Dam — Style Deposit. Preview, Issue 122 (June 2006). CSIRO Publishingpp. 26–30.

CHAPTER 5

CRYSTAL STRUCTURAL MODIFICATION AND MINERAL INCLUSIONS IN APATITE FROM OLYMPIC DAM, SOUTH AUSTRALIA

Sasha Krneta[1], Cristiana L. Ciobanu[2], Kornelis van der Kerke[2], Nigel J. Cook[2], Kathy Ehrig[3], Animesh Basak[4]

[1]*School of Physical Sciences, The University of Adelaide, Adelaide, S.A., 5005, Australia*

[2]*School of Chemical Engineering, The University of Adelaide, Adelaide, S.A., 5005, Australia*

[3]*BHP Olympic Dam, Adelaide, SA 5000, Australia*

[4]*Adelaide Microscopy, The University of Adelaide, Adelaide, S.A., 5005, Australia*

Manuscript to be submitted in revised and abridged form

Statement of Authorship

Title of Paper	Crystal structural modification and mineral inclusions in apatite from Olympic Dam, South Australia
Publication Status	☐ Published ☐ Accepted for Publication ☐ Submitted for Publication ☑ Unpublished and Unsubmitted w ork w ritten in manuscript style
Publication Details	Krneta, S., Ciobanu, C.L., van der Kerke, K., Cook, N.J., Ehrig, K. and Basak, A.,. Crystal structural modification and mineral inclusions in apatite from Olympic Dam, South Australia. (to be submitted in revised and abridged form)

Principal Author

Name of Principal Author (Candidate)	Sasha Krneta
Contribution to the Paper	Collected sample material, devised a plan for and performed analytical work, interpreted data , co-wrote manuscript
Overall percentage (%)	50
Certification:	This paper reports on original research I conducted during the period of my Higher Degree by Research candidature and is not subject to any obligations or contractual agreements with a third party that would constrain its inclusion in this thesis. I am the primary author of this paper.
Signature	Date 13/9/17

Co-Author Contributions

By signing the Statement of Authorship, each author certifies that:

i. the candidate's stated contribution to the publication is accurate (as detailed above);

ii. permission is granted for the candidate in include the publication in the thesis; and

iii. the sum of all co-author contributions is equal to 100% less the candidate's stated contribution.

Name of Co-Author	Cristiana Ciobanu
Contribution to the Paper	Supervised development of work, assisted in defining direction of research, provided assistance in the collection of analytical data, assisted with data interpretation and helped with manuscript preparation.
Overall percentage (%)	30
Signature	Date 17 Sept 2012

Name of Co-Author	Kornelis van der Kerke
Contribution to the Paper	, Provided assistance in the collection of analytical data and assisted with data interpretation.
Overall percentage (%)	10
Signature	Date 13/9/17

Name of Co-Author	Nigel Cook		
Contribution to the Paper	Assisted in defining the direction of research, assisted with data interpretation and evaluated manuscript.		
Overall percentage (%)	5		
Signature		Date	13/9/17

Name of Co-Author	Kathy Ehrig		
Contribution to the Paper	Assisted in defining the direction of research, assisted with data interpretation and evaluated manuscript.		
Overall percentage (%)	3		
Signature		Date	13/09/17

Name of Co-Author	Animesh Basak		
Contribution to the Paper	Assisted with collection of analytical data.		
Overall percentage (%)	2		
Signature		Date	13/9/2017

CHAPTER 5: CRYSTAL STRUCTURAL MODIFICATION AND MINERAL INCLUSIONS IN APATITE FROM OLYMPIC DAM, SOUTH AUSTRALIA.

Abstract

Apatite, $Ca_5(PO_4)_3(F,Cl,OH)$, incorporates a wide range of trace elements (e.g., REE, Th) during processes leading to formation of ore deposits. This study is aimed at understanding how apatite from the giant iron oxide-copper-gold (IOCG) deposit at Olympic Dam (South Australia) tracks deposit evolution at the nanoscale. Apatite of different origin, both magmatic and early hydrothermal, was selected for study. Focused Ion Beam-Scanning Electron Microscopy was used to prepare samples for Transmission Electron Microscopy. Results show changes in apatite symmetry due to nanometre-scale inclusions. Fluorite (CaF_2) is associated with pyrrhotite ($Fe_{1-x}S$; x=0-0.125), and monazite [$(Ce,La,Nd,Th)PO_4$] + thorite ($ThSiO_4$) in magmatic and hydrothermal apatite, respectively. The study demonstrates that the transition from magmatic to hydrothermal regimes is paramount for setting conditions of metal deposition in giant IOCG deposits.

Keywords: Olympic Dam; transmission electron microscopy; apatite; pyrrhotite; fluorite; monazite; thorite; magmatic; hydrothermal

5.1. Introduction

Apatite, with the general formula $Ca_5(PO_4)_3(F,Cl,OH)$ (Pasero et al., 2010) is a minor constituent in magmatic rocks of various types and commonly hosts the majority of the P and

often most of the rare earth element (REE) budget (e.g., Piccoli and Candela, 2002, Hughes, 2015). The apatite structure can accommodate roughly half the elements in the periodic table (Hughes and Rakovan, 2015), making it a powerful geochemical and petrologic tool for unravelling complex evolution trends in magmatic-hydrothermal systems (e.g., Krause et al., 2013, Harlov, 2015, Bouzari et al., 2016). Apatite can also host inclusions of various types (e.g., Gottesman and Wirth, 1997; Harlov, 2015, Xing and Wang et al., 2017). These inclusions can be either the result of co-crystallisation together with apatite, or the product of hydrothermal alteration of the apatite. Understanding the speciation of these inclusions and their relationship with the host apatite is of critical importance for genetic models of rock and ore-forming processes.

For example, pyrrhotite inclusions were found in apatite with dark cores from granites in the Erzgebirge orefield, Germany (Gottesman and Wirth, 1997). These authors undertook a nanoscale study and showed that such dark cores contain an abundance of pyrrhotite inclusions which are coherently oriented within the apatite host. Such orientation could only result from a primary growth process, inferring that both apatite and pyrrhotite have co-crystallised from the same granitic magma. However, magmatic pyrrhotite is more commonly found in mafic and ultramafic melts such as those of the Hongge layered intrusion, SW China, where apatite containing pyrrhotite inclusions almost identical to those described in the Erzgebirge study have also been noted (Xing and Wang et al., 2017). The presence of pyrrhotite within the dark cores of apatites was cited by Gottesman and Wirth, (1997) as strong evidence for the incorporation of foreign material originating from older and/or marginal parts of the intrusions or from the country rocks.

The presence of trace elements or mineral inclusions can also lead to changes in crystal symmetry of the host apatite (Hughes and Rakovan, 2015). An interesting topic is the

presence of monazite in association with one of the $ThSiO_4$ polymorphs: thorite (tetragonal); or huttonite (monoclinic). Identification requires crystal structural investigation (Table 5.1). Recent experimental studies have shown that huttonite can crystallise within apatite, alongside monazite, during alteration by Th-enriched fluids. In contrast to the aforementioned inclusions hosted in magmatic apatite, inclusions of $ThSiO_4$, if formed as a result of overprinting, can be considered products of secondary replacement (Harlov et al., 2007). Determining the character of such inclusions could potentially offer significant insights into the trace element behaviour during the formation of Olympic Dam.

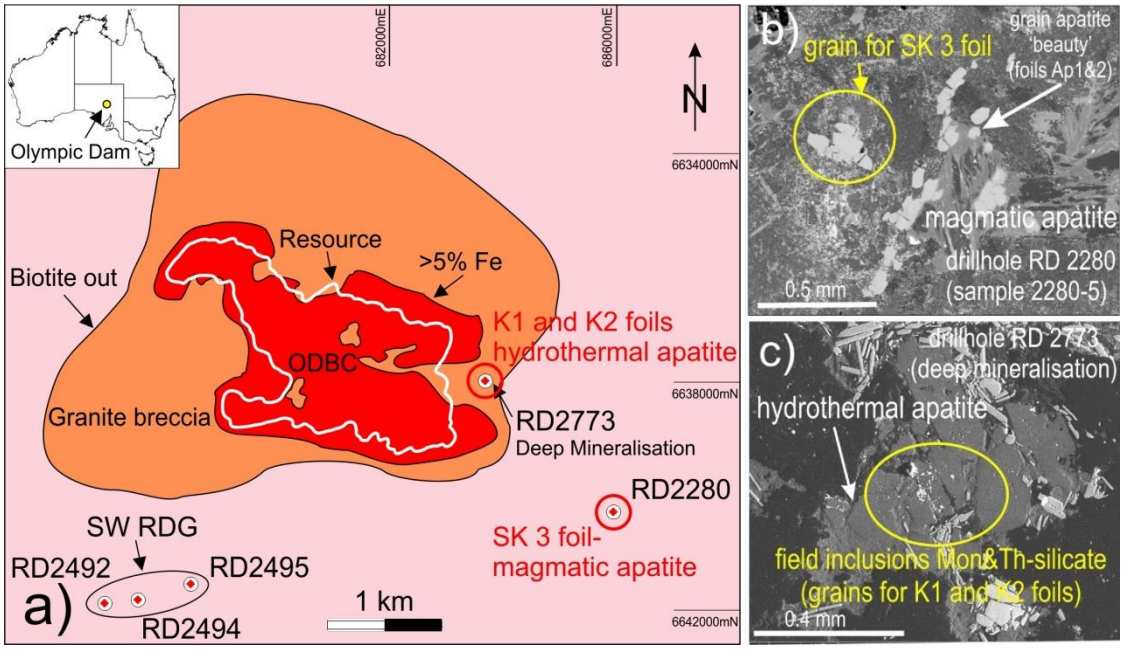

Fig. 5.1: Sample location (a) and Back Scatter Electron (BSE) images showing petrography (b, c) of samples used for this study. In (a), the geology of the Olympic Dam area (from Krneta et al., 2016, modified after Ehrig et al., 2012). Pink: Roxby Downs Granite. Inset in (a) shows location of OD in South Australia.

Apatite from the Olympic Dam (OD) iron oxide copper gold (IOCG) deposit (South Australia; Fig. 5.1a) is a petrogenetic tool for understanding trace element changes during the transition from magmatic to hydrothermal stages (Krneta et al., 2016). Olympic Dam is a

supergiant Cu-U-Au-Ag deposit (e.g., Ehrig et al., 2012) located 550 km NNW of Adelaide, and is not only one of the world's largest metalliferous deposits, but also the largest single uranium deposit on Earth. The OD orebody is hosted by the Olympic Dam Breccia Complex (ODBC; Fig. 5.1a), derived by Fe-metasomatism of the Roxby Downs Granite (RDG; Reeve et al., 1990) emplaced at ~1.6 Ga (Johnson and Cross, 1995). RDG-hosted apatite from OD has been found to host a variety of mineral inclusions (Fig. 5.1b, c; Krneta et al., 2015; 2016). Such inclusions, ranging in size from micron- to nanometre-scale, were reported in magmatic, i.e., pyrrhotite and fluorite, and hydrothermal apatite, i.e., monazite and a Th-silicate, $ThSiO_4$ (Fig. 5.1b, c).

Magmatic apatite from drillhole RD2880 in the SE part of the deposit (Fig. 5.1a) is hosted within the RDG, rich in mafic enclaves. Their origin is difficult to interpret since they are intensively altered. Calculation of halogen partitioning between melts and fluids using data from apatite at OD has shown that the apatite from this location differs significantly from apatite from other locations at OD, i.e., the SW location (Fig. 5.1a; Krneta et al., 2016). Such differences can be used to interpret magma mixing during emplacement, as well as the potential for metal budget evaluation within the hydrothermal fluids released towards the end of the magma cooling.

Hydrothermal apatite associated with early, magnetite-dominant assemblages is found within the mineralised satellite termed 'Deep Mineralization' (Fig. 5.1a), where Cu-ores are found at levels deeper than 1,500 m (Cu-mineralization is still open at 2,200 m) in drillhole RD2773 on the same SE side of the deposit (Apukhtina et al., 2017). Samples from deep, altered granitoids and breccias at this location show abundant, coarse (up to cm-size) apatite, in which trails of various mineral inclusions are associated with domains of variable composition in host apatite (Krneta et al., 2016). The present study uses samples from the two

locations shown on Fig. 5.1 with the aim of understanding changes in magmatic and hydrothermal apatite with respect to: (i) apatite crystal structural modifications due to the presence of mineral inclusions and (ii) speciation and associations of these inclusions if studied down to the nanoscale. Results are discussed with respect to the magmatic to hydrothermal transition regimes at OD, and the relevance of nanoscale studies for constraining trace elements distribution in IOCG systems.

5.2. Methodology

All equipment used is hosted at Adelaide Microscopy.

5.2.1 Sample preparation

Considering the high variability in textures, composition and mineral inclusions found in the OD apatite (Krneta et al., 2015; 2016), sample preparation for Transmission Electron Microscopy (TEM) study was performed using *in-situ* extraction of slices from polished blocks. The FEI-Helios nanoLab Dual Focused Ion Beam and Scanning Electron Microscope (FIB-SEM) instrument under the Australian microscopy and microanalysis research facility (AMMRF) flagship was used. Procedures outlined by Ciobanu et al., (2011) were followed in extraction and thinning (to <100 nm) of TEM foils by ion beam (Ga^{+}) milling. The TEM foils were attached to Cu grids. Three foils were prepared from two polished blocks; details of the procedures are shown in Fig. 5.2.

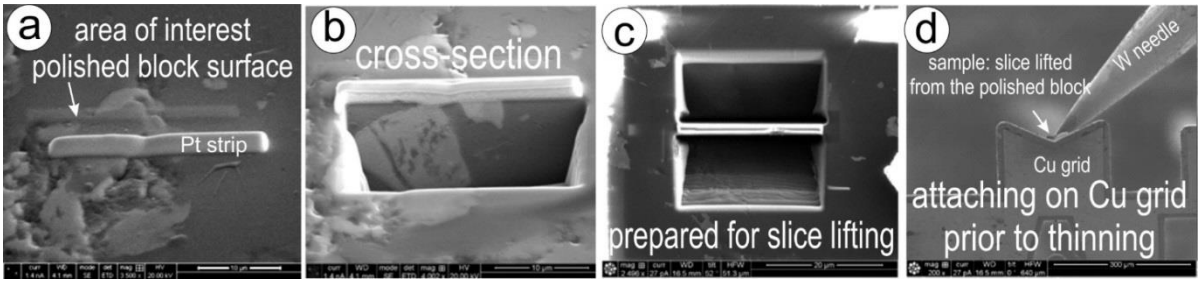

Fig. 5.2: Secondary electron (SE) images showing the sequence of FIB-SEM procedures (as

marked) for obtaining TEM foils. The example shown is for hydrothermal apatite – foil K1 (see below).

5.2.2 Data acquisition and processing

A Philips 200CM TEM equipped with a Gatan digital camera was used at 200 kV for obtaining electron diffractions (ED) and imaging including high-resolution HR-TEM in bright field (BF) mode. The TEM has a double-tilt holder with the "a" and "b" having tilts up to 60º and 30º, respectively. A range of electron diffractions representing different zone axes for each mineral in a given foil were acquired by specimen tilting. Chemical composition assisting with identification of phases present as nanometre-scale inclusions and their host minerals was measured from energy-dispersive X-Ray spectra (EDS) acquired on an Oxford Instruments X-Max 65T SDD detector, and processed in Aztec Energy TEM SP. DigitalMicrograph™ was used for diffraction measurements and image analysis.

5.2.3 Experimental characterisation and data analysis

Characterisation and indexation of relevant electron diffraction patterns was undertaken using WinWulff™ software and crystallographic information files (cif) obtained from the American Mineralogist Crystal Structure Database (Rruff.geo.arizona.edu; Downs and Hall-Wallace, 2003). Space group conversions were made using International Tables for Crystallography, volume A (Hahn, 2005). Table 5.1 gives crystal structural details for each of the minerals characterised and indexed. WinWulff™ was also used to calculate angles between *hlk* vectors, where *h*, *k* and *l* are each expressed as integers and denote the family of planes which are orthogonal to $h\mathbf{b}_1+k\mathbf{b}_2+l\mathbf{b}_3$.

5.3. Background on crystal structures

Chemistry and crystal structures of apatite and associated minerals studied here are shown in Table 5.1. A brief introduction to the crystal structures, with emphasis on apatite, is given below.

5.3.1 Apatite

The crystal structure of apatite $Ca_5(PO_4)_3(F,Cl,OH)$, consists of three types of polyhedra for Ca and P cations (Fig. 5.3; Hughes, 2015; Luo et al., 2011). There are two sites for Ca: (i) a nine-fold coordinated tri-capped trigonal prism: Me_1O_9 (Mercier et al., 2005); and (ii) a seven-fold coordinated distorted pentagonal bipyramid (Dolivo-Dobrovolsky, 2006): Me_2O_6X, where X is host to one of the anions F, Cl, OH; whereas P is placed in the rigid PO_4 tetrahedron. The X anions are placed along the edges of the unit cell. There are three varieties of apatite depending upon the dominance of the X anion: fluorapatite (F-dominant); chlorapatite (Cl-dominant) and hydroxylapatite (OH-dominant; e.g., Pasero et al., 2010). Apatite chemistry in F-Cl-OH^- space is very complex with all three components commonly present in measurable amounts in natural apatite. However, fluorapatite is by far the most common species (Webster and Piccoli, 2015), as is the case here (Krneta et al., 2016).

Table 5.1: Chemistry and crystal structures of apatite and associated minerals as discussed.

Mineral	Chemical formula	Space group	No.	a (Å)	b (Å)	c (Å)	α (°)	β (°)	γ (°)
Apatite	$Ca_5(PO_4)_3(OH,F,Cl)$	(1) *P*11 $2_1/b$	13	9.4877	18.9628	6.8224	90		119.9773
		(2) *P* $6_3/m$	176	9.3973		6.8782	90		120
		(*) *P*6/*m*	175						
Monazite	$(Ce,La,Nd,Th)PO_4$	(3) *P*1 $2_1/n$1	14	6.792	7.0203	6.4674	90	103.38	90
		(*) *P*2	3						
Thorite	$ThSiO_4$	(4) *I* $4_1/amd$	141	7.142		6.327	90		
		(*) *I* $4_2/ncm$	138						
Huttonite	$ThSiO_4$	(5) *P*1 $2_1/n$1	14	6.784	6.974	6.5	90	104.92	90
Fluorite	CaF_2	(6) *Fm*3*m*	225	5.42695			90		
Pyrrhotite (6C Po)	$Fe_{1-x}S$; x=0-0.125 ($Fe_{11}S_{12}$)	(7) **Fd*	227-228	6.8973	11.954	34.521	90	90.003	90

(1) Monoclinic apatite: Hughes et al. (1990); (2) Hexagonal Apatite: Hughes et al. (1989); (3) Monazite: Ni et al. (1995); (4) Thorite: Fuchs and Gebert (1958); (5) Huttonite: Taylor and Ewing (1978); (6) Fluorite: Wyckoff (1963); (7) Pyrrhotite 6C: Villiers and Liles (2010); (*) – space groups used for indexing in this study.

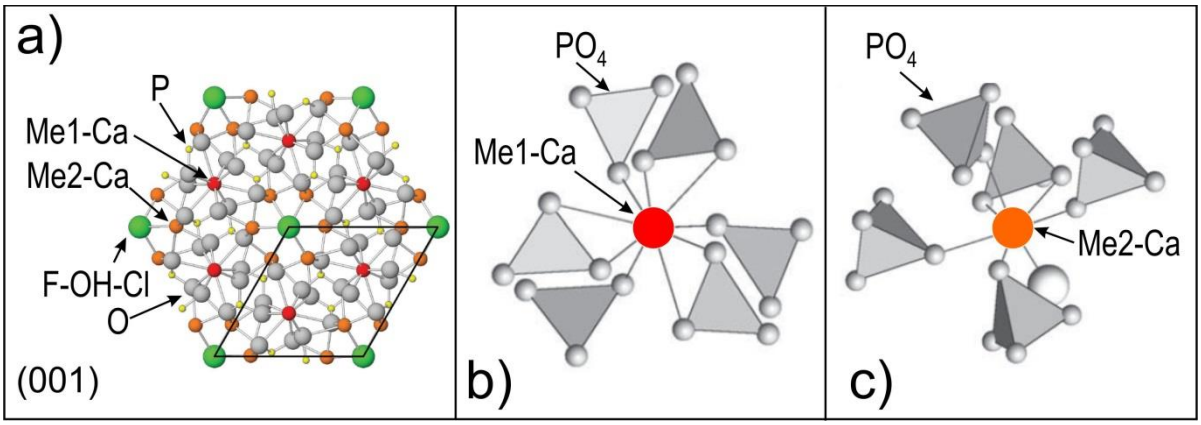

Fig. 5.3: Crystal structure of apatite. (a) Atomic arrangement projected down to (001) (from Hughes, 2015). (b, c) Environment of Me1 and Me2 sites, respectively, (from Luo et al., 2011). The different grey shadings of the PO_4 tetrahedra show their orientation relative to projection planes.

Apatite has a hexagonal symmetry in space group $P6_3/m$ but monoclinic varieties are also known and may be indicative of low temperature formation (Hughes, 2015; Table 5.1). The two Ca and single P cations in apatite can be substituted by a wide variety of other elements (including REE, Y and Th) leading to the apatite supergroup (Pasero et al., 2010). Such substitutions affect the apatite crystal structure significantly, leading to the wide variety of structural variations observed (e.g., Demartin et al., 2010, Yi et al., 2013, Gianfagna and Mazziotti, 2014). Hughes and Rakovan (2002) distinguish fluorapatite, chlorapatite and hydroxylapatite as " apatite *sensu stricto*" and define the structure of the other minerals within the supergroup as sub-symmetries of the apatite *sensu stricto* structure.

Incorporation of Th in apatite crystal structure has been studied using single crystal X-ray diffraction and X-ray absorption spectroscopy (Luo et al., 2011) showing this element substituted for the Me2 site (Fig. 5.3c). This replacement, studied for natural and synthetic samples with ~2,000 ppm and ~20,0000 ppm Th, respectively, was refined using extended X-ray absorption fine-structure spectroscopy. The results show that Th incorporation in the Me2 site leads to a ~0.05-0.08 Å decrease in the Me-O bond distances and crystal distortions that are not measurable by the single-crystal technique.

5.3.2 Other phases accompanying apatite

Among the most common REE-phosphates, generically $REE(PO_4)$ present as an accessory in rocks of various types is monazite $[(Ce,La,Nd,Th)PO_4]$. The mineral is monoclinic and has a dimorph, xenotime, with a tetragonal crystal structure (Table 5.1; Ni et al. 1995). Studies of crystal chemistry of the two phases have shown that the structures consist of chains of TO_4 (T=P) with a REE-oxygen polyhedra that preferentially accommodates light (La-Gd) and heavy (Tb-Lu) REE in monazite and xenotime, respectively (Ni et al., 1995).

Replacement between apatite and monazite is known in a variety of geological environments (e.g., Harlov, 2015). Often such replacement results in nucleation of a Th-silicate, $ThSiO_4$. The latter is known as two dimorphs: tetragonal thorite and monoclinic huttonite (Table 5.1). Both apatite and monazite can accommodate a few and several 10's of wt. % Th in the crystal structure, respectively. Formation of discrete Th-silicate inclusions may be often observed in rocks of various origin. Interpretations of their formation rely on two main mechanisms: (i) primary, as exsolutions from higher temperature solid solutions and (ii) secondary, as host phosphate mineral replacement takes place, e.g., monazite replacing apatite (Harlov et al., 2007).

Fluorite (CaF_2), a typical ionic structure, has a simple cubic symmetry (Table 5.1; Wyckoff, 1963) characterised by cubic close packed atoms of Ca, where Ca atoms are found on all corners and at the centre of each face of the unit cell cube whereas F is found within tetrahedral coordination (surrounded by 4 Ca atoms).

Pyrrhotite group minerals are non-stoichiometric phases with general formula $Fe_{1-x}S$ (x = 0-0.125. Non-stoichiometry relates to Fe-vacancies leading to superstructures of various types, causing drastic changes in magnetic and surface properties (e.g., Becker et al., 2010). Pyrrhotite structures derive from the hexagonal close-packed NiAs structure. Troilite (FeS, 2C-pyrrhotite) is rare in terrestrial rocks but common in meteorites since sub-solidus re-equilibration is observed <300 °C. At such conditions, 4C-pyrrhotite (Fe_7S_8) and NC-pyrrhotite (between FeS and Fe_7S_8) dominate. Prefixes indicate the superstructure lattice repeats along the axis of layer stacking relative to c-axis periodicity in the NiAs substructure; 4C- and NC-pyrrhotite correspond to 'monoclinic' and 'hexagonal' pyrrhotite, respectively. NC-type pyrrhotites are a structurally-diverse group with widely variable N*c* values, including both periodic (Fe_9S_{10} [5C], $Fe_{10}S_{11}$ [5.5C] and $Fe_{11}S_{12}$ [6C]) and non-periodic NC-pyrrhotites.

Superstructures can be easily recognised from electron diffractions from satellite, weaker reflections between two main (Bragg) reflections (Amelinckx et al., 1989). The 6C variety (Villiers and Liles, 2010) is listed in Table 5.1, since this was identified in the present study.

5.4. Results

The three foils obtained from the OD samples and studied here are: (i) one from the magmatic apatite in RD2280, i.e., SK3 and, (ii) two from the hydrothermal apatite in RD2773, i.e., K1 and K2. The foils were imaged and briefly characterised on the FIB platform prior to TEM study. Results are shown in Figures 5.4-5.12.

5.4.1 Magmatic apatite

Foil SK3 was obtained from one of the largest apatite (several hundred µm), typical of the contact between granite and mafic enclaves, showing parallel, dense trails of inclusions (Fig. 5.4a). Foil imaging shows this apatite contains nanometre-scale inclusions with two phases (Fig. 5.4b) which were identified by EDS-TEM spectra as pyrrhotite and fluorite (Fig. 5.5c, d). TEM imaging shows that the inclusions occur as parallel rods (Fig. 5.6a) and pyrrhotite is coherently intergrown with host apatite along the *c** axis as seen from both (Selected Area of Electron Diffraction, SAED, in Fig. 5.6b).

No pores or crystal defects are present in the apatite but indexing of SAEDs from apatite was possible using space group P6/m instead of P63/m (ideal hexagonal symmetry for apatite; Hughes et al., 1989; Table 5.1) due to the presence of reflections violating the 3-axis symmetry law (see below). Pyrrhotite shows 3 x fold satellite reflections (arrowed on Fig. 5.6b) along the *c** axis typical of 6C variety.

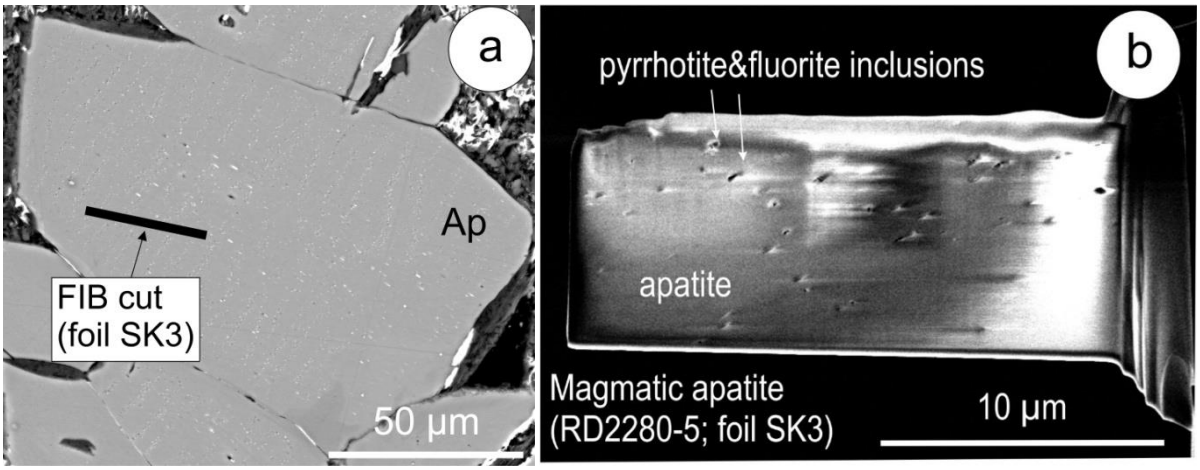

Fig. 5.4: Secondary electron (SE) images showing magmatic apatite with sub-micron inclusions of pyrrhotite and fluorite (a) grain on the surface of the polished block (b) TEM foil.

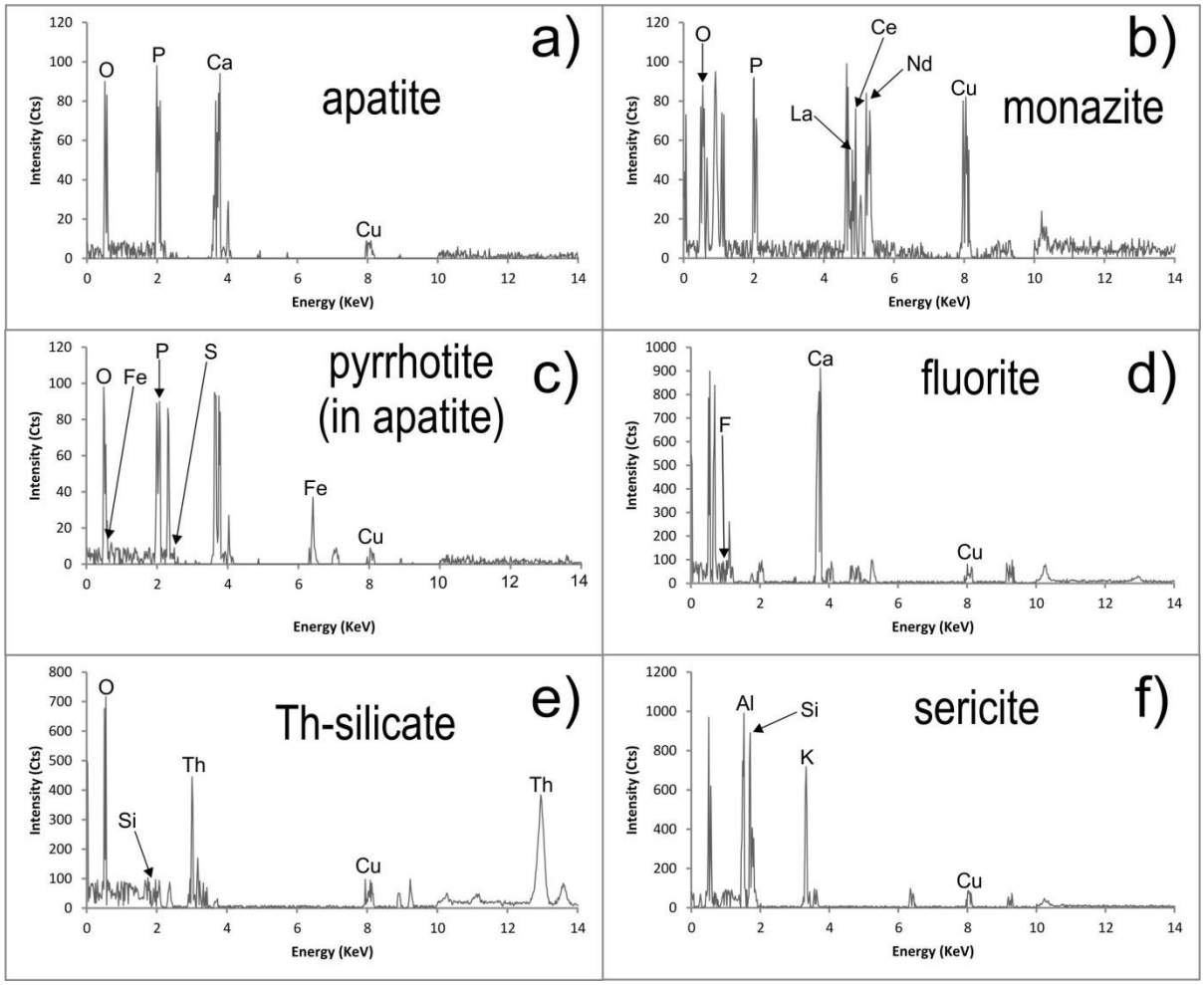

Fig. 5.5: Selected EDS-TEM spectra showing the composition of phases (as marked) in the three foils. The smallest inclusions Cu peak is due to the interference from the grid (copper). The smallest pyrrhotite inclusions (<50 nm) in c) are difficult to analyse even when decreasing the beam size to ~40 nm.

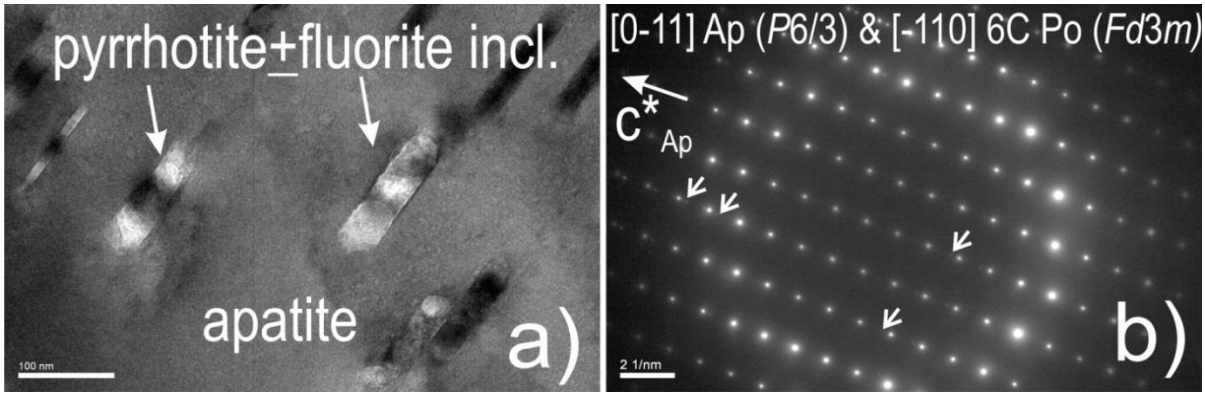

Fig. 5.6: (a) Bright-field TEM image showing nm-scale inclusions of apatite (+ fluorite). (b) Selected Area of Electron Diffraction (SAED) showing coherent intergrowths between host apatite (Ap) and pyrrhotite inclusion (Po) along the c* axis. Satellite reflections due to the long range superstructuring in Po (Villiers and Liles, 2010) are marked by arrows.

5.4.2 Hydrothermal apatite

Foils K1 and K2 were obtained from two different grains of large (mm-size) apatite, typical of the Deep mineralization (e.g., Fig. 5.1c). Such grains also feature trails of inclusions but these are more erratically distributed than in the case of magmatic apatite (Krneta et al., 2016). The inclusions are dominantly monazite + $ThSiO_4$ but include other phases such as hematite and a variety of sulphides, all of which vary greatly with regards to grain size (from nanometre-scale up to several μm in size; Krneta et al., 2016). Most typical are the associations between monazite and the Th-silicate (Fig. 5.7a, b), which is also the association that was targeted by the present study. TEM imaging shows these are present in both foils, albeit in close association with one another (Fig. 5.7c). Foil K1 is cut across a boundary between apatite and

a larger monazite that contains abundant inclusions of fluorite and also sericite; smaller grains of quartz (SiO_2) were also found within apatite from foil K2. EDS-TEM spectra obtained for all these minerals (except quartz) are shown in Fig. 5.4.

Relevant SAEDs down to 1st and 2nd order zone axes obtained from apatite in both foils show this has a lower symmetry group (*P*6/*m* instead of *P*6$_3$/*m*; Fig. 5.7). Measurements of distances ~8.1Å corresponding to *c* axis in apatite (Table 5.1; SAEDs in Fig. 5.8a, b) indicate the presence (00*l*) reflections where *l*=*n* rather than 2*n* violates symmetry in space group P6$_3$/m (00*l*: *l*=2*n*).

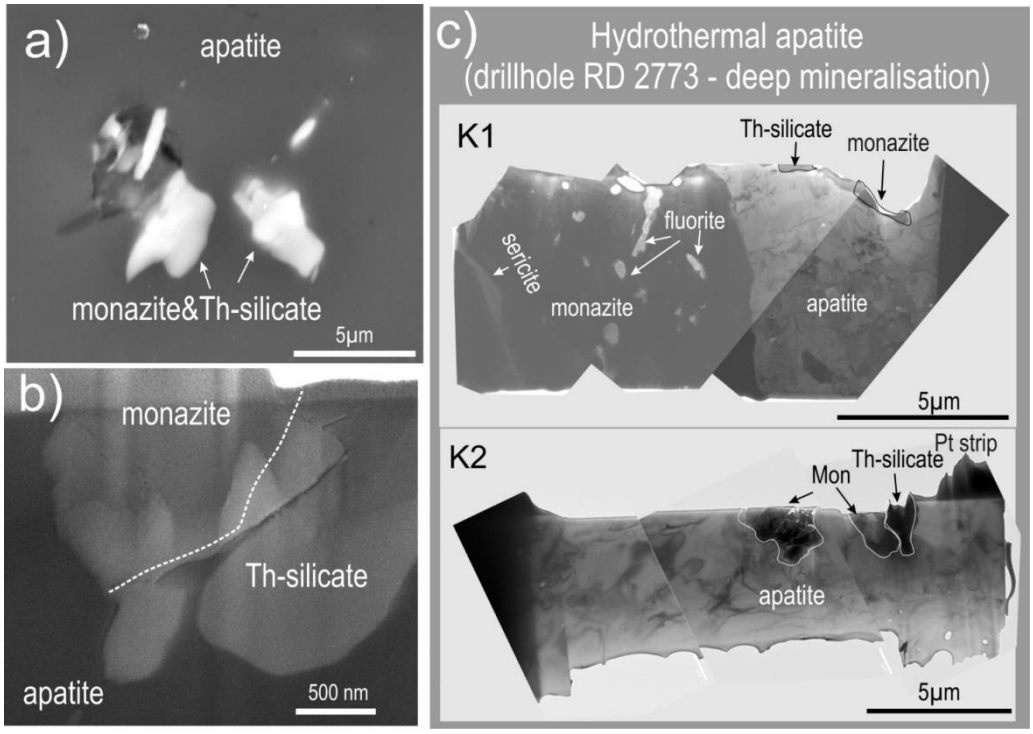

Fig. 5.7: (a) SE image showing the monazite-Th-silicate inclusions that were sliced for TEM sample. (b) SE image showing a detail of the inclusion after the foil was prepared. (c) Low-resolution TEM images showing the two foils obtained for hydrothermal apatite. Identification of inclusion composition was obtained using EDS-TEM spectra in Fig. 5.7.

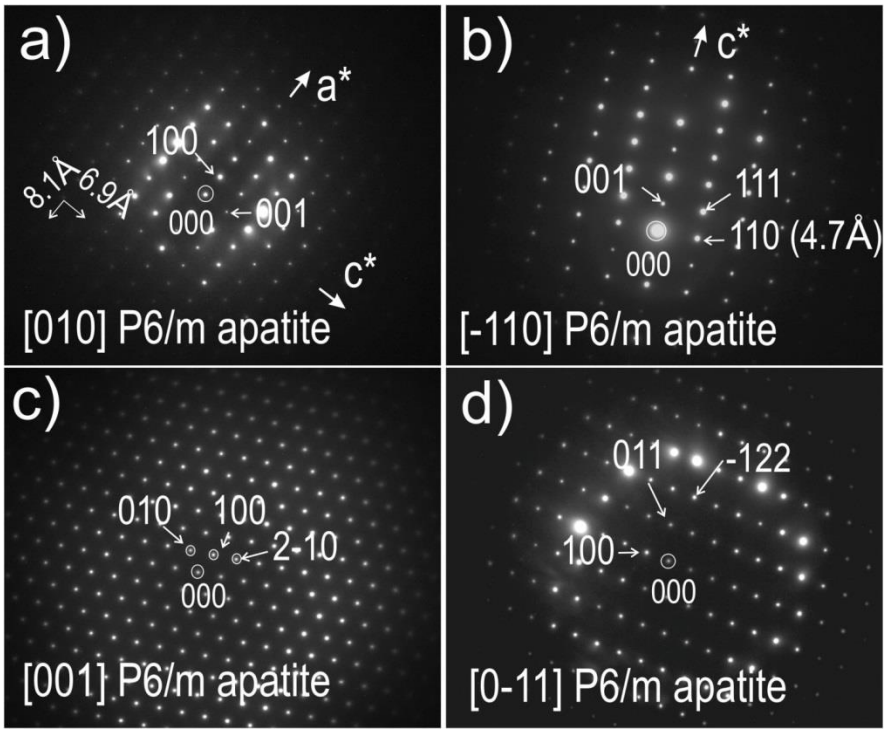

Fig. 5.8: SAEDs on first and second zone axes (as marked in square brackets) in apatite. The presence of (00l) reflections in (a) and (b) where l=n rather than 2n violates symmetry in space group $P6_3/m$.

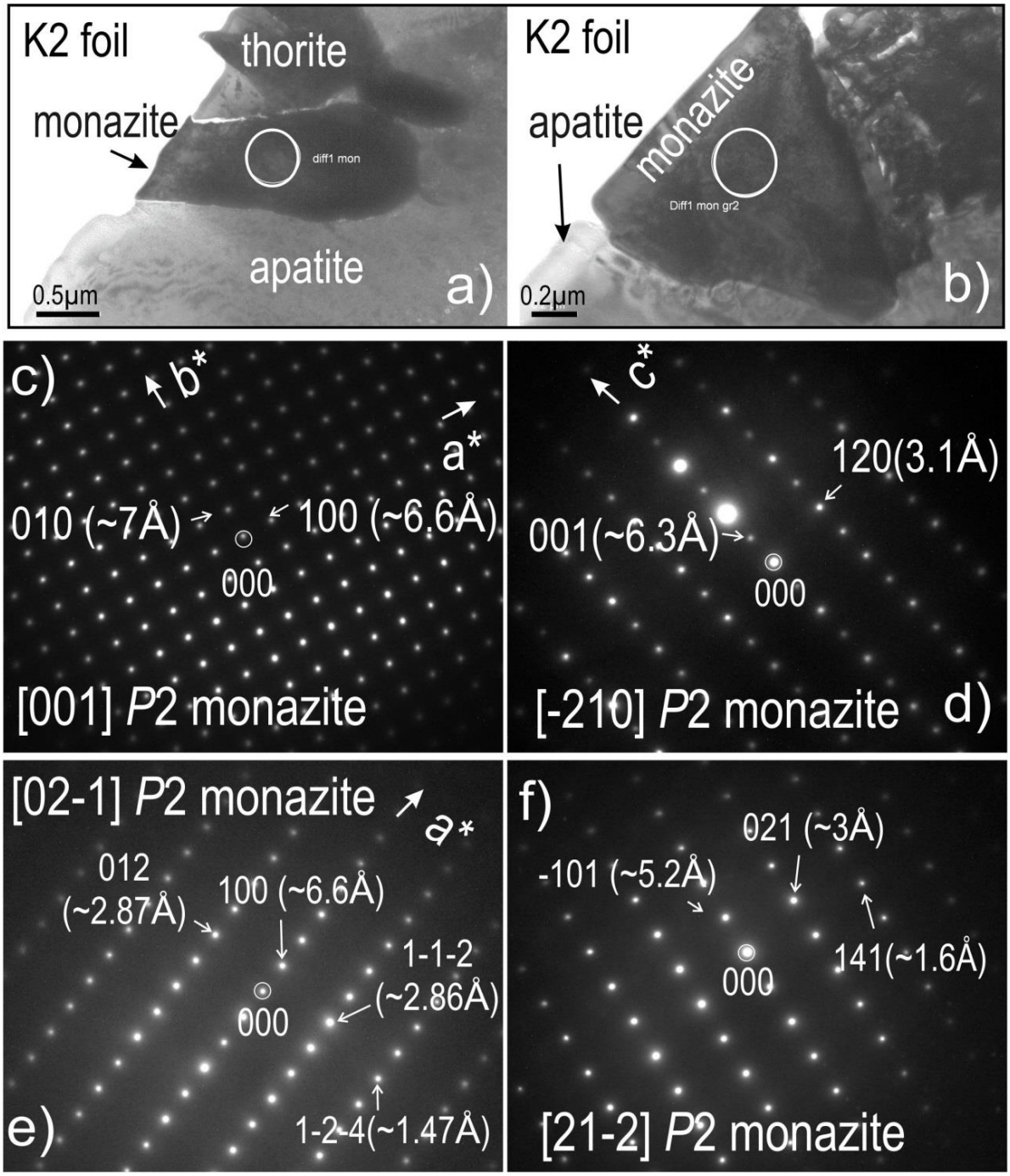

Fig. 5.9: (a-b) TEM images of inclusions of monazite in foil K2. (d-f) SAEDs on zone axes as marked obtained from monazite in foil K2. Note violation of symmetry for the ideal space group P1 2_1/n1 (see text) in (c-e).

Four distinct zone axes were indexed from monazite present as small inclusions in apatite from foil K2 (Fig. 5.9a). The SAEDs (Fig. 5.9c-f) could not be indexed using the ideal space

group $P1\ 2_1/n1$ but (Table 5.1; Ni et al., 1995) due to violation of symmetry rules ($h00=2n$; $0k0$; $k=2n$; $00l$; $l=2n$; $h0l$; $h+l=2n$). A space group of lower symmetry $P2$ could be used instead (Fig. 5.9e-f). The [001] zone axis (Fig. 5.9c) was obtained from both inclusions at the same tilt, whereas different zone axes were obtained when tilting (Fig. 5.9d-e), albeit orthogonal orientation between the c^* and a^* axes for the two grains. This suggests that the small inclusions of monazite, although with random orientation relative to host apatite, share partial crystallographic orientation with one another, rather than being random.

Similar SAEDs as those in Figure 5.9c-f were also obtained for the large monazite in foil K1. HR-TEM imaging down to [001] zone axis shows lattice fringes with no defects (Fig. 5.10a). At the same tilt, the larger fluorite inclusions are oriented down to [1-10] zone axis (Fig. 5.10b). Although such fluorite inclusions have commonly euhedral morphology, small veinlets and protrusions are also observed along the boundary with monazite.

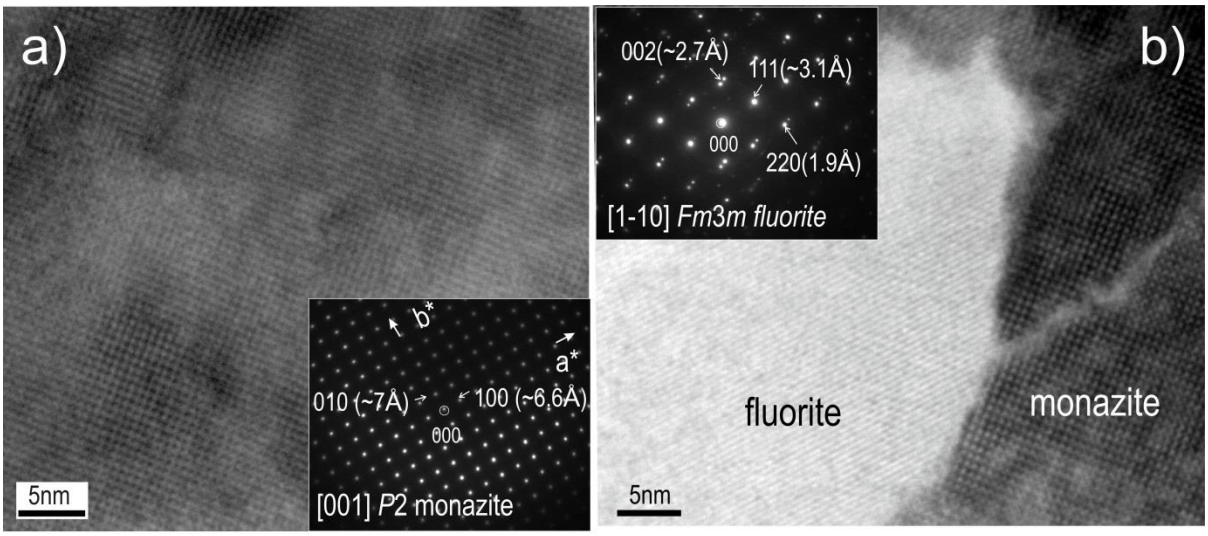

Fig. 5.10: HR-TEM images and SAEDs (insets) obtained from monazite (a) and fluorite (b) in foil K1. The uneven colouring in (a) indicate monazite is beam sensitive. Note protrusions and veinlets of fluorite in monazite along their mutual boundary in (b).

SAEDs obtained from the Th-silicate occurring as inclusions at the top of foil K2 allow identification of thorite rather than huttonite (Fig. 5.11). Measurements on SAEDs down to [001] zone axis in thorite (Fig. 5.11a) are compatible with the ideal space group $I4_1/amd$ (Table 5.1). However, violation of reflections conditions for this space group are observed in all the other three zone axes (Fig. 5.11b-d) and thus the indexing is done using a lower space group such as $I4_2/ncm$. The thorite inclusions show coherent intergrowths with apatite (Fig. 5.12), whereby the a^* axis in thorite and apatite are parallel to one another. Surprisingly, there is no preferential orientation between the orientation of thorite and monazite despite their close associations throughout the samples.

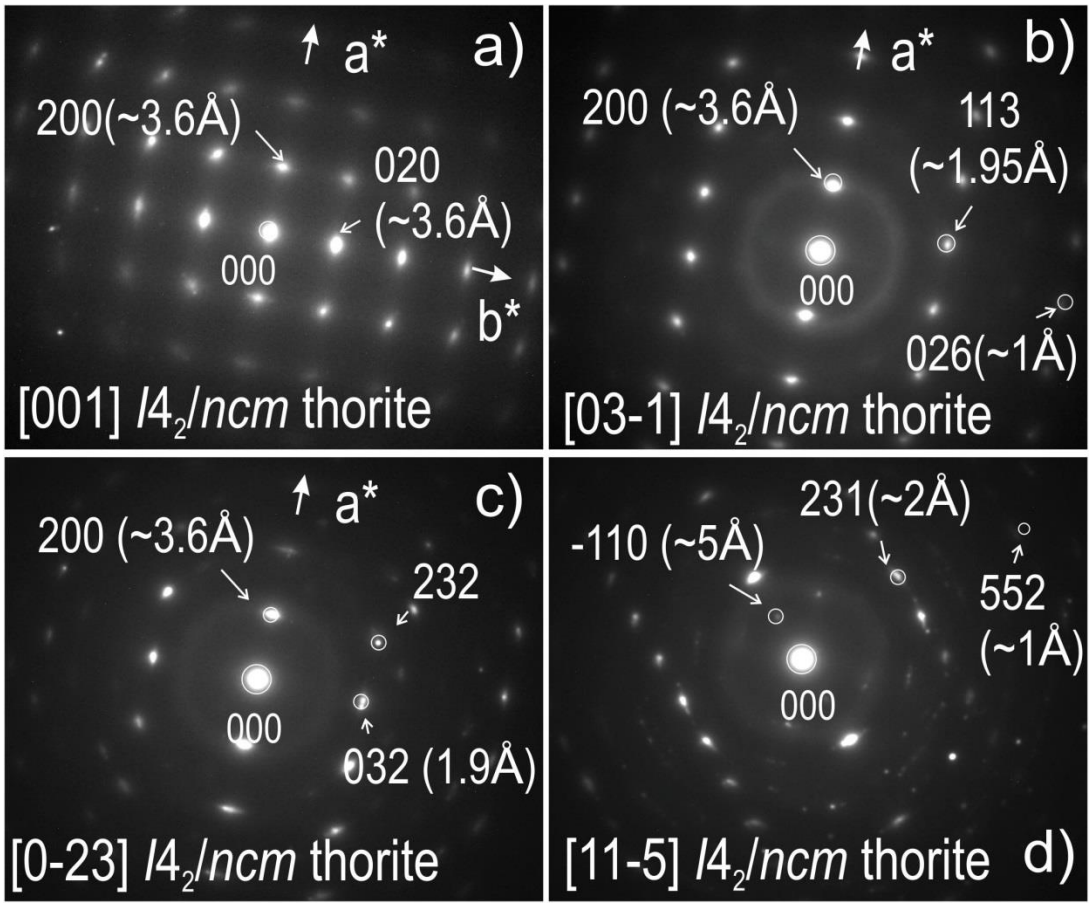

Fig. 5.11: SAEDs down to zone axes in thorite as marked obtained from inclusion at the top in foil K2. SAED in (a) can be indexed using the ideal space group for thorite ($I4_1/amd$) but those in (c-d) contain measurements that violate reflection conditions: hk0; h, k=2n; hhl:

2h+l=4n; hkl: h+k+l=2n; 0kl; k+l=2n.One of the lower space groups, e.g., $I4_2/ncm$ could be used instead for indexing.

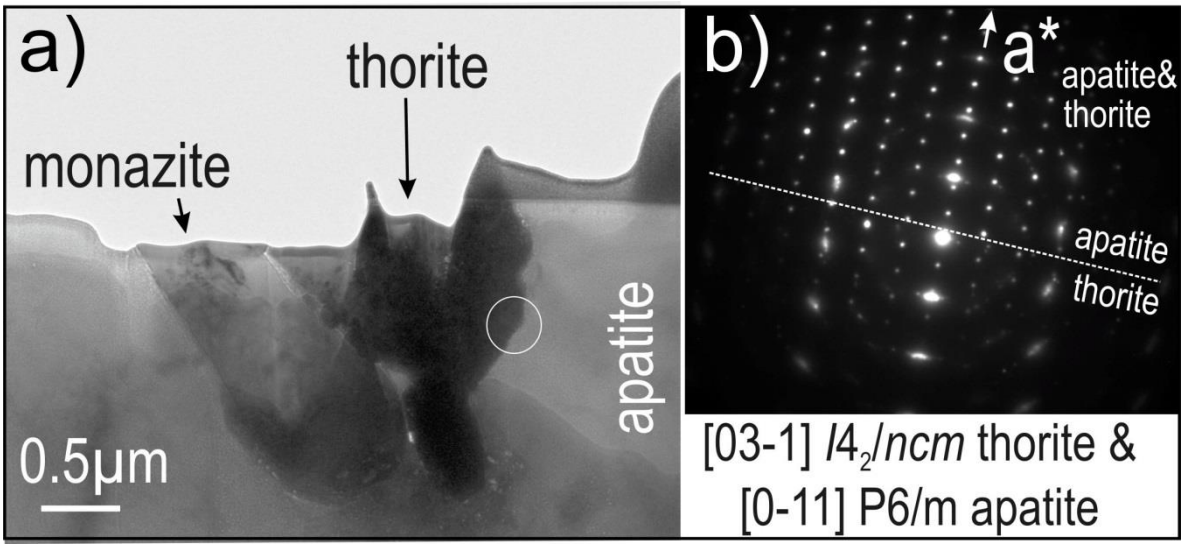

Fig. 5.12: TEM image (a) and SAED (b) showing coherent crystallographic relationships between thorite and apatite.

5.5. Discussion and conclusions

The TEM study here confirms the distinct mineral associations previously found in magmatic and hydrothermal apatite (Krneta et al., 2016) and show how these extend down to the nanoscale. In the case of hydrothermal apatite these associations are more varied than previously recognised as they also contain abundant fluorite, sericite and quartz. Identification of such inclusions and their association down to the nanoscale are paramount to understand petrogenetic models proposed so far (Gottesmann and Wirth, 1997; Krneta et al., 2016).

The results show coherence between pyrrhotite and magmatic apatite concurrent with the results of Gottesman and Wirth (1997) for apatite in granitoids, and that of Xing and Wang (2017) for similar assemblages in layered mafic intrusions. However, the presence of fluorite in association with pyrrhotite backs up the model of magma mixing suggested by Krneta et al.

(2016). In contrast, Broska et al. (2014) suggested that the formation of such pyrrhotite inclusions is the result of reduced sulphur infiltration in apatite which binds with pre-existing Fe present in the apatite. Although an interesting proposition, such a mechanism in the case of RDG magmatic apatite is considered unlikely given the lack of evidence for hydrothermal alteration.

Identification of thorite rather than huttonite as the Th-silicate polymorph supports a model of primary exsolution of this mineral from the host apatite rather than replacement as suggested by Harlov et al. (2007) based on hydrothermal experiments. Apatite, monazite and thorite, all show lower than ideal symmetries, a fact which could be corroborated with lattice distortion introduced by formation of inclusions. The present study also underlines the importance of slice cutting and extraction from a site of petrogenetic interest using FIB-TEM technique for TEM sample preparation (Ciobanu et al., 2011).

In conclusion, the presence of fluorite in both magmatic and hydrothermal apatite shows that F is available from both the granitic melt and early hydrothermal fluid. This is important in the context of understanding the unusual enrichment of the Olympic Dam deposit in U and LREE since fluoride complexes can be the preferred metal ligands in the deposition of LREE (Migdisov et al., 2016). The present study also shows that the transition from magmatic to hydrothermal regimes in IOCG deposits can be a fertile stage for trace element enrichment and/or metal deposition when felsic magmas (granitoids) are responsible for the onset of the mineralising hydrothermal system.

Acknowledgements

This is a contribution to the FOX project (Trace elements in iron oxides), supported by BHP Olympic Dam and the South Australian Mining and Petroleum Services Centre of Excellence. Staff at Adelaide Microscopy are thanked for their invaluable assistance.

References

Amelinckx, S., Van Tendeloo, G., Van Dyck, D. and Van Landuyt, J., 1989. The study of modulated structures, mixed layer polytypes and 1-D quasi-crystals by means of electron microscopy and electron diffraction. Phase Transitions 16, 3–40.

Apukhtina, O.B., Kamenetsky, V.S., Ehrig, K., Kamenetsky, M.B., Mass, R., McPhie, J., Ciobanu, C.L. and Cook, N.J., 2017. Deep, early mineralisation at the Olympic Dam Cu-U-Au-Ag deposit, South Australia. Economic Geology, 112 (6), 1531-1542.

Becker, M., de Villiers, J.P.R. and Bradshaw, D., 2010. The flotation of magnetic and non-magnetic pyrrhotite from selected nickel ore deposits. Minerals Engineering 23, 1045-1052.

Bouzari, F., Hart, J.R.H., Bissig, T. and Barker, S., 2016. Hydrothermal alteration revealed by apatite luminescence and chemistry: A potential indicator mineral for exploring covered Porphyry Copper Deposits. Economic Geology 111, 1397-1410.

Broska, I., Krogh Ravna, E.J., Vojtko, P., Janak, M., Konecny, P., Pentrak, M., Bacik, P., Luptakova, J. and Kullerud, K., 2014. Oriented inclusions in apatite in a post-UHP fluid-mediated regime (Tromson Nappe, Norway). European Journal of Mineralogy 26, 623-634.

Ciobanu, C.L., Cook, N.J., Utsunomiya, S., Pring, A. and Green, L., 2011. Focussed ion beam-transmission electron microscopy applications in ore mineralogy: Bridging micro- and nanoscale observations. Ore Geology Reviews 42, 6–31.

Demartin, F., Gramaccioli, C.M., Campostrini, I. and Pilati, T. 2010. Aiolosite, $Na_2(Na_2Bi)(SO_4)_3Cl$, a new sulfate isotypic to apatite from La Fossa Crater, Vulcano, Aeolian Islands, Italy. American Mineralogist 95, 382–385.

Dolivo-Dobrovolsky, V.V. 2006. About a common mistake in treating the crystal structure of apatite. Zapiski Vserossijskogo mineralogičeskogo obseŝtva 135, 123–125.

Downs, R.T. and Hall-Wallace, M., 2003. The American Mineralogist Crystal Structure Database. American Mineralogist 88, 247–250.

Ehrig, K., McPhie, J. and Kamenetsky, V.S., 2012. Geology and mineralogical zonation of the Olympic Dam iron oxide Cu–U–Au–Ag deposit, South Australia. In: Hedenquist, J.W., Harris, M., Camus, F. (Eds.), Geology and Genesis of Major Copper Deposits and Districts of the World, a Tribute to Richard Sillitoe. Society of Economic. Geologists Special Publication Vol. 16, pp. 237–268.

Fuchs, L.H. and Gebert, E, 1958. X-ray studies of synthetic coffinite, thorite and uranothorites. American Mineralogist 43, 243–248.

Gianfagna, A. and Mazziotti-Tagliani, S. 2014. As-rich apatite from Mt. Calvario: Characterization by micro-raman spectroscopy. The Canadian Mineralogist 52, 799-808.

Gottesmann, B. and Wirth, R., 1997. Pyrrhotite inclusions in dark pigmented apatite from granitic rocks. European Journal of Mineralogy 9, 491–500.

Hahn, T., ed., 2005. International Tables for Crystallography, Volume A. Space Group Symmetry, 5th edition, Springer, Dordrecht, The Netherlands, 911 pp.

Harlov, D.E., 2015. Apatite: A fingerprint for metasomatic processes. Elements 11, 171–176.

Harlov, D.E., Wirth, R. and Hetherington, C.J., 2007. The relative stability of monazite and huttonite At 300-900 ^{o}C and 200-1000 MPa: metasomatism and the propagation of metastable mineral phases. American Mineralogist 92, 1652–1664.

Hughes, J.M., 2015. The many facets of apatite. American Mineralogist 100, 1033–1039.

Hughes, J.M. and Rakovan, J.F., 2002. The crystal structure of apatite, $Ca_5 (PO_4)_3 (F,OH,Cl)$. Reviews in Mineralogy and Geochemistry 48, 1–12.

Hughes, J.M. and Rakovan, J., 2015. Structurally robust, chemically diverse: Apatite and Apatite Supergroup Minerals. Elements 11, 165–170.

Hughes, J.M., Cameron, M. and Crowley, K.D., 1989. Structural variations in natural F, OH, and Cl apatites. American Mineralogist 74, 870–876.

Hughes, J.M., Cameron, M. and Crowley, K.D., 1990. Crystal structures of natural ternary apatites: Solid solution in the $Ca_5(PO_4)_3X$ (X = F,OH,Cl) system. American Mineralogist 75, 295–304.

Johnson, J.P. and Cross, K.C., 1995. U–Pb geochronological constraints on the genesis of Olympic Dam Cu–U–Au–Ag deposit, South Australia. Economic Geology 88, 1046–1063.

Krause, J., Harlov, D.E., Pushkarev, E.V. and Brugmann, E.G., 2013. Apatite and clinopyroxene as tracers for metasomatic processes in nepheline clinopyroxenites of Uralian-Alaskan-type complexes in the Ural Mountains, Russian Federation. Geochimica et Cosmochimica Acta 121, 503–521.

Krneta, S., Ciobanu, C.L., Cook, N.J., Ehrig, K. and Kamenetsky, V.S., 2015. Apatite in the Olympic Dam Cu-Au-U-Ag deposit. In: Proceedings, Mineral Resources in a Sustainable World, 13th Biennial SGA Meeting, Nancy, France, August 2015, volume 3, p. 1103–1106.

Krneta, S., Ciobanu, C.L., Cook, N.J., Ehrig, K. and Kontonikas-Charos, A., 2016. Apatite at Olympic Dam, South Australia: a petrogenetic tool. Lithos 262, 470–485.

Luo, Y., Rakovan, J., Tang, Y., Lupulescu, M., Hughes, J.M. and Pan, Y., 2011. Crystal chemistry of Th in fluorapatite. American Mineralogist, 96, 23–33.

Mercier, P.H.J., Le Page, Y., Whitfield, P.S., Mitchell, L.D., Davidson, I.J. and White, T.J. 2005. Geometrical parameterization of the crystal chemistry of P63/m apatites: comparison with experimental data and *ab initio* results. Acta Crystallographica B61, 635–655.

Migdisov, A.A., Williams-Jones, A.E., Brugger, J., and Caporuscio, F.A., 2016. Hydrothermal transport, deposition, and fractionation of the REE: Experimental data and thermodynamic calculations. Chemical Geology 439, 13–42.

Ni, Y., Hughes. J.M. and Mariano, A.N., 1995. Crystal chemistry of monazite and xenotime structures $Ce(PO_4)$. American Mineralogist 80, 21–26.

Pasero, M., Kampf, A., Ferraris, C., Pekov, I.V., Rakovan, J. and White, T., 2010. Nomenclature of the apatite supergroup minerals. European Journal of Mineralogy 22, 163–179.

Piccoli, P.M. and Candela, P.A., 2002. Apatite in Igneous Systems. Reviews in Mineralogy and Geochemistry 48, 255–292.

Reeve, J.S., Cross, K.C., Smith, R.N. and Oreskes, N., 1990. Olympic Dam copper-uranium-gold-silver deposit. In: Hughes, F.E. (Ed.), Geology of the Mineral Deposits of Australia and Papua New Guinea: Australasian Institute of Mining and Metallurgy. Monograph Vol. 14, 1009–1035.

Taylor, M. and Ewing, R.C., 1978. The crystal structure of the $ThSiO_4$ polymorphs: huttonite and thorite. Acta Crystallographica, Section B, 34, 1074–1079.

Villiers, J.P.R. and Liles, D.C., 2010. The crystal-structure and vacancy distribution in 6*C* pyrrhotite. American Mineralogist 95, 148–152.

Webster, J.D. and Piccoli, P.M., 2015. Magmatic apatite: a powerful, yet deceptive mineral. Elements 11, 177–182.

Wyckoff, R.W.G., 1963. Crystal Structures, 2nd edition, Wiley, New York.

Xing, C.M. and Wang, C.Y., 2017. Cathodoluminescence images and trace element compositions of fluorapatite from the Hongge layered intrusion in SW China: A record of prolonged crystallization and overprinted fluid metasomatism. American Mineralogist 102, 1390–1401.

Yi, H., Balan, E., Gervais, C., Segalen, L., Fayon, F., Roche, D., Person, A., Morin, G., Guillaumet, M., Blanchard, M., Lazzeri, M. and Babonneau, F. 2013. A carbonate-fluoride defect model for carbonate-rich fluorapatite. American Mineralogist 98, 1066–1069.

CHAPTER 6

MODELING REE TRENDS IN FLUORAPATITE FROM OLYMPIC DAM: SNAPSHOTS OF FLUID EVOLUTION IN A GIANT HYDROTHERMAL SYSTEM

Sasha Krneta[1], Cristiana L. Ciobanu[2], Nigel J. Cook[2], Kathy Ehrig[3]

[1]*School of Physical Sciences, The University of Adelaide, Adelaide, S.A., 5005, Australia*

[2]*School of Chemical Engineering, The University of Adelaide, Adelaide, S.A., 5005, Australia*

[3]*BHP Olympic Dam, Adelaide, SA 5000, Australia*

Manuscript to be submitted in revised and abridged form to *Geology*

Statement of Authorship

Title of Paper	Modeling REE trends in fluorapatite from Olympic Dam: snapshots of fluid evolution in a giant hydrothermal system
Publication Status	☐ Published ☐ Accepted for Publication ☐ Submitted for Publication ☑ Unpublished and Unsubmitted w ork w ritten in manuscript style
Publication Details	Krneta, S., Ciobanu, C.L., Cook, N.J., Ehrig, K., and Kontonikas-Charos, A.,. Modeling REE trends in fluorapatite from Olympic Dam: snapshots of fluid evolution in a giant hydrothermal system. (to be submitted in revised and abridged form to *Geology*)

Principal Author

Name of Principal Author (Candidate)	Sasha Krneta
Contribution to the Paper	Devised research plan and objectives, performed relevant research and undertook training in the use of relevant modeling programs, wrote manuscript
Overall percentage (%)	70
Certification:	This paper reports on original research I conducted during the period of my Higher Degree by Research candidature and is not subject to any obligations or contractual agreements with a third party that would constrain its inclusion in this thesis. I am the primary author of this paper.
Signature	Date 13/9/17

Co-Author Contributions

By signing the Statement of Authorship, each author certifies that:

the candidate's stated contribution to the publication is accurate (as detailed above);

permission is granted for the candidate in include the publication in the thesis; and

the sum of all co-author contributions is equal to 100% less the candidate's stated contribution.

Name of Co-Author	Cristiana Ciobanu
Contribution to the Paper	Supervised research development, assisted in defining direction of research, assisted with chapter writing and evaluation.
Overall percentage (%)	25
Signature	Date 13 Sept 2017

Name of Co-Author	Nigel Cook
Contribution to the Paper	Supervised research development, assisted in defining direction of research, assisted with chapter writing and evaluation.
Overall percentage (%)	3
Signature	Date 13/9/17

Name of Co-Author	Kathy Ehrig		
Contribution to the Paper	Supervised research development and evaluated chapter.		
Overall percentage (%)	2		
Signature		Date	13/09/17

CHAPTER 6: NUMERICAL MODELING OF REE TRENDS IN FLUORAPATITE: SNAPSHOTS OF FLUID EVOLUTION IN A GIANT HYDROTHERMAL SYSTEM

Abstract

Trace element signatures in apatite are used to study hydrothermal processes due to the ability of this mineral to chemically record and preserve the impact of individual hydrothermal events. Interpretation of rare earth element (REE)-signatures in hydrothermal apatite can be complex due to not only evolving fO_2, fS_2 and fluid composition, but also to the broad variety of different REE-complexes (Cl-, F-, P-, SO_4, CO_3, oxide, OH^- etc.) in the fluid, and the wide variety of solubilities and stabilities that these complexes exhibit. To facilitate interpretation of evolving REE-signatures within the giant Olympic Dam iron-oxide-copper-gold deposit, South Australia, the REE-signatures of three unique apatite types from hydrothermal assemblages crystallized under partially constrained conditions have been numerically modeled, and the partitioning coefficients between apatite and fluid calculated. Results of these calculations duplicate the measured data showing a transition from early LREE- to later MREE-enriched apatite, which can be achieved by an evolution in the proportion of different REE-complexes, each with inherent stabilities and solubilities. Modeling also efficiently explains the switch from REE-signatures with negative to positive Eu-anomalies. REE transport in hydrothermal fluids is attributed to REE-Cl complexes, thus explaining both the LREE-enriched character of the deposit and the relatively LREE-depleted nature of later generations of apatite. The presence of apatite with positive Eu-anomalies is attributed to crystallization from late neutral to alkaline fluids characterized by the presence of Eu^{3+} species.

Keywords: apatite; numerical modeling; Olympic Dam; rare earth elements.

6.1 Introduction

Trace elements (concentrations <<1 wt.%) and their variation within hydrothermal minerals can provide valuable information on fluid parameters and conditions of ore deposition for assemblages which are well constrained with respect to paragenetic position. Studies have demonstrated the interdependency between hydrothermal conditions and the compositions of specific minerals (e.g., Smith et al., 2004, Brugger et al., 2008, van Hinsberg et al., 2010). Many of these studies have focused on the rare earth elements (REE), which display a coherent behavior to one another due to similar electronic configurations, common trivalent oxidation state, and systematic decrease in atomic radius with increased atomic number. This typically leads to smooth fractionation across the group (e.g., Haas et al., 1995) but since Eu and Ce may also occur as Eu^{2+} and Ce^{4+}, redox-sensitive anomalies may result.

The behavior of the REE in hydrothermal fluids is affected by parameters such as pH, temperature, salinity, redox conditions and fluid composition (e.g., Bau, 1991, Haas et al., 1995, Migdisov and Williams-Jones, 2014, Migdisov et al., 2016), thus allowing REE to be used as geochemical tracers in hydrothermal systems. Emphasis has been placed on determining the thermodynamic properties of various REE complexes in hydrothermal fluids at temperatures typical of ore deposit formation (Migdisov and Williams-Jones, 2014, Migdisov et al., 2016), which can support numerical modeling of REE behavior.

Modeling of REE patterns for zoned calcic garnet (Smith et al., 2004) and scheelite (Brugger et al., 2000, 2008) have shown the sensitivity of these minerals to changes in fluid parameters. In both cases, modeling addressed compositionally-zoned minerals, in which core-to-rim compositional variation was modeled in terms of partitioning between mineral and fluid, involving evolving fluid parameters, successfully reproducing the patterns measured. The work of Brugger et al. (2008), which focused on high-grade orogenic gold

ores, emphasized the sensitivity of REE patterns in scheelite to pH variation, and suggested that apatite should behave similarly and display analogous signatures enriched in middle REE (MREE).

Chondrite-normalized REE fractionation patterns of apatite-group minerals are recognized as valuable tools for understanding hydrothermal processes (Harlov, 2015). Despite being widespread in a wide range of magmatic to metamorphic rocks (Belousova et al., 2001,2002, Cao et al., 2012, Teiber et al., 2015, Mao et al., 2016), apatite chemistry has not previously been modeled in the same way as scheelite or calc-silicates. Chondrite-normalized REE fractionation trends for apatite are widely reported from a variety of rocks but such trends are, in general, remarkably consistent with one another, conspicuous by consistent, downward-sloping trends featuring relative enrichment in light REE (LREE) (Cao et al., 2012, Teiber et al., 2015, Mao et al., 2016). Variation in the size and sign of Eu anomalies across rock suites from across metallogenic provinces have been used to infer variability or change in redox conditions (e.g., Cao et al., 2012).

Apatite is a conspicuous component of iron-oxide-copper-gold IOCG systems, including those within the Olympic Cu-Au Province of South Australia. Apatite is particularly abundant within early apatite-magnetite assemblages, which resemble those of the iron-oxide-apatite (IOA) subgroup, such as Kiruna, Sweden (Krneta et al., 2016, 2017a, b, Apukhtina et al., 2017, Ehrig et al., 2017). Recent study of apatite from Olympic Dam (Krneta et al., 2016), which is by far the largest deposit in the Olympic Cu-Au Province (Ehrig et al., 2012), has demonstrated a systematic compositional variation with regards to F, Cl, S, As, and most prominently REE, which correlates with changes in the host intrusive or hydrothermal assemblage. Distinct REE-signatures are characteristic of apatite from certain hydrothermal assemblages; these vary from LREE-enriched types within early reduced, high-temperature magnetite-apatite-chlorite-carbonate±pyrite±chalcopyrite, assemblages preserved on the

margins of the deposit and at depth, to MREE-enriched signatures within shallow zones in which hematite is dominant. Finally, apatite within late-stage massive bornite mineralization is both MREE-enriched and displays marked positive Eu-anomalies (Krneta et al., 2017a).

The transition from early high-temperature magnetite-dominant to later hematite-dominant assemblages in the Olympic Dam area coincided with significant changes in the mineralizing fluids as determined by fluid inclusion studies (Oreskes and Einaudi, 1992; Bastrakov et al. 2007). Given the well documented association between apatite with a specific chemistry and hydrothermal assemblages formed under known fluid conditions, numerical modeling of apatite/fluid partitioning can offer significant insights into the behavior of REE during formation of Olympic Dam. Using empirical mineral compositional data and newly published thermodynamic values for REE complexes (Migdisov et al., 2016), along with assumptions for other fluid parameters grounded in the stabilities of the host assemblage, REE behavior and partitioning coefficients between apatite and fluid are modeled numerically. Using three examples of unique apatite REE-signatures, the transition from LREE- to MREE-enriched and finally MREE-enriched signatures with positive Eu-anomalies, is shown to be the direct result of changes in the character of the hydrothermal fluids during formation of Olympic Dam.

6.2 Background and Rationale

6.2.1 Apatite chemistry and controls on elemental uptake

The apatite supergroup (Pasero et al., 2010) constitutes a large group of named minerals made possible by the extraordinary flexibility of the apatite structure (e.g., White and Dong, 2002), which allows for incorporation of approximately half the elements in the periodic table (Hughes and Rakovan, 2015). The general formula of apatite supergroup minerals is defined

as $A_5(XO_4)_3Z$, where the A position is most commonly occupied by Ca^{2+} but can be substituted by a variety of other di-, tri- and tetravalent cations, such as Na^{+}, Sr^{2+}, Pb^{2+}, Ba^{2+}, Mn^{2+}, Fe^{2+}, Mg^{2+}, Ni^{2+}, Co^{2+}, Cu^{2+}, Zn^{2+}, Sn^{2+}, Cd^{2+}, Eu^{2+}, REE^{3+}, Y^{3+}, Zr^{4+}, Ti^{4+}, Th^{4+}, U^{4+}, and S^{4+}, as well as U^{6+}. The X position is dominantly occupied by P, as PO_4^{3-}, but can also accommodate SO_4^{2-}, AsO_4^{3-}, VO_4^{3-}, SiO_4^{4-}, CO_3^{2-}, CrO_4^{2-}, CrO_4^{3-}, GeO_4^{4-}, SeO_4^{4-} and WO_4^{3-}. Finally, the Z position hosts F, Cl and OH^{-} defining the three end-members fluorapatite, chlorapatite and hydroxyapatite, termed apatite "*sensu stricto*" (Hughes and Rakovan, 2002).

Three cation polyhedra make up the apatite structure, a single, rigid PO_4 tetrahedron and two Ca polyhedra Ca1 and Ca2 (Hughes and Rakovan, 2002). Of these, the Ca2 position dominantly hosts LREE and the Ca1 position the heavy-REE (HREE), with Nd expressing no preference for either position (Hughes and Rakovan, 2015). The size of these positions exerts the dominant control on trace element substitution through the proximity principle (Goldschmidt, 1937), meaning that elements with atomic radii closest to that of the substituting position are most readily substituted. In instances where an elements valance state is different to that of the position it is substituting, such as in the case of REE^{3+} substituting for Ca^{2+}, overall charge balance is maintained through a variety of different coupled charge-compensated substitutions (Pan and Fleet, 2002, Rønsbo, 1989).

In the magmatic environment, once the effects of the proximity principle, whole rock composition and the co-partitioning of REE between apatite and other minerals are taken into account, apatite REE-signatures are largely predictable. In contrast, REE-trends in hydrothermal apatite are far more complex since the wide array of fluids capable of crystallizing apatite can carry variable concentrations of REE as a range of soluble complexes (e.g., Migdisov et al., 2016). These factors, combined with temperature, pH, fO_2 and others, dictate the dominance or absence of an individual REE at the conditions of apatite

crystallization, in turn resulting in a wide variety of REE-signatures among hydrothermal apatites.

For example, redox-sensitive Eu, can be present as Eu^{3+} and Eu^{2+} giving it the ability to partition away from the other trivalent REE. This behavior has been used to infer variability or change in redox conditions (e.g., Cao et al., 2012), as well as changes in fluid parameters due to the sensitivity of Eu^{3+}/Eu^{2+} complexing to pH (Brugger et al., 2008). Similarly, the common tendency for the LREE to speciate as stable and soluble LREE-Cl complexes to a greater extent than for HREE can lead to spatial disassociation from LREE (Migdisov et al., 2016).

6.2.2 Apatite within the Olympic Dam deposit

Olympic Dam is the largest expression of IOCG mineralization within the Olympic Cu-Au Province (10,400 Mt at 0.77% Cu, 0.25 kg/t, 0.32 g/t Au and 1 g/t Ag; BHP, 2016). The deposit is hosted within the Olympic Dam Breccia Complex, a collective term used to describe a range of breccias, intrusives and other lithologies associated with the Olympic Dam ore environment (Reeve et al., 1990, Ehrig et al., 2012). This in turn is hosted within the Roxby Downs Granite (RDG), a pink, hydrothermally altered yet undeformed, two-feldspar granite belonging to the ~1.6 Ga Hiltaba Suite (Creaser, 1989, Johnson and Cross, 1995, Kontonikas-Charos et al., 2017).

Mineralogical zoning is expressed across the deposit as variations in the dominant Fe-oxide and Cu-(Fe)-sulfide species (Ehrig et al., 2012) whereby reduced magnetite±pyrite± chalcopyrite assemblages grade laterally from the peripheries of the deposit and upwards from depth to oxidized, hematite-dominant chalcopyrite+bornite assemblages, and finally to chalcocite-dominant assemblages at shallow levels. Similarly, the dominant silicate alteration minerals vary from chlorite-dominant in association with reduced magnetite assemblages (in

which magmatic feldspars are also often preserved) to sericite-dominant in association with hematite (Ehrig et al., 2012, Kontonikas-Charos et al., 2017).

The work of Krneta et al. (2016, 2017a) defined the morphological and chemical characteristics of apatite across the Olympic Dam deposit and showed that apatite associated with a specific intrusive rock or hydrothermal assemblage displays chemical characteristics unique to that particular assemblage. Moreover, apatite was found to record subsequent hydrothermal overprinting events expressed within zoned grains.

Hydrothermal apatite is abundant within the magnetite-dominant assemblages such as the *deep mineralization* (Krneta et al., 2016, Apukhtina et al., 2017), where it occurs as coarse (> several mm) grains, or large aggregates consisting of multiple ~500 µm grains commonly interstitial to magnetite. Compositionally, such apatite is LREE-enriched with moderate negative Eu-anomalies (Figure 6.1, Table 6.1).

Although hematite-sericite alteration is best developed in the higher, central portions of the deposit, it significantly overprints early magnetite-dominant mineralization throughout the deposit (Ehrig et al., 2012). Here, pre-existing apatite is altered along fractures and grain rims and depleted in LREE, S, and Cl. In instances where hematite-sericite alteration is pervasive, particularly *hematite-sericite associated apatite* within the RDG, the apatite is strongly MREE-enriched with a weak negative Eu-anomaly (Figure 6.1, Table 6.1; Krneta et al., 2016, 2017a). MREE-enrichment in association with hematite-sericite alteration has also been documented from the Wirrda Well and Acropolis IOCG prospects SSE and SSW of Olympic Dam as well, suggesting that such a feature may be generic and linked to ore genesis (Krneta et al., 2017a, b).

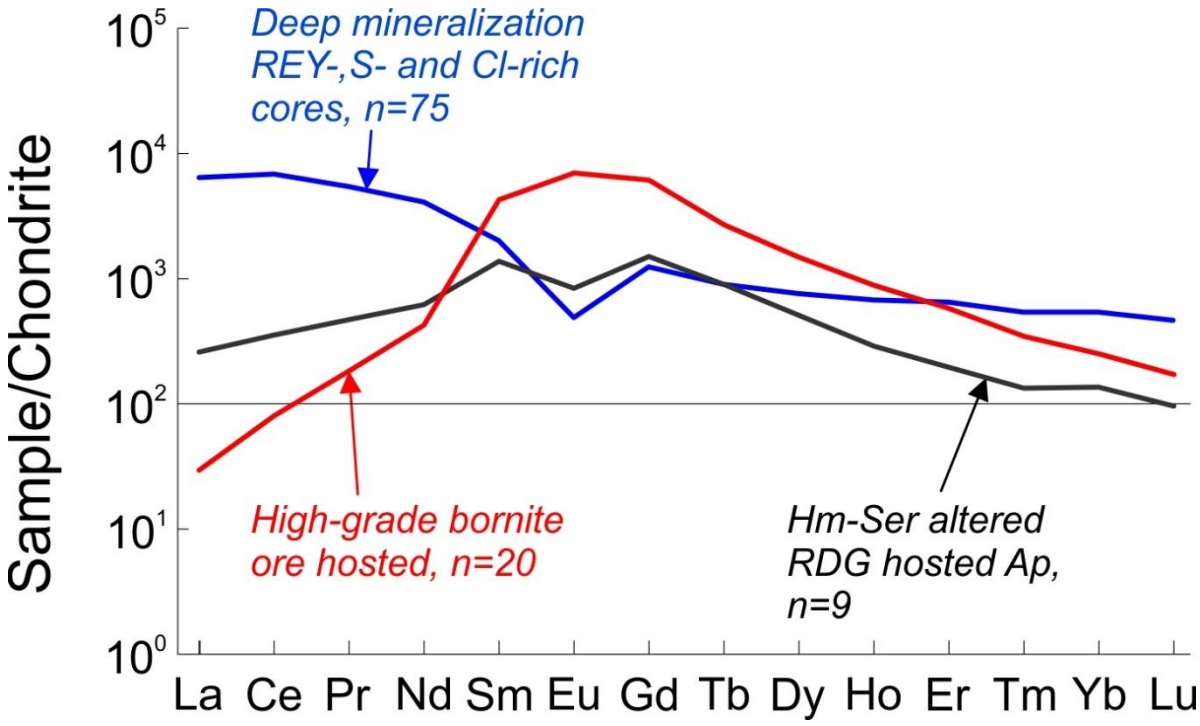

Figure 6.1: Chondrite-normalized REE-signatures of three apatite types hosted within the Olympic Dam mineralized system (Krneta et al., 2016, 2017a) used in the numerical modeling of partitioning between apatite and fluid.

Within upper levels of the deposit, volumetrically limited, massive, high-grade bornite mineralization hosts apatite with extreme MREE-enrichment. Unlike the hematite-sericite associated mineralization, such apatite displays a positive Eu-anomaly (*high-grade bornite ore hosted apatite*, Figure. 6.1, Table 6.1; Krneta et al., 2017a). Such a signature is very unusual for apatite (e.g., Belousova et al., 2002, Cao et al., 2012, Teiber et al., 2015, Mao et al., 2016), however it has been observed within the Acropolis deposit where Krneta et al. (2017b) showed it to be the result of crystallization from late-stage neutral to alkaline fluids on the basis of mineral stabilities and Eu-speciation.

	Deep mineralization REY-, S- and Cl-rich cores	Hematite-sericite altered RDG hosted	High-grade bornite ore hosted
La	1520	84	7
Ce	4192	258	49
Pr	504	47	17
Nd	1868	280	194
Sm	298	195	631
Eu	27	45	391
Gd	247	290	1217
Tb	32	32	97
Dy	187	125	365
Ho	37	16	49
Er	104	33	92
Tm	13	4	9
Yb	83	24	39
Lu	11	3	4

Table 6.1: REE concentrations (in ppm) of three apatite types hosted within the Olympic Dam mineralized system (Krneta et al., 2016, 2017a) used as examples in the numerical modeling of partitioning between apatite and fluid.

6.2.3 Fluid evolution within IOCG systems, REE speciation and the controls on apatite/fluid partitioning

Study of fluid inclusions within IOCG mineralization in the Olympic Cu-Au Province (Oreskes and Einaudi, 1992, Morales Ruano et al., 2002, Bastrakov et al., 2007, Ismail et al., 2014, Schlegel, 2015), as well as from IOCG globally (Chiaradia et al., 2006, Baker et al., 2008, Gleeson and Smith, 2009) has provided crucial insights into the formation of these deposits by defining the temperatures and salinities of fluids associated with each hydrothermal assemblage in any given deposit. In the case of Olympic Dam, early magnetite-dominant mineralization was found to have formed at temperatures in excess of 400 °C from fluids with salinities between 20 and 45 wt. NaCl equiv. (Oreskes and Einaudi, 1992). Similar magnetite-dominant assemblages throughout the Olympic Cu-Au Province formed under similar conditions (Bastrakov et al., 2007). However, Olympic Dam hematite-dominant

mineralization crystallized from cooler (150-300 °C), low-salinity (1-8 wt.% NaCl) fluids (Oreskes and Einaudi, 1992). Numerous authors have speculated that this transition was largely responsible for deposition of Cu-Au within many of the IOCG systems given that the early magnetite-stage ore fluids were rich in copper (>500 ppm Cu based on PIXE analysis; Bastrakov et al., 2007), but lacked a suitable depositional mechanism. Similarly, Haynes et al. (1995) modeled this transition and found that changes in fluid salinity, temperature and other parameters, such as pH, were sufficient to bring about deposition of Cu-Au-U-Ag mineralization.

None of these authors considered, however, the behavior of the REE during this transition despite the presence of REE within the deposit at elevated concentrations compared to crustal values, particularly in the case of La and Ce. The work of Migdisov et al. (2016) provides the most comprehensive account of REE behavior in hydrothermal fluids along with thermodynamic properties for a suite of REE complexes derived from experiments conducted at elevated temperatures. The new thermodynamic data disputes the ambient temperature extrapolated values of Haas et al. (1995) and defines the roles of the various REE complexes within hydrothermal systems formed at elevated temperatures and neutral to acidic conditions. The authors emphasize that the low solubility of REE-F, -P, -oxide, -OH and -CO_3 complexes makes them unlikely to be involved in REE transport. Conversely, the high solubility and stability of REE-Cl and SO_4 complexes along with their likely high concentration in hydrothermal fluids (e.g., highly saline hydrothermal fluids) suggests that they are central to REE transport. Significant variability is, however, observed among the REE with regards to complexing behavior. LREE are much more stable than HREE as Cl-complexes suggesting that they should also be more readily transported and concentrated upon precipitation. Such a hypothesis is proven directly by modeling (Migdisov et al., 2016), and indirectly by the predominance of LREE-enriched hydrothermal systems as opposed to those enriched in

HREE (e.g., Cook et al., 2013, Weng et al., 2015), although the unique geological settings of specific hydrothermal systems will facilitate further complexities.

6.3 Methodology

6.3.1 Numerical modeling of apatite/fluid partitioning coefficients

Brugger et al. (2000, 2008), Smith et al. (2004) and Migdisov et al. (2016) have outlined the methodology for calculation of fluid partitioning coefficients in minerals where Ca is a major component. Substitution mechanisms must be defined as a preliminary requisite step. These can either be direct, e.g., Eu^{2+} for Ca^{2+} substitution, or via charge-compensated coupled substitutions involving elements such as Na or Si in the case of REE^{3+}. For calculation of partitioning coefficients between apatite and fluid, the two substitution mechanisms are proposed to be:

$$(1)\ Ca_{Ap}^{2+} + Eu_{aq}^{2+} \leftrightarrow Ca_{aq}^{2+} + Eu_{Ap}^{2+}$$

$$(2)\ 2Ca_{Ap}^{2+} + REE_{aq}^{3+} + Na_{aq}^{+} \leftrightarrow 2Ca_{aq}^{2+} + REE_{Ap}^{3+} + Na_{Ap}^{+}$$

Although REE incorporation into the apatite types used here (Figure 6.1, Table 6.1) appears to be primarily accommodated by Si^{4+}-for-P^{5+} substitution based on EPMA analysis (Krneta et al., 2016), the simplifying assumption that the dominant substitution involves charge compensation by Na^{+} has been made to eliminate the complications involved in considering multiple elements in this role. This is considered prudent and in line with analogous approaches (e.g., Smith et al., 2004).

Using equations (1) and (2) we can define the equilibrium constants (K) expressed in equations (3) and (4), respectively, where 'a_i' is the activity of element 'i' in the fluid (aq) or in apatite (Ap).

$$(3)\ \mathrm{K}_1(P,T)=\frac{a_{Eu^{2+}_{Ap}}}{a_{Eu^{2+}_{aq}}}\frac{a_{Ca^{2+}_{aq}}}{a_{Ca^{2+}_{Ap}}}$$

$$(4)\ \mathrm{K}_2(P,T)=\frac{a^2_{Ca^{2+}_{aq}}}{a^2_{Ca^{2+}_{Ap}}}\frac{a_{REE^{3+}_{Ap}}}{a_{REE^{3+}_{aq}}}\frac{a_{Na^{+}_{Ap}}}{a_{Na^{+}_{aq}}}$$

The apatite/fluid partitioning coefficient (D_i) is related to the equilibrium constant K_i by equations (5) and (6), where 'Y_i' denotes the activity coefficient of element 'i' and the square brackets in (6) define the concentration of the elements in the fluid in molal terms, and as mole fraction in the apatite.

$$(5)\ D^{\frac{Ap}{fluid}}_{Eu^{2+}} = \mathrm{K}_1(P,T)\frac{Y_{Eu^{2+}_{aq}}}{Y_{Ca^{2+}_{aq}}}\frac{Y_{Ca^{2+}_{Ap}}}{Y_{Eu^{2+}_{Ap}}}$$

$$(6)\ D^{\frac{Ap}{fluid}}_{REE^{3+}} = \mathrm{K}_2\ (P,T)\ \frac{Y_{REE^{3+}_{aq}}}{Y^2_{Ca^{2+}_{aq}}}\frac{Y_{Na^{+}_{aq}}}{Y_{REE^{3+}_{Ap}}}\frac{Y^2_{Ca^{2+}_{Ap}}}{Y_{Na^{+}_{Ap}}}\frac{\lfloor Na^{+}_{aq}\rfloor}{\lfloor Ca^{2+}_{aq}\rfloor}\frac{\lfloor Ca^{2+}_{Ap}\rfloor}{\lfloor Na^{+}_{Ap}\rfloor}$$

Assuming that the solid solution is dilute and ideal, the activity coefficients for Ca and each individual REE can be assumed to be at unity. Moreover, if the fluid is considered dilute and ideal, then Ca and each of the other REE are equally at unity allowing (6) to be reduced to (7).

$$(7)\ D^{Ap/fluid}_{REE^{3+}} = K_2(\mathrm{P,\ T})\frac{\lfloor Na^{+}_{aq}\rfloor}{\lfloor Ca^{2+}_{aq}\rfloor}\frac{\lfloor Ca^{2+}_{Ap}\rfloor}{\lfloor Na^{+}_{Ap}\rfloor}$$

Using values obtained for individual REE from equations (5) and (7) together with equation (8) modified from Smith et al. (2004), we can model the crystallization of apatite in an open system involving a constantly replenished fluid accounting for the common lack of intra-grain zoning observed in the apatite types used as the basis for the preceding models. This methodology also largely follows Brugger et al. (2000).

$$(8)\ C_{Ap} = D^{\frac{Ap}{fluid}}_{REE^{3+}}\ \mathrm{x}\ C^{(D-1)}_{aq}$$

Activities of REE and other relevant components were calculated using Geochemist's Workbench® 11 (Bethke and Yeakel, 2016) after updating the database for REE-Cl and -F aqueous species according to thermodynamic values given by Migdisov et al. (2016). In the

case of LREE, the activity is most commonly represented by a single chloride complex whereas the activity of MREEs and HREEs are distributed among multiple species (chloride, fluoride, hydroxide and oxide). As such these were combined and a total value, $a_{REE_{total}}$, was used in the calculations. Although this method may be a simplification of the natural hydrothermal system, it is nevertheless in line with the approach followed elsewhere. Previous studies (e.g., Smith et al., 2004) have resolved the complication of an individual REE being present as multiple complexes by not defining the various species, and treating the activity of an individual REE as a single parameter. In other published work, notably Brugger et al. (2008), the scenario investigated involved the speciation of Eu under two sets of conditions, each of which contained Eu exclusively as a single species.

6.3.2 Study cases and determination of fluid conditions

Three unique study cases of apatite sub-types from Olympic Dam were selected from the work of Krneta et al. (2016, 2017a) based on their well-defined REE-signatures and associations with particular hydrothermal assemblages (Figure 6.1, Table 6.1). To perform the numerical modeling and determine apatite/fluid REE partitioning, a set of fluid conditions for each scenario must be defined along with the concentrations of crucial elements such as the REE, complexing ligands, Ca and Na. In the case of the reduced, magnetite-dominant mineralization (*deep mineralization*) and the oxidized, *hematite-sericite associated* apatite, empirical fluid inclusion measurements (Oreskes and Einaudi, 1992) provide temperature and salinity data. Other required input parameters, such as pH and fO_2 were determined based on the stabilities of constituent minerals within the assemblages and incorporating the modeling work of Haynes et al. (1995). These are outlined in Table 6.2 and shown in Figure 6.2.

	Deep min. hosted apatite		hematite-sericite associated apatite		high-grade bornite ore hosted apatite	
Model	**1.1**	**1.2**	**2.1**	**2.2**	**3.1**	**3.2**
O_2 aq (log g)	-36.8	-36.8	-31.7	-31.7	-31.7	-32
H^+ (pH)	5.2	5.2	4.4	4.4	8.5	6.6
NaCl (wt%)	20	20	10	10	5	5
Ca (wt%)	0.61	3	0.37	4	1.06	3.5
HCO_3^- (wt%)	0.37	0.37	0.94	0.94	2.40	2.40
F- (wt%)	0.005	0.005	0.005	0.005	0.005	0.005
SO_4^{--} (wt%)	0.15	0.15	0.15	0.15	2.00	2.00
Temperature	300	300	300	300	300	300
La (ppm)	100	100	100	100	1200	1200
Ce (ppm)	200	200	200	200	1700	1700
Pr (ppm)	21	21	24	24	150	150
Nd (ppm)	70	70	80	80	393	393
Sm (ppm)	12.4	12.4	14	14	41.2	41.2
Eu (ppm)	1.7	1.7	1.9	1.9	12.4	12.4
Gd (ppm)	10.3	10.3	11.8	11.8	28	28
Tb (ppm)	1.6	1.6	1.7	1.7	3.4	3.4
Dy (ppm)	9.5	9.5	10.3	10.3	16.7	16.7
Ho (ppm)	1.9	1.9	2	2	3	3
Er (ppm)	5.7	5.7	6.1	6.1	9.1	9.1
Tm (ppm)	0.5	0.5	0.7	0.7	1.2	1.2
Yb (ppm)	5.6	5.6	6.3	6.3	8.6	8.6
Lu (ppm)	0.9	0.9	1.1	1.1	1.3	1.3

Table 6.2: Numerical model fluid parameters and fluid chemistry.

Given that no empirical measurements of fluid REE, Ca or complexing ligand concentrations currently exist, these need to be assumed. Following Smith et al. (2004), the various element concentrations are assumed to be equal to the whole rock concentrations of the interpreted fluid source (this is unaltered RDG in the case of the *deep mineralization*), or the whole rock concentrations in the rock host in the case of the *hematite-sericite associated* and the *high-grade bornite ore hosted apatite*. Whole rock values given by Ehrig et al. (2012) for the unaltered RDG, sericite-altered RDG and mineralized RDG (10-20 wt. % Fe, Cu ≥3000 ppm) were used for the *deep mineralization, hematite-sericite associated* and *high-grade bornite ore hosted* apatite, respectively, as outlined in Table 6.2.

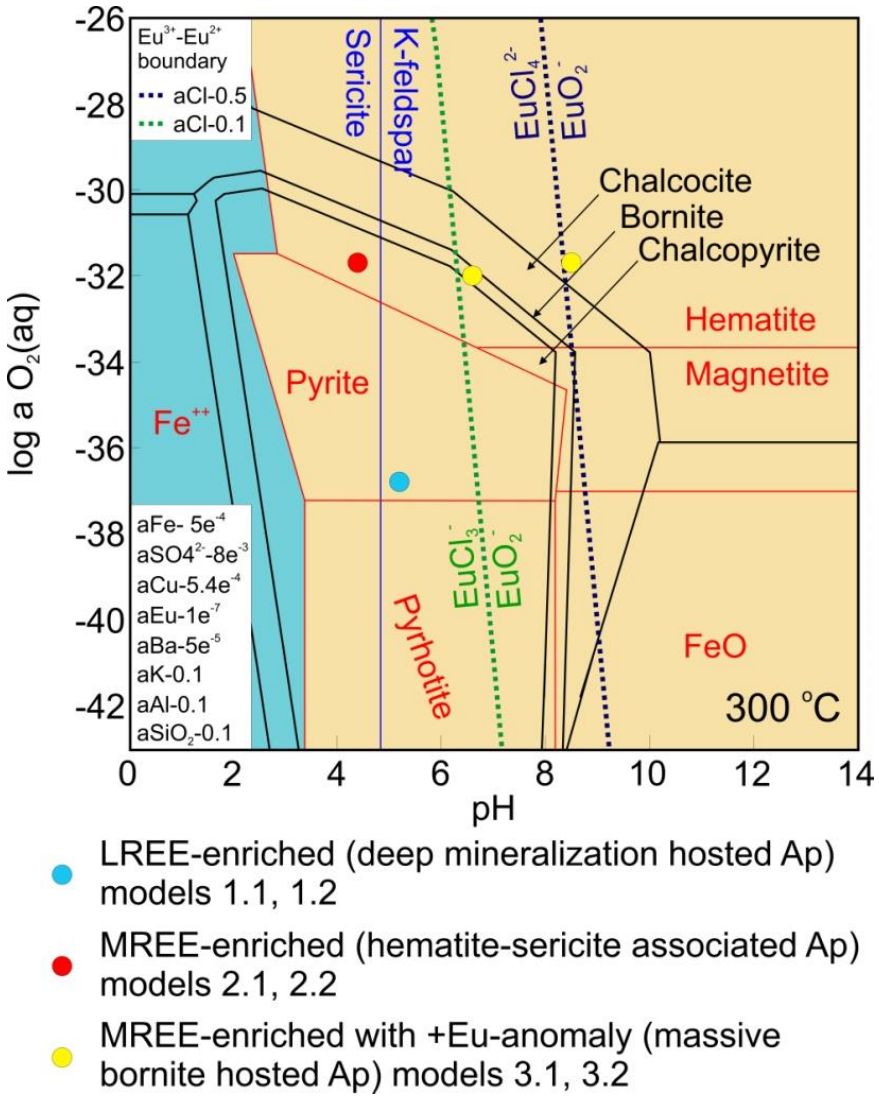

Figure 6.2: Diagram showing the relative stabilities of Cu-Fe sulfides, Fe-oxides and K-feldspar-sericite. The various model scenarios are shown as colored circles demonstrating their agreement with the wider mineral assemblage (Krneta et al., 2016, 2017a).

6.4 Results and Discussion

6.4.1 Apatite/fluid REE partitioning and the effects of evolving fluid conditions

Using the methods and fluid parameters described and chemistry as outlined in Table 6.2, six models were generated, two for each apatite type (*deep mineralization, hematite-sericite*

associated and *massive bornite hosted apatite*). Results of the modeling and calculations are shown in Appendix A with the model apatite and apatite/fluid partitioning coefficient D shown graphically as Figure 6.3.

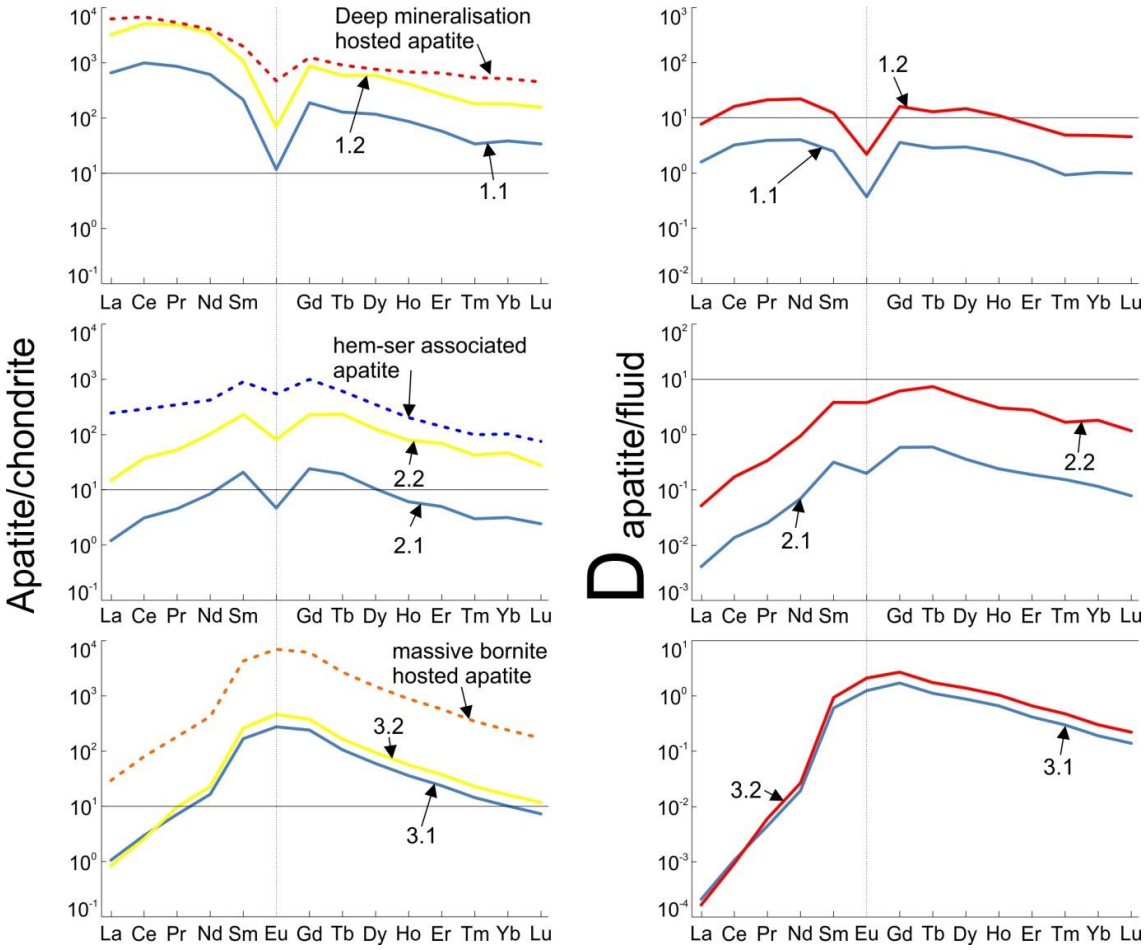

Figure 6.3: (a) Measured (dashed line) and model (full lines) chondrite-normalized concentrations of REE, and **(b)** the corresponding calculated apatite/fluid partitioning coefficients D for each model.

Within the generated models, by far the best fits to the measured apatite compositions are provided by models 1.2 and 2.2. The remaining models significantly understate the observed absolute REE concentrations, but nonetheless successfully replicate the shape of the measured chondrite-normalized REE fractionation trends. Many of these however are within the concentration ranges obtained for the measured apatite. To replicate the absolute mean REE

concentrations, models 1.2 and 2.2 required an assumption of high Ca concentrations in the fluid (3 and 4 wt.%), respectively which may be excessive for such fluids, even if it is noted that Haynes et al. (1995) proposed fluids containing ~2.5 wt.% Ca. As suggested, the primary effect of increasing Ca concentrations is an increase in the absolute REE levels within model apatite. However, this is not the case in models 3.1 and 3.2, suggesting that at the pH values proposed for these models (8.5 and 6.6, respectively) the effects of increasing Ca concentration is minor. Similarly, varying Na concentrations within all models, in isolation, primarily effects the absolute levels of REE but to a lesser extent than variation in Ca.

The various model groups are primarily distinguished with respect to changes in apatite/fluid partitioning coefficients, D, and the speciation of individual REE. For example, models 1.1 and 1.2 display relatively flat fractionation behavior, varying across a single order of magnitude, whereas in the case of the models attempting to replicate the MREE-enriched apatite varieties, they vary across at least 4 orders of magnitude with very low D values for LREE, increasing towards the MREE, and decreases slightly for HREE (Figure 6.3). These very low rates of LREE fractionation are, to a certain extent, artefacts of the highly LREE-enriched nature of the fluids chosen to represent models 2.1, 2.2, 3.1 and 3.2. However, in the case of models 2.1 and 2.2, an explanation for this fractionation can be observed in the increased proportion of fluid LREE activity being represented by Cl complexes (Table 6.3), a change which can be expected to increase the likelihood of these elements remaining mobile (Migdisov et al., 2016) and thus inhibit incorporation into apatite. Moreover, this would explain the commonly observed LREE depletion associated with hematite-sericite overprinting of pre-existing apatite (Krneta et al., 2016, 2017a). An increase in the dominance of Cl complexes is primarily caused by a drop in pH from 5.2 to 4.4, and does not exhibit a sensitivity to changes in NaCl concentrations since sufficient Cl is available in all the models to facilitate formation of REE-Cl species.

	% of REE activity as Cl complexes						Proportion of REE activity as oxide and OH^- complexes					
Model	1.1	1.2	2.1	2.2	3.1	3.2	1.1	1.2	2.1	2.2	3.1	3.2
La	91.9	94.0	97.5	99.1	0	3.5E-03	6.21	4.57	0.20	0.11	100	100
Ce	63.7	70.8	93.8	97.1	1.2E-10	4.9E-04	31.7	27.0	1.89	1.09	100	100
Pr	67.0	73.6	96.1	98.2	0	1.6E-04	29.6	25.0	1.67	0.97	100	100
Nd	30.7	36.9	84.6	92.6	0	2.9E-05	65.3	61.9	6.01	4.39	100	100
Sm	10.2	13.1	64.5	79.7	0	1.7E-06	85.5	84.8	12.9	10.4	100	100
Eu	100	100	100	100	0	0	0	0	0	0	100	100
Gd	13.3	18.3	57.3	77.1	0	1.7E-06	72.4	73.9	7.40	5.32	100	100
Tb	5.04	7.65	34.4	58.8	0	7.4E-07	79.4	83.8	8.49	8.37	100	100
Dy	5.96	2.02	30.3	56.0	0	5.1E-07	69.3	83.4	5.36	5.05	100	100
Ho	7.82	6.79	31.2	56.5	0	4.7E-07	75.2	83.8	7.85	7.24	100	100
Er	1.06	1.47	16.4	34.7	0	0	89.1	93.3	12.3	13.6	100	100
Tm	1.30	1.80	3.72	36.0	0	8.4E-08	91.8	95.2	17.8	47.9	100	100
Yb	0.60	0.82	11.2	26.7	0	0	93.4	97.2	20.5	24.5	100	100
Lu	0.18	0.25	3.01	6.51	0	0	88.7	94.1	14.0	30.7	100	100
	% of REE activity as F complexes						Proportion of REE activity as SO_4 complexes					
Model	1.1	1.2	2.1	2.2	3.1	3.2	1.1	1.2	2.1	2.2	3.1	3.2
La	1.85	1.38	1.94	0.74	2.3E-08	0	0	0	0.38	0.10	3.3E-09	1.5E-04
Ce	4.54	2.21	4.28	1.76	3.1E-09	7.9E-10	0	0	0	0	0	0
Pr	3.44	1.42	2.19	0.83	4.2E-10	0	0	0	0	0	0	0
Nd	4.02	1.20	5.76	2.00	1.5E-10	1.2E-10	0	0	3.59	1.04	7.5E-11	1.3E-05
Sm	4.34	2.09	18.4	8.57	1.9E-11	0	0	0	4.17	1.34	6.5E-12	1.4E-06
Eu	0	0	0	0	0	0	0	0	0	0	0	0
Gd	14.3	7.77	35.3	17.5	7.5E-11	2.9E-10	0	0	0	0	0	0
Tb	15.5	8.60	53.8	32.8	8.5E-11	4.4E-10	0	0	3.38	0	2.9E-12	0
Dy	24.7	14.6	62.7	38.9	1.1E-10	3.5E-10	0	0	1.73	0	1.7E-12	0
Ho	17.0	9.41	59.2	36.3	8.6E-11	1.1E-10	0	0	1.76	0	1.5E-12	0
Er	9.81	5.19	69.7	51.7	2.5E-11	7.2E-11	0	0	1.59	0	3.5E-13	7.7E-08
Tm	6.89	2.96	74.2	10.7	2.7E-11	8.2E-11	0	0	4.32	5.34	4.0E-13	8.7E-08
Yb	5.96	1.96	66.6	48.8	1.7E-11	5.5E-10	0	0	1.69	0	3.5E-13	7.7E-08
Lu	11.1	5.68	82.3	62.8	3.1E-11	1.2E-10	0	0	0.68	0	0	2.8E-08

Table 6.3: Percentages of REE activity represented within the model fluids as various complexes. Chloride complexes dominate LREE speciation in models 1.1 and 1.2. This proportion increases within models 2.1 and 2.2, in which Cl complexes increasingly represent all REE. Models 3.1 and 3.2 are entirely dominated by oxide and hydroxide species. REE-SO_4 species are absent in most models and only minor constituents in models that assume very high SO_4 concentrations (~2 wt.%).

Within all models chosen, with the exceptions of 3.1 and 3.2, REE-F species account for a portion of each REE's activity. This is particularly true in the case of models 2.1 and 2.2 where a major proportion of HREE activity is represented by these complexes. In comparison to models 1.1 and 1.2 where these species are carried largely by oxide and hydroxide species, the transition to lower pH conditions would inhibit the crystallization of F as fluorite and increase its availability for REE complexing (Migdisov et al., 2016).

In all cases, the majority of HREE activity is represented by low-solubility F-, oxide- and hydroxide-complexes, all of which are considered highly immobile (Migdisov et al., 2016). This may explain the much smaller variability that these elements exhibit compared to LREE with respect to both REE-signatures and absolute concentrations.

The significant variability in REE speciation present in models 1.1, 1.2, 2.1 and 2.2 are lacking in models 3.1 and 3.2, in which all REE species are dominated by oxide and hydroxide species. This suggests that the unusual MREE-enriched signature of this apatite cannot be explained in terms of solubility and stability discrepancies between the REE. Given the relative lack of co-crystallizing LREE-enriched species within these samples, except for very minor florencite, it could be reasonable to suggest that the fluids from which this apatite formed were already slightly MREE-enriched and that the preferential partitioning of REE closest to the Sm-Gd range into apatite (Pan and Fleet, 2002) led to further MREE-enrichment as was suggested for scheelite under similar conditions (Brugger et al., 2000). Crucially, within these models, Eu is present as the trivalent species EuO_2^-, a form much more easily incorporated into apatite compared to the $EuCl_4^{2-}$ species present within the other models. Given that the di- vs. trivalent speciation of Eu is primarily controlled by pH in hydrothermal systems (Brugger et al., 2008), the presence of a positive Eu anomaly in the *massive bornite hosted apatite* can be readily attributed to crystallization under pH conditions significantly

higher than those proposed for the other apatites, which display negative Eu anomalies. Moreover, Brugger et al. (2008) noted that transition of $EuCl_4^{2-}$ to EuO_2^- is very sensitive to Cl activity, as shown in Figure 6.2. This suggests that lower salinity, in addition to higher pH, was responsible for formations of this apatite.

6.4.2 REE-mobility in IOCG systems

Modeling of REE partitioning between apatite and fluid along with the consideration of REE-speciation in fluid during formation of various hydrothermal assemblages within Olympic Dam offers valuable insights into the transport and deposition of REE within the deposit. It is apparent that REE transport was primarily facilitated by REE-Cl complexes due to their high solubility and dominance (at least for LREE) in both early magnetite-stable and later hematite-stable ore-forming fluids. Such a scenario is concordant with the findings of van Dongen et al. (2010) in their studies of REE behavior within porphyry Cu-Au mineralization and with arguments put forward by Migdisov et al. (2016). The latter authors also emphasized the importance of SO_4 complexes for REE transport This is, however, found to have been negligible at Olympic Dam due to the very low activity of REE-SO_4 complexes under all conditions considered, even at high SO_4 concentrations (e.g., models 3.1 and 3.2).

Despite the mobility of REE during formation of both magnetite- and hematite-dominant mineralization, the latter appears to have made a much more considerable contribution to the overall enrichment of the deposit in REE. Specifically, pervasive sericite alteration results in the destruction of feldspars and apatite (Krneta et al., 2016, Kontonikas-Charos et al., 2017), liberating significant volumes of REE (as these minerals account for most of the REE budget within the RDG and other intrusive rocks) under conditions exceptionally well suited for their transport. Such a coupled process of REE liberation and transport could account for a portion of the elevated REE concentrations within the deposit. Moreover, the significantly higher

enrichment in LREE is easily explained through such a model given their dominance as REE-Cl complexes within fluids causing hematite-sericite alteration.

Within the deposit, REE are dominantly hosted in the REE-fluorocarbonate mineral bastnäsite ($REECO_3F$), in florencite, with subordinate amounts within synchysite, crandallite-group phases, xenotime and monazite (Ehrig et al., 2012, Schmandt et al., 2017). All these minerals contain P, F and/or CO_3, supporting the hypothesis that deposition of REE was achieved via a weakening of REE-Cl activity and subsequent REE complexation with the aforementioned species. Further modeling is required to precisely determine under which parameters REE deposition occurred.

The modeling outlined here successfully reproduces the measured REE fractionation in apatite from Olympic Dam and satellite prospects in the region. This not only highlights that the observed trends can be efficiently and plausibly explained in terms of IOCG fluid evolution, but also that these trends are rooted in constrainable regional-scale phenomena. These in turn carry significance for understanding formation of large IOCG deposits, and may assist refinement of genetic models essential for successful mineral exploration.

Acknowledgments

This work is supported by BHP Olympic Dam. We gratefully acknowledge microanalytical assistance from the staff at Adelaide Microscopy, notably Ben Wade. N.J.C. and K.E. acknowledge support from the ARC Research Hub for Australian Copper–Uranium. CLC acknowledges support from the ‘FOX’ project (Trace elements in iron oxides), supported by BHP Olympic Dam and the South Australian Mining and Petroleum Services Centre of Excellence.

Supplementary materials

Appendix A- Numerical modeling input values and results (models 1.1-3.2). The $a_{(aq)}$ total values represents the sum of activity for a particular element. In the case of Ca and Na these are commonly represented by a single species whereas the $a_{(aq)}$ total values in the case of the REE are represented by multiple complexes. The fluid REE concentrations used to calculate the model apatite are equivalent to the whole rock values for the respective models.

References

Baker, T., Mustard, R., Fu, B., Williams, P.J., Dong, G., Fisher, L., Mark, G. and Ryan, C.G., 2008. Mixed messages in iron oxide-copper-gold systems of the Cloncurry district, Australia: insights from PIXE analysis of halogens and copper in fluid inclusions. Mineralium Deposita 43, 599-608.

Bastrakov, E.N., Skirrow, R.G. and Davidson, G.J., 2007. Fluid evolution and origins of iron oxide Cu-Au prospects in the Olympic Dam District, Gawler Craton, South Australia. Economic Geology 102, 1415-1440.

Bau, M., 1991. Rare-earth element mobility during hydrothermal and metamorphic fluid-rock interaction and the significance of the oxidation state of europium. Chemical Geology 93, 219-230.

Belousova, E.A., Walters, S., Griffin, W.L. and O'Reilly, S.Y., 2001. Trace-element signatures of apatites in granitoids from the Mt Isa Inlier, northwestern Queensland. Australian Journal of Earth Sciences 48, 603-619.

Belousova, E.A., Griffin, W.L., O'Reilly, S.Y. and Fisher, N.I. 2002. Apatite as an indicator mineral for mineral exploration: trace-element compositions and their relationship to host rock type. Journal of Geochemical Exploration 76, 45–69.

Bethke, C. and Yeakel, S., 2016. The Geochemist's Workbench® Release 11 - GWB Essentials Guide. https://www.gwb.com/pdf/GWB11/GWBessentials.pdf

BHP, 2016. http://www.bhp.com/-/media/bhp/documents/investors/annual-reports/2016/bhpbillitonannualreport2016.pdf?la=en

Brugger, J., Lahaye, Y., Costa, S., Lambert, D. and Bateman, R. 2000. Inhomogenous distribution of REE in scheelite and dynamics of Archean hydrothermal systems (Mt. Charlotte and Drysdale gold deposits, Western Australia). Contributions to Mineralogy and Petrology 139, 251-264.

Brugger, J., Etschmann, B., Pownceby, M., Liu, W., Grundler, P. and Brewe, D., 2008. Oxidation state of europium in scheelite: Tracking fluid-rock interaction in gold deposits. Chemical Geology 257, 26-33.

Cao, M., Li, G., Qin, K., Seitmuratova, E.Y. and Liu, Y., 2012. Major and Trace element characteristics of apatites in granitoids from Central Kazakhstan: Implications for petrogenesis and mineralization. Resource Geology 62, 63-83.

Chiaradia, M., Banks, D., Cliff, R., Marschik, R. and de Haller, A., 2006. Origin of fluids in iron oxide–copper–gold deposits: Constraints from $\delta^{37}Cl$, $^{87}Sr/^{86}Sr$, and Cl/Br. Mineralium Deposita 41, 565–573.

Cook, N.J., Ciobanu, C.L., O'Reilly, D., Wilson, R., Das, K., Wade, B., 2013. Mineral chemistry of rare earth element (REE) mineralization, Browns Range, Western Australia. Lithos 172, 192-213.

Creaser, R.A., 1989. The geology and petrology of Middle Proterozoic felsic magmatism of the Stuart Shelf, South Australia. Unpublished Ph.D. thesis, La Trobe University, Melbourne.

Ehrig, K., McPhie, J. and Kamanetsky, V.S., 2012. Geology and mineralogical zonation of the Olympic Dam iron oxide Cu-U-Au-Ag deposit, South Australia. In: Hedenquist, J.W.,

Harris, M., Camus, F. (Eds.), Geology and Genesis of Major Copper Deposits and Districts of the World, a Tribute to Richard Sillitoe. Society of Economic Geologists Special Publication 16, 237-268.

Ehrig, K., Kamenetsky, V.S., McPhie, J., Apukhtina, O., Ciobanu, C.L., Cook, N.J., Kontonikas-Charos, A. and Krneta, S. 2017. The IOCG-IOA Olympic Dam Cu-U-Au-Ag deposit and nearby prospects, South Australia. In: Mineral Resources to Discover, Proceedings 14th SGA Biennial Meeting, Quebec, Canada, August 2017, Volume 3, p. 823-826.

Gleeson, S.A. and Smith, M.P., 2009. The sources and evolution of mineralising fluids in iron oxide–copper–gold systems, Norrbotten, Sweden: Constraints from Br/CI ratios and stable CI isotopes of fluid inclusion leachates. Geochimica et Cosmochimica Acta 73, 5658–5672.

Goldschmidt, V.M. 1937. The principles of distribution of chemical elements in minerals and rocks. The seventh Hugo Müller Lecture, delivered before the Chemical Society on March 17th, 1937. Journal of the Chemical Society (Resumed), 655-673.

Haas, J.R., Shock, E.L. and Sassani, D.C., 1995. Rare earth elements in hydrothermal systems: Estimates of standard partial molal thermodynamic properties of aqueous complexes of the rare earth elements at high pressures and temperatures. Geochimica at Cosmochimica Acta 59, 4329-4350.

Harlov, D.E., 2015. Apatite: a fingerprint for metasomatic processes. Elements 11, 171-176.

Haynes, D.W., Cross, K.C., Bills, R.T. and Reed, M.H., 1995. Olympic Dam ore genesis: a fluid-mixing model. Economic Geology 90, 281-307.

Hughes, J.M. and Rakovan, J.F., 2002. The crystal structure of apatite, $Ca_5(PO4)_3(F,OH,Cl)$. Reviews in Mineralogy and Geochemistry 48, 1-12.

Hughes, J.M. and Rakovan, J.F., 2015. Structurally robust, chemically diverse: Apatite and apatite supergroup minerals. Elements 11, 165–170.

Ismail, R., Ciobanu, C.L., Cook, N.J., Teale, G.S., Giles, D., Schmidt Mumm, A. and Wade, B., 2014. Rare earths and other trace elements in minerals from skarn assemblages, Hillside iron oxide–copper–gold deposit, Yorke Peninsula, South Australia. Lithos 184–187, 456-477.

Johnson, J.P. and Cross, K.C., 1995. U-Pb geochronological constraints on the genesis of Olympic Dam Cu-U-Au-Ag deposit, South Australia. Economic Geology 88, 1046–1063.

Kontonikas-Charos, A., Ciobanu, C.L., Cook, N.J., Ehrig, K., Krneta, S. and Kamenetsky, V.S. 2017. Feldspar evolution in the Roxby Downs Granite, host to Fe-oxide Cu-Au-(U) mineralisation at Olympic Dam, South Australia. Ore Geology Reviews 80, 838-859.

Krneta, S., Ciobanu, C.L., Cook, N.J., Ehrig, K. and Kontonikas-Charos, A., 2016. Apatite at Olympic Dam, South Australia: a petrogenetic tool. Lithos, 262, 470-485.

Krneta, S., Ciobanu, C.L., Cook, N.J., Ehrig, K. and Kontonikas-Charos, A., 2017a. The Wirrda Well and Acropolis prospects Gawler Craton, South Australia: insights into evolving fluid conditions through apatite chemistry. Journal of Geochemical Exploration 181, 276-291.

Krneta, S., Ciobanu, C.L., Cook, N.J., Ehrig, K. and Kontonikas-Charos, A. 2017b. Rare earth element behaviour in apatite from the Olympic Dam Cu-U-Au-Ag deposit, South Australia. Minerals 7(8), 135.

Mao, M., Rukhlov, A.S., Rowins, S.M., Spence, J. and Coogan, L.A., 2016. Apatite trace element compositions: A robust new tool for mineral exploration. Economic Geology 111, 1187-1222.

Migdisov, A.A. and Williams-Jones, A.E., 2014. Hydrothermal transport and deposition of the rare earth elements by fluorine-bearing aqueous liquids. Mineralium Deposita 49, 987-997.

Migdisov, A.A., Williams-Jones, A.E. and Wagner, T., 2009. An experimental study of the solubility and speciation of the Rare Earth Elements (III) in fluoride- and chloride-bearing aqueous solutions at temperatures up to 300 ^{o}C. Geochimica et Cosmochimica Acta 73, 7087-7109.

Migdisov, A.A., Williams-Jones, A.E., Brugger, J., and Caporuscio, F.A., 2016. Hydrothermal transport, deposition, and fractionation of the REE: Experimental data and thermodynamic calculations. Chemical Geology 439, 13-42.

Morales Ruano, S. Both, R.A. and Golding, S.D., 2002. A fluid inclusion and stable isotope study of the Moonta copper-gold deposits, South Australia: evidence for fluid immiscibility in a magmatic hydrothermal system. Chemical Geology 192, 211-226.

Oreskes, M. and Einaudi M.T., 1992. Origin of hydrothermal fluids at Olympic Dam: preliminary results from fluid inclusions and stable isotopes. Economic Geology 87, 64-90.

Pan, Y. and Fleet, M.E., 2002. Compositions of the apatite-group minerals: Substitution mechanisms and controlling factors. Reviews in Mineralogy and Geochemistry 48, 13-49.

Pasero, M., Kampf, A., Ferraris, C., Pekov, I.V., Rakovan, J. and White, T., 2010. Nomenclature of the apatite supergroup minerals. European Journal of Mineralogy 22, 163-179.

Reeve, J.S., Cross, K.C., Smith, R.N. and Oreskes, N., 1990. Olympic Dam copper-uranium-gold-silver deposit. In: Hughes, F.E. (ed.), Geology of the Mineral Deposits of Australia and Papua New Guinea: Australasian Institute of Mining and Metallurgy, Monograph 14, p. 1009–1035.

Rønsbo, J.G., 1989. Coupled substitutions involving REE's and Na and Si in apatites in alkaline rocks from Ilimaussaq, South Greenland, and the petrological implications. American Mineralogist 74, 896–901.

Schlegel, T.U., 2015. The Prominent Hill iron oxide-Cu-Au deposit in South Australia. A deposit formation model based on geology, geochemistry and stable isotopes and fluid inclusions. Unpublished PhD thesis, ETH Zurich, Switzerland.

Schmandt, D.S., Cook, N.J., Ciobanu, C.L., Ehrig, K., Wade, B.P. and Gilbert, S., and Kamenetsky, V.S., 2017. Rare earth element fluorocarbonate minerals from the Olympic Dam Cu-U-Au-Ag deposit, South Australia. Minerals 7 (10), 202.

Smith, M., Henderson, P., Jeffries, T., Long, J. and Williams, C., 2004. The rare earth elements and uranium in garnets from the Beinn an Dubhaich Aureole, Skye, Scotland, UK: constraints on processes in a dynamic hydrothermal system. Journal of Petrology 45, 457-484.

Teiber, H., Marks, M.A.W., Arzamastsev, A.A., Wenzel, T. and Markl, G., 2015. Compositional variation in apatite from various host rocks: clues with regards to source composition and crystallization conditions. Journal of Mineral Geochemistry 192, 151-167.

van Dongen, M., Weinberg, R.F. and Tomkins, A.G., 2010. REE-Y, Ti, and P remobilization in magmatic rocks by hydrothermal alteration during Cu-Au deposit formation. Economic Geology 105, 763-776.

van Hinsberg, V.J., Migdisov, A.A and Williams-Jones, A.E. 2010. Reading the mineral record of fluid composition from element partitioning. Geology 38, 847-850.

Weng, Z., Jowitt, S.M., Mudd, G.M. and Haque, N., 2015. A detailed assessment of global Rare Earth Element resources: opportunities and challenges. Economic Geology 110, 1925-1952.

White, T.J. and Dong, Z.L., 2002. Structural derivation and crystal chemistry of apatites. Acta Crystallographica B59, 1-16.

CHAPTER 7

CONCLUSIONS AND RECOMMENDATIONS

CHAPTER 7: CONCLUSIONS AND RECOMENDATIONS

7.1 Summary of main findings

Through their major and trace element chemistry, morphology, textures and mineral associations, the magmatic and hydrothermal apatite investigated in the course of this research have both offered significant insights into the formation and evolution of IOCG deposits in the Olympic Cu-Au province. Some broader geochemical trends confirmed here, relating to parameters such as whole rock chemistry and fluid characteristics, have been observed and reported elsewhere, albeit from contrasting geological settings (e.g., Belousova et al., 2001, 2002, Cao et al., 2012, Mao et al., 2016). Others, however, notably the association of a characteristically MREE-enriched apatite with the most intense hydrothermal activity, and apatite rich in inclusions of pyrrhotite + fluorite are described here for the first time from an IOCG deposit setting.

The hydrothermal assemblages detailed in the preceding chapters, although varying with respect to host rock, are marked by apatite with comparable chemistry wherever the host hydrothermal assemblage is sufficiently similar. Moreover, the chemistry of apatite alteration during overprinting of one particular hydrothermal assemblage by another is characterised by similar losses and gains of the same elements, irrespective of deposit/prospect, or host rock. When combined with the abundance of apatite throughout each studied ore system, these findings demonstrate the utility of apatite for fingerprinting hydrothermal assemblages, tracking metasomatic processes, and potentially acting as a spatially resolvable vector in mineral exploration.

The evolution of apatite within and surrounding the Olympic Dam IOCG deposit and nearby Wirrda Well and Acropolis prospects is outlined in the chapters of this thesis, and the role of apatite in formation of the ore systems is discussed. Beyond this, however, this research has highlighted areas in which our current understanding of both apatite ("a common mineral, yet uncommonly versatile"; Hughes and Rakovan, 2015) and its significance within the deposits and prospects of the Olympic Cu-Au Province can be further improved. The following sub-sections provide a short summary of the findings of this work and their implications, and provide some suggestions of future research avenues.

7.1.1 The evolution of apatite within IOCG mineralization

Results described in the preceding chapters were reached through careful consideration of the chemical and morphological characteristics of apatite and its relationships with other minerals. These were studied using a combination of petrographic observation, microanalysis and investigation at the nanoscale. On the basis of this work, the apatite can be classified according to its origin and associations as: 1) magmatic; 2) hydrothermal (magnetite-dominant assemblage); 3) hydrothermal (hematite-sericite associated); and 4) late hydrothermal. The evolution of apatite within the Olympic Dam deposit is graphically illustrated in Figure 1, whereas that of apatite from the Wirrda Well and Acropolis prospects in shown in Figure 2.

These four apatite types are expressed within all three study cases with varying abundance, and are representative of the distinct spatial and temporal evolution of IOCG-type systems in South Australia. Commonly, however, an individual hydrothermal event undergone by one part of a deposit may be expressed as a new generation of apatite whereas the same event might be recorded elsewhere as distinct chemical domains formed by the overprinting of an earlier generation of apatite. Nevertheless, as these mineralised systems evolve, apatite

becomes a decreasingly abundant component of the various hydrothermal assemblages, primarily through obliteration during hematite-sericite alteration of the host. Moreover, its significance as a repository for a range of different trace elements becomes reduced in the course of evolution from magmatic to late hydrothermal types.

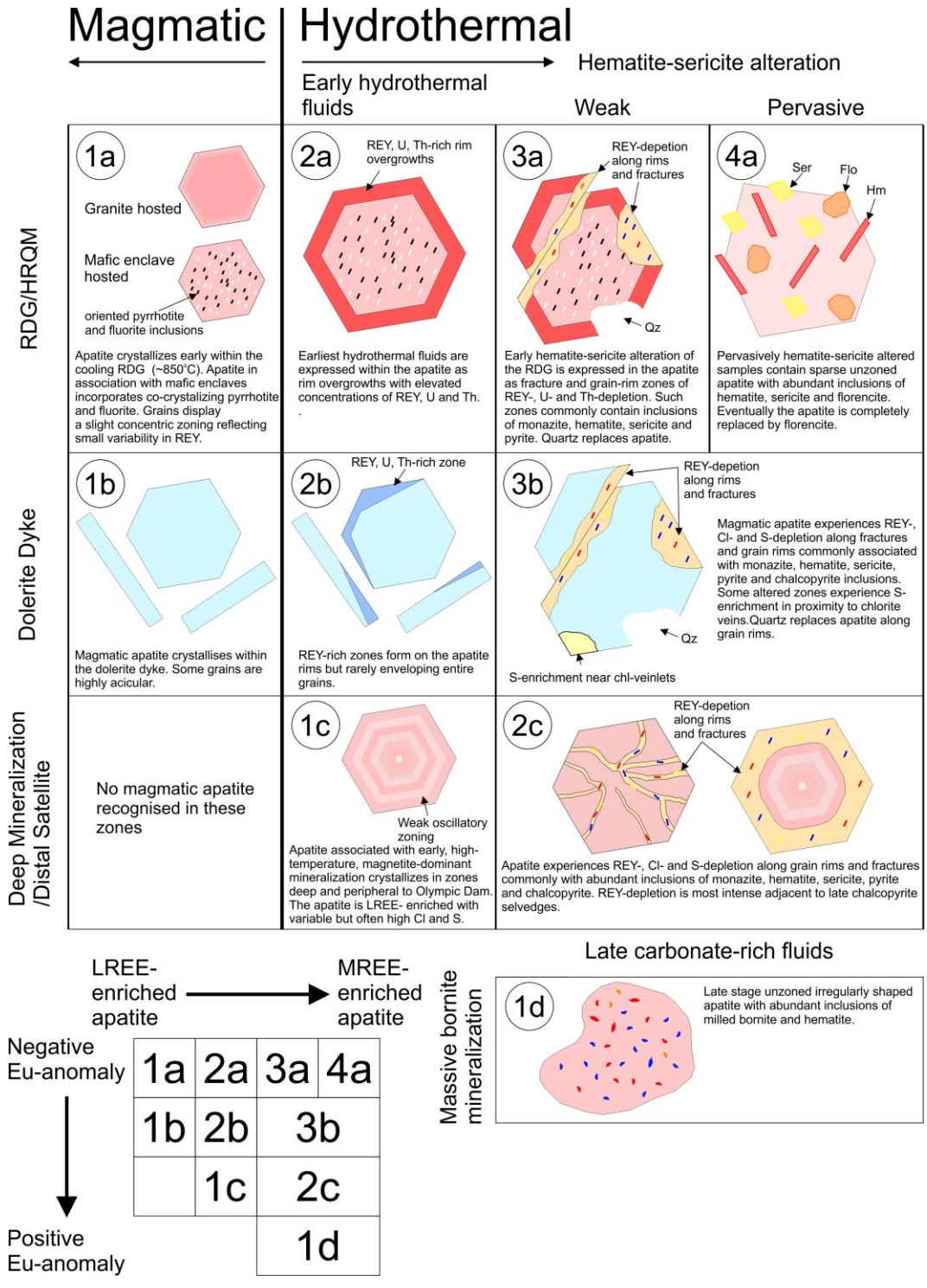

Figure 7.1- Schematic illustrating apatite evolution in different rocks within the Olympic Dam ore environment with particular emphasis on the effects of various alteration assemblages. Abbreviations: Flo-florencite; Hm-hematite; Qz-quartz; Ser-sericite.

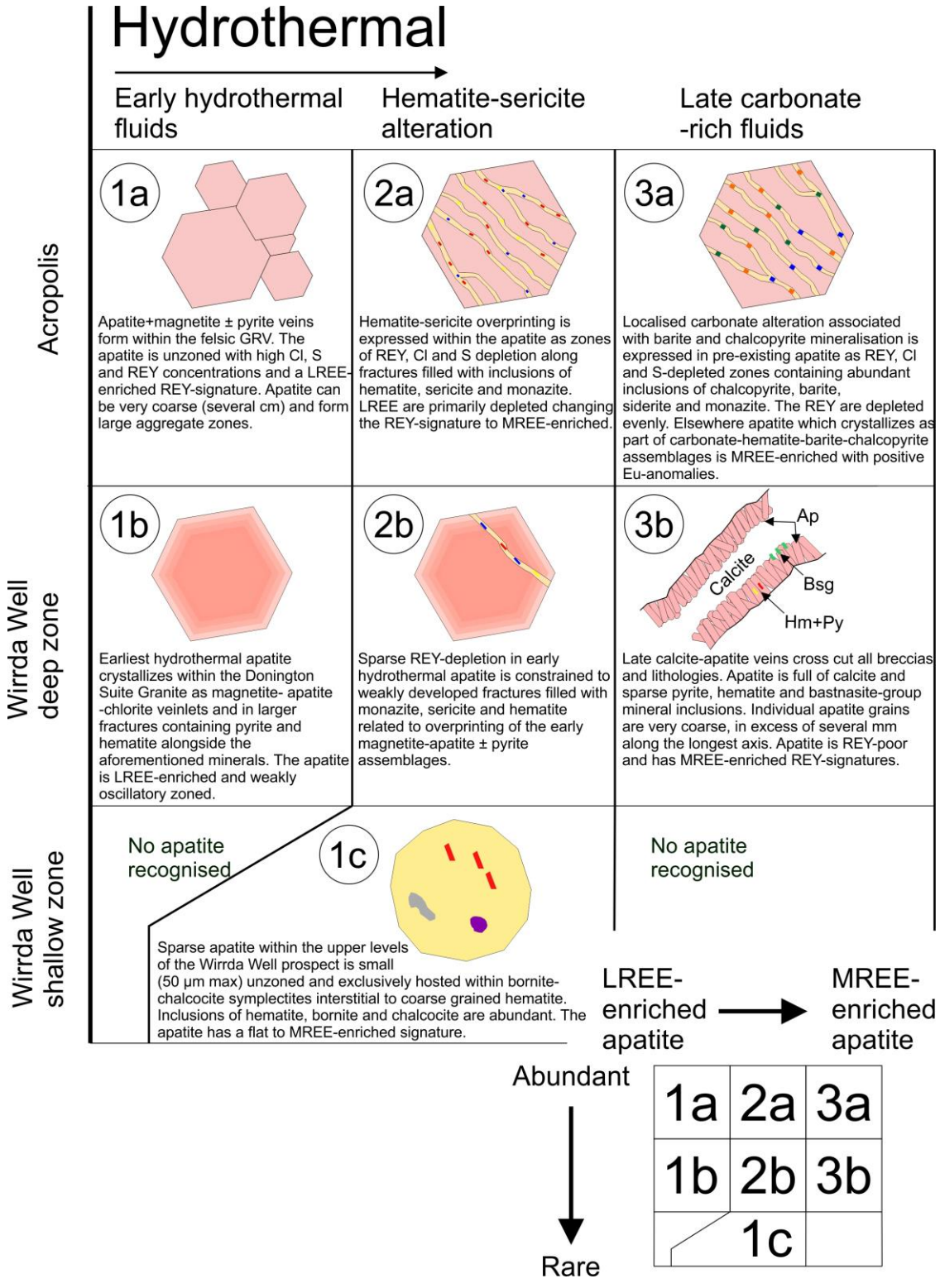

Figure 7.2- Schematic illustrating apatite evolution in rocks critical to the ore environment within the Acropolis and Wirrda Well prospects. Particular emphasis is given to the effects of various alteration assemblages. Abbreviations: Ap-apatite; Bsg-fluorocarbonate minerals of the bastnäsite group; Hm-hematite; Py-pyrite.

Group 1- Magmatic apatite

The earliest generation of apatite encountered within the study area are magmatic grains associated with ~1.6 Ga intrusive rocks such as the Roxby Downs Granite (RDG), Hornridge Quartz Monzonite (HRQM) and dolerite dyke (DD; Creaser, 1989, Jagodinski et al., 2005, Huang et al., 2016). Wherever these rocks are unaffected by hydrothermal alteration, the contained apatite primarily reflects the composition and magmatic history of the host rock.

All apatites in these rocks are fluorapatite with variable concentrations of Cl and (calculated) OH^-. Chlorine concentrations are highest in the DD, lesser in the HRQM and lowest in the RDG apatite, where they are commonly below the minimum limit of detection by electron microprobe. Such halogen concentrations are in agreement with apatite from intrusive rocks with similar whole rock compositions (Webster and Piccoli, 2015). Similarly, the concentrations of other minor and trace elements, including REY, are concordant with well-established and documented trends since these relate to, and are controlled by whole rock chemistry (Cao et al., 2012, Teiber et al., 2015, Mao et al., 2016).

With a few exceptions, apatite in these intrusive rocks is always equant with low aspect ratios, a characteristic indicative of crystallisation within a slowly cooling intrusive (Piccoli and Candela, 2002). The highly acicular grains encountered within the DD and the mafic enclaves of the RDG stand out however. Such morphology is commonly interpreted as the product of rapid crystallisation under conditions of undercooling brought about by the intrusion of hot magmas into cool host rocks, or by magma mixing (Reid et al., 1983, Holden et al., 1987,

Bargossi et al., 1999, Sha, 1995), supporting an interpretation in which the RDG-hosted mafic enclaves represent foreign material (Krneta et al., 2016, Chapters 2 and 5). Further evidence supporting this interpretation can be observed in the tendency for mafic enclave hosted apatite to contain cores containing abundant, oriented, elongate pyrrhotite + fluorite inclusions (Krneta et al., 2016, Chapters 2 and 5), commonly observed in mafic rocks (Xing and Wang, 2017) but rarer in granites (Gottesman and Wirth, 1997). Given the widespread nature of the mafic enclaves and the strong lines of evidence for their external mafic origin, we can conclude that the RDG experienced significant interaction with mafic rocks. Such an observation supports the assertion of Groves et al. (2010) that magma mixing and metal + volatile exchange are critical to the formation of IOCG deposits.

Group 2- Magnetite-dominant assemblage associated

This variety of apatite is prolific throughout the magnetite-dominant mineralization confined to the lateral and vertical peripheries of the Olympic Dam deposit, the Wirrda Well prospect, and throughout the Acropolis mineralization. In cases where the apatite is unaffected by later overprinting, grains are inclusion-free and display only weak oscillatory zoning. ΣREY-concentrations and chondrite-normalized REY-signatures are comparable to those of magmatic RDG-hosted apatite, although S- and Cl-concentrations can be significantly higher, as is the case in deep and distal satellite mineralization of Olympic Dam (Krneta et al., 2016, Chapter 2). This variability most probably reflects slight localized variations in Cl and S activity. Moreover, the higher Na and S concentrations observed in some apatite within the Distal satellite mineralization are indicative of the effects of albitization which is preserved within this mineralization (Kontonikas-Charos et al., 2017a).

Magnetite-dominant assemblage associated apatite is extremely well represented within the vein and breccia mineralization of the Acropolis prospect (Krneta et al., 2017b) where it

resembles, both chemically and morphologically, the apatite within Iron Oxide Apatite (IOA) type deposits (Harlov et al., 2002, Bonyadi et al., 2011, Day et al., 2016). By way of comparison, the hydrothermal conditions which prevailed during formation of this apatite more closely resemble those of IOA deposits than the hematite-dominant mineralization hosting Cu-U-Au-Ag ore at Olympic Dam. This was recently pointed out by Ehrig et al. (2017), who sought to link IOCG- and IOA-style mineralization across the broader region surrounding Olympic Dam.

Group 3- Hematite-sericite associated

Both Group 1 and 2 apatite display a significant overprint by fluids responsible for hematite-sericite alteration within the Olympic Dam deposit and Acropolis prosects but this is less marked in Wirrda Well. The overprint is expressed by a depletion of a variety of elements along grain rims and fractures. REY (most commonly LREE), as well as Cl, S, U and Th, are depleted along such zones, which are also characterised by the presence of hematite, sericite and monazite inclusions. Unlike the sericite and hematite whose origin is considered external to the apatite, the monazite inclusions are formed by incorporation of REY liberated from apatite via coupled dissolution reprecipitation reaction, as proposed by Harlov et al. (2002).

This mechanisms for the formation of monazite inclusions in apatite has been recognised elsewhere and this is considered characteristic of IOA mineralization (Bonyadi et al., 2011). Synchronous with the depletion of the aforementioned elements are increases in Ca, P, F, and locally also of As, within the apatite. Arsenic enrichment is considered particularly instructive with regards to the overprinting hematite-sericite assemblage due to the associations of higher fO_2 conditions and the presence of As in the 5+ valance state, which is most easily and directly incorporated into apatite (Perseil et al., 2000, Mao et al., 2016).

Elsewhere within the studied mineralization, hematite-sericite alteration is expressed as a new generation of apatite grains with significantly weakened negative Eu-anomalies and MREE-enriched REY-signatures when compared to Group 1 and 2 apatite. In the case of pervasively altered RDG these apatite grains are rich with inclusions of hematite and sericite, as well as florencite, which eventually replace the apatite entirely.

Within the shallow zone of the Wirrda Well prospect (Krneta et al., 2017b, Chapter 4) Group 3 apatite is represented by small unzoned grains hosted in bornite-chalcocite symplectites interstitial to coarse hematite. Apatite crystallisation is coeval with that of the symplectites and lies temporally between two hematite crystallisation events. The apatite contains abundant inclusions of hematite, bornite and chalcocite. REY-signatures are characteristically MREE-enriched with weak negative Eu- and Y-anomalies.

Group 4- Late hydrothermal

This group of apatite are the expressions of late, volumetrically limited but spatially widespread fluid pulses responsible for the formation of (in the case of Olympic Dam) small zones of massive high-grade bornite mineralization. This apatite commonly contains abundant inclusions of milled fragments of bornite, hematite and very rare florencite. REY-signatures stand in stark contrast to those of the LREE-enriched Group 1 and 2 apatite and are extremely MREE-enriched with strong positive Eu-anomalies (Krneta et al., 2017a, Chapter 3). Similarly, apatite formed as part of carbonate-barite-apatite-chalcopyrite assemblages within the Acropolis prospect displays the same distinctive signature with MREE-enrichment and a strong positive Eu-anomaly (Krneta et al., 2017b, Chapter 4).

7.1.2 Apatite and the evolution of hydrothermal fluids

The evolving character of hydrothermal fluids within IOCG deposits of the Olympic Cu-Au province are best expressed by the transition from early and peripheral magnetite- to later and central hematite-dominant mineralization. Empirically, this transition has been shown to correspond to radical changes in multiple fluid parameters (temperature, pH, salinity) (Oreskes and Einaudi, 1992, Bastrakov et al., 2007). Several authors have speculated as to the causes of this transition, invoking various processes such as fluid mixing into the multiple proposed formation mechanisms (Hitzman et al., 1992, Haynes et al., 1995, Pollard, 2006, Groves et al., 2010). However, regardless of the mechanism involved, the preceding chapters show that the changing apatite REY-signatures are the direct result of this transition. In detail, the change in fluid characteristics impacts apatite REY-signatures by:

- An increased proportion of the LREE speciating as stable and soluble REY-Cl complexes in hematite-sericite altering fluids. This results in their partitioning away from the apatite creating MREE-enriched signatures. This is manifested by the liberation of LREE from pre-existing apatite and re-deposition of the REE within newly formed grains of monazite.
- Increasing the proportion of Eu in the fluid with regards to the other REY through the alteration of feldspars. This results in the weakening of the negative Eu-anomalies in hematite-sericite alteration associated apatite.
- Changing the dominance of Eu species from Eu^{2+} to Eu^{3+} in apatite associated with late stage alkaline CO_2 - HCO_3^- buffered fluids resulting in the crystallisation of apatite with positive Eu-anomalies.

7.1.3 Apatite trace element contributions to REY concentrations in IOCG mineralization

In the mineralized systems examined as part of this work, magmatic and paragenetically early hydrothermal apatite (Group 1 and 2) contain much higher concentrations of impurity elements (REY, U, Th) than later Group 3 and 4 grains. Such a contrast emphasises the evolving role of apatite as a host for trace elements within IOCG mineralization. This evolution is primarily attributed to the co-partitioning of trace elements between apatite and other phases in later Group 3 and 4 types (Krneta et al., 2016, 2017a, b, Chapters 2, 3 and 4), and the ability of the hydrothermal fluids responsible for hematite-sericite alteration to alter pre-existing apatite. This results in element release and remobilization of trace elements away from the apatite to form new species.

In the case of Olympic Dam, hematite-sericite alteration affects a huge volume of rocks hosting Group 1 and 2 apatite, ultimately leading to their obliteration. This process warrants consideration in terms of the genetic models of IOCG formation as the destruction of so much apatite and feldspar may contribute to the REY budget, which was subsequently incorporated within the developing IOCG mineralization (Kontonikas-Charos et al., 2017b, Krneta et al., 2017a, Chapter 3).

According to the speculative calculations of Weng et al. (2015), the Olympic Dam deposit contains an approximate 53 million tonnes of contained La + Ce at concentrations of 1,705 and 2,561 ppm, respectively. Comparatively, unaltered RDG contains an average of approximately 100 ppm La and 200 ppm Ce (Ehrig et al., 2012). Using these concentrations along with the average La and Ce concentrations in apatite given by Krneta et al. (2017a, Chapter 3), we can calculate that apatite is host to 5.58 and 5.97 % of whole rock La and Ce, respectively in the unaltered RDG (Table 7.1). As such, total destruction of apatite within the

RDG would liberate approximately 45,000 tonnes of combined La and Ce per km^3. This amount of metal, although substantial would still require that in excess of 1,100 km^3 of RDG be altered in order to account for the 53 million tonnes of combined La + Ce in the Olympic Dam deposit. The calculations thus suggest that the destruction of apatite may have made some contribution to the overall REY-budget, but cannot account for all of it.

Despite the RDG feldspars having much lower REY-concentrations, their very high modal abundance make them more substantial carriers of REY within the RDG than apatite. Combining the La + Ce liberated through apatite and feldspar destruction during hematite-sericite alteration, the volume of RDG required to account for the La + Ce budget at Olympic Dams is substantially reduced.

Lithology	Mean density (g/cm^3)	Mean P (wt. %)	Mean kg apatite /tonne	Mean kg La in apatite/tonne	Mean kg Ce in apatite/tonne
RDG	2.64	0.03	1.67	0.0055	0.0116
	% of whole rock La in apatite	% of whole rock Ce in apatite	Tonnes of La in apatite/km^3	Tonnes of Ce in apatite/km^3	
	5.58	5.97	14592	30708	

Table 7.1. Calculated concentrations of Ce and La hosted in apatite within the unaltered RDG.

7.2 Research gaps and future work

Although comprehensive in many ways, this body of work has highlighted several avenues in which additional research may offer more comprehensive insights into the formation of IOCG deposits along with providing an affirmation of the findings presented here. The established associations between apatite and particular intrusive rocks, or hydrothermal assemblages can be further exploited through the study of stable isotopes (Cl and Sr), and the determination of oxidation states of some elements within the apatite (notably Eu). The assessment of various types of apatite through methods such as cathodoluminescence responses could (as was

shown by Bouzari et al., 2016) offer a practical means of classifying apatite and enable its use in exploration as a pathfinder mineral without the need for expensive and time-consuming microanalytical work.

This research has highlighted several geochemical and morphological trends in apatite which are intimately associated with distinct processes associated with IOCG mineralization. This suggests, in turn, that their occurrence is not restricted to the studied systems but is instead widespread throughout the Olympic Cu-Au Province. Testing this hypothesis would require the study of other deposits throughout the Province, such as Carrapateena, Prominent Hill and Cairn Hill (in which apatite is particularly abundant), as well as the many nearby prospects in various stages of exploration. Further study might focus on expressions of IOCG mineralization within calc-silicate horizons of the Wallaroo Group, such as Groundhog (Reid et al., 2011) and mineralization encountered within drillhole SAR9.

Although some detailed studies have been done on apatite from IOA deposits of Sweden and Iran (Harlov et al., 2002, Bonyadi et al., 2011), there exists considerable opportunity for study of apatite from IOCG deposits *sensu stricto*. Such studies should be considered particularly important given that some preliminary results of apatite chemistry from other deposits appear contradictory or at odds with the findings of the research presented herein. For example, the published compositional data for hydrothermal apatite hosted in the Ernest Henry IOCG deposit, Mt. Isa Inlier, Queensland, shows these grains to be extremely As-rich (up to 5 wt. %; Rusk et al., 2010, Liu et al., 2017). Such high As-concentrations are extremely anomalous not only when compared to apatite hosted within the Olympic Dam, Wirrda Well and Acropolis mineralised systems but globally as well, suggesting either significantly different hydrothermal conditions or the increased presence of As within the hydrothermal fluids,

possibly sourced from the alteration of sedimentary secessions, which commonly concentrate As, as suggested by Mao et al. (2016).

7.2.1 XANES studies of apatite

The strength of chondrite-normalized Eu anomalies in apatite are critical to the understanding of the dominant physiochemical conditions during apatite crystallization. However, due to the ability of apatite to incorporate the element in both 2+ and 3+ states unequivocally resolving the cause of Eu-anomaly fluctuations requires the determination of Eu^{2+} and Eu^{3+} concentrations within apatite. The Eu^{2+}/Eu^{3+} ratio in apatite has been successfully measured using X-ray absorption near-edge structure (XANES) analysis (Rakovan et al., 2001, Takahashi et al., 2005), a method which has the capacity to resolve the spectra of the two Eu species (Figure 7.3) even when concentrations are only on the order of several tens of ppm, making the method suitable for analysis of the apatite presented in this research (Krneta et al., 2017a, b, Chapter 3, 4).

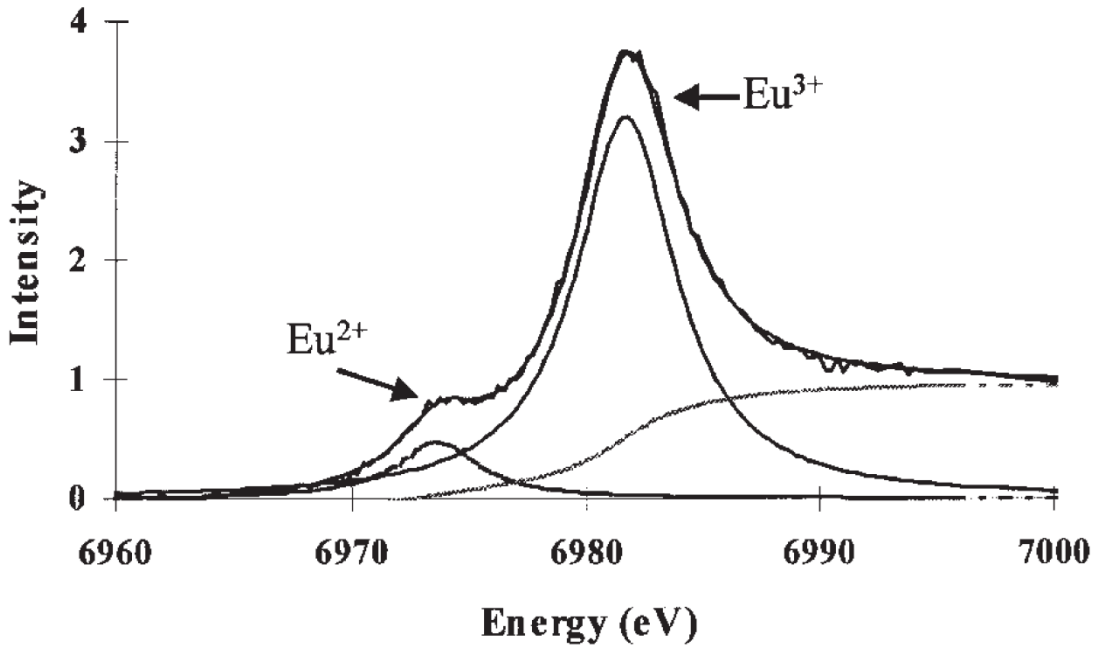

Figure 7.3- Characteristic XANES spectra for europium species, after Rakovan et al. (2001)

Changes in the strength of the Eu-anomaly in apatite can be brought about by either varying the proportions of Eu^{3+} to Eu^{2+} in the fluid (Brugger et al., 2008), or through disproportionately large increases of Eu over the remainder of the REE (Mao et al., 2016). Given that the modelling of REY-speciation during the transition from magnetite-dominant to hematite-sericite alteration did not indicate any changes in the proportion of Eu^{2+} to Eu^{3+} (Chapter 6), the observed weakening of the negative Eu anomaly was most likely caused by the introduction of large amounts of Eu into the fluid through feldspar alteration.

Therefore, XANES analysis is recommended as a means of testing this hypothesis as the implications are wide-reaching. Namely, the sericitization of feldspars is not only found in IOCG deposits but others such as Porphyry Cu-Au and Orogenic Au deposits as well.

7.2.2 Chlorine isotopes in apatite

Several studies have sought to determine the source(s) of mineralizing fluids in IOCG deposits through the use of halogen ratios such as Br/Cl, and I/Cl, as well as the measurement of Cl isotopes (Chiaradia et al., 2006, Kendrick et al., 2008, Fisher and Kendrick, 2008, Gleeson and Smith, 2009, Williams et al., 2010). These studies have shown that multiple signatures, including those of magmatic, metamorphic and basinal fluids may be present in IOCG systems globally. The incorporation of Cl, Br and I in apatite is non-ideal and as such does not reflect the concentrations of these elements in hydrothermal fluids (Hughes et al., 2014). However, the isotopic composition of Cl in apatite can be considered as representative of the isotopic signature of the hydrothermal fluids (Chiaradia et al., 2006).

The study of Cl isotopes in the geological environment is very much in its infancy if compared to other isotopic systems (Barnes et al., 2017). On the basis of Cl isotopic compositions, the World's Cl-reservoirs can be separated into the crustal (dominated by the oceans and evaporites) and the mantle (Gleeson and Smith, 2009). Although both display

internal heterogeneities resulting from the localised effects of processes such as kinetic fractionation (Sharp et al., 2010, Barnes et al., 2017), crustal values fall, for the most part, within the range of $\delta^{37}Cl$ = 0.0‰ ± +0.9‰. Conversely, the mantle represents a significant although highly heterogeneous source of negative Cl isotopic compositions (Gleeson and Smith, 2009). The study of fluid provenance in hydrothermal systems exploits this discrepancy and assumes the transference of the fluid isotopic signature into the crystallising hydrothermal mineral that incorporates Cl.

Given the ability of apatite to host Cl, often in high concentrations, direct measurement of Cl isotopes in apatite is recommended as it can offer insights into the source of fluids responsible for the formation of a particular hydrothermal assemblage. The measurement of several different apatite from distinct hydrothermal assemblages can be used as a means of gaining insights into how the sources of these fluids evolve. Measurement should be performed using either thermal ionization mass spectrometry (TIMS) or Laser ablation inductively coupled plasma mass spectrometry (LA–ICP–MS). However, with regards to the latter significant effort may need to be invested in developing a suitable method as the use of LA–ICP–MS with regards to Cl-isotopes is in its infancy (Barnes et al., 2017).

Similarly, some authors have drawn connections between world class IOCG deposits and mantle-derived Cl isotopic signatures (e.g., Chiaradia et al., 2006) suggesting that the development of an early stage prospect prioritisation tool could be developed using Cl isotopes in apatite.

7.2.3 Fluid inclusion studies

The Olympic Dam deposit along with other examples of IOCG mineralization in the Olympic Cu-Au province are relatively poorly studied with regards to fluid inclusions (Oreskes and

Einaudi, 1992, Morales Ruano et al., 2002, Bastrakov et al., 2007, Ismail et al., 2014, Schlegel, 2015). Given the global significance of Olympic Dam as a supergiant orebody hosting a huge portion of the worlds defined uranium reserves (BHP, 2016), this may seem surprising but needs to be viewed in the context of the brecciation, mineralogical complexity, fine grain size and evidence for extensive overprinting since initial formation which may hamper interpretation. As such the character of the mineralizing fluids is somewhat poorly defined.

Given that Olympic Dam is a huge and extremely varied orebody which experienced several episodes of overprinting (e.g., Ciobanu et al., 2013; Apukhtina et al., 2017), the study of fluid inclusions spaning the deposit vertically, laterally and through time could offer a clearer picture of fluid evolution during the main ~1.6 Ga event along with characterising the nature of subsequent overprints. Very little is known about the later overprinting fluids but given that there is strong evidence for their involvement in the redistribution and potentially introduction of some of the U in the deposit (Kirchenbaur et al., 2016), further study is warranted.

As such an exhaustive campaign of fluid inclusion work is recommended, focusing not only on inclusions in quartz but other minerals such as feldspars and apatite, and potentially also in opaque phases such as Fe-oxides using an infra-red light source. The direct measurement of fluid inclusions in apatite in particular could provide the most accurate data (homogenization temperatures and salinities) for use in the modelling of REY-behaviour.

In concert with traditional microthermometry such fluid inclusion studies might take advantage of techniques such as Laser Raman spectroscopy as a means of determining the composition of vapour and liquid phases (e.g., Zhong et al., 2017). The trace element compositions of the fluid inclusions could be determined using the leachate method or by proton ion probe (PIXE) microanalysis, both of which have proven very useful in determining

the concentrations of elements such as Br and I and in study of Cl-isotopes (e.g., Gleeson and Smith, 2009). These elements, and particularly their ratios (Br/Cl, I/Cl), should be studied across the various hydrothermal assemblages as they are expected to evolve in response to the postulated processes of fluid mixing.

7.3 Exploration implications

The use of apatite as a pathfinder mineral is a topic of increasing research due to its: 1) abundance, 2) resitate nature and 3) ability to chemically fingerprint a target lithology (Kelley et al., 2011, Hashmi et al., 2015). The apatite studied as part of this research has been shown to fulfil all three requirements, as is the case with apatite hosted in a range of other deposit types (Belusova et al., 2001, 2002, Cao et al., 2012, Mao et al., 2016).

Globally, research examining the use of apatite as a mineral pathfinder has been most strongly focused on Cu-Au-porphyry type deposits in North America (e.g., Averill, 2011, Kelley et al., 2011, Hashmi et al., 2015, Bouzari et al., 2016). This is largely attributable to the favourable combination of a deposit type with extensive alteration haloes coupled with the presence of a suitable sampling medium in the form of widespread glacial sediments. Despite this near ideal combination, results have been variably successful, particularly in instances where the concentrations of apatite have been used in isolation without any characterisation using microanalytical analysis (e.g., Kelley et al., 2011). These studies have highlighted the shortcomings of such an approach due to the potential for false positives attributable to apatite sourced from non-target lithologies.

The work of Bouzari et al. (2016) showed that cathodoluminescence (CL) was a practical means of distinguishing between ore-related and other apatite once the former had been characterised with regards to CL response.

Unlike the North American Cu-Au porphyry terrains, the Olympic Cu-Au Province poses several problems for the use of apatite as a pathfinder. Specifically, the presence of tens but more commonly hundreds of metres of barren cover restrict the collection of samples to drillcore material which can be prohibitively expensive to obtain. However, the widespread presence of suitable basal sediments in the form of Permian glacial diamictites, moraines and eskers (Alley, 1995), as well as the Mesoproterozoic fluvial red beds of the Pandurra Formation (Preiss, 1993) bode well for its effectiveness, perhaps not in exclusivity but alongside geophysically targeted exploration.

Investigating the dispersion of monazite through the glacial sediments overlying the Prominent Hill deposit, Forbes et al. (2015) found that monazite sourced from the deposit was detectable in cover several hundred meters in the interpreted down-ice direction. Similar studies of apatite would be required in order to assess its dispersion and suitability as a pathfinder.

References

Alley, N.F 1995. Late Palaeozoic. In: Drexel, J.F., Preiss, W.V. (Eds.), The Geology of South Australia. Vol. 2. The Phanerozoic, Geological Survey of South Australia, Bulletin 54, 63–92.

Apukhtina, O.B., Kamenetsky, V.S., Ehrig, K., Kamenetsky, M.B., Mass, R., McPhie, J., Ciobanu, C.L. and Cook, N.J., 2017. Deep, early mineralisation at the Olympic Dam Cu-U-Au-Ag deposit, South Australia: Economic Geology, 112 (6), 1531-1542.

Averill, S.A. 2011. Viable indicators in surficial sediments for two major base metal deposit types: Ni-Cu-PGE and Porphyry Cu. Geochemistry: Exploration, Environment, Analysis 11, 279–292.

Bargossi, G.M., Del Moro, A., Ferrari M., Gesparotto, G., Mordenti, A., Rottura, A. and Tateo, F., 1999. Caratterizzazione petrografico-geochimica e significato dell'associazione

monzogranito-inclusi femici microgranulari della Vetta di Cima d'Asta (Alpi Meridionali). Mineralogica et Petrographica Acta 42, 155–179.

Bastrakov, E.N., Skirrow, R.G., and Davidson, G.J., 2007. Fluid evolution and origins of iron oxide Cu-Au prospects in the Olympic Dam District, Gawler Craton, South Australia: Economic Geology 102, 1415–1440.

Belousova, E.A., Walters, S., Griffin, W.L. and O'Reilly, S.Y., 2001. Trace-element signatures of apatites in granitoids from the Mt Isa Inlier, northwestern Queensland. Australian Journal of Earth Sciences 48, 603–619.

Belousova, E.A., Griffin, W.L., O'Reilly, S.Y. and Fisher, N.I., 2002. Apatite as an indicator mineral for mineral exploration: trace-element compositions and their relationship to host rock type. Journal of Geochemical Exploration 76, 45–69.

BHP, 2016. http://www.bhp.com/-/media/bhp/documents/investors/annual-reports/2016/bhpbillitonannualreport2016.pdf?la=en

Bonyadi, Z., Davidson, G.J., Mehrabi, B., Meffre, S. and Ghazban, F., 2011. Significance of apatite REE depletion and monazite inclusions in the brecciated Se–Chahun iron oxide–apatite deposit, Bafq district, Iran: Insights from paragenesis and geochemistry. Chemical Geology 281, 253–269.

Bouzari, F., Hart, J.R.H., Bissig, T. and Barker, S., 2016. Hydrothermal alteration revealed by apatite luminescence and chemistry: A potential indicator mineral for exploring covered Porphyry Copper Deposits. Economic Geology 111, 1397–1410.

Brugger, J., Etschmann, B., Pownceby, M., Liu, W., Grundler, P. and Brewe, D., 2008. Oxidation state of europium in scheelite: Tracking fluid-rock interaction in gold deposits. Chemical Geology. 257, 26–33.

Cao, M., Li, G., Qin, K., Seitmuratova, E.Y. and Liu, Y., 2012. Major and Trace element characteristics of apatites in granitoids from Central Kazakhstan: Implications for petrogenesis and mineralization. Resource Geology 62, 63–83.

Chiaradia, M., Banks, D., Cliff, R., Marschik, R. and de Haller, A., 2006. Origin of fluids in iron oxide–copper–gold deposits: Constraints from $\delta^{37}Cl$, $^{87}Sr/^{86}Sr_i$, and Cl/Br. Mineralium Deposita 41, 565–573.

Ciobanu, C.L., Wade, B., Cook, N.J., Schmidt Mumm, A. and Giles, D., 2013. Uranium-bearing hematite from the Olympic Dam Cu-U-Au deposit, South Australia; a geochemical tracer and reconnaissance Pb-Pb geochronometer. Precambrian Research 238, 129–147.

Creaser, R.A., 1989. The geology and petrology of Middle Proterozoic felsic magmatism of the Stuart Shelf, South Australia. Unpublished Ph.D. thesis, La Trobe University, Melbourne.

Day, W.C., Slack, J.F., Auyso, R. and Seeger, C.M., 2016. Regional geologic and petrologic Framework for Iron Oxide ± Apatite ± Rare Earth Element and Iron Oxide Copper-Gold deposits of the Mesoproterozoic St. Francois Mountains Terrane, Southeast Missouri, USA. Economic Geology 11, 1825–1858.

Ehrig, K., McPhie, J. and Kamanetsky, V.S., 2012. Geology and mineralogical zonation of the Olympic Dam iron oxide Cu-U-Au-Ag deposit, South Australia. In: Hedenquist, J.W., Harris, M., Camus, F. (Eds.), Geology and Genesis of Major Copper Deposits and Districts of the World, a Tribute to Richard Sillitoe. Society of Economic Geologists Special Publication 16, 237–268.

Ehrig, K., Kamenetsky, V.S., McPhie, J., Apukhtina, O., Ciobanu, C.L., Cook, N.J., Kontonikas-Charos, A., and Krneta, S. 2017. The IOCG-IOA Olympic Dam Cu-U-Au-Ag deposit and nearby prospects, South Australia. In: Mineral Resources to Discover,

Proceedings 14th SGA Biennial Meeting, Quebec, Canada, August 2017, Volume 3, p. 823-826.

Fisher, L.A. and Kendrick, M.A., 2008. Metamorphic fluid origins in the Osborne Fe oxide Cu–Au deposit, Australia: Evidence from noble gases and halogens. Mineralium Deposita 43, 483–497.

Forbes, C., Giles, D., Freeman, H., Sawyer, M. and Normington, V., 2015. Glacial dispersion of hydrothermal monazite in the Prominent Hill deposit: An exploration tool. Journal of Geochemical Exploration 156, 10–33.

Gleeson, S.A. and Smith, M.P., 2009. The sources and evolution of mineralising fluids in iron oxide–copper–gold systems, Norrbotten, Sweden: Constraints from Br/CI ratios and stable CI isotopes of fluid inclusion leachates. Geochimica et Cosmochimica Acta 73, 5658–5672.

Gottesmann, B. and Wirth, R., 1997. Pyrrhotite inclusions in dark pigmented apatite from granitic rocks. European Journal of Mineralogy 9, 491–500.

Groves, D.I., Bierlein, F.P., Meinert, L.D. and Hitzman, M.W., 2010. Iron Oxide Copper-Gold (IOCG) Deposits through Earth History: Implications for origin, lithospheric setting, and distinction from other epigenetic Iron Oxide Deposits. Economic Geology 105, 641–654.

Harlov, D.E., Andersson, U.B., Förster, H-J., Nyström, J.O., Dulski, P. and Broman, C., 2002. Apatite–monazite relations in the Kiirunavaara magnetite–apatite ore, northern Sweden: Chemical Geology 191, 47–72.

Hashmi, S., Ward, B.C., Plouffe, A., Leybourne, M.I. and Ferbey, T., 2015. Geochemical and mineralogical dispersal in till from the Mount Polley Cu-Au porphyry deposit, central British Columbia, Canada. Geochemistry: Exploration, Environment, Analysis 15, 234–249.

Haynes, D.W., Cross, K.C., Bills, R.T. and Reed, M.H., 1995. Olympic Dam ore genesis: a fluid-mixing model. Economic Geology 90, 281–307.

Hitzman, M.W., Oreskes, N. and Einaudi, M.T., 1992. Geological characteristics and tectonic setting of Proterozoic iron oxide (Cu-U-Au-REE) deposits. Precambrian Research 58, 241–287.

Holden, P., Halliday, A.N. and Stephens, W.E., 1987. Neodymium and strontium isotope content of microdiorite enclaves points to mantle input to granitoid production. Nature 330, 53–56.

Huang, Q., Kamenetsky, V.S., Ehrig, K., McPhie, J., Kamenetsky, M., Cross, K., Meffre, S., Agangi, A., Chambefort, I., Direen, N.G., Maas, R. and Apukhtina, O., 2016. Olivine-phyric basalt in the Mesoproterozoic Gawler silicic large igneous province, South Australia: Examples at the Olympic Dam Iron Oxide Cu–U–Au–Ag deposit and other localities. Precambrian Research 281, 185–199.

Hughes, J.M. and Rakovan, J.F., 2015. Structurally robust, chemically diverse: Apatite and apatite supergroup minerals. Elements 11, 165–170.

Hughes, J.M., Heffernan, K.M., Goldoff, B. and Nakvasil, H. 2014. Cl-rich fluorapatite, devoid of OH, from the three peaks area, Utah: The first reported structure of natural Cl-rich fluorapatite. The Canadian Mineralogist 52, 643–652.

Ismail, R., Ye, L., Ciobanu, C.L. and Cook, N.J., 2014. The Hillside Cu-Au deposit, South Australia: A preliminary fluid inclusion study. Acta Geologica Sinca 88, 1454–1456.

Jagodzinski, E.A., 2005. Compilation of SHRIMP U-Pb Geochronological Data. Olympic Domain, Gawler Craton, South Australia, 2001-2003. Geoscience Australia, Record 2005/20.

Kelley, K.D., Eppinger, R.G., Lang, J., Smith, S.M. and Fey, D.L., 2011. Porphyry Cu indicator minerals in till as an exploration tool: example from the giant Pebble porphyry

Cu-Au-Mo deposit, Alaska, USA. Geochemistry: Exploration, Environment, Analysis 11, 321–334.

Kendrick, M.A., Honda, M., Gillen, D., Baker, T. and Phillips, D., 2008. New constraints on regional brecciation on the Wernecke Mountains, Canada, from He, Ne, Ar, Kr, Xe, Cl, Br and I. Chemical Geology 255, 33–46.

Kirchenbaur, M., Maas, R., Ehrig, K., Kamenetsky, V.S., Strub, E., Ballhaus, C. and Munker, C., 2016. Uranium and Sm isotope studies of the supergiant Olympic Dam Cu-Au-U-Ag deposit, South Australia. Geochimica et Cosmochimica Acta 180, 15–32.

Kontonikas-Charos, A., Ciobanu, C.L., Cook, N.J., Ehrig, K., Krneta, S. and Kamenetsky, V.S. 2017a. Feldspar evolution in the Roxby Downs Granite, host to Fe-oxide Cu-Au-(U) mineralisation at Olympic Dam, South Australia. Ore Geology Reviews 80, 838–859.

Kontonikas-Charos, A., Ciobanu, C.L., Cook, N.J., Ehrig, K., Ismail, R., Krneta, S. and Basak, A., 2017b. Feldspar mineralogy and rare earth element (re)mobilization in iron-oxide copper gold systems from South Australia: a nanoscale study. Mineralogical Magazine (in press). DOI: 10.1180/minmag.2017.081.040

Krneta, S., Ciobanu, C.L., Cook, N.J., Ehrig, K. and Kontonikas-Charos, A., 2016. Apatite at Olympic Dam, South Australia: a petrogenetic tool. Lithos 262, 470–485.

Krneta, S., Ciobanu, C.L., Cook, N.J., Ehrig, K. and Kontonikas-Charos, A., 2017a. The Wirrda Well and Acropolis prospects Gawler Craton, South Australia: insights into evolving fluid conditions through apatite chemistry. Journal of Geochemical Exploration 181, 276–291.

Krneta, S., Ciobanu, C.L., Cook, N.J., Ehrig, K. and Kontonikas-Charos, A. 2017b. Rare earth element behaviour in apatite from the Olympic Dam Cu-U-Au-Ag deposit, South Australia. Minerals 7(8), 135.

Liu, W., Mei, Y., Etschmann, B., Brugger, J., Pearce, M., Ryan, C.G., Borg, S., Wykes, J., Kappen, P., Paterson, D., Boesenberg, U., Garrevoet, J., Moorhead, G. and Falkenberg, G., 2017. Arsenic in hydrothermal apatite: Oxidation state, mechanism of uptake, and comparison between experiments and nature. Geochimica et Cosmochimica Acta 196, 144–159.

Mao, M., Rukhlov, A.S., Rowins, S.M., Spence, J. and Coogan, L.A., 2016. Apatite trace element compositions: A robust new tool for mineral exploration. Economic Geology 111, 1187–1222.

Morales Ruano, S. Both, R.A. and Golding, S.D., 2002. A fluid inclusion and stable isotope study of the Moonta copper-gold deposits, South Australia: evidence for fluid immiscibility in a magmatic hydrothermal system. Chemical Geology 192, 211–226.

Oreskes, M. and Einaudi M.T., 1992. Origin of hydrothermal fluids at Olympic Dam: Preliminary results from fluid inclusions and stable isotopes. Economic Geology 87, 64–90.

Perseil, E-A., Blanc, P. and Ohnenstetter, D., 2000. As-bearing fluorapatite in manganiferous deposits from St. Marcel-Praborna, Val D'aosta, Italy. Canadian Mineralogist 38, 101–117.

Piccoli, P.M. and Candela, P.A., 2002. Apatite in Igneous Systems. Reviews in Mineralogy and Geochemistry 48, 255–292.

Pollard, P.J., 2006. An intrusion-related origin for Cu–Au mineralization in iron oxide–copper–gold (IOCG) provinces. Mineralium Deposita 41, 179.

Preiss, W.V., 1993. Neoproterozoic. In: Drexel J.F., Preiss W.V., Parker A.J. (eds.), The Geology of South Australia, Volume 1, The Precambrian. Geological Survey of South Australia Bulletin 54, 170–203.

Rakovan, J., Newville, M., and Sutton, S., 2001. Evidence of heterovalent europium in zoned Llallagua apatite using wavelenght dispersive XANES. American Mineralogist 86, 697–700.

Reid, A. J., Swain, G. S. Mason, D. and Maas, R. 2011. Nature and timing of Cu-Au Zn-Pb mineralisation at Punt Hill, eastern Gawler Craton. MESA Journal 60, 7–17.

Reid, J.B. Jr., Evans, O.,C. and Fates, D.G., 1983. Magma mixing in granitic rocks of the central Sierra Nevada, California. Earth Planetary Science Letters 66, 243–261.

Rusk, B., Oliver, N., Cleverley, J., Blenkinsop, T., Zhang, D., Williams, P. and Habermann, P., 2010. Physical and chemical characteristics of the Ernest Henry iron oxide copper gold deposit, Australia; implications for IOGC genesis. Hydrothermal Iron Oxide Copper-Gold & Related Deposits: A Global Perspective - Advances in the Understanding of IOCG Deposits. Global Perspective Series, 3 (ed. T. M. Porter). PGC Publishing, Linden Park, SA, Australia pp. 201–218.

Schlegel, T.U., 2015. The Prominent Hill iron oxide-Cu-Au deposit in South Australia. A deposit formation model based on geology, geochemistry and stable isotopes and fluid inclusions. Unpublished PhD thesis, ETH Zurich, Switzerland.

Sha, L-K., 1995. Genesis of zoned hydrous ultramafic/mafic-silicic intrusive complexes: an MHFC hypothesis. Earth Science Reviews 39, 59–90.

Sharp, Z.D., Barnes, J.D., Fischer, T.P. and Halick, M., 2010. A laboratory determination of chlorine isotope fractionation in acid systems and applications to volcanic fumaroles. Geochimica et Cosmochimica Acta 74, 264–273.

Takahashi, Y., Kolonin, G.R., Shironosova, G.P., Kupriyanova, I.I., Uruga, T. and Shimizu, H., 2005. Determination of the Eu(II)/Eu(III) ratios in minerals by X-ray absorption near-edge structure (XANES) and its application to hydrothermal deposits. Mineralogical Magazine 69, 179–190.

Teiber, H., Marks, M.A.W., Arzamastsev, A.A., Wenzel, T. and Markl, G., 2015. Compositional variation in apatite from various host rocks: clues with regards to source composition and crystallization conditions. Journal of Mineral Geochemistry 192, 151–167.

Webster, J.D. and Piccoli, P.M., 2015. Magmatic apatite: a powerful, yet deceptive mineral. Elements 11, 177–182.

Weng, Z., Jowitt, S.M., Mudd, G.M. and Haque, N., 2015. A detailed assessment of global Rare Earth Element resources: opportunities and challenges. Economic Geology 110, 1925–1952.

Williams, P.J., Kendrick, M.A. and Xavier, R.P., 2010. Sources of ore fluid components in IOCG deposits. In: Porter TM (ed.) Hydrothermal Iron Oxide Copper–Gold and Related Deposits: A Global Perspective, pp. 107–116. Adelaide: PGC Publishing.

Xing, C.M. and Wang, C.Y., 2017. Cathodoluminescence images and trace element compositions of fluorapatite from the Hongge layered intrusion in SW China: A record of prolonged crystallization and overprinted fluid metasomatism. American Mineralogist 102, 1390–1401.

Zhong, J., Chen, Y-J., Qi, J-P., Chen, J., Dai, M-C. and Li, J., 2017. Geology, fluid inclusion and stable isotope study of the Yueyang Ag-Au-Cu deposit, Zijinshan orefield, Fujian Province, China. Ore Geology Reviews 86, 254–270.

CHAPTER 8

ADDITIONAL MATERIALS

ADDITIONAL MATERIAL A

SUPPLEMENTARY DATA FOR CHAPTER 2

APATITE AT OLYMPIC DAM, SOUTH AUSTRALIA: A PETROGENETIC TOOL

Sasha Krneta[1], Cristiana L. Ciobanu[2], Nigel J. Cook[2], Kathy Ehrig[3], Alkis Kontonikas-Charos[1]

[1]*School of Physical Sciences, The University of Adelaide, Adelaide, S.A., 5005, Australia*

[2]*School of Chemical Engineering, The University of Adelaide, Adelaide, S.A., 5005, Australia*

[3]*BHP Olympic Dam, Adelaide, SA 5000, Australia*

Paper published in Lithos, 262, 470-485

ELECTRONIC APPENDIX A FOR CHAPTER 2

Standards, X-ray lines, count times and typical minimum detection limits (mdl) for electron probe microanalysis are summarized in the table below.

	University of Adelaide				**University of Tasmania**			
Element	**Standard**	**X-ray line**	**Count time (s)** unknown/ background	**Average mdl** (ppm)	**Standard**	**X-ray line**	**Count time (s)** unknown/ background	**Average mdl** (ppm)
Na	Albite	Na Kα	15/7.5	245	Albite	Na Kα	20/10	143
K	Sanadine	K Kα	15/7.5	108	Sanadine	K Kα	20/10	79
Ca	Plagioclase	Ca Kα	15/7.5	154	Plagioclase	Ca Kα	20/3	228
Mn	Rhodonite	Mn Kα	15/15	273	Rhodonite	Mn Kα	20/10	265
Mg	Almandine	Mg Kα	15/7.5	135	Almandine	Mg Kα	10/5	140
Fe	Almandine	Fe Kα	15/7.5	296	Almandine	Fe Kα	20/10	293
Al	Albite	Al Kα	15/7.5	107	Albite	Al Kα	10/5	132
Si	Albite	Si Kα	15/7.5	122	Albite	Si Kα	20/10	103
Ti	Rutile	Ti Kα	15/7.5	131	Rutile	Ti Kα	50/25	79
F	Synthetic CaF_2	F Kα	15/15	383	Synthetic CaF_2	F Kα	60/50	340
Cl	Tugtupite	Cl Kα	15/7.5	133	Tugtupite	Cl Kα	30/15	74
P	Apatite	P Kα	15/7.5	123	Apatite	P Kα	20/10	157
Sr	Celestite	Sr Lα	15/15	331	Celestite	Sr Lα	40/20	205
Y	REE1	Y Lα	15/15	312	REE1	Y Lα	70/35	174
La	La Glass	La Lα	30/15	562	La Glass	La Lα	60/30	234
Ce	Ce Glass	Ce Lα	30/15	529	Ce Glass	Ce Lα	50/25	467
Nd	Nd Glass	Nd Lß	30/15	479	Nd Glass	Nd Lß	60/30	411
Cr	Chromite	Cr Kα	15/7.5	274	Chromite	-	-	
As	Gallium Arsenide	As Kα	15/15	240	Gallium Arsenide	As Kα	30/15	210
S	Marcasite	S Kα	10/5	123	Marcasite	S Kα	30/15	68

ELECTRONIC APPENDIX B1-B5 FOR CHAPTER 2

Electronic Appendix B1. Summary of EPMA data for apatite from Roxby Downs granite

Magmatic Apatite cores

	2280-2					2280-3		2280-4		2280-5			2280-6
	1	2	3	4	5	1	2	1	2	1	2	3	1
	Mean	Mean	Mean	Mean	Mean	Mean	Mean	Mean	Mean	Mean	Mean	Mean	Mean
	n=3	n=2	n=3	n=5	n=6	n=8	n=11	n=4	n=2	n=7	n=23	n=11	n=2
F	3.10	3.17	3.58	3.57	3.35	3.31	3.28	3.09	3.50	3.29	3.36	3.56	3.61
Cl	0.03	0.03	0.02	0.06	0.03	0.07	0.14	0.04	0.04	0.08	0.10	0.11	0.05
Na_2O	0.08	0.02	0.06	0.08	0.07	0.11	0.10	<mdl	<mdl	0.06	0.09	0.09	0.03
SiO_2	0.53	0.63	0.32	0.60	0.39	0.46	0.46	0.46	0.38	0.85	0.47	0.46	0.85
Al_2O_3	<mdl	<mdl	<mdl	<mdl	<mdl	<mdl	<mdl	<mdl	0.01	<mdl	<mdl	<mdl	<mdl
MgO	<mdl	<mdl	<mdl	<mdl	<mdl	<mdl	<mdl	<mdl	<mdl	<mdl	<mdl	<mdl	0.01
P_2O_5	39.82	39.55	39.89	38.38	39.30	41.30	41.14	41.76	41.76	38.46	41.50	41.40	39.19
SO_3	0.02	0.53	0.01	0.09	0.08	0.33	0.68	0.10	0.03	0.03	0.28	0.20	0.02
K_2O	<mdl	<mdl	<mdl	<mdl	<mdl	0.02	0.04	<mdl	<mdl	0.02	<mdl	0.08	0.01
CaO	54.11	54.09	54.82	54.54	55.21	54.06	53.89	54.41	54.37	53.64	54.29	54.51	54.33
TiO_2	<mdl	0.12	<mdl	<mdl	<mdl	<mdl	<mdl	<mdl	<mdl	<mdl	<mdl	<mdl	<mdl
Cr_2O_3	<mdl	<mdl	<mdl	<mdl	<mdl	<mdl	<mdl	<mdl	<mdl	<mdl	<mdl	<mdl	<mdl
MnO	0.06	0.05	0.05	0.07	0.05	0.06	0.05	<mdl	0.04	0.04	0.04	0.05	0.04
FeO	0.15	0.82	0.54	0.17	0.25	0.56	0.86	0.08	0.06	0.31	0.63	0.64	0.06
As_2O_3	<mdl	<mdl	<mdl	<mdl	<mdl	<mdl	<mdl	<mdl	<mdl	<mdl	<mdl	<mdl	<mdl
SrO	na	na	na	na	na	0.03	0.02	<mdl	<mdl	<mdl	0.02	0.02	na
Y_2O_3	na	na	na	na	na	0.17	0.15	0.11	0.12	<mdl	0.15	0.11	na
La_2O_3	0.37	0.53	0.33	0.39	0.32	0.39	0.39	0.37	0.34	0.45	0.41	0.46	0.61
Ce_2O_3	0.83	0.86	0.60	0.80	0.68	0.76	0.68	0.60	0.49	0.96	0.74	0.71	0.91
Nd_2O_3	0.28	0.20	0.16	0.35	0.22	0.29	0.27	0.15	0.15	0.36	0.26	0.20	0.19
Total	99.37	100.62	100.39	**99.10**	**99.96**	**101.91**	**102.16**	**101.18**	**101.29**	**98.54**	**102.37**	**102.60**	**99.91**
Calculated formulae (9 apfu)													
Ca	**5.018**	**4.965**	**5.064**	**5.137**	**5.125**	**4.878**	**4.847**	**4.906**	**4.916**	**5.060**	**4.879**	**4.904**	**5.054**
Mg	-	-	-	-	-	-	-	-	-	-	-	-	0.002
Mn	0.004	0.004	0.003	0.006	0.004	0.005	0.004	-	0.003	0.003	0.003	0.003	0.003
Sr													
Y													
La	0.012	0.017	0.011	0.013	0.010	0.012	0.012	0.012	0.011	0.015	0.013	0.014	0.019
Ce	0.026	0.027	0.019	0.026	0.022	0.023	0.021	0.019	0.015	0.031	0.023	0.022	0.029
Nd	0.009	0.006	0.005	0.011	0.007	0.009	0.008	0.005	0.004	0.011	0.008	0.006	0.006
Na	0.013	0.003	0.009	0.013	0.012	0.018	0.017	-	-	0.010	0.014	0.015	0.005
K	-	-	-	-	-	0.002	0.004	-	-	0.002	-	0.009	0.001
Fe	0.011	0.059	0.039	0.012	0.018	0.040	0.061	0.006	0.004	0.023	0.044	0.045	0.005
Ti	-	0.007	-	-	-	-	-	-	-	-	-	-	-
Al	-	-	-	-	-	-	-	-	0.001	-	-	-	-
Cr	-	-	-	-	-	0.000	-	-	-	-	-	-	-
Total	**5.093**	**5.088**	**5.150**	**5.218**	**5.198**	**4.986**	**4.973**	**4.946**	**4.955**	**5.155**	**4.984**	**5.018**	**5.123**
ΣREY	0.047	0.050	0.035	0.050	0.039	0.044	0.041	0.035	0.030	0.057	0.043	0.042	0.054
P	2.918	2.868	2.912	2.856	2.882	2.945	2.924	2.976	2.984	2.867	2.947	2.943	2.880
S	0.001	0.034	0.001	0.006	0.005	0.021	0.043	0.006	0.002	0.002	0.018	0.013	0.001
As	-	-	-	-	-	-	-	-	-	-	-	-	-
Si	0.046	0.054	0.028	0.053	0.034	0.038	0.039	0.039	0.032	0.075	0.040	0.039	0.074
Total	**2.965**	**2.957**	**2.940**	**2.915**	**2.921**	**3.004**	**3.006**	**3.021**	**3.018**	**2.944**	**3.005**	**2.994**	**2.956**
F	0.847	0.860	0.976	0.993	0.917	0.880	0.870	0.821	0.933	0.916	0.891	0.945	0.991
Cl	0.005	0.005	0.003	0.008	0.005	0.009	0.020	0.006	0.006	0.012	0.015	0.016	0.008
OH	0.148	0.135	0.022	0.000	0.079	0.110	0.110	0.173	0.061	0.072	0.094	0.040	0.001
Total	**1.000**	**1.000**	**1.000**	**1.001**	**1.000**	**1.000**	**1.000**	**1.000**	**1.000**	**1.000**	**1.000**	**1.000**	**1.000**

Electronic Appendix B1. Summary of EPMA data for apatite from Roxby Downs granite (continued)

Hydrothermal REY-rich rims

	2280-2					2280-3				2280-5
	1	**2**	**3**	**4**	**5**	**1**	**2**	**3**	**4**	**1**
	Mean	**Mean**	**Mean**	**Mean**	**Mean**	**Mean**	**Mean**	**Mean**	**Mean**	**Mean**
	n=2	n=6	n=3	n=3	n=3	n=1	n=6	n=5	n=6	n=2
F	3.10	3.25	3.38	3.48	3.56	3.31	3.29	3.39	3.28	3.26
Cl	0.03	0.03	0.03	0.03	0.03	0.03	0.04	0.03	0.03	0.08
Na_2O	0.03	0.04	0.05	0.02	0.04	0.06	0.04	0.07	0.08	0.08
SiO_2	1.59	2.05	1.71	1.83	1.53	2.19	1.94	2.17	2.12	1.46
Al_2O_3	0.02	0.01	<mdl	<mdl	<mdl	<mdl	<mdl	<mdl	<mdl	<mdl
MgO	<mdl	<mdl	<mdl	<mdl	<mdl	0.02	<mdl	<mdl	<mdl	<mdl
P_2O_5	37.62	37.10	37.38	36.61	37.06	36.73	36.67	38.45	38.66	37.12
SO_3	0.01	0.01	<mdl	0.02	<mdl	0.02	<mdl	0.00	0.01	0.11
K_2O	0.01	<mdl	<mdl	<mdl	<mdl	<mdl	<mdl	<mdl	<mdl	<mdl
CaO	51.94	51.88	52.22	52.66	52.89	51.75	51.46	51.27	51.22	52.42
TiO_2	<mdl	0.08	<mdl	<mdl	<mdl	<mdl	<mdl	<mdl	<mdl	<mdl
Cr_2O_3	<mdl	<mdl	<mdl	<mdl	<mdl	<mdl	<mdl	<mdl	<mdl	<mdl
MnO	0.04	0.05	0.06	0.04	0.06	0.06	0.04	0.06	0.05	0.04
FeO	0.15	0.33	0.71	0.12	0.34	0.38	0.16	0.36	0.15	0.27
As_2O_3	<mdl	<mdl	<mdl	<mdl	<mdl	<mdl	<mdl	<mdl	<mdl	<mdl
SrO	na	na	na	na	na	na	na	0.03	0.02	na
Y_2O_3	na	na	na	na	na	na	na	0.61	0.59	na
La_2O_3	0.98	1.28	1.06	1.01	0.82	1.31	1.01	1.24	1.26	0.83
Ce_2O_3	1.92	2.38	2.07	1.96	1.66	2.58	2.26	2.50	2.46	1.68
Nd_2O_3	0.50	0.61	0.49	0.58	0.55	0.72	0.85	0.99	0.90	0.46
Total	**97.95**	**99.10**	**99.15**	**98.36**	**98.56**	**99.13**	**97.75**	**101.18**	**100.82**	**97.80**
Calculated formulae (9 apfu)										
Ca	**4.949**	**4.926**	**4.955**	**5.048**	**5.052**	**4.931**	**4.955**	**4.779**	**4.772**	**5.019**
Mg	-	-	-	-	-	0.002	-	-	-	-
Mn	0.003	0.003	0.005	0.003	0.005	0.004	0.003	0.005	0.004	0.003
Sr										
Y										
La	0.032	0.042	0.035	0.033	0.027	0.043	0.033	0.040	0.041	0.028
Ce	0.063	0.077	0.067	0.064	0.054	0.084	0.074	0.080	0.078	0.055
Nd	0.016	0.019	0.015	0.018	0.018	0.023	0.027	0.031	0.028	0.015
Na	0.005	0.007	0.008	0.004	0.008	0.011	0.007	0.012	0.013	0.013
K	0.001	-	-	-	-	-	-	-	-	-
Fe	0.011	0.024	0.053	0.009	0.025	0.028	0.012	0.026	0.011	0.020
Ti	-	0.005	-	-	-	-	-	-	-	-
Al	0.002	0.001	-	-	-	-	-	-	-	-
Cr	-	-	-	-	-	-	-	-	-	-
Total	**5.082**	**5.104**	**5.137**	**5.180**	**5.189**	**5.126**	**5.112**	**4.972**	**4.946**	**5.153**
ΣREY	0.111	0.138	0.117	0.116	0.099	0.150	0.135	0.150	0.147	0.097
P	2.832	2.784	2.802	2.773	2.797	2.765	2.790	2.832	2.846	2.809
S	0.001	0.001	-	0.001	-	0.001	-	0.000	0.000	0.007
As	-	-	-	-	-	-	-	-	-	-
Si	0.141	0.181	0.151	0.164	0.137	0.195	0.174	0.188	0.185	0.131
Total	**2.974**	**2.966**	**2.954**	**2.938**	**2.934**	**2.961**	**2.964**	**3.021**	**3.032**	**2.947**
F	0.873	0.911	0.947	0.984	1.003	0.930	0.936	0.932	0.901	0.922
Cl	0.005	0.005	0.004	0.005	0.005	0.005	0.006	0.005	0.004	0.013
OH	0.122	0.084	0.049	0.011	0.000	0.065	0.058	0.063	0.095	0.066
Total	**1.000**	**1.000**	**1.000**	**1.000**	**1.008**	**1.000**	**1.000**	**1.000**	**1.000**	**1.000**

<mdl-Below minimum detection limit

Electronic Appendix B1. Summary of EPMA data for apatite from Roxby Downs granite (continued

Hydrothermal REY-depleted apatite							Hydrothermal sericite-hosted (florencite inclusions)		
2280-2	**2280-3**			**2280-5**		**2280-6**	**2280-6**		
1	**1**	**2**	**1**	**2**	**3**	**1**	**1**	**2**	**3**
Mean	**Mean**	**Mean**	**Mean**	**Mean**	**Mean**	**Mean**	**Mean**	**Mean**	**Mean**
n=2	n=1	n=1	n=7	n=2	n=3	n=2	n=2	n=2	n=7
3.55	3.54	3.15	3.35	3.19	3.46	3.45	3.53	3.42	3.57
<mdl	<mdl	0.02	0.03	0.05	0.03	<mdl	<mdl	<mdl	<mdl
<mdl	0.04	<mdl	<mdl	<mdl	0.02	0.13	0.15	0.05	<mdl
0.19	0.09	0.21	0.13	0.12	0.14	0.21	0.14	0.05	0.06
<mdl	0.02	<mdl	0.02	0.01	<mdl	0.19	0.02	<mdl	<mdl
<mdl	<mdl	<mdl	<mdl	<mdl	<mdl	<mdl	<mdl	<mdl	<mdl
39.62	40.11	42.20	39.59	40.27	42.22	39.62	39.98	40.40	41.85
0.01	0.06	0.02	0.01	0.01	0.01	0.58	0.45	0.10	0.05
<mdl	0.01	<mdl	0.03	0.05	<mdl	0.14	0.09	0.04	0.03
56.20	55.83	55.30	55.61	56.67	55.43	56.77	56.56	56.31	55.70
<mdl	<mdl	<mdl	0.02	<mdl	<mdl	<mdl	<mdl	<mdl	<mdl
<mdl	<mdl	<mdl	<mdl	<mdl	<mdl	0.02	<mdl	<mdl	<mdl
<mdl	<mdl	<mdl	0.02	0.02	<mdl	0.02	<mdl	<mdl	<mdl
0.04	0.08	<mdl	0.36	0.26	0.37	0.11	0.11	0.07	0.06
<mdl	<mdl	<mdl	<mdl	<mdl	<mdl	<mdl	<mdl	<mdl	0.02
na	na	0.03	<mdl	<mdl	0.02	<mdl	na	na	<mdl
na	na	0.11	<mdl	<mdl	0.05	<mdl	na	na	0.06
0.06	<mdl	0.05	<mdl	<mdl	<mdl	<mdl	<mdl	0.04	<mdl
0.05	0.07	0.11	0.03	<mdl	0.09	<mdl	0.05	0.07	<mdl
0.06	0.07	0.16	0.04	<mdl	0.06	0.06	0.07	0.05	<mdl
99.78	**99.92**	**101.35**	**99.25**	**100.65**	**101.91**	**101.31**	**101.13**	**100.60**	**101.39**
5.205	**5.149**	**4.964**	**5.168**	**5.181**	**4.967**	**5.166**	**5.157**	**5.151**	**5.020**
-	-	-	-	-	-	-	-	-	-
-	-	-	0.002	0.001	-	0.002	-	-	-
0.002	-	0.001	-	-	-	-	-	0.001	-
0.002	0.002	0.003	0.001	-	0.003	-	0.002	0.002	-
0.002	0.002	0.005	0.001	-	0.002	0.002	0.002	0.002	-
-	0.007	-	-	-	0.003	0.021	0.024	0.008	-
-	0.001	-	0.004	0.005	-	0.015	0.010	0.004	0.003
0.003	0.006	-	0.026	0.018	0.026	0.008	0.007	0.005	0.004
-	-	-	0.001	-	-	-	-	-	-
-	0.002	-	0.002	0.001	-	0.019	0.002	-	-
-	-	-	-	-	-	0.002	-	-	-
5.214	**5.168**	**4.973**	**5.205**	**5.207**	**5.001**	**5.235**	**5.203**	**5.173**	**5.028**
0.005	0.004	0.010	0.002	0.000	0.004	0.002	0.004	0.005	0.000
2.900	2.922	2.993	2.907	2.909	2.990	2.849	2.880	2.920	2.981
0.001	0.004	0.001	0.001	0.001	0.000	0.037	0.029	0.007	0.003
-	-	-	-	-	-	-	-	-	0.001
0.016	0.007	0.018	0.011	0.010	0.012	0.018	0.012	0.005	0.005
2.917	**2.934**	**3.012**	**2.919**	**2.920**	**3.002**	**2.905**	**2.921**	**2.932**	**2.990**
0.971	0.964	0.836	0.920	0.861	0.916	0.928	0.949	0.924	0.949
-	-	0.002	0.004	0.007	0.005	-	-	-	-
0.029	0.036	0.162	0.076	0.132	0.079	0.072	0.051	0.076	0.051
1.000	**1.000**	**1.000**	**1.000**	**1.000**	**1.000**	**1.000**	**1.000**	**1.000**	**1.000**

<mdl-Below minimum detection limit

na-Not applicable (element not measured)

Electronic Appendix B1. Summary of EPMA data for apatite from Roxby Downs granite (continued)

Magmatic apatite cores							Hydrothermal REY-rich rims					Hydrothermal REE depleted apatite
RX7860					RX7864	RX7866	RX7860			RX7864	RX7866	RX7866
1	2	3	4	5	1	2	1	2	3	1	1	1
Mean	Mean	Mean	Mean	Mean	Mean	Mean	Mean	Mean	Mean	Mean	Mean	Mean
n=2	n=2	n=3	n=10	n=4	n=7	n=1	n=5	n=3	n=1	n=1	n=4	n=4
3.22	3.40	3.42	3.19	3.85	3.13	3.15	3.13	3.20	3.45	3.03	3.40	3.23
0.10	0.05	0.05	0.08	0.11	0.07	0.04	0.10	0.07	0.05	0.08	0.07	0.02
0.10	0.09	0.07	0.08	0.12	0.05	<mdl	0.09	0.11	0.04	0.08	0.03	<mdl
0.91	0.76	0.83	0.44	0.39	0.64	0.78	2.35	2.15	1.52	1.54	2.83	0.52
<mdl	0.04	<mdl	<mdl	<mdl	<mdl	<mdl	0.02	<mdl	<mdl	<mdl	<mdl	0.01
<mdl	0.04	<mdl	<mdl	0.01	<mdl	<mdl	0.04	<mdl	<mdl	<mdl	<mdl	0.01
41.14	41.80	41.92	41.35	40.98	41.79	41.81	38.13	38.89	40.61	40.24	37.80	42.25
<mdl	<mdl	<mdl	0.10	0.13	0.04	0.01	<mdl	0.01	0.03	0.01	<mdl	0.02
0.02	0.01	<mdl	<mdl	0.01	0.00	<mdl	0.02	<mdl	0.02	<mdl	<mdl	0.01
52.90	52.98	53.74	54.29	53.90	52.99	52.90	49.84	50.01	52.30	51.13	48.85	53.96
<mdl	<mdl	<mdl	0.05	<mdl	<mdl	<mdl	<mdl	<mdl	<mdl	<mdl	<mdl	0.05
<mdl	<mdl	<mdl	<mdl	<mdl	<mdl	<mdl	<mdl	<mdl	<mdl	<mdl	<mdl	<mdl
0.03	0.04	0.05	0.06	0.05	0.04	<mdl	0.05	0.03	0.05	<mdl	0.01	0.01
0.06	0.85	0.10	0.75	0.31	0.15	0.08	0.20	0.64	0.11	0.19	0.07	0.21
<mdl	<mdl	<mdl	<mdl	<mdl	<mdl	<mdl	<mdl	<mdl	<mdl	<mdl	<mdl	<mdl
na	na	na	<mdl	<mdl	na	na	<mdl	na	na	na	na	<mdl
na	na	na	0.15	0.16	na	na	<mdl	na	na	na	na	<mdl
0.43	0.25	0.42	0.33	0.33	0.39	0.39	1.06	0.86	0.69	0.84	1.24	0.06
1.14	0.74	0.88	0.65	0.65	0.86	1.14	2.60	2.22	1.69	1.89	2.92	0.30
0.58	0.42	0.34	0.26	0.26	0.30	0.46	1.18	1.24	0.62	0.77	1.27	0.20
100.63	**101.48**	**101.82**	**101.77**	**101.25**	**100.45**	**100.76**	**98.81**	**99.41**	**101.17**	**99.78**	**98.48**	**100.87**
4.822	**4.777**	**4.828**	**4.903**	**4.922**	**4.806**	**4.790**	**4.705**	**4.676**	**4.768**	**4.716**	**4.638**	**4.852**
-	0.005	-	-	0.001	-	-	0.006	-	-	-	-	0.002
0.002	0.003	0.004	0.004	0.003	0.003	-	0.004	0.002	0.004	-	0.001	0.001
0.014	0.008	0.013	0.010	0.011	0.012	0.012	0.035	0.028	0.022	0.027	0.040	0.002
0.035	0.023	0.027	0.020	0.020	0.027	0.035	0.084	0.071	0.053	0.060	0.095	0.009
0.017	0.013	0.010	0.008	0.008	0.009	0.014	0.037	0.039	0.019	0.024	0.040	0.006
0.016	0.015	0.011	0.013	0.019	0.007	-	0.016	0.019	0.006	0.014	0.005	-
0.002	0.001	-	-	0.001	0.000	-	0.002	-	0.002	-	-	0.001
0.004	0.060	0.007	0.053	0.022	0.010	0.006	0.014	0.046	0.008	0.014	0.005	0.015
-	-	-	0.003	-	-	-	-	-	-	-	-	0.003
-	0.004	-	-	-	-	-	0.002	-	-	-	-	0.001
-	-	-	0.000	-	-	-	-	-	-	-	-	-
4.913	**4.909**	**4.901**	**5.014**	**5.008**	**4.875**	**4.857**	**4.905**	**4.881**	**4.881**	**4.853**	**4.824**	**4.892**
0.067	0.043	0.050	0.038	0.039	0.048	0.061	0.156	0.137	0.093	0.110	0.175	0.017
2.963	2.979	2.976	2.951	2.957	2.995	2.991	2.845	2.873	2.925	2.933	2.836	3.002
-	-	-	0.006	0.008	0.003	0.001	-	0.000	0.002	0.000	-	0.001
-	-	-	-	-	-	-	-	-	-	-	-	-
0.077	0.064	0.070	0.037	0.033	0.054	0.066	0.207	0.187	0.130	0.133	0.250	0.044
3.041	**3.043**	**3.046**	**2.994**	**2.998**	**3.052**	**3.058**	**3.051**	**3.061**	**3.056**	**3.066**	**3.086**	**3.047**
0.867	0.904	0.906	0.851	1.038	0.838	0.840	0.873	0.884	0.928	0.824	0.952	0.858
0.014	0.008	0.007	0.012	0.016	0.010	0.005	0.015	0.010	0.007	0.012	0.010	0.003
0.119	0.089	0.087	0.137	0.000	0.152	0.154	0.112	0.107	0.066	0.165	0.038	0.139
1.000	**1.000**	**1.000**	**1.000**	**1.054**	**1.000**	**1.000**	**1.000**	**1.000**	**1.000**	**1.000**	**1.000**	**1.000**

<mdl-Below minimum detection limit

na-Not applicable (element not measured)

Electronic Appendix B2. Summary of EPMA data for apatite from Horn Ridge Quartz Monzonite

	Cl-rich magmatic apatite										REY-rich Magmatic apatite					Small magnetite-hosted Cl-rich magmatic apatite			F-rich hydrothermal apatite		
	1	2	3	4	5	6	7	8	9	10	1	2	3	4	5	1	2	3	1	2	3
	Mean (n=5)	Mean (n=3)	Mean (n=5)	Mean (n=8)	Mean (n=10)	Mean (n=5)	Mean (n=4)	Mean (n=2)	Mean (n=4)	Mean (n=3)	Mean (n=2)	Mean (n=2)	Mean (n=2)	Mean (n=3)	Mean (n=1)	Mean (n=2)	Mean (n=1)	Mean (n=1)	Mean (n=5)	Mean (n=4)	Mean (n=2)
F	2.77	2.81	2.75	2.79	3.11	3.05	2.61	2.69	2.88	3.04	2.72	2.81	2.43	2.62	2.71	1.92	2.49	2.73	3.43	3.30	3.34
Cl	0.57	0.60	0.59	0.55	0.58	0.53	0.58	0.60	0.46	0.48	0.67	0.57	0.64	0.65	0.54	0.96	0.91	0.95	0.10	0.08	0.02
Na_2O	0.15	0.13	0.12	0.11	0.18	0.10	0.16	0.14	0.06	0.04	0.21	0.11	0.15	0.11	0.17	0.14	0.12	0.07	0.01	0.02	<mdl
SiO_2	0.63	0.48	0.50	0.46	0.47	0.47	0.56	0.57	0.37	0.61	0.66	0.99	1.30	0.95	0.93	0.72	1.44	0.45	0.20	0.14	0.17
Al_2O_3	<mdl	<mdl	<mdl	<mdl	<mdl	<mdl	<mdl	<mdl	0.02	0.01	0.01	<mdl	<mdl	<mdl	0.00	0.01	<mdl	0.01	0.05	<mdl	0.03
MgO	0.01	0.01	0.01	0.01	0.02	<mdl	<mdl	0.03	<mdl	<mdl	0.01	<mdl	0.02	0.02	0.03	0.01	<mdl	0.01	0.02	<mdl	0.08
P_2O_5	40.73	40.59	40.10	40.04	41.51	41.23	41.17	40.88	42.32	41.80	40.39	40.37	40.11	38.73	41.88	40.80	40.41	41.97	41.36	42.22	41.89
SO_3	0.10	0.03	0.03	0.05	0.03	0.05	0.05	0.01	0.02	0.05	0.04	0.04	0.01	0.01	0.11	0.00	<mdl	0.01	<mdl	<mdl	<mdl
K_2O	<mdl	<mdl	<mdl	<mdl	<mdl	<mdl	0.09	<mdl	<mdl	<mdl	0.01	<mdl	<mdl	<mdl	0.00	<mdl	<mdl	0.01	<mdl	0.06	<mdl
CaO	53.58	53.51	53.67	54.87	53.86	54.14	53.59	53.83	54.71	53.95	52.79	53.24	52.69	52.87	52.98	52.90	51.50	53.26	55.40	55.45	55.87
TiO_2	<mdl	<mdl	<mdl	<mdl	<mdl	<mdl	0.02	0.00	0.06	<mdl	-0.01	<mdl	0.05	<mdl	0.00	0.01	<mdl	0.01	<mdl	0.01	<mdl
Cr_2O_3	<mdl	<mdl	<mdl	<mdl	<mdl	na	na	na	na	na	na	na	na	<mdl	na	na	na	na	na	na	na
MnO	0.09	0.08	0.07	0.07	0.07	0.09	0.06	0.12	0.06	0.05	0.10	0.06	0.08	0.06	0.10	0.10	0.07	0.06	0.02	0.01	<mdl
FeO	0.29	0.25	0.26	0.15	0.06	0.35	0.17	0.24	1.55	0.11	0.16	0.23	0.34	0.23	0.21	1.95	1.79	1.93	0.10	0.09	0.29
As_2O_3	<mdl	<mdl	<mdl	<mdl	0.01	<mdl	<mdl	<mdl	<mdl	<mdl	<mdl	<mdl	<mdl	<mdl	0.00	<mdl	<mdl	<mdl	<mdl	<mdl	0.01
SrO	na	na	na	na	0.03	0.04	0.02	0.03	0.00	0.00	0.02	na	0.03	0.03	0.00	0.05	0.00	0.00	0.02	0.02	0.01
Y_2O_3	na	na	na	na	0.26	0.23	0.27	0.28	0.17	0.30	0.35	na	0.43	0.56	0.40	0.32	0.64	0.16	0.11	0.15	0.12
La_2O_3	0.34	0.30	0.32	0.21	0.32	0.23	0.32	0.37	0.20	0.16	0.46	0.45	0.59	0.41	0.41	0.46	0.62	0.39	0.02	0.01	0.01
Ce_2O_3	0.76	0.67	0.74	0.55	0.69	0.49	0.70	0.85	0.44	0.47	0.97	1.00	1.41	1.11	0.83	0.94	1.67	0.58	0.04	0.02	0.03
Nd_2O_3	0.36	0.38	0.35	0.29	0.34	0.29	0.41	0.49	0.22	0.20	0.50	0.62	0.78	0.55	0.43	0.48	0.74	0.29	0.09	0.07	<mdl
Total	**100.53**	**99.95**	**99.58**	**100.16**	**101.52**	**101.28**	**100.80**	**101.16**	**103.57**	**101.28**	**100.04**	**100.97**	**101.18**	**98.31**	**101.72**	**101.76**	**102.38**	**102.86**	**100.96**	**101.60**	**101.86**
Calculated formulae (9 apfu)																					
Ca	**4.893**	**4.920**	**4.961**	**5.052**	**4.879**	**4.914**	**4.874**	**4.904**	**4.848**	**4.866**	**4.868**	**4.869**	**4.816**	**4.985**	**4.7549**	**4.797**	**4.679**	**4.775**	**5.023**	**4.972**	**5.009**
Mg	0.002	0.002	0.001	0.001	0.002	-	-	0.004	-	-	0.001	<mdl	0.003	0.003	0.0041	0.001	-	0.001	0.002	<mdl	0.010
Mn	0.006	0.006	0.005	0.005	0.005	0.007	0.004	0.009	0.004	0.004	0.007	0.004	0.006	0.005	0.0071	0.007	0.005	0.004	0.001	0.001	<mdl
Sr	na	na	na	na	0.002	0.002	0.001	0.001	0.000	0.000	0.001	na	0.002	0.002	0	0.002	0.000	0.000	0.001	0.001	0.001
Y	na	na	na	na	0.012	0.010	0.012	0.013	0.008	0.014	0.016	na	0.020	0.025	0.0179	0.014	0.029	0.007	0.005	0.007	0.005
La	0.011	0.010	0.010	0.007	0.010	0.007	0.010	0.012	0.006	0.005	0.015	0.014	0.019	0.013	0.0125	0.014	0.019	0.012	0.001	0.000	0.000
Ce	0.024	0.021	0.023	0.017	0.021	0.015	0.022	0.026	0.013	0.015	0.031	0.031	0.044	0.036	0.0254	0.029	0.052	0.018	0.001	0.001	0.001
Nd	0.011	0.012	0.011	0.009	0.010	0.009	0.012	0.015	0.007	0.006	0.015	0.019	0.024	0.017	0.0129	0.014	0.022	0.009	0.003	0.002	<mdl
Na	0.025	0.022	0.020	0.018	0.029	0.017	0.026	0.024	0.009	0.006	0.035	0.018	0.024	0.019	0.0273	0.023	0.019	0.011	0.002	0.003	-
K	-	-	-	-	-	-	0.010	-	-	-	0.001	-	-	-	0	-	-	0.001	<mdl	0.007	<mdl
Fe	0.021	0.018	0.019	0.011	0.005	0.025	0.012	0.017	0.107	0.008	0.011	0.016	0.024	0.017	0.0146	0.138	0.127	0.135	0.007	0.006	0.020
Ti	-	-	-	-	-	-	0.001	0.000	0.004	-	-	-	0.003	-	0	0.001	-	0.000	<mdl	0.001	<mdl
Al	-	-	-	-	-	-	-	-	0.002	0.001	0.001	-	-	-	0	0.001	-	0.001	0.005	<mdl	0.003
Cr	-	-	-	-	-	-	-	-	-	-	-	-	-	-	0	0.000	-	-	0.000	0.000	0.000
Total	**5.008**	**5.023**	**5.065**	**5.120**	**4.974**	**5.005**	**4.985**	**5.025**	**5.008**	**4.923**	**5.001**	**4.994**	**4.989**	**5.094**	**4.8767**	**5.043**	**4.952**	**4.973**	**5.051**	**4.998**	**5.048**
ΣREY	0.046	0.042	0.045	0.033	0.054	0.041	0.056	0.066	0.034	0.039	0.076	0.064	0.106	0.092	0.0688	0.072	0.122	0.045	0.010	0.009	0.007
P	2.939	2.949	2.929	2.913	2.971	2.958	2.959	2.942	2.963	2.979	2.943	2.918	2.897	2.885	2.9699	2.924	2.901	2.973	2.963	2.991	2.968
S	0.006	0.002	0.002	0.003	0.002	0.003	0.003	0.001	0.002	0.003	0.002	0.002	0.001	0.001	0.0071	0.000	-	0.000	<mdl	<mdl	<mdl
As	-	-	-	-	0.000	-	-	-	-	-	-	-	-	-	0	-	-	-	<mdl	<mdl	0.000
Si	0.054	0.041	0.043	0.039	0.039	0.040	0.048	0.048	0.031	0.051	0.057	0.085	0.111	0.084	0.0783	0.061	0.122	0.037	0.017	0.011	0.014
Total	**2.999**	**2.992**	**2.974**	**2.956**	**3.013**	**3.001**	**3.010**	**2.991**	**2.995**	**3.033**	**3.003**	**3.005**	**3.009**	**2.970**	**3.0553**	**2.984**	**3.023**	**3.011**	**2.980**	**3.003**	**2.982**
F	0.747	0.764	0.751	0.758	0.832	0.818	0.700	0.723	0.754	0.809	0.741	0.760	0.656	0.730	0.7166	0.513	0.668	0.723	0.918	0.873	0.884
Cl	0.082	0.087	0.086	0.080	0.083	0.076	0.084	0.087	0.065	0.068	0.098	0.082	0.093	0.097	0.0762	0.138	0.131	0.135	0.014	0.011	0.003
OH	0.171	0.149	0.162	0.162	0.086	0.106	0.216	0.190	0.182	0.122	0.161	0.158	0.251	0.173	0.2072	0.349	0.201	0.142	0.068	0.116	0.113
Total	**1.000**	**1.000**	**1.000**	**1.000**	**1.000**	**1.000**	**1.000**	**1.000**	**1.000**	**1.000**	**1.000**	**1.000**	**1.000**	**1.000**	**1.000**	**1.000**	**1.000**	**1.000**	**1.000**	**1.000**	**1.000**

<mdl-Below minimum detection limit na-Not applicable (element not measured)

Electronic Appendix B3. Summary of EPMA data for apatite from Mesoproterozoic dolerites

	Cl-rich magmatic apatite								REY-rich hydrothermal apatite						Cl-S-rich hydrothermal apatite				F-rich hydrothermal apati			
	RX7913				RX7914				RX7913		RX7914				RX7914				RX7913	RX7914		
	1	2	3	4	1	2	3	4	1	2	1	2	3	4	1	2	3	4	1	1	2	3
	Mean	Mean	Mean	Mean	Mean	Mean	Mean	Mean	Mean	Mean	Mean	Mean	Mean	Mean	Mean	Mean	Mean	Mean	Mean	Mean	Mean	Mean
	(n=5)	(n=3)	(n=5)	(n=7)	(n=1)	(n=2)	(n=5)	(n=10)	(n=5)	(n=3)	(n=4)	(n=3)	(n=5)	(n=1)	(n=4)	(n=1)	(n=2)	(n=6)	(n=3)	(n=2)	(n=2)	(n=4)
F	2.61	2.45	2.03	2.17	2.47	2.45	2.57	2.47	2.39	2.39	2.50	2.55	2.44	2.51	2.48	2.36	2.36	2.43	3.46	3.56	3.46	3.40
Cl	1.17	1.16	1.46	1.19	1.08	1.26	1.14	1.21	1.19	1.29	1.17	1.15	1.10	1.17	1.21	1.22	1.36	1.15	0.19	0.08	0.02	0.22
Na_2O	0.03	0.06	0.08	0.08	0.05	0.07	0.07	0.08	0.15	0.18	0.07	0.10	0.10	0.08	0.10	0.14	0.11	0.14	0.03	0.04	0.01	0.03
SiO_2	0.27	0.30	0.38	0.30	0.32	0.42	0.33	0.36	0.74	0.61	0.50	0.56	0.55	0.56	0.41	0.46	0.34	0.43	0.09	0.05	0.16	0.10
Al_2O_3	<mdl	<mdl	<mdl	0.02	<mdl	<mdl	0.02	0.02	0.01	<mdl	0.01	<mdl	0.02	<mdl	<mdl	<mdl	<mdl	0.02	0.01	<mdl	0.13	0.01
MgO	0.31	0.20	0.18	0.34	0.25	0.27	0.26	0.29	0.15	0.14	0.23	0.21	0.24	0.29	0.28	0.27	0.34	0.25	<mdl	0.02	0.02	0.04
P_2O_5	40.32	40.52	40.10	41.70	39.21	41.51	40.85	41.52	39.20	39.78	38.79	38.36	41.34	41.48	39.38	38.31	38.45	41.12	41.43	41.18	39.79	39.48
SO_3	0.03	0.11	0.12	0.19	0.03	0.07	0.18	0.11	0.11	0.13	<mdl	0.09	0.04	0.08	0.42	0.51	0.33	0.45	0.03	0.02	0.03	0.05
K_2O	<mdl	<mdl	<mdl	0.02	<mdl	<mdl	0.01	0.01	<mdl	<mdl	<mdl	0.01	0.03	<mdl	<mdl	<mdl	0.01	0.04	<mdl	<mdl	0.01	<mdl
CaO	54.28	54.22	53.59	54.31	54.19	53.87	54.38	54.06	52.99	53.47	53.25	53.54	53.81	53.45	54.18	54.31	54.22	54.07	55.75	56.16	55.94	55.93
TiO_2	<mdl	<mdl	<mdl	0.01	<mdl	<mdl	<mdl	0.02	<mdl	<mdl	<mdl	<mdl	<mdl	<mdl	<mdl	<mdl	<mdl	<mdl	<mdl	<mdl	<mdl	<mdl
Cr_2O_3	<mdl	<mdl	0.01	na	<mdl	na	<mdl	na	<mdl	<mdl	<mdl	<mdl	<mdl	na	0.01	<mdl	<mdl	na	<mdl	<mdl	<mdl	<mdl
MnO	0.08	0.07	0.09	0.06	0.09	0.08	0.07	0.07	0.04	0.07	0.08	0.06	0.04	0.13	0.08	0.10	0.07	0.06	0.04	0.04	0.03	0.01
FeO	0.42	0.41	0.50	0.54	0.35	0.49	0.41	0.64	0.35	0.42	0.32	0.47	0.33	0.46	0.34	0.38	0.43	0.41	0.51	0.14	0.33	0.20
As_2O_3	0.01	<mdl	<mdl	<mdl	<mdl	<mdl	<mdl	<mdl	<mdl	<mdl	<mdl	<mdl	0.03	0.02	<mdl	<mdl	<mdl	0.02	<mdl	<mdl	<mdl	<mdl
SrO	na	na	na	0.16	na	0.17	0.15	0.17	na	na	na	na	0.13	0.19	na	na	na	0.15	na	na	na	na
Y_2O_3	na	na	na	0.03	na	0.07	0.03	0.05	na	na	na	na	0.09	0.06	na	na	na	0.04	na	na	na	na
La_2O_3	0.18	0.15	0.17	0.12	0.19	0.26	0.18	0.21	0.55	0.49	0.31	0.42	0.36	0.30	0.12	0.15	0.09	0.16	0.07	0.05	<mdl	0.02
Ce_2O_3	0.36	0.35	0.37	0.23	0.35	0.56	0.32	0.43	1.20	1.12	0.77	0.81	0.67	0.63	0.26	0.26	0.17	0.26	0.21	0.13	0.07	0.09
Nd_2O_3	0.17	0.16	0.19	0.11	0.16	0.25	0.15	0.22	0.46	0.43	0.37	0.37	0.34	0.25	0.13	0.13	0.09	0.14	0.15	0.12	0.10	0.01
Total	**100.24**	**100.16**	**99.27**	**101.53**	**98.74**	**101.81**	**101.09**	**101.91**	**99.53**	**100.53**	**98.38**	**98.70**	**101.58**	**101.67**	**99.39**	**98.62**	**98.36**	**101.30**	**101.97**	**101.60**	**100.10**	**99.59**
Calculated formulae (9 apfu)																						
Ca	**5.000**	**4.980**	**4.965**	**4.884**	**5.077**	**4.865**	**4.952**	**4.875**	**4.949**	**4.942**	**5.032**	**5.064**	**4.869**	**4.830**	**5.028**	**5.101**	**5.107**	**4.886**	**5.031**	**5.087**	**5.159**	**5.196**
Mg	0.040	0.025	0.024	0.042	0.033	0.034	0.033	0.036	0.019	0.018	0.031	0.028	0.030	0.037	0.036	0.036	0.042	0.031	-	0.003	0.003	0.006
Mn	0.005	0.005	0.007	0.005	0.007	0.006	0.005	0.005	0.003	0.005	0.006	0.004	0.003	0.009	0.006	0.008	0.006	0.004	0.003	0.003	0.002	0.001
Sr	-	-	-	0.008	-	0.008	0.007	0.008	-	-	-	-	0.006	0.009	-	-	-	0.007	-	-	-	-
Y	-	-	-	0.001	-	0.003	0.001	0.002	-	-	-	-	0.004	0.003	-	-	-	0.002	-	-	-	-
La	0.006	0.005	0.006	0.004	0.006	0.008	0.005	0.007	0.018	0.016	0.010	0.014	0.011	0.009	0.004	0.005	0.003	0.005	0.002	0.001	-	0.001
Ce	0.011	0.011	0.012	0.007	0.011	0.017	0.010	0.013	0.038	0.035	0.025	0.026	0.021	0.020	0.008	0.008	0.006	0.008	0.006	0.004	0.002	0.003
Nd	0.005	0.005	0.006	0.003	0.005	0.007	0.005	0.007	0.014	0.013	0.012	0.012	0.010	0.007	0.004	0.004	0.003	0.004	0.004	0.004	0.003	-
Na	0.006	0.010	0.013	0.013	0.009	0.012	0.012	0.013	0.025	0.030	0.012	0.018	0.017	0.013	0.016	0.024	0.020	0.024	0.005	0.006	0.002	0.005
K	-	-	-	0.000	-	-	0.001	0.000	-	-	-	0.001	0.001	-	-	-	0.001	0.001	-	-	0.001	-
Fe	0.030	0.029	0.036	0.038	0.025	0.034	0.029	0.045	0.026	0.030	0.023	0.035	0.023	0.032	0.025	0.028	0.030	0.029	0.036	0.010	0.024	0.014
Ti	-	-	-	0.000	-	-	0.000	0.000	-	-	-	-	0.000	-	-	-	-	-	-	-	-	-
Al	-	-	-	0.001	-	-	0.000	0.001	0.001	-	0.001	-	0.000	-	-	-	-	0.001	0.001	-	0.014	0.001
Cr	-	-	0.001	-	-	-		-	-	-	-	-			0.001	-	-	-	-	-	-	-
Total	**5.103**	**5.071**	**5.069**	**5.005**	**5.174**	**4.996**	**5.061**	**5.013**	**5.094**	**5.090**	**5.152**	**5.201**	**4.996**	**4.970**	**5.127**	**5.214**	**5.219**	**5.220**	**5.089**	**5.118**	**5.210**	**5.227**
ΣREY	0.022	0.021	0.023	0.014	0.022	0.033	0.021	0.027	0.070	0.064	0.047	0.051	0.046	0.039	0.016	0.017	0.013	0.011	0.013	0.009	0.005	0.004
P	2.934	2.941	2.935	2.963	2.903	2.963	2.938	2.959	2.893	2.905	2.897	2.866	2.956	2.962	2.887	2.843	2.857	2.936	2.954	2.948	2.900	2.899
S	0.002	0.007	0.008	0.012	0.002	0.005	0.012	0.007	0.007	0.009	-	0.006	0.002	0.005	0.027	0.034	0.026	0.029	0.002	0.001	0.002	0.003
As	0.001	-	-	-	-	0.000	0.000	-	-	-	-	-	0.000	0.001	-	-	-	0.000	-	-	-	-
Si	0.023	0.025	0.032	0.025	0.028	0.036	0.028	0.030	0.065	0.053	0.044	0.049	0.046	0.048	0.036	0.040	0.033	0.036	0.008	0.004	0.014	0.008
Total	**2.960**	**2.973**	**2.975**	**3.000**	**2.933**	**3.003**	**2.977**	**2.996**	**2.965**	**2.966**	**2.941**	**2.922**	**3.005**	**3.016**	**2.951**	**2.917**	**2.916**	**3.002**	**2.964**	**2.953**	**2.915**	**2.910**
F	0.710	0.664	0.555	0.577	0.682	0.653	0.690	0.657	0.658	0.651	0.698	0.710	0.651	0.670	0.679	0.655	0.655	0.647	0.922	0.951	0.941	0.933
Cl	0.171	0.168	0.214	0.170	0.160	0.179	0.164	0.172	0.175	0.189	0.175	0.172	0.158	0.167	0.177	0.181	0.195	0.164	0.027	0.012	0.003	0.032
OH	0.119	0.168	0.230	0.254	0.157	0.167	0.146	0.171	0.167	0.160	0.127	0.117	0.192	0.162	0.144	0.164	0.149	0.188	0.051	0.049	0.056	0.039
Total	**1.000**	**1.000**	**1.000**	**1.000**	**1.000**	**1.000**	**1.000**	**1.000**	**1.000**	**1.000**	**1.000**	**1.000**	**1.000**	**1.000**	**1.000**	**1.000**	**1.000**	**1.000**	**1.000**	**1.011**	**1.000**	**1.004**

<mdl-Below minimum detection limit

na-Not applicable (element not measured)

Electronic Appendix B4. Summary of EPMA data for apatite from Olympic Dam Deep Mineralisation

	Grain cores with high REY, S and Cl													Grain rims and fracture domains with low REY, S and Cl							
	2773-1		2773-2		2773-4	2773-3	2773-5							2773-3	2773-1		2773-2	2773-4		2773-5	
	1	2	1	2	1	1	1	2	3	4	5	6	7	1	1	2	1	1	1	2	3
	Mean	Mean	Mean	Mean	Mean	Mean	Mean	Mean	Mean	Mean	Mean	Mean	Mean	Mean	Mean	Mean	Mean	Mean	Mean	Mean	Mean
	n=2	n=2	n=5	n=4	n=6	n=10	n=3	n=5	n=5	n=2	n=3	n=4	n=1	n=13	n=4	n=4	n=6	n=6	n=4	n=5	n=3
F	3.21	3.32	3.47	3.08	3.06	3.30	3.08	3.02	3.23	3.32	3.17	3.03	3.50	3.34	3.35	3.65	3.32	3.38	3.63	3.55	3.80
Cl	0.48	0.34	0.32	0.17	0.30	0.32	0.44	0.34	0.38	0.33	0.47	0.49	0.36	0.03	0.07	<mdl	0.04	<mdl	0.36	0.02	0.15
Na_2O	0.20	0.11	0.14	0.11	0.16	0.16	0.19	0.23	0.20	0.14	0.23	0.20	0.16	<mdl	0.04	<mdl	<mdl	<mdl	0.07	<mdl	0.06
SiO_2	0.67	0.50	0.58	0.55	0.49	0.58	0.58	0.58	0.58	0.49	0.54	0.54	0.53	0.09	0.14	0.06	0.07	0.06	0.18	0.14	0.09
Al_2O_3	<mdl	<mdl	<mdl	<mdl	<mdl	0.01	<mdl	<mdl	<mdl	<mdl	<mdl	<mdl	<mdl	<mdl	<mdl	<mdl	<mdl	<mdl	<mdl	<mdl	<mdl
MgO	<mdl	<mdl	<mdl	<mdl	<mdl	0.02	0.01	<mdl	0.02	<mdl	0.02	0.03	<mdl	<mdl	<mdl	<mdl	<mdl	<mdl	<mdl	<mdl	<mdl
P_2O_5	40.42	39.46	39.40	39.06	38.80	38.25	40.34	40.89	41.09	40.99	40.34	41.20	41.70	39.70	41.02	40.86	40.19	40.08	41.54	42.45	42.12
SO_3	0.38	0.24	0.24	0.25	0.26	0.27	0.27	0.27	0.21	0.23	0.30	0.26	0.22	0.04	0.05	<mdl	<mdl	<mdl	0.09	<mdl	0.03
K_2O	0.05	<mdl	<mdl	<mdl	<mdl	0.01	0.02	<mdl	<mdl	0.01	<mdl	<mdl	0.01	<mdl	0.01	<mdl	<mdl	<mdl	0.03	<mdl	0.01
CaO	54.31	54.29	54.68	54.07	53.67	54.55	54.13	53.81	54.09	54.68	52.62	54.22	54.38	56.20	55.10	55.99	55.44	55.36	54.84	55.68	55.27
MnO	<mdl	0.02	<mdl	<mdl	<mdl	<mdl	<mdl	<mdl	<mdl	<mdl	<mdl	0.02	0.05	<mdl	0.04	0.03	<mdl	<mdl	0.02	<mdl	<mdl
FeO	0.14	0.49	0.12	0.10	0.06	0.11	0.25	0.16	0.11	0.33	0.15	0.27	0.75	0.04	0.13	0.38	<mdl	0.11	0.18	0.20	0.55
As_2O_3	<mdl	0.02	<mdl	<mdl	<mdl	<mdl	<mdl	<mdl	0.03	0.02	<mdl	0.02	<mdl	<mdl	<mdl	<mdl	<mdl	<mdl	<mdl	<mdl	<mdl
SrO	na	na	na	na	na	na	0.05	0.06	0.07	0.06	0.05	0.07	0.05	<mdl	na	na	na	na	0.05	0.05	0.06
Y_2O_3	na	na	na	na	na	na	0.20	0.17	0.18	0.14	0.18	0.17	0.17	<mdl	na	na	na	na	0.09	0.07	0.05
La_2O_3	0.23	0.22	0.24	0.21	0.22	0.25	0.31	0.34	0.34	0.24	0.34	0.32	0.24	<mdl	0.07	<mdl	<mdl	<mdl	0.08	<mdl	0.06
Ce_2O_3	0.63	0.54	0.63	0.60	0.64	0.64	0.74	0.89	0.87	0.52	0.77	0.79	0.58	<mdl	0.15	<mdl	<mdl	<mdl	0.07	0.05	0.16
Nd_2O_3	0.31	0.25	0.29	0.24	0.28	0.27	0.33	0.36	0.35	0.26	0.37	0.33	0.26	0.05	0.07	<mdl	<mdl	<mdl	0.05	<mdl	0.10
Total	**101.04**	**99.83**	**100.11**	**98.48**	**97.96**	**98.75**	**100.99**	**101.16**	**101.77**	**101.77**	**99.59**	**101.95**	**102.97**	**99.63**	**100.27**	**101.10**	**99.33**	**99.10**	**101.31**	**102.31**	**102.55**
Calculated formulae (9 apfu)																					
Ca	**4.950**	**5.036**	**5.066**	**5.060**	**5.060**	**5.141**	**4.946**	**4.889**	**4.897**	**4.948**	**4.863**	**4.893**	**4.953**	**5.202**	**5.032**	**5.100**	**5.125**	**5.133**	**4.970**	**4.966**	**4.953**
Mg	-	-	-	-	-	0.001	0.002	-	0.003	-	0.003	0.003	-	-	-	-	-	-	-	-	0.001
Mn	-	0.002	-	-	-	-	-	-	-	-	-	0.001	-	-	0.003	0.002	-	-	0.002	-	0.000
Sr	na	na	na	na	na	na	0.002	0.003	0.003	0.003	0.003	0.004	0.003	-	-	-	-	-	0.002	0.002	0.003
Y	na	na	na	na	na	na	0.009	0.008	0.008	0.006	0.008	0.008	0.002	-	-	-	-	-	0.004	0.003	0.002
La	0.007	0.007	0.008	0.007	0.007	0.008	0.010	0.011	0.011	0.008	0.011	0.010	0.002	-	0.002	-	-	-	0.003	-	0.002
Ce	0.020	0.017	0.020	0.019	0.021	0.021	0.023	0.027	0.027	0.016	0.024	0.024	0.005	-	0.005	-	-	-	0.002	0.002	0.005
Nd	0.009	0.008	0.009	0.007	0.009	0.009	0.010	0.011	0.011	0.008	0.012	0.010	0.003	0.001	0.002	-	-	-	0.002	-	0.003
Na	0.033	0.019	0.024	0.019	0.028	0.027	0.032	0.038	0.033	0.024	0.038	0.032	0.010	-	0.006	-	-	-	0.012	-	0.010
K	0.005	-	-	-	-	0.000	0.002	-	-	0.001	-	-	0.002	-	0.001	-	-	-	0.003	-	0.002
Fe	0.010	0.035	0.008	0.007	0.005	0.008	0.018	0.012	0.008	0.023	0.011	0.019	0.038	0.003	0.009	0.027	-	0.008	0.012	0.014	0.038
Al	-	-	-	-	-	0.000	-	-	-	-	-	-	-	-	-	-	-	-	-	-	0.001
Total	**5.036**	**5.127**	**5.136**	**5.125**	**5.132**	**5.216**	**5.056**	**5.001**	**5.001**	**5.037**	**4.974**	**5.005**	**5.020**	**5.215**	**5.064**	**5.133**	**5.138**	**5.146**	**5.013**	**4.992**	**5.020**
ΣREY	0.036	0.032	0.037	0.033	0.037	0.037	0.052	0.057	0.057	0.038	0.055	0.052	0.012	0.003	0.009	0.004	0.003	0.001	0.010	0.006	0.012
P	2.911	2.892	2.884	2.889	2.890	2.849	2.913	2.936	2.939	2.931	2.946	2.937	2.983	2.904	2.960	2.941	2.936	2.936	2.975	2.992	2.983
S	0.024	0.016	0.016	0.016	0.017	0.018	0.017	0.017	0.013	0.015	0.019	0.017	0.002	0.003	0.003	-	-	-	0.006	-	0.002
As	-	0.001	-	-	-	-	-	-	0.002	0.001	-	0.001	-	-	-	-	-	-	-	-	0.000
Si	0.057	0.043	0.050	0.048	0.043	0.051	0.050	0.049	0.049	0.042	0.046	0.045	0.008	0.008	0.012	0.005	0.006	0.005	0.016	0.012	0.008
Total	**2.992**	**2.953**	**2.950**	**2.953**	**2.951**	**2.919**	**2.980**	**3.003**	**3.003**	**2.988**	**3.013**	**3.000**	**2.993**	**2.915**	**2.975**	**2.947**	**2.945**	**2.942**	**2.997**	**3.004**	**2.993**
F	0.863	0.910	0.949	0.852	0.852	0.918	0.831	0.811	0.863	0.886	0.865	0.806	1.004	0.912	0.903	0.981	0.905	0.924	0.970	0.935	1.004
Cl	0.069	0.050	0.046	0.025	0.044	0.048	0.064	0.049	0.055	0.047	0.068	0.070	0.021	0.005	0.011	-	0.006	-	0.052	0.003	0.021
OH	0.068	0.040	0.005	0.124	0.104	0.034	0.105	0.141	0.082	0.067	0.066	0.124	-0.024	0.083	0.086	0.019	0.089	0.075	0.000	0.062	0.000
Total	**1.000**	**1.000**	**1.000**	**1.000**	**1.000**	**1.000**	**1.000**	**1.000**	**1.000**	**1.000**	**1.000**	**1.000**	**1.000**	**1.000**	**1.000**	**1.000**	**1.000**	**1.000**	**1.022**	**1.000**	**1.024**

<mdl-Below minimum detection limit

na-Not aplicable (element not measured)

Electronic Appendix B5. Summary of EPMA data for apatite from Distal Satellite

	High REY+S hydrothermal grains							High REY-S-Na, Kfs-hosted grains			Low REY + S overprinted grains			
	RX6687					RX6691		RX6687			RX6687		RX6691	
	1	2	3	4	5	1	2	1	2	3	1	2	1	2
	Mean	Mean	Mean	Mean	Mean	Mean	Mean	Mean	Mean	Mean	Mean	Mean	Mean	Mean
	(n=9)	(n=1)	(n=1)	(n=1)	(n=2)	(n=4)	(n=5)	(n=4)	(n=2)	(n=1)	(n=4)	(n=1)	(n=2)	(n=1)
F	3.34	3.17	3.63	3.03	3.56	3.64	3.55	3.49	3.67	2.91	3.47	3.73	3.44	3.47
Cl	0.05	0.02	0.03	0.03	0.02	0.02	0.02	0.03	0.03	0.03	<mdl	<mdl	<mdl	0.03
Na_2O	0.13	0.18	0.16	0.12	0.12	0.15	0.18	0.32	0.25	0.19	<mdl	0.07	<mdl	<mdl
SiO_2	0.48	0.48	0.36	0.58	0.49	0.36	0.59	0.60	0.52	0.55	0.01	0.10	0.08	0.05
Al_2O_3	<mdl	0.01	<mdl	<mdl	0.08	<mdl	<mdl	<mdl	0.01	<mdl	<mdl	0.03	<mdl	0.02
MgO	<mdl	<mdl	<mdl	<mdl	<mdl	<mdl	<mdl	<mdl	0.01	<mdl	<mdl	0.03	<mdl	0.01
P_2O_5	38.84	38.42	41.46	40.76	40.80	38.34	37.88	38.22	40.63	40.42	40.09	41.63	39.35	40.71
SO_3	0.24	0.31	0.24	0.23	0.20	0.21	0.27	0.62	0.58	0.53	<mdl	0.05	0.04	0.01
K_2O	<mdl	<mdl	0.10	0.04	0.09	0.01	<mdl	<mdl	0.07	0.02	<mdl	0.10	<mdl	0.10
CaO	54.11	54.56	54.88	54.30	54.46	54.47	54.53	54.69	54.25	54.42	56.57	55.31	56.43	55.55
TiO_2	<mdl	<mdl	<mdl	<mdl	<mdl	<mdl	<mdl	<mdl	<mdl	<mdl	<mdl	<mdl	<mdl	<mdl
Cr_2O_3	<mdl	<mdl	<mdl	<mdl	<mdl	0.02	<mdl	<mdl	<mdl	0.00	<mdl	<mdl	<mdl	<mdl
MnO	<mdl	<mdl	<mdl	<mdl	0.02	<mdl	<mdl	<mdl	<mdl	<mdl	<mdl	<mdl	<mdl	<mdl
FeO	0.11	0.05	0.21	0.23	0.57	0.35	0.71	0.03	0.23	0.32	<mdl	0.34	0.66	0.26
As_2O_3	<mdl	<mdl	<mdl	<mdl	<mdl	<mdl	<mdl	0.02	<mdl	<mdl	<mdl	<mdl	<mdl	<mdl
SrO	na	na	0.03	0.04	0.03	na	na	na	0.03	0.04	na	0.04	na	na
Y_2O_3	na	na	0.11	0.13	0.11	na	na	na	0.13	0.14	na	0.04	na	na
La_2O_3	0.30	0.32	0.14	0.37	0.21	0.25	0.35	0.33	0.25	0.26	<mdl	0.05	<mdl	<mdl
Ce_2O_3	0.69	0.71	0.44	0.77	0.47	0.66	0.87	0.72	0.65	0.64	0.04	<mdl	<mdl	0.08
Nd_2O_3	0.22	0.28	0.21	0.26	0.18	0.22	0.27	0.31	0.29	0.24	<mdl	0.05	<mdl	<mdl
Total	**98.55**	**98.53**	**102.03**	**100.95**	**101.42**	**98.73**	**99.27**	**99.38**	**101.61**	**100.73**	**100.27**	**101.61**	**100.01**	**100.16**
Calculated formulae (9 apfu)														
Ca	**5.083**	**5.132**	**4.941**	**4.935**	**4.945**	**5.144**	**5.143**	**5.116**	**4.918**	**4.945**	**5.207**	**4.995**	**5.229**	**5.090**
Mg	-	-	-	-	-	-	-	-	0.001	-	-	0.004	-	0.002
Mn	-	-	-	-	0.001	-	-	-	-	-	-	-	-	-
Sr	-	-	0.001	0.002	0.002	-	-	-	0.002	0.002	-	0.002	-	-
Y	-	-	0.005	0.006	0.005	-	-	-	0.006	0.006	-	0.002	-	-
La	0.010	0.010	0.004	0.012	0.007	0.008	0.011	0.011	0.008	0.008	-	0.002	-	-
Ce	0.022	0.023	0.013	0.024	0.014	0.021	0.028	0.023	0.020	0.020	0.001	-	-	0.002
Nd	0.007	0.009	0.006	0.008	0.006	0.007	0.008	0.010	0.009	0.007	-	0.001	-	-
Na	0.021	0.031	0.026	0.020	0.020	0.026	0.031	0.055	0.041	0.032	-	0.011	-	-
K	-	-	0.011	0.004	0.009	0.001	-	-	0.007	0.002	-	0.011	-	0.011
Fe	0.008	0.004	0.015	0.016	0.040	0.026	0.052	0.002	0.016	0.023	0.000	0.024	0.048	0.019
Ti	-	-	-	-	-	-	-	-	-	-	-	-	-	-
Al	-	0.001	-	-	0.008	-	-	-	0.001	-	-	0.003	-	0.002
Cr	-	-	-	-	-	0.003	-	-	-	0.000	-	-	-	-
Total	**5.152**	**5.209**	**5.023**	**5.027**	**5.056**	**5.236**	**5.275**	**5.216**	**5.028**	**5.047**	**5.208**	**5.054**	**5.277**	**5.125**
ΣREY	0.039	0.042	0.029	0.050	0.032	0.036	0.048	0.043	0.043	0.041	0.001	0.005	0.000	0.002
P	2.883	2.856	2.949	2.927	2.927	2.861	2.823	2.825	2.910	2.902	2.916	2.971	2.880	2.947
S	0.016	0.020	0.015	0.015	0.013	0.014	0.018	0.040	0.037	0.034	-	0.003	0.003	0.001
As	-	-	-	-	-	-	-	0.001	-	-	-	-	-	-
Si	0.042	0.043	0.031	0.049	0.041	0.032	0.052	0.052	0.044	0.047	0.001	0.008	0.007	0.004
Total	**2.941**	**2.918**	**2.996**	**2.991**	**2.981**	**2.907**	**2.893**	**2.919**	**2.991**	**2.982**	**2.917**	**2.982**	**2.890**	**2.952**
F	0.927	0.881	0.964	0.813	0.954	1.015	0.987	0.962	0.982	0.782	0.942	0.993	0.940	0.939
Cl	0.007	0.003	0.004	0.004	0.002	0.003	0.003	0.004	0.004	0.005	-	-	-	0.005
OH	0.066	0.116	0.031	0.183	0.044	0.000	0.010	0.034	0.014	0.213	0.058	0.007	0.060	0.056
Total	**1.000**	**1.000**	**1.000**	**1.000**	**1.000**	**1.018**	**1.000**	**1.000**	**1.000**	**1.000**	**1.000**	**1.000**	**1.000**	**1.000**

<mdl-Below minimum detection limit

na-Not aplicable (element not measured)

ELECTRONIC APPENDIX C FOR CHAPTER 2

Procedure for AST and apatite-fluid-melt partitioning

Whole rock assays from drillhole RD2495 (Fig. 1) were used to calculate AST for the RDG. This drillhole was chosen due to the low level of alteration inferred from the preservation of mafic minerals, and by the low levels of hydrothermal minerals such as hematite and sericite. Individual assays were selected on the basis of K_2O/Na_2O ratios and Fe concentrations (Kontonikas-Charos et al., 2015). The use of whole rock samples with little hydrothermal alteration allows for the more accurate AST estimates as the assumption must be made that whole rock P_2O_5 concentrations approximate to those at the time of AST, and that the majority of P_2O_5 in whole rock is hosted by apatite. Both assumptions are considered valid as apatite is the only primary phosphate identified, and the phase is present as inclusions in all minerals, pointing to its early crystallisation. Whole rock compositions vary from slightly metaluminous to slightly peraluminous.

AST calculations were performed using the formulae of Harrison and Watson (1984) and Bea et al. (1992), yielding mean AST temperatures of 857±26 °C (n=10) and 854.5±40.3 °C (n=11), respectively. Potential errors are largely dependent on assumptions made with respect to the proportion of crystallisation of the host melt prior to apatite saturation. Neither Harrison and Watson (1984) nor Bea et al. (1992) provide an approach to their error quantification. Piccoli and Candela (1994), however, state that in granitic melts, apatite would, as a general rule, crystallise within 30 °C of the AST, and cite the distinct lack of zoning in apatite from the Plinian phase of the Mt. Bishop Tuff, Long Valley Caldera, USA, as evidence for rapid crystallisation. Zoning in RDG apatite would thus infer a protracted or perhaps discontinuous crystallisation history, providing further evidence for contamination of the RDG by exotic, potentially mafic material.

Calculations were performed using *Saturnin* (Janoušek, 2006) with formulae presented therein.

Roxby Downs Granite apatite saturation estimates (RD2495)

Sample interval depth (m)	Al_2O_3	P_2O_5	SiO_2	CaO	K_2O	Na_2O	A/CNK	AST (Harrison and Watson 1984) ^oC	AST (Bea et al. 1992) ^oC
440-445	13.06	0.069	68.46	0.85	5.20	3.79	0.973	851.3	na
455-460	13.45	0.046	71.03	0.94	5.24	3.76	0.992	840.5	na
460-465	13.66	0.069	72.10	0.84	5.14	3.80	1.023	na	872.1
465-470	13.81	0.069	72.74	0.80	5.14	3.90	1.029	na	874.9
470-475	13.34	0.092	69.96	1.15	4.90	3.79	0.979	894.9	na
495-500	13.45	0.069	70.39	0.34	5.88	2.76	1.168	na	749
510-515	13.60	0.069	69.53	0.98	5.23	3.81	0.992	862.5	na
515-520	13.40	0.092	68.46	1.06	5.17	3.72	0.982	879.4	na
545-550	13.51	0.092	68.67	1.06	5.14	3.88	0.973	881.7	na
585-590	13.57	0.069	69.74	1.18	5.30	3.92	0.947	864.7	na
625-630	12.96	0.069	68.03	0.67	5.97	3.18	1.003	na	844.6
630-635	12.91	0.092	66.75	0.70	5.88	3.10	1.013	na	851.1
660-665	12.92	0.069	66.96	0.59	5.99	3.11	1.02	na	820.6
665-670	12.53	0.069	66.75	0.83	5.73	3.13	0.975	832.9	na
690-695	12.64	0.069	64.40	0.77	6.16	3.06	0.965	806.5	na
760-765	12.89	0.069	68.89	1.15	5.24	3.92	0.907	855.8	na
770-775	13.96	0.069	72.10	1.16	4.95	3.79	1.019	na	875.2
780-785	14.23	0.069	72.95	0.85	5.06	3.98	1.048	na	863.4
785-790	13.98	0.069	72.53	0.84	4.96	4.07	1.028	na	873
790-795	13.96	0.069	72.53	1.01	4.91	4.12	1.002	na	891.2
795-800	14.19	0.069	72.53	1.11	5.01	4.02	1.011	na	885.3
							Average	857.0	854.6
							Stdev	26.0	40.3
							n	10	11

Table showing selected whole-rock assays used in the calculation of apatite saturation temperatures. AST calculations for whole-rock assays of subaluminous composition were performed using formulae of Harrison and Watson (1984), whereas the AST for peraluminous samples was calculated using the formula given by Bea et al. (1992).

Cl-concentrations were calculated in melt and coexisting volatile phase at the time of AST using the methodology outlined in Piccoli and Candela (1994), specifically formulae 18, 19

and 27 therein. Average values of F and Cl, as measured by EPMA, and calculated OH values assuming stoichiometric apatite were grouped according to sample and an averaged AST temperature of 855.74 ^{o}C was used in the calculation. A pressure of 2.2 kbar from Al-in hornblende geothermobarometry (Creaser (1989); Kontonikas-Charos (unpublished data)) was used for all samples.

References

Bea, F., Fershater, G. and Corretge, L.G., 1992. The geochemistry of phosphorus in granite rocks and the effect of aluminium. Lithos 29, 43-56.

Creaser, R.A., 1989. The geology and petrology of Middle Proterozoic felsic magmatism of the Stuart Shelf, South Australia. Unpublished Ph.D. thesis, La Trobe University, Melbourne.

Harrison, T.M. and Watson, E.B., 1984. The behaviour of apatite during crustal anatexis: equilibrium and kinetic considerations. Geochimica et Cosmochimica Acta 48, 1467-1477.

Janoušek, V., 2006. Saturnin, R language script for application of accessory-mineral saturation models in igneous geochemistry. Geologica Carpathica 57, 131-142.

Kontonikas-Charos, A., Ciobanu, C.L., Cook, N.J., Ehrig, K. and Kamenetsky, V.S., 2015. Deuteric coarsening and albitization in Hiltaba granites from the Olympic Dam IOCG deposit, South Australia. In: Proceedings, Mineral Resources in a Sustainable World, 13th Biennial SGA Meeting, Nancy, France, August 2015, volume 3, p. 1099-1102.

Piccoli, P.M. and Candela, P.A., 1994. Apatite in felsic rocks: a model for the estimation on initial halogen concentrations in the Bishop Tuff (Long Valley) and Tuolumne Intrusive Suite (Sierra Nevada Batholith) magmas. American Journal of Science 294, 92-135.

ADDITIONAL MATERIAL B

SUPPLEMENTARY DATA FOR CHAPTER 3

RARE EARTH ELEMENT BEHAVIOUR IN APATITE FROM THE OLYMPIC DAM CU-U-AU-AG DEPOSIT, SOUTH AUSTRALIA

Sasha Krneta[1], Cristiana L. Ciobanu[2], Nigel J. Cook[2], Kathy Ehrig[3], Alkis Kontonikas-Charos[1]

[1]*School of Physical Sciences, The University of Adelaide, Adelaide, S.A., 5005, Australia*

[2]*School of Chemical Engineering, The University of Adelaide, Adelaide, S.A., 5005, Australia*

[3]*BHP Olympic Dam, Adelaide, SA 5000, Australia*

Paper published in Minerals, 7(8), 135

SUPPLEMENTARY MATERIAL TABLE S1 FOR CHAPTER 3

Supplementary Material Table S1
Typical minimum detection limits (mdl) for LA-ICP-MS are summarized in the table below.

Element	mdl (ppm)	Element	mdl (ppm)	Element	mdl (ppm)
Na	2.19	**Rb**	0.34	**Gd**	0.15
Mg	0.12	**Sr**	0.07	**Tb**	0.02
Al	0.61	**Zr**	0.09	**Dy**	0.12
Si	63.81	**Nb**	0.05	**Y**	0.08
S	7.23	**Mo**	0.25	**Ho**	0.03
K	3.58	**Sn**	0.29	**Er**	0.08
Sc	0.17	**Cs**	0.17	**Tm**	0.03
Ti	2.43	**Ba**	0.40	**Yb**	0.11
V	0.06	**Ta**	0.02	**Lu**	0.03
Mn	0.71	**W**	0.09	**^{204}Pb**	3.98
Fe	5.48	**La**	0.10	**^{206}Pb**	0.12
Co	0.06	**Ce**	0.16	**^{208}Pb**	0.06
Ni	0.27	**Pr**	0.07	**Th**	0.04
Cu	2.30	**Nd**	0.37	**U**	0.02
Zn	0.56	**Sm**	0.27		
As	1.75	**Eu**	0.03		

SUPPLEMENTARY MATERIAL TABLE S2 FOR CHAPTER 3

Standards, X-ray lines, count times and typical minimum detection limits (mdl) for electron probe microanalysis are summarized in the table below.

	CAMECA SX-Five			
Element	**Standard**	**X-ray line**	**Count time (s)** unknown/ background	**Average mdl** (ppm)
Na	Albite	Na Kα	15/7.5	265
K	Sanadine	K Kα	15/7.5	141
Ca	Plagioclase	Ca Kα	15/7.5	219
Mn	Rhodonite	Mn Kα	15/15	465
Mg	Almandine	Mg Kα	15/7.5	158
Fe	Almandine	Fe Kα	15/7.5	609
Al	Albite	Al Kα	15/7.5	132
Si	Albite	Si Kα	15/7.5	140
Ti	Rutile	Ti Kα	15/7.5	200
F	Synthetic CaF_2	F Kα	15/15	428
Cl	Tugtupite	Cl Kα	15/7.5	171
P	Apatite	P Kα	15/7.5	153
Sr	Celestite	Sr Lα	15/15	523
Y	REE1	Y Lα	15/15	552
La	La Glass	La Lα	30/15	856
Ce	Ce Glass	Ce Lα	30/15	853
Nd	Nd Glass	Nd Lß	30/15	827
Cr	Chromite	Cr Kα	15/7.5	270
As	Gallium Arsenide	As Kα	15/15	282
S	Marcasite	S Kα	10/5	183

ADDITIONAL MATERIAL C

SUPPLEMENTARY DATA FOR CHAPTER 4

THE WIRRDA WELL AND ACROPOLIS PROSPECTS, GAWLER CRATON, SOUTH AUSTRALIA: INSIGHTS INTO EVOLVING FLUID CONDITIONS THROUGH APATITE CHEMISTRY

Sasha Krneta[1], Nigel J. Cook[2], Cristiana L. Ciobanu[2], Kathy Ehrig[3], Alkis Kontonikas-Charos[1]

[1]*School of Physical Sciences, The University of Adelaide, Adelaide, S.A., 5005, Australia*

[2]*School of Chemical Engineering, The University of Adelaide, Adelaide, S.A., 5005, Australia*

[3]*BHP Olympic Dam, Adelaide, SA 5000, Australia*

Paper published in Journal of Geochemical Exploration 181, 276-291.

ELECTRONIC APPENDIX A

Standards, X-ray lines, count times and typical minimum detection limits (mdl) for electron probe microanalysis are summarized in the table below.

	University of Adelaide				University of Tasmania			
Element	**Standard**	**X-ray line**	**Count time (s)** unknown/ background	**Average mdl** (ppm)	**Standard**	**X-ray line**	**Count time (s)** unknown/ background	**Average mdl** (ppm)
Na	Albite	Na Kα	15/7.5	265	Albite	Na Kα	20/10	228
K	Sanadine	K Kα	15/7.5	141	Sanadine	K Kα	20/10	110
Ca	Plagioclase	Ca Kα	15/7.5	219	Plagioclase	Ca Kα	20/3	150
Mn	Rhodonite	Mn Kα	15/15	465	Rhodonite	Mn Kα	20/10	267
Mg	Almandine	Mg Kα	15/7.5	158	Almandine	Mg Kα	10/5	131
Fe	Almandine	Fe Kα	15/7.5	609	Almandine	Fe Kα	20/10	287
Al	Albite	Al Kα	15/7.5	132	Albite	Al Kα	10/5	106
Si	Albite	Si Kα	15/7.5	140	Albite	Si Kα	20/10	124
Ti	Rutile	Ti Kα	15/7.5	200	Rutile	Ti Kα	50/25	126
F	Synthetic CaF_2	F Kα	15/15	428	Synthetic CaF_2	F Kα	60/50	381
Cl	Tugtupite	Cl Kα	15/7.5	171	Tugtupite	Cl Kα	30/15	131
P	Apatite	P Kα	15/7.5	153	Apatite	P Kα	20/10	120
Sr	Celestite	Sr Lα	15/15	523	Celestite	Sr Lα	40/20	339
Y	REE1	Y Lα	15/15	552	REE1	Y Lα	70/35	310
La	La Glass	La Lα	30/15	856	La Glass	La Lα	60/30	554
Ce	Ce Glass	Ce Lα	30/15	853	Ce Glass	Ce Lα	50/25	519
Nd	Nd Glass	Nd Lß	30/15	827	Nd Glass	Nd Lß	60/30	475
Cr	Chromite	Cr Kα	15/7.5	270	Chromite	-	-	-
As	Gallium Arsenide	As Kα	15/15	282	Gallium Arsenide	As Kα	30/15	233
S	Marcasite	S Kα	10/5	183	Marcasite	S Kα	30/15	121

Typical minimum detection limits (mdl) for LA-ICP-MS are summarized in the table below.

Element	mdl (ppm)	Element	mdl (ppm)	Element	mdl (ppm)
Na	2.20	**Rb**	0.49	**Gd**	0.15
Mg	0.12	**Sr**	0.06	**Tb**	0.02
Al	0.49	**Zr**	0.10	**Dy**	0.09
Si	59.1	**Nb**	0.05	**Y**	0.03
S	6.50	**Mo**	0.28	**Ho**	0.03
K	3.52	**Sn**	0.35	**Er**	0.07
Sc	0.18	**Cs**	0.25	**Tm**	0.02
Ti	2.51	**Ba**	0.40	**Yb**	0.11
V	0.06	**Ta**	0.02	**Lu**	0.02
Mn	0.77	**W**	0.09	**Pb204**	3.67
Fe	5.09	**La**	0.05	**Pb206**	0.12
Co	0.09	**Ce**	0.04	**Pb208**	0.06
Ni	0.40	**Pr**	0.04	**Th**	0.03
Cu	1.37	**Nd**	0.22	**U**	0.02
Zn	0.57	**Sm**	0.27		
As	1.76	**Eu**	0.04		

APPENDIX B FOR CHAPTER 4

Appendix B. Summary of EPMA data for apatite from the Wirrda Well prospect

	Magnetite associated apatite				Hematite-pyrite associated apatite			Calcite vein hosted apatite			Bornite-chalcocite hosted apatite		
	WRD33-3	WRD33-7	WRD33-8	WRD33-9	WRD33-4	WRD33-5	WRD33-6	WRD33-1	WRD33-2	WRD33-3	rx7577	rx7579	rx7578
	Mean n=10	Mean n=42	Mean n=1	Mean n=2	Mean n=19	Mean n=19	Mean n=14	Mean n=6	Mean n=9	Mean n=10	Mean n=6	Mean n=6	Mean n=6
F	3.675	3.443	2.946	3.590	3.215	3.325	3.401	3.627	3.450	3.281	3.715	3.699	3.617
Cl	0.050	0.086	0.086	0.130	0.040	0.047	0.093	0.048	0.044	0.076	0.022	<mdl	<mdl
Na_2O	<mdl	0.074	<mdl	<mdl	0.141	0.105	0.135	<mdl	<mdl	<mdl	0.033	<mdl	<mdl
SiO_2	0.642	0.206	0.236	0.335	0.302	0.258	0.228	0.029	0.027	0.071	0.066	<mdl	0.099
Al_2O_3	<mdl	<mdl	<mdl	<mdl	<mdl	<mdl	<mdl	0.016	<mdl	<mdl	0.023	0.046	0.034
MgO	<mdl	<mdl	<mdl	0.015	<mdl	<mdl	<mdl	<mdl	<mdl	<mdl	0.014	<mdl	<mdl
P_2O_5	41.311	42.251	42.578	42.512	41.935	42.296	42.160	39.892	41.584	41.874	41.993	41.801	41.945
SO_3	0.038	0.077	0.005	0.017	0.198	0.202	0.154	0.029	0.019	<mdl	0.135	<mdl	<mdl
K2O	<mdl	<mdl	<mdl	0.073	<mdl	<mdl	<mdl	<mdl	<mdl	<mdl	0.022	<mdl	<mdl
CaO	54.988	55.249	54.851	55.318	53.641	54.711	53.981	56.095	55.865	55.542	55.240	54.777	55.467
TiO_2	<mdl	<mdl	<mdl	<mdl	<mdl	<mdl	<mdl	<mdl	<mdl	<mdl	<mdl	<mdl	<mdl
Cr_2O_3	<mdl	<mdl	na	na	na	na	na	<mdl	<mdl	<mdl	na	na	na
MnO	<mdl	<mdl	0.046	0.034	<mdl	<mdl	0.040	0.083	0.069	0.072	<mdl	<mdl	<mdl
FeO	0.084	0.274	0.149	0.085	0.307	0.269	0.233	0.411	<mdl	0.205	0.323	1.200	0.448
As_2O_3	<mdl	<mdl	<mdl	<mdl	<mdl	<mdl	<mdl	<mdl	<mdl	<mdl	<mdl	<mdl	<mdl
SrO	na	0.055	<mdl	<mdl	<mdl	<mdl	<mdl	na	na	na	0.164	<mdl	<mdl
Y_2O_3	na	0.144	0.228	0.172	0.160	0.166	0.140	na	na	na	0.163	0.163	0.159
La_2O_3	0.124	0.081	0.065	0.120	0.161	0.122	0.149	<mdl	<mdl	<mdl	<mdl	<mdl	<mdl
Ce_2O_3	0.396	0.189	0.121	0.169	0.297	0.219	0.296	<mdl	<mdl	<mdl	0.068	0.095	0.116
Nd_2O_3	0.357	0.130	0.098	0.210	0.222	0.176	0.159	<mdl	<mdl	<mdl	0.060	0.116	0.132
Total	**101.566**	**102.169**	**101.472**	**102.771**	**100.479**	**101.824**	**100.967**	**100.335**	**101.294**	**101.186**	**102.622**	**102.154**	**103.051**
Calculated formulae (9 apfu)													
Ca	4.967	4.938	4.900	4.921	4.851	4.890	4.866	5.175	5.047	5.004	4.914	4.923	4.947
Mg	-	-	-	0.002	-	-	-	-	-	-	0.001	-	-
Mn	-	-	0.003	0.002	-	-	0.003	0.006	0.005	0.005	-	-	-
Sr	-	0.003	-	-	-	-	-	-	-	-	0.004	-	-
Y	-	0.006	0.010	0.008	0.007	0.007	0.006	-	-	-	0.012	0.012	0.012
La	0.004	0.003	0.002	0.004	0.005	0.004	0.005	-	-	-	-	-	-
Ce	0.012	0.006	0.004	0.005	0.009	0.007	0.009	-	-	-	0.002	0.002	0.004
Nd	0.011	0.004	0.003	0.006	0.007	0.005	0.005	-	-	-	0.002	0.003	0.004
Na	-	0.012	-	-	0.023	0.017	0.022	-	-	-	0.008	-	0.004
K	-	-	-	0.008	-	-	-	-	-	-	0.004	-	-
Fe	0.006	0.019	0.010	0.006	0.022	0.019	0.016	0.030	-	0.014	0.022	0.084	0.031
Ti	-	-	-	-	-	-	-	-	-	-	-	-	-
Al	-	-	-	-	-	-	-	0.002	-	-	0.007	0.004	0.010
Cr	-	-	0.000	-	0.000	0.000	-	-	-	-	-	-	-
Total	**5.002**	**4.989**	**4.937**	**4.963**	**4.914**	**4.944**	**4.918**	**5.220**	**5.069**	**5.029**	**4.980**	**5.040**	**5.021**
SREY	0.022	0.015	0.019	0.021	0.023	0.020	0.019	0.003	0.003	0.003	0.016	0.018	0.020
P	2.948	2.984	3.005	2.988	2.996	2.987	3.003	2.908	2.969	2.981	2.952	2.969	2.956
S	0.002	0.005	0.000	0.001	0.013	0.013	0.010	0.002	0.001	-	0.033	-	-
As	-	-	-	-	-	-	-	-	-	-	-	-	-
Si	0.055	0.017	0.020	0.028	0.026	0.022	0.019	0.002	0.002	0.006	0.017	-	-
Total	**3.006**	**3.005**	**3.026**	**3.018**	**3.035**	**3.022**	**3.033**	**2.912**	**2.972**	**2.988**	**3.002**	**2.980**	**2.989**
F	0.980	0.908	0.777	0.942	0.858	0.877	0.905	0.988	0.920	0.872	0.976	0.981	0.997
Cl	0.007	0.012	0.012	0.018	0.006	0.007	0.013	0.007	0.006	0.011	0.002	<mdl	<mdl
OH	0.012	0.080	0.211	0.039	0.137	0.116	0.082	0.007	0.075	0.122	0.022	0.016	0.003
Total	**1.000**	**1.000**	**1.000**	**1.000**	**1.000**	**1.000**	**1.000**	**1.000**	**1.000**	**1.000**	**1.000**	**1.000**	**1.000**

<mdl-below minimum detection; na-not measured

APPENDIX C FOR CHAPTER 4

Appendix C. Summary of EPMA data for apatite from the Acropolis prospect

	Early Cl-,REY-rich apatite			LREE-,Cl-depleted zones		REY-,Cl-depleted zones	Chalcopyrite-barite associated apatite	Sericite associated apatite	
	ACD2-1	ACD2-2	ACD21.2A	ACD2-1	ACD2-2	ACD21.2A	ACD1-3	ACD2-3	ACD2-4
	mean	mean	mean	mean	mean	mean	mean	mean	mean
	n=12	n=8	n=8	n=11	n=9	n=4	n=7	n=20	n=40
F	3.305	3.436	3.674	3.302	3.325	3.812	3.634	3.300	3.389
Cl	0.231	<mdl	0.168	<mdl	<mdl	0.049	<mdl	<mdl	<mdl
Na2O	0.082	0.195	0.094	<mdl	<mdl	0.042	<mdl	<mdl	<mdl
SiO2	0.622	0.135	0.627	0.045	0.118	0.208	0.182	0.082	<mdl
Al2O3	<mdl	0.085	0.015	<mdl	0.093	0.008	0.103	<mdl	<mdl
MgO	0.028	0.092	0.019	<mdl	<mdl	<mdl	<mdl	<mdl	<mdl
P2O5	39.235	40.089	41.459	40.405	39.828	42.218	39.280	40.592	41.587
SO3	0.167	<mdl	0.392	<mdl	<mdl	0.158	<mdl	<mdl	<mdl
K2O	<mdl	<mdl	<mdl	<mdl	<mdl	<mdl	0.081	0.052	<mdl
CaO	54.127	54.094	54.853	55.658	55.437	55.280	55.194	55.213	55.402
TiO2	<mdl	<mdl	<mdl	<mdl	<mdl	<mdl	<mdl	<mdl	<mdl
Cr2O3	<mdl	<mdl	-	<mdl	<mdl	-	<mdl	<mdl	<mdl
MnO	0.044	<mdl	<mdl	<mdl	0.126	<mdl	0.063	0.106	0.118
FeO	0.141	0.382	0.120	0.348	0.342	0.532	0.421	0.348	0.196
As2O3	<mdl	<mdl	0.021	<mdl	<mdl	<mdl	<mdl	<mdl	<mdl
SrO	-	-	0.012	-	-	0.060	-	-	0.057
Y2O3	-	-	0.170	-	-	0.086	-	-	0.140
La2O3	0.296	0.179	0.316	<mdl	<mdl	0.070	<mdl	<mdl	<mdl
Ce2O3	0.779	0.599	0.821	<mdl	0.093	0.194	<mdl	<mdl	<mdl
Nd2O3	0.326	0.396	0.294	0.086	<mdl	0.138	0.095	<mdl	<mdl
Total	99.416	99.619	103.051	100.153	99.505	102.881	99.119	99.881	100.966
Calulted formulae (9 apfu)									
Ca	5.043	5.019	4.900	5.113	5.133	4.927	5.156	5.071	5.019
Mg	0.004	0.012	0.002	-	-	-	-	-	-
Mn	0.003	-	-	-	-	-	0.005	-	0.008
Sr	-	-	0.001	-	-	0.003	-	-	0.003
Y	-	-	0.012	-	-	0.006	-	-	0.006
La	0.010	0.006	0.010	-	-	0.002	-	-	-
Ce	0.025	0.019	0.025	-	-	0.006	-	-	-
Nd	0.010	0.012	0.009	0.003	-	0.004	0.003	-	-
Na	0.014	0.033	0.015	-	-	0.007	-	-	-
K	-	-	-	-	-	-	0.009	0.006	-
Fe	0.010	0.028	0.008	0.023	0.025	0.037	0.031	0.025	0.013
Ti	-	-	-	-	-	-	-	-	-
Al	-	0.009	0.001	-	0.009	0.001	0.011	-	-
Cr	-	-	-	-	-	-	-	-	-
Total	5.120	5.132	4.984	5.155	5.192	4.996	5.216	5.119	5.053
SREY	0.044	0.037	0.056	0.007	0.004	0.018	0.005	0.003	0.007
P	2.888	2.939	2.926	2.933	2.914	2.973	2.900	2.946	2.976
S	0.011	-	0.025	-	-	0.010	-	-	-
As	-	-	0.001	-	-	-	-	-	-
Si	0.054	0.012	0.052	0.004	0.010	0.017	0.016	0.007	-
Total	2.954	2.947	3.004	2.938	2.924	3.001	2.917	2.954	2.978
F	0.909	0.941	0.969	0.895	0.909	1.003	1.002	0.894	0.906
Cl	0.034	-	0.024	-	-	0.007	-	-	-
OH	0.057	0.058	0.008	0.094	0.090	-0.010	-0.003	0.104	0.093
Total	1.000	1.000	1.000	1.000	1.000	1.000	1.000	1.000	1.000

<mdl-below minimum detection; na-not measured

APPENDIX D FOR CHAPTER 4

Appendix D. Summary of LA-ICP-MS data for apatite from the Wirrda Well prospect

Magnetite associated apatite

WRD33-9	Na	Mg	Al	Si	S	K	Sc	Ti	V	Mn	Fe	Co	Ni	Cu	Zn	As	Rb	Sr	Zr	Nb	Mo	Sn	Cs	Ba
Mean n=(15)	713	989	2642	21615	242	2652	2.43	213	5.34	229	6231	0.68	2.36	15.7	12.0	38.1	34.0	226	0.37	1.03	<mdl	0.86	3.78	7.64
S.D.	276	1286	3082	19217	24.3	2365	2.70	347	5.51	87.8	11095	1.22	4.63	16.3	8.61	14.1	25.1	53.0	0.31	2.28	<mdl	0.58	2.96	6.89
Min	253	30.2	2.96	1471	203	4.47	0.48	27.1	0.60	142	241	0.12	0.30	1.50	2.23	14.6	1.99	116	0.07	0.02	<mdl	0.31	0.21	0.67
Max	1280	5206	9359	65483	299	6455	11.4	1120	20.0	453	34584	4.48	17.6	43.6	29.9	69.3	71.4	300	1.02	8.37	<mdl	2.22	9.4	20.6

	Ta	W	La	Ce	Pr	Nd	Sm	Eu	Gd	Tb	Dy	Y	Ho	Er	Tm	Yb	Lu	ΣREY	^{204}Pb	^{206}Pb	^{208}Pb	Th	U
	0.03	0.53	367	1277	205	992	297	33.9	341	55.2	332	1777	65.0	173	21.9	134	17.9	6089	6.62	61.3	6.33	19.6	24.4
	0.02	0.41	129	449	80.1	449	162	10.5	186	28.0	167	911	33.5	91.2	11.5	69.0	9.4	2785	2.85	88.2	5.70	20.7	15.2
	0.01	0.10	213	737	111	515	136	22.7	172	28.2	183	915	34.5	88.5	11.0	66.9	8.11	3242	2.86	7.41	0.67	3.39	4.03
	0.07	1.06	616	1975	383	2147	743	57.6	859	132	780	4219	154	416	52.1	313	42.1	12890	9.2	371	23.3	85.0	54.7

WRD33-3	Na	Mg	Al	Si	S	K	Sc	Ti	V	Mn	Fe	Co	Ni	Cu	Zn	As	Rb	Sr	Zr	Nb	Mo	Sn	Cs	Ba
Mean n=(6)	252	1646	891	2537	273	539	4.38	43.6	5.93	175	683	0.95	<mdl	<mdl	22.3	39.1	72.8	203	0.98	0.09	<mdl	2.18	0.78	11.4
S.D.	205	3778	907	1473	87.0	561	6.50	19.3	12.4	75.5	801	1.28	<mdl	<mdl	30.1	11.8	155	44.4	1.10	0.09	<mdl	3.13	0.53	24.6
Min	134	32.9	0.62	850	210	14.6	0.49	25.8	0.42	85.2	183	0.20	<mdl	<mdl	2.87	19.5	0.66	134	0.07	0.02	<mdl	0.18	0.40	0.27
Max	667	9357	1815	4079	443	1130	17.4	75.6	31.2	269	2081	2.42	<mdl	<mdl	57.0	53.4	350	247	2.57	0.27	<mdl	5.79	1.15	61.5

	Ta	W	La	Ce	Pr	Nd	Sm	Eu	Gd	Tb	Dy	Y	Ho	Er	Tm	Yb	Lu	ΣREY	^{204}Pb	^{206}Pb	^{208}Pb	Th	U
	<mdl	0.62	457	1700	287	1543	441	38.1	529	78.9	470	2691	95.3	250	32.4	199	29.1	8841	<mdl	66.3	9.2	49.9	38.0
	<mdl	0.38	340	1226	213	1145	317	21.3	367	54.6	326	1767	66.6	174	22.3	138	20.2	6197	<mdl	66.1	11.4	77.4	37.2
	<mdl	0.14	123	503	90.0	510	168	18.6	238	35.0	218	1401	47.1	125	15.8	98.2	12.1	3603	<mdl	8.92	1.17	4.43	7.84
	<mdl	0.98	1118	4083	704	3782	1057	71.1	1233	182	1087	5946	222	578	73.7	454	66.0	20656	<mdl	179	31.8	205	93.7

WRD33-7	Na	Mg	Al	Si	S	K	Sc	Ti	V	Mn	Fe	Co	Ni	Cu	Zn	As	Rb	Sr	Zr	Nb	Mo	Sn	Cs	Ba
Mean n=(5)	806	679	862	3713	253	380	1.63	54.6	1.68	240	1998	0.65	1.52	2.22	116	35.0	62.3	244	0.43	0.16	<mdl	<mdl	8.68	13.7
S.D.	570	1103	1363	1516	19.0	365	1.14	29.1	1.53	70.4	2893	0.88	1.03	0.25	209	20.2	114	103	0.48	0.15	<mdl	<mdl	13.7	25.8
Min	181	42.1	0.42	2008	238	7.40	0.59	33.8	0.45	177	282	0.13	0.79	2.04	0.93	18.4	1.49	144	0.04	0.04	<mdl	<mdl	0.62	0.13
Max	1446	2325	2865	4906	281	736	3.02	97.6	3.91	317	6296	1.97	2.24	2.39	429	59.3	234	361	1.04	0.38	<mdl	<mdl	24.5	52.4

	Ta	W	La	Ce	Pr	Nd	Sm	Eu	Gd	Tb	Dy	Y	Ho	Er	Tm	Yb	Lu	ΣREY	^{204}Pb	^{206}Pb	^{208}Pb	Th	U
	<mdl	0.16	335	1244	209	1059	318	29.6	365	57.5	367	2261	79.4	225	29.9	188	27.0	6794	<mdl	51.5	6.07	20.6	27.5
	<mdl	0.05	134	308	49.7	362	176	14.6	239	39.2	254	1518	54.3	158	20.9	127	18.2	3473	<mdl	41.0	3.71	17.0	26.9
	<mdl	0.13	176	767	137	690	179	18.3	187	28.1	181	1101	40.0	107	14.6	91.8	13.4	3731	<mdl	9.8	1.36	4.32	6.96
	<mdl	0.22	486	1564	275	1605	579	50.0	708	114	732	4422	157	453	60.4	371	53.8	11631	<mdl	98.3	10.8	44.3	69.2

Magnetite associated apatite continued…

WRD33-8	Na	Mg	Al	Si	S	K	Sc	Ti	V	Mn	Fe	Co	Ni	Cu	Zn	As	Rb	Sr	Zr	Nb	Mo	Sn	Cs	Ba
Mean n=(19)	310	555	2675	10345	259	1548	2.58	48.3	3.53	306	2748	<mdl	<mdl	<mdl	14.5	25.5	24.6	159	0.91	<mdl	<mdl	<mdl	<mdl	2.21
S.D.	133	1624	5968	15824	25.5	2996	3.19	35.3	6.77	74.9	5813	<mdl	<mdl	<mdl	31.4	6.81	59.1	42.0	0.68	<mdl	<mdl	<mdl	<mdl	3.29
Min	163	47.0	1.00	1663	232	6.42	0.87	20.2	0.61	207	328	<mdl	<mdl	<mdl	0.64	16.9	0.51	118	0.07	<mdl	<mdl	<mdl	<mdl	0.16
Max	547	6983	18409	56799	331	9306	14.3	148	28.0	539	19989	<mdl	<mdl	<mdl	111	41.6	233	282	2.65	<mdl	<mdl	<mdl	<mdl	10.2

Ta	W	La	Ce	Pr	Nd	Sm	Eu	Gd	Tb	Dy	Y	Ho	Er	Tm	Yb	Lu	ΣREY	^{204}Pb	^{206}Pb	^{208}Pb	Th	U
<mdl	0.26	365	1406	254	1311	408	36.9	465	73.4	444	2415	88.1	242	30.9	195	26.8	7761	<mdl	43.3	5.11	26.6	32.9
<mdl	0.31	174	687	126	650	197	13.9	213	32.9	195	1025	38.5	105	13.7	86.2	11.8	3571	<mdl	33.0	3.85	25.7	23.8
<mdl	0.11	123	467	84.3	445	162	15.1	178	27.5	165	902	33.5	90.2	11.1	65.9	9.1	2779	<mdl	7.45	0.99	2.42	5.95
<mdl	3.07	732	2726	486	2482	758	62.8	850	134	793	4184	160	433	56.3	354	47.2	14258	<mdl	127	15.8	97.9	84.2

Hematite-pyrite associated apatite

WRD33-4	Na	Mg	Al	Si	S	K	Sc	Ti	V	Mn	Fe	Co	Ni	Cu	Zn	As	Rb	Sr	Zr	Nb	Mo	Sn	Cs	Ba
Mean n=(23)	893	49.7	<mdl	1886	274	88.7	0.61	34.7	1.82	73.6	1091	<mdl	<mdl	<mdl	4.97	102	<mdl	363	0.09	0.48	<mdl	<mdl	<mdl	2.29
S.D.	525	23.3	<mdl	1381	85.5	140	0.51	14.1	2.05	37.0	1285	<mdl	<mdl	<mdl	3.04	28.9	<mdl	116	0.08	0.74	<mdl	<mdl	<mdl	1.65
Min	187	17.6	<mdl	580	214	7.73	0.21	20.0	0.29	37.5	101	<mdl	<mdl	<mdl	1.03	52.8	<mdl	140	0.03	0.02	<mdl	<mdl	<mdl	0.53
Max	2262	107	<mdl	7295	654	591	2.28	69.9	7.38	212	5049	<mdl	<mdl	<mdl	10.8	154	<mdl	501	0.34	3.48	<mdl	<mdl	<mdl	5.50

Ta	W	La	Ce	Pr	Nd	Sm	Eu	Gd	Tb	Dy	Y	Ho	Er	Tm	Yb	Lu	ΣREY	^{204}Pb	^{206}Pb	^{208}Pb	Th	U
<mdl	0.98	789	2383	332	1434	285	29.8	260	33.7	191	1199	37.5	101	12.6	76.6	11.6	7175	<mdl	12.8	2.57	11.8	7.82
<mdl	0.64	474	1378	182	745	129	10.4	108	14.8	85.9	518	17.2	46.2	5.8	36.1	4.8	3754	<mdl	12.5	1.88	12.2	5.18
<mdl	0.17	176	522	81.5	389	76.3	14.3	77.1	9.1	50.2	346	10.3	28.4	3.58	21.9	4.49	1809	<mdl	0.97	0.42	0.74	0.91
<mdl	2.26	1817	5411	728	2991	518	53.4	430	62.3	366	2080	74.7	205	25.5	162	21.6	14946	<mdl	64.9	8.43	46.5	18.6

WRD33-5	Na	Mg	Al	Si	S	K	Sc	Ti	V	Mn	Fe	Co	Ni	Cu	Zn	As	Rb	Sr	Zr	Nb	Mo	Sn	Cs	Ba
Mean n=(24)	594	96.4	56.5	1838	310	16.9	0.71	27.2	10.7	74.3	1019	<mdl	<mdl	<mdl	3.69	99	<mdl	332	0.13	0.23	<mdl	<mdl	<mdl	2.08
S.D.	338	243	122	1542	114	16.4	0.61	14.0	19.9	36.7	1413	<mdl	<mdl	<mdl	2.30	29.3	<mdl	108	0.07	0.27	<mdl	<mdl	<mdl	2.51
Min	222	17.5	0.47	623	228	3.86	0.14	14.4	0.19	39.5	54.6	<mdl	<mdl	<mdl	0.66	54.3	<mdl	144	0.04	0.02	<mdl	<mdl	<mdl	0.17
Max	1426	1233	464	7228	724	67.8	2.61	83.1	65.1	212	4847	<mdl	<mdl	<mdl	9.2	155	<mdl	471	0.24	1.02	<mdl	<mdl	<mdl	11.5

Ta	W	La	Ce	Pr	Nd	Sm	Eu	Gd	Tb	Dy	Y	Ho	Er	Tm	Yb	Lu	ΣREY	^{204}Pb	^{206}Pb	^{208}Pb	Th	U
<mdl	1.53	531	1649	233	1037	217	24.8	223	29.7	169	1087	34.4	94.7	12.1	76.4	12.1	5430	<mdl	12.1	2.83	14.3	7.35
<mdl	2.60	320	931	123	512	94.4	7.05	93.1	13.2	78.2	503	16.0	45.6	6.04	38.9	6.02	2787	<mdl	7.34	1.93	14.8	5.97
<mdl	0.03	201	666	96.2	435	86.7	15.7	86.1	10.0	57.1	369	11.5	29.8	3.82	24.1	4.43	2096	<mdl	1.13	0.50	1.07	0.80
<mdl	11.3	1418	3950	518	2137	372	39.5	355	50.3	302	1802	59.7	165	21.9	147	23.1	11359	<mdl	27.3	7.73	56.3	20.3

Hematite-pyrite associated apatite continued…

WRD33-6	Na	Mg	Al	Si	S	K	Sc	Ti	V	Mn	Fe	Co	Ni	Cu	Zn	As	Rb	Sr	Zr	Nb	Mo	Sn	Cs	Ba
Mean n=(22)	1024	136	233	1948	295	29.2	<mdl	34.3	3.08	200	1078	<mdl	<mdl	<mdl	8.26	67.8	<mdl	377	<mdl	0.23	<mdl	<mdl	<mdl	1.15
S.D.	509	210	524	968	91.9	40.0	<mdl	24.7	6.60	170	1008	<mdl	<mdl	<mdl	8.56	12.2	<mdl	46.4	<mdl	0.27	<mdl	<mdl	<mdl	1.28
Min	334	47.4	0.83	815	207	4.15	<mdl	11.7	0.16	84.2	328	<mdl	<mdl	<mdl	0.23	43.9	<mdl	309	<mdl	0.02	<mdl	<mdl	<mdl	0.17
Max	2609	788	1639	4301	562	154	<mdl	134	23.5	953	3916	<mdl	<mdl	<mdl	32.8	90.7	<mdl	550	<mdl	1.15	<mdl	<mdl	<mdl	5.21

Ta	W	La	Ce	Pr	Nd	Sm	Eu	Gd	Tb	Dy	Y	Ho	Er	Tm	Yb	Lu	ΣREY	^{204}Pb	^{206}Pb	^{208}Pb	Th	U
<mdl	0.32	806	2535	338	1405	262	25.6	246	34.0	203	1290	42.0	120	16.3	105	16.4	7444	<mdl	17.8	4.40	22.8	12.0
<mdl	0.25	451	1313	159	594	86.5	6.23	69.5	8.47	48.4	285	10.0	27.1	3.83	26.6	3.95	3092	<mdl	10.0	1.78	12.1	5.76
<mdl	0.04	237	797	117	551	123	13.3	132	17.2	108	723	22.1	61.5	7.91	46.9	8.10	2966	<mdl	3.30	0.85	1.97	1.61
<mdl	0.88	2089	6291	780	2977	478	39.2	388	48.8	269	1647	54.6	157	21.1	142	22.2	15402	<mdl	44.2	7.82	51.9	23.4

Calcite vein hosted apatite

WRD33-2	Na	Mg	Al	Si	S	K	Sc	Ti	V	Mn	Fe	Co	Ni	Cu	Zn	As	Rb	Sr	Zr	Nb	Mo	Sn	Cs	Ba
Mean n=(13)	260	24.3	1.91	355	270	42.3	0.55	45.6	0.16	414	1263	0.25	<mdl	<mdl	5.83	<mdl	<mdl	302	<mdl	0.05	<mdl	<mdl	0.19	13.6
S.D.	127	8.50	1.07	37.8	9.2	23.2	0.36	7.49	0.12	161	651	0.27	<mdl	<mdl	3.07	<mdl	<mdl	129	<mdl	0.05	<mdl	<mdl	0.04	6.31
Min	142	14.8	0.71	278	252	21.9	0.28	36.6	0.06	152	292	0.08	<mdl	<mdl	2.34	<mdl	<mdl	149	<mdl	0.01	<mdl	<mdl	0.16	3.13
Max	613	44.1	4.07	394	285	104	1.50	63.4	0.45	739	2398	1.04	<mdl	<mdl	11.5	<mdl	<mdl	532	<mdl	0.18	<mdl	<mdl	0.26	22.6

Ta	W	La	Ce	Pr	Nd	Sm	Eu	Gd	Tb	Dy	Y	Ho	Er	Tm	Yb	Lu	ΣREY	^{204}Pb	^{206}Pb	^{208}Pb	Th	U
<mdl	0.09	37.7	148	26.9	141	57.7	15.4	66.8	9.3	44.2	153	7.05	14.2	1.32	5.88	0.63	730	13.2	16.3	11.8	0.36	0.53
<mdl	0.09	8.72	22.9	4.31	26.5	13.1	3.67	15.0	1.53	6.51	17.7	0.81	1.74	0.17	1.19	0.11	124	10.6	11.3	9.8	0.23	0.44
<mdl	0.02	29.2	122	22.3	94.6	31.3	9.1	41.2	6.59	35.1	129	6.01	12.6	1.15	4.40	0.47	545	4.73	3.17	2.05	0.01	0.10
<mdl	0.27	58.1	201	36.4	198	83.7	22.0	97.2	12.6	59.2	192	9.1	19.4	1.68	8.16	0.85	1000	36.2	40.1	31.8	0.66	1.50

WRD33-3	Na	Mg	Al	Si	S	K	Sc	Ti	V	Mn	Fe	Co	Ni	Cu	Zn	As	Rb	Sr	Zr	Nb	Mo	Sn	Cs	Ba
Mean n=(4)	277	43.3	1.49	318	274	44.3	0.89	33.7	0.12	670	924	0.21	<mdl	<mdl	6.96	<mdl	<mdl	179	<mdl	<mdl	<mdl	<mdl	<mdl	13.0
S.D.	67.8	22.5	0.73	37.1	3.88	17.4	0.23	2.52	0.01	253	256	0.06	<mdl	<mdl	2.32	<mdl	<mdl	38.6	<mdl	<mdl	<mdl	<mdl	<mdl	4.89
Min	192	21.6	0.70	280	269	26.6	0.68	29.9	0.11	316	622	0.16	<mdl	<mdl	4.42	<mdl	<mdl	145	<mdl	<mdl	<mdl	<mdl	<mdl	8.20
Max	350	74.7	2.38	369	278	65.5	1.19	35.4	0.13	856	1247	0.25	<mdl	<mdl	10.0	<mdl	<mdl	231	<mdl	<mdl	<mdl	<mdl	<mdl	18.4

Ta	W	La	Ce	Pr	Nd	Sm	Eu	Gd	Tb	Dy	Y	Ho	Er	Tm	Yb	Lu	ΣREY	^{204}Pb	^{206}Pb	^{208}Pb	Th	U
0.02	0.13	38.4	146	24.4	120	38.5	9.7	43.2	6.49	35.6	144	6.25	12.7	1.17	5.38	0.61	633	12.3	26.9	11.0	0.25	0.17
0.00	0.04	5.59	18.0	2.96	16.0	4.27	1.44	6.53	1.00	4.52	19.0	0.83	1.89	0.13	1.14	0.12	83.5	6.85	12.5	5.37	0.06	0.06
0.02	0.11	32.3	129	21.8	107	34.2	8.26	37.0	5.59	32.0	127	5.39	10.7	1.06	3.88	0.44	556	4.31	11.2	4.86	0.20	0.09
0.03	0.16	44.6	166	28.1	141	42.5	11.3	51.9	7.70	41.4	171	7.39	15.2	1.33	6.49	0.73	737	20.4	39.0	17.5	0.32	0.23

Bornite-chalcocite hosted apatite

RX7578	Na	Mg	Al	Si	S	K	Sc	Ti	V	Mn	Fe	Co	Ni	Cu	Zn	As	Rb	Sr	Zr	Nb	Mo	Sn	Cs	Ba
Mean n=(10)	267	33.6	55.0	414	315	46.6	1.71	126	<mdl	121	403	<mdl	<mdl	<mdl	7.63	8.21	1.00	311	32.3	<mdl	<mdl	<mdl	<mdl	6.71
S.D.	123	17.0	89.1	155	33.4	25.6	1.21	37.2	<mdl	17.1	348	<mdl	<mdl	<mdl	4.51	4.13	0.51	94.2	23.9	<mdl	<mdl	<mdl	<mdl	2.50
Min	159	16.7	3.44	284	272	14.6	0.67	95.1	<mdl	83.8	15.3	<mdl	<mdl	<mdl	3.73	2.44	0.74	234	9.2	<mdl	<mdl	<mdl	<mdl	2.30
Max	556	70.8	294	795	373	78.0	4.47	218	<mdl	145	945	<mdl	<mdl	<mdl	18.9	15.3	1.91	482	78.3	<mdl	<mdl	<mdl	<mdl	9.6

Ta	W	La	Ce	Pr	Nd	Sm	Eu	Gd	Tb	Dy	Y	Ho	Er	Tm	Yb	Lu	ΣREY	^{204}Pb	^{206}Pb	^{208}Pb	Th	U
<mdl	<mdl	196	742	128	692	221	46.2	326	46.7	249	875	36.9	75.1	6.27	27.9	3.36	3672	268	284	284	181	19.7
<mdl	<mdl	73.9	250	39.6	166	39.7	7.15	46.7	7.29	35.9	215	7.65	20.0	1.97	8.79	1.60	921	90.6	75.7	82.0	196	17.2
<mdl	<mdl	96.5	409	81.2	465	148	33.8	242	34.1	188	578	26.2	49.8	4.02	16.4	1.45	2373	108	170	165	4.13	7.96
<mdl	<mdl	329	1194	203	952	279	58.3	383	58.2	301	1244	49.2	109	9.7	42.7	5.97	5218	431	406	409	540	62.4

RX7579	Na	Mg	Al	Si	S	K	Sc	Ti	V	Mn	Fe	Co	Ni	Cu	Zn	As	Rb	Sr	Zr	Nb	Mo	Sn	Cs	Ba
Mean n=(6)	196	71.5	118	1073	1093	76.0	2.22	232	2.80	103	7117	1.27	<mdl	<mdl	35.4	7.78	<mdl	283	83.8	0.49	7.05	<mdl	<mdl	8.10
S.D.	88.3	49.9	159	873	913	116	1.64	156	2.10	41.6	1946	1.44	<mdl	<mdl	43.9	4.34	<mdl	68.0	117	0.37	3.78	<mdl	<mdl	5.82
Min	96.1	26.0	23.3	289	507	9.4	1.04	104	1.08	75.9	5741	0.19	<mdl	<mdl	10.8	3.55	<mdl	215	8.74	0.15	4.17	<mdl	<mdl	2.73
Max	329	156	397	2192	2683	282	4.84	534	6.91	184	8493	3.70	<mdl	<mdl	124	13.5	<mdl	396	296	1.01	14.2	<mdl	<mdl	18.2

Ta	W	La	Ce	Pr	Nd	Sm	Eu	Gd	Tb	Dy	Y	Ho	Er	Tm	Yb	Lu	ΣREY	^{204}Pb	^{206}Pb	^{208}Pb	Th	U
<mdl	1.80	152	536	88.7	470	142	37.7	242	38.7	209	584	29.1	51.6	3.60	15.3	1.53	2601	168	184	161	4.31	12.2
<mdl	1.90	58.5	181	23.0	121	26.1	6.69	47.2	7.56	48.7	189	8.66	13.5	0.69	3.31	0.17	734	69.4	93.4	67.7	3.31	7.26
<mdl	0.20	80.6	319	59.4	330	102	26.3	176	28.7	147	359	19.0	32.0	2.77	9.8	1.23	1693	99	103	94.6	1.34	3.42
<mdl	5.43	234	781	117	644	175	44.0	291	45.8	260	898	41.9	70.2	4.58	20.1	1.69	3628	283	350	279	8.80	22.9

APPENDIX E FOR CHAPTER 4

Appendix E. Summary of LA-ICP-MS data for apatite from the Acropolis prospect

Early Cl-,REY-rich apatite

ACD2-1	Na	Mg	Al	Si	S	K	Sc	Ti	V	Mn	Fe	Co	Ni	Cu	Zn	As	Rb	Sr	Zr	Nb	Mo	Sn	Cs	Ba
Mean n=(20)	638	190	18.3	1445	259	22.6	1.03	35.1	1.79	252	909	0.16	0.45	2.85	4.15	117	<mdl	349	0.83	<mdl	<mdl	<mdl	<mdl	1.98
S.D.	176	40.5	20.9	487	13.8	19.7	0.65	3.58	0.73	180	303	0.09	0.11	2.11	2.69	59.0	<mdl	151	1.63	<mdl	<mdl	<mdl	<mdl	1.74
Min	350	108	1.00	675	221	4.50	0.28	30.1	0.58	163	638	0.02	0.27	1.26	0.67	53.4	<mdl	183	0.03	<mdl	<mdl	<mdl	<mdl	0.32
Max	907	249	63.8	2214	282	59.2	3.04	44.2	3.20	942	1675	0.31	0.66	8.60	8.38	260	<mdl	699	6.85	<mdl	<mdl	<mdl	<mdl	7.27

	Ta	W	La	Ce	Pr	Nd	Sm	Eu	Gd	Tb	Dy	Y	Ho	Er	Tm	Yb	Lu	ΣREY	^{204}Pb	^{206}Pb	^{208}Pb	Th	U
	<mdl	0.12	1577	4309	503	1901	310	36.4	285	34.8	186	1083	35.3	92.5	11.7	70.6	10.3	10446	<mdl	13.6	10.5	69.7	11.1
	<mdl	0.08	734	2093	213	756	103	12.2	96.3	11.1	61.1	384	12.2	34.3	4.70	30.8	4.52	4550	<mdl	7.85	6.04	51.1	7.19
	<mdl	0.02	674	2017	270	1180	191	21.7	154	18.5	90.8	567	17.3	44.2	6.04	35.9	5.19	5294	<mdl	2.72	1.93	8.70	2.14
	<mdl	0.29	3921	11291	1197	4397	633	66.8	523	64.2	360	2201	71.4	193	25.7	164	23.6	25130	<mdl	34.8	24.2	194	30.9

ACD2-2	Na	Mg	Al	Si	S	K	Sc	Ti	V	Mn	Fe	Co	Ni	Cu	Zn	As	Rb	Sr	Zr	Nb	Mo	Sn	Cs	Ba
Mean n=(8)	1030	251	257	1092	256	39.5	1.76	51.2	10.8	221	3148	0.70	1.29	4.56	104	29.1	0.99	686	0.43	0.16	0.66	<mdl	<mdl	8.15
S.D.	416	281	399	851	18.5	39.5	0.75	14.8	11.5	150	2997	0.66	0.64	2.66	61.1	22.5	0.75	495	0.40	0.18	0.39	<mdl	<mdl	7.60
Min	465	22.4	2.87	334	229	8.78	0.90	36.1	1.38	89.3	67.2	0.10	0.67	1.79	21.6	11.7	0.38	198	0.08	0.03	0.12	<mdl	<mdl	0.23
Max	1501	628	933	2394	274	105	3.17	78.4	25.8	502	6988	1.61	2.08	8.06	178	78.7	2.18	1293	0.97	0.44	1.32	<mdl	<mdl	17.6

	Ta	W	La	Ce	Pr	Nd	Sm	Eu	Gd	Tb	Dy	Y	Ho	Er	Tm	Yb	Lu	ΣREY	^{204}Pb	^{206}Pb	^{208}Pb	Th	U
	<mdl	0.20	1378	3654	534	2071	354	49.4	348	56.0	359	2002	75.1	196	21.9	114	13.8	11225	7.72	400	18.0	67.2	384
	<mdl	0.12	528	1228	204	839	147	19.5	106	21.8	186	1161	43.7	118	12.9	60.7	6.60	4682	3.77	468	4.27	38.7	475
	<mdl	0.09	662	1699	200	719	140	23.3	217	33.2	140	543	21.6	47.3	5.65	36.6	5.34	4493	3.05	52.4	12.1	25.5	35.5
	<mdl	0.40	2114	4907	741	2969	555	76.3	498	82.7	578	3386	126	330	36.7	182	22.4	16603	13.0	1209	22.6	146	1241

ACD212A	Na	Mg	Al	Si	S	K	Sc	Ti	V	Mn	Fe	Co	Ni	Cu	Zn	As	Rb	Sr	Zr	Nb	Mo	Sn	Cs	Ba
Mean n=(20)	951	190	<mdl	2888	317	<mdl	1.51	97.1	2.22	188	537	0.15	0.44	<mdl	<mdl	84.5	<mdl	204	0.36	<mdl	<mdl	<mdl	<mdl	2.36
S.D.	186	35.1	<mdl	429	13.1	<mdl	0.38	8.46	0.41	16.8	134	0.05	0.27	<mdl	<mdl	6.91	<mdl	18.2	0.13	<mdl	<mdl	<mdl	<mdl	3.32
Min	713	142	<mdl	2163	297	<mdl	0.88	79.8	1.57	162	403	0.03	0.16	<mdl	<mdl	67.2	<mdl	177	0.16	<mdl	<mdl	<mdl	<mdl	0.57
Max	1225	234	<mdl	3422	341	<mdl	2.01	113	2.96	208	1014	0.22	1.10	<mdl	<mdl	97.2	<mdl	231	0.61	<mdl	<mdl	<mdl	<mdl	13.1

	Ta	W	La	Ce	Pr	Nd	Sm	Eu	Gd	Tb	Dy	Y	Ho	Er	Tm	Yb	Lu	ΣREY	^{204}Pb	^{206}Pb	^{208}Pb	Th	U
	<mdl	<mdl	3390	8273	897	2968	391	50.2	305	36.6	213	1322	43.0	117	15.5	102	15.8	18139	<mdl	18.5	12.2	82.8	16.6
	<mdl	<mdl	904	1932	197	600	59.9	7.56	50.9	5.77	33.4	190	6.63	19.7	2.52	16.7	2.62	4028	<mdl	1.84	3.47	23.6	1.73
	<mdl	<mdl	2282	5790	640	2210	304	37.9	228	26.4	157	1002	31.6	84.4	10.6	73.2	12.1	12888	<mdl	14.8	7.16	51.5	13.0
	<mdl	<mdl	4436	10501	1126	3712	477	59.3	359	44.0	260	1546	51.3	141	18.6	121	20.0	22872	<mdl	21.1	16.6	110	19.2

LREE-,Cl-depleted zones

ACD2-1	Na	Mg	Al	Si	S	K	Sc	Ti	V	Mn	Fe	Co	Ni	Cu	Zn	As	Rb	Sr	Zr	Nb	Mo	Sn	Cs	Ba
Mean n=(8)	321	28.3	35.7	338	264	188	<mdl	43.4	5.92	217	958	2.52	1.12	2.67	6.49	21.1	13.3	428	0.71	<mdl	<mdl	<mdl	<mdl	6.4
S.D.	178	10.7	55.0	41.1	55.1	406	<mdl	9.9	11.0	309	802	3.43	1.76	2.50	5.38	10.9	26.8	247	0.90	<mdl	<mdl	<mdl	<mdl	8.9
Min	114	14.7	3.42	280	206	6.93	<mdl	30.4	0.08	49.2	92.1	0.10	0.09	0.79	2.84	2.90	0.33	217	0.03	<mdl	<mdl	<mdl	<mdl	0.4
Max	570	39.3	118	385	365	1106	<mdl	60.0	31.7	845	1984	8.29	4.25	6.99	15.0	38.1	61.2	892	2.36	<mdl	<mdl	<mdl	<mdl	24.4

Ta	W	La	Ce	Pr	Nd	Sm	Eu	Gd	Tb	Dy	Y	Ho	Er	Tm	Yb	Lu	ΣREY	^{204}Pb	^{206}Pb	^{208}Pb	Th	U
<mdl	0.09	92.2	367	79.6	487	200	34.5	266	28.1	112	356	15.5	28.6	2.44	10.7	1.24	2079	4.84	5.46	15.2	94.7	1.32
<mdl	0.05	63.2	253	50.2	274	84.4	13.0	107	10.9	43.6	144	5.99	11.7	0.95	3.72	0.55	1066	1.19	2.71	7.02	60.1	0.81
<mdl	0.04	30.2	156	37.8	232	86.6	17.1	122	12.4	47.6	141	6.47	11.0	1.06	5.22	0.52	907	3.49	1.43	7.85	35.1	0.43
<mdl	0.15	191	869	189	1069	333	52.5	416	43.3	171	547	23.5	43.8	3.77	15.1	2.14	3970	6.17	9.6	26.5	218	2.53

REY-,Cl-depleted zones

ACD212A	Na	Mg	Al	Si	S	K	Sc	Ti	V	Mn	Fe	Co	Ni	Cu	Zn	As	Rb	Sr	Zr	Nb	Mo	Sn	Cs	Ba
Mean n=(10)	263	436	7.44	720	314	<mdl	2.06	80.8	1.41	198	610	<mdl	<mdl	<mdl	10.1	82.9	<mdl	135	<mdl	<mdl	<mdl	<mdl	<mdl	3.46
S.D.	190	607	5.96	158	23.0	<mdl	2.06	15.8	0.76	191	904	<mdl	<mdl	<mdl	7.40	52.9	<mdl	67.9	<mdl	<mdl	<mdl	<mdl	<mdl	3.23
Min	117	38.4	0.81	480	287	<mdl	0.26	57.4	0.53	52.2	145	<mdl	<mdl	<mdl	1.55	18.3	<mdl	69.8	<mdl	<mdl	<mdl	<mdl	<mdl	0.45
Max	739	1494	14.6	936	349	<mdl	6.58	109	2.64	508	1965	<mdl	<mdl	<mdl	21.8	165	<mdl	256	<mdl	<mdl	<mdl	<mdl	<mdl	10.6

Ta	W	La	Ce	Pr	Nd	Sm	Eu	Gd	Tb	Dy	Y	Ho	Er	Tm	Yb	Lu	ΣREY	^{204}Pb	^{206}Pb	^{208}Pb	Th	U
<mdl	<mdl	942	2313	235	780	128	29.2	118	11.8	52.5	280	9.6	23.8	2.97	17.9	2.89	4947	<mdl	6.47	4.90	28.5	4.45
<mdl	<mdl	790	1977	223	797	121	23.5	96.5	9.9	48.3	286	9.5	25.7	3.48	21.7	3.58	4436	<mdl	4.64	3.28	30.0	4.29
<mdl	<mdl	305	689	48.3	130	13.6	3.71	14.3	1.62	9.5	49.0	1.61	3.21	0.38	1.87	0.29	1272	<mdl	0.74	1.12	1.08	0.14
<mdl	<mdl	2763	6754	741	2600	340	72.4	262	30.1	168	1028	34.0	91.2	12.2	75.9	12.3	14984	<mdl	16.7	9.5	77.5	14.3

Chalcopyrite-barite associated apatite

ACD1-3	Na	Mg	Al	Si	S	K	Sc	Ti	V	Mn	Fe	Co	Ni	Cu	Zn	As	Rb	Sr	Zr	Nb	Mo	Sn	Cs	Ba
Mean n=(14)	721	1291	7709	19298	275	8346	8.69	170	8.60	184	23203	2.66	1.70	4.25	21.0	8.05	13.8	3833	0.39	0.08	0.65	0.62	<mdl	291
S.D.	332	1047	1726	3461	21.2	1964	6.30	54.8	4.43	154	5804	2.73	1.20	1.57	19.0	1.34	3.45	1993	0.34	0.05	0.50	0.10	<mdl	124
Min	389	15.7	5345	13754	246	4582	0.75	84.4	2.59	88.4	15313	0.19	0.41	2.50	1.41	6.23	7.56	658	0.12	0.04	0.18	0.50	<mdl	107
Max	1549	2959	10151	23480	321	9653	21.0	283	18.2	679	31727	6.53	3.70	6.63	54.8	9.9	18.7	6436	0.93	0.24	2.04	0.82	<mdl	558

Ta	W	La	Ce	Pr	Nd	Sm	Eu	Gd	Tb	Dy	Y	Ho	Er	Tm	Yb	Lu	ΣREY	^{204}Pb	^{206}Pb	^{208}Pb	Th	U
<mdl	0.60	40.6	324	101	919	849	620	989	88.6	341	1308	47.7	89.2	7.62	35.2	4.23	5763	19.0	58.7	62.7	333	38.5
<mdl	0.27	9.2	83.8	28.7	303	473	417	680	52.2	171	577	20.6	34.9	2.97	15.1	1.84	2870	10.4	38.2	23.4	178	33.3
<mdl	0.19	19.5	187	61.3	516	341	165	306	33.6	146	630	22.6	47.1	2.99	11.5	1.54	2491	7.70	6.98	20.9	63.2	0.54
<mdl	1.21	55.5	457	152	1475	1788	1639	2771	230	814	2855	103	173	14.2	73.9	9.0	12610	47.4	150	101	659	121

Sericite associated apatite

ACD2-3	Na	Mg	Al	Si	S	K	Sc	Ti	V	Mn	Fe	Co	Ni	Cu	Zn	As	Rb	Sr	Zr	Nb	Mo	Sn	Cs	Ba
Mean n=(10)	290	260	525	1048	223	431	3.35	31.6	0.88	543	534	0.54	0.54	2.52	34.9	2.88	3.41	594	4.51	0.04	<mdl	<mdl	<mdl	9.6
S.D.	117	260	278	505	64.4	265	1.72	14.2	0.88	246	377	0.43	0.24	2.85	22.7	1.29	2.78	218	6.45	0.02	<mdl	<mdl	<mdl	7.93
Min	78.3	13.1	51.3	386	56.1	126	0.60	7.29	0.13	90.0	92.0	0.12	0.13	0.22	7.50	0.93	0.95	106	0.05	0.01	<mdl	<mdl	<mdl	2.05
Max	407	713	737	1882	266	890	6.66	58.3	2.49	963	1108	1.16	0.80	7.76	73.7	4.34	8.57	901	18.7	0.08	<mdl	<mdl	<mdl	23.3

	Ta	W	La	Ce	Pr	Nd	Sm	Eu	Gd	Tb	Dy	Y	Ho	Er	Tm	Yb	Lu	ΣREY	^{204}Pb	^{206}Pb	^{208}Pb	Th	U
	<mdl	0.11	74.1	336	57.1	276	82.0	33.7	146	30.4	207	1066	43.4	120	15.0	89.9	12.1	2589	20.3	156	42.5	203	146
	<mdl	0.07	26.9	115	19.4	94.5	30.7	14.1	63.5	13.9	101	509	20.5	56.2	6.83	39.4	5.34	1116	7.36	58.8	27.3	285	54.4
	<mdl	0.01	21.4	101	17.5	84.3	25.3	10.2	45.6	9.4	63.3	321	12.8	34.4	4.10	23.3	3.02	777	5.97	46.1	21.1	1.50	43.6
	<mdl	0.18	119	496	78.3	359	119	53.0	225	48.2	354	1715	69.1	184	22.3	137	19.0	3999	31.3	244	99	818	227	

ACD2-4	Na	Mg	Al	Si	S	K	Sc	Ti	V	Mn	Fe	Co	Ni	Cu	Zn	As	Rb	Sr	Zr	Nb	Mo	Sn	Cs	Ba
Mean n=(14)	206	404	653	1641	264	388	16.4	111	2.79	721	5672	1.31	1.61	13.1	17.8	10.7	5.83	348	7.14	0.06	2.15	<mdl	<mdl	55.5
S.D.	103	311	552	858	9.2	365	7.02	67.2	2.65	237	3042	1.08	1.19	6.11	11.8	12.8	7.15	129	10.0	0.04	1.24	<mdl	<mdl	121
Min	113	15.2	23.9	441	250	5.27	0.98	51.7	0.24	297	1209	0.11	0.40	6.31	2.74	2.42	0.66	160	0.46	0.01	0.23	<mdl	<mdl	1.17
Max	501	903	1439	3177	276	950	25.3	257	7.60	981	9959	3.58	3.80	25.9	44.8	51.1	24.2	596	34.1	0.13	4.49	<mdl	<mdl	457

	Ta	W	La	Ce	Pr	Nd	Sm	Eu	Gd	Tb	Dy	Y	Ho	Er	Tm	Yb	Lu	ΣREY	^{204}Pb	^{206}Pb	^{208}Pb	Th	U
	<mdl	0.23	86.5	285	50.6	292	115	46.2	213	35.1	195	973	34.6	79.4	8.17	44.2	6.02	2463	95.4	428	95.0	9.7	319
	<mdl	0.14	24.7	97.7	17.7	92.7	32.4	18.7	56.7	9.2	41.6	173	6.24	14.8	1.77	10.3	1.39	599	58.1	201	55.3	3.91	141
	<mdl	0.11	51.6	158	28.8	176	76.5	27.7	141	23.6	141	748	26.0	60.8	5.67	31.2	4.16	1700	12.7	86.2	13.6	3.22	73.8
	<mdl	0.56	141	506	83.8	469	168	83.4	307	56.4	293	1253	47.2	103	11.4	65.1	9.4	3598	185	698	182	18.8	488

ADDITIONAL MATERIAL D

SUPPLEMENTARY DATA FOR CHAPTER 6 NUMERICAL MODELING OF REE TRENDS IN FLUORAPATITE: SNAPSHOTS OF FLUID EVOLUTION IN A GIANT HYDROTHERMAL SYSTEM

Sasha Krneta[1], Cristiana L. Ciobanu[2], Nigel J. Cook[2], Kathy Ehrig[3]

[1]*School of Physical Sciences, The University of Adelaide, Adelaide, S.A., 5005, Australia*

[2]*School of Chemical Engineering, The University of Adelaide, Adelaide, S.A., 5005, Australia*

[3]*BHP Olympic Dam, Adelaide, SA 5000, Australia*

APPENDIX A FOR CHAPTER 6

Numerical modeling input values and results (models 1.1-3.2). The $a_{(aq)}$ total values represents the sum of activity for a particular element. In the case of Ca and Na these are commonly represented by a single species whereas the $a_{(aq)}$ total values in the case of the REE are represented by multiple complexes. The fluid REE concentrations used to calculate the model apatite are equivalent to the whole rock values for the respective models.

Model 1.1	$a_{(aq)}$ total	$a_{(Apatite)}$	Concentration in apatite (mole fraction)	Concentration fluid (molal)	K	$D_{apatite/fluid}$	Concentrations REE fluid (ppm)	Model apatite (ppm)	Model apatite /chondrite
Ca	0.141	0.974	0.974	0.195					
Na	3.05	0.013	0.013	4.39					
La	1.35E-04	2.25E-03			1.51E-03	1.58	98.4	156	658
Ce	1.82E-04	6.15E-03			3.05E-03	3.20	194	622	1014
Pr	1.80E-05	7.35E-04			3.70E-03	3.89	21.1	81.9	881
Nd	6.35E-05	2.66E-03			3.79E-03	3.98	72.2	287	629
Sm	1.57E-05	4.07E-04			2.35E-03	2.47	13.0	32.0	216
Eu	1.03E-07	3.70E-05			0.032	0.370	1.76	0.65	11.6
Gd	8.63E-06	3.23E-04			3.39E-03	3.56	10.8	38.3	192
Tb	1.41E-06	4.20E-05			2.69E-03	2.83	1.65	4.68	130
Dy	7.59E-06	2.36E-04			2.81E-03	2.95	9.92	29.3	119
Ho	1.90E-06	4.63E-05			2.21E-03	2.32	2.08	4.82	87.5
Er	7.62E-06	1.28E-04			1.52E-03	1.59	5.81	9.26	57.9
Tm	1.70E-06	1.64E-05			8.72E-04	0.916	0.922	0.84	33.8
Yb	9.21E-06	9.90E-05			9.72E-04	1.02	6.04	6.17	38.3
Lu	1.30E-06	1.34E-05			9.38E-04	0.985	0.846	0.83	33.9
Y Eu++ (aq)	7.22E-03								

Model 1.2	a(aq) total	a(Apatite)	Concentration in apatite (mole fraction)	Concentration fluid (molal)	K	$D_{apatite/fluid}$	Concentrations REE fluid (ppm)	Model apatite (ppm)	Model apatite /chondrite
Ca	0.789	0.974	0.974	1.05					
Na	3.39	0.013	0.013	4.80					
La	1.59E-04	2.25E-03			0.036	7.68	98.4	756	3189
Ce	2.08E-04	6.15E-03			0.075	16.1	194	3117	5084
Pr	1.89E-05	7.35E-04			0.099	21.1	21.1	445	4785
Nd	6.59E-05	2.66E-03			0.103	22.0	72.2	1587	3473
Sm	1.82E-05	4.07E-04			0.057	12.2	13.0	158	1067
Eu	9.78E-08	3.70E-05			0.965	2.19	1.76	3.85	68.7
Gd	1.10E-05	3.23E-04			0.075	16.0	10.8	172	864
Tb	1.78E-06	4.20E-05			0.060	12.8	1.65	21.2	588
Dy	8.80E-06	2.36E-04			0.068	14.6	9.92	145	589
Ho	2.31E-06	4.63E-05			0.051	10.9	2.08	22.6	412
Er	9.50E-06	1.28E-04			0.034	7.32	5.81	42.5	266
Tm	1.84E-06	1.64E-05			0.023	4.86	0.922	4.48	179
Yb	1.13E-05	9.90E-05			0.022	4.77	6.04	28.8	179
Lu	1.61E-06	1.34E-05			0.021	4.54	0.846	3.84	156
Y Eu++ (aq)	6.25E-03								

Model 2.1	a(aq) total	a(Apatite)	Concentration in apatite (mole fraction)	Concentration fluid (molal)	K	$D_{apatite/fluid}$	Concentrations REE fluid (ppm)	Model apatite (ppm)	Model apatite /chondrite
Ca	0.068	0.996	0.996	0.105					
Na	1.28	1.96E-03	1.96E-03	1.94					
La	1.42E-04	9.31E-05			4.73E-06	4.10E-03	100.0	0.41	1.73
Ce	1.49E-04	3.27E-04			1.58E-05	0.014	200	2.74	4.47
Pr	1.62E-05	6.56E-05			2.93E-05	0.025	24.0	0.61	6.54
Nd	3.74E-05	4.15E-04			8.01E-05	0.069	80.0	5.55	12.1
Sm	5.63E-06	2.86E-04			3.67E-04	0.318	14.0	4.45	30.0
Eu	1.60E-07	6.52E-05			27.9	0.199	1.90	0.38	6.76
Gd	4.26E-06	4.01E-04			6.78E-04	0.587	11.8	6.93	34.8
Tb	4.50E-07	4.29E-05			6.88E-04	0.596	1.70	1.01	28.2
Dy	2.89E-06	1.66E-04			4.15E-04	0.359	10.3	3.70	15.0
Ho	5.46E-07	2.10E-05			2.78E-04	0.241	2.00	0.48	8.75
Er	1.37E-06	4.14E-05			2.17E-04	0.188	6.10	1.15	7.18
Tm	1.79E-07	4.40E-06			1.78E-04	0.154	0.700	0.11	4.31
Yb	1.48E-06	2.75E-05			1.34E-04	0.116	6.30	0.73	4.53
Lu	2.48E-07	3.10E-06			9.03E-05	0.078	1.10	0.086	3.50
Y Eu++ (aq)	0.012								

Model 2.2	a(aq) total	a(Apatite)	Concentration in apatite (mole fraction)	Concentration fluid (molal)	K	$D_{apatite/fluid}$	Concentrations REE fluid (ppm)	Model apatite (ppm)	Model apatite /chondrite
Ca	0.906	0.996	0.996	1.28					
Na	1.48	1.96E-03	1.96E-03	2.19					
La	1.58E-04	9.31E-05			6.46E-04	0.052	100.0	5.18	21.8
Ce	1.67E-04	3.27E-04			2.14E-03	0.172	200	34.4	56.0
Pr	1.70E-05	6.56E-05			4.22E-03	0.338	24.0	8.11	87.2
Nd	3.85E-05	4.15E-04			0.012	0.946	80.0	75.7	166
Sm	6.55E-06	2.86E-04			0.048	3.83	14.0	53.6	362
Eu	1.27E-07	6.52E-05			468	3.79	1.90	7.21	129
Gd	5.71E-06	4.01E-04			0.077	6.15	11.8	72.6	365
Tb	5.09E-07	4.29E-05			0.092	7.38	1.70	12.5	349
Dy	3.19E-06	1.66E-04			0.057	4.56	10.3	47.0	191
Ho	6.08E-07	2.10E-05			0.038	3.03	2.00	6.06	110
Er	1.31E-06	4.14E-05			0.035	2.78	6.10	16.9	106
Tm	2.30E-07	4.40E-06			0.021	1.67	0.700	1.17	46.9
Yb	1.33E-06	2.75E-05			0.023	1.81	6.30	11.4	70.9
Lu	2.32E-07	3.10E-06			0.015	1.17	1.10	1.29	52.5
Y Eu++ (aq)	8.10E-03								

Model 3.1	a(aq) total	a(Apatite)	Concentration in apatite (mole fraction)	Concentration fluid (molal)	K	$D_{apatite/fluid}$	Concentrations REE fluid (ppm)	Model apatite (ppm)	Model apatite /chondrite
Ca	0.224	0.992	0.992	0.292					
Na	0.439	4.10E-03	4.10E-03	0.944					
La	3.47E-03	1.01E-05			1.39E-06	2.10E-04	1200	0.252	1.06
Ce	4.71E-03	6.99E-05			7.10E-06	1.07E-03	1700	1.82	2.98
Pr	3.94E-04	2.42E-05			2.93E-05	4.44E-03	150	0.665	7.16
Nd	1.01E-03	2.69E-04			1.28E-04	0.019	393	7.58	16.6
Sm	1.01E-04	8.41E-04			3.99E-03	0.603	41.2	24.9	168
Eu	2.99E-05	5.15E-04			8.22E-03	1.24	12.4	15.4	275
Gd	6.54E-05	1.55E-03			0.011	1.71	28.0	47.9	241
Tb	7.87E-06	1.22E-04			7.40E-03	1.12	3.40	3.80	106
Dy	3.78E-05	4.58E-04			5.80E-03	0.877	16.7	14.6	59.5
Ho	6.69E-06	6.10E-05			4.36E-03	0.659	3.00	1.98	36.0
Er	2.00E-05	1.15E-04			2.74E-03	0.415	9.10	3.78	23.6
Tm	2.61E-06	1.08E-05			1.98E-03	0.299	1.20	0.359	14.4
Yb	1.83E-05	4.82E-05			1.26E-03	0.191	8.60	1.64	10.2
Lu	2.73E-06	5.25E-06			9.18E-04	0.139	1.30	0.180	7.34

Y Eu++ (aq)	NA

Model 3.2	a(aq) total	a(Apatite)	Concentration in apatite (mole fraction)	Concentration fluid (molal)	K	$D_{apatite/fluid}$	Concentrations REE fluid (ppm)	Model apatite (ppm)	Model apatite /chondrite
Ca	0.645	0.992	0.992	1.05					
Na	0.652	4.10E-03	4.10E-03	1.03					
La	7.37E-03	1.01E-05			3.63E-06	1.66E-04	1200	0.199	0.841
Ce	9.16E-03	6.99E-05			2.03E-05	9.29E-04	1700	1.58	2.58
Pr	4.88E-04	2.42E-05			1.32E-04	6.03E-03	150	0.904	9.72
Nd	1.23E-03	2.69E-04			5.81E-04	0.027	393	10.4	22.9
Sm	1.10E-04	8.41E-04			0.020	0.933	41.2	38.4	260
Eu	2.99E-05	5.15E-04			0.046	2.10	12.4	26.0	464
Gd	7.01E-05	1.55E-03			0.059	2.69	28.0	75.3	378
Tb	8.49E-06	1.22E-04			0.038	1.75	3.40	5.93	165
Dy	4.02E-05	4.58E-04			0.030	1.39	16.7	23.2	94.3
Ho	7.17E-06	6.10E-05			0.023	1.04	3.00	3.11	56.5
Er	2.11E-05	1.15E-04			0.014	0.661	9.10	6.01	37.6
Tm	2.77E-06	1.08E-05			0.010	0.475	1.20	0.570	22.8
Yb	1.95E-05	4.82E-05			6.59E-03	0.301	8.60	2.59	16.1
Lu	2.89E-06	5.25E-06			4.83E-03	0.221	1.30	0.287	11.7

Y Eu++ (aq)	NA

ADDITIONAL MATERIAL E

CONFERENCE ABSTRACT:

REY-SIGNATURES IN APATITE MONITOR THE EVOLUTION OF IOCG SYSTEMS: EXAMPLES FROM OLYMPIC DAM AND ACROPOLIS, SOUTH AUSTRALIA

Sasha Krneta[1], Cristiana L. Ciobanu[2], Nigel J. Cook[2], Kathy Ehrig[3], Vadim S. Kamenetsky[4]

[1]*School of Physical Sciences, The University of Adelaide, Adelaide, S.A., 5005, Australia*

[2]*School of Chemical Engineering, The University of Adelaide, Adelaide, S.A., 5005, Australia*

[3]*BHP Olympic Dam, Adelaide, SA 5000, Australia*

[4]*School of Physical Sciences, University of Tasmania, Hobart, TAS, Australia, 7001*

REY-signatures in apatite monitor the evolution of IOCG systems: examples from Olympic Dam and Acropolis, South Australia

Krneta, Sasha[1], Ciobanu, Cristiana L.[2], Cook, Nigel J.[2], Ehrig, Kathy[3], Kamenetsky, Vadim S.[4]

[1]*School of Physical Sciences, University of Adelaide, North Terrace, SA 5005, Australia,*
[2]*School of Chemical Engineering, University of Adelaide, Adelaide S.A. 5005, Australia*
[3]*BHP Billiton Olympic Dam, Adelaide, SA 5000, Australia*
[4]*School of Physical Sciences, University of Tasmania, Hobart, TAS, Australia 7001*

The Olympic Cu-Au Province, South Australia hosts numerous Mesoproterozoic iron-oxide-copper-gold (IOCG) deposits, of which the largest is Olympic Dam (OD). Mineralization is hosted within the Olympic Dam Breccia Complex (ODBC) which is, in turn, located within the Roxby Downs Granite (RDG), a member of the ~1.595 Ga Hiltaba magmatic suite. Breccia-hosted mineralisation contains dominant hematite, Cu-(Fe)-sulphides, carbonates, sericite, chlorite and a range of discrete U- and REY-bearing minerals (Ehrig et al. 2012). Apatite is an important and, locally very abundant component of both the pre-existing host rocks and mineralisation. The Acropolis (AC) prospect, approximately 25 SW of OD, is hosted in altered felsic Gawler Range Volcanics (GRV) and ~1.85 Ga Donington suite granite. Mineralisation at AC occurs in veins and breccias containing iron-oxides, apatite, K-feldspar, sericite, chlorite, carbonates, Cu-(Fe)-sulphides and discrete U- and REY-bearing minerals.

Due to its widespread occurrence and capacity to incorporate a wide array of elements sensitive to changes in mineralising conditions, apatite chemistry has been used as a means of gaining insights into processes of metallogenic interest (e.g. Harlov 2015). We present new LA-ICP-MS data for apatite hosted in weakly- to pervasively-altered RDG within drillholes S and SE of the ODBC and for apatite from GRV-hosted veins and breccias from two drillholes intersecting the AC prospect: ACD1 (magnetite-dominant); and ACD2 (martite-dominant). The two drillholes are ~5 km apart.

RDG-hosted magmatic apatite has high REY concentrations (mean ~50,000 ppm), and commonly consists of inclusion-rich cores overgrown by zones of extreme REY enrichment (mean ~105,000 ppm). Both zones display a LREE-enriched chondrite-normalised fractionation trend with strong negative Eu-anomaly, with a weak Ce-anomaly in the rims. Both zones undergo depletion of REY along fractures filled by hematite, sericite and monazite. Chondrite-normalised fractionation trends show preferential removal of both LREE and HREE, but not MREE, and a weakening of the negative Eu-anomaly.

Earliest hydrothermal apatite is seen in pervasively hematite-sericite altered RDG as small grains intimately intergrown with sericite, hematite and florencite. Such apatite displays a strongly MREE-enriched chondrite-normalised fractionation trend with a weak negative Eu-anomaly. Early hydrothermal apatite from the AC prospect shows a LREE-enriched chondrite-normalised fractionation trend in grains intimately associated with early magnetite mineralisation comparable to that seen in magmatic RDG apatite. However, such grains contain altered domains of MREE-enrichment and depletion in ∑REY along fractures and grain rims. Apatite intimately intergrown with and containing inclusions of sericite, hematite and monazite displays a flat to MREE-enriched chondrite-normalised fractionation trend.

Although numerous parameters may be responsible for the change from LREE- to MREE-enriched apatite signature, it would appear that LREE-enrichment is more commonly a feature of magmatic and early hydrothermal apatite whereas MREE-enriched trends are characteristic of later, more advanced stages of mineralisation. Changes in fluid chemistry, in particular those affecting REY transport, could be responsible. Alternatively, the strong MREE-enrichment may relate to co-

crystallisation of later apatite with LREE-consuming minerals such as monazite, florencite and bastnäsite and with HREE-consuming xenotime.

References:

Ehrig, K. et al. (2012) SEG Spec vol 16, 237-267.
Harlov D.E. (2015) Elements 11, 171-176.

ADDITIONAL MATERIAL F

CONFERENCE ABSTRACT:

APATITE IN THE OLYMPIC DAM FE-OXIDE CU-U-AU-AG DEPOSIT

Sasha Krneta[1], Cristiana L. Ciobanu[2], Nigel J. Cook[2], Kathy Ehrig[3], Vadim S. Kamenetsky[4]

[1]*School of Physical Sciences, The University of Adelaide, Adelaide, S.A., 5005, Australia*

[2]*School of Chemical Engineering, The University of Adelaide, Adelaide, S.A., 5005, Australia*

[3]*BHP Olympic Dam, Adelaide, SA 5000, Australia*

[4]*School of Physical Sciences, University of Tasmania, Hobart, TAS, Australia, 7001*

Apatite in the Olympic Dam Fe-oxide Cu-U-Au-Ag deposit

Sasha Krneta
School of Physical Sciences, University of Adelaide, North Terrace, SA 5005, Australia

Cristiana L. Ciobanu, Nigel J. Cook
School of Chemical Engineering, University of Adelaide, Adelaide S.A. 5005, Australia

Kathy Ehrig
BHP Billiton Olympic Dam, Adelaide, SA 5000, Australia

Vadim S. Kamenetsky
ARC Centre of Excellence in Ore Deposits (CODES), School of Physical Sciences, University of Tasmania, Hobart, TAS, Australia 7001

Abstract. Apatite from igneous rocks hosting the World-class Olympic Dam iron-oxide-copper-gold deposit, South Australia is characterized with respect to morphology, chemistry, mineral assemblage and grain-scale compositional zoning. In granites, apatite displays a characteristic core-to rim zonation due to REE content. Fields of dusty monazite as 'emulsion'-like cores or symplectite intergrowths with host apatite are recognized. Compositional data, and their correlation with textures, show a complexity but nevertheless, potential for characterizing the igneous-to-hydrothermal evolution at Olympic Dam. Knowledge of the evolution and geochemistry of apatite at Olympic Dam may offer insights into deposit formation, and, potentially, be a tool to discriminate Cu-Au mineralized and barren Fe-oxide dominated hydrothermal systems.

Keywords. Olympic Dam, apatite, mineral chemistry

1 Introduction

The utility of apatite in geological studies has long been known. Apatite can also contain high levels of rare earth elements (REE) and in many rocks it is the main host. Apatite can contain a large number of other elements, the incorporation of which is controlled by physiochemical parameters during crystallization. Due to the nature of hydrothermal systems where the precipitation of metals is often instigated by changes in parameters such as temperature, pressure and chemistry, the ability of apatite to record such changes, and its relatively resistant character, gives it the potential to offer great insights into the formation history of ore deposits.

The Olympic Dam Cu-Au-U-Ag deposit (9840 Mt tonnes @ 0.78% Cu, 0.25kg/t U_3O_8, 0.3g/t Au, 2g/t Ag (BHP Billiton 2014) is the largest deposit in the Olympic Cu-Au province, South Australia, the World's premier Iron-Oxide-Copper-Gold (IOCG) province. At Olympic Dam, apatite whereas abundant throughout all igneous lithologies; lesser amounts are present in the hematite breccias hosting sulfide ore. Collectively, this apatite represents numerous generations that span the evolutionary history of the deposit, and thus offer insights into how the deposit formed.

Variation in apatite chemistry, particularly REE-fractionation trends, in the Hillside deposit, South Australia (Ismail et al. 2014) allowed a reconstruction of deposit evolution from magmatic to early hydrothermal to late-stage hydrothermal events. Similarly, in the Moonta-Wallaroo region, northwest of Hillside, Kontonikas-Charos et al. (2014) showed that the complex textures displayed by apatite backed up the interpreted changes in fluid characteristics during albitization and subsequent potassic alteration.

2 Background

2.1 Apatite chemistry

Minerals of the apatite supergroup (Pasero et al. 2010) have the general formula $A_5(XO_4)_3Z$, where the A site accommodates elements such as Ca^{2+}, Sr^{2+}, Ba^{2+}, Mg^{2+}, Mn^{2+},Fe^{2+}, Cd^{2+}, Na^{2+}, Eu^{2+} and REE^{3+}. The X site is occupied by P^{5+} as $(PO_4)^{3+}$ but other small highly-charged cations (SiO_4^{4+}, SO_4^{2-}, AsO_4^{3-}, VO_4^{3-} etc.) can occupy this structural position. Halogens, F^- and Cl^-, occupy the Z site along with OH^-.

REE substitution for Ca in apatite is controlled predominantly by the proximity principle whereby the REE with atomic radii most similar to that of the Ca position are most easily substituted. As a result most natural apatite REE contents peak in the area of Sm-Nd. Given the REE valence state of REE^{3+} with the exception of Eu^{2+} and Ce^{4+}, coupled compensation mechanisms are necessary to maintain charge balance (Pan and Fleet 2002):

$$REE^{3+} + O^{2-} = Ca^{2+} + F^-$$
$$REE^{3+} + Na^+ = 2\ Ca^{2+}$$
$$REE^{3+} + SiO_4^{4-} = Ca^{2+} + PO_4^{3-}$$
$$2\ REE^{3+} + \square = 3\ Ca^{2+}$$

The atomic radius of Eu^{3+} is almost identical to that of Ca^{2+} and as such, apatite has a preference for Eu^{3+} over Eu^{2+}. The Eu^{2+}/Eu^{3+} ratio in melts is dependent on fO_2, bulk rock composition, temperature and, possibly, pressure. These parameters, particularly fO_2 exert a control on the substitution of Eu in magmatic apatite.

Several published studies have successfully used variations in apatite geochemistry to correlate certain intrusive rocks with particular styles of mineralization in large-scale mineralized belts (e.g. Cao et al. 2011). Other studies on the deposit scale (e.g. Harlov et al. 2002,

Bonyadi et al. 2011) have successfully tracked changes in hydrothermal fluid chemistry by the evolution of apatite chemistry.

2.2 The Olympic Dam deposit

Olympic Dam is located in the north of the Olympic Cu-Au province, an elongate mineralized region on the eastern edge of the late Archean to Mesoproterozoic Gawler Craton. The deposit (Fig. 1) is hosted exclusively within the Olympic Dam Breccia Complex (ODBC) (Reeve et al. 1990), a term used to describe the mineralized breccias, felsic and mafic-ultramafic volcanic units and bedded clastic facies. In turn the ODBC is hosted within the Roxby Downs Granite (RDG), a member of the ~1590 Ma Hiltaba Suite (Creaser and White 1991). The RDG is an undeformed, medium- to coarse-grained granite consisting of alkali feldspar, quartz, sodic plagioclase, and minor biotite and amphibole with trace magnetite, titanite, fluorapatite, zircon and fluorite (Ehrig et al. 2012). Other granites, such as the Horn Ridge Granite (HG), dated at 1594.4 ± 3.4 Ma (Jagodzinski 2005), are also present. Mafic-ultramafic rocks occur as dikes, with ages spanning from ~1590 Ma (picrites) to ~800 Ma (Gairdiner dolerite dykes) (e.g. Huang et al 2015). The RDG has experienced pervasive, texturally destructive hematite-sericite alteration and brecciation. Alteration and brecciation intensifies towards the deposit center with the granite-breccia contacts being largely gradational. The majority of the resource is hosted in hematite- or granite-rich breccias.

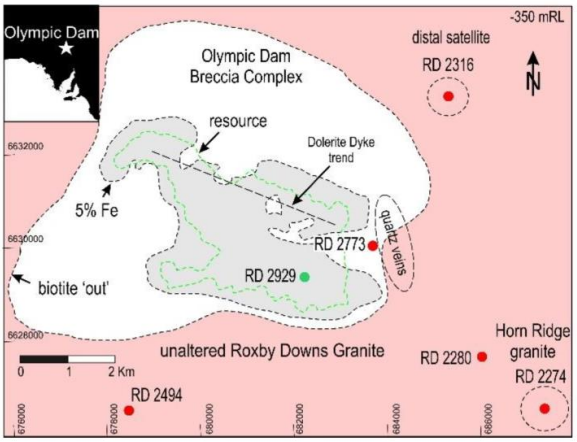

Fig. 1. Sketch map of Olympic Dam, modified from Ehrig et al. (2012), showing the location of drillholes (circles in red for apatite in granite, and green for apatite in picrite). The trend of one of the ca. 800 Ma Gairdner syke swarms is also shown.

Analyzed samples are from 5 drillholes intersecting granites outside, or at the immediate edge of the deposit, and from one of the highly altered picrites (Fig. 1). Granites intersected a few km outside the deposit outline are considered 'fresh' (biotite preserved), but are typically heterogeneous, altered on the m- to dm-scale, or include cm- to dm-sized mafic enclaves (e.g. RD2280; Fig. 2). Alteration correlates with hematite and sericite replacement of feldspars during albitization.

Distal and proximal satellites, i.e. weak chalcopyrite mineralization, associated with hematite ± magnetite alteration of variable intensity, are hosted in granites that were also sampled. In the distal satellite, intersected by RD2316, abundant, coarse molybdenite occurs at upper levels, whereas in the proximal satellite (drillhole RD2773), mineralization increases at a depth of ~2000 m, and has a distinct base metal (sphalerite ± galena) signature.

Polished blocks and thin sections were analyzed by optical microscopy, scanning electron microscopy in back-scattered electron (BSE) mode and by electron microprobe (EPMA). The aim of the present, preliminary study is to texturally and geochemically characterize apatite from altered and unaltered intrusive rocks in an effort to identify whether apatite may be an effective pathfinder for magmatic and hydrothermal processes in the IOCG environment.

4 Results

4.1 Apatite textures and petrographic context

Apatite from igneous rocks occurs as grains with morphologies ranging from equant (in granites) to elongate or bladed (in mafic enclaves in RDG and picrite), and of variable sizes (up to several hundred μm). Apatite is characterized by chemical heterogeneity with variable complexity (e.g. Fig. 3). In the granites, apatite displays characteristic core-to rim zonation which is mostly due to REE content (REE-poor and REE-richer as darker cores and brighter rims on the BSE images; Fig. 3a). In both enclaves and host RDG, apatite (e.g. in drillhole RD2280) shows fields of dusty monazite as 'emulsion'-like cores or symplectite intergrowths with host apatite (Fig. 3a, b, respectively).

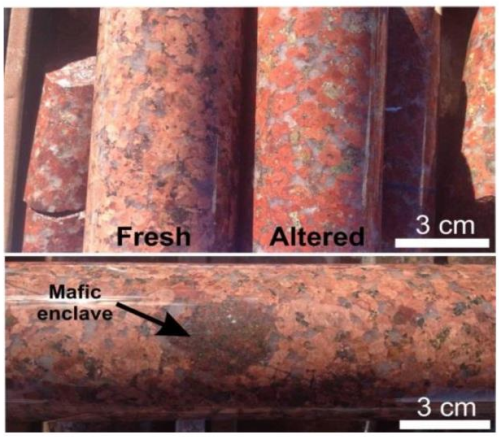

Fig. 2. Drillcore photographs showing characteristics of RDG (drillhole RD2280).

Quartz cores are conspicuously seen in apatite from the mafic enclaves (Fig. 3c). Reworking of initial core-rim zonation patterns, mainly corresponding to REE-depletion, is seen as a darkening of apatite on the BSE images in and along fractures where sericite + hematite alteration occurs (Fig. 3d), as well as irregular inliers from margins towards the cores in equant grains (Fig. 3a).

Incipient development of porosity, microfracturing and coarsening of monazite from the areas of dusty inclusions are also observed. Advanced fracture- and pore-controlled replacement of apatite is seen in samples

where sericite + hematite alteration is more prominent (Fig. 3e). In such cases, nucleation of coarser florencite is conspicuous.

Apatite from mineralized granites differs markedly in terms of appearance since it does not occur as single grains but rather as aggregates interstitial to other minerals, e.g. between hematite pseudomorphically replacing pre-existing magnetite (Fig. 3f). However, as in the case of apatite from the igneous rocks without any mineralization, it also shows strong chemical heterogeneity - corroded darker (early) cores and brighter (late) margins are evident on BSE images (Fig. 3f). Porosity, fracturing, and replacement of apatite are also associated with nucleation of discrete inclusions of REE-minerals.

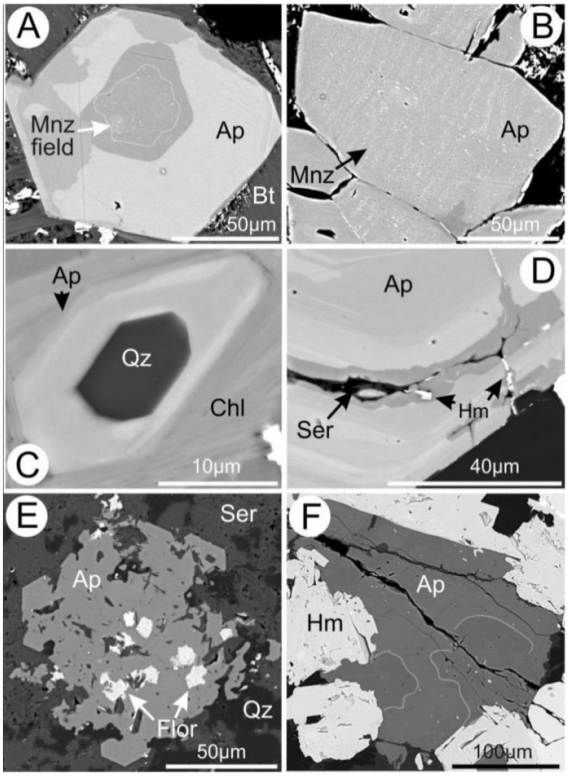

Fig. 3. BSE images showing textures of apatite from RDG granite (a, d, e) and enclaves (b, c), and in mineralized granite (f) in sample from ~2,000m, drillhole RD2773. Abbreviations: Ab-albite; Ap-apatite; Bt-biotite; Chl-chlorite; Flor-florencite; Hm-hematite; Mnz-monazite; Qz-quartz; Ser-sericite.

4.2 Compositional patterns

EPMA data was collected on grains with various textural complexities as described above. Results show that, for zones of apatite that display no textural evidence of overprinting (termed 'unaltered' on Fig. 4a), there is a strong correlation between the type of igneous rock and halogen content. Both are fluorapatite but whereas those in the RDG are end-member fluorapatite, apatite in the picrite is characterized by marked Cl-enrichment.

Apatite from the HG contains both F and Cl, and plots half way along the line between Cl- and F-rich groups on Fig. 4a. Both types of Cl-bearing fluorapatite show a decrease in Cl-content in areas where there is evidence of alteration (porosity, fractures, inclusions, etc). Calculated formulae show full occupancy of the Z site by (F+Cl), implying negligible OH component. Analyzed apatites display varying REE contents, up to > 5 wt% REE_2O_3 (Fig. 4b) concordant with zoning (Fig. 3a). REE content correlates with (Na_2O+SiO_2), indicating coupled substitution(s) to maintain charge balance

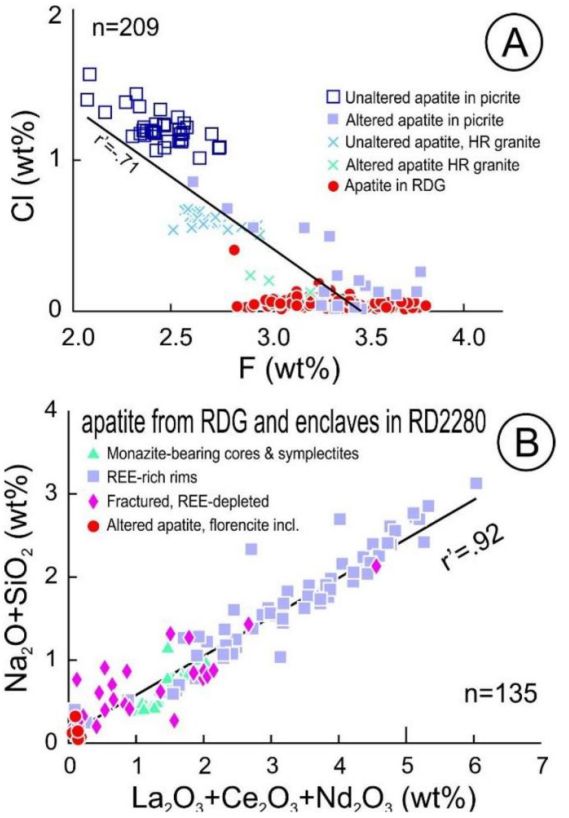

Fig. 4. **(a)** Plot of Cl (wt.%) vs. F (wt.%), and **(b)** Na_2O+SiO_2 (wt.%) vs. La_2O_3+Ce_2O_3+Nd_2O_3 (wt.%) for apatite from igneous rocks.

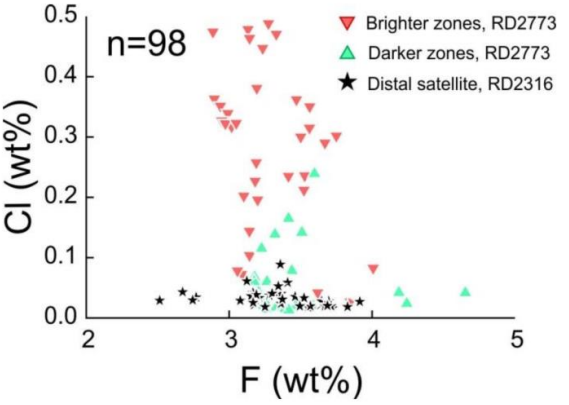

Fig. 5. Plot of Cl (wt.%) vs. F (wt.%) for apatite from granites containing sulfide mineralization.

A plot of Cl vs. F in apatite from the drillcores intersecting satellite mineralization (Fig. 5) also shows that deeper mineralization in drillhole RD2773 is also characterized by modest enrichment in Cl in parts of the grains that do not show evidence of alteration. The same analyses (and also those from RD2316) also show the presence of both sulfur and silica (Fig. 6), even if REE are only present at concentrations around the detection limit as measured by EPMA.

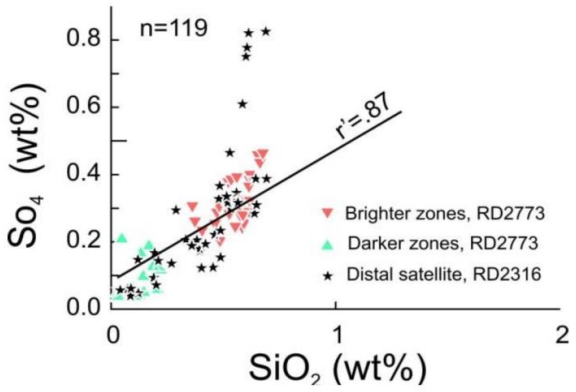

Fig. 6. Plot of SO_4 (wt.%) vs. SiO_2 (wt.%) for apatite from granites containing sulfide mineralization.

5 Discussion and concluding remarks

The presence of numerous small monazite inclusions in apatite has been observed in magmatic, metamorphic and hydrothermal systems, including the Kiirunavaara magnetite-apatite ore, northern Sweden (Harlov et al., 2002). The range of apatite-monazite relationships shown here, i.e. from emulsion-like and symplectites to pore-attached and coarsening of monazite, are of particular interest as such features have not been seen elsewhere in the Olympic IOCG Province.

The emulsion-like and symplectite intergrowths are indicative of exsolution from a higher-temperature, homogenous phase. However, no such field of immiscibility is known between the two phosphates. Experiments (Wolf and London 1995) show that monazite formation could be due to partial incongruent dissolution of early-formed apatite grains in peraluminous granitic melts. Such apatite-monazite relationships thus indicate that pristine, magmatic apatite is preserved in our samples. Porosity development, fracturing and inclusion coarsening are features that can all be attributed to progressive hydrothermal alteration leading to depletion of the overall REE concentration in apatite, as seen in the present samples. Hydrothermal experiments (e.g. Harlov et al. 2005) show that growth of monazite inclusions can be induced by reaction with KCl-rich fluids, removing Si+Na from apatite, thus destabilizing the coupled substitution, releasing REE and forming monazite. This argument could apply here but as a hydrothermal overprint on primary igneous apatite.

The difference in grain habit of apatite in the RDG and the mafic enclaves hosted within it can be explained by variable rates of cooling. Wyllie et al. (1962) found that at, a near equilibrium cooling rate, small equant apatite grains are formed whereas conditions of signif-icant undercooling lead to skeletal acicular grains often with central cavities. In the case of the RDG enclaves, these central cavities appear to have been subsequently filled with quartz. Other studies (e.g. Holden et al. 1987) used observations of acicular grains in and around mafic enclaves to imply rapid cooling of the mafic component upon emplacement into a felsic magma.

The compositional data, and their correlation with textures, show a complexity but nevertheless, potential for characterizing the igneous-to-hydrothermal evolution at Olympic Dam. The Cl component of magmatic apatite from granite and picrite differs. Taken together with S, the Cl component of apatite also appears to be a tracer for the magmatic-to-hydrothermal evolution of the deposit and may also assist understanding subsequent reworking of primary mineral generations.

Further work will focus on determining the REY fractionation trends of different textural categories of apatite in and surrounding the Olympic Dam deposit, including apatite within sulfide-hosting hematite breccias of the deposit itself. We will also compare and contrast the textural and chemical signature of apatite with that in other IOCG systems in the Gawler Craton, including those with both comparable and distinct alteration features, as well as worldwide.

References

BHP Billiton (2014) http://www.bhpbilliton.com/home/investors/reports/Documents/2014/BHPBillitonAnnualReport2014.pdf

Bonyadi Z, Davidson GJ, Mehrabi B, Meffre S, Ghazban F (2011) Significance of apatite REE depletion and monazite inclusions in the brecciated Se–Chahun iron oxide–apatite deposit, Bafq district, Iran: Insights from paragenesis and geochemistry. Chem Geol 281:253-269

Cao M, Li G, Qin K, Seitmuratova EY, Liu Y (2012) Major and Trace element characteristics of apatites in granitoids from Central Kazakhstan: Implications for petrogenesis and mineralization. Resource Geol 62:63-83

Creaser RA, White A (1991) Large volume, high temperature felsic volcanism from the Middle Proterozoic of South Australia. Geology 19:48–51.

Ehrig K, McPhie J, Kamenetsky V (2013) Geology and Mineralogical Zonation of the Olympic Dam Iron Oxide CuU-Au-Ag Deposit, South Australia. SEG Spec vol 16:237-267

Harlov DE, Andersson UB, Förster HJ, Nyström JO, Dulski P, Broman C (2002) Apatite monazite relations in the Kiirunavaara magnetite-apatite ore, northern Sweden. Chem Geol 191:47–72

Harlov DE, Wirth R, Förster HJ (2005) An experimental study of dissolution-reprecipitation in fluorapatite: fluid infiltration and the formation of monazite. Contrib Miner Petrol 150:268–286

Holden P, Halliday AN, Stephens WE (1987) Neodymium and strontium isotope content of microdiorite enclaves points to mantle input to granitoid production. Nature 330:53-56

Huang QY, Kamenetsky VS, McPhie J and 10 co-authors (2015) The link between the break-up of the supercontinent Rodinia and the supergiant Olympic Dam deposit. This volume.

Ismail R, Ciobanu CL, Cook NJ, Giles D, Schmidt-Mumm A, Teale GS, Wade B (2014) Rare earths and other trace elements in minerals from skarn assemblages, Hillside iron oxide–copper–gold deposit, Yorke Peninsula, South Australia. Lithos 184–187:456-477

Jagodzinski EA (2005) Compilation of SHRIMP U-Pb geochronological data. Geoscience Australia Record 2005/20

Kontonikas-Charos A, Ciobanu CL, Cook NJ (2014) Albitization and redistribution of REE and Y in IOCG systems: Insights from Moonta-Wallaroo, Yorke Peninsula, South Australia. Lithos, 208:178-201

Pasero M, Kampf A, Ferraris C, Pekov IV, Rakovan J, White T (2010) Nomenclature of the apatite supergroup minerals: Eur J Mineral 22:163-179

Pan Y, Fleet ME (2002) Compositions of the Apatite-Group Minerals: Substitution Mechanisms and Controlling Factors. Rev Mineral Geochem 48:13-49

Reeve JS, Cross KC, Smith RN, Oreskes N (1990) Olympic Dam copper-uranium-gold-silver deposit. AusIMM Monogr 14:1009–1035

Wolf MB, London D (1995) Incongruent dissolution of REE- and Sr-rich apatite in peraluminous granitic liquids: Differential apatite, monazite, and xenotime solubilities during anatexis. Am Mineral 80:765-775

Wyllie PJ, Cox KG, Biggar GM (1962) The habit of apatite in synthetic systems and igneous rocks. J Petrol 3:238-242

ADDITIONAL MATERIAL G

CONFERENCE ABSTRACT:

REY-SIGNATURES IN APATITE MONITOR THE EVOLUTION OF IOCG SYSTEMS: EXAMPLES FROM OLYMPIC DAM AND WIRRDA WELL, SOUTH AUSTRALIA

Sasha Krneta[1], Cristiana L. Ciobanu[2], Nigel J. Cook[2], Kathy Ehrig[3], Vadim S. Kamenetsky[4]

[1]*School of Physical Sciences, The University of Adelaide, Adelaide, S.A., 5005, Australia*

[2]*School of Chemical Engineering, The University of Adelaide, Adelaide, S.A., 5005, Australia*

[3]*BHP Olympic Dam, Adelaide, SA 5000, Australia*

[4]*School of Physical Sciences, University of Tasmania, Hobart, TAS, Australia, 7001*

REY-signatures in apatite monitor the evolution of IOCG systems: examples from Olympic Dam and Wirrda Well, South Australia

Krneta S.[1], Ciobanu C.L.[2], Cook N.J.[2], Ehrig K.[3], Kamenetsky V.S.[4]

[1]School of Physical Sciences, University of Adelaide, SA 5005, Australia, sasha.krneta@adelaide.edu.au
[2]School of Chemical Engineering, University of Adelaide, Adelaide S.A. 5005, Australia
[3]BHP Billiton Olympic Dam, Adelaide, SA 5000, Australia
[4]School of Physical Sciences, University of Tasmania, Hobart, TAS, Australia 7001

Apatite is a common magmatic accessory in the intrusive rocks hosting the World-class Olympic Dam (OD) orebody and the nearby Wirrda Well (WW) prospect. Moreover, hydrothermal apatite is a locally abundant mineral throughout the altered and mineralized rocks. We evaluate whether changes in the morphology and chemistry (particularly the rare earth element and Y content; REY) of apatite can be used to constrain the evolution of these iron-oxide-copper-gold (IOCG) systems.

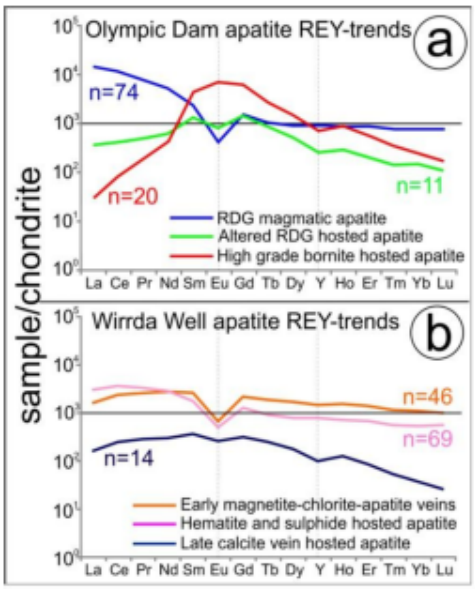

The ~1.6 Ga Roxby Downs Granite (RDG), host to the Olympic Dam deposit contains apatite as a magmatic accessory, locally in high concentrations associated with mafic enclaves. Magmatic apatite commonly contains inclusion-rich cores and REY-enriched rims. The cores show a LREE-enriched chondrite-normalised fractionation trend with a strong negative Eu-anomaly (Fig. 1a). Apatite intimately associated with intense hematite-sericite alteration display convex, MREE-enriched patterns with a weak negative Eu-anomaly (Fig. 1a). Such grains contain abundant inclusions of florencite and sericite. Florencite inclusions are also observed in apatite within high-grade breccia-hosted, bornite dominant mineralisation where apatite displays a highly MREE-enriched fractionation trend.

Figure 1- Chondrite-normalised REY-fractionation trends presented as means calculated from multiple analyses.

The magnetite-dominant WW prospect, hosted in ~1.85 Ga Donington suite granite and contemporaneous mafic dykes displays a deposit wide mineralogical zoning similar to that seen at OD some 20 km to the north. Chalcocite and bornite occur in upper levels of the prospect with a pyrite-chalcopyrite assemblage prevailing at depth. Altered Donington granite-hosted vein and breccia mineralisation was examined from the latter. Apatite from early magnetite-chlorite-apatite veinlets displays a flat to slightly LREE-enriched chondrite-normalised fractionation trend whereas later hematite- and sulphide-hosted apatite is slightly LREE-enriched (Fig. 1b). Both trends display relatively strong negative Eu-anomalies. Concentrations of As and U/Th ratios are higher in the case of the hematite-sulphide hosted apatite. Late calcite veins crosscutting both the altered granite and breccias contain extremely coarse-grained apatite (~2mm) which displays a MREE-enriched chondrite-normalised fractionation trend and a weak negative Eu-anomaly and ∑REY-concentrations much lower than apatite associated with earlier mineralisation (Fig. 1b).

In both IOCG systems, magmatic and early hydrothermal apatite shows LREE-enriched fractionation trends with strong negative Eu-anomalies whereas later apatite displays more MREE-enriched trends, albeit with lower ∑REY-concentrations. This change in REY-partitioning behaviour could be due to changes in the physiochemical character of the mineralizing fluid, or alternatively, may indicate crystallisation of MREE-enriched apatite in the presence of LREE- and HREE-consuming minerals such as monazite, florencite and xenotime. These dynamics are important evidence for a change from early primitive low-grade pyrite-chalcopyrite mineralisation to higher grade bornite mineralization reflected in apatite chemistry by a switch from LREE- to MREE-enriched REY-trends.

ADDITIONAL MATERIAL H

CONFERENCE ABSTRACT:

APATITE IN THE OLYMPIC DAM IOCG SYSTEM AND ADJACENT PROSPECTS: INSIGHTS INTO MAGMATIC AND HYDROTHERMAL EVOLUTION

Sasha Krneta[1], Cristiana L. Ciobanu[2], Nigel J. Cook[2], Kathy Ehrig[3], Vadim S. Kamenetsky[4]

[1]*School of Physical Sciences, The University of Adelaide, Adelaide, S.A., 5005, Australia*

[2]*School of Chemical Engineering, The University of Adelaide, Adelaide, S.A., 5005, Australia*

[3]*BHP Olympic Dam, Adelaide, SA 5000, Australia*

[4]*School of Physical Sciences, University of Tasmania, Hobart, TAS, Australia, 7001*

Apatite in the Olympic Dam IOCG system and adjacent prospects: insights into magmatic and hydrothermal evolution

Sasha Krneta[1*], Cristiana L. Ciobanu[2], Nigel J.Cook[2], Kathy Ehrig[3] and Vadim S. Kamenetsky[4]

[1] School of Physical Sciences, University of Adelaide, North Terrace, SA 5005, Australia
[2] School of Chemical Engineering, University of Adelaide, Adelaide S.A. 5005, Australia
[3] BHP Billiton Olympic Dam, Adelaide, SA 5000, Australia
[4] School of Physical Sciences, University of Tasmania, Hobart, TAS, Australia 7001

The utility of apatite-group geochemistry to gain insights into evolving physiochemical conditions during mineralization in a magmatic-to-hydrothermal environment is a topic of expanding research. Apatite is a widespread pre-, syn- and post-mineralization accessory in the Olympic Dam (OD) IOCG-system and in nearby Wirrda Well (WW) and Acropolis prospects (25 km SW and SE of OD, respectively). Although broadly tied to the same 1.6Ga IOCG mineralization event, differences exist both in the tenor of Cu-Au mineralization and host lithologies.

Magmatic apatite in the ~1.6Ga Roxby Downs Granite (RDG) displays core-to-rim ΣREE-zoning. Monazite inclusion-rich cores are overgrown by REE-rich rims; both are depleted along hematite-sericite-filled fractures crosscutting apatite. REE loss and SO_4 increase, together with nucleation of florencite inclusions, accompany apatite destruction during hematite-sericite alteration of the RDG.

Halogen variation, in terms of an increase in Cl relative to F, is seen in altered picrite dykes within the deposit area and the less-evolved Horn Ridge granite some 5 km SE of the deposit. Both igneous rocks are broadly coeval with the RDG which hosts mineralized hematite-sericite breccias at OD. Irregular grain-scale zoning in apatite from picritic dykes is geochemically expressed by increased F and corresponding drop in ΣREE and Cl. These zones coincide with domains of monazite inclusion-nucleation and subsequent overprint during hematite-sericite alteration of host picrite.

Hydrothermal apatite within Cu±Mo±Zn mineralization ~5km NE of OD (distal-satellite), as well as in mineralization at ~2km depth, ~1km E of the deposit (deep-proximal satellite), occurs as aggregates interstitial to Fe-oxides; similar apatite is observed at Acropolis. Two distinct types of apatite are observed at WW in veins and breccias hosted by deformed and altered 1.85Ga Donington granite and Fe-oxide-altered mafic dykes. Apatite associated with magnetite-pyrite-chlorite-siderite±sericite breccia displays equant to irregular morphologies and contains magnetite and REE-mineral inclusions. Second generation apatite occurs along late calcite veins crosscutting all lithologies. Vein apatite contains lower SO_4 and ΣREE than the first type.

In summary, changes in apatite morphology, textures, REE, halogen and newly-formed REE-minerals clearly show the magmatic-to-hydrothermal transition throughout igneous lithologies undergoing hematite-sericite alteration at OD. Hydrothermal apatite in deep-proximal and distal satellites at OD shows similarities, albeit with variation, with apatite from both WW and Acropolis in terms of morphology, REE-zoning and mineral inclusions, and most importantly in terms of SO_4 and Cl content. In all these prospects, sulfide (chalcopyrite±pyrite) stability is at fO_2 conditions defined by magnetite+hematite

ADDITIONAL MATERIAL I

CONFERENCE POSTER:

APATITE IN THE OLYMPIC DAM IOCG SYSTEM AND ADJACENT PROSPECTS: INSIGHTS INTO MAGMATIC AND HYDROTHERMAL EVOLUTION

Sasha Krneta[1], Cristiana L. Ciobanu[2], Nigel J. Cook[2], Kathy Ehrig[3], Vadim S. Kamenetsky[4]

[1]*School of Physical Sciences, The University of Adelaide, Adelaide, S.A., 5005, Australia*

[2]*School of Chemical Engineering, The University of Adelaide, Adelaide, S.A., 5005, Australia*

[3]*BHP Olympic Dam, Adelaide, SA 5000, Australia*

[4]*School of Physical Sciences, University of Tasmania, Hobart, TAS, Australia, 7001*

Apatite in the Olympic Dam IOCG system and adjacent prospects: insights into magmatic and hydrothermal evolution

Sasha Krneta[1*], Cristiana L. Ciobanu[2], Nigel J.Cook[2], Kathy Ehrig[3] and Vadim S. Kamenetsky[4]

[1] School of Physical Sciences, University of Adelaide, North Terrace, SA 5005, Australia
[2] School of Chemical Engineering, University of Adelaide, Adelaide S.A. 5005, Australia
[3] BHP Billiton Olympic Dam, Adelaide, SA 5000, Australia
[4] School of Physical Sciences, University of Tasmania, Hobart, TAS, Australia 7001

Rationale

- The ~1.6 Ga Olympic Dam IOCG deposit (9576 Mt @ 0.82% Cu, 0.31 g/t Au, 260 g/t U, 1.39 g/t Ag) is hosted within the Olympic Dam Breccia Complex (Fig. 1a), which is composed of hydrothermal breccias, mafic-ultramafic and felsic intrusives and a suite of laminated volcaniclastic and sedimentary facies (Ehrig et al. 2012). Wirrda Well and Acropolis are adjacent prospects containing magnetite-dominant IOCG-style mineralisation.
- Apatite is widespread through all three systems, as both a magmatic accessory and the product of hydrothermal alteration. Apatite textures, grain habit, size, mineral associations and geochemistry vary depending on host rock and level of fluid interaction.
- Substitution of elements into the apatite structure is largely controlled by physicochemical conditions, including temperature, and by activities of substituting elements in the fluid.
- Our study of apatite from Olympic Dam and other deposits in the Olympic Cu-Au Province offers insights into formation mechanisms for of IOCG deposits and potentially, a pathfinder to economic mineralisation.

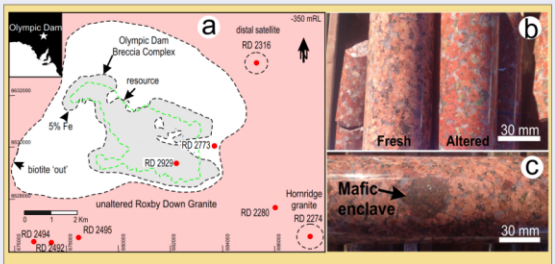

***Figure 1**- (a) Sketch map of the Olympic Dam deposit and location of sampled drillholes (after Ehrig et al. 2012), (b) Altered and Fresh RDG. The reddening of the feldspars is due to an increase of fine-grained hematite during alteration, (c) Mafic enclave in RDG.*

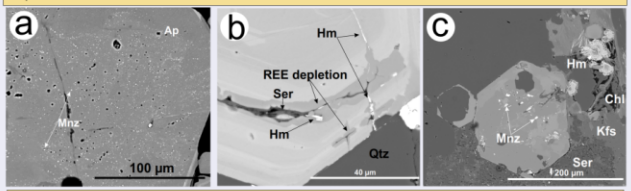

Figure 2- *(a) Monazite emulsion in RDG apatite, (b) REY depletion along fractures and grain rims in RDG apatite. The fractures contain sericite and hematite infill. (c) REY depletion in RDG apatite associated with formation of coarse-grained monazite. Ap-apatite, Mnz-monazite, Hm-hematite, Ser-sericite, Qtz-Quartz, Chl-chlorite, Kfs-K-feldspar.*

Roxby Downs Granite (RDG), Horn Ridge Quartz Monzonite (HRQM) and Mafic Dyke

- RDG and HRQM contain an early magmatic apatite rich in monazite inclusions (Fig. 2a).
- Progressive hematite-sericite alteration sees depletion of REY, Cl and S from magmatic apatite and formation of a second generation of coarse monazite inclusions (Fig. 1c and 4b).
- Mafic enclaves in the RDG contain a higher proportion of acicular apatite
- Cl concentrations are low in RDG apatite, higher in HRQM and highest in Mafic Dyke apatite (Fig. 3a).

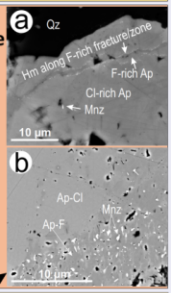

Figure 4-*(a) F-rich, REY-depleted hematite-lined fracture cutting through Cl- and REY-rich apatite, (b) Cl-, REY- and S-rich apatite being altered to a F-rich ap with loss of REY and Cl. Alteration of the apatite is associated with the formation of irregular and elongate monazite inclusions and pores. Ap-apatite, Mnz-monazite, Qz-quartz*

Deep mineralisation

- Deep Mineralisation apatite occurs as large grains or aggregates, commonly interstitial to magnetite.
- These display zoning with cores rich in Cl, S and REY, and grain rims and altered zoned along fractures depleted in these elements (Fig. 3a).
- Alteration and REY loss is associated with formation of monazite inclusions.

***Figure 3**- Binary compositional plots for RDG, HRQM and Mafic Dyke - (a) F vs. Cl (apfu). Note altered apatite in both HRQM and mafic dyke are depleted in Cl, (b) REY vs. Si (apfu). Early Deep mineralisation apatite is REY-, S- and Cl-rich with grain rims and fractures being depleted in these elements, (c)RDG REY vs. Si showing the core to rim REY zoning and subsequent REY-delpetion associated with hematite-sericite alteration.*

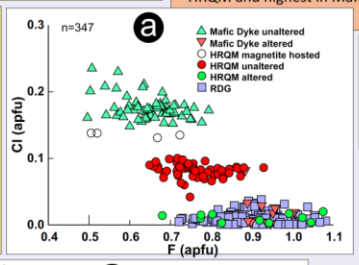

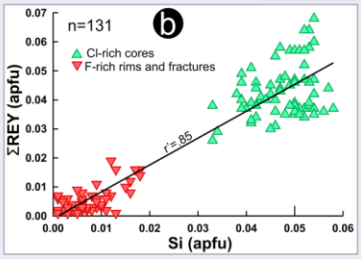

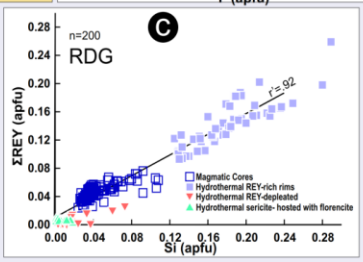

Wirrda Well and Acropolis

- Both prospects contain coarse, initially REY-, S- and in the case of Acropolis, Cl-rich apatite.
- Apatite depleted in REY, S and Cl along rims and grain fractures (Fig. 5b).
- REY-depleted zones host discrete REY- bearing minerals (dominantly monazite) (Fig. 5b)
- These share similarities with grains observed in Deep mineralisation at Olympic Dam.
- What appear to be post-mineralisation calcite veins host coarse pore-rich apatite with very low REY and S concentrations at Wirrda Well

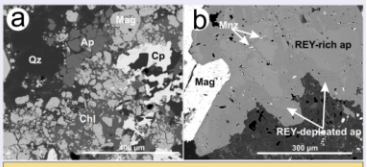

Figure 5-*(a) Wirrda Well apatite aggregates in a magnetite-sulphide-chlorite vein. The apatite grains display a subtle chemical zoning with some grains being unzoned, (b) Acropolis apatite on the edge of a magnetite grain. The bright areas of the apatite are REY-rich and the darker zones REY-depleted and full of monazite inclusions. Ap-apatite, Qz-quartz, Mag-magnetite, Chl-chlorite, Cp-chalcopyrite*

Conclusions

- Changes in apatite morphology, textures, REY and halogen concentration, and presence/absence of newly-formed REE-minerals, clearly define the magmatic-to-hydrothermal transition throughout igneous lithologies undergoing hematite-sericite alteration at OD.
- Hydrothermal apatite in Deep mineralisation at OD shows similarities, albeit with variation, with apatite from both WW and Acropolis in terms of morphology, REE-zoning and mineral inclusions, and most importantly, in terms of SO_3 and Cl content.
- Further work will examine apatite from high-grade ore samples within the OD deposit. Characterisation of REY fractionation trends will be achieved using LA-ICP-MS.
- Chondrite-normalised REY fractionation trends, particularly size and sign of the Eu- and Ce-anomalies, will offer insight into fluid chemistry during apatite evolution at OD.

Reference

Ehrig, K., McPhie, J., Kamenetsky, V. (2012). Geology and mineralogical zonation of the Olympic Dam Iron Oxide Cu-U-Au-Ag deposit, South Australia. In: Hedenquist, J. W., Harris, M., Camus, F. (ed) Geology and Genesis of Major Copper Deposits and Districts of the World: A Tribute to Richard H. Sillitoe, Society of Economic Geologists Inc., 237-267.

Acknowledgements

We thank BHP Billiton for access to Olympic Dam, Wirrda Well & Acropolis sample material and financial support. We also acknowledge the team at Adelaide Microscopy and the Central Science Laboratory for help and advice in regards to data collection.

ADDITIONAL MATERIAL J

CO-AUTHORED PAPER

FELDSPAR EVOLUTION IN THE ROXBY DOWNS GRANITE HOST TO FE-OXIDE CU-AU-(U) MINERALISATION AT OLYMPIC DAM, SOUTH AUSTRALIA

Alkis Kontonikas-Charos[1], Cristiana L. Ciobanu[2], Nigel J. Cook[2], Kathy Ehrig[3], Sasha Krneta[1], Vadim S. Kamenetsky[4]

[1]*School of Physical Sciences, The University of Adelaide, Adelaide, S.A., 5005, Australia*

[2]*School of Chemical Engineering, The University of Adelaide, Adelaide, S.A., 5005, Australia*

[3]*BHP Olympic Dam, Adelaide, SA 5000, Australia*

[4]*School of Physical Sciences, University of Tasmania, Hobart, TAS, Australia, 7001*

Paper published in Ore Geology Reviews 80, 838-859.

Ore Geology Reviews 80 (2017) 838–859

Contents lists available at ScienceDirect

Ore Geology Reviews

journal homepage: www.elsevier.com/locate/oregeorev

Feldspar evolution in the Roxby Downs Granite, host to Fe-oxide Cu-Au-(U) mineralisation at Olympic Dam, South Australia

Alkis Kontonikas-Charos [a,*], Cristiana L. Ciobanu [b], Nigel J. Cook [b], Kathy Ehrig [c], Sasha Krneta [a], Vadim S. Kamenetsky [d]

[a] School of Physical Sciences, University of Adelaide, Adelaide, SA 5000, Australia
[b] School of Chemical Engineering, University of Adelaide, Adelaide, SA 5000, Australia
[c] BHP Billiton Olympic Dam, Adelaide, SA 5000, Australia
[d] School of Physical Sciences, University of Tasmania, Hobart, TAS, 7001, Australia

ARTICLE INFO

Article history:
Received 14 March 2016
Received in revised form 8 August 2016
Accepted 20 August 2016
Available online 24 August 2016

Keywords:
Feldspars
Albitisation
Iron-oxide copper-gold mineralisation
Olympic dam

ABSTRACT

The textural relationships and geochemistry of feldspars from least-altered to sericite-hematite altered and mineralised ~1.595 Ga Roxby Downs Granite (RDG) at Olympic Dam, South Australia, were examined. The sample suite is representative of RDG both distal (>5 km) and proximal (<1 km) to the hydrothermal breccias of the Olympic Dam Breccia Complex (ODBC), which host Fe-oxide Cu-Au-(U) mineralisation at Olympic Dam. Microscopic observations and quantitative analyses indicate that a range of feldspar reactions have taken place within the RDG hosting the Olympic Dam deposit. An early phase of igneous plagioclase (~An_{27-34}) is recognised, along with a more abundant, less-calcic plagioclase (~An_{12-20}) both displaying rapakivi and anti-rapakivi textures with alkali feldspar. Alkali feldspars (~$Or_{55}Ab_{43}An_2$) record post-magmatic evolution from cryptoperthite to patch perthite. Subsequent patch perthite is overprinted by highly porous, near end-member albite and K-feldspar, while plagioclase undergoes replacement by albite + sericite ± Ba-rich K-feldspar. In sericite-hematite altered and mineralised RDG along the margin of the ODBC, sericite replaces all plagioclase, whereas red-stained, Fe-rich K-feldspar persists. Sulphide-uranium-rare earth element mineralisation is observed in association with hydrothermal feldspars, and increases in abundance with proximity to the orebody. Petrographic observations and whole-rock geochemistry illustrate the transformation of plagioclase and alkali feldspar from igneous to hydrothermal processes, and indicate that hydrothermal albite and K-feldspar formed within the RDG without the need for an external source of alkalis. Feldspar geothermometry indicates a minimum crystallisation temperature of 765 °C at 2.2 kbar for alkali feldspar (pressure estimate obtained using plagioclase-amphibole geobarometry) followed by a range of lower temperature transformations. Late-stage magma mixing/contamination is postulated from supportive temperature and pressure estimates along with feldspar and mafic mineral relationships.

1. Introduction

The presence of feldspar replacement reactions has long been recognised as a diagnostic property of iron-oxide copper-gold (IOCG) systems (*e.g.*, Groves et al., 2010); however the exact role they play in the genesis of such deposits remains poorly constrained. Detailed studies of deuteric coarsening (e.g., Parsons and Lee, 2009) and albitisation (*e.g.*, Putnis, 2002; Plümper and Putnis, 2009) have highlighted the ability of such reactions to alter the physical and chemical properties of the host rocks from the macro- down to the nanoscale during fluid-rock interaction. This invokes the idea that feldspar replacement reactions might be more important than once thought, and may even be a required stage for deposition of IOCG mineralisation.

The Olympic Dam IOCG-U deposit, South Australia, is widely regarded as the archetype of the IOCG *sensu stricto* deposit class (*e.g.*, Hitzman et al., 1992; Groves et al., 2010). At Olympic Dam, all IOCG mineralisation is localised within the ~1.595 Ga Roxby Downs Granite (RDG) (*e.g.*, Reeve et al., 1990; Johnson and Cross, 1995). Therefore, Olympic Dam provides an outstanding opportunity to understand the relationship between magmatism, alteration and mineralisation. New insights into the formation of Olympic Dam can be obtained by constraining the major mineralogical changes preserved in the host rocks, which cannot be unambiguously interpreted on the basis of whole rock geochemistry alone. In this contribution, changes in feldspar textures and chemistry in the RDG from magmatic to hydrothermal stages are documented at various (sub-μm to dm) scales.

* Corresponding author.
E-mail address: alkiviadis.kontonikas-charos@adelaide.edu.au (A. Kontonikas-Charos).

http://dx.doi.org/10.1016/j.oregeorev.2016.08.019
0169-1368/

2. Background

2.1. Feldspar reactions and nomenclature

Feldspar microtextures provide a valuable tool for understanding subsolidus re-equilibration in slowly cooled igneous rocks (*e.g.*, Parsons et al., 2015). As fluid-feldspar interaction readily occurs during cooling, feldspars are often subject to post-crystallisation modification (Brown and Parsons, 1989). This typically involves circulation of a deuteric fluid (post-magmatic, internally exsolved), and results in the formation of highly porous, strain-free regions of albite- and orthoclase-rich subgrains within perthitic feldspars (Lee and Parsons, 1997). This process is known as 'deuteric coarsening' (Brown and Parsons, 1984), and the resultant intergrowth texture is termed 'patch perthite' (Parsons, 1978).

Deuteric coarsening is generally considered isochemical (*e.g.*, Parsons et al., 2005) but albitisation, one of the most common metasomatic aluminosilicate reactions in the Earth's upper crust (Perez and Boles, 2005), involves non-isochemical replacement of feldspar by albite. Regional-scale albitisation has been documented from a number of igneous-metamorphic terranes including the Bamble Sector, Norway (Engvik et al., 2008), the Cloncurry District, Queensland, Australia (*e.g.*, Oliver et al., 2004), and recently from the southern part of the Gawler Craton, South Australia (Conor et al., 2010; Ismail et al., 2014; Kontonikas-Charos et al., 2014). Albitisation is also spatially and temporally associated with iron-oxide copper-gold (IOCG) mineralisation (Barton, 2014; and references therein). In this case, albitisation typically forms a broad halo surrounding the deposit, and results in an assemblage dominated by albite (replacing feldspars), chlorite (replacing mafic minerals) and rutile (replacing Fe-Ti-oxides). In extreme cases, almost monomineralic albitites can result (Barton, 2014).

Previous authors (*e.g.*, Engvik et al., 2008; Plümper and Putnis, 2009) have concluded that albitisation occurs through a coupled dissolution-precipitation mechanism (Putnis, 2002), whereby porosity generated is crucial for advancement of the replacement interface between the parent and product phases. It is clear that feldspar reactions are capable of altering the physical properties and chemistry of rocks by significantly enhancing rock permeability (*e.g.*, Putnis, 2002), allowing for subsequent element remobilisation (*e.g.*, Parsons et al., 2009; Hövelmann et al., 2010; Kontonikas-Charos et al., 2014).

2.2. Olympic Dam geology

The Olympic Dam deposit (10,100 Mt @ 0.78% Cu, 250 ppm U_3O_8, 0.3 ppm Au, 1 ppm Ag; BHP Billiton, 2015) is situated within the Olympic Cu-Au Province, a large metallogenic belt which strikes roughly N-S for over 500 km along the eastern margin of the Gawler Craton. The Olympic Cu-Au province also encompasses numerous other IOCG deposits and prospects, including Prominent Hill, Carrapateena, Hillside and Moonta-Wallaroo (Hayward and Skirrow, 2010). The province comprises Palaeo- to Mesoproterozoic sediments, granites, volcanics and conglomerates (Ferris et al., 2002). Rocks of the Hutchison Group (~2 Ga), Donington Granitoid Suite (~1845–1810 Ma) and Wallaroo Group equivalents (~1.75 Ga) form the Palaeoproterozoic basement of the Olympic Dam region (Creaser, 1989; Ferris et al., 2002; Jagodzinski, 2005). These units are unconformably overlain and intruded by felsic and mafic lithologies of the Hiltaba Intrusive Suite (HIS) and Gawler Range Volcanics (GRV); both are the products of a regional-scale magmatic event at ~1.6 Ga (*e.g.*, Skirrow et al., 2007).

Deposition of Cu-Au mineralisation has been considered contemporaneous with the ~1.6 Ga event, based on dating of hydrothermal minerals at Olympic Dam and other prospects (*e.g.*, Johnson and Cross, 1995, Jagodzinski, 2005; Skirrow et al., 2007; Ciobanu et al., 2013; Reid et al., 2013). The hydrothermal breccias of the Olympic Dam Breccia Complex (ODBC), which host the Olympic Dam deposit, are contained within the RDG, which is unconformably overlain by Neoproterozoic to Cambrian sediments of the Stuart Shelf (Reeve et al., 1990). Compositions and textures within the ODBC are gradational, and comprise a continuum from sericite-altered granite through mineralised hematite-rich breccias to barren hematite-quartz breccias in the centre of the deposit (Ehrig et al., 2012). Such changes can be expressed by Fe-Si relationships of whole rock compositions (Fig. 3 in Ehrig et al., 2012). Sericite and hematite, as well as quartz, chlorite, siderite, fluorite, barite and minor magnetite, are the dominant minerals within the complex. Degree of alteration and intensity of brecciation increase from the edges of the ODBC towards the deposit centre (Haynes et al., 1995; Ehrig et al., 2012).

The RDG is relatively undeformed, equigranular and medium- to coarse-grained. It is primarily composed of alkali feldspar (~50%), quartz (21–25%), plagioclase (17–23%) and minor biotite, amphibole and opaques/accessories (5–7%) (Creaser, 1989). The latter include magnetite (containing exsolution of relic ilmenite, which is altered to hematite and rutile), titanite, apatite, zircon, as well as allanite, fluorite, tourmaline, ankerite, uranothorite, synchysite and trace sulphides (Creaser, 1989; Ehrig et al., 2012). Plagioclase forms euhedral grains with core-to-rim compositional zoning (An_{34-20}). Alkali feldspars are coarsely perthitic and may be mantled by plagioclase ('rapakivi' texture); occasionally, granophyric textures with quartz are also observed (Creaser, 1989). Alteration of feldspars to an assemblage of sericite and hematite, and to a lesser extent chloritisation of mafic minerals, is seen throughout the RDG (Creaser, 1989; Oreskes and Einaudi, 1990).

Despite its prominence elsewhere throughout the Gawler Craton (*e.g.*, Yorke Peninsula; Conor et al., 2010; Ismail et al., 2014; Kontonikas-Charos et al., 2014), sodic alteration (particularly albitisation) has not been considered to be significant at Olympic Dam (*e.g.*, Hayward and Skirrow, 2010). Furthermore, hydrothermal K-feldspar has not been previously recognised at Olympic Dam.

3. Approach and methodology

A mineralogical and petrological study was carried out on representative granite samples from various parts of the Olympic Dam region. Drillholes RD2492, -2494 and -2945, ~3 km SW of the deposit ('Area 1' on Fig. 1), were sampled for granite to investigate the chemical and mineralogical homogeneity of the RDG around the Olympic Dam deposit. Drillholes along a 5 km-long NW-SE transect (from RD2274 to RD2511; 'Area 2' on Fig. 1) were also selected to understand feldspar modifications in granite towards the margin of the deposit. In addition, the sample suite includes mineralised granites located both proximal (Drillhole RD3554), and distal (Drillhole RD2316), relative to the ODBC. All samples were obtained from drill core which had been previously assayed by BHP Billiton (see Ehrig et al., 2012 for assay methodology). Initial mineral identification and sample characterisation was made on thin sections and polished blocks by optical microscopy.

All instruments used for analytical characterisation of thin sections and polished blocks are hosted at Adelaide Microscopy, University of Adelaide. A FEI Quanta 450 scanning electron microscope (SEM) with energy-dispersive X-ray spectrometry and back-scatter electron (BSE) imaging capabilities was used at an accelerating voltage of 20 kV and beam current of 10 nA.

Quantitative compositions of feldspars within representative samples were determined using a Cameca SX-Five electron probe microanalyser (EPMA). All feldspars, amphibole and Fe-Ti-minerals were analysed in samples from least-altered RDG (drillholes RD2492, RD2494, RD2495, RD2280 and RD2774), whereas only albite and red-stained K-feldspar were analysed from sericite-hematite altered and mineralised RDG (drillholes RD2531, RD2511, RD3554 and RD2316). Appendix A provides further details of EPMA methodology, including standards, wavelengths, count times and minimum detection limits (mdl).

Transmission electron microscopy (TEM) was performed on foils prepared using the focussed ion beam (FIB)-SEM technique for

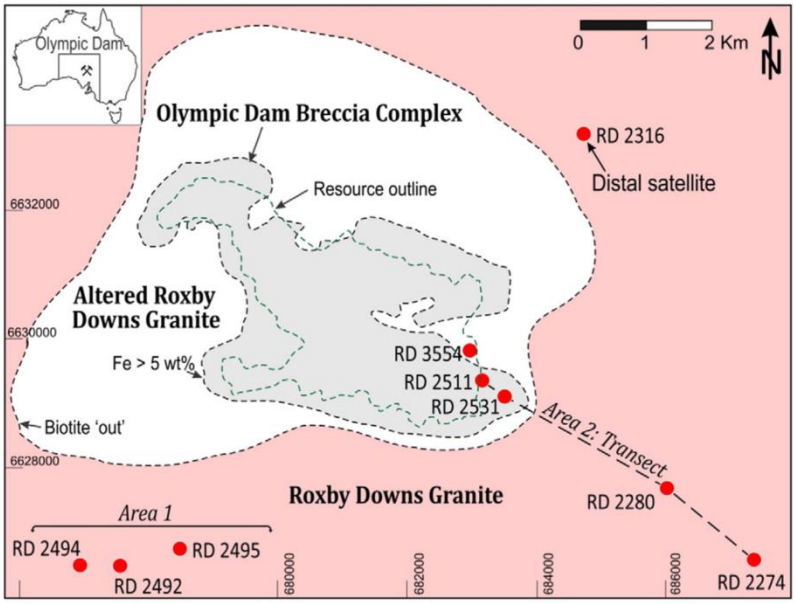

Fig. 1. Sketch map outlining the Olympic Dam deposit and sampled drillhole locations. The map is representative of geology 350 m below the surface, which is overlain by metasediments of the Stuart Shelf. For simplicity, geological structures are ignored. Note that the 3D morphology of the deposit is variable and drillholes marked within the ODBC may cross over respective zones at various depths. For a detailed 3D outline see Ehrig et al. (2012). The white area represents weakly hematite-sericite altered RDG, whereas the area within the Fe >5 wt.% contour contains granite-breccias, hematite-breccias and barren hematite-quartz breccias towards the centre.
Sketch map was modified after Ehrig et al. (2012).

characterisation of feldspars in cryptoperthites. FIB-SEM work was carried out on a Dual Beam FEI Helios Nanolab 600 platform allowing for cross-section imaging, as well as cutting, extraction and thinning of foils for TEM study. Procedures for cutting, extraction and thinning of TEM foils followed Ciobanu et al. (2011). High-resolution (HR)-TEM images in bright field mode (BF) and electron diffractions were obtained using a Philips CM200 TEM equipped with LaB6 source, double-tilt holder and Gatan digital camera, operated at 200 kV. Diffraction measurements were performed using DigitalMicrograph™ 3.11.1 Winwulff© 1.4.0 (JCrystalSoft) software. Publicly available data from the American Mineralogist Crystal Structure Database (http://rruff.geo.arizona.edu/AMS/amcsd.php) were used for indexing of electron diffractions. Energy-dispersive X-ray spectra (EDS) for cryptoperthite analysis were performed on an ultra-high resolution, probe-corrected, FEI Titan Themis S/TEM operated at 200 kV, with an EDS spot size ~5 nm. The Titan Themis is equipped with a FEI Super-X and Fischione HAADF detector. The Super-X detector provides geometrically symmetric EDS detection with an effective solid angle of 0.8 Sr Probe correction delivering sub-Angstrom-scale spatial resolution.

4. Results

4.1. Samples and whole-rock geochemistry

The ubiquitous pink-red colouration of the RDG throughout the sample suite indicates that it is not completely free of alteration. There are, however, important differences in the intensity of alteration. This variability makes it imperative to outline the mineralogical differences between samples from individual drillholes or areas within the Olympic Dam region. This was achieved *via* a combination of macroscopic observation of drillcores and whole-rock geochemistry. Least-altered RDG is most abundant in drillholes >3 km outside the ODBC and is primarily recognised by the pink colouration of feldspars, preservation of mafic minerals and rapakivi textures (Fig. 2). Least-altered RDG is typically characterised by K_2O:Na_2O ratios between 1 and 3 (this varies with degrees of hydrothermal alteration), FeO <4 wt.%, and trace amounts (~25 ppm) of Cu (Table 1a).

In hand specimen, red-staining of alkali feldspar, yellow-green coloration of plagioclase (sericite replacement) and destruction of mafic minerals are diagnostic of alteration in the RDG (Fig. 2), which is more intense and abundant in drillholes proximal to the ODBC. A low Na_2O content (<0.5 wt.%) and Fe content of ~7 wt.% are also characteristic (Table 1b). Such properties define the 'sericite-hematite altered RDG' sample suite. Mineralised RDG (Table 1c) is typical within drillholes closest to the ODBC, and features elevated Fe (>10 wt.%), a drop in K_2O (from ~7 to ~5.5 wt.%), and Cu concentrations exceeding 1 wt.%. Note, however, that the data in Table 1c is restricted to intervals in the drillhole from which samples were collected for this study. Fig. 3 depicts the progressive alteration and mineral replacement of the RDG associated with mineralisation, using whole-rock analyses over an ~300 m-thick section from drillhole RD2316. In this drillhole the mineralisation (Cu, Mo, LREE and U) strongly correlates with depletion in Na_2O and increase in FeO. Mineralogical changes taking place along this downhole profile are discussed in more detail in the next section. Based on characteristics outlined in this section, three sample suites are defined: (1) least altered RDG; (2) sericite-hematite altered RDG; and (3) mineralised RDG.

Whole-rock analyses for least-altered RDG (Table 1a), show values for the main oxides (*e.g.*, SiO_2 ~ 70%; Al_2O_3 ~ 13%; K_2O ~ 5%, Na_2O ~ 3–4%; FeO ~ 3–4, CaO < 1%, P_2O_5 < 1% and MgO + Ti_2O < 1.5%; LOI ~ 1–2.2%) close to those of granites. Such analyses are used to discriminate among different types of granitoids and their geochemical affiliation (Fig. 4). Two diagrams based on CIPW normative calculations are used, QAP (Streckeisen, 1976; LeMaitre et al., 1989) and Ab-An-Or (Barker, 1979), to show the differences in terms of rock types within the least-altered RDG (Fig. 4a, b). The QAP diagram is modified by dividing the albite (Ab) norm between the orthoclase (Or + Ab * 0.33) and plagioclase (An + Ab * 0.66) apexes, which is based on EPMA spot analyses of cryptoperthite in the least-altered RDG. This approximation is checked by the petrographic study (see below). Least-altered RDG

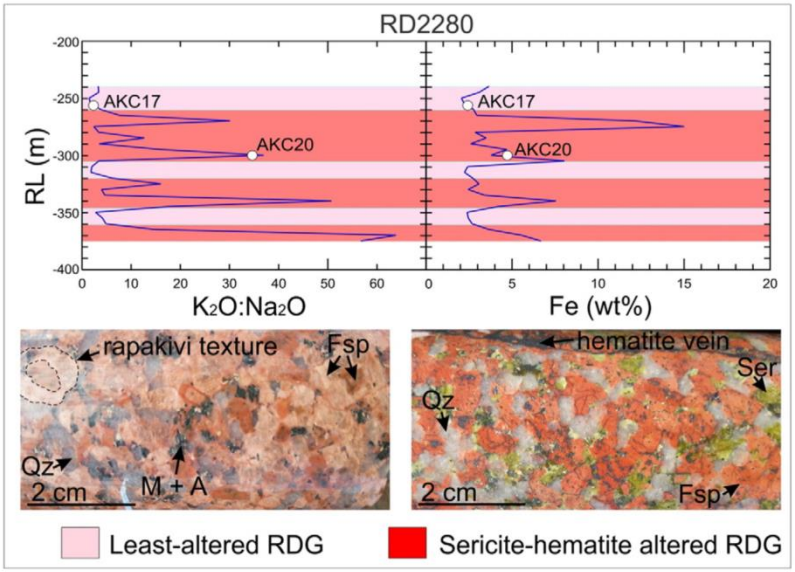

Fig. 2. Binary plots of whole-rock analyses for drillhole RD2280 and hand specimen photographs showing differences in appearance between least-altered and altered RDG. Pink sections represent least-altered RDG (low K_2O:Na_2O ratios and low Fe content), whereas red sections represent altered RDG (high K_2O:Na_2O ratios and high Fe content). Note the change from pink to red colouration of feldspars and the yellow-green colour of sericite in altered RDG. Abbreviations: Fsp — feldspar, M + A — mafic and accessory minerals, Qz — quartz, RL — relative depth of drillhole, Ser — sericite.

plots as a tight cluster on both the QAP and Ab-An-Or diagrams (Fig. 4a, b), however some of the data begins to extend towards the 'alkali feldspar granite' field and the Or-apex, respectively. Fig. 4c indicates the least-altered RDG ranges from weakly metaluminous to moderately peraluminous. The sample suite is further discriminated by the modified alkali-lime index (Fig. 4d). The least-altered RDG plots between the alkalic and alkali calcic fields due to high Na_2O and K_2O relative to CaO. It also straddles the fields for A- and I-type granitoids, as defined by published data (*e.g.*, Frost et al., 2001).

4.2. Petrography

The petrographic and mineralogical differences between the sample suites are summarised in Table 2. Importantly, although RDG from Area 2 retains the geochemical hallmarks of the least-altered RDG outlined above, it is more altered than RDG from Area 1. Feldspars are more extensively altered and markedly microporous, while all igneous mafic minerals are altered to chlorite + rutile. Thus, Area 2 represents a transition between the least-altered and altered RDG categories. Subsequent feldspar descriptions and interpretations regarding the magmatic history of the RDG hinge primarily on observations from the Area 1 sample suite.

Despite differences in degrees of alteration, least-altered RDG from both Areas 1 and 2 display many petrographic similarities. Feldspars are characterised by various textural overprints (see below) and also form rapakivi and anti-rapakivi textures, while quartz occurs interstitial to other minerals as small groundmass crystals, as well as larger grains (>2 mm). Large microgranular mafic enclaves (>2 mm), consisting of amphibole, biotite and Fe-Ti-minerals (ilmenite, titanite and magnetite), are also found throughout the RDG and have been partially (Area 1) and completely altered (Area 2). In this case, amphibole and biotite are altered to chlorite + hematite ± rutile ± albite, whereas ilmenite breaks down to hematite + rutile symplectites, titanite is replaced by rutile + quartz and magnetite is replaced by hematite. Photomicrographs (Fig. 5) highlight some textural characteristics of minerals in least-altered RDG.

Sericite-hematite altered RDG occurs irregularly throughout all drillholes along the transect (Fig. 1), increasing in abundance and intensity with proximity to the ODBC. Dominant minerals are K-feldspar, quartz, sericite, Fe-oxides (both magnetite and hematite), chlorite,

Table 1a
Sample list and whole-rock assay data for least-altered RDG.

Sample	Drillhole	Depth (mRL)	Whole rock assay data															
			SiO_2	TiO_2	Al_2O_3	FeO	MnO	MgO	CaO	BaO	Na_2O	K_2O	P_2O_5	Total	LOI	K_2O: Na_2O	Cu (ppm)	U_3O_8 (ppm)
RX7860	RD2494	−480.3 to 485.3	71.2	0.48	13.5	3.07	0.05	0.90	0.94	0.10	3.81	5.36	0.07	99.48	1.18	1.41	<50	14
RX7864	RD2492	−653.1 to 658.1	69.3	0.42	13.5	3.36	0.06	0.73	0.76	0.10	3.24	5.55	0.09	97.11	1.40	1.72	<50	8
RX7865	RD2495	−448.1 to 453.1	68.7	0.48	13.1	3.05	0.08	0.99	0.85	0.09	3.73	5.30	0.09	96.46	1.27	1.42	<50	12
RX7866		−483.1 to 488.1	69.7	0.43	13.3	3.06	0.06	0.81	0.88	0.10	3.71	5.36	0.07	97.48	1.04	1.45	<50	12
AKC16	RD2280	−244.9 to 249.9	70.8	0.45	13.8	3.98	0.04	0.83	0.42	0.11	2.16	6.53	0.09	99.21	1.92	3.03	200	<4
AKC17		−259.9 to 264.9	71.4	0.43	13.7	3.56	0.05	1.19	0.57	0.09	1.91	6.59	0.05	99.54	2.24	3.44	<50	5
AKC21		−309.9 to 314.9	70.0	0.45	13.7	3.11	0.05	0.76	0.59	0.09	3.15	5.64	0.09	97.63	1.64	1.79	350	15
AKC22		−314.9 to 319.9	70.6	0.42	13.9	2.88	0.06	0.86	0.76	0.09	3.41	5.57	0.07	98.62	1.62	1.63	200	20
AKC27	RD2274	−214.9 to 217.9	69.1	0.27	12.7	4.80	0.03	0.63	0.14	0.16	1.02	7.05	0.01	95.91	1.55	6.88	<50	<4

Note: 'Total' column only refers to elements given in tables, which are used for rock classification diagrams in Fig. 4. All values given are in wt.% aside from Cu and U_3O_8. Intervals for whole-rock assay data are 5 m. Depth (mRL) is relative to sea level.

Table 1b
Sample list and whole-rock assay data for sericite-hematite altered RDG.

Sample	Drillhole	Depth (mRL)	Whole rock assay data														
			SiO_2	TiO_2	Al_2O_3	FeO	MnO	MgO	CaO	BaO	Na_2O	K_2O	P_2O_5	Total	LOI	K_2O: Na_2O	Cu (ppm)	U_3O_8 (ppm)
AKC1	RD2531	−315.6 to 316.6	62.0	0.37	12.2	12.4	0.63	0.45	0.07	0.04	0.12	5.65	0.12	94.05	5.89	47.1	850	50
AKC2		−423.4 to 424.4	67.0	0.33	12.5	7.08	0.37	0.38	0.08	0.36	0.12	6.13	0.07	94.42	4.09	51.1	200	40
AKC3		−619.1 to 620.1	66.3	0.40	12.8	5.70	0.23	0.32	0.21	0.11	0.18	8.00	0.07	94.32	3.42	44.4	100	25
AKC5		−718.8 to 719.8	65.9	0.40	12.7	7.17	0.31	0.43	0.31	0.07	0.13	6.58	0.14	94.14	4.08	50.6	700	35
AKC8	RD2511	−274.7 to 275.7	65.7	0.35	11.8	7.74	0.04	0.46	0.59	0.61	0.16	6.65	0.07	94.17	2.27	41.6	2400	72
AKC9		−295.1 to 296.1	65.5	0.40	12.9	7.00	0.19	0.33	0.62	0.12	0.19	7.81	0.07	95.13	3.26	41.1	3350	145
AKC10		−338.7 to 339.7	67.8	0.35	12.1	8.45	0.09	0.38	0.21	0.09	0.15	6.38	0.07	96.07	2.62	42.5	2200	38
AKC11		*−510.5 to 515.5*	69.7	0.38	13.5	3.80	0.08	0.81	0.34	0.09	0.16	7.90	0.07	96.83	4.56	49.4	450	26
AKC12		*−510.5 to 515.5*	69.7	0.38	13.5	3.80	0.08	0.81	0.34	0.09	0.16	7.90	0.07	96.83	4.56	49.4	450	26
AKC13		−664.6 to 665.6	67.6	0.38	13.5	6.69	0.05	0.35	0.11	0.17	0.13	6.34	0.07	95.39	2.70	48.8	450	32
AKC18	RD2280	*−294.9 to 299.9*	68.5	0.42	13.2	6.05	0.04	0.83	0.31	0.07	0.47	6.75	0.12	96.76	2.13	14.4	<50	<4
AKC19		*−294.9 to 299.9*	68.5	0.42	13.2	6.05	0.04	0.83	0.31	0.07	0.47	6.75	0.12	96.76	2.13	14.4	<50	<4
AKC20		*−299.9 to 304.9*	70.2	0.45	13.4	4.86	0.03	0.68	0.21	0.09	0.23	7.56	0.05	97.76	1.95	32.9	<50	<4
AKC23		*−324.9 to 329.9*	70.8	0.47	14.4	3.96	0.03	0.60	0.18	0.09	0.54	7.73	0.09	98.89	1.81	14.3	250	10
AKC24		*−354.9 to 359.9*	67.4	0.40	12.6	3.16	0.23	1.38	1.72	0.07	1.70	6.32	0.07	95.05	3.80	3.7	<50	10
AKC25		*−369.9 to 374.9*	66.3	0.42	13.2	8.59	0.01	0.36	0.06	0.04	0.13	6.83	0.05	95.99	1.73	52.5	3800	10
AKC26		*−369.9 to 374.9*	66.3	0.42	13.2	8.59	0.01	0.36	0.06	0.04	0.13	6.83	0.05	95.99	1.73	52.5	3800	10
RX6698	RD2316	−634.7 to 635.7	52.2	0.30	8.0	20.9	0.22	3.10	2.36	0.19	0.85	3.85	0.37	92.34	5.20	4.53	1800	330
RX6700		−662.7 to 663.7	68.2	0.35	12.9	5.84	0.09	0.71	0.49	0.09	2.87	5.72	0.07	97.33	1.67	1.99	300	50
RX6702		−664.7 to 665.7	60.8	0.27	10.3	13.5	0.28	1.74	1.89	0.08	1.62	4.38	0.16	95.02	4.79	2.70	1400	110
RX6703		−664.7 to 665.7	60.8	0.27	10.3	13.5	0.28	1.74	1.89	0.08	1.62	4.38	0.16	95.02	4.79	2.70	1400	110
RX6704		−670.7 to 671.7	61.8	0.30	10.9	13.6	0.14	1.19	0.94	0.08	1.33	5.07	0.16	95.51	3.19	3.81	1400	74
RX6706		−674.7 to 675.7	68.2	0.35	13.0	6.06	0.17	0.83	0.94	0.08	2.78	5.67	0.07	98.15	2.04	2.04	1800	76
RX7322	RD3554	−491.3 to 492.3	71.7	0.32	13.3	3.15	0.01	0.15	0.06	0.27	0.18	7.26	0.02	96.42	2.63	40.3	890	50
RX7323		−−513.8 to 514.8	68.5	0.32	11.9	5.85	0.21	0.27	0.10	0.11	0.15	6.04	0.02	93.47	3.61	40.3	4500	65
RX7331		−764.3 to 765.3	64.2	0.35	12.9	7.42	0.15	0.18	0.87	0.36	0.27	8.37	0.09	95.16	3.82	31.0	4500	35

Note: 'Total' column only refers to elements given in tables, which are used for rock classification diagrams in Fig. 4. All values given are in wt.% aside from Cu and U_3O_8. Italics indicates whole-rock assay data intervals of 5 m, whereas others are 1 m. Depth (mRL) is relative to sea level.

sulphides (chalcopyrite, pyrite, sphalerite, galena and molybdenite), rutile, REE- and U-minerals, as well as minor albite. In terms of major mineralogical changes, sericite replaces all igneous plagioclase, while the abundance of hematite and minor, disseminated Cu-Fe-sulphides increases compared to least-altered RDG. Primary mafic minerals are not preserved in sericite-hematite altered RDG. Accessory minerals are generally sparse; however metamict zircon is occasionally preserved. Hydrothermal rutile contains measurable concentrations of Nb and W, and is also morphologically distinct from the rutile forming symplectites with hematite. Samples of mineralised RDG contain a greater abundance of Cu-Fe-sulphides (chalcopyrite, minor chalcocite and bornite) and hematite, which predominates over sericite. Albite is still preserved at depth in both sericite-hematite altered and mineralised RDG.

4.2.1. Alkali feldspars in least-altered RDG

The majority of alkali feldspars observed in least-altered RDG display perthitic textures. Due to their complexity, textural characterisation of alkali feldspars requires a careful systematic approach. Categorisation of feldspar textures follows terminology outlined by Parsons et al. (2005), with compositional data obtained by EPMA. A total of four textural categories are preserved within the least-altered RDG: cryptoperthite; patch perthite; film perthite and highly porous albite and K-feldspar. Their features and compositions are summarised in Tables 3 and 4, respectively. Optical properties routinely used to discriminate between feldspar phases are not apparent using transmitted light microscopy alone, even in the least-altered samples. Thus, SEM was primarily used in feldspar characterisation.

Table 1c
Sample list and whole-rock assay data for mineralised RDG.

Sample	Drillhole	Depth (mRL)	Whole rock assay data														
			SiO_2	TiO_2	Al_2O_3	FeO	MnO	MgO	CaO	BaO	Na_2O	K_2O	P_2O_5	Total	LOI	K_2O: Na_2O	Cu (ppm)	U_3O_8 (ppm)
RX7307	RD3554	−261.3 to 262.3	65.9	0.20	10.4	7.46	0.06	0.51	0.50	0.40	0.12	4.60	0.01	90.16	3.53	38.3	36,800	20
RX7315		−341.3 to 342.3	59.7	0.25	10.3	14.4	0.27	0.20	0.17	0.27	0.11	3.25	0.14	89.06	3.58	29.5	25,800	235
RX7321		−392.9 to 393.9	41.5	0.18	7.4	28.3	0.87	0.28	0.15	0.22	0.08	2.34	0.23	81.55	8.18	29.3	16,900	495
RX7324		−520.4 to 521.4	66.5	0.28	11.9	5.71	0.13	0.33	0.15	0.09	0.16	6.08	0.01	91.34	2.63	38.0	28,500	175
RX7325		−524.1 to 525.1	64.6	0.28	12.2	4.57	0.01	0.18	0.06	0.33	0.16	5.36	0.01	87.76	2.43	33.5	45,000	100
RX7326		−527.9 to 528.9	61.4	0.30	12.3	3.86	0.01	0.18	0.04	0.09	0.13	5.66	0.01	83.98	3.52	43.5	83,700	80
RX7327		−535.4 to 536.4	67.0	0.30	11.2	5.67	0.01	0.17	0.04	0.29	0.16	5.24	0.02	90.10	5.30	32.8	33,800	185
RX7328		−561.6 to 562.6	35.3	0.13	4.7	45.4	0.01	0.05	0.03	0.11	0.05	1.92	0.12	87.82	1.92	38.4	45,400	600
RX7329		−585.9 to 586.9	64.8	0.28	11.7	9.94	0.01	0.13	0.04	0.31	0.23	6.40	0.07	93.91	1.75	27.8	13,800	225
RX6685	RD2316	−481.8 to 482.8	47.5	0.20	7.2	29.6	0.06	0.45	0.22	0.06	0.07	4.35	0.16	89.87	6.72	62.1	7300	155
RX6686		−489.8 to 490.8	64.6	0.32	10.5	11.7	0.06	0.48	0.28	0.10	0.12	7.20	0.14	95.50	2.13	60.0	3900	155
RX6687		−489.8 to 490.8	64.6	0.32	10.5	11.7	0.06	0.48	0.28	0.10	0.12	7.20	0.14	95.50	2.13	60.0	3900	155
RX6690		−545.8 to 546.8	49.4	0.25	8.4	23.5	0.25	1.79	1.39	0.08	0.09	4.35	0.18	89.68	5.46	48.3	11,500	490
RX6691		−546.8 to 547.8	39.6	0.15	5.1	34.6	0.22	1.56	1.76	0.03	0.05	1.99	0.28	85.34	8.73	39.8	26,800	950
RX6693		−576.8 to 577.8	44.9	0.20	6.2	29.9	0.18	1.41	1.79	0.40	0.07	2.83	0.37	88.25	6.77	40.4	15,000	650
RX6694		−599.7 to 600.7	48.3	0.18	5.6	28.4	0.23	1.18	1.53	0.03	0.07	2.61	0.34	88.47	7.31	37.3	5400	550

Note: 'Total' column only refers to elements given in tables, which are used for rock classification diagrams in Fig. 4. All values given are in wt.% aside from Cu and U_3O_8. Depth (mRL) is relative to sea level.

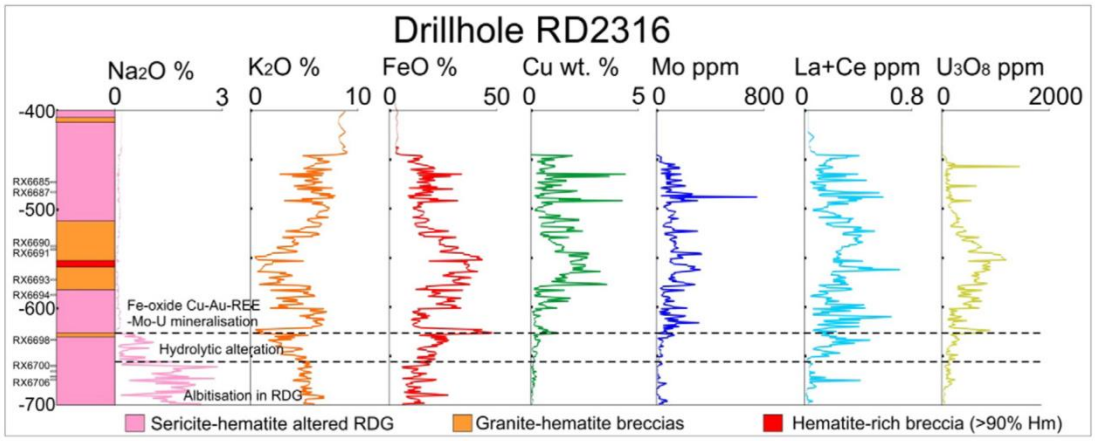

Fig. 3. Down-hole profile of drillhole RD2316 illustrating major elemental changes in whole-rock analyses. Note the transition in alteration and subsequent mineralisation styles in the RDG across an ~80 m section. There is a clear positive correlation between FeO, Cu, Mo, La + Ce and U_3O_8 in mineralised RDG.

Cryptoperthite, more frequently preserved in Area 1 than in Area 2, occurs as fields of fully coherent, sub-μm-sized Ab-rich lamellae with sub-μm periodicities within Or-rich feldspar (Fig. 6a). Depending on grain orientation, it may also form a braid texture. Measured bulk compositions of cryptoperthite vary from ~$Or_{68.3}Ab_{30.1}An_{1.6}$ to $Or_{48.3}Ab_{50.1}An_{1.6}$ (mean values given in Table 4), while individual analyses indicate that the interiors of cryptoperthite are more Ab-rich and Or-poor relative to the rims. In addition, it is apparent that this change in composition coincides with a loss in lamellar coherency at field boundaries. Micropores are extremely scarce.

Cryptoperthites have been partially overprinted by clusters of incoherent, Or-rich (~$Or_{85.1}$) and Ab-rich (~$Ab_{83.3}$) subgrains which are noticeably microporous near subgrain junctions, and may also be associated with sub-μm-sized hematite inclusions (Fig. 6b). Depending upon the viewing plane, this 'patch perthite' may appear as sets of intragranular anastomosing veinlets occurring along, or crosscutting Ab-rich lamellae within the cryptoperthite.

Film perthite is very scarce and typically only preserved towards the centres of some Or-rich grains of patch perthite. It is characterised by semi-coherent, <500 nm-thick Ab-rich lamellae with a sub-μm

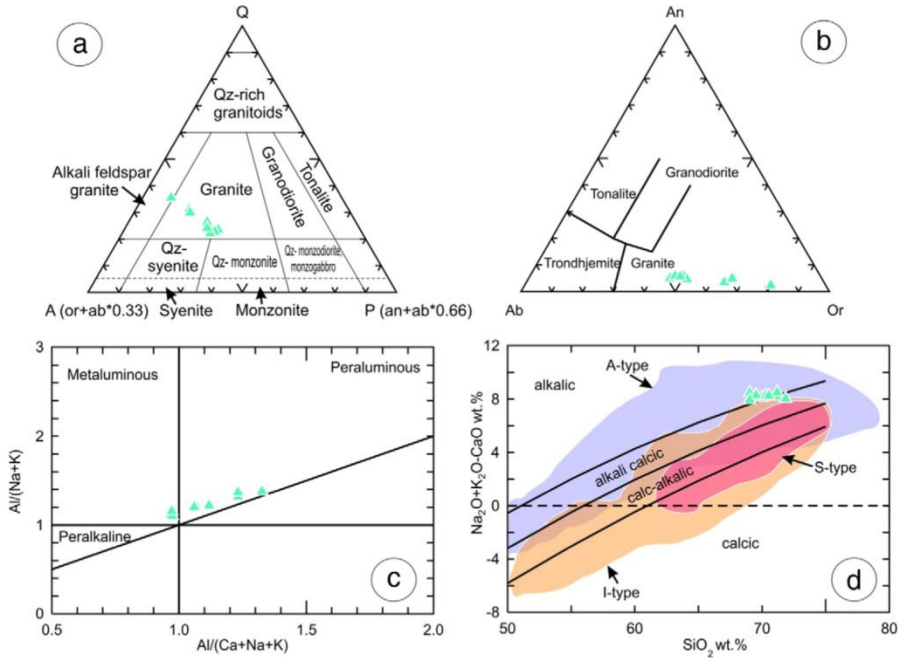

Fig. 4. Ternary and binary plots of whole-rock analytical data used for least-altered RDG classification at Olympic Dam. (a) QAP diagram (Streckeisen, 1976; LeMaitre et al., 1989) from CIPW normalised whole-rock data. The diagram is modified for the proportions of Ab in A and P which is based on the presence of normative albite within the alkali feldspars of the least-altered RDG. (b) CIPW normalised data plotted on a Ab-An-Or diagram after Barker (1979). See text for explanation. (c) Alumina saturation index diagram after Shand (1943), using ratios of molecular Al, Ca, K and Na. (d) Binary plot of the modified alkali-lime index, ($Na_2O + K_2O$-CaO)/SiO_2, and approximate fields for the alkalic, alkali calcic, calc-alkalic and calcic rock series. Granite field types are based on existing data from plutonic rocks in various terranes (see Frost et al., 2001 and references therein).

Table 2
Summary of mineralogy and geochemistry for the RDG.

Lithology	Drillholes	Texture	Mineralogy	Whole-rock geochemistry
Least-altered RDG (Area 1)	RD2492, RD2494, RD2495	Medium- to coarse-grained, granitic, equigranular-porphyritic	Alkali feldspar (40%), plagioclase (25%), quartz (20%), amphibole and biotite (10%), and accessories (5%) — zircon, apatite, magnetite, Fe-Ti-minerals (ilmenite, titanite), REE-U-minerals (synchysite, uraninite, uranothorite). Mafic minerals are partially altered. (Amphibole and biotite to chlorite, magnetite to hematite, ilmenite to rutile + hematite and titanite to rutile + quartz)	K_2O:Na_2O ~ 1–2, FeO < 4 wt.%, Cu < 50 ppm
Least-altered RDG (Area 2)	RD2280, RD2274	Medium- to coarse-grained, granitic, equigranular	Alkali feldspar (40%), plagioclase (25%), quartz (20%), amphibole and biotite (10%) and accessories (5%) — zircon, apatite, magnetite, Fe-Ti-minerals, REE-U-minerals (synchysite, uraninite, uranothorite). All mafic minerals are completely altered (see above).	K_2O:Na_2O ~ 1–3.5, FeO < 4 wt.%, Cu ~ <50–350 ppm
Sericite-hematite altered RDG	RD2280, RD2531, RD2511, RD2316, RD3554	Coarse-grained, highly-fractured,	K-feldspar (35%), sericite (25%), quartz (20%), chlorite (10%), variable amounts (up to 10%) of magnetite, hematite, rutile, carbonates (calcite, siderite, ankerite), disseminated sulphides (chalcopyrite, pyrite, sphalerite, galena, molybdenite), REE-U-minerals (synchysite, bastnäsite, uraninite, florencite). Trace amounts of albite.	Na_2O < 0.5 wt.%, FeO ~ 7 wt.%
Mineralised RDG (distal)	RD2316	Coarse-grained, brecciated	K-feldspar (25%), sericite (25%), quartz (25%), variable amounts (up to 25%) of magnetite, hematite, chlorite, rutile, carbonates (calcite, siderite, ankerite), sulphides (chalcopyrite, bornite, chalcocite, pyrite, sphalerite, galena, molybdenite), REE-U minerals (bastnäsite, uranothorite, brannerite, coffinite, florencite). Albite preserved at depth.	FeO > 10 wt.%, K_2O ~ 5.5 wt.%, Cu > 1 wt.%, (Na_2O ~ 1–2 wt.% at depth)
Mineralised RDG (proximal)	RD3554	Coarse-grained, brecciated	K-feldspar (25%), sericite (25%), quartz (25%), variable amounts (up to 25%) of magnetite, hematite, chlorite, rutile, carbonates (calcite, siderite, ankerite), sulphides (chalcopyrite, bornite, chalcocite, pyrite, sphalerite, galena, molybdenite), REE-U minerals (bastnäsite, uranothorite, brannerite, coffinite, florencite).	FeO > 10 wt.%, K_2O ~ 5.5 wt.%, Cu > 1 wt.%

periodicity (Fig. 6c). Measured bulk compositions of film perthite vary from $Or_{78}Ab_{21.4}An_{0.6}$ to $Or_{88.4}Ab_{11.3}An_{0.3}$, likely due to variability in lamellae size, and thus the initial composition of the Or-rich phase.

All feldspar microtextures have been extensively overprinted by highly porous, incoherent, near-end member albite and K-feldspar (Fig. 6d). As with the cryptoperthites, the overprinted feldspars are more abundant in RDG from Area 2, but are also quite widespread in Area 1. Initially coherent and semi-coherent lamellae of cryptoperthite and film perthite may be irregularly thickened, or feature trails of micropores. These highly porous feldspars have similar composition to the feldspars they replace; however some grains are almost entirely comprised of highly porous K-feldspar. The Ab-rich phase of patch perthite is typically overprinted by highly porous albite which may also contain sub-μm inclusions of sericite. This albite is compositionally similar to

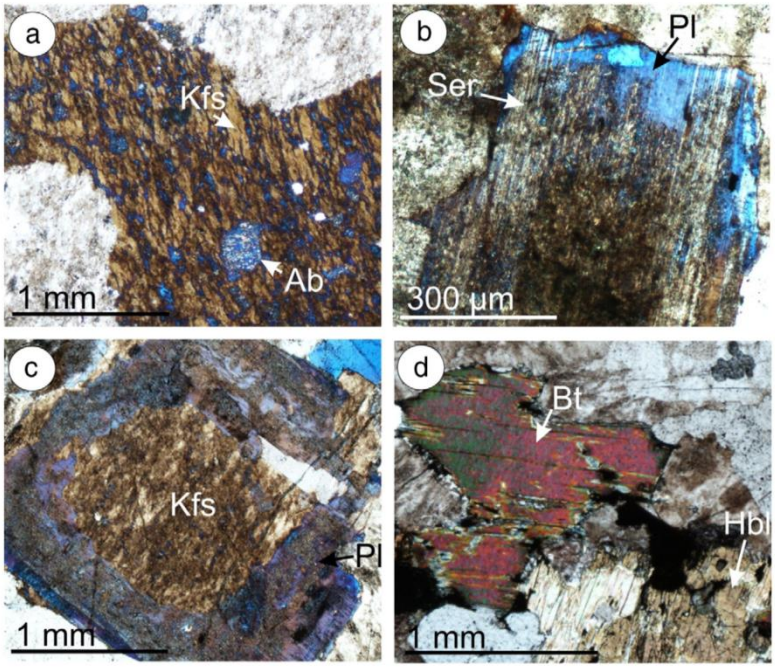

Fig. 5. Photomicrographs in transmitted light (crossed polars) showing primary minerals in the least-altered RDG. (a) Large perthitic alkali feldspar grain displaying various turbid areas related to recrystallisation. (b) Typical appearance of plagioclase; note the zonation and sericite alteration along polysynthetic twins. (c) Alkali feldspar grain mantled by plagioclase. (d) Cluster of variably altered hornblende and biotite. Abbreviations: Ab — albite, Bt — biotite, Hbl — hornblende, Kfs — K-feldspar, Pl — plagioclase, Ser — sericite.

Table 3
Summary of feldspar textures and bulk compositions in the RDG.

Microtexture	Phases	Description	Composition range (bulk)	Textural relationships	Figures
Plagioclase	Andesine-oligoclase	Large (>2 mm) phenocrysts, displaying typical calcic-sodic core to rim compositional zoning. Only preserved within least-altered RDG from Area 1.	~An_{27-34}	Phenocrysts are extremely altered and overprinted by replacive albite and highly porous K-feldspar.	8a
Plagioclase	Oligoclase	Forms individual grains and rims on pre-existing feldspars. Hosts inclusions of worm-like quartz, fluorite and alkali feldspar.	~An_{12-20}	Forms mantles around alkali feldspars (rapakivi), and discontinuous rims around andesine-oligoclase.	8a, b, d, 9a, 15
Cryptoperthite	Ab- and Or-rich feldspar	Fully coherent intergrowth of sub-μm sized Ab-rich lamellae with sub-μm periodicities in Or-rich feldspar. Micropores are scarce.	~$Or_{42-74}Ab_{25-55}An_{1-3}$	Preserved as regions within feldspar grains.	6a, d, 7a–d, 14
Patch perthite	Subgrains of Ab- and Or-rich feldspar	Incoherent clusters of Ab- and Or-rich subgrains, highly porous near subgrain boundaries, may be associated with sub-μm-sized hematite inclusions.	~$Ab_{84}An_{14}Or_2$ ~$Or_{85}Ab_{14}An_1$	Forms mosaics or veins, depending upon viewing plane, which crosscut cryptoperthite.	6a, b, d, 8a, 14
Film perthite	Ab- and Or-rich feldspar	Semi-coherent, <500 nm-thick Ab-rich lamellae with a sub-μm periodicity within Or-rich phase of patch perthite.	~$Or_{83}Ab_{16}An_1$	Only partially preserved towards the centre of the Or-rich phase of patch perthite.	6b, c
Replacive albite, highly porous albite	Albite ± sericite	Highly porous, incoherent, near-end member albite.	~$Ab_{97}An_1Or_2$	Crosscuts and partially replaces all pre-existing alkali and plagioclase feldspars.	6d, 8c, d, 9a, b, 10a, 15
Highly porous K-feldspar	K-feldspar ± Ba-rich K-feldspar	Highly porous, incoherent, near-end member K-feldspar. Variably red-stained.	~$Or_{98}Ab_2$	Crosscuts and partially replaces all pre-existing alkali and plagioclase feldspars.	6b–d, 9a–d, 10a, b, 17

albite directly replacing plagioclase grains (discussed below). In addition, both highly porous feldspars are intimately associated with sub-μm-sized inclusions of hematite.

Nanoscale characterisation of the cryptoperthite is shown in Fig. 7. Low-resolution TEM imaging shows typical cryptoperthite appearance with albite lamellae tens to hundreds of nm in width, generally parallel to one another but with variation in thickness and branching (Fig. 7a, b). High-resolution TEM imaging shows coherent lattice fringes between host orthoclase and exsolved albite, both down to the same [1 − 12] zone axis (Fig. 7c). The spinodal and slightly disordered character of the exsolution is seen on selected areas of electron diffraction (SAED) as distortion of main reflections, with streaks along (*hk*0)* directions (Fig. 7d). Based on several zero- and second-order SAEDs obtained from perthites, the host is orthoclase rather than microcline; the latter interpretation is concordant with the lack of typical tartan twinning. The composition of both host and lamellae was checked using EDS

Table 4
Mean electron probe microanalyses of alkali feldspars in the RDG.

	Cryptoperthite ($n = 61$)	Ab-rich phase of patch perthite ($n = 11$)	Or-rich phase of patch perthite ($n = 18$)	Film perthite ($n = 17$)	Highly porous albite ($n = 18$)	Highly porous K-feldspar ($n = 39$)	Ba-rich K-feldspar ($n = 21$)	Red-stained areas of K-feldspar ($n = 52$)
Sample wt.%								
SiO_2	65.89 (0.28)	64.31 (0.61)	64.21 (0.65)	65.41 (0.27)	68.86 (1.72)	65.21 (0.51)	55.82 (1.57)	63.29 (1.06)
Al_2O_3	18.71 (0.12)	21.69 (0.32)	18.39 (0.39)	18.20 (0.17)	20.04 (0.36)	18.17 (0.47)	20.51 (0.52)	17.71 (0.37)
FeO	0.16 (0.02)	0.22 (0.04)	0.12 (0.14)	0.12 (0.02)	0.12 (0.91)	0.19 (0.25)	0.06 (0.12)	1.42 (1.33)
CaO	0.38 (0.07)	3.16 (0.37)	0.08 (0.05)	0.07 (0.09)	0.24 (0.1)	<mdl	0.01 (0.03)	0.04 (0.11)
SrO	0.33 (0.01)	0.25 (0.02)	0.35 (0.10)	0.35 (0.02)	<mdl	<mdl	0.25 (0.02)	<mdl
BaO	0.31 (0.07)	0.03 (0.01)	1.03 (0.30)	0.25 (0.30)	<mdl	0.27 (0.05)	10.81 (1.73)	0.24 (0.15)
Na_2O	5.18 (0.44)	10.19 (0.25)	1.67 (0.47)	1.85 (0.44)	11.85 (0.49)	0.23 (0.11)	0.21 (0.12)	0.23 (0.06)
K_2O	9.64 (0.30)	0.31 (0.08)	14.57 (1.05)	14.79 (0.69)	0.27 (0.08)	16.12 (0.95)	12.09 (0.63)	16.71 (0.32)
Total	100.69 (0.30)	100.11 (0.49)	100.45 (0.70)	101.12 (0.16)	101.26 (1.22)	100.11 (0.73)	99.59 (0.51)	99.89 (0.98)
a.p.f.u.								
Ca	0.02	0.15	0.00	0.00	0.02	0.00	0.00	0.00
Sr	0.01	0.01	0.01	0.01	0.00	0.00	0.01	0.00
Ba	0.01	0.00	0.02	0.00	0.00	0.00	0.21	0.00
Na	0.45	0.87	0.15	0.16	0.98	0.02	0.02	0.02
K	0.56	0.02	0.86	0.86	0.01	1.01	0.77	1.00
Total	1.06	1.05	1.04	1.05	1.02	1.03	1.00	1.02
Al	1.00	1.13	1.01	0.98	1.02	0.99	1.21	0.98
Si	2.98	2.84	2.98	2.99	2.97	3.00	2.79	2.97
Fe	0.01	0.01	0.00	0.01	0.01	0.01	0.00	0.06
mol.%								
Ab %	43.51 (3.54)	83.29 (1.81)	14.51 (0.94)	15.61 (3.70)	97.41 (0.83)	2.17 (0.45)	2.03 (1.26)	2.02 (0.48)
An %	1.74 (0.31)	14.31 (1.68)	0.39 (0.20)	0.35 (0.40)	1.10 (0.55)	0	0.06 (0.18)	0.18 (0.54)
Or %	54.89 (3.67)	1.71 (0.42)	85.09 (1.14)	82.89 (3.89)	1.15(0.43)	97.79 (0.54)	97.39 (1.45)	96.79 (0.65)
Feldspar geothermometry (Fuhrman and Lindsley, 1988)								
Minimum T (°C)	765	430	430	<430	*	*	*	*

Note: figures in parentheses represent standard deviations. <mdl indicate values below the minimum detection limits. Geothermometry uncertainties of ±40 °C.
Analyses represent transects of cryptoperthite grains from interior to rim. For maximums and minimums see Appendices.
* No reliable estimates calculated.

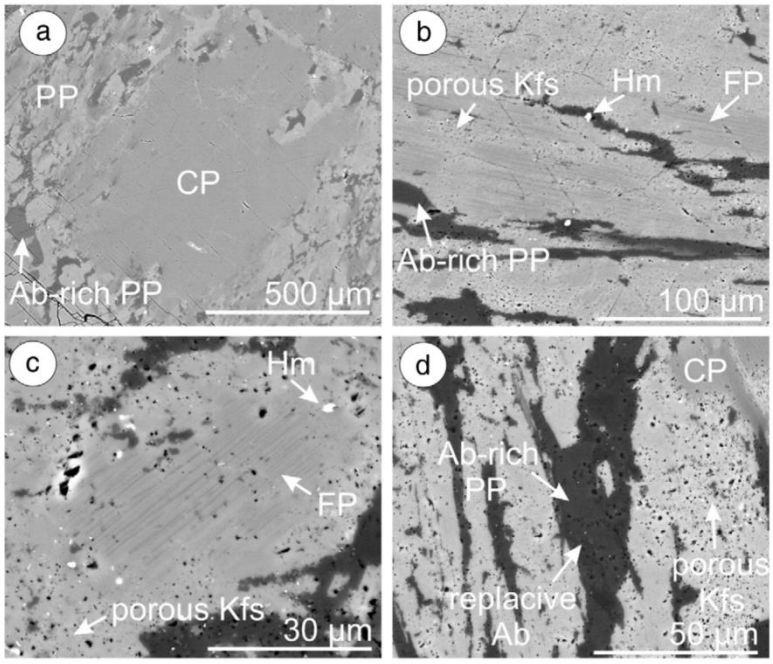

Fig. 6. Back scatter electron images detailing important features of alkali feldspar microtextures in least-altered RDG. (a) Large fields of cryptoperthite (CP) cross-cut by patch perthite (PP). Note the anastomosing nature of the patch perthite. (b) Area of alkali feldspar phenocryst displaying exsolution lamellae of film perthite (FP) crosscut by highly porous albite and K-feldspar. Note the presence of hematite (Hm). (c) High-magnification image of film perthite surrounded by porous K-feldspar. (d) Albite-rich subgrain of patch perthite overprinted by replacive albite (Ab).

spectra with a spot size of ~5 nm (Fig. 7e, f). Although the sample is sensitive to beam damage, the data clearly shows the lack of Na in the host potassium feldspar.

4.2.2. Plagioclase in least-altered RDG

Two distinct compositions of igneous plagioclase are identified in the RDG: andesine-oligoclase (~An_{27-34}); and oligoclase (~An_{12-20}). Similar to the alkali feldspars, plagioclase commonly exhibits complex overprints.

In Area 1, andesine-oligoclase (~An_{27-34}) forms the cores of plagioclase grains surrounded by oligoclase (An_{12-20}) mantles (Fig. 8a). These andesine-oligoclase cores have been extensively altered and are only partially preserved in Area 1. In both areas, oligoclase with a lower An component (~An_{12-20}) occurs as rapakivi mantles and as individual grains without andesine cores. Irrespective of textural type, this oligoclase is characterised by high K_2O content (~0.73 wt.%, Table 5) and often contains worm-like quartz, fluorite (<20 µm-sized) and irregular alkali feldspar (cryptoperthite and patch perthite) inclusions (Fig. 8b).

Alteration of plagioclase is predominantly in the form of albitisation, where the replacive albite is typically concentrated within grain cores (*e.g.*, Figs. 5b and 8a). This replacement can be seen to extend from core to margin along polysynthetic twins (*e.g.*, Fig. 5b), and eventually form completely albitised pseudomorphs. In detail, replacive albite is extremely porous and forms fine-grained intergrowths with sericite ± hematite (Fig. 8c). Due to the presence of sub-µm-scale sericite, K_2O (from *in-situ* EPMA spot analysis) may be overestimated. Inclusions of dolomite and calcite may also occur within this albite. In addition to pervasive albitisation, a thin layer of homogenous albite commonly forms rims around oligoclase, which is in direct contact with recrystallised alkali feldspar. This rim is devoid of micropores and is superposed by replacive albite (Fig. 8d).

Importantly, Ba-bearing K-feldspar is observed within RDG from both areas, even in samples preserving the mafic minerals. Such K-feldspar occurs along twin planes and compositional zones of albitised plagioclase (Fig. 9a, b) to which it is restricted. This K-feldspar varies widely with respect to Ba content, ranging from <1 wt.% BaO up to as much as ~15 wt.% BaO. In detail, this K-feldspar is very fine-grained (<10 µm) and highly porous (Fig. 9c, d).

4.2.3. Feldspars in sericite-hematite altered and mineralised RDG

As documented above, sericite-hematite altered RDG occurs irregularly throughout all drillholes along the transect (Fig. 1), however the intensity of alteration increases with proximity to the ODBC. The only feldspars preserved in sericite-hematite altered and/or mineralised granite are replacive albite and porous K-feldspar, described above. There are, however, significant differences in the abundance of feldspars between sericite-hematite altered and mineralised RDG. This can be observed in the ~300 m-thick profile from drillhole RD2316 (Fig. 3). The deeper part retains significant replacive albite and porous K-feldspar. Importantly, this K-feldspar displays heterogeneous zones of intense red-staining (Fig. 10a), averaging ~1.5 wt.% FeO (Table 4). In detail, dusty sub-µm sized Fe-oxide inclusions (hematite) are observed, likely contributing to the characteristic red-staining (Fig. 10b). The abundance of these red-stained zones increases upwards, over ~100 m, as replacive albite is progressively destroyed by sericite and Cu-Au mineralisation starts to predominate.

The stability of sericite over albite at this stage is not only evident from whole-rock analyses (Table 1a, 1b, 1c), but also from textural observations of mm-sized grains of sericite resembling plagioclase pseudomorphs (Fig. 10c). Importantly, some of these pseudomorphs are partially replaced by hematite ± chlorite. In addition, some rapakivi textures survive; however they are now defined by porous, red-stained, K-feldspar cores rimmed by fine-grained sericite (Fig. 10d). Granophyric textures between quartz and K-feldspar (partially replaced by

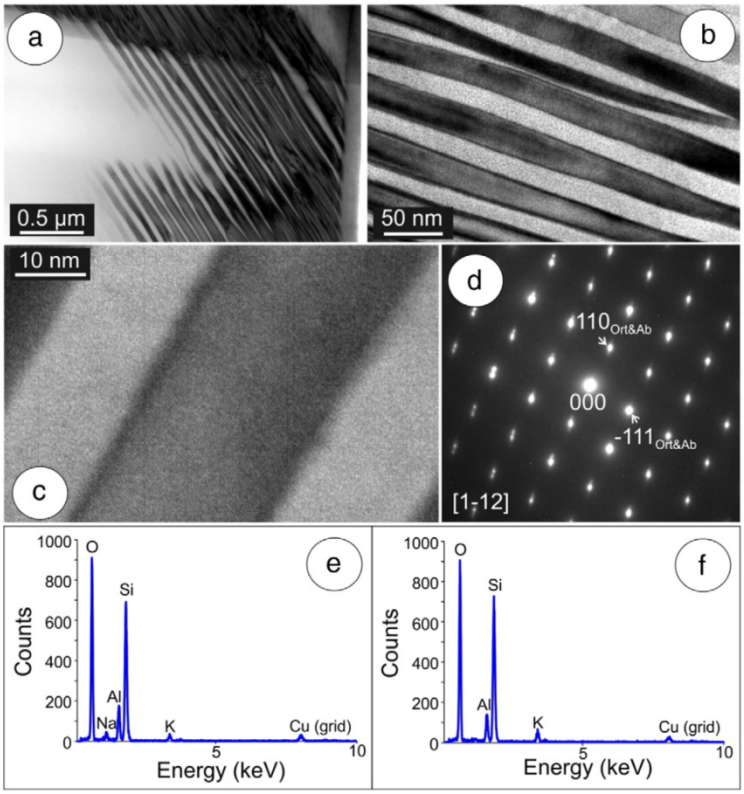

Fig. 7. Transmission electron microscope images of cryptoperthite from least-altered RDG. (a, b) Low-resolution images of albite lamellae (dark) within orthoclase host (light). Note the varying thickness of lamellae. (c) High-resolution image displaying coherent lattice fringes between both albite and orthoclase along a zone axis of cryptoperthite. (d) Selected Area of Electron Diffraction (SAED) along zone axis from (c). (e, f) TEM-EDX spectra obtained from Ab lamellae and Or host in cryptoperthite, respectively. A spot size of 5 nm was used.

sericite) are also occasionally observed along the margin of the ODBC (*e.g.*, drillhole RD2511). Such textures are characteristic of sericite-hematite altered RDG from drillhole RD2316 and from drillholes along the transect in Area 2 (RD2274, RD2280, RD2511, RD2531 and RD3554).

Mineralised RDG within drillholes RD2316 and RD3554 contains variable amounts of chalcopyrite, bornite, chalcocite, sphalerite, galena, native gold and molybdenite, but is devoid of replacive albite, whereas red-stained K-feldspar becomes more abundant. A spatial association between the porous, red-stained K-feldspar and sulphides (*e.g.*, sphalerite, chalcopyrite and galena) is notable throughout all RDG sample suites. Remarkably, some feldspar grains are pervasively replaced by intimate intergrowths of sericite + synchysite + bastnäsite + parisite (not previously recognised at Olympic Dam) + molybdenite (Fig. 11). Discrete uranium minerals (uraninite, coffinite and brannerite) are also present within reaction zones at the margins of sulphide disseminations. In addition, W- and Nb-zoned rutile is also abundant.

5. Geothermobarometric estimates for least-altered RDG

Compositional variation among amphiboles, amphibole-plagioclase pairs, magnetite-ilmenite pairs and feldspars can be used to place constraints on the T-P-fO_2 conditions of crystallisation from the magmatic to early hydrothermal stage. This was achieved by analysing distinct zones and mineral associations within feldspar phenocrysts from the RDG, principally from Area 1. Such phenocrysts (*e.g.*, Fig. 12) were found to contain feldspars representative of all stages of evolution from magmatic to hydrothermal (see Discussion), and also to host abundant magmatic amphibole (edenite), biotite and Fe-(Ti)-oxides. In addition, the phenocrysts contain discrete areas of alteration also containing sulphides (galena, sphalerite, and pyrite as inclusions in apatite), and coarse REE-minerals such as synchysite.

5.1. Amphibole chemistry, geobarometry and geothermometry

A common method to estimate pressures for granitic rocks is Al-in-hornblende geobarometry (Hammarstrom and Zen, 1986; Hollister et al., 1987; Schmidt, 1992). The geobarometer has been experimentally calibrated, and is suitable for an assemblage of quartz + alkali feldspar + + plagioclase + hornblende + biotite + Fe-Ti-oxide + titanite + melt + fluid. It is assumed that following solidification and cooling, the equilibration of hornblende with the above assemblage would eventually cease, and thus the Al content would reflect the final crystallisation depth of the magma. The Al content in hornblende is also affected by temperature, addressed by Blundy and Holland (1990) who propose an amphibole-plagioclase thermometer. It is recommended to apply this to rocks equilibrated between 500 and 1000 °C, plagioclase with $<An_{92}$ and amphiboles containing <7.8 a.p.f.u. However, the geothermometer requires pressure information, thus using the Al-in-hornblende method of Schmidt (1992) and correcting for the effects of temperature and fO_2 (Anderson and Smith, 1995) was necessary.

Compositional data for amphibole from three locations contained within a phenocryst from sample RX7865 are compared with amphibole in the groundmass from sample RX7860 (Table 6). The amphibole shows bright and dark areas on BSE images, corresponding to differences in Fe/(Fe + Mg). The brighter areas are compositionally similar to amphibole in the rock groundmass, and on the rapakivi margin of the phenocryst. This suggests that the darker areas represent retrogression followed by chlorite alteration (also observed to replace coexisting

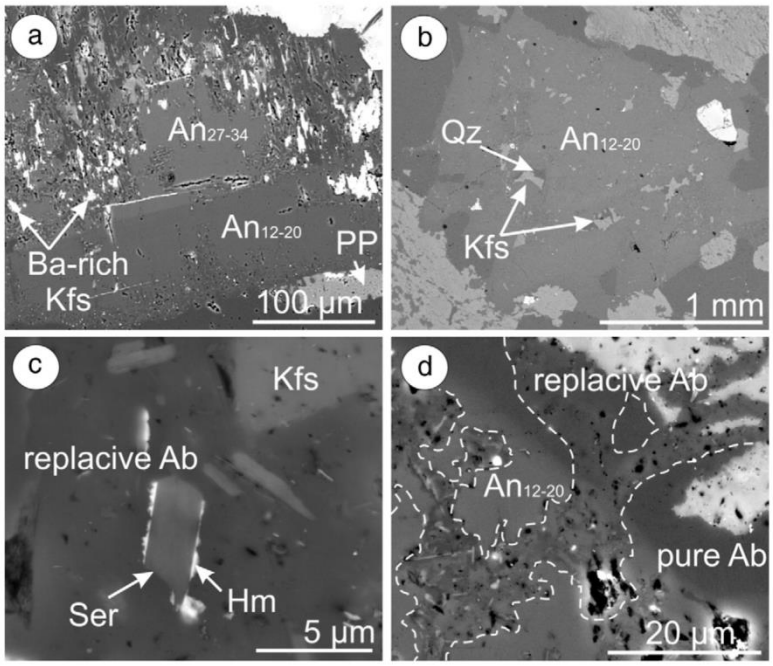

Fig. 8. Back scatter electron images outlining features of plagioclase and associated alteration textures. (a) Typical andesine-oligoclase core sharing a discontinuous boundary with low-An oligoclase. Note the Ba-rich K-feldspar and patch perthite (PP). (b) Large low-An oligoclase grain with random, irregularly-shaped perthitic K-feldspar and quartz (Qz) inclusions. (c) High-magnification image of the replacive albite ± sericite intergrowth texture. Note the rim of hematite (Hm) around sericite (Ser). (d) BSE image showing the homogeneous albite rim on low-An oligoclase superposed by the replacive albite ± sericite texture.

biotite). The compositions of biotite co-existing with amphibole in the same samples (Table 6) are broadly comparable with one another. However, biotite replacing amphibole in sample RX7860 is slightly Mg-richer, consistent with the loss of Fe during overprinting described for amphibole above.

Table 5
Mean electron probe microanalyses of plagioclase feldspar in the RDG.

	Andesine-oligoclase cores	Rapakivi oligoclase	Replacive albite
	($n = 25$)	($n = 47$)	($n = 63$)
wt.%			
SiO_2	59.71 (0.48)	63.59 (0.51)	68.56 (1.11)
Al_2O_3	24.48 (0.28)	22.10 (0.27)	19.84 (0.23)
FeO	0.41 (0.11)	0.25 (0.04)	0.11 (1.37)
CaO	6.61 (0.41)	3.86 (0.34)	0.19 (0.15)
SrO	0.22 (0.01)	0.24 (0.02)	<mdl
BaO	0.05 (0.03)	0.04 (0.03)	<mdl
Na_2O	7.89 (0.21)	9.42 (0.43)	11.88 (0.76)
K_2O	0.44 (0.21)	0.73 (0.36)	0.43 (0.29)
TOTAL	99.92 (0.21)	100.30 (0.23)	101.26 (1.58)
a.p.f.u.			
Ca	0.32	0.18	0.01
Sr	0.01	0.00	0.00
Ba	0.00	0.00	0.00
Na	0.69	0.81	1.00
K	0.03	0.04	0.02
TOTAL	1.04	1.04	1.03
Al	1.30	1.16	1.02
Si	2.68	2.82	2.98
Fe	0.02	0.01	0.00
mol.%			
Ab %	66.21 (1.58)	77.71 (3.21)	96.80 (0.90)
An %	30.60 (1.91)	17.60 (1.59)	0.86 (0.33)
Or %	2.52 (1.20)	4.04 (1.99)	2.31(0.78)

Note: figures in parentheses represent standard deviations.

Application of the Al-in-hornblende geobarometer based on total Al content (Schmidt, 1992) gives pressure estimates between 2.08 and 2.85 kbar. However, these estimates are not corrected for temperature. Applying the modified geobarometer of Anderson and Smith (1995), using temperatures derived from the amphibole-plagioclase geothermometer of Blundy and Holland (1990; Table 7), a fit is obtained at pressures of ~2.2 kbar (corresponding to a final crystallisation depth of 6–8 km) and minimum crystallisation temperatures of 710 and 731 °C for the assemblages within the rapakivi mantle and groundmass, respectively. Overprinted assemblages in the phenocryst core and rapakivi mantle give temperature ranges of 703 to 657 °C, and 710 to 700 °C, respectively, at the same pressure; the lower estimate in each case being for the darker amphibole. Overprinting during uplift is unlikely since, on the basis of the measured compositions, this would infer an unrealistic temperature increase. Instead, a fit between temperature decrease at constant pressure (~2.2 kbar) is reasonable. Creaser (1996) also applied Al-in-hornblende geobarometry to a quartz-monzodiorite from the same pluton as the RDG (following Schmidt, 1992) using the average composition of hornblende. A pressure estimate of 200 MPa (2 kbar) was obtained, corresponding to a final crystallisation at a depth of approximately 6–8 km.

5.2. Fe-Ti-mineral chemistry, geothermometry and fO_2 estimates

The association of Fe-(Ti)-minerals is variable throughout the least-altered RDG samples, from magnetite to magnetite-ilmenite-titanite. All these associations can be present in samples where amphibole is preserved (*e.g.*, sample RX7860). In samples where no mafic silicates survive, ilmenite commonly breaks down to rutile + hematite, while magnetite is replaced by hematite. Magnetite displays skeletal exsolution of other spinels that vary from extremely dense to scattered (whether coexisting with ilmenite or not). Moreover, trellis exsolution of ilmenite in magnetite is observed, particularly in areas where

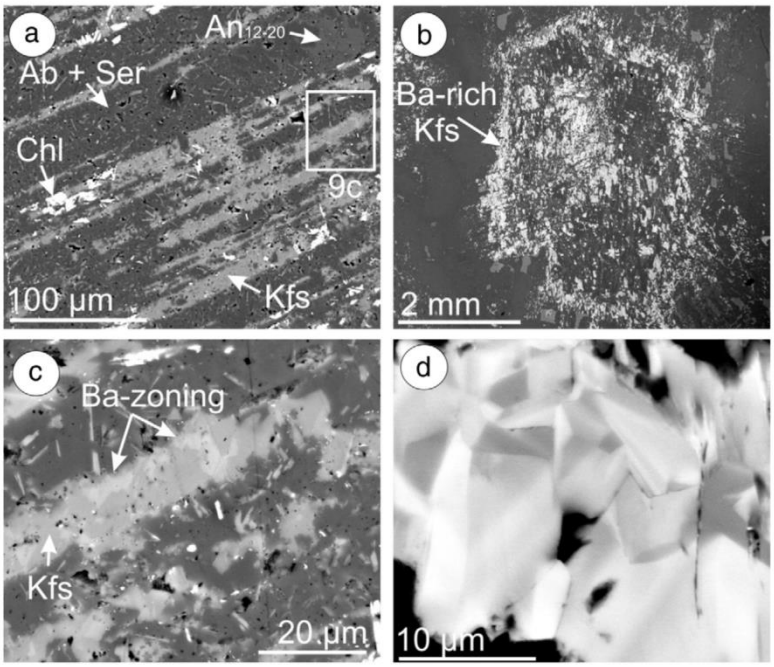

Fig. 9. Back scatter electron images of K-feldspar textures associated with altered plagioclase. (a) K-feldspar forming along twins of albitized low-An oligoclase. Note the presence of chlorite. (b) Large pseudomorph of albitized oligoclase rimmed and dominated by Ba-rich K-feldspar. (c) High-magnification image of (a), revealing Ba-zoning and porosity of the K-feldspar. (d) High-magnification image of complex Ba-zonation in fine-grained, Ba-rich K-feldspar found within a large albitised andesine core. BaO concentration varies from 5 to 14 wt.% in dark and bright areas, respectively. Abbreviations: Ab — albite, Chl — chlorite, Kfs — K-feldspar, Olg — oligoclase, Ser — sericite.

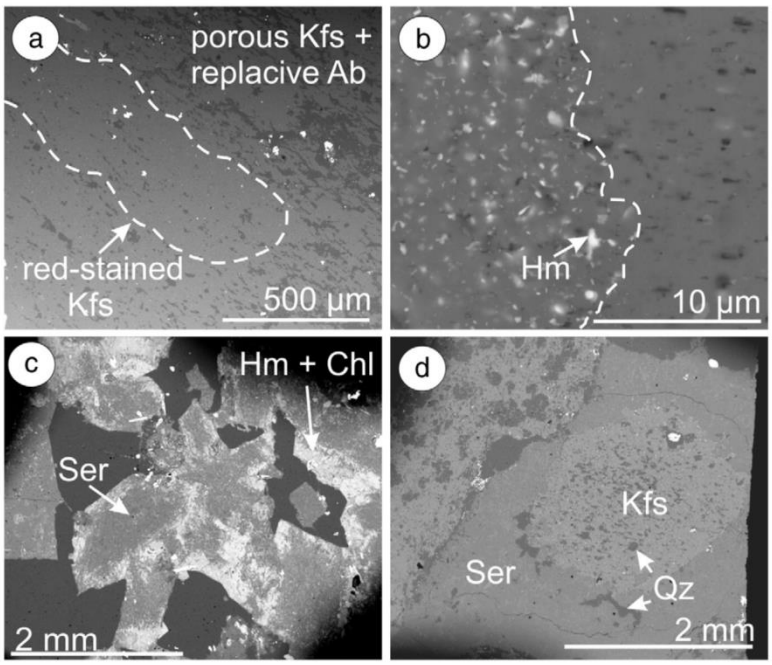

Fig. 10. Back scatter electron images highlighting important features of feldspars in sericite-hematite altered and mineralised RDG. (a) Typical perthitic K-feldspar (Kfs) observed in sericite-hematite altered RDG at depth or to the peripheries of the ODBC. Note the destruction of perthitic texture by red-stained K-feldspar. (b) High-magnification image illustrating the presence of sub-µm-sized hematite (Hm) corresponding to the red-stained areas of K-feldspar. (c) Large sericite pseudomorph grains being replaced by fine-grained hematite ± chlorite. (d) Altered rapakivi texture. Plagioclase mantle has been completely replaced by sericite, whereas the core, although similar in appearance to patch perthite, is comprised of porous K-feldspar with quartz.

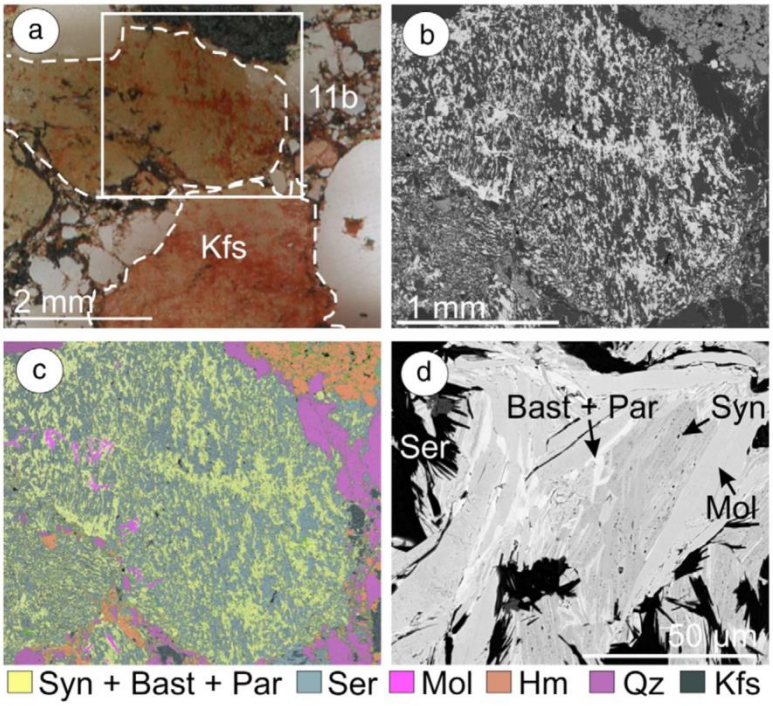

Fig. 11. Back scatter electron and scanned images of REE-mineral + molybdenite association overprinting K-feldspar in mineralised RDG within drillhole RD2316. (a) Scanned area of polished thin section from drillhole RD2316, highlighting the preserved shape of perthitic K-feldspar grains. (b) Low-magnification BSE image of area in (a). (c) False colour BSE map of the image in (b), showing the various minerals within the texture. (d) BSE image, and highlighting rhythmic interlayering of fine-grained molybdenite + synchysite + bastnäsite + sericite overprint. Abbreviations: Bast — bastnäsite, Hm — hematite, Kfs — K-feldspar, Mol — molybdenite, Qz — quartz, Ser — sericite, Syn — synchysite.

sulphides occur, such as on the rapakivi mantle of the phenocryst in Fig. 12. The TiO_2 content of magnetite (Table 8) varies from 0.34 (associated with hematite) to 3.17 wt.% (dense exsolution of spinels). Ilmenite contains ~10 wt.% MnO along with measurable Nb_2O_5 (thousands of ppm). The Nb content increases when associated with titanite. Both magnetite and ilmenite contain measurable V_2O_5, and magnetite with trellis exsolution or from the groundmass also contains ZnO.

Table 8 also shows estimates of re-equilibration temperatures from pairs of coexisting magnetite-ilmenite in the phenocryst and in sample RX7860, following routines developed by Lepage (2003). Temperature-fO_2 estimates based on the calibrations of Andersen and Lindsley (1985), that acknowledge the effect of minor elements such as Mn, Mg and Cr, are in the range 567–624 °C and −20.6 to −18.5 logfO_2. The higher temperature range (611 to 624 °C), consistent with amphibole-plagioclase geothermometry (654 °C from areas where amphibole has been overprinted), is from magnetite-ilmenite pairs in sample RX7860 in which the magnetite contains dense exsolutions. Such a temperature is close to that obtained from magnetite-ilmenite pairs in the andesine-oligoclase core of the phenocryst (609 °C). The lowest temperature estimates are from magnetite-ilmenite pairs in the same core (567 °C) and from the rapakivi mantle (577 °C), in both cases associated with amphibole. The fO_2 estimate is consistent with the stability field of magnetite at temperatures of 550–650 °C. The discrepancy between the lowest temperatures from magnetite-ilmenite pairs (567–577 °C, taken to reflect solid-state Fe-Ti re-equilibration) and magmatic temperatures derived from amphibole-plagioclase geothermometry can be explained by the much faster compositional re-equilibration in Fe-Ti-oxide system (*e.g.*, presence of trellis exsolution of ilmenite) down-temperature after crystallisation of the amphibole-plagioclase assemblage.

5.3. Feldspar geothermometry

Temperature estimates were obtained using SOLVCALC software following the ternary feldspar model of Fuhrman and Lindsley (1988) based on phase equilibria for disordered feldspars. Minimum temperature estimates for crystal growth can be obtained from ternary solvus isotherms. Using the average An composition of cryptoperthite (0.174 mol.%; Table 4), along with a reasonable pressure of 2.2 kbar (see above), a minimum temperature estimate for crystal growth of 765 °C was obtained. Following crystallisation, subsequent exsolution, ordering and coarsening likely occurred *via* similar mechanisms outlined by Brown and Parsons (1984) whereby processes such as spinodal decomposition and diffusion occurred around 700 °C to form cryptoperthite.

Exsolution likely continued down temperature until fluid-feldspar interaction resulted in formation of patch perthite. Application of the Fuhrman and Lindsley (1988) feldspar geothermometer using the average compositions of Ab- and Or-rich phases within patch perthite from Table 4 yields a temperature of 430 °C for formation at 2.2 kbar. A secondary stage of coherent exsolution took place following patch perthite formation, leading to development of film perthite within the Or-rich phase of the patch perthite, at some temperature range below 430 °C.

6. Discussion

Plagioclase and alkali feldspar textures and chemistry both define a transition from magmatic to hydrothermal processes within the RDG. The following sections and Fig. 13 summarise and discuss each stage within this evolutionary sequence.

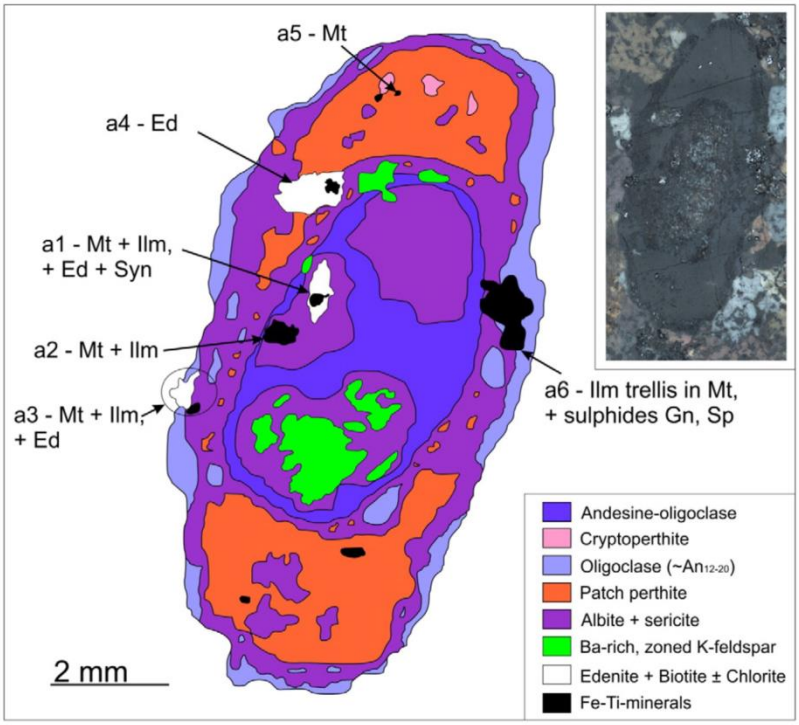

Fig. 12. Inset: reflected light image of a large feldspar phenocryst from least-altered RDG in Area 1. Schematic of the large feldspar phenocryst showing all stages within feldspar evolution. Highlighted areas indicate mafic and Fe-Ti-mineral locations used for geobarometry and geothermometry. Abbreviations: Ed — edenite, Gn — galena, Ilm — ilmenite, Mt — magnetite, Sp — sphalerite, Syn — synchysite.

6.1. Plagioclase crystallisation and significance of rapakivi texture

The timing of plagioclase crystallisation relative to other feldspars is critical to understand the magmatic evolution of the RDG. Compositions and textural observations indicate the presence of at least two generations of igneous plagioclase in the RDG. The first generation is defined by the andesine-oligoclase cores (~$An_{27–34}$), which show calcic-sodic core to rim compositional zoning. The low-An oligoclase is interpreted as a second generation based on the fact that it forms rapakivi mantles and discontinuous rims around andesine-oligoclase cores. Commonalities in textural features between all low-An oligoclase (*e.g.*, inclusions of alkali feldspar, fluorite and quartz), suggest that they are contemporaneous. Moreover, this low-An plagioclase shows evidence of replacing pre-existing alkali feldspar. Such an interpretation is based on the continuity of lamellae within the perthitic alkali feldspar inclusions.

Previous authors (*e.g.*, Plümper and Putnis, 2009) have attributed the replacement of microcline by oligoclase in granites to a late-stage alkali ion exchange process (Orville, 1963), in which Na^+ and K^+ preferentially partition to feldspars and a post-magmatic fluid, respectively. This interpretation was based on the marked microporosity in the oligoclase relative to microcline, which is consistent with fluid-feldspar interaction. However, in the RDG, low-An oligoclase is relatively porosity-free, and is also implied to have crystallised prior to fluid-rock interaction. This requires a physical and/or chemical change in melt conditions which would alter the stability of feldspars to the point where plagioclase would nucleate on K-feldspar, and vice versa. Decreases in pressure and/or temperature, or an increase in Ca and mafic components in the melt, are the preferred catalysts (*e.g.*, Müller et al., 2008). Feldspar resorption textures in the RDG, interpreted to have occurred prior to deuteric coarsening, are supportive of late-stage magma mixing/contamination and/or ascent (*e.g.*, Emslie, 1991; Wark and Stimac, 1992; Dempster et al., 1994; Rämö and Haapala, 1995). Such processes would increase the degree of crustal melting and can also initiate magma convection, explaining the partial (rapakivi mantles) and complete resorption of some alkali feldspars observed in the RDG. The coexistence of mantled and non-mantled alkali feldspars along with the heterogeneity in rapakivi mantle morphology (*e.g.*, tabular, ovoid) may be explained by the relative timing of crystallisation among other factors. Alkali feldspars which have ovoid morphologies or have undergone complete resorption would likely have crystallised early in the magma chamber (*e.g.*, Ryan, 1991) or could be evidence for incomplete mingling between magmas (Hibbard, 1981). Crystal migration has been proposed as an alternative explanation for the presence of mantled feldspars in the past (*e.g.*, Słaby and Goetze, 2004; Słaby et al., 2011). In this case, feldspar phenocryst chemistry would reflect the different magma conditions under which each feldspar mantle formed, making it difficult to relate this to the surrounding groundmass. Regardless, feldspar textures and geochemistry, in conjunction with the presence of microgranular mafic enclaves, two generations of igneous magnetite (Ti-rich and Ti-poor) and magmatic apatite textures (see Krneta et al., 2016), point towards late-stage magma mixing/contamination in the RDG. In addition, this is supported by geobarometric estimates along with amphibole-plagioclase geothermometry (Tables 6 and 7) which indicate that formation of the rapakivi mantle occurred at the same depth *via* a change in temperature rather than through magma ascent.

The presence of fluorite inclusions within low-An oligoclase has significant implications. Firstly, this suggests that the melt was at least supersaturated with respect to F at the time of rapakivi formation. Fluorine has been demonstrated to greatly increase the alkali ion interdiffusion rates in alkali feldspars (Snow and Kidman, 1991), and has also been reported from other rapakivi granites (Troeng, 1982; Wilson and

Table 6
EPMA compositional data for amphibole and biotite in least-altered RDG and Al-in-hornblende geobarometry.

	Amphibole: edenite							Biotite		
	RX7865					RX7860		RX7865	RX7860 (groundmass)	
	Phenocryst							Phenocryst	Magmatic	Hydrothermal
	a3	a1 'bright'	a1 'dark'	a4 'bright'	a4 'dark'	a4		a4	a5	a4
	n = 4	n = 4	n = 4	n = 4	n = 4	n = 12		n = 4	n = 19	n = 15
SiO_2	42.94	44.06	45.29	43.29	44.04	42.87	SiO_2	36.73	36.70	37.06
TiO_2	1.13	1.18	0.77	1.42	1.37	0.94	TiO_2	2.14	2.56	1.77
Al_2O_3	6.48	6.17	5.92	6.68	6.40	6.60	Al_2O_3	11.32	11.35	10.84
FeO	20.64	19.44	15.29	18.87	17.50	21.19	FeO	20.84	20.34	20.03
MnO	0.45	0.48	0.46	0.43	0.43	0.49	MnO	0.16	0.26	0.16
MgO	9.29	10.18	13.30	10.48	11.50	9.30	MgO	12.74	12.81	13.43
CaO	10.88	11.13	11.51	10.90	11.12	10.97	CaO	0.02	0.01	0.03
Na_2O	2.19	2.04	2.06	2.37	2.23	2.19	Na_2O	0.18	0.26	0.17
K_2O	1.10	1.04	1.01	1.12	1.08	1.18	K_2O	9.42	9.65	9.50
P_2O_5	0.01	0.01	0.01	0.01	0.01	0.01	P_2O_5	0.01	0.01	0.02
Cl	0.20	0.17	0.14	0.23	0.18	0.23	Cl	0.29	0.27	0.29
F	1.40	1.42	1.93	1.57	1.78	1.53	F	2.50	2.89	2.66
Total	96.72	97.32	97.69	97.37	97.64	97.51	Total	93.84	94.23	93.31
Amphibole: formulae based on: $Ca_2(Mg,Fe^{2+},Fe^{3+},Mn,Al^{vi})_5(Si,Al^{iv})_8O_{22}(OH,F,Cl)_2$							Biotite: formulae based on $K(Mg,Fe,Mn)_3AlSi_3O_{10}(OH,F,Cl)_2$			
Si	6.811	6.884	6.937	6.775	6.828	6.779	Si	2.93	2.92	2.97
Al (iv)	1.189	1.116	1.063	1.225	1.172	1.221	Al	1.07	1.06	1.02
Total (T)	8.000	8.000	8.000	8.000	8.000	8.000	Total (T)	4.00	3.98	3.99
Al (vi)	0.023	0.020	0.006	0.007	0.000	0.010	Ti	0.13	0.16	0.11
Ti	0.135	0.139	0.089	0.167	0.160	0.112	Mn	0.01	0.02	0.01
Fe (iii)	0.274	0.254	0.196	0.247	0.227	0.281	Mg	1.52	1.52	1.60
Fe (ii)	2.737	2.539	1.958	2.469	2.268	2.802	Fe	1.39	1.35	1.34
Mn	0.060	0.063	0.059	0.057	0.056	0.066	Total (M)	4.13	4.13	4.09
Mg	2.197	2.371	3.034	2.443	2.658	2.190	Na	0.03	0.04	0.03
Total (C)	5.426	5.387	5.342	5.391	5.369	5.460	K	0.96	0.98	0.97
Ca	1.849	1.864	1.889	1.828	1.847	1.858	Ca	0.00	0.00	0.00
Na	0.674	0.619	0.612	0.718	0.671	0.673	Total (I)	0.99	1.02	1.00
K	0.222	0.207	0.198	0.223	0.213	0.239	F	0.63	0.73	0.67
Total (A + B)	2.745	2.689	2.699	2.769	2.730	2.770	Cl	0.04	0.04	0.04
F	0.704	0.703	0.936	0.778	0.871	0.764	OH	1.33	1.24	1.29
Cl	0.055	0.045	0.035	0.061	0.048	0.061	Total (A)	2.000	2.000	2.000
OH*	1.241	1.252	1.028	1.161	1.080	1.175	Mg/(Fe + Mg + Mn)	0.520	0.526	0.542
Total (W)	2.000	2.000	2.000	2.000	2.000	2.000				
Fe/(Fe + Mg + Mn)	0.56	0.52	0.40	0.51	0.47	0.57				
Al-in-hornblende geobarometry (kbar)										
	1.67	1.35	1.06	1.75	1.49	1.74	Johnson and Rutherford (1989)			
	2.18	1.79	1.46	2.28	1.97	2.27	Hammarstrom and Zen (1986)			
	2.76	2.40	2.08	2.85	2.56	2.84	Schmidt (1992)			
	1.84	1.52	1.23	1.93	1.66	1.92	Anderson and Smith (1995) @ 750 °C			
	2.11	1.77	1.46	2.20	1.92	2.19	Mean of all estimates			

Note: compositions for amphibole are based on 24 oxygens. Compositions for biotite are based on 11 oxygens.

Åkerblom, 1982). Moreover, experimental work (Manning, 1981) indicates that interaction between F- and H_2O-saturated granitic melts can reduce the minimum temperature of the melt, and also shift the eutectic point in the Qz-Ab-Or ternary system. Given that F would likely concentrate towards the later stages of crystallisation, plagioclase crystallising at this point is expected to be more sodic. High F concentrations would shift the Qz-Ab-Or eutectic point towards the Ab-apex and thus the melt composition would enter the quartz field. Following crystallisation of quartz at this stage, the melt composition would subsequently enter the quartz-alkali feldspar cotectic and both quartz and alkali feldspar would crystallise. Finally, as the melt composition reaches the new eutectic point, sodic plagioclase would crystallise together with quartz and alkali feldspar. This behaviour explains the presence of both rapakivi (plagioclase mantling alkali feldspar) and anti-rapakivi (alkali feldspar mantling plagioclase-calcic in this case) textures observed throughout the RDG.

6.2. Alkali feldspars and deuteric coarsening

Textural observations of cryptoperthite are consistent with interpretations and models proposed by previous authors (*e.g.*, Parsons et al., 2015; references therein), involving continuous interdiffusion of Na and K in the aluminosilicate tetrahedral framework during cooling from the solvus. Conversely, the incoherency and microporosity of

Table 7
Results of amphibole-plagioclase geothermometry.

Ed-Plag	Phenocryst (RX7865)					RX7860
	Core-overprinted		Rapakivi mantle overprinted			Edenite-Ads-Olig
Amphibole (from Table 6)	a1 bright	a1 dark	a4 bright	a4 dark	a3	a4
Plag X_{Ab}	0.66	0.97	0.85	0.85	0.75	0.66
Pressure estimate (kbar)	2.2	2.2	2.2	2.2	2.2	2.2
T (°C)	731	657	710	700	703	754

Calibration of Blundy and Holland (1990). Uncertainties of ±75 °C.

Table 8
EPMA compositional data for selected magnetite-ilmenite pairs and geothermometric estimates.

	Phenocryst (RX7865)								RX7860								
	a1		a2		a3		a5	a6	Dense inclusions (a3)				Scarce inclusions (a1)			Hm-associated	
	Mt	Ilm	Mt	Ilm	Mt	Ilm	Mt		Mt	Ilm	Mt	Ilm	Mt			Mt	
SiO_2	0.01	0.10	0.01	1.17	0.01	0.32	0.02	0.06	<mdl	0.04	0.03	0.04	0.06	<mdl	0.02	0.03	<mdl
TiO_2	1.13	48.97	1.42	48.16	1.13	48.92	0.89	1.27	3.17	49.54	2.45	49.54	1.27	1.37	0.56	0.69	0.34
Al_2O_3	0.33	0.05	0.52	0.28	0.45	0.13	0.27	0.44	0.36	<mdl	0.33	<mdl	0.44	0.24	0.14	0.17	0.07
Fe_2O_3	63.79	3.63	63.0	4.83	64.23	3.99	65.50	63.49	60.81	4.50	62.23	4.50	63.49	64.97	66.41	65.81	66.62
FeO	30.92	34.08	31.2	33.9	31.11	33.49	29.47	31.13	33.17	33.97	32.39	33.97	31.13	31.66	30.98	31.05	30.66
MnO	0.17	9.70	0.13	9.30	0.14	10.07	0.11	0.15	0.20	9.83	0.31	9.83	0.15	0.25	0.07	0.05	<mdl
MgO	<mdl	0.12	0.03	0.19	0.02	0.25	0.02	0.04	0.02	0.02	0.02	0.02	0.04	0.01	0.02	0.02	<mdl
CaO	0.01	0.03	<mdl	0.81	0.07	0.20	<mdl	<mdl	0.01	0.50	0.01	0.50	<mdl	0.02	0.02	<mdl	0.02
Cr_2O_3	0.02	0.03	0.02	<mdl	0.02	<mdl	<mdl	<mdl	0.02	0.02	0.02	0.02	<mdl	0.02	<mdl	0.02	<mdl
ZnO	<mdl	<mdl	<mdl	<mdl	<mdl	<mdl	<mdl	0.06	<mdl	<mdl	0.04	<mdl	0.06	<mdl	<mdl	<mdl	<mdl
V_2O_5	0.21	0.25	0.22	0.27	0.18	0.27	0.18	0.17	0.18	0.27	0.18	0.27	0.17	0.18	0.18	0.13	0.11
Nb_2O_5	<mdl	<mdl	<mdl	0.11	<mdl	<mdl	<mdl	<mdl	<mdl	<mdl	<mdl	<mdl	<mdl	<mdl	<mdl	<mdl	<mdl
Total	96.60	96.95	96.58	99.04	97.36	97.64	96.45	96.82	97.95	98.69	98.01	98.69	96.82	98.73	98.39	97.97	97.84
Cation proportions (Carmichael, 1967)																	
Si	0.000	0.003	0.001	0.030	0.001	0.008	0.001	0.003	0.000	0.001	0.001	0.001	0.003	0.000	0.001	0.001	0.000
Ti	0.034	0.958	0.042	0.917	0.033	0.948	0.027	0.038	0.093	0.953	0.072	0.953	0.038	0.040	0.017	0.020	0.010
Al	0.015	0.002	0.024	0.008	0.021	0.004	0.013	0.021	0.017	0.000	0.015	0.000	0.021	0.011	0.006	0.008	0.003
Fe^{3+}	1.909	0.071	1.882	0.092	1.905	0.077	1.927	1.893	1.790	0.087	1.832	0.087	1.893	1.902	1.954	1.944	1.973
Fe^{2+}	1.028	0.742	1.037	0.718	1.025	0.722	1.023	1.032	1.085	0.726	1.060	0.726	1.032	1.030	1.013	1.019	1.009
Mn	0.006	0.214	0.004	0.199	0.005	0.220	0.004	0.005	0.007	0.213	0.010	0.213	0.005	0.008	0.002	0.002	0.000
Mg	0.000	0.005	0.002	0.007	0.001	0.009	0.001	0.002	0.001	0.001	0.001	0.001	0.002	0.001	0.001	0.001	0.000
Ca	0.001	0.001	0.000	0.022	0.003	0.006	0.000	0.000	0.000	0.014	0.000	0.014	0.000	0.001	0.001	0.000	0.001
Cr	0.001	0.001	0.001	0.000	0.001	0.000	0.000	0.000	0.001	0.000	0.001	0.000	0.000	0.001	0.000	0.001	0.000
Zn	0.000	0.000	0.000	0.000	0.000	0.000	0.000	0.002	0.000	0.000	0.001	0.000	0.002	0.000	0.000	0.000	0.000
V	0.007	0.005	0.007	0.006	0.006	0.006	0.006	0.006	0.006	0.005	0.006	0.005	0.006	0.006	0.005	0.004	0.004
Nb	0.000	0.000	0.000	0.001	0.000	0.000	0.000	0.000	0.000	0.000	0.000	0.000	0.000	0.000	0.000	0.000	0.000
Total	3.000	2.000	3.000	2.000	3.000	2.000	3.000	3.000	3.000	2.000	3.000	2.000	3.000	3.000	3.000	3.000	3.000
Calc. methods:	mol.% Usp		mol.% Ilm		mol.% Usp		mol.% Ilm		mol.% Usp		mol.% Ilm		mol.% Usp		mol.% Ilm		mol.% Ilm
Carmichael (1967)	3.4%		96.1%		4.3%		94.6%		3.4%		95.7%		9.3%		95.4%		7.2%		95.4%
Anderson (1968)	3.1%		95.3%		4.1%		93.4%		3.1%		94.7%		9.1%		95.2%		6.6%		95.2%
Lindsley and Spencer (1982)	3.4%		95.3%		4.3%		93.5%		3.4%		94.8%		9.4%		95.2%		7.2%		95.2%
Stormer (1983)	3.4%		96.0%		4.4%		94.6%		3.4%		95.5%		9.5%		95.0%		7.2%		95.0%
Geothermobarometer by Andersen and Lindsley (1985)																	
X'Usp & X'Ilm from:	T (°C)		$\log fO_2$		T (°C)		$\log fO_2$		T (°C)		$\log fO_2$		T (°C)		$\log fO_2$		T (°C)		$\log fO_2$
Carmichael (1967)	559				600				569				620				609		
Anderson (1968)	573		−20.3		617		−18.1		584		−19.6		622		−19.3		608		−19.6
Lindsley and Spencer (1982)	576		−20.3		618		−18.2		586		−19.6		624		−19.3		612		−19.5
Stormer (1983)	562		−21.2		601		−19.2		572		−20.5		629		−19.1		616		−19.3
Average:	567		−20.6		609		−18.5		577		−19.9		624		−19.2		611		−19.5

patch perthite support formation through fluid-feldspar interaction. Recrystallisation of cryptoperthite, at this stage, is generally isochemical with respect to major elements. Fig. 14 illustrates the behaviour of alkali elements during this process. The Ca and Na contents positively correlate with one another; both elements appear to be concentrated within the cryptoperthite grain interiors. In contrast, K increases towards the rims.

Trails of micropores observed to replace Ab-rich lamellae of cryptoperthite point to direct removal of Na. This is supported by interpretations in Walker et al. (1995), who conclude that the microporosity in patch perthite cannot be fully accounted for by molar volume reduction, and that some feldspar components are inevitably lost to the fluid. Such an observation may in fact represent an initial stage of Na remobilisation, leading to subsequent albitisation observed in the RDG. In addition, it may explain the homogeneous albite rim observed in plagioclase adjacent to recrystallised alkali feldspar in the RDG.

The generation of microporosity in feldspars has also been discussed by Putnis (2002), who concludes that pores may form due to differences in solubility and/or molar volume between the parent (cryptoperthite) and product (patch perthite) phases. In addition, microporosity development in patch perthite has long been documented (*e.g.*, Worden et al., 1990). Given the intragranular nature of deuteric coarsening, microporosity in patch perthite opens up the possibility of elements entering the mineral from adjacent grains. In the RDG, nearby biotite alteration of amphibole and/or re-equilibration of high Fe/low Mg igneous biotite may provide a source of Fe (*e.g.*, Brimhall et al., 1985), and explain the presence of sub-μm-sized hematite associated with patch perthite. Moreover, generation of microporosity in patch perthite, critical for the advancement of the replacement reaction interface (Putnis, 2002), could also promote subsequent fluid-feldspar interaction (Lee and Parsons, 1997). Consequently, the majority of patch perthite reported here has been altered by the highly porous albite and K-feldspar.

6.3. Albitisation of plagioclase

Albitisation of plagioclase is a ubiquitous feature of the RDG. The resultant albite + sericite texture is mostly localised within the plagioclase cores; however, it may also progress along cleavage planes to form pseudomorphs of albitised plagioclase. The pseudomorphic character and sharp boundaries between plagioclase and replacive albite are consistent with coupled dissolution-precipitation reactions (*e.g.*, Putnis, 2002). Such reactions proceed from grain boundaries inwards, and thus plagioclase cores with albite rims would be expected. However, the opposite is commonly observed throughout the RDG, inferring that fluids were able to access plagioclase cores. Such a mechanism was discussed by Que and Allen (1996), who postulated that hydrothermal fluids penetrated plagioclase cores *via* microfractures, which formed prior to hydraulic fracturing in the Rosses granite complex, Ireland. Element maps in Fig. 15 illustrate this core to rim albitisation process in the RDG. The grain interior comprises replacive albite (dark

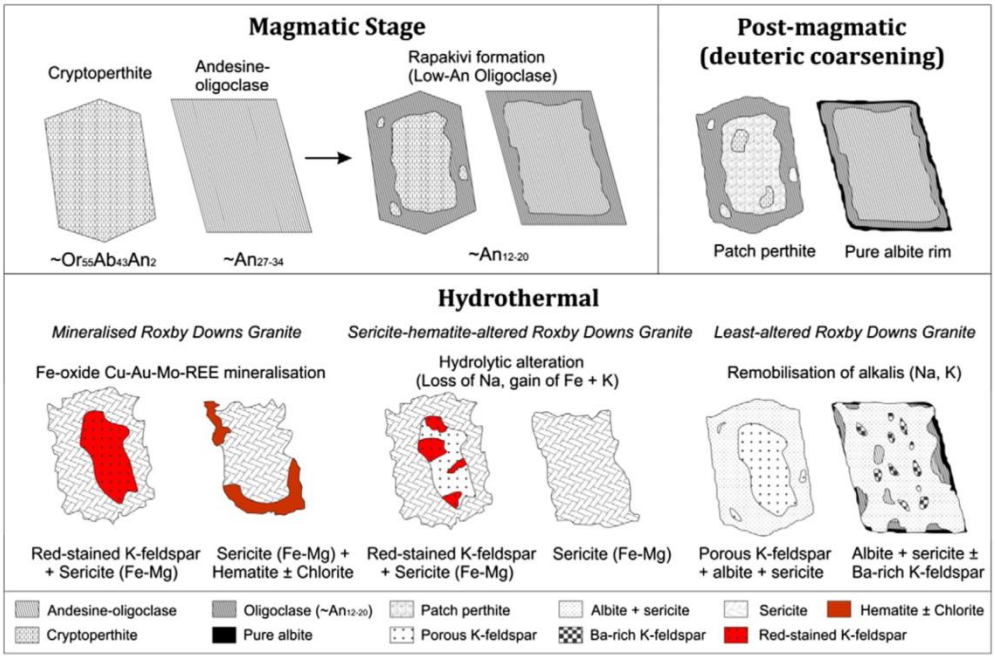

Fig. 13. Schematic diagram outlining the evolutionary sequence of feldspars in the RDG. Relationships between zones preserve magmatic, post-magmatic and hydrothermal feldspar replacement reactions. See text for detailed explanation.

blue) ± sericite (light blue), with oligoclase relicts observed along the grain boundary. In addition, a homogeneous albite rim can be seen between the grain boundary and oligoclase relicts on the Ca and K maps. This feature is observed in all plagioclase grains adjacent to patch perthite (see also Fig. 8d), and is interpreted to represent liberation of Na during recrystallisation of cryptoperthite (deuteric coarsening stage). The circled areas on the BSE image represent K-feldspar inclusions and are thus depleted in both Ca and Na.

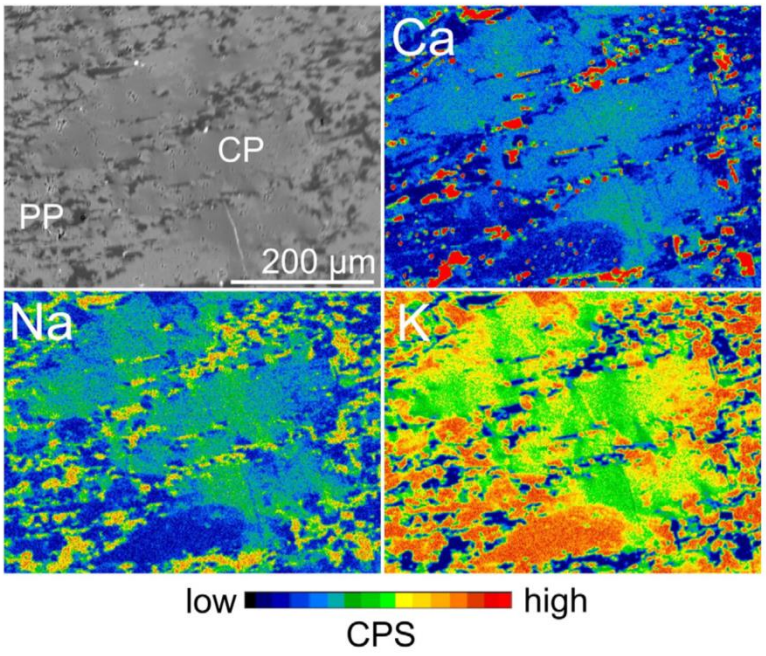

Fig. 14. Back scatter electron image (top left) and EPMA major element maps of cryptoperthite (CP) and patch perthite (PP). See text for explanation. Counts per second scales range from 0 to 92 (Ca), 0 to 52 (Na) and 0 to 245 (K).

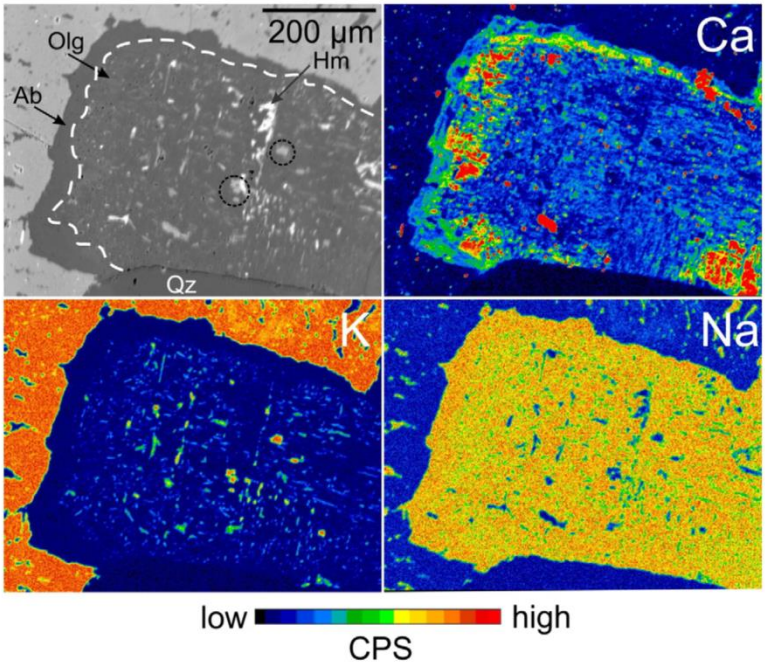

Fig. 15. Back scatter electron image (top left) and EPMA major element maps for an albitized oligoclase grain in the RDG. Circled areas on BSE image represent K-feldspar. See text for explanation. Counts per second scales range from 0 to 158 (Ca), 0 to 52 (Na) and 0 to 248 (K).

Previous authors have attempted to constrain the chemical reactions that best represents the albitisation of plagioclase. Applying the equations proposed by Merino (1975); Boles (1982) and Engvik et al. (2008), replacement of plagioclase by albite in the RDG may be given by:

$$Na_{0.8}Ca_{0.2}Al_{1.2}Si_{2.8}O_8(\text{oligoclase}) + 0.2Na^+(\text{aq.}) + 0.2H_4SiO_4(\text{aq.}) \rightarrow NaAlSi_3O_8(\text{albite}) + 0.2Ca^{2+}(\text{aq.}) + 0.2Al^{3+}(\text{aq.}) + 0.8OH^-(\text{aq.}) \quad (1)$$

$$Na_{0.8}Ca_{0.2}Al_{1.2}Si_{2.8}O_8(\text{oligoclase}) + 0.4Na^+(\text{aq.}) + 0.8H_4SiO_4(\text{aq.}) \rightarrow 1.2NaAlSi_3O_8(\text{albite}) + 0.2Ca^{2+}(\text{aq.}) + 1.6H_2O(\text{aq.}) \quad (2)$$

Eq. (1) implies mobility of Al^{3+}, which, given the close association of sericite with replacive albite, may in fact be released from plagioclase and incorporated in sericite. This hypothesis is preferred in the case of the RDG due to the close association with sericite. Eq. (2) conserves Al within the product albite, and may be more relevant for the formation of the pure albite rim discussed above. Regardless of which equation is most suitable, the albitisation of plagioclase principally involves consumption of Na^+, Si^{-4} and H^+, and the release of Ca^{2+} and Al^{3+}. Whole-rock analyses of least-altered RDG do not show a gain of Na, which indicates that Na for albitisation was locally sourced from within the RDG. A potential source is the widespread replacement of patch perthite by highly porous albite and K-feldspar. Observed textures indicate the grain-scale removal of Na from alkali feldspar (collectively patch perthite) at this later stage. Moreover, the alteration of edenite to chlorite involves liberation of Na from the sodic amphibole. Beyond these potential sources, a seminal study by Orville (1963) showed that Na-rich fluids are not necessarily required for albitisation, and that a fluid simply has to be of suitable temperature to facilitate exchange between Na^+ and K^+. The source of Si for albitisation in the RDG is also of importance. Previous authors (Plümper and Putnis, 2009) interpreted nearby corroded quartz as a source of Si for albitisation in granitoids of the Trans-Scandinavian Igneous Belt in SE Sweden. However, no corroborative textures have been observed in the RDG and thus an alternative source of Si for the albitisation reaction is required. A potential source may be the chloritisation of biotite in the RDG, based on the cogenetic precipitation of hydrothermal quartz with chlorite (*e.g.*, Parry and Downey, 1982).

Using EPMA spot analyses of plagioclase and albite, an isocon plot (Gresens, 1967; Grant, 1986) was constructed to observe the behaviour of elements during the albitisation of low-An oligoclase in the RDG (Fig. 16). Assuming constant volume or mass, Al is slightly mobile, and K increases in the resultant albite. This may represent contamination of sub-µm-sized inclusions of sericite in albite. Variations in albite:sericite ratio may reflect local fluctuations in a_{K+} in the fluids, or a decrease in temperature, since sericite is more stable at lower temperatures than albite (Johnson et al., 1992). Despite the high K content of plagioclase in the RDG (Table 6), sericite would still require K from an external source. Similarly to Si, the chloritisation of biotite typically releases K^+ (Parry and Downey, 1982), and thus might represent such a potential source.

In addition to sericite, sub-µm-sized inclusions of hematite are also associated with replacive albite. This is highlighted in the isocon, which shows an increase of Fe in albite. A likely source of Fe in this case might be the hydrothermal conversion of amphibole to biotite (Brimhall et al., 1985), a phenomenon seen throughout the RDG, and possibly also from plagioclase, even if FeO is well below 0.5 wt.%.

Calcite and dolomite inclusions are also observed within albitised plagioclase and have likely sourced Ca from the igneous plagioclase. However, such inclusions are not ubiquitously present, indicating grain-scale removal of Ca during albitisation, as well as CO_2 within the albitising fluid. Dissolution experiments (Słaby, 1995), in which oligoclase was dissolved in K_2CO_3 solution, produced a similar assemblage consisting of K-feldspar + albite + calcite + dolomite, and may indicate a similar environment for the alteration of plagioclase in the RDG.

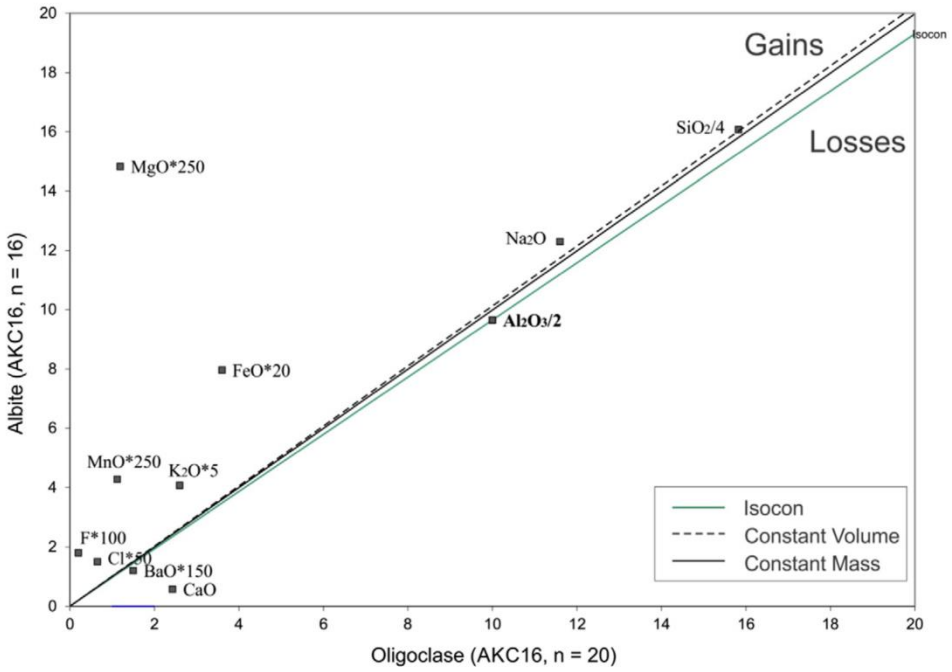

Fig. 16. Isocon plot (Gresens, 1967; Grant, 1986) showing elemental gains and losses during albitization of low-An oligoclase. This plot assumes the immobility of Al^{3+}, which may be incorporated into sericite (see text).

6.4. Hydrothermal K-feldspar

Hydrothermal K-feldspar has not previously been reported from Olympic Dam. However, a change in physico-chemical conditions from albite- to K-feldspar-stable is apparent in even the least-altered RDG. This is evident from a compositionally and texturally distinct K-feldspar which is restricted to previously albitised zones of plagioclase (Fig. 8; Table 2). Fluctuation in Ba content of this K-feldspar could reflect the initial composition of plagioclase, but is more likely related to differential flow of hydrothermal fluids. Similar Ba-zoned K-feldspar was associated with albitisation in granites from Proterozoic terranes in the Fennoscandian Shield (*e.g.*, Morad et al., 2010). This type of feldspar is also reported from Hiltaba suite granites in the Moonta-Wallaroo region (Kontonikas-Charos et al., 2014).

Similarly to plagioclase, alkali feldspar is also affected by hydrothermal K-feldspar formation. This highly porous, near end-member K-feldspar is the most common form of hydrothermal K-feldspar observed in the RDG. Analogous to replacive albite, sub-μm hematite inclusions in the red-stained areas of this K-feldspar are related to Fe release *via* local mineral reactions (*e.g.*, breakdown of primary mafic minerals). A similar mechanism has been suggested for rocks containing red-stained K-feldspar and contemporaneous alteration of biotite and hornblende (*e.g.*, Putnis et al., 2007; Drake et al., 2008). Moreover, the increased FeO content in between hematite inclusions of red-stained K-feldspar (*e.g.*, Fig. 17) indicates that Fe could be present as either nm-scale inclusions, or incorporated within the feldspar crystal lattice. The heterogeneous distribution of hematite throughout the red-stained areas of K-feldspar could relate to porosity generation and locally variable rates of nucleation in the RDG. Putnis et al. (2007) concluded that such red-staining, characteristic of many granitic rocks, is a direct product of fluid-feldspar interaction rather than solid-state exsolution.

The decrease in Na_2O and increase in K_2O between least-altered and sericite-hematite altered RDG observed in whole-rock analyses (*e.g.*, Fig. 2) likely reflects Na/K exchange of the type typical for IOCG systems (*e.g.*, Barton, 2014). Similar to patch perthite, the generation of porosity in hydrothermal albite and K-feldspar likely promotes further fluid-feldspar interaction, and would thus partly influence the apparent shift of alteration style.

The association of red-stained K-feldspar with various sulphides, gold and REE-(U)-minerals strongly implies a genetic relationship between them. Moreover, the replacement of red-stained K-feldspar by interlayered sericite + molybdenite + REE-minerals (Fig. 10d) further emphasises the link between mineralisation and K-feldspar at this hydrothermal stage. All the evidence presented here highlights the ability of feldspars to preserve distinct stages within an evolving magmatic-hydrothermal system.

6.5. Significance of feldspar evolution for IOCG mineralisation

The magmatic evolution of feldspars supports late-stage magma mixing/contamination, a critical component of crustal continuum models for generation of fertile IOCG systems (*e.g.*, Groves et al., 2010). The present study also highlights the preservation of alteration styles, from the grain- to cm-scale that occurs as the granite cools from >750 °C (see Table 9 for summary of geothermobarometry). Post-crystallisation uplift and brecciation of the RDG likely contributed to hydrothermal alteration of feldspars at Olympic Dam. An increase in abundance of hematite and sulphides progressively obliterates the features described for the RDG. Evidence for remobilisation of Na and subsequent albitisation and formation of hydrothermal K-feldspar, are nevertheless preserved within the granite immediately adjacent to the ODBC.

The results collectively point to a process in which initial fluids exsolved from the melt and evolved through cooling and subsequent convection within the granitoid pluton. The abundant microporosity and presence of additional phases (*e.g.*, hematite and sericite) associated with feldspar replacement reactions indicate that each feldspar grain represents an open system, which at least extends to adjacent grains.

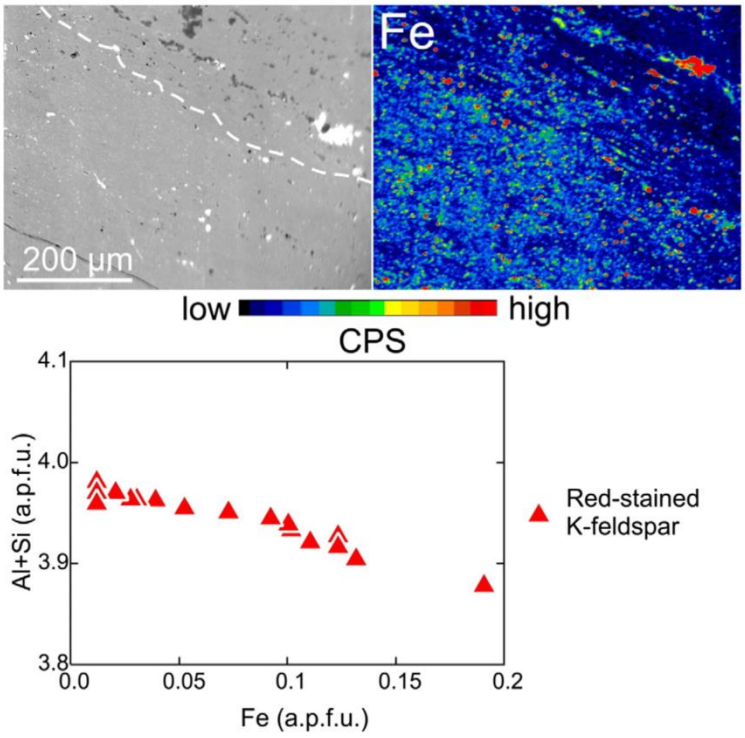

Fig. 17. Back scatter electron image, EPMA Fe element map and binary plot of variably red-stained K-feldspar within altered RDG. See text for explanation. Counts per second scales range from 0 to 155.

Microfracturing and repeated fracture reactivation could be effective mechanisms by which multiple open systems link up. Whole-rock analyses of least-altered RDG at one-metre intervals (Table 1a) are consistent with existing data for granites (*e.g.*, Frost et al., 2001; references therein). In addition, the data plots in the same area on the modified QAP and Ab-An-Or diagrams, irrespective of textures and mineralogy suggesting that Area 2 is more altered than Area 1. Thus, regardless of the extent of feldspar replacement textures in the least-altered RDG samples, the rock still maintains its overall granitic composition at the m-scale. Such evidence further supports recycling of feldspar components within the RDG and implies that hydrothermal albite and K-feldspar can form *in-situ* without the need for an external source of alkalis (*e.g.*, evaporites; Barton and Johnson, 1996, 2000; Conor et al., 2010).

The presence of albite at depth within the ODBC is concordant with proposed models for IOCG systems, in which deep sodic alteration transitions to intermediate potassic alteration followed by shallower hydrolytic alteration (*e.g.*, Hitzman et al., 1992; Barton, 2014). This telescoping of alteration assemblages is supported by higher $a\mathrm{Na}^+$ than $a\mathrm{K}^+$ at higher temperatures (Orville, 1963). However, it is important to highlight that in the case of the RDG, albitisation does not produce the barren, monomineralic albitites as reported from other IOCG terranes, *e.g.*, from Cloncurry, Queensland (Mark, 1998; Bertelli and Baker, 2010). There is a clear remobilisation of Na from the host RDG, which indeed leads to local albitisation; and may also lead to albitisation elsewhere in the Olympic Dam area. Nevertheless, the preservation of albitisation at depth and to the peripheries of the ODBC is an important observation and one which reflects the critical role that successive alteration events play in the formation of giant orebodies such as Olympic Dam. In addition, the significant geochemical and textural changes related to feldspar recrystallisation in the RDG clearly played a role in facilitating fluids and subsequent or synchronous hydrothermal alteration/mineralisation at Olympic Dam.

7. Conclusions

The results of this study allow the following conclusions:

- Major element exchange occurring at Olympic Dam can be tracked from feldspar textures in the surrounding RDG. There is a remobilisation and eventual loss of Na occurring in the least-altered RDG and a gain of Fe and K in sericite-hematite altered and mineralised RDG. This corresponds to observed albitisation, sericite-hematite alteration and

Table 9
Summary of geothermobarometric estimates for the RDG.

Technique	Minerals	*P* (kbar)	*T* (°C)	Implications
Al-in-hornblende geobarometry	Edenite	2.2	N/A	Corresponds to crystallisation depths of ~8 km
Feldspar geothermometry	Cryptoperthite	2.2	~765	Minimum crystallisation *T* for ternary feldspars
Amphibole-plagioclase geothermometry	Edenite, plagioclase	2.2	700–710	Minimum crystallisation *T* for rapakivi mantles
Magnetite-ilmenite geothermometry	Magnetite, ilmenite	N/A	574–624	Minimum re-equilibration *T* of Fe-Ti-oxides
Feldspar geothermometry	Patch perthite	2.2	~430	*T* for onset of deuteric coarsening
	Film perthite	2.2	<430	Secondary exsolution in Or-rich phase of patch perthite

subsequent Fe-oxide Cu-Au-REE-Mo-U mineralisation. In addition, there is a significant association between increased red-staining of K-feldspar and abundance of sulphide mineralisation.

- Textural relationships and geochemistry of feldspars and mafic minerals in the least-altered RDG point to late-stage magma mixing/contamination.
- Geothermometry indicates minimum crystallisation temperatures of 765 °C for ternary feldspar at a pressure of ~2.2 kbar (using Al-in-hornblende geobarometry corrected for temperature by amphibole-plagioclase geothermometry), followed by re-equilibration of Fe-Ti-minerals and feldspars at ~550–650 °C and ~430 °C, respectively. Pre-existing feldspars have been extensively overprinted by highly porous albite and K-feldspar.
- The presence of hydrothermal albite and K-feldspar at Olympic Dam illustrate the ability for these forms of alteration, characteristic of IOCG systems, to be internally sourced from within the host rock (granite). Such widespread physical and chemical changes resulting from these reactions may indeed facilitate subsequent mineralisation.

Acknowledgements

We thank BHP Billiton for financial support and access to Olympic Dam samples and facilities. We also thank Adelaide Microscopy for assistance with microanalysis, in particular Animesh Basak for assistance operating the Titan Themis TEM and Benjamin Wade for assistance with various software packages. We acknowledge the insightful comments of Ewa Słaby and two anonymous reviewers. Constructive comments from Ian Parsons on an earlier version of this manuscript are greatly appreciated and helped us present our ideas with greater clarity. We also acknowledge support from the 'FOX' project (Trace elements in iron oxides), supported by BHP Billiton and the South Australian Mining and Petroleum Services Centre of Excellence.

References

Andersen, D.J., Lindsley, D.H., 1985. New (and final!) models for the Ti-magnetite/ilmenite geothermometer and oxygen barometer. AGU Spring Meeting. Eos 66 (18), p. 416.
Anderson, A.T., 1968. The oxygen fugacity of alkaline basalt and related magmas. Am. J. Sci. 266, 704–727.
Anderson, J.L., Smith, D.R., 1995. The effects of temperature and fO_2 on the Al-in-hornblende barometer. Am. Mineral. 80, 549–559.
Barker, F., 1979. Trondhjemite: definition, environment and hypotheses of origin. Trondhjemites, dacites and related rocks. 1-12, Elsevier, Amsterdam, p. 659.
Barton, M., 2014. Iron oxide (-Cu–Au–REE–P–Ag–U–Co) systems. Treatise on Geochemistry, second edition vol. 13. Elsevier, Amsterdam, pp. 515–541.
Barton, M.D., Johnson, D.A., 1996. Evaporitic-source model for igneous-related Fe oxide–(REE-Cu-Au-U) mineralisation. Geology 24, 259–262.
Barton, M.D., Johnson, D.A., 2000. Alternative brine sources for Fe-oxide (-Cu-Au) systems: implications for hydrothermal alteration and metals. Hydrothermal Iron Oxide Copper-Gold & Related Deposits: A Global Perspective. vol. 1, pp. 43–60.
Bertelli, M., Baker, T., 2010. A fluid inclusion study of the Suicide Ridge Breccia Pipe, Cloncurry district, Australia: implication for breccia genesis and IOCG mineralisation. Precambrian Res. 179, 69–87.
BHP Billiton, 2015. http://www.bhpbilliton.com/home/investors/annualreporting2015.pdf.
Blundy, J.D., Holland, T.J.B., 1990. Calcic amphibole equilibria and a new amphibole-plagioclase geothermometer. Contrib. Mineral. Petrol. 104, 208–224.
Boles, J.R., 1982. Active albitization of plagioclase, Gulf Coast Tertiary. Am. J. Sci. 282, 165–180.
Brimhall, G.H., Agee, C., Stoffregen, R., 1985. The hydrothermal conversion of hornblende to biotite. Can. Mineral. 23, 369–379.
Brown, W., Parsons, I., 1984. Exsolution and coarsening mechanisms and kinetics in an ordered cryptoperthite series. Contrib. Mineral. Petrol. 86, 3–18.
Brown, W.L., Parsons, I., 1989. Alkali feldspars: ordering rates, phase transformations and behaviour diagrams for igneous rocks. Mineral. Mag. 53, 25–42.
Carmichael, I.S.E., 1967. The iron-titanium oxides of salic volcanic rocks and their associated ferromagnesian silicates. Contrib. Mineral. Petrol. 14, 36–64.
Ciobanu, C.L., Cook, N.J., Utsunomiya, S., Pring, A., Green, L., 2011. Focussed ion beam-transmission electron microscopy applications in ore mineralogy: bridging micro- and nanoscale observations. Ore Geol. Rev. 42, 6–31.
Ciobanu, C.L., Wade, B.P., Cook, N.J., Schmidt Mumm, A., Giles, D., 2013. Uranium-bearing hematite from the Olympic Dam Cu–U–Au deposit, South Australia: a geochemical tracer and reconnaissance Pb–Pb geochronometer. Precambrian Res. 238, 129–147.
Conor, C., Raymond, O., Baker, T., Teale, G., Say, P., Lowe, G., 2010. Alteration and mineralisation in the Moonta-Wallaroo Cu–Au mining field region, Olympic domain, South Australia. Hydrothermal Iron Oxide Copper–Gold and Related Deposits: A Global Perspective. vol. 3, pp. 1–24.
Creaser, R.A., 1989. The Geology and Petrology of Middle Proterozoic Felsic Magmatism of the Stuart Shelf, South Australia. La Trobe University, Melbourne.
Creaser, R.A., 1996. Petrogenesis of a Mesoproterozoic quartz latite-granitoid suite from the Roxby Downs area, South Australia. Precambrian Res. 79, 371–394.
Dempster, T., Jenkin, G., Rogers, G., 1994. The origin of rapakivi texture. J. Petrol. 35, 963–981.
Drake, H., Tullborg, E.-L., Annersten, H., 2008. Red-staining of the wall rock and its influence on the reducing capacity around water conducting fractures. Appl. Geochem. 23, 1898–1920.
Ehrig, K., McPhie, J., Kamenetsky, V., 2012. Geology and mineralogical zonation of the Olympic Dam iron oxide Cu-U-Au-Ag deposit, South Australia. In: Hedenquist, J.W., Harris, M., Camus, F. (Eds.), Geology and Genesis of Major Copper Deposits and Districts of the World: A Tribute to Richard H. Sillitoe vol. 16. Society of Economic Geologists Special Publication, pp. 237–267.
Emslie, R., 1991. Granitoids of rapakivi granite-anorthosite and related associations. Precambrian Res. 51, 173–192.
Engvik, A.K., Putnis, A., Gerald, J.D.F., Austrheim, H., 2008. Albitization of granitic rocks: the mechanism of replacement of oligoclase by albite. Can. Mineral. 46, 1401–1415.
Ferris, G.M., Schwarz, M.P., Heithersay, P., 2002. The geological framework, distribution, and controls of Fe-oxide Cu–Au mineralisation in the Gawler Craton, South Australia: Part 1—Geological and tectonic framework. Hydrothermal Iron Oxide Copper–Gold and Related Deposits: A Global Perspective. vol. 2, pp. 9–32.
Frost, B.R., Barnes, C.G., Collins, W.J., Arculus, R.J., Ellis, D.J., Frost, C.D., 2001. A geochemical classification for granitic rocks. J. Petrol. 42, 2033–2048.
Fuhrman, M.L., Lindsley, D.H., 1988. Ternary-feldspar modeling and thermometry. Am. Mineral. 73, 201–215.
Grant, J.A., 1986. The isocon diagram; a simple solution to Gresens' equation for metasomatic alteration. Econ. Geol. 81, 1976–1982.
Gresens, R.L., 1967. Composition–volume relationships of metasomatism. Chem. Geol. 2, 47–65.
Groves, D.I., Bierlein, F.P., Meinert, L.D., Hitzman, M.W., 2010. Iron oxide copper-gold (IOCG) deposits through earth history: implications for origin, lithospheric setting, and distinction from other epigenetic iron oxide deposits. Econ. Geol. 105, 641–654.
Hammarstrom, J.M., Zen, E., 1986. Aluminium in hornblende: an empirical geobarometer. Am. Mineral. 71, 1297–1313.
Haynes, D.W., Cross, K.C., Bills, R.T., Reed, M.H., 1995. Olympic Dam ore genesis; a fluid-mixing model. Econ. Geol. 90, 281–307.
Hayward, N., Skirrow, R., 2010. Geodynamic setting and controls on iron oxide Cu-Au (±U) ore in the Gawler Craton, South Australia. Hydrothermal Iron Oxide Copper-Gold and Related Deposits: A Global Perspective. vol. 3, pp. 105–131.
Hibbard, M.J., 1981. The magma mixing origin of mantled feldspars. Contrib. Mineral. Petrol. 76, 158–170.
Hitzman, M.W., Oreskes, N., Einaudi, M.T., 1992. Geological characteristics and tectonic setting of proterozoic iron oxide (Cu-U-Au-REE) deposits. Precambrian Res. 58, 241–287.
Hollister, L.S., Grissom, G.C., Peters, E.K., Stowell, H.H., Sisson, V.B., 1987. Confirmation of the empirical correlation of aluminium in hornblende with pressure of solidification of calcalkaline plutons. Am. Mineral. 72, 231–239.
Hövelmann, J., Putnis, A., Geisler, T., Schmidt, B.C., Golla-Schindler, U., 2010. The replacement of plagioclase feldspars by albite: observations from hydrothermal experiments. Contrib. Mineral. Petrol. 159, 43–59.
Ismail, R., Ciobanu, C.L., Cook, N.J., Teale, G.S., Giles, D., Schmidt Mumm, A., Wade, B., 2014. Rare earths and other trace elements in minerals from skarn assemblages, Hillside iron oxide–copper–gold deposit, Yorke Peninsula, South Australia. Lithos 184–187, 456–477.
Jagodzinski, E.A., 2005. Compilation of SHRIMP U-Pb geochronological data. Geoscience Australia Record 2005/20.
Johnson, J.P., Cross, K.C., 1995. U-Pb geochronological constraints on the genesis of the Olympic Dam Cu-U-Au-Ag deposit, South Australia. Econ. Geol. 90, 1046–1063.
Johnson, M.C., Rutherford, M.J., 1989. Experimental calibration of the aluminium-in-hornblende geobarometer with application to Long Valley caldera (California). Geology 17, 837–841.
Johnson, J.W., Oelkers, E.H., Helgeson, H.C., 1992. SUPCRT92: a software package for calculating the standard molal thermodynamic properties of minerals, gases, aqueous species, and reactions from 1 to 5000 bar and 0 to 1000 °C. Comput. Geosci. 18, 899–947.
Kontonikas-Charos, A., Ciobanu, C.L., Cook, N.J., 2014. Albitization and redistribution of REE and Y in IOCG systems: insights from Moonta-Wallaroo, Yorke Peninsula, South Australia. Lithos 208–209, 178–201.
Krneta, S., Ciobanu, C.L., Cook, N.J., Ehrig, K., Kontonikas-Charos, A., 2016. Apatite at Olympic Dam, South Australia: a petrogenetic tool. Lithos 262, 470–485.
Lee, M.R., Parsons, I., 1997. Dislocation formation and albitization in alkali feldspars from the Shap granite. Am. Mineral. 82, 557–570.
LeMaitre, R.W., Streckeisen, A., Zanettin, B., Le Bas, M.J., Bonin, B., Bateman, P. (Eds.), 1989. A Classification of Igneous Rocks and Glossary of Terms: Recommendations of the International Union of Geological Sciences Subcommission on the Systematics of Igneous Rocks. Blackwell Scientific, Oxford (193 pp.).
Lepage, L.D., 2003. ILMAT: an Excel worksheet for ilmenite-magnetite geothermometry and geobarometry. Comput. Geosci. 29, 673–678.
Lindsley, D.H., Spencer, K.J., 1982. Fe-Ti oxide geothermometry: reducing analyses of coexisting Ti-magnetite (Mt) and ilmenite (Ilm). EOS Trans. Am. Geophys. Union 63, 471.
Manning, D., 1981. The effect of fluorine on liquidus phase relationships in the system Qz-Ab-Or with excess water at 1 kb. Contrib. Mineral. Petrol. 76, 206–215.

Mark, G., 1998. Albitite formation by selective pervasive sodic alteration of tonalite plutons in the Cloncurry district, Queensland. Aust. J. Earth Sci. 45, 765–774.
Merino, E., 1975. Diagenesis in Tertiary sandstones from Kettleman North Dome, California: I. Diagenetic mineralogy. J. Sediment. Petrol. 45, 320–336.
Morad, S., El-Ghali, M., Caja, M., Sirat, M., Al-Ramadan, K., Mansurbeg, H., 2010. Hydrothermal alteration of plagioclase in granitic rocks from Proterozoic basement of SE Sweden. Geol. J. 45, 105–116.
Müller, A., Seltmann, R., Kober, B., Eklund, O., Jeffries, T., Kronz, A., 2008. Compositional zoning of rapakivi feldspars and coexisting quartz phenocrysts. Can. Mineral. 46, 1417–1442.
Oliver, N.H., Cleverley, J.S., Mark, G., Pollard, P.J., Fu, B., Marshall, L.J., Rubenach, M.J., Williams, P.J., Baker, T., 2004. Modeling the role of sodic alteration in the genesis of iron oxide-copper-gold deposits, Eastern Mount Isa block, Australia. Econ. Geol. 99, 1145–1176.
Oreskes, N., Einaudi, M.T., 1990. Origin of rare earth element-enriched hematite breccias at the Olympic Dam Cu-U-Au-Ag deposit, Roxby Downs, South Australia. Econ. Geol. 85, 1–28.
Orville, P.M., 1963. Alkali ion exchange between vapor and feldspar phases. Am. J. Sci. 261, 201–237.
Parry, W., Downey, L., 1982. Geochemistry of hydrothermal chlorite replacing igneous biotite. Clay Clay Miner. 30, 81–90.
Parsons, I., 1978. Feldspars and fluids in cooling plutons. Mineral. Mag. 42, 1–17.
Parsons, I., Thompson, P., Lee, M.R., Cayzer, N., 2005. Alkali feldspar microtextures as provenance indicators in siliciclastic rocks and their role in feldspar dissolution during transport and diagenesis. J. Sediment. Res. 75, 921–942.
Parsons, I., Lee, M.R., 2009. Mutual replacement reactions in alkali feldspars I: microtextures and mechanisms. Contrib. Mineral. Petrol. 157 (5), 641–661.
Parsons, I., Magee, C.W., Allen, C.M., Shelley, J., Lee, M.R., 2009. Mutual replacement reactions in alkali feldspars II: trace element partitioning and geothermometry. Contrib. Mineral. Petrol. 157, 663–687.
Parsons, I., Fitz Gerald, J.D., Lee, J.K.W., Ivanic, T., Golla-Schindler, U., 2010. Time-temperature evolution of microtextures and contained fluids in a plutonic alkali feldspar during heating. Contrib. Mineral. Petrol. 160, 155–180.
Parsons, I., Gerald, J.D.F., Lee, M.R., 2015. Review. Routine characterization and interpretation of complex alkali feldspar intergrowths. Am. Mineral. 100, 1277–1303.
Perez, R.J., Boles, J.R., 2005. An empirically derived kinetic model for albitization of detrital plagioclase. Am. J. Sci. 305, 312–343.
Plümper, O., Putnis, A., 2009. The complex hydrothermal history of granitic rocks: multiple feldspar replacement reactions under subsolidus conditions. J. Petrol. 50, 967–987.
Putnis, A., 2002. Mineral replacement reactions: from macroscopic observations to microscopic mechanisms. Mineral. Mag. 66, 689–708.
Putnis, A., Hinrichs, R., Putnis, C.V., Golla-Schindler, U., Collins, L.G., 2007. Hematite in porous red-clouded feldspars: evidence of large-scale crustal fluid–rock interaction. Lithos 95, 10–18.
Que, M., Allen, A.R., 1996. Sericitization of plagioclase in the Rosses granite complex, Co. Donegal, Ireland. Mineral. Mag. 60, 927–936.
Rämö, O., Haapala, I., 1995. One hundred years of rapakivi granite. Mineral. Petrol. 52, 129–185.
Reeve, J., Cross, K., Smith, R., Oreskes, N., 1990. Olympic Dam copper-uranium-gold-silver deposit. Geology of the Mineral Deposits of Australia and Papua New Guinea vol. 2. AusIMM, Melbourne, pp. 1009–1035.
Reid, A., Smith, R.N., Baker, T., Jagodzinski, E.A., Selby, D., Gregory, C.J., Skirrow, R.G., 2013. Re-Os dating of molybdenite within hematite breccias from the Vulcan Cu-Au prospect, Olympic Cu-Au province, South Australia. Econ. Geol. 108, 883–894.
Ryan, B., 1991. Makhavinekh Lake pluton, Labrador, Canada: geological setting, subdivisions, mode of emplacement, and a comparison with Finnish rapakivi granites. Precambrian Res. 51, 193–225.
Schmidt, M.W., 1992. Amphibole composition in tonalite as a function of pressure: an experimental calibration of the Al-in-hornblende barometer. Contrib. Mineral. Petrol. 110, 304–310.
Shand, S.J., 1943. The Eruptive Rocks. 2nd edition. John Wiley, New York.
Skirrow, R.G., Bastrakov, E.N., Barovich, K., Fraser, G.L., Creaser, R.A., Fanning, C.M., Raymond, O.L., Davidson, G.J., 2007. Timing of iron oxide Cu-Au-(U) hydrothermal activity and Nd isotope constraints on metal sources in the Gawler craton, South Australia. Econ. Geol. 102, 1441–1470.
Słaby, E., 1995. TAS classification — how to overcome problems with post-magmatic feldspar formation in Permian volcanic rocks. Zbl. Geol. Paläontol. 5, 541–552.
Słaby, E., Goetze, J., 2004. Feldspar crystallization under magma-mixing conditions shown by cathodoluminescence and geochemical modelling — a case study from the Karkonosze pluton (SW Poland). Mineral. Mag. 68, 561–577.
Słaby, E., Śmigielski, M., Śmigielski, T., Domonik, A., Simon, K., Kronz, A., 2011. Chaotic three-dimensional distribution of Ba, Rb and Sr in feldspar megacrysts grown in an open magmatic system. Contrib. Mineral. Petrol. 162, 909–927.
Snow, E., Kidman, S., 1991. Effect of fluorine on solid-state alkali interdiffusion rates in feldspar. Nature 349, 231–233.
Stormer, J.C., 1983. The effects of recalculation on estimates of temperature and oxygen fugacity from analyses of multicomponent iron-titanium oxides. Am. Mineral. 68, 586–594.
Streckeisen, A.L., 1976. Classification and nomenclature of igneous rocks. Earth-Sci. Rev. 12, 1–35.
Troeng, B., 1982. Uranium-rich granites in the Olden Window, Sweden. Mineral. Mag. 46, 217–226.
Walker, F.D.L., Lee, M.R., Parsons, I., 1995. Micropores and micropermeable texture in alkali feldspars: geochemical and geophysical implications. Mineral. Mag. 59, 505–534.
Wark, D.A., Stimac, J.A., 1992. Origin of mantle (rapakivi) feldspars: experimental evidence of a dissolution- and diffusion-controlled mechanism. Contrib. Mineral. Petrol. 111, 345–361.
Wilson, M., Åkerblom, G., 1982. Geological setting and geochemistry of uranium-rich granites in the Proterozoic of Sweden. Mineral. Mag. 46, 233–245.
Worden, R.H., Walker, F.D.L., Parsons, I., Brown, W.L., 1990. Development of microporosity, diffusion channels and deuteric coarsening in perthitic alkali feldspars. Contrib. Mineral. Petrol. 104, 507–515.

CHAPTER 9

REFERENCES

CHAPTER 9: REFERENCES

Alderton, D.H.M., Pearce, J.A. and Potts, P.J., 1980. Rare earth element mobility during granite alteration: Evidence from southwest England. Earth and Planetary Science Letters 49, 149–165.

Allen, S., McPhie, J., Ferris, G. and Simpson, C., 2008. Evolution and architecture of a large felsic igneous province in western Laurentia: the 1.6 Ga Gawler Range Volcanics, South Australia. Journal of Volcanology and Geothermal Research 172, 132–147.

Alley, N.F., 1995. Late Palaeozoic. In: Drexel, J.F., Preiss, W.V. (Eds.), The Geology of South Australia. Vol. 2. The Phanerozoic, Geological Survey of South Australia, Bulletin. 54, 63–92.

Amelinckx, S., Van Tendeloo, G., Van Dyck, D. and Van Landuyt, J., 1989. The study of modulated structures, mixed layer polytypes and 1-D quasi-crystals by means of electron microscopy and electron diffraction. Phase Transitions 16, 3–40.

Apukhtina, O.B., Kamenetsky, V.S., Ehrig, K., Kamenetsky, M.B., McPhie, J., Maas, R., Meffre, S., Goermann, K., Rodermann, T., Cook, N.J. and Ciobanu, C.L., 2016. Postmagmatic magnetite–apatite assemblage in mafic intrusions: a case study of dolerite at Olympic Dam, South Australia. Contributions to Mineralogy and Petrology 171:2 DOI 10.1007/s00410-015-1215-7

Apukhtina, O.B., Kamenetsky, V.S., Ehrig, K., Kamenetsky, M.B., Mass, R., McPhie, J., Ciobanu, C.L. and Cook, N.J., 2017. Deep, early mineralisation at the Olympic Dam Cu-U-Au-Ag deposit, South Australia. Economic Geology, 112 (6), 1531-1542.

Averill, S.A. 2007. Recent advances in base metal indicator mineralogy. EXPLORE, 134, 2-6.

Averill, S.A. 2011. Viable indicators in surficial sediments for two major base metal deposit types: Ni-Cu-PGE and Porphyry Cu. Geochemistry: Exploration, Environment, Analysis 11, 279–292.

Baker, T., Mustard, R., Fu, B., Williams, P.J., Dong, G., Fisher, L., Mark, G. and Ryan, C.G., 2008. Mixed messages in iron oxide-copper-gold systems of the Cloncurry district, Australia: insights from PIXE analysis of halogens and copper in fluid inclusions. Mineralium Deposita 43, 599–608.

Barkov, A.Y. and Nikiforov, A.A., 2016. Compositional variations of apatite, fractionation trends, and a PGE-bearing zone in the Kivakka layered intrusion, nothern Karelia, Russia. The Canadian Mineralogist 54, 475–490.

Barton, M., 2014. Iron oxide (–Cu–Au–REE–P–Ag–U–Co) systems. Treatise on Geochemistry (second edition, volume 13): Amsterdam, Elsevier, 515–541.

Bastrakov, E.N., Skirrow, R.G. and Davidson, G.J., 2007. Fluid evolution and origins of iron oxide Cu-Au prospects in the Olympic Dam District, Gawler Craton, South Australia: Economic Geology 102, 1415–1440.

Bargossi, G.M., Del Moro, A., Ferrari M., Gesparotto, G., Mordenti, A., Rottura, A. and Tateo, F., 1999. Caratterizzazione petrografico-geochimica e significato dell'associazione monzogranito-inclusi femici microgranulari della Vetta di Cima d'Asta (Alpi Meridionali). Mineralogica et Petrographica Acta 42, 155–179.

Bau, M., 1991. Rare-earth element mobility during hydrothermal and metamorphic fluid-rock interaction and the significance of the oxidation state of europium. Chemical Geology 93, 219–230.

Bau, M. and Dulski, P., 1995. Comparative study of yttrium and rare-earth element behaviours in flourine-rich hydrothermal fluids. Contributions to Mineral Petrology 119, 213–223.

Bea, F., Fershater, G. and Corretge, L.G., 1992. The geochemistry of phosphorus in granite rocks and the effect of aluminium. Lithos 29, 43–56.

Becker, M., de Villiers, J.P.R. and Bradshaw, D., 2010. The flotation of magnetic and non-magnetic pyrrhotite from selected nickel ore deposits. Minerals Engineering 23, 1045–1052.

Belousova, E.A., Walters, S., Griffin, W.L. and O'Reilly, S.Y., 2001. Trace-element signatures of apatites in granitoids from the Mt Isa Inlier, northwestern Queensland. Australian Journal of Earth Sciences 48, 603–619.

Belousova, E.A., Griffin, W.L., O'Reilly, S.Y. and Fisher, N.I., 2002. Apatite as an indicator mineral for mineral exploration: trace-element compositions and their relationship to host rock type. Journal of Geochemical Exploration 76, 45–69.

Belperio, A., Flint, R. and Freeman, H., 2007. Prominent Hill: A Hematite-Dominated, Iron Oxide Copper-Gold System. Economic Geology 102, 1499–1510.

Bethke, C. and Yeakel, S., 2016, The Geochemist's Workbench® Release 11 - GWB Essentials Guide. https://www.gwb.com/pdf/GWB11/GWBessentials.pdf

BHP, 2014. http://www.bhp.com/~/media/bhp/documents/investors/annual-reports/bhpbillitonannualreport2014.pdf

BHP, 2015. http://www.bhp.com/~/media/bhp/documents/investors/annual-reports/2015/bhpbillitonannualreport2015.pdf?la=en

BHP, 2016. http://www.bhp.com/-/media/bhp/documents/investors/annual-reports/2016/bhpbillitonannualreport2016.pdf?la=en

Blissett, A.H., Creaser, R.A., Daly, S.J, Flint, D.J. and Parker, A.J., 1993. Gawler Range Volcanics. In: Drexel, J. F., Preiss, W.V., Parker, A.J. (eds.), The Geology of South Australia. Volume 1, The Precambrian: Adelaide, Geological Survey of South Australia, Bulletin 54, 107–131.

Bonyadi, Z., Davidson, G.J., Mehrabi, B., Meffre, S. and Ghazban, F., 2011. Significance of apatite REE depletion and monazite inclusions in the brecciated Se–Chahun iron oxide–

apatite deposit, Bafq district, Iran: Insights from paragenesis and geochemistry. Chemical Geology 281, 253–269.

Boudreau A.E. and Krugger F.J. 1990. Variation in the composition of apatite through the Merensky cyclic unit in the western Bushveld Complex. Economic Geology 85, 737–745.

Boudreau, A.E. and McCallum, I.S., 1990. Low temperature alteration of REE-rich chlorapatite from the Stillwater Complex, Montana. American Mineralogist 75, 687–693.

Bouzari, F., Hart, J.R.H., Bissig, T. and Barker, S., 2016. Hydrothermal alteration revealed by apatite luminescence and chemistry: A potential indicator mineral for exploring covered Porphyry Copper Deposits. Economic Geology 111, 1397–1410.

Bowden, B., Fraser, G., Davidson, G.J., Meffre, S., Skirrow, R., Bull, S. and Thompson, J., 2017. Age constraints on the hydrothermal history of the Prominent Hill iron oxide copper-gold deposit, South Australia. Mineralium Deposita 52, 863–881.

Brauand, E., Fowler, M., Storey, C. and Darling, J., 2017. Apatite trace element and isotope applications to petrogenesis and provenance. American Mineralogist, 102, 75–84.

Broom-Fendley, S., Styles, M.T., Appleton, J.D., Gunn, G. and Wall, F., 2016. Evidence for dissolution-reprecipitation of apatite and preferential LREE mobility in carbonatite-derived late-stage hydrothermal processes. American Mineralogist 101, 596–611.

Broom-Fendley, S., Brady, A.E., Wall, F., Gunn, G. and Dawes, W., 2017. REE minerals at the Songwe Hill carbonatite, Malawi: HREE-enrichment in late-stage apatite. Ore Geology Reviews 81, 23–41.

Broska, I., Krogh Ravna, E.J., Vojtko, P., Janak, M., Konecny, P., Pentrak, M., Bacik, P., Luptakova, J. and Kullerud, K., 2014. Oriented inclusions in apatite in a post-UHP fluid-mediated regime (Tromson Nappe, Norway). European Journal of Mineralogy 26, 623-634.

Brugger, J., Lahaye, Y., Costa, S., Lambert, D. and Bateman, R. 2000. Inhomogenous distribution of REE in scheelite and dynamics of Archean hydrothermal systems (Mt. Charlotte and Drysdale gold deposits, Western Australia). Contributions to Mineralogy and Petrology 139, 251–264.

Brugger, J., Etschmann, B., Pownceby, M., Liu, W., Grundler, P. and Brewe, D., 2008. Oxidation state of europium in scheelite: Tracking fluid-rock interaction in gold deposits. Chemical Geology 257, 26–33.

Candela, P.A., 1986. Generalized mathematical models for the fractional evolution of vapor from magmas in terrestrial planetary crusts. In: Saxena, S.K. (Ed.), Advances in Physical Geochemistry Physics and Chemistry of the Terrestrial Planets Vol. 6. Springer-Verlag, New York, pp. 362–398.

Cao, M., Li, G., Qin, K., Seitmuratova, E.Y. and Liu, Y., 2012. Major and Trace element characteristics of apatites in granitoids from Central Kazakhstan: Implications for petrogenesis and mineralization. Resource Geology 62, 63–83.

Cawthorn, R.G., 2013. Rare earth element abundances in apatite in the Bushveld Complex- A consequence of the trapped liquid shift effect. Geology 41, 603–606.

Chemtob, S.M., Rossman, G.R., Young, E.D., Ziegler, K., Moynier, F., Eiler, J.M. and Hurowitz, J.A., 2015. Silicon isotope systematics of acidic weathering of fresh basalts, Kilauea volcano, Hawai'i. Geochimica et Cosmochimica Acta 169, 63–81.

Chen, H.Y., Clark, A.H. and Kyser, T.K., 2010. The Marcona magnetite deposit, Ica, central south Peru: A product of hydrous, iron oxide-rich melt. Economic Geology 105, 1441–1456.

Chen, B., Wang, J., Kong, L., Mai, X., Zheng, N., Zhong, Q., Liang, J. and Chen, D., 2017. Adsorption of uranium from uranium mine contaminated water using phosphate rock

apatite using (PRA): Isotherm, kinetic and characterization studies. Colloids and Surfaces A: Physicochemical and Engineering Aspects 520, 612–621.

Chew, D.M. and Spikings, R.A., 2015. Geochronology and Thermochronology using apatite: time and temperature, lower crust to surface. Elements 11, 189–194.

Chiaradia, M., Banks, D., Cliff, R., Marschik, R. and de Haller, A., 2006. Origin of fluids in iron oxide–copper–gold deposits: Constraints from δ37Cl, $^{87}Sr/^{86}Sr_i$ and Cl/Br. Mineralium Deposita 41, 565–573.

Ciobanu, C.L., Cook, N.J., Utsunomiya, S., Pring, A. and Green, L., 2011. Focussed ion beam-transmission electron microscopy applications in ore mineralogy: Bridging micro- and nanoscale observations. Ore Geology Reviews 42, 6–31.

Ciobanu, C.L., Wade, B., Cook, N.J., Schmidt Mumm, A. and Giles, D., 2013. Uranium-bearing hematite from the Olympic Dam Cu-U-Au deposit, South Australia; a geochemical tracer and reconnaissance Pb-Pb geochronometer: Precambrian Research 238, 129–147.

Ciobanu, C.L., Cook, N.J. and Ehrig, K., 2017. Ore minerals down to the nanoscale: Cu-(Fe)-sulphides from the Iron Oxide Copper Gold deposit at Olympic Dam, South Australia. Ore Geology Reviews 81, 1218–1235.

Clark, J.M., Cook, N.J., Reid, A., Ciobanu, C.L. and Hill, P., 2014. Defining the Style of Mineralisation at the Cairn Hill Magnetite-Sulphide Deposit, Mount Woods Inlier, Gawler Craton, South Australia. Gold14@Kalgoorlie – Western Australia Abstract volume, p. 19–20.

Conor, C., Raymond, O., Baker, T., Teale, G., Say, P. and Lowe, G., 2010. Alteration and Mineralisation in the Moonta-Wallaroo Cu-Au Mining Field Region, Olympic Domain, South Australia. Hydrothermal Iron Oxide Copper-Gold and Related Deposits: A Global Perspective 3, 1–24.

Cook, N.J., Ciobanu, C.L., O'Reilly, D., Wilson, R., Das, K., Wade, B., 2013. Mineral chemistry of rare earth element (REE) mineralization, Browns Range, Western Australia. Lithos 172, 192–213.

Cook, N.J., Ciobanu, C.L., George, L. and Ehrig, K., 2016. Trace Element Analysis of Minerals in Magmatic-Hydrothermal Ores by Laser Ablation Inductively-Coupled Plasma Mass Spectrometry: Approaches and Opportunities. Minerals 6, 111.

Courtney-Davies, L., Zhu, Z., Ciobanu, C.L., Wade, B.P., Cook, N.J., Ehrig, K., Cabral, A.R. and Kennedy, A., 2016. Matrix-matched iron-oxide laser ablation ICP-MS U-Pb geochronology using mixed solutions standards. Minerals 6, 85.

Courtney-Davies, L., Ciobanu, C.L., Tapster, S., Condon, D., Kennedy, A., Cook, N., Ehrig, K., Wade, B. and Richardson, M., 2017. Steps to developing iron-oxide U-Pb geochronology for robust temporal insights into IOCG and BIF mineralisation. Applied Earth Sciences 126, 51–52.

Creaser, R.A., 1989. The geology and petrology of Middle Proterozoic felsic magmatism of the Stuart Shelf, South Australia. Unpublished Ph.D. thesis, La Trobe University, Melbourne.

Creaser, R.A. and White, A., 1991. Large volume, high temperature felsic volcanism from the Middle Proterozoic of South Australia. Geology 19, 48–51.

Cross, K.C., 1993. Acropolis and Wirrda Well, in: Drexel, J.F., Preiss, W.V., Parker, A.J., (Eds.), The geology of South Australia. Vol. 1, The Precambrian. Geological Survey of South Australia, South Australia, pp. 138.

Day, W.C., Slack, J.F., Auyso, R. and Seeger, C.M., 2016. Regional Geologic and Petrologic Framework for Iron Oxide ± Apatite ± Rare Earth Element and Iron Oxide Copper-Gold Deposits of the Mesoproterozoic St. Francois Mountains Terrane, Southeast Missouri, USA. Economic Geology 11, 1825–1858.

Daliran, F., Stosch, H.-G., Williams, P.J., Jamali, H. and Dorri, M.B., 2010. Early Cambrian iron oxide-apatite-REE (U) deposits of the Bafq district, east-central Iran. Geological Association of Canada short course notes 20, 147–159.

Demartin, F., Gramaccioli, C.M., Campostrini, I. and Pilati, T. 2010. Aiolosite, $Na_2(Na_2Bi)(SO_4)_3Cl$, a new sulfate isotypic to apatite from La Fossa Crater, Vulcano, Aeolian Islands, Italy. American Mineralogist 95, 382–385.

Dolivo-Dobrovolsky, V.V. 2006. About a common mistake in treating the crystal structure of apatite. Zapiski Vserossijskogo mineralogičeskogo obseŝtva 135, 123–125.

Downs, R.T. and Hall-Wallace, M., 2003. The American Mineralogist Crystal Structure Database. American Mineralogist 88, 247–250.

Ehrig, K., 2013. Geology of the Wirrda Well IOCG deposit. Powerpoint presentation, 10th Annual SA Exploration and Mining Conference, Adelaide. http://www.saexplorers.com.au

Ehrig, K., 2016. The Olympic Dam Fe-oxide Cu-U-Au-Ag deposit: 40 years since discovery. Powerpoint presentation, Australian Earth Sciences Convention 2016, Adelaide.

Ehrig, K., McPhie, J. and Kamanetsky, V.S., 2012. Geology and mineralogical zonation of the Olympic Dam iron oxide Cu-U-Au-Ag deposit, South Australia. In: Hedenquist, J.W., Harris, M., Camus, F. (Eds.), Geology and Genesis of Major Copper Deposits and Districts of the World, a Tribute to Richard Sillitoe. Society of Economic Geologists Special Publication 16, 237–268.

Ehrig, K., Kamenetsky, V.S., McPhie, J., Apukhtina, O., Ciobanu, C.L., Cook, N.J., Kontonikas-Charos, A. and Krneta, S. 2017. The IOCG-IOA Olympic Dam Cu-U-Au-Ag deposit and nearby prospects, South Australia. In: Mineral Resources to Discover, Proceedings 14th SGA Biennial Meeting, Quebec, Canada, August 2017, Volume 3, p. 823-826.

Fanning, C.M., Reid, A. and Teale, G., 2007. A geocronological framework for the Gawler Craton, South Australia. South Australian Geological Survey Bulletin 55, 258.

Fisher, L.A. and Kendrick, M.A., 2008. Metamorphic fluid origins in the Osborne Fe oxide Cu–Au deposit, Australia: Evidence from noble gases and halogens. Mineralium Deposita 43, 483–497.

Forbes, C., Giles, D., Freeman, H., Sawyer, M. and Normington, V., 2015. Glacial dispersion of hydrothermal monazite in the Prominent Hill deposit: An exploration tool. Journal of Geochemical Exploration 156, 10–33.

Fuchs, L.H. and Gebert, E, 1958. X-ray studies of synthetic coffinite, thorite and uranothorites. American Mineralogist 43, 243–248.

Gianfagna, A. and Mazziotti-Tagliani, S., 2014. As-rich apatite from Mt. Calvario: Characterization by micro-raman spectroscopy. The Canadian Mineralogist 52, 799–808.

Gleeson, S.A. and Smith, M.P., 2009. The sources and evolution of mineralising fluids in iron oxide–copper–gold systems, Norrbotten, Sweden: Constraints from Br/CI ratios and stable CI isotopes of fluid inclusion leachates. Geochimica et Cosmochimica Acta 73, 5658–5672.

Goldschmidt, V.M. 1937. The principles of distribution of chemical elements in minerals and rocks. The seventh Hugo Müller Lecture, delivered before the Chemical Society on March 17th, 1937. Journal of the Chemical Society (Resumed), 655–673.

Gottesmann, B. and Wirth, R., 1997. Pyrrhotite inclusions in dark pigmented apatite from granitic rocks. European Journal of Mineralogy 9, 491–500.

Groves, D.I., Bierlein, F.P., Meinert, L.D. and Hitzman, M.W., 2010. Iron Oxide Copper-Gold (IOCG) Deposits through Earth History: Implications for Origin, Lithospheric Setting, and Distinction from Other Epigenetic Iron Oxide Deposits. Economic Geology 105, 641–654.

Haas, J.R., Shock, E.L. and Sassani, D.C., 1995. Rare earth elements in hydrothermal systems: Estimates of standard partial molal thermodynamic properties of aqueous complexes of the rare earth elements at high pressures and temperatures. Geochimica at Cosmochimica Acta 59, 4329–4350.

Hahn, T., ed., 2005. International Tables for Crystallography, Volume A. Space Group Symmetry, 5th edition, Springer, Dordrecht, The Netherlands, 911 pp.

Harlov, D.E., 2015. Apatite: a fingerprint for metasomatic processes. Elements 11, 171–176.

Harlov, D.E., Andersson, U.B., Förster, H-J., Nyström, J.O., Dulski, P. and Broman, C., 2002a. Apatite–monazite relations in the Kiirunavaara magnetite–apatite ore, northern Sweden: Chemical Geology 191, 47–72.

Harlov, D.E., Förster, H-J., Nijland, T.G. 2002b. Fluid-induced nucleation of REE-phosphate minerals in apatite: Nature and experiment. Part I. Chlorapatite. American Mineralogist 87, 245–261.

Harlov, D.E., Forster, H.J.. 2004. Fluid-induced nucleation of (Y+REE)-phosphate minerals within apatite: nature and experiment. Part II. Fluorapatite. American Mineralogist 88,1209–1221.

Harlov, D.E., Wirth, R. and Forster, H.J.. 2005. An experimental study of dissolution-reprecipitation in fluorapatite: Fluid infiltration and the formation of monazite. Contributions to Mineral Petrology 150, 268–286.

Harlov, D.E., Wirth, R. and Hetherington, C.J., 2007. The relative stability of monazite and huttonite at 300–900 °C and 200–1000 MPa: metasomatism and the propagation of metastable mineral phases. American Mineralogist 92, 1652–1664.

Harrison, T.M. and Watson, E.B., 1984. The behaviour of apatite during crustal anatexis: equilibrium and kinetic considerations. Geochimica et Cosmochimica Acta 48, 1467–1477.

Hashmi, S., Ward, B.C., Plouffe, A., Leybourne, M.I. and Ferbey, T., 2015. Geochemical and mineralogical dispersal in till from the Mount Polley Cu-Au porphyry deposit, central British Columbia, Canada. Geochemistry: Exploration, Environment, Analysis 15, 234–249.

Haynes, D.W., Cross, K.C., Bills, R.T. and Reed, M.H., 1995. Olympic Dam ore genesis: A fluid-mixing model. Economic Geology 90, 281–307.

Hayward, N. and Skirrow, R.G., 2010. Geodynamic setting and controls on iron oxide Cu-Au (±U) ore in the Gawler Craton, South Australia. In: Porter, T.M (Ed.), Hydrothermal iron oxide copper-gold & related deposits: A global perspective, Volume 3, PGC Publishing, Adelaide,1–27.

Hitzman, M.W., Oreskes, N. and Einaudi, M.T., 1992. Geological characteristics and tectonic setting of Proterozoic iron oxide (Cu-U-Au-REE) deposits. Precambrian Research 58, 241–287.

Holden, P., Halliday, A.N. and Stephens, W.E., 1987. Neodymium and strontium isotope content of microdiorite enclaves points to mantle input to granitoid production. Nature 330, 53–56.

Hodgkin, T., 1996. High-grade gold occurrence at Olympic Dam Mine. Mesa Journal 1, 24.

Hovis, G.L. and Harlov, D.E., 2010. Solution calorimetric investigation of fluor-chlorapatite crystalline solutions. American Mineralogist 95, 946–952.

Hovis, G.L., McCubbin, F.M., Nekvasil, H., Ustunisik, G., Woerner, W.R. and Lindsley, D.H., 2014. A novel technique for fluorapatite synthesis and the thermodynamic mixing behaviour of F–OH apatite crystalline solutions. American Mineralogist 99, 890–897.

Huang, Q., Kamenetsky, V.S., McPhie, J., Ehrig, K., Meffre, S., Maas, R., Thompson, J., Kamenetsky, M., Chambefort, I., Apukhtina, O. and Hu, Y., 2015. Neoproterozoic (ca.

820-830 Ma) mafic dykes at Olympic Dam, South Australia: Links with the Gairdner Large Igneous Province. Precambrian Research 271, 160–172.

Huang, Q., Kamenetsky, V.S., Ehrig, K., McPhie, J., Kamenetsky, M., Cross, K., Meffre, S., Agangi, A., Chambefort, I., Direen, N.G., Maas, R. and Apukhtina, O., 2016. Olivine-phyric basalt in the Mesoproterozoic Gawler silicic large igneous province, South Australia: Examples at the Olympic Dam Iron Oxide Cu–U–Au–Ag deposit and other localities. Precambrian Research 281, 185–199.

Hughes, J.M., 2015. The many facets of apatite. American Mineralogist 100, 1033–1039.

Hughes, J.M. and Rakovan, J.F., 2002. The crystal structure of apatite, Ca5 (PO4) 3 (F,OH,Cl). Reviews in Mineralogy and Geochemistry 48, 1–12.

Hughes, J.M. and Rakovan, J.F., 2015. Structurally robust, chemically diverse: Apatite and apatite supergroup minerals. Elements 11, 165–170.

Hughes, J.M., Cameron, M. and Crowley, K.D. 1989. Structural variations in natural F, OH and Cl apatites. American Mineralogist 74, 870–876.

Hughes, J.M., Cameron, M. and Crowley, K.D., 1990. Crystal structures of natural ternary apatites: Solid solution in the $Ca_5(PO_4)_3X$ (X = F,OH,Cl) system. American Mineralogist 75, 295–304.

Hughes, J.M., Cameron, M., Crowley, K.D., 1991. Ordering of divalent cations in apatite structure: crystal 3 structure refinements of natural Mn- and Sr-bearing apatites. American Mineralogist 76, 1857–1862.

Hughes, J.M., Heffernan, K.M., Goldoff, B. and Nakvasil, H. 2014. Cl-rich fluorapatite, devoid of OH, from the three peaks area, Utah: The first reported structure of natural Cl-rich fluorapatite. The Canadian Mineralogist 52, 643–652.

Ismail, R., Ciobanu, C.L., Cook, N.J., Teale, G.S., Giles, D., Schmidt Mumm, A. and Wade, B., 2014. Rare earths and other trace elements in minerals from skarn assemblages,

Hillside iron oxide–copper–gold deposit, Yorke Peninsula, South Australia. Lithos 184–187, 456–477.

Jagodzinski, E.A., 2005. Compilation of SHRIMP U-Pb Geochronological Data. Olympic Domain, Gawler Craton, South Australia, 2001-2003. Geoscience Australia, Record 2005/20.

Jagodzinski, E.A., 2014. The age of magmatic and hydrothermal zircon at Olympic Dam, Australian Earth Sciences Convention Proceedings, Geological Society of Australia Abstracts 110, 260.

Johnson, J.P. and Cross, K.C., 1995. U-Pb geochronological constraints on the genesis of Olympic Dam Cu-U-Au-Ag deposit, South Australia. Economic Geology 88, 1046–1063.

Jonsson, E., Harlov, D.E., Majka, J., Högdahl, K., Persson-Nilsson, K., 2016. Fluorapatitemonazite-allanite relations in the Grängesberg apatite-iron oxide ore district, Bergslagen, Sweden. American Mineralogist 101, 1769–1782.

Janoušek, V., 2006. Saturnin, R language script for application of accessory-mineral saturation models in igneous geochemistry. Geologica Carpathica 57, 131–142.

Jungck, M.H.A. and Niederer, F.R., 2017. From supernova to Solar System: Few years only; first Solar System components apatite and spinel determined. Polar Science 11, 54–71.

Kampf, A.R. and Housley, R.M. 2011. Fluorphosphohedyphane, $Ca_2Pb_3(PO_4)_3F$, the first apatite supergroup mineral with essential Pb and F. American Mineralogist 96, 423–429.

Kelley, K.D., Eppinger, R.G., Lang, J., Smith, S.M. and Fey, D.L., 2011. Porphyry Cu indicator minerals in till as an exploration tool: example from the giant Pebble porphyry Cu-Au-Mo deposit, Alaska, USA. Geochemistry: Exploration, Environment, Analysis 11, 321–334.

Kelly, S.R., Rakovan, J. and Hughes, J.M., 2017. Column anion arrangements in chemically zoned ternary chlorapatite and fluorapatite from Kurokura, Japan. American Mineralogist 102, 720–727.

Kendrick, M.A., Honda, M., Gillen, D., Baker, T. and Phillips, D., 2008. New constraints on regional brecciation on the Wernecke Mountains, Canada, from He, Ne, Ar, Kr, Xe, Cl, Br and I. Chemical Geology 255, 33–46.

Kirchenbaur, M., Maas, R., Ehrig, K., Kamenetsky, V.S., Strub, E., Ballhaus, C. and Munker, C., 2016. Uranium and Sm isotope studies of the supergiant Olympic Dam Cu-Au-U-Ag deposit, South Australia. Geochimica et Cosmochimica Acta 180, 15–32.

Konecke, B.A., Fiege, A., Simon, A.C., Parat, F. and Stechern, A., 2017. Co-variability of S^{6+}, S^{4+}, and S^{2-} in apatite as a function of oxidation state: Implications for a new oxybarometer. American Mineralogist 102, 548–557.

Kontonikas-Charos, A., Ciobanu, C.L. and Cook, N.J., 2014. Albitization and redistribution of REE and Y in IOCG systems: Insights from Moonta-Wallaroo, Yorke Peninsula, South Australia. Lithos 208, 178–201.

Kontonikas-Charos, A., Ciobanu, C.L., Cook, N.J., Ehrig, K., Kamenetsky, V.S., 2015. Deuteric coarsening and albitization in Hiltaba granites from the Olympic Dam IOCG deposit, South Australia. Proceedings, Mineral Resources in a Sustainable World, 13th Biennial SGA Meeting, Nancy, France, August 2015 Vol. 3, pp. 1099–1102.

Kontonikas-Charos, A., Ciobanu, C.L., Cook, N.J., Ehrig, K., Krneta, S. and Kamenetsky, V.S. 2017a Feldspar evolution in the Roxby Downs Granite, host to Fe-oxide Cu-Au-(U) mineralisation at Olympic Dam, South Australia. Ore Geology Reviews. 80, 838–859.

Kontonikas-Charos, A., Ciobanu, C.L., Cook, N.J., Ehrig, K., Ismail, R., Krneta, S. and Basak, A., 2017b. Feldspar mineralogy and rare earth element (re)mobilization in iron-oxide copper gold systems from South Australia: a nanoscale study. Mineralogical

Magazine (in press). DOI: 10.1180/minmag.2017.081.040

Kontonikas-Charos, A., Ciobanu, C.L., Cook, N.J., Ehrig, K., Krneta, S. and Kamenetsky, V.S., 2017c. Rare earth element geochemistry of feldspars: Examples from Fe-oxide Cu-Au systems in the Olympic Cu-Au Province, South Australia. Mineralogy and Petrology (in revision).

Krause, J., Harlov, D.E., Pushkarev, E.V. and Brugmann, E.G., 2013. Apatite and clinopyroxene as tracers for metasomatic processes in nepheline clinopyroxenites of Uralian-Alaskan-type complexes in the Ural Mountains, Russian Federation. Geochimica et Cosmochimica Acta 121, 503–521.

Krneta, S., Ciobanu, C.L., Cook, N.J., Ehrig, K., Kamenetsky, V.S., 2015. Apatite in the Olympic Dam Cu–U–Au–Ag deposit. Proceedings, Mineral Resources in a Sustainable World, 13th Biennial SGA Meeting, Nancy, France, August 2015 Vol. 3, pp. 1103-1106.

Krneta, S., Ciobanu, C.L., Cook, N.J., Ehrig, K. and Kontonikas-Charos, A., 2016. Apatite at Olympic Dam, South Australia: a petrogenetic tool. Lithos, 262, 470–485.

Krneta, S., Ciobanu, C.L., Cook, N.J., Ehrig, K. and Kontonikas-Charos, A., 2017a. The Wirrda Well and Acropolis prospects Gawler Craton, South Australia: insights into evolving fluid conditions through apatite chemistry. Journal of Geochemical Exploration 181, 276–291.

Krneta, S., Ciobanu, C.L., Cook, N.J., Ehrig, K. and Kontonikas-Charos, A. 2017b. Rare earth element behaviour in apatite from the Olympic Dam Cu-U-Au-Ag deposit, South Australia. Minerals 7(8), 135.

Ladenburger, S., Marks, M.A.W., Upton, B., Hill, P., Wenzel, T., and Markl, G., 2016. Compositional variation of apatite from rift-related alkaline igneous rocks of the Gardar Province, South Greenland. American Mineralogist, 101, 612–626.

Li, H., and Hermann, J., 2017. Chlorine and fluorine partitioning between apatite and sediment melt at 2.5 GPa, 800 ^{o}C: A new experimentally derived thermodynamic model. American Mineralogist 102, 580–594.

Liu, W., Mei, Y., Etschmann, B., Brugger, J., Pearce, M., Ryan, C.G., Borg, S., Wykes, J., Kappen, P., Paterson, D., Boesenberg, U., Garrevoet, J., Moorhead, G. and Falkenberg, G., 2017. Arsenic in hydrothermal apatite: Oxidation state, mechanism of uptake, and comparison between experiments and nature. Geochimica et Cosmochimica Acta 196, 144–159.

Lottermoser, B.G., 1992. Rare earth elements and hydrothermal ore formation processes. Ore Geology Reviews 7, 25–41.

Luo, Y., Hughes, J.M., Rakovan, J. and Pan, Y.M. 2009. Site preference of U and Th in Cl, F, and Sr apatites. American Mineralogist 94, 345–351.

Luo, Y., Rakovan, J., Tang, Y., Lupulescu, M., Hughes, J.M. and Pan, Y., 2011. Crystal chemistry of Th in fluorapatite. American Mineralogist 96, 23–33.

Macmillan, E., Cook, N.J., Ehrig, K., Ciobanu, C.L. and Pring, A., 2016. Uraninite from the Olympic Dam IOCG-U-Ag deposit: Linking textural and compositional variation to temporal evolution. American Mineralogist 101, 1295–1320.

Macmillan, E., Cook, N.J., Ehrig, K. and Pring, A., 2017. Chemical and textural interpretation of late stage coffinite and brannerite from the Olympic Dam IOCG-Ag-U deposit. Mineralogical Magazine (*in-press*) https://doi.org/10.1180/minmag.2017.081.006

Majka, J., Harlov, D.E., Jonsson, E., Högdahl, K. and Persson-Nilsson, K., 2016. Fluorapatite-monazite-allanite relations in the Grängesberg apatite-iron oxide ore district, Bergslagen, Sweden. American Mineralogist 101, 1769–1783.

Mao, M., Rukhlov, A.S., Rowins, S.M., Spence, J. and Coogan, L.A., 2016. Apatite trace element compositions: A robust new tool for mineral exploration. Economic Geology 111, 1187–1222.

Marks, M.A.W., Thomas, W., Whitehouse, M.J., Loose, M., Zack, T., Barth, M., Worgard, L., Krasz, V., Eby, G.N., Stosnach, H. and Markl, G., 2012. The volatile inventory (F, Cl, Br, S, C) of magmatic apatite: An integrated analytical approach. Chemical Geology 291, 241–255.

Marks, A.W., Scharrer, M., Landenburger, S. and Markl, G., 2014. Comment on "Apatite: A new redox proxy for silicic magmas?". Geochimica et Cosmochimica Acta 183, 267–270.

Mauger, A.J., Ehrig, K., Kontonikas-Charos, A., Ciobanu, C.L., Cook, N.J. and Kamenetsky, V.S., 2016. Alteration at the Olympic Dam IOCG-U deposit: Insights into distal to proximal feldspar and phyllosilicate chemistry from infrared reflectance spectroscopy. Australian Journal of Earth Sciences 63, 959–972.

McCubbin, F.M., Jones, R.H., 2015. Extraterrestrial apatite: planetary geochemistry to astrobiology. Elements 11, 183–188.

McDonough, W.F. and Sun, S.-S., 1995. Composition of the Earth. Chemical Geology 120, 223–253.

McPhie, J., Kamenetsky, V., Chambefort, I., Ehrig, K. and Green, N., 2011. Origin of the supergiant Olympic Dam Cu-U-Au-Ag deposit, South Australia: Was a sedimentary basin involved? Geology 39, 795–798.

McPhie, J., Orth, K., Kamenetsky, V., Kamenetsky, M. and Ehrig, K., 2016. Characteristics, origin and significance of Mesoproterozoic bedded clastic facies at the Olympic Dam Cu-U-Au-Ag deposit, South Australia. Precambrian Research 276, 85–100.

Mercier, P.H.J., Le Page, Y., Whitfield, P.S., Mitchell, L.D., Davidson, I.J. and White, T.J., 2005. Geometrical parameterization of the crystal chemistry of P63/m apatites: comparison with experimental data and *ab initio* results. Acta Crystallographica B61, 635–655.

Migdisov, A.A. and Williams-Jones, A.E., 2006a. A spectrophotometric study of erbium (III) speciation in chloride solutions at elevated temperatures. Chemical Geology 234, 17–27.

Migdisov, A.A. and Williams-Jones, A.E., 2006b. An experimental study of the solubility and speciation of neodymium (III) fluoride in F-bearing aqueous solutions. Geochimica et Cosmochimica Acta 71, 3056–3069.

Migdisov, A.A. and Williams-Jones, A.E., 2008. A spectrophotometric study of Nd(III), Sm(III) and Er(III) complexation in sulfate-bearing solutions at elevated temperatures. Geochimica et Cosmochimica Acta 72, 5291–5303.

Migdisov, A.A. and Williams-Jones, A.E., 2014. Hydrothermal transport and deposition of the rare earth elements by fluorine-bearing aqueous liquids. Mineralium Deposita 49, 987–997.

Migdisov, A.A., Reukov, V.V. and Williams-Jones, A.E., 2006. A spectrophotometric study of neodymium(III) complexation in sulfate solutions at elevated temperatures. Geochimica et Cosmochimica Acta 70, 983–992.

Migdisov, A.A., Williams-Jones, A.E., Normand, C. and Wood, S.A., 2008. A spectrophotometric study of samarium (III) speciation in chloride solutions at elevated temperatures. Geochimica et Cosmochimica Acta 72, 1611–1625.

Migdisov, A.A., Williams-Jones, A.E. and Wagner, T., 2009. An experimental study of the solubility and speciation of the Rare Earth Elements (III) in fluoride- and chloride-bearing aqueous solutions at temperatures up to 300 ^{o}C. Geochimica et Cosmochimica Acta 73, 7087–7109.

Migdisov, A.A., Williams-Jones, A.E., Brugger, J., and Caporuscio, F.A., 2016. Hydrothermal transport, deposition, and fractionation of the REE: Experimental data and thermodynamic calculations. Chemical Geology 439, 13–42.

Miles, A.J., Graham, C.M., Hawkesworth, C.J., Gillespie, M.R., Hinton, R.W., Bromiley, G.D. and EMMAC, 2014. Apatite: A new redox proxy for silicic magmas?". Geochimica et Cosmochimica Acta 132, 101–119.

Morales Ruano, S. Both, R.A. and Golding, S.D., 2002. A fluid inclusion and stable isotope study of the Moonta copper-gold deposits, South Australia: evidence for fluid immiscibility in a magmatic hydrothermal system. Chemical Geology 192, 211–226.

Ni, Y., Hughes. J.M. and Mariano, A.N., 1995. Crystal chemistry of monazite and xenotime structures Ce(PO_4). American Mineralogist 80, 21–26.

Oelkers, E.H. and Montel, J-M., 2008. Phosphates and nuclear waste storage. Elements 4, 113–116.

Oreskes, M. and Einaudi M.T., 1990. Origin of rare earth element-enriched heamatite breccias at the Olympic Dam Cu-U-Au-Ag deposit, Roxby Downs, South Australia. Economic Geology 85, 1–28.

Oreskes, M. and Einaudi M.T., 1992. Origin of Hydrothermal Fluids at Olympic Dam: Preliminary Results from Fluid Inclusions and Stable Isotopes. Economic Geology 87, 64–90.

Pan, Y. and Fleet, M.E., 2002. Compositions of the apatite-group minerals: Substitution mechanisms and controlling factors. Reviews in Mineralogy and Geochemistry 48, 13–49.

Parker, A.J., 1990. Gawler Craton and Stuart Shelf- regional geology and mineralisation. In: Hughes, F.C. (Ed.) Geology of the Mineral Deposits of Australia and Papua New Guinea, Australasian Institute of Mining and Metallurgy. Monograph Series 14, p. 999–1008.

Pasero, M., Kampf, A., Ferraris, C., Pekov, I.V., Rakovan, J. and White, T., 2010.

Nomenclature of the apatite supergroup minerals. European Journal of Mineralogy 22, 163–179.

Paterson, A.J., 1986. The Acropolis Prospect. In: A.J Parker, C.M. Horn, B.P.J Stevens, H.L Paterson (eds.), Geological Excursions of the Adelaide Geosyncline, Gawler Craton and Broken Hill Regions. Geological Society of Australia (S.A. Division), p. 17–27.

Peng, G., Luhr, J.F. and McGee, J.J., 1997. Factors controlling sulfur concentrations in volcanic apatite. American Mineralogist 82, 1210–1224.

Perseil, E-A., Blanc, P. and Ohnenstetter, D., 2000. As-bearing fluorapatite in manganiferous deposits from St. Marcel-Praborna, Val D'aosta, Italy. Canadian Mineralogist 38, 101–117.

Piccoli, P.M. and Candela, P.A., 1994. Apatite in felsic rocks: a model for the estimation on initial halogen concentrations in the Bishop Tuff (Long Valley) and Tuolumne Intrusive Suite (Sierra Nevada Batholith) magmas. American Journal of Science 294, 92–135.

Piccoli, P.M. and Candela, P.A., 2002. Apatite in Igneous Systems. Reviews in Mineralogy and Geochemistry 48, 255–292.

Pollard, P.J., 2006. An intrusion-related origin for Cu–Au mineralization in iron oxide–copper–gold (IOCG) provinces. Mineralium Deposita 41, 187.

Porter, T.M., 2010. Current understanding of iron oxide associated-alkali altered mineralised systems. Part 1. An overview, in Porter, T.M., ed., Hydrothermal iron oxide copper-gold & related deposits: A global perspective: Adelaide, Australia, PGC Publishing, v. 3, p. 5–32.

Preiss, W.V., 1993. Neoproterozoic. In: Drexel J.F., Preiss W.V., Parker A.J. (eds.), The Geology of South Australia, Volume 1, The Precambrian. Geological Survey of South Australia Bulletin 54, 170–203.

Putnis, A., 2002. Mineral replacement reactions: from macroscopic observations to microscopic mechanisms. Mineralogical Magazine 66, 689–708.

Rakovan, J., Newville, M. and Sutton, S., 2001. Evidence for heterovalent europium in zoned

Llallagua apatite using wavelength dispersive XANES. American Mineralogist 86, 697–700.

Reeve, J.S, 1990. The discovery and evaluation of gold mineralization within the Olympic Dam deposit, South Australia, in Glasson, K.R., Rattigan, J.H. (eds.), Geological aspects of the discovery of some important mineral deposits in Australia: Australasian Institute of Mining and Metallurgy, Monograph 17, p. 57–58.

Reeve, J.S., Cross, K.C., Smith, R.N. and Oreskes, N., 1990. Olympic Dam copper-uranium-gold-silver deposit. In: Hughes, F.E. (ed.), Geology of the Mineral Deposits of Australia and Papua New Guinea: Australasian Institute of Mining and Metallurgy, Monograph 14, p. 1009–1035.

Reid, J.B., Jr., Evans, O.,C. and Fates, D.G., 1983. Magma mixing in granitic rocks of the central Sierra Nevada, California. Earth Planetary Science Letters 66, 243–261.

Reid, A.J., Hand, M., Jagodzinski, E., Kelsey, D. and Pearson, N., 2008. Paleoproterozoic orogenesis in the southeastern Gawler Craton, South Australia. Australian Journal of Earth Sciences 55, 449–471.

Reid, A.J., Swain, G.S., Mason, D. and Maas, R., 2011. Nature and timing of Cu-Au-Zn-Pb mineralisation at Punt Hill, eastern Gawler Craton. MESA Journal 60, 7–17.

Roberts, D.E. and Hudson, G.R.T., 1983. The Olympic Dam copper-uranium-gold deposit, Roxby Downs, South Australia. Economic Geology 78, 799–822.

Rønsbo, J.G., 1989. Coupled substitutions involving REE's and Na and Si in apatites in alkaline rocks from Ilimaussaq, South Greenland, and the petrological implications. American Mineralogist 74, 896–901.

Rusk, B., Oliver, N., Cleverley, J., Blenkinsop, T., Zhang, D., Williams, P. and Habermann, P., 2010. Physical and chemical characteristics of the Ernest Henry iron oxide copper gold deposit, Australia; implications for IOGC genesis. Hydrothermal Iron Oxide Copper-Gold

& Related Deposits: A Global Perspective - Advances in the Understanding of IOCG Deposits. Global Perspective Series, 3 (ed. T. M. Porter). PGC Publishing, Linden Park, SA, Australia. pp. 201–218.

Schlegel, T.U., 2015. The Prominent Hill iron oxide-Cu-Au deposit in South Australia. A deposit formation model based on geology, geochemistry and stable isotopes and fluid inclusions. Unpublished PhD thesis, ETH Zurich, Switzerland.

Schlegel, T.U. and Heinrich, C.A., 2015. Lithology and hydrothermal alteration control the distribution of copper grade in the Prominent Hill Iron Oxide-Copper-Gold deposit (Gawler Craton, South Australia). Economic Geology 110, 1953–1994.

Schlegel, T.U., Wagner, T., Boyce, A., Heinrich, C.A., 2016. A magmatic source of hydrothermal sulfur for the Prominent Hill deposit and associated prospects in the Olympic iron oxide copper-gold (IOCG) province of South Australia, Ore Geology Reviews (*in press*) doi: 10.1016/j.oregeorev.2016.09.002

Schmandt, D.S., Cook, N.J., Ehrig, K., Ciobanu, C.L., Wade, B.P. and Gilbert, S., 2017. Rare earth element fluorocarbonate minerals from the Olympic Dam Cu-U-Au-Ag deposit, South Australia. Minerals (in review).

Sha, L-K., 1995. Genesis of zoned hydrous ultramafic/mafic-silicic intrusive complexes: an MHFC hypothesis. Earth Science Reviews 39, 59–90.

Sharp, Z.D., Barnes, J.D., Fischer, T.P. and Halick, M., 2010. A laboratory determination of chlorine isotope fractionation in acid systems and applications to volcanic fumaroles. Geochimica et Cosmochimica Acta 74, 264–273.

Skirrow, R.G., Bastrakov, E.N., Davidson, G., Raymond, O.L. and Heithersay, P., 2002. The geological framework, distribution and controls of Fe-oxide Cu-Au mineralisation in the Gawler Craton, South Australia. Part II- Alteration and mineralisation. In: Porter, T.M

(Ed.), Hydrothermal Iron Oxide Copper-Gold & Related Deposits: A Global Perspective, Volume 2, PGC Publishing, Adelaide, 33–47.

Skirrow, R.G., Bastrakov, E.N., Barovich, K., Fraser, G.L., Creaser, R., Fanning, M.C., Raymond, O.L. and Davidson, G.J., 2007. Timing of iron oxide Cu-Au-(U) hydrothermal activity and Nd isotope constraints on metal sources in the Gawler craton, South Australia. Economic Geology 102, 1441–1470.

Smith, M. and Henderson, P., 2000. Preliminary fluid inclusions constraints on fluid evolution in the Bayan Obo Fe-REE-Nb deposit, Inner Mongolia, China. Economic Geology 95, 1371.

Smith, M., Henderson, P., Jeffries, T., Long, J. and Williams, C., 2004. The rare earth elements and uranium in garnets from the Beinn an Dubhaich Aureole, Skye, Scotland, UK: constraints on processes in a dynamic hydrothermal system. Journal of Petrology 45, 457–484.

Storey, C.D. and Smith, M.P., 2017. Metal source and tectonic setting of iron oxide-copper-gold (IOCG) deposits: Evidence from an in situ Nd isotope study of titanite from Norrbotten, Sweden. Ore Geology Reviews 81, 1287–1302.

Streck, M.J. and Dilles, J.H., 1998. Sulfur evolution of oxidized magmas as recorded in apatite from a porphyry copper batholith. Geology 26, 523–526.

Takahashi, Y., Kolonin, G.R., Shironosova, G.P., Kupriyanova, I.I., Uruga, T. and Shimizu, H., 2005. Determination of the Eu(II)/Eu(III) ratios in minerals by X-ray absorption near-edge structure (XANES) and its application to hydrothermal deposits. Mineralogical Magazine 69, 179–190.

Takashima, R., Kuwabara, S., Sato, T., Takemura, K. and Nishi, H., 2017. Utility of trace elements in apatite for discrimination and correlation of Quaternary ignimbrites and co-ignimbrite ashes, Japan. Quaternary Geochronology 41, 151-162.

Taylor, M. and Ewing, R.C., 1978. The crystal structure of the $ThSiO_4$ polymorphs: huttonite and thorite. Acta Crystallographica, Section B 34, 1074–1079.

Teiber, H., Marks, M.A.W., Arzamastsev, A.A., Wenzel, T. and Markl, G., 2015. Compositional variation in apatite from various host rocks: clues with regards to source composition and crystallization conditions. Journal of Mineral Geochemistry 192, 151–167.

Ustunisik, G., Nekvasil, H. and Lindsley, D., 2011. Differential degassing of H_2O, Cl, F and S: Potential effects on lunar apatite. American Mineralogist 96, 1650–1653.

van Dongen, M., Weinberg, R.F. and Tomkins, A.G., 2010. REE-Y, Ti, and P Remobilization in Magmatic Rocks by Hydrothermal Alteration during Cu-Au Deposit Formation. Economic Geology 105, 763–776.

van Hinsberg, V.J., Migdisov, A.A and Williams-Jones, A.E. 2010. Reading the mineral record of fluid composition from element partitioning. Geology 38, 847–850.

Vella, L., 1997. Interpretation and modelling, based on petrophysical measurements, of the Wirrda Well potential field anomaly, South Australia. Exploration Geophysics 28, 299–306.

Vella, L. and Cawood, M., 2006. Carrapateena: discovery of an Olympic Dam – style deposit. Preview, Issue 122 (June 2006), CSIRO Publishing, 26–30.

Verdugo-Ihl, M.R., Ciobanu, C.L., Cook, N.J., Courtney-Davies, L., Ehrig, K. and Gilbert, S., 2017. Trace element signatures in U-W-Sn-Mo zoned hematite from the IOCG deposit at Olympic Dam, South Australia. In: Mineral Resources to Discover, Proceedings 14th SGA Biennial Meeting, Quebec, Canada, August 2017, Volume 3, p. 967-970.

Villiers, J.P.R. and Liles, D.C., 2010. The crystal-structure and vacancy distribution in 6*C* pyrrhotite. American Mineralogist 95, 148–152.

Wang, Y., Wang, Y. and Merino, E., 1995. Dynamic weathering model: Constraints required by coupled dissolution and pseudomorphic replacement. Geochimica et Cosmochimica Acta 59, 1559–1570.

Webster, J.D. and Piccoli, P.M., 2015. Magmatic apatite: a powerful, yet deceptive mineral. Elements 11, 177–182.

Webster, J.D., Tappen, D. and Mandeville, C.W., 2009. Partitioning behaviour of chlorine and fluorine in the system apatite-melt-fluid: II. Felsic silicate systems at 200 MPa. Geochimica et Cosmochimica Acta 73, 559–581.

Weng, Z., Jowitt, S.M., Mudd, G.M. and Haque, N., 2015. A detailed assessment of global Rare Earth Element resources: opportunities and challenges. Economic Geology 110, 1925–1952.

White, T.J. and Dong, Z.L., 2002. Structural derivation and crystal chemistry of apatites. Acta Crystallographica B59, 1–16.

Williams, P.J., Barton, M.D., Johnson, D.A., Fontboté, L., De Haller, A., Mark, G., Oliver, N.H. and Marschik, R., 2005. Iron oxide copper-gold deposits: Geology, space-time distribution, and possible modes of origin. Economic Geology, 371–405.

Williams, P.J., Kendrick, M.A. and Xavier, R.P., 2010. Sources of ore fluid components in IOCG deposits. In: Porter TM (ed.) Hydrothermal Iron Oxide Copper–Gold and Related Deposits: A Global Perspective, pp. 107–116. Adelaide: PGC Publishing.

Williams-Jones, A.E., Samson, I.M. and Olivo, G.R., 2000. The genesis of hydrothermal fluorite-REE deposits in the Gallinas Mountains, New Mexico. Economic Geology 95, 327–341.

Wolf, M.B., London, D., 1995. Incongruent dissolution of REE- and Sr-rich apatite in peraluminous granitic liquids: differential apatite, monazite, and xenotime solubilities during anatexis. American Mineralogist 80, 765–775.

Wyckoff, R.W.G., 1963. Crystal Structures, 2nd edition, Wiley, New York.

Wyllie, P.J., Cox, K.G. and Biggar, G.M., 1962. The habit of apatite in synthetic systems and igneous rocks. Journal of Petrology 3, 238–242.

Xing, C.M. and Wang, C.Y., 2017. Cathodoluminescence images and trace element compositions of fluorapatite from the Hongge layered intrusion in SW China: A record of prolonged crystallization and overprinted fluid metasomatism. American Mineralogist 102, 1390–1401.

Yi, H., Balan, E., Gervais, C., Segalen, L., Fayon, F., Roche, D., Person, A., Morin, G., Guillaumet, M., Blanchard, M., Lazzeri, M. and Babonneau, F., 2013. A carbonate-fluoride defect model for carbonate-rich fluorapatite. American Mineralogist 98, 1066–1069.

Zhong, J., Chen, Y-J., Qi, J-P., Chen, J., Dai, M-C. and Li, J., 2017. Geology, fluid inclusion and stable isotope study of the Yueyang Ag-Au-Cu deposit, Zijinshan orefield, Fujian Province, China. Ore Geology Reviews 86, 254–270.

Zhu, C. and Sverjensky, D.A., 1991. Partitioning of F–Cl–OH between minerals and hydrothermal fluids. Geochimica et Cosmochimica Acta 55, 1837–1858.